This document does not contain any export controlled data

THE SCIENCE OF EMISSIONS FROM ALTERNATIVE FUELS

WP-2145

FINAL REPORT

March 2017

Dr. W.M. Roquemore
(Principal Investigator)
Air Force Research Laboratory

Prof. T.A. Litzinger
(Co-Principal Investigator)
The Pennsylvania State University

Approved for Public Release
Distribution Unlimited

PERFORMING ORGANIZATIONS AND RESEARCHERS

Air Force Research Laboratory
Well-stirred Reactor, T-63, Referee Combustor
W. M. Roquemore (Principal Investigator)
A. Lynch
J. Miller
D. Blunck
E. Corporan
T. Edwards
J. Gord

Pennsylvania State University
Jet Flames, Model combustor
T. A. Litzinger (Co-Principal Investigator)
R. J. Santoro
J. O'Connor
S. Iyer
A. Makwana
Y. Wang
A. G. Mouis
V. Iyer
M. Linevsky

University of Dayton Research Institute
Shock Tube, Well-stirred Reactor, Referee Combustor
S. S. Sidhu
M. S. Kahandawala
J. S. Heyne
S. D. Stouffer
G. Flora
R. D. Stachler
A. Lagounov
J. P. Cain
M. J. De Witt
R. Striebich
D. Annekan
C. Klingshirn
M. Arstingstall
D. Brigalli
J. Mantz

United Technologies Research Center
Kinetics, Modeling
M. B. Colket
S. Zeppieri

Innovative Scientific Solutions, Inc. (ISSI)
Modeling
V. R. Katta

Aerodyne Research, Inc.
Aircraft Engine Emissions
R. C. Miake-Lye

Spectral Energies
Laser Diagnostics
S. Roy

TABLE OF CONTENTS

LIST OF FIGURES ..... **vi**

LIST OF TABLES ..... **xxiii**

LIST OF ACRONYMS ..... **xxv**

1 EXECUTIVE SUMMARY **1**

1.1 Background *1*

1.2 Objectives and Approach *1*

1.3 Summary of Major Results from Research *2*

1.3.1 Alternate Fuel Effects on Emissions in T-63 Engine Studies 2

1.3.2 Alternative Fuel Effects on Emissions in Referee Combustor (Low Power) 3

1.3.3 Fundamental Mechanism Producing UHC Emissions at Low Power 4

1.3.4 Effects of Alternative Fuels at High Power 5

1.4 Summary of Major Conclusions and Contributions of this Project *6*

1.5 Science-based Methodology for Evaluating Alternative Fuels *9*

1.6 Contents of Final Report *10*

2 INTRODUCTION **11**

2.1 Motivation for Program *11*

2.2 Program Objectives *11*

2.3 Background *12*

2.3.1 Linear Behavior of UHC Emissions at Low Power 12

2.3.2 Unburned Fuel contribution to UHC Emissions 13

2.3.3 Emissions Trends at High Power 14

2.4 Overall Research Approach *16*

3 EXPERIMENTAL FACILTIES AND METHODS **18**

3.1 Shock Tube Studies *18*

3.1.1 Shock Tube Facilities 18

3.1.2 Experimental Methods 20

3.2 Well-stirred Reactor Studies *29*

3.2.1 Fuel-rich Studies 29

3.2.2 Fuel-lean Studies 31

3.3 Laminar Co-flow Flame Studies *34*

3.3.1 Laminar Co-flow Flame Burner 34

3.3.2 Experimental Methods 37

3.3.3 Experimental Conditions 39

3.4 Model Combustor *40*

3.4.1 Model Combustor Test Facility 40

3.4.2 Experimental Methods 43

3.4.3 Experimental Conditions 44

3.5 Referee Combustor Studies 45
3.5.1 Referee Combustor Facilities 45
3.5.2 Experimental Methods 46
3.5.3 Experimental Conditions 48

3.6 T-63 Engine Studies 49
3.6.1 T-63 Engine Facilities 49
3.6.2 Experimental Methods 50

3.7 Test Fuel Matrix 52

4 MODELING AN D SIMULATION METHODS 54

4.1 Chemical Mechanisms 54

4.2 UNICORN 58

4.3 CHEMKIN 60

4.4 SHOCKIN 62

5 FUNDAMENTAL PROCESSES LEADING TO ENGINE EMISSIONS 63

5.1 Introduction 63

5.2 Reaction Models for the Formation of Polycyclic Aromatic Hydrocarbons 63

5.3 Model Predictions of Linear Scaling of UHC Emissions at Low Power 66
5.3.1 Exploratory Investigations 66
5.3.2 Quench Requirements to Freeze Hydrocarbon Emissions 69
5.3.3 NETPSR Reactor Analysis 69
5.3.4 Quantitative Comparisons 73
5.3.5 Predictions for Different Surrogate Fuels 74
5.3.6 Impact of Engine Cycle on Emissions Trends 75

5.4 Computational Study of Formation of UHC Emissions in Opposed-jet Flames 76

5.5 Primary Flame Zone Structure - the role of preferential diffusion 83

5.6 Flame-Turbulence Interaction 97

5.7 Flame Propagation through Stratified Mixtures 104

5.8 Simulation of Emissions from Low-Temperature Combustion in Opposed-Jet Flames 110

6 SHOCK TUBE STUDIES 120

6.1 Ignition Delay Times 120
6.1.1 Experimental Results 120
6.1.2 Chemical kinetic analysis 125

6.2 Emissions 137
6.2.1 Experimental Results 137
6.2.2 Chemical kinetic analysis 158
6.2.3 Effect of Dwell (Reaction) Time 166

7 WELL-STIRRED REACTOR STUDIES 175

7.1 Fuel-rich Studies *175*
7.1.1 m-xylene/n-dodecane, JP-8 and Sasol Fuels 175
7.1.2 Heptane/Dodecane Experiments 179
7.1.3 Methylcyclohexane/n-Dodecane Experiments 181
7.1.4 Discussion of Results for Fuel-rich Mixtures 181

7.2 Lean Blowout Experiments *182*
7.2.1 Discussion of Reactor Temperature and LBO Results 183
7.2.2 Discussion of Major and Minor Emissions 185
7.2.3 Discussion of HAPs During LBO Testing 190

7.3 Modeling of Lean Well-Stirred Reactor Experiments *197*
7.3.1 Kinetic Mechanisms and Surrogate Formulations 200
7.3.2 JP-8 Results from WSR and Analysis 202
7.3.3 Predictions of HAPs from JP-8 204
7.3.4 Simulation of Emissions for LBO Experiments for Binary Fuel Blends 207

7.4 UNICORN Modeling Results for m-xylene/dodecane *218*

8 LAMINAR CO-FLOW FLAME STUDIES 224

8.1 Fuel Composition Effects in Non-premixed Co-flow Flames *224*
8.1.1 Visible Light Images and Flame Heights 224
8.1.2 Spatial Distribution of Aromatic Species and Soot 225

8.2 Fuel Composition Effects in Partially-premixed Co-flow Flames *233*
8.2.1 Visible Light Images and Flame Heights 233
8.2.2 Spatial Distribution of Aromatic Species and Soot 234

8.3 Simulation of Fuel Effects in Co-flow Flames *238*
8.3.1 Initial Studies using 2-Equation Soot Model 238
8.3.2 Improved Soot Model in UNICORN Code 243
8.3.3 Simulation of Fuel Effects using the Improved Soot Model in UNICORN 247

8.4 Comparisons of Test Fuels and Actual Fuels *257*

9 MODEL COMBUSTOR STUDIES 260

9.1 Experimental Results *260*

9.2 Simulation of Soot in Model Combustor *263*

10 REFEREE COMBUSTOR STUDIES 270

10.1 Gas-phase Emissions *273*

10.2 PM Emissions *281*

10.3 Summary of findings *283*

11 T63 ENGINE STUDIES 284

11.1 Effects on Engine Performance *284*

11.2 Speciation of Minor Combustion Products *285*

11.3 Physical Properties of Soot Emissions *288*

11.4 Chemical Properties of Soot Emissions 290
11.4.1 Chemical Properties with n-Heptane/n-Dodecane Fuel 291
11.4.2 Chemical Properties with iso-Octane/n-Dodecane Fuel 292
11.4.3 Chemical Properties with m-Xylene/n-Dodecane Fuel 293
11.4.4 Chemical Properties with Methylcyclohexane/n-Dodecane Fuel 294
11.4.5 Discussion of Chemical Properties of Soot 295
11.5 Unburned Fuel Emissions 298

12 CONCLUSIONS AND RECOMMENDATION 302

ACKNOWLEDGEMENTS 303

REFERENCES 304

Appendix A: Results from Initial Lean Blowout Experiments 313

Appendix B Composition of Actual Fuels included in Final Report 315

PUBLICATIONS 316

LIST OF FIGURES

Figure 1.1. National Jet Fuel Combustion Program Organization Chart……....……09

Figure 2-1. UHC emission data for a broad range of engines at Oakland airport. (Herndon et.al., 2009) 12

Figure 2-2. Variable Benzene to Formaldehyde ratios for JP-8 and two FT fuels (Miake-Lye, 2010) 12

Figure 2-3. General reaction scheme for high temperature hydrocarbon oxidation for fuel-lean and fuel-rich conditions. 13

Figure 2-4. Variation of Emission Index of CO with engine power for JP-8, two FT fuels and two JP-8/FT blends. (Bulzan et.al., 2010).....15

Figure 2-5. Variation of Emission Index of UHC with engine power for JP-8, two FT fuels and two JP-8/FT blends. (Bulzan et.al., 2010).....15

Figure 2-6. Variation of Emission Index of black carbon portion of PM with engine power for JP-8, two FT fuels and two JP-8/FT blends. (Bulzan et.al., 2010).....16

Figure 3-1. Schematic of the heated shock tube. 19

Figure 3-2. Schematic of the sample preparation unit (SPU). 19

Figure 3-3. Example of time interval measurements of the incident shock wave passage and total experimental observation time (dwell time).....21

Figure 3-4. Example of linear regression analysis used to calculate the incident shock velocity at the end wall of the test section. 22

Figure 3-5. Ignition delay time measurement. 23

Figure 3-6. Schematic of the product sampling unit (PSU). 24

Figure 3-7. Cross-section of the WSR (Stouffer, et. al., 2005, Stouffer, et. al., 2007). 29

Figure 3-8. Illustration of experimental arrangement for collecting fuel-rich combustion products from well-stirred reactor 30

Figure 3-9. A transverse cross-section of the toroidal WSR is shown with dimensions listed in mm. Reactor volume is 250 mL. Reactor components (red) are fused silica and the jet ring (blue) is Inconel.....31

Figure 3-10. Experimental Schematic for WSR Emission Studies. A heated line takes the sample from the reaction region in the WSR to the FTIR. Charcoal tube and bag samples are taken after the FTIR before being exhausted.....34

Figure 3-11. Cross-section of burner used in jet flame studies.....36

Figure 3-12. Original vaporizer system 36

Figure 3-13. Experimental setup for laser extinction.....37

Figure 3-14. Experimental setup for planar laser induced incandescence 38

Figure 3-15. Schematic of model gas turbine combustor facility 40

Figure 3-16. Cross-sectional view of combustion chamber.....42

Figure 3-17. Schematic of the liquid fuel injection system. Source, Mordaunt (2005) 43

Figure 3-18. Optical setup for laser extinction on the model gas turbine combustor 44

Figure 3-19. (a) Combustor Rig (b) Close-up of Pressure Vessel 46

Figure 3-20. (a) Swirl Stabilized Single Cup Combustor (b) Close-up of Fuel Nozzle 46

Figure 3-21. Close up of the Emission Probes (Note: During Measurements the Probes Tips are Further Downstream) 47

Figure 4-1. Chemkin II – PSR Model.....61

Figure 4.2. Schematic illustration of the computational method used by SHOCKIN for each time step Δt. From point 1 to 1' the mixture reacts at constant U, V. Subsequently, the mixture composition is frozen and isentropically expanded or compressed to match the experimental pressure at the point 2. 62

Figure 5-1. Comparison of predictions of different PAH mechanism from heptane.....64

Figure 5-2. Comparison of predictions of different PAH mechanism from iso-octane.....65

Figure 5-3. Comparison of predictions of different PAH mechanism from m-xylene 65

Figure 5-4. Schematic Depicting the Sequence of Hydrocarbon Oxidation. 67

Figure 5-5. Selected Hydrocarbon EI vs. Formaldehyde EI Profiles for a Premixed Flame at Phi=0.6. 67

Figure 5-6. Heat Release and Temperature Profiles of Opposed-Jet (Strained) Flame. 68

Figure 5-7. Select Hydrocarbon EI Profiles for Opposed-Jet Flame. 68

Figure 5-8. Hydrocarbon EI vs. Formaldehyde EI for Opposed-Jet Flame. 69

Figure 5-9. Residence Time Comparisons of Unstrained and Strained Premixed Flames. 69

Figure 5-10. Schematic of Reactor Series (T_3 = 477K, P_3 = 4.08 atm).....70

Figure 5-11. Trends in Emission Indices for a Variation in Equivalence Ratio of 1st Quench Reactor. 71

Figure 5-12. Trends in Indices for Variations in Equivalence Ratio of 1st Quench Reactor...71

Figure 5-13. Trends in Indices for Variations in Quench Times 72

Figure 5-14. Variations in Ethylene Emission Indices for Different Initial Equivalence Ratios 72

Figure 5-15. Emission Indices of Several Hydrocarbons (HCEI) for Three Fuels. 74

Figure 5-16. Predicted Emission Indices of Benzene for Three Different Fuels. 75

Figure 5-17. Prediction of Hydrocarbon Emissions from the Network Reactor code, starting with lean 76

Figure 5-18. Peak temperatures of the opposing-jet nonpremixed flames formed between air and hydrocarbon fuels at different strain rates. (a) Data are shown with respect to global strain rate and (b) data are shown with respect to airside strain rate. 79

Figure 5-19. (a) Flame structure and (b) various hydrocarbon species produced in a near-extinction opposing-jet flame formed between air and methane. Global strain rate is 448 s^{-1}. 80

Figure 5-20. (a) Flame structure and (b) various hydrocarbon species produced in a near-extinction opposing-jet flame formed between air and propane. Global strain rate is 377 s^{-1}. 81

Figure 5-21. (a) Flame structure and (b) various hydrocarbon species produced in a near-extinction opposing-jet flame formed between air and heptane. Global strain rate is 233 s^{-1}....82

Figure 5-22. (a) Flame structure and (b) various hydrocarbon species produced in a near-extinction opposing-jet flame formed between air and JP-8. Global strain rate is 83 s^{-1}. 83

Figure 5-23. Premixed flame stabilized on a 12.7-mm diameter bluff-body burner. Iso-concentration contours of H_2O (broken lines) and streamlines are superimposed on CO_2 distribution in the left half. Streamlines and contours (broken lines) representing a heat-release-rate value of 200-w/cm^3 are superimposed on C/H-atom-ratio distribution in the right half. 90

Figure 5-24. Distributions of CO_2 and H_2O concentrations and C/H atom ratio with respect to temperature (along a radial line) at different heights above the burner surface. (a), (c) and (e) are for 3.8-m/s fuel-jet velocity and (b), (d) and (f) are for 6.4-m/s fuel-jet velocity. Results for an unstrained laminar 1D flame are included in (e) and (f)....91

Figure 5-25. Results of the simulation performed for the flame shown in the previous figure after assuming diffusion coefficients of all the species are equal. (a) Iso concentration contours of H_2O (broken lines) and streamlines are superimposed on CO_2 distribution in the left half. Streamlines and contours (broken lines) representing a heat-release-rate value of 200-w/cm^3 are superimposed on C/H-atom-ratio distribution in the right half. (b) Distributions of C/H

atom ratio and H_2O and CO_2 concentrations with respect to temperature (along a radial line) in the recirculation zone (h = 3.3 mm) and in the downstream flame (h = 12.5 mm).....92

Figure 5-26. Opposing jet premixed flames simulated with UNICORN code. C/H-atom-ratio distributions with respect to temperature along the centerline for weakly (60 s^{-1}) and moderately (280 s^{-1}) stretched flames are compared with the data obtained for an unstretched 1D flame.....93

Figure 5-27. Normalized species concentrations and axial velocity near the bluff-body surface (z = 0.5 mm). Flame location is identified based on maximum heat release rate.....93

Figure 5-28. Distributions of C/H atom ratio with respect to temperature (along a radial line) at (a) 2 mm and (b) 6.5 mm above the burner surface. Results for an unstrained laminar 1D flame obtained with Chemkin are included.....94

Figure 5-29. Premixed flame stabilized on a 12.7-mm diameter bluff-body burner. Iso-concentration contours of H_2O (broken lines) are superimposed on CO_2 distribution in the left halves. Heat-release-rate contour (broken lines) of 150-w/cm^3 are superimposed on C/H-atom-ratio distribution in the right halves. (a) Instantaneous, (b) time-averaged flames. Streamlines are superimposed on time-averaged image. 94

Figure 5-30. Distributions of C/H atom ratio with respect to temperature (along a radial line) at (a) 2 mm and (b) 6.5 mm above the burner surface. Results for an unstrained laminar 1D flame obtained with Chemkin are included.....95

Figure 5-31. Turbulent flame obtained in (a) experiment and (b) calculations for the Cambridge burner operating with non-swirling fuel jets. 95

Figure 5-32. Comparison between computed and measured axial velocities obtained at four different heights in the recirculation zone. 96

Figure 5-33. Computed and measured distributions of C/H-atom ratio with respect to temperature near the bluff-body surface (x = 2 mm). Direct simulation is obtained without using any turbulence model. 96

Figure 5-34. Schematic diagram of opposing-jet-flow burner used for the investigations of vortex/flame interactions. Nitrogen-diluted hydrogen fuel and air introduced from upper and lower nozzles, respectively. 99

Figure 5-35. Laminar and near-turbulent opposing jet flames are shown in the left and right halves, respectively. Temperature distributions are plotted. Time-averaged temperature over a period is used for the near-turbulent case. 100

Figure 5-36. Instantaneous flame visualized with temperature and velocity fields. 100

Figure 5-37. Instantaneous flame visualized using vorticity. 101

Figure 5-38. Instantaneous flame visualized using scalar dissipation rate. 101

Figure 5-39. Instantaneous flame visualized using OH concentration and particle-tracking technique. 102

Figure 5-40. Evolutions of the vortices and temperature field in a flame transitioning to a turbulent one. 103

Figure 5-41. Flame system used for studying UHCs. 106

Figure 5-42. Initial equivalence ratio distributions used for the simulation of stratified-combustion experiment of Kang and Kyritsis (2005, 2007). 106

Figure 5-43. Effect of diffusion on equivalence-ratio distribution as flame propagates through tube. 106

Figure 5-44. Computed and measured flame speed for different equivalence ratio distributions.107

Figure 5-45. Propagation of n-dodecane flame through constant phi. (a) Initial phi distribution, (b) temperature at mid-section at different times. 107

Figure 5-46. Propagation of n-dodecane flame through linearly varying phi. (a) Initial phi distribution, (b) temperature at different times. 108

Figure 5-47. (a) Variations in averaged temperature and species mass fractions as the flame propagated through the stratified mixture. (b)-(h) Correlations between mass fractions of various species and ethylene after the flame is extinguished. 109

Figure 5-48. Ignition-delay times calculated for stoichiometric n-heptane-air mixture at 1-atm pressure by Farouk et al [4]. Results from the simulations of UNICORN code integrated with the reduced mechanism of Farouk et al. are shown with symbols. 114

Figure 5-49. History of temperature and heat release rate recorded during the ignition process of a fuel pocket with 600 K initial temperature. Time scales are broken into two parts for providing details during the "cool" and "hot" ignition events. Plot using the time scale covering both the ignition events is shown in the inset. 115

Figure 5-50. Schematic diagram of the opposing-jet-diffusion-flame burner used in the simulations for forming a "cool" diffusion flame. 115

Figure 5-51. Steady-state distributions of heat release rate and temperature along the centerline of the opposing-jet-diffusion-flame burner obtained for different air temperatures. Locations of the stagnation planes are marked with dashed lines with corresponding colors. Note, stagnation planes for 724-K and 725-K cases are identically located. 116

Figure 5-52. “Cool” flame obtained without (left half) and with (right half) gravitational force. Temperature distributions and streamlines obtained between the fuel and air nozzles are shown. 116

Figure 5-53. Two types of diffusion flames formed in opposing-jet burner under identical conditions. "Cool" flame is shown in the left halves and normal flame is shown in the right

halves. (a) Temperature distributions and streamlines, (b) H_2-concentration distributions and iso-heat-release-rate contours, and (c) C_2H_4-concentration distributions and iso-concentration contours of OH radicals between the fuel (z = 0) and air (z = 10 mm) nozzles. 117

Figure 5-54. "Cool" diffusion flame structure along the centerline. Distributions of velocity, temperature and stretch rate are shown in (a) and those of reactants, products, intermediate species and low-temperature intermediates are shown in (b), (c) and (d), respectively. .118

Figure 5-55. Variations in peak temperature and maximum HRR of a "cool" diffusion flame subjected to increasing stretch rate. Flame extinguished for stretch rates > 14.7 s^{-1}.....119

Figure 6-1. Ignition delay measurements for (a) n-dodecane/n-heptane blend, (b) n-dodecane/iso-octane blend, (c) n-dodecane/methylcyclohexane blend and (d) n-dodecane/m-xylene blend. Filled symbols are measurements from OH* emissions whereas open symbols are from the pressure profiles recorded at the end plate of the test section. 122

Figure 6-2. Comparison experimental (a) and modeled (b) ignition delay times for ■: n-dodecane/n-heptane; ▲: n-dodecane/iso-octane; ◆: n-dodecane/methylcyclohexane; ●: n-dodecane/m-xylene. 123

Figure 6-3. Comparison of experimental ignition delay times measured under similar experimental conditions: □: *n*-dodecane (Flora et al., 2011); ○: *m*-xylene (Saxena et al., 2011); ◇: methylcyclohexane (Nagulapalli, 2015); ★: *n*-heptane/toluene (Kahandawala et al., 2008); ▼: JP-8 POSF 3773 (Balagurunathan, 2012); ▸: S-8 POSF 4820 (Balagurunathan, 2012).124

Figure 6-4. Sensitivity analysis results comparison targeting ignition delay time at T ~ 1000 K, P ~ 16.9 atm at Φ = 3, Ar = 93%. For each surrogate fuel, the 15 top reactions with the highest absolute sensitivity coefficient were considered. 128

Figure 6-5. Sensitivity analysis results comparison targeting ignition delay time at T ~ 1250 K, P ~ 16.5 atm at Φ = 3, Ar = 93%. For each surrogate fuel, the 15 top reactions with the highest absolute sensitivity coefficient were considered. 129

Figure 6-6. Sensitivity analysis results comparison targeting ignition delay time at T ~ 1470 K, P ~ 16.5 atm at Φ = 3, Ar = 93%. For each surrogate fuel, the 15 top reactions with the highest absolute sensitivity coefficient were considered. 130

Figure 6-7. Local rate of production analysis at T ~ 1000 K and time equals to half of the ignition delay for all the surrogate mixtures. The CHBR model with constant U, V assumption was used. 131

Figure 6-8. Local rate of production analysis at T ~ 1250 K and time equals to half of the ignition delay for all the surrogate mixtures. The CHBR model with constant U, V assumption was used. 132

Figure 6-9. Local rate of production analysis at T ~ 1470 K and time equals to half of the ignition delay for all the surrogate mixtures. The CHBR model with constant U, V assumption was used. 133

Figure 6-10. Comparison of the molecular oxygen conversion among the surrogate mixtures at time equal to half of the ignition delay; (a) T ~ 1000 K, (b) T ~ 1250 K, (c) T ~ 1470 K. Computation performed using the CHBR model with the constant U, V assumption. 135

Figure 6-11. Comparison of n-dodecane decomposition pathways among the surrogate mixtures at time equal to half of the ignition delay; (a) T ~ 1000 K, (b) T ~ 1250 K, (c) T ~ 1470 K. Computation performed using the CHBR model with the constant U, V assumption. 136

Figure 6-12. Experimental carbon recoveries measured for (a) n-dodecane/n-heptane blend, (b) n-dodecane/iso-octane, (c) n-dodecane/methylcyclohexane, (d) n-dodecane/m-mxylene. All the experiments were at an equivalence ratio of 3, argon concentration of 93% (mol), pre-ignition pressure of ~16 atm, and dwell time of ~7.5–8.0 ms. 138

Figure 6-13. Example of time history profiles for pressure, temperature and density from the application of the three computational approaches. 139

Figure 6-14. CO (a) and CO_2 (b) emissions comparisons among the binary fuel blends. 140

Figure 6-15. Comparison of measured and predicted formaldehyde and acetaldehyde emissions. 141

Figure 6-16. Methane (a) and ethane (b) emissions comparisons among the binary fuel blends 143

Figure 6-17. Ethylene (a) and acetylene (b) emissions comparisons among the binary fuel blends. 144

Figure 6-18. Benzene (a) and toluene (b) emissions comparisons among the binary fuel blends. 145

Figure 6-19. Naphthalene emissions comparisons among the binary fuel blends. 146

Figure 6-20. Semi-volatile emissions comparisons among the binary fuel blends. 147

Figure 6-21. Non-volatile emissions comparisons among the binary fuel blends. 149

Figure 6-22. Non-volatile emissions comparisons among the binary fuel blends. 150

Figure 6-23. Non-volatile emissions comparisons among the binary fuel blends. 151

Figure 6-24. Soot yields (a) and mass percentages (b) measured for volatile and elemental carbon collected on the soot filters. 153

Figure 6-25. Volatile (a) and elemental (b) carbon collected on the soot filters expressed in terms of carbon yields as function of the pre-ignition temperature. 154

Figure 6-26. Measured particulate matter pre-cursors including acetylene, benzene, naphthalene and soot for *n*-dodecane/*n*-heptane mixture. 156

Figure 6-27. Carbon yields of benzene, naphthalene and soot as functions of acetylene yields for the base binary fuel blends over the temperature range of 978–1263 K. 157

Figure 6-28. Carbon yields of benzene, naphthalene and soot as functions of acetylene yields for the base binary fuel blends over the temperature range of 1263–1554 K. 157

Figure 6-29. Global rate of production analysis for carbon monoxide (CO). 159

Figure 6-30. Global rate of production analysis for carbon dioxide (CO_2).....159

Figure 6-31. Global rate of production analysis for methane (CH_4). 161

Figure 6-32. Global rate of production analysis for ethane (C_2H_6).....161

Figure 6-33. Global rate of production analysis for acetylene (C_2H_2). 162

Figure 6-34. Global rate of production analysis for ethylene (C_2H_4).....162

Figure 6-35. Global rate of production analysis for benzene (C_6H_6). 164

Figure 6-36. Global rate of production analysis for toluene ($C_6H_5CH_3$).....164

Figure 6-37. Global rate of production analysis for naphthalene ($C_{10}H_8$).....165

Figure 6-38. Experimental pressure profiles showing the different swell times obtained maintaining similar pre- and post- ignition conditions. 167

Figure 6-39. Ignition delay times and dwell times for each of the experiments. 168

Figure 6-40. Time-dependent emission yields for CO, CO_2 and C_1-C_2 hydrocarbons. 170

Figure 6-41. Time-dependent emission yields for aldehyde species. 171

Figure 6-42. Time-dependent emission yields for benzene and toluene. 172

Figure 6-43. Time-dependent emission yields for semi-volatile organic compounds (SVOC). 173

Figure 6-44. Time-dependent emission yields for the particulate matter (PM). 174

Figure 7-1. Emission indicies of methane, formaldehyde, acetylene with respect to ethylene for JP-8 (top), Sasol (middle), and dodecane/m-xylene (bottom) fuels. 176

Figure 7-2. Emission indicies of actylene and methane with respect to formaldehyde (left and middle) and methane (right) for ethylene/air reactions. 177

Figure 7-3. Emission indicies of ethylene (1st column), acetylene (2nd column), formaldehyde (3st column), and methane (4th column) for varying equivalence ratios for JP-8 (top), Sasol (middle), and dodecane/m-xylene (bottom) fuels. 178

Figure 7-4. Emission indicies of ethylene (1st column), acetylene (2nd column), formaldehyde (3st column), and methane (4th column) for varying equivalence ratios for ethylene air reactions.178

Figure 7-5. Emission indices of methane, formaldehyde, acetylene with respect to ethylene for JP-8 (top), Sasol (middle), and dodecane/m-xylene (bottom) fuels. The scale of the plots are reduced relative to Figure 2.....179

Figure 7-6. Emission Indices of Methane, Acetylene, Ethylene and Formaldehyde for the n-Heptane/n-Dodecane Surrogate. 180

Figure 7-7. Emission Indices of Formaldehyde, Methane and Acetylene vs. Emission Indices for Ethylene for the Heptane/Dodecane Surrogate. 180

Figure 7-8. Emissions from the WSR on the Approach to Lean Blowout. 181

Figure 7-9. WSR reactor temperature effects with equivalence ratio. Temperature trends to decrease when decreasing equivalence ratio, thus reducing fuel flow. (P = 1 atm, τ = 6-7ms).....183

Figure 7-10. WSR LBO effects with H/C number of the given surrogate fuel mixture is listed for each fuel and its respective color. (P = 1 atm, τ = 6.5ms). For a constant enthalpy system, decreases in H/C ratio trend to increase the state of LBO, thus reducing resistance to LBO.184

Figure 7-11. WSR heat release rate with equivalence ratio. Decreases in fuel flow trends to reduce energy released in the combustion process. Fuel mass flow rates were multiplied by their corresponding heat of combustion to determine heat release rate. (P = 1 atm, τ = 6-7ms, $Vfuel$ = ~22-26 mL/min).....184

Figure 7-12. Carbon dioxide (a) and carbon monoxide (b) concentration (ppm) a function of equivalence ratio at atmospheric conditions and a residence time of approximately 6.5 ms. Temperatures for these experiments are reported in Figure 7-10. 185

Figure 7-13. Formaldehyde concentration (ppm) as a function of equivalence ratio at atmospheric conditions and a residence time of approximately 6.5 ms. Measurements from methane were recorded from the FTIR. 186

Figure 7-14. Methane concentration (ppm) as a function of equivalence ratio (a) and as a function of formaldehyde concentrations (b) at atmospheric conditions and a residence time of approximately 6.5 ms. Measurements from methane were recorded from the FTIR.....187

Figure 7-15. Ethane concentration (ppm) as a function of equivalence ratio (a) and as a function of formaldehyde concentrations (b) at atmospheric conditions and a residence time of approximately 6.5 ms. Measurements from ethane were recorded from the FTIR. 187

Figure 7-16. Ethylene concentration (ppm) as a function of equivalence ratio (a) and as a function of formaldehyde concentrations (b) at atmospheric conditions and a residence time of approximately 6.5 ms. Measurements from ethylene were recorded from the FTIR.....188

Figure 7-17. Acetylene concentration (ppm) as a function of equivalence ratio (a) and as a function of formaldehyde concentrations (b) at atmospheric conditions and a residence time of approximately 6.5 ms. Measurements from acetylene were recorded from the FTIR. 189

Figure 7-18. Propene concentration (ppm) as a function of equivalence ratio (a) and as a function of formaldehyde concentrations (b) at atmospheric conditions and a residence time of approximately 6.5 ms. Measurements from propene were recorded from the FTIR. 189

Figure 7-19. Propene concentration (ppm) as a function of equivalence ratio (a) and as a function of formaldehyde concentrations (b) at atmospheric conditions and a residence time of approximately 6.5 ms. Measurements from propene were recorded from the gas bag sampling technique. 190

Figure 7-20. 1,3 butadiene concentration (ppm) as a function of equivalence ratio (a) and as a function of formaldehyde concentrations (b) at atmospheric conditions and a residence time of approximately 6.5 ms. Measurements from 1,3 butadiene were recorded from the FTIR.191

Figure 7-21. 1,3 butadiene concentration (ppm) as a function of equivalence ratio (L) and as a function of formaldehyde concentrations (b) at atmospheric conditions and a residence time of approximately 6.5 ms. Measurements from 1,3 butadiene were recorded from the gas bag sampling technique.....191

Figure 7-22. Butene and 1,3 butadiene concentration (ppm) as a function of equivalence ratio (a) and as a function of formaldehyde concentrations (b) at atmospheric conditions and a residence time of approximately 6.5 ms. Measurements from butene and 1,3 butadiene were recorded from the charcoal tube sampling technique.....192

Figure 7-23. Acetaldehyde concentration (ppm) as a function of equivalence ratio (a) and as a function of formaldehyde concentrations (b) at atmospheric conditions and a residence time of approximately 6.5 ms. Measurements from acetaldehyde were recorded from the FTIR.193

Figure 7-24. Methanol concentration (ppm) as a function of equivalence ratio (a) and as a function of formaldehyde concentrations (b) at atmospheric conditions and a residence time of approximately 6.5 ms. Measurements from methanol were recorded from the FTIR and deviate slightly out of the calibration range of 0-10 ppm towards lean blowout conditions. 194

Figure 7-25. Isobutene concentration (ppm) as a function of equivalence ratio (a) and as a function of formaldehyde concentrations (b) at atmospheric conditions and a residence time of approximately 6.5 ms. Measurements from isobutene were recorded from the FTIR. 194

Figure 7-26. Benzene concentration (ppm) as a function of equivalence ratio (a) and as a function of formaldehyde concentrations (b) at atmospheric conditions and a residence time of approximately 6.5 ms. Measurements from benzene were recorded from the charcoal tube technique. 195

Figure 7-27. Toluene concentration (ppm) as a function of equivalence ratio (a) and as a function of formaldehyde concentrations (b) at atmospheric conditions and a residence time of approximately 6.5 ms. Measurements from toluene were recorded from the charcoal tube technique. 196

Figure 7-28. p&m-xylene concentration (ppm) as a function of equivalence ratio (a) and as a function of formaldehyde concentrations (b) at atmospheric conditions and a residence time

of approximately 6.5 ms. Measurements from p&m-xylene were recorded from the charcoal tube technique. 196

Figure 7-29. Progression of Reactor Equivalence Ratio, Temperature, and Residence Times (Large symbols: Simulations, Small symbols: Experiments) 197

Figure 7-30. Temperature Profiles as LBO is Approached (Large symbols: Simulations, Small symbols: Experiments).....198

Figure 7-31. Ethene Emissions as Function of Formaldehyde Emissions as LBO is Approached198

Figure 7-32. Comparison of LBO Temperature Profiles: Experimental, Adiabatic, Fixed-Temperature, and Non-Adiabatic for JP-8/Air System. 199

Figure 7-33. Non-Adiabatic Simulations Major Species Sensitivities to System Reactions (1250 K). 200

Figure 7-34. Ethene as Function of Formaldehyde for Both Experiment and Simulations 203

Figure 7-35. Methane as Function of Formaldehyde for Both Experiment and Simulations ..203

Figure 7-36. Acetylene as Function of Formaldehyde for Both Experiment and Simulations 204

Figure 7-37. Simulations of Propene as Function of Formaldehyde.....205

Figure 7-38. Simulations of 1-Butene as Function of Formaldehyde 205

Figure 7-39. Simulations of Iso-Butene as Function of Formaldehyde 206

Figure 7-40. Simulations of 1,3-Butadiene as Function of Formaldehyde 206

Figure 7-41. Simulations of Benzene as Function of Formaldehyde.....207

Figure 7-42. Comparison of Experimental and Simulation Ethene Profiles as Functions of Equivalence Ratio and Fuel Compositions (Dashed line represents simulation results at fixed temperature) 208

Figure 7-43. Comparison of Experimental and Simulation Methane Profiles as Functions of Equivalence Ratio and Fuel Compositions. 209

Figure 7-44. Comparison of Experimental and Simulation Acetylene Profiles as Functions of Equivalence Ratio and Fuel Compositions. 209

Figure 7-45. Comparison of Experimental and Simulation Formaldehyde Profiles as Functions of Equivalence Ratio and Fuel Compositions. 210

Figure 7-46. Comparison of Experimental and Simulation CO Profiles as Functions of Equivalence Ratio and Fuel Compositions. 211

Figure 7-47. Formaldehyde Production (solid) and Consumption (dashed) Rates and Formaldehyde Mole Fraction Levels (dotted) as Functions of Reactor Temperature for All Tested Fuels (simulations).....212

Figure 7-48. Net Fuel and O2 Consumption Rates for the n-Dodecane/n-Heptane Fuel Blend. 212

Figure 7-49. Comparison of Experimental and Simulation Ethene Profiles as Functions of Formaldehyde Emissions and Fuel Compositions 213

Figure 7-50. Comparison of Experimental and Simulation iso-Butene Profiles as Functions of Formaldehyde Emissions and Fuel Compositions 214

Figure 7-51. Comparison of Experimental and Simulation Toluene Profiles as Functions of Formaldehyde Emissions and Fuel Compositions 214

Figure 7-52. Comparison of Experimental and Simulation 1,3-Butadiene Profiles as Functions of Formaldehyde Emissions and Fuel Compositions 215

Figure 7-53. Comparison of Potential Core Convection Time and Ignition Times as Functions of Equivalence Ratio and Mixture Fraction for n-Dodecane/Air Mixtures.....216

Figure 7-54. Equilibrium Gas Temperatures as functions of Equivalence Ratio (and resulting correlation) for n-Dodecane/Air Mixtures. 217

Figure 7-55. Ignition Delay Times as functions of Initial Mixture Temperature (and resulting correlation) for n-Dodecane/Air Mixtures. 217

Figure 7-56. Critical Blowout Equivalence Ratios for the Five Tested Fuel Blends. 218

Figure 7-57. Measured and computed temperatures obtained for WSR operating at different equivalence ratios.....220

Figure 7-58. Measured and computed concentrations of major species obtained in WSR. 220

Figure 7-59. Measured and computed concentrations of minor species obtained in WSR.....220

Figure 7-60. Correlations between emission indices obtained for acetylene and ethylene in WSR (a) computed and (b) measured distributions. 221

Figure 7-61. Correlations between emission indices obtained for formaldehyde and ethylene in WSR (a) computed and (b) measured distributions. 221

Figure 7-62. Correlations between emission indices obtained for methane and ethylene in WSR (a) computed and (b) measured distributions. 222

Figure 7-63. Temperature sensitivity in WSR to mixture composition for m-xylene and n-dodecane components. 222

Figure 7-64. Changes in major species concentrations in WSR due to variations in composition for m-xylene-n-dodecane mixtures. 223

Figure 7-65. Changes in UHC in WSR due to variations in composition for m-xylene-n-dodecane mixtures. 223

Figure 7-66. Changes in UHC concentrations in WSR due to variations in composition for m-xylene-n-dodecane mixtures. 223

Figure 8-1. Visible light images of non-premixed co-flow flames (phi = infinity) with 0.2 slpm nitrogen. 225

Figure 8-2. Aromatic species distributions for non-premixed co-flow flames with 0.2 slpm nitrogen. 227

Figure 8-3. Soot species distributions for non-premixed co-flow flames with 0.2 slpm nitrogen. Note that the m-xylene fuel (m-X) is on a different scale than the paraffinic fuels. 228

Figure 8-4. Centerline profiles for small aromatics, large aromatics and soot for non-premixed flames with 0.2 slpm of nitrogen. 229

Figure 8-5. Comparison of aromatic species and soot in non-premixed flames of m-xylene fuel with 0.2 and 0.48 slpm of nitrogen. Note that each 2-D plot has a separate scale. 231

Figure 8-6. Comparison of centerline profiles of aromatics and soot in the non-premixed m-xylene flames with 0.2 and 0.48 slpm of nitrogen. 232

Figure 8-7. Visible light images of non-premixed co-flow flames (phi = 6) with 0.2 slpm nitrogen. 233

Figure 8-8. Aromatic species distributions for partially-premixed co-flow flames (phi = 6) with 0.2 slpm nitrogen. Note that the m-xylene fuel (m-X) is on a different scale than the paraffinic fuels. 235

Figure 8-9. Soot distributions for partially-premixed co-flow flames (phi = 6) with 0.2 slpm nitrogen. Note that the m-xylene fuel (m-X) is on a different scale than the paraffinic fuels.236

Figure 8-10. Centerline profiles for small aromatics, large aromatics and soot for partially premixed fuel jet at phi=6 237

Figure 8-11. Jet diffusion flames obtained with (a) n-heptane-n-dodecane, (b) iso-octane-n-dodecane, (c) mch-n-dodecane, and (d) m-xylene-n-dodecane fuel blends. Direct photographs of the flames are superimposed on computed soot volume fraction (red represents maximum value of 4.5 ppm). 240

Figure 8-12. Computed (a) and measured (b) soot volume fractions along the centerline for various jet diffusion flames. 240

Figure 8-13. Distributions of temperature and acetylene concentration along the centerline in n-heptane and m-xylene flames. 241

Figure 8-14. Distributions of (a) OH (left) and soot nucleation rate (right) and (b) soot growth rate (left) and soot oxidation rate (right) in n-dodecane-n-heptane flame. 241

Figure 8-15. Distributions of (a) OH (left) and soot nucleation rate (right) and (b) soot growth rate (left) and soot oxidation rate (right) in n-dodecane-m-xylene flame. 242

Figure 8-16. Distributions of fuel components along the centerline in n-heptane (red), iso-octane (blue), mch (green) and m-xylene (purple) flames. 242

Figure 8-17. M-xylene/n-dodecane flame calculated with new soot model. (a) Comparison of measured (left) and computed (right) distributions of soot. (b) Measured and computed soot distributions along the centerline. 244

Figure 8-18. M-xylene/n-dodecane flame calculated with new soot model after modifying the soot oxidation rate. (a) Comparison of measured (left) and computed (right) distributions of soot. (b) Measured and computed soot distributions along the centerline. 245

Figure 8-19. Comparison of radial distributions of soot at different heights for n-decane flame of University of Toronto. Symbols, broken lines and solid lines, represent measurements, University of Toronto predictions and our predictions, respectively. (a) h = 30 mm, (b) h = 40 mm, (c) h = 50 mm, (d) h = 60 mm, and (e) h = 70 mm. 245

Figure 8-20. Comparison of radial distributions of soot at different heights for Jet-A flame of University of Toronto. Symbols, broken lines and solid lines, represent measurements, University of Toronto predictions and our predictions, respectively. (a) h = 30 mm, (b) h = 40 mm, (c) h = 50 mm, (d) h = 60 mm, and (e) h = 70 mm. 246

Figure 8-21. Comparison of predicted soot distributions with the direct photographs of flames formed with various fuels. Experiments were performed at University of San Diego. ... 246

Figure 8-22. Comparison of measured (top) and predicted soot distributions for non-premixed co-flow flames (phi = infinity) with 0.2 slpm nitrogen 249

Figure 8-23. Comparison of measured (top) and predicted soot distributions for partially-premixed co-flow flames (phi = 6) with 0.2 slpm nitrogen 250

Figure 8-24. Comparison of measured (top) and predicted centerline profiles of soot for non-premixed co-flow flames (phi = infinity) with 0.2 slpm nitrogen. 251

Figure 8-25. Comparison of measured (top) and predicted centerline profiles of soot for partially-premixed co-flow flames (phi = 6) with 0.2 slpm nitrogen. 252

Figure 8-26. Comparison of measured (top) and predicted distributions of small aromatic species for non-premixed co-flow flames (phi = infinity) with 0.2 slpm nitrogen 253

Figure 8-27. Comparison of measured (top) and predicted distributions of small aromatic species for partially-premixed co-flow flames (phi = 6) with 0.2 slpm nitrogen 254

Figure 8-28. Comparison of measured (top) and predicted distributions of large aromatic species for non-premixed co-flow flames (phi = infinity) with 0.2 slpm nitrogen.....255

Figure 8-29. Comparison of measured (top) and predicted distributions of large aromatic species for partially-premixed co-flow flames (phi = 6) with 0.2 slpm nitrogen 256

Figure 8-30. m-xylene/n-dodecane vs. JP8 for (phi = ∞): Experimental soot volume fraction and aromatic species for co-flow jet diffusion flame.....258

Figure 8-31. m-xylene/n-dodecane vs. JP8 for (phi = 6): Experimental soot volume fraction and aromatic species for co-flow jet diffusion flame.....258

Figure 8-32. Iso-octane/n-dodecane vs. FT for (phi = ∞): Experimental soot volume fraction and aromatic species for co-flow jet diffusion flame.....259

Figure 8-33. Iso-octane/n-dodecane vs. FT for (phi = 6): Experimental soot volume fraction and aromatic species for co-flow jet diffusion flame.....259

Figure 9-1. Comparison of Soot at Combustor Exit for n-heptane/n-dodecane fuels and JP-8 as a function of equivalence ratio.....261

Figure 9-2. Comparison of Soot fields in n-heptane/n-dodecane, pure n-dodecane and n-hexadecane/n-dodecane for non-premixed and partially-premixed (jet phi=6) conditions. 262

Figure 9-3. Comparison of centerline soot profiles for n-heptane/n-dodecane (C7) and n-hexadecane/n-dodecane (C16) for non-premixed and partially-premixed (jet phi=6) conditions.. 262

Figure 9-4. Axisymmetric model of the dump combustor used in CFD analysis. Conjugate heat transfer through the combustor outer wall between the burned gases and cooling air is modeled. 266

Figure 9-5. Computed temperature fields (left halves) and soot distributions (right halves) in the combustor for different equivalence ratios. Premixed mixtures of JP-8 and air with equivalence ratios of (a) 1.2, (b) 1.4, (c) 1.5, (d) 1.6, and (e) 1.7 are injected into the combustion chamber. Instantaneous flowfields obtained at random times are shown.....267

Figure 9-6. Flowfields near the dump section for equivalence ratios 1.2 (a, c, and e) and 1.7 (b, d, and f). Temperature and soot radiation are shown in the left and right halves, respectively in frames (a) and (b). Velocity field (left half) and heat-release-rate contours (right half) are superimposed. OH and CO distributions are shown in frames (c) and (d) in the left and right halves, respectively. O_2 contours are superimposed on the left halves. Fuel and H_2 distributions are shown in frames (e) and (f) in the left and right halves, respectively. CH_4 contours are superimposed on the left halves. 268

Figure 9-7. Computed (dashed line) and measured (solid line) soot volume fractions at the exit plane of the dump combustor for m-xylene fuel as function of equivalence ratio. Predicted soot volume fraction for paraffinic fuels at phi=1.6 are shown as individual points. The bars between + symbols show the data scatter among experiments performed on different runs and while increasing and decreasing the equivalence ratio. 269

Figure 10-1. Referee combustor operating on Jet A fuel at 207 kPa, T_{air} = 394 K, and phi = 0.1270

Figure 10-2. LBO Equivalence Ratio for the Test Conditions.....271

Figure 10-3. Apparent Combustion Efficiency calculated from SAE ARP 1533.....272

Figure 10-4. CO_2 Emissions at Equivalence Ratios Near LBO 273

Figure 10-5. CO Emissions at Equivalence Ratios Near LBO 274

Figure 10-6. UHC Emissions at Equivalence Ratios Near LBO 274

Figure 10-7. C_1-C_4 components in Combustor Exhaust (1-Alkenes and Propadiene).....276

Figure 10-8. C_1-C_4 Components in Combustor Exhaust (Alkanes).....277

Figure 10-9. Benzene Emissions Index.....278

Figure 10-10. Toluene Emissions Index 279

Figure 10-11. Formaldehyde Emissions Index 279

Figure 10-12. Unreacted Fuel Fraction in the UHC.....280

Figure 10-13. Relative Reactivity of Second Surrogate Component Compared to that of n-C_{12}. 281

Figure 10-14. Particle number Emission Indices 282

Figure 10-15. Particle Number Density vs HC ratio.....282

Figure 11-1. Comparison of measured mass fuel flow rate for T-63 engine testing with six fuels.284

Figure 11-2. Comparison of total NO_x Emission Index for T-63 engine testing with six fuels. 285

Figure 11-3. Comparison of the emission indices of benzene as a function of power setting and fuel type.....286

Figure 11-4. Correlation between emission indices for benzene and ethylene. Symbols denote the fuels tested and numbers displayed are the linear slopes. 287

Figure 11-5. Correlation between emission indices for and acetaldehyde to ethylene. Symbols denote the fuels tested and numbers displayed are the linear slopes.....288

Figure 11-6. Particle Number emission indices as a function of engine power for fuel type. .289

Figure 11-7. Estimated (a) number and (b) mass of particles deposited on stages 7-13 for each fuel (symbols) at low-speed ground idle. Values are representative of one deposition spot (*i.e.*, nozzle) for the sampled PSDs, experiment sampling times and a density of ρ = 1.5 g cm^{-3}.290

Figure 11-8. A processed (averaged, baseline-corrected and smoothed) micro-FTIR spectrum for T63 aircraft soot that is typical of the six fuels tested. The sample shown is for Fischer-Tropsch, 85% power and stage 9. 291

Figure 11-9. Group concentration ratio as a function of particle size for *n*-heptane/*n*-dodecane blend. Colors denote functionality and symbols denote engine power. 292

Figure 11-10. Group concentration ratio as a function of particle size for *iso*-octane/*n*-dodecane blend. Colors denote functionality and symbols denote engine power. 293

Figure 11-11. Group concentration ratio as a function of particle size for *m*-xylene/*n*-dodecane blend. Colors denote functionality and symbols denote engine power. 294

Figure 11-12. Group concentration ratio as a function of particle size for *methylcyclohexane*/*n*-dodecane blend. Colors denote functionality and symbols denote engine power. 295

Figure 11-13. Plot showing the number of particles emitted-per-kilometer traveled for various engine technologies. Values assume an aircraft speed of 1 mi hr^{-1}. Symbol colors denote the engine power (% maximum power), as shown in the figure. Data from this work is shown between the data of [a](Lobo *et al.*, 2011) and [b](Bulzan, *et al.*, 2010).....297

Figure 11-14. Plot showing the mass of particles emitted-per-kilometer traveled for various engine technologies. Values assume an aircraft speed of 1 mi hr^{-1}. Symbol colors denote the engine power (% maximum power), as shown in the figure. Data from this work is shown between the data of [a](Lobo *et al.*, 2011) and [b](Bulzan, *et al.*, 2010). 298

Figure 11-15. Comparison of neat fuel (top) and hydrocarbons captured from T63 idle engine emissions. 299

Figure 11-16. Comparison of major components in jet fuel and emissions of T63 (idle condition).299

Figure 11-17. Changes observed in distribution of emissions show that less volatile components are more likely to be combusted and that alkyl aromatics are formed during combustion. 301

Figure A-1. Temperature and Equivalence ratio of the Reactor Operating on Heptane/Dodecane Surrogate as the Lean Blowout Limit is Approached 313

Figure A-2. Emissions from the WSR on the Approach to Lean Blowout for n-Heptane/n-Dodecane Surrogate Fuel 314

Figure A-3. Emissions from the WSR as Lean Blowout is approached for MCH/Dodecane .314

LIST OF TABLES

Table 3-1. Light gases analytical details. 25

Table 3-2. Aldehydes species analytical details. 26

Table 3-3. Aromatic species and fuel component residues analytical details. 27

Table 3-4. Semi-volatile organic species analytical details. 27

Table 3-5. Experimental matrix. 28

Table 3-6. Experimental conditions for jet flame studies. 39

Table 3-7. Experimental Conditions for the AFRL Single Cup Rig. 48

Table 3-8. Composition of Fuels Tested. 49

Table 3-9. Hazardous Air Pollutants Measured in Combustion Emissions. 51

Table 3-10. Matrix of binary fuel blends; major component in mixtures is n-dodecane (BP=216°C) 53

Table 4-1. Added Reaction steps to account for mass growth, decomposition and oxidation of methylstyrene (MCSTYREN). 56

Table 4-2. Added reactions to account for PAH formation. 56

Table 5-1. Comparison of various predicted HCEI ratios against Formaldehyde Emission Indexes (EI) with engine exhaust data. 73

Table 6-1. Ignition delay time correlations for the binary fuel blends studied in this work and for other surrogate and practical fuel investigated at the UDRI shock tube facilities under similar experimental conditions. 125

Table 6-2. Modified Gaussian expressions used to interpolate soot yields measurements vs. pre-ignition temperature. 155

Table 6-3. Experimental condition and ignition delay measurements for the quenching effects studies 168

Table 7-1 Different Fuel Blends and Surrogates Used with SERDP Kinetic Mechanism 201

Table 7-2 Experimental matrix for n-Dodecane/m-Xylene study 202

Table 7-3. Limiting Equivalence Ratios, Ignition Temperatures and Times. 218

Table 8-1. Flame heights for non-premixed co-flow flames 225

Table 8-2. Flame heights for partially-premixed co-flow flames 234

Table 8-3. Details of the fuel jet at burner exit. 238

Table 8-4. Comparison of Test Fuels and Actual Fuels.....257

Table 11-1. Charcoal tube response versus continuous monitor (UHC) response for T63 at idle power conditions. 300

LIST OF ACRONYMS

AF	Air Force
AFB	Air Force Base
AFRL	Air Force Research Lab
AIAA	American Institute of Aeronautics and Astronautics
Ar	Argon
ASME	American Society of Mechanical Engineers
ASTM	American Society for Testing and Materials
C7	n-heptane and n-heptane/n-dodecane fuel
C2H2	Acetylene
C2H4	Ethylene
C12H26	Dodecane
CBB	Centerbody burner
CFD	computational fluid dynamic
CFM	Specific type of combustor
CHBR	Closed homogeneous batch reactor
CHEMKIN	Combustion Modeling Program
CH4	Methane
CH2O	Formaldehyde
CO	Carbon monoxide
CO2	Carbon dioxide
CPC	Condensation particle counter
CRECK	Chemical Reaction Engineering and Chemical Kinetics (research group at University of Milan, Italy)
CW	Continuous wave (i.e. Non-pulsed)
DNPH	Di-nitrophenylhydrazine (used in analysis of aldehyde emissions)
DoD	Department of Defense
DOE	Department of Energy
EI	Emission Index (gram emission/kg fuel)
ESTCP	Environmental security technology certification program
EPA	Environmental protection agency
FFT	Fast Fourier transform
FT	Fischer-Tropsch
FTIR	Fourier transform infrared
GASKIN	Chemical kinetic modeling code for shock tubes
GC	Gas chromatograph
GC-MS	Gas chromatograph-mass spectrometer
GRI	Gas research institute
GT	Gas turbine
H	Atomic hydrogen
H2	Molecular hydrogen
H2O	Water
H/C	Ratio of fuel hydrogen to carbon
HACA	Hydrogen-abstraction-carbon addition
HAP	Hazardous air pollutant
HP	High pressure

iC8	iso-octane and iso-octane/n-dodecane fuel
ICCD	Intensified charge coupled device
ID	Internal Diameter
IR	Infra-red
ISSI	Innovative Scientific Solutions, Inc.
JP-8	Jet propulsion 8 (u.s. Military jet fuel)
LBO	Lean blowout
LIF	Laser-induced fluorescence
LII	Laser-induced incandescence
LLNL	Lawrence Livermore National Laboratory
LOS	Line-of-sight
MATLAB	Software/programming language
MCH	Methyl cyclohexane and methylcyclohexane/n-dodecane fuel
MJ	Mega-Joule
MOM	Method of Moments
MS	Mass spectrometer
MURI	Multi-University Research Initiative
m-X	Meta-xylene and meta-xylene/n-dodecane fuel
MXYLYL	m-methylbenzyl radical
N2	Molecular Nitrogen
NJFCP	National Jet Fuel Combustion Program
NAAQS	National Ambient Air Quality Standards
NETPSR	NETwork of Perfectly-Stirred Reactors
NIST	NIST National Institute of Standards and Technology
NO	Nitric oxide
NO2	Nitrogen dioxide
NOx	N-O emissions including NO, NO_2, and N_2O
O	Atomic oxygen
O2	Molecular oxygen
OH/OH*	Hydroxyl radical (* denotes excited state)
PAH	Polycyclic aromatic hydrocarbons
PC	Personal computer
PLIF	Planar laser-induced fluorescence
PLII	Planar laser-induced incandescence
PM	Particulate matter
PM2.5	Particulate matter with an aerodynamic diameter less than 2.5 micron
PREMIX	Premixed flame module within CHEMKIN
PMT	Photomultiplier tube
PRZ	Primary recirculation zone
PSD	Power spectral density or particle size distribution
PSR	perfectly stirred reactor
PSU	Penn State University and Product Sampling Unit
RMS	Root-mean square
RRF	Relative response factor
RZ	Recirculation zone
SCFM	Standard cubic feet per minute
SERDP	Strategic Environmental Research and Development Program
SERDP v1.0	First chemical kinetic mechanism developed under WP-1577

SERDP-2011-PAH	Current version of chemical kinetic mechanism developed under WP-1577
SHOCKAL	Computer program used to compute pre-ignition shock tube temperature
SHOCKIN	Shock Tube Modeling option within CHEMKIN
SIP	State implementation plan
SLPM	Standard liters per minute
SNETPSR	Sooting NETwork of Perfectly-Stirred Reactors
SPK	Synthetic paraffinic kerosene
SPU	Sample preparation unit
SRZ	Secondary recirculation zone
ST	Shock Tube
TCD	Thermal conductivity detector
TP	Triple point in centerbody burner flame
TPO	Temperature programmed oxidation
TQMS	Triple quadrupole mass spectrometer
TSI	Threshold Soot Index
TTL	Transistor-transistor logic
UC	University of California
UDRI	University of Dayton Research Institue
UHC	Unburned Hydrocarbons
UHP	Ultra-high purity
UIC	University of Illinois at Chicago
UNICORN	UNsteady, Ignition, and COmbustion with ReactioNs
U.S.	United States
USC	University of Southern California
UTRC	United Technologies Research Center
UV	Ultraviolet
VSU	Volatile Sampling Unit
WP	Weapon Systems and Platforms
WSR	Well-stirred Reactor
XAD-2	Polymeric sorbent used to capture semi-volatile compounds
YAG	Yttrium aluminum garnet

1 EXECUTIVE SUMMARY

1.1 Background

Gas turbine engines (GTEs) consume approximately 70% of the total fuel purchased by the DoD and are the major source of carbon monoxide (CO), unburned hydrocarbons (UHC), oxides of nitrogen (NOx), and particulate matter (PM) emissions produced at military airbases. The DoD has established goals for use of synthetic derived alternative JP-8, which will consist of blends of petroleum-based JP-8 and synthetic fuels and potentially fully synthetic fuels. These goals present new challenges for low emissions combustors that will burn alternative fuels. First, the alternative fuels, that could be in the DoD inventory in the next ten to twenty years, are in the early stages of being defined, and second, there is very little fundamental data on the combustion of possible alternative fuels. This SERDP program described in this report was designed to address these challenges by establishing a scientific base for modeling all emissions from GTEs burning alternative fuels and by developing a methodology for selecting future alternative fuels based on their emissions characteristics.

Field studies of aircraft engine emissions have identified clear effects of alternative fuels. Alternative fuels have been demonstrated to have an impact on the composition of the UHC emissions. Blending paraffinic alternative fuels into JP-8 has also been found to substantially reduce particulate matter emissions. Field and laboratory studies have also shown that each of the emissions vary substantially as engine power varies. At low power conditions, emissions of unburned hydrocarbons and CO are the highest, and they decrease with increasing power. Soot and NOx emissions are most significant at higher engine power. Thus, it is important to understand the effects of alternative fuels at both low and high power conditions. At low engine power, the field studies yielded a very surprising result - that the distributions of gaseous emissions show substantial similarity when burning conventional petroleum fuels, independent of engine type. As a consequence of this similarity, cross-plots of emissions indices against the emission index of a reference species, such as C_2H_4 or H_2CO, show linear behavior for low engine power operation.

1.2 Objectives and Approach

The objectives of this program are to: (1) establish a science-base needed to develop accurate models for PM, CO, NOx, total UHC and individual HAPs emissions from military gas turbine engines burning alternative fuels and (2) establish a science-based methodology for selecting practical alternative fuels that minimize emissions.

The research approach involves mutually supportive, tightly coupled experimental and computational efforts. A series of well-controlled laboratory experiments were designed and conducted that systematically progress in complexity in a way that permits collective analysis of the data to develop a fundamental understanding of the production of emissions from burning alternative fuels under a wide range of conditions. Experimental facilities being used in the program include: a well-stirred reactor in which chemical kinetics are the controlling process; shock tube experiments focusing on kinetics at realistic pressures; premixed and non-premixed co-flow flame experiments with dependence on kinetics and molecular diffusion at variable pressure; and two combustor test rigs - a model combustor at Penn State and the Referee Combustor at WPAFB, which include the composite effects of all the processes occurring in a gas turbine combustor operated at pressure including spray atomization, vaporization, diffusion, turbulent

mixing, stretch, kinetics, and turbulent/chemistry interactions. Early in the program, the systematic increase in complexity was extended by the addition of emissions experiments from a T-63 engine to the original program plan. In support of the SERDP program, the Air Force initiated a study of the emissions from a T-63 engine using the test fuels designed for this SERDP program as well as JP-8 and several practical alternative fuels. Thus, the test devices in this program systematically cover key chemical and physical processes from devices in which chemical kinetics are the controlling process to a small gas turbine.

In parallel to the experimental efforts, computations were performed for each of the experiments, except the Referee Combustor and the T-63 engine, using the two computational tools. The well-stirred reactor and shock-tube are modeled using the commercial CHEMKIN/SHOCKIN software package. A unique Navier-Stokes based CFD code called UNICORN was used to simulate the co-flow flames and the model combustor at Penn State. The modeling studies resulted in a hypothesis for the linear behavior of cross-plotted UHC emissions from actual engines. A new set of laboratory experiments were conducted test the hypothesis.

To achieve the objective of evaluating and developing accurate models for predicting emissions from alternative fuels, a set of alternative fuels with known chemical kinetics is required. Unfortunately, there were no practical alternative fuels with known chemical kinetics at the time the program was initiated. As a result, a set of test fuels comprised of pure components, for which chemical kinetic mechanisms exist, was used to cover a range of compositions expected in future alternative fuels. Each of the fuels consists of a binary mixture of n-dodecane and a second hydrocarbon representative of one of the four main classes of hydrocarbons that are present in alternative fuels – normal alkanes, iso-alkanes, cycloalkanes and aromatics. Normal and iso-alkanes are present in alternate fuels produced from Fischer-Tropsch (FT) processes, and cyclo-alkanes are present in alternative fuels produced from coal by liquefaction processes. The compounds selected to represent each of the major classes of alkanes present in alternative fuels were: n-heptane, iso-octane, and methyl-cyclohexane. Because the m-xylene/n-dodecane fuel is a simple surrogate for jet fuel, the combustion studies provide direct experimental evidence of the effects of changing jet fuel composition on emissions. The three purely paraffinic fuels, n-heptane/n-dodecane, iso-octane/n-dodecane, and methyl-cyclohexane/n-dodecane, represent possible alternative fuels created via a Fischer-Tropsch or coal liquefaction processes. The fuel set includes a fifth fuel, n-dodecane/n-hexadecane, to investigate the effect of fuel volatility on emissions. The test fuel set is discussed in Section 3.7.

1.3 Summary of Major Results from Research

1.3.1 Alternate Fuel Effects on Emissions in T-63 Engine Studies

The experiments conducted with the T-63 engine yielded a wealth of results on fuel effects on emissions as engine power was varied. The results from the study established a basis for comparison between the results from the laboratory devices and an actual gas turbine engine. Experiments were conducted with the four binary fuel mixtures designed to study chemical effects of alternative fuels on emissions and covered the power range from idle to 85% of maximum power

CO_2 emissions were lower by 1 to 3% for the purely paraffinic fuels compared to the JP-8 surrogate; this reduction correlates with the H/C ratio of the fuels. CO emissions were lower by approximately 10% for the purely paraffinic fuels compared to m-xylene fuel. Within measurement uncertainty, the NO_x emissions were the same for the four test fuels. PM emissions for the three paraffinic fuel mixtures were substantially lower than the PM emissions for the m-xylene/n-dodecane fuel, which is a surrogate for JP-8.

The overall trends in NOx and PM are consistent with trends found in studies of prototype alternative fuels in military aircraft engines.

The lowest level of PM emissions was observed for the test fuel comprised of normal alkanes, n-heptane/n-dodecane almost 10 times less than the m-xylene/n-dodecane fuel at 85% power. The iso-octane and methyl-cyclohexane fuels had similar PM emissions that were approximately twice as high as the PM from the n-heptane fuel. (These same relative trends in PM were observed in the co-flow flame experiments.) For all four test fuels, total UHC emissions decreased by more than an order of magnitude between idle and 85% power. The UHC emissions did not show any consistent trend among the four test fuels. Speciation of the UHC emissions showed that the major components comprising the UHC emissions were similar among the fuels and included: ethylene, formaldehyde, acetaldehyde, and methane. However, speciation of the UHC emissions also showed some direct effects of fuel composition on hazardous air pollutants (HAPs). The m-xylene and methyl-cyclohexane fuels produced approximately twice as much benzene as the n-heptane and iso-octane fuels. (The higher production of benzene was also observed in the well-stirred reactor studies.) Cross-plots of the speciated UHC emissions showed the same linear behavior that was observed in the field studies of aircraft emissions, although slopes may be different.

Another key finding from the detailed speciation of the UHC emissions was that a substantial fraction of the UHC emissions at idle and low power was from unreacted fuel. *The presence of unreacted fuel in the UHC means that the composition of any alternative fuel will have a substantial, direct effect on UHC emissions when engines are operated at idle and near-idle power levels.*

1.3.2 Alternative Fuel Effects on Emissions in Referee Combustor (Low Power)

Experiments conducted in the Referee Combustor at WPAFB provided additional insights into the effects of the fuel composition on emissions at low power. The experiments were conducted at test conditions that are similar to the idle and near-idle conditions in the T-63 experiments and included the four binary fuel mixtures designed to study effects of chemical composition as well as the fifth fuel designed to study volatility effects.

Emissions of CO_2, CO, and total UHC were similar for all of the fuels, and the data set did not show clear trends among the test fuels. However, detailed speciation of the UHC emissions showed that fuel composition was having a direct effect on some of the UHC emissions. Formaldehyde emissions were lowest for the m-xylene fuel and highest for the fuel comprised of n-heptane/n-dodecane fuel. Although the difference in formaldehyde emissions was only about 20%, the difference is important because formaldehyde is typically a large component in UHC emissions at low power. Consistent with the T-63 results, benzene was substantially higher for the m-xylene and methyl-cyclohexane fuels than for the iso-octane and n-heptane fuels. In the Referee Combustor results, the difference in benzene emission levels was nearly a factor of four. Toluene emissions were produced by the m-xylene fuel, but not for the three paraffinic fuels. In addition to effects on HAPs emissions, the detailed speciation studies also demonstrated the unreacted fuel contributes substantially to UHC emissions at near idle conditions. Analysis of the speciated UHC emissions indicates that approximately 40% of the total UHC emissions is produced by unreacted fuel. This result is consistent with the finding from the T-63 studies.

The PM emissions from the Referee Combustor provide insights into the effects of fuel composition and volatility at low power conditions. Consistent with the T-63 results, a substantial effect of chemical composition is evident in the results. For example, the PM emissions for the m-xylene fuel were more than ten times higher than those for the three paraffinic fuels. The effect of fuel volatility is also evident in these

results. For the low volatility n-hexadecane/n-dodecane fuel, the PM emissions were more than a factor of 10 larger than the emissions for the high volatility n-heptane/n-dodecane fuel. Given the low power conditions under which these experiments were conducted, the PM emissions from the paraffinic fuels are likely to consist primarily of condensed fuel.

1.3.3 Fundamental Mechanism Producing UHC Emissions at Low Power

From the beginning, a major focus of this program was to understand the fundamental mechanism underlying the linear behavior in UHC emissions observed in the field data when aircraft engines are operating at low power. When we started this research, we believed that chemical kinetics was the primary cause of the observed linear behavior. However, modeling studies revealed that quenching of the combusting fuel-air mixture is essential in the process of UHC emission formation. Through a series of systematic computational experiments, a conceptual model of the chemical and physical processes that lead to hydrocarbon emissions from gas turbine combustors was established. Contrary to our conceptual understanding at the start of the program, the studies demonstrated that regions of fuel-lean, premixed combustion are the main source of hydrocarbon emissions at low engine power, not regions of non-premixed combustion. A key insight from this computational investigation is that the hydrocarbon emissions result from fuel-air mixtures that have been mixed to very low fuel-air ratios, which are outside the flammability limits. Thus, these studies indicate that the coupling of chemical kinetics and quenching, associated with turbulence and mixing of secondary air, play crucial roles in determining engine emissions.

The importance of the coupling of chemistry and quenching led us to reevaluate our experimental plan and add experiments to verify one of the possible quenching mechanisms in the well-stirred reactor experiments. The experiments were designed to study conditions at which reaction stops because the mixture has become too fuel-lean to be self-sustaining. This condition is referred to as lean-blowout and occurs when the rate of energy release from reaction is no longer sufficient to sustain combustion at a given residence time.

Before the well-stirred reactor experiments were conducted, a series of computations were made to predict the effects of fuel composition on emissions when the well-stirred reactor is near and under lean-blowout conditions. The computations also included predictions of the fuel-air ratio at which lean blowout occurred and the emissions that were produced as the fuel-air ratio approached the value at which lean blowout occurred. Emissions predicted as the reactor approached lean-blowout showed a linear relationship in cross-plots of hydrocarbon species at different fuel to air ratios of the reactor just as was observed in field studies of aircraft emissions. The predicted emissions also indicated possible fuel effects.

The emissions data from the experiments confirmed some of the fuel effects predicted in the modeling. Iso-butene was produced only by the iso-octane fuel, and toluene was produced only by the m-xylene fuel. Benzene emissions were highest in concentration for the m-xylene fuel and the methyl-cyclohexane fuel. These trends are consistent with the T-63 and Referee Combustor results.

Computational and experimental results for the equivalence ratio and the temperature at lean blowout showed reasonably good agreement, given the high sensitivity of the results to the accuracy of the kinetic model. In the experiment, the equivalence ratio[1] at lean blowout was 0.414, 0.420, 0.422 and 0.425,

[1] Equivalence ratio is a normalized fuel-air ratio that indicates whether the fuel-air mixture has the stoichiometric amount of air ($\Phi=1$), has more air than the stoichiometric amount (fuel lean, $\Phi<1$) or has less air than the stoichiometric amount (fuel rich, $\Phi>1$).

respectively, n-heptane/n-dodecane, methyl-cyclohexane/n-dodecane, iso-octane/n-dodecane and m-xylene/n-dodecane. The simulations matched the relative ordering of the fuels in terms of equivalence ratio at lean blowout, but the simulations predicted that blowout would occur at lower equivalence ratios in the range of 0.34 to 0.37. The experiments showed that reactor temperature at lean blowout ranged from 1401K for the n-heptane fuel to 1415K for the m-xylene fuel. Because the simulations predicted blowout at lower equivalence ratios, the simulations also predicted lower temperatures at blowout than were observed in the experiments. In spite of the differences in predicted and experimental values of equivalence ratio at which lean blowout occurs in the well-stirred reactor, the predicted levels of major emissions like CO and ethylene show good agreement with the experiments.

1.3.4 Effects of Alternative Fuels at High Power

At high power levels in gas turbine engines, the major emissions are PM and NOx. A major constituent of PM emissions will be soot that forms in fuel-rich regions. Under high power conditions, the UHC and CO emissions are much lower than at idle and lower power due to increased temperatures in the combustor. At high power conditions, the composition of UHC emissions will include greater amounts of high molecular weight species characteristic of fuel-rich combustion. The shock tube, co-flow flame, and model combustor experiments were designed to study fundamental processes related to emission formation at high power.

Shock tube experiments provided data on variation in reaction products under conditions where chemical kinetics alone determine the differences among the fuels. Experiments and simulations were completed over a range of initial temperatures at a fuel-rich equivalence ratio of 3. Detailed speciation was completed for all fuels from CO and methane to high molecular weight intermediates such as coronene that are important for soot formation. Simulations and reaction pathway analyses were completed for the fuel set designed to study chemical effects on emissions, using the latest version of the chemical kinetic mechanism developed during this program (SERDP 2015). Under the conditions selected for the shock tube studies in this program, both the experiments and simulations indicate that the three paraffinic fuels share similar concentrations of reaction intermediates. This similarity can be attributed to the common presence of n-dodecane in these fuels and the commonality of reaction products among the alkanes used in this study. Contrary to expectations, the m-xylene fuel showed substantially higher production of CO_2 than the paraffinic fuels at low temperature. This higher reactivity was not captured by the chemical kinetic model indicating a need for further improvements in the low-temperature kinetics.

In addition to the shock tube experiments, the experiments in the non-premixed and partially premixed co-flow flames also provide data on the effects of alternative fuels on emissions under high power conditions, specifically on soot volume fraction and qualitative aromatic species including polycyclic hydrocarbons (PAHs). Measurements were completed for the five test fuels. These data show that replacing an aromatic species, m-xylene, with any type of paraffin, normal, iso or cyclo, substantially reduced the soot volume fraction and the aromatic levels in the flames. The trends in soot emissions are consistent with the T-63 results at high power and with trends in field studies of engine emissions.

Initial simulations of the co-flow flame experiments were obtained with the UNICORN code using a chemical mechanism from a research group at the Polytechnic Institute in Milan, Italy. (At the time that the simulations were performed, the mechanism developed in this program did not yet include kinetics for all of the compounds in the test fuels.) Comparison of experimental and modeling studies in the co-flow flame demonstrated that the simulations of aromatic species and soot are in reasonably good for the three

purely paraffinic test fuels. However, the model did not predict soot as well for the test fuel that contains m-xylene, which is an aromatic species. The simulations substantially under-predicted soot for both non-premixed and partially premixed co-flow flames, which is a major shortcoming evident not only in our work but generally throughout the soot modeling community.

Subsequent work within this SERDP program to improve the chemical kinetic mechanism and to enhance the soot model in UNICORN led to dramatic improvements in the ability to capture the effects of the m-xylene on soot emissions. For the first time, the simulation of the co-flow flames not only capture the increase in soot associated with the aromatic species, they also capture the change in the structure of the soot field that occurs. For the sooting m-xylene flame, the soot peak is located in an annular region whereas for the non-sooting flames of the paraffinic fuels, the soot field is annular at lower heights in the flame, but soot is distributed throughout the flame at higher heights.

The model combustor experiments and simulations were directed at formation of soot and the effect of fuel volatility on soot formation. The simulations conducted using UNICORN were completed prior to the experiments. The simulations predicted a reduction by a factor of 2 in average soot emissions at the combustor exit plane between the m-xylene fuel and the paraffinic fuels. The magnitude of the emissions for the alkane fuels was matched well by the simulations. The simulations predicted a soot volume fraction of approximately 1ppm at an equivalence ratio of 1.6; whereas, the experiments showed average soot levels of 0.7 ppm. Given the complexity of the processes that must be simulated in the model combustor, this agreement is excellent. The simulations of the soot levels from the m-xylene fuel, which is a simple surrogate for sooting of JP-8, predicted soot levels at the combustor exit of approximately 2 ppm at an equivalence ratio of 6. The most recent experiments in the model combustor with JP-8 show an exit soot level at an equivalent ratio of 1.6 to be approximately 4 ppm. So the increase of soot between the aromatic fuel and the paraffinic fuels is somewhat under-predicted.

The experiments in the model combustor included experiments with the n-heptane/n-dodecane and n-hexadecane/n-dodecane fuels to investigate the effect of fuel volatility on soot emissions. The results show no effect of volatility on soot within experimental uncertainty. Therefore, the hypothesis of increasing soot volume fraction with decreasing fuel volatility was not confirmed. It is possible that the design injector and bluff-body in the model combustor leads to such rapid levels of droplet vaporization and mixing that the fuel-air mixture is nearly homogeneous prior to the start of combustion. These results could not be simulated due to the fact that the kinetic mechanism had not been extended to include n-hexadecane.

1.4 Summary of Major Conclusions and Contributions of this Project

The findings from the experimental and modeling work conducted in this program and reported in 10 peer review journals and 30 conference papers support the following statements when comparing the binary mixtures of paraffinic compounds representative of alternate fuels to the m-xylene fuel, which is a surrogate for JP-8:

- Effects on NOx, CO and total hydrocarbons were small, generally 10% or less.
- Effect on PM emissions was substantial, with reductions in PM emissions by one order of magnitude.
- Low molecular weight components of UHC emissions were not strongly affected.

- Some high molecular weight UHC species increased in concentration depending on the fuel composition, e.g., benzene emissions were higher for the m-xylene fuel and the methyl-cyclohexane fuel.
- Unique UHC species were present for some of the fuels, e.g., iso-butene for the iso-octane fuel and toluene for the m-xylene fuel.

The experimental results on the impact of fuel volatility while holding chemical composition fixed support the following statements:

- Decreasing fuel volatility resulted in substantially increased PM emissions for the Referee Combustor operating at condition near engine idle although these PM emissions are likely due to increased UHC (or fuel) emissions rather than soot.
- Decreasing fuel volatility did not affect soot emissions for a model combustor operating at rich fuel-air ratios corresponding to high power engine operation. Due to the unique design of this combustor, however, this conclusion should be considered as tentative pending tests in other types of combustors.

In addition to these specific findings on alternative fuel effects, the program led to three major insights that advance the state of the art understanding of engine emissions:

- The experimental work in the T-63 engine and the Referee Combustor demonstrated that substantial fractions (30 to 50%) of the UHC emissions can be traced to unreacted fuel. This finding means that the composition of any fuel directly affects the UHC emissions, including emissions of HAPs that are present in the fuel.
- The experimental and modeling studies conducted to understand the linear behavior in UHC emissions at low power led to the important new insight that UHC emissions form in a gas turbine combustor when reacting premixed fuel-air mixtures are quenched. Thus the emissions are not determined by reaction kinetics alone, but rather by coupling of chemical kinetics, fluid mechanics, and flame extinction processes. Furthermore, multiple quenching mechanisms can lead to UHC emissions, including mixing to very lean fuel-air ratios, quenching due to flame propagation into regions of low fuel-air ratio, and flame stretch. Accurate modeling of the emissions from a gas turbine combustor will require that each of the multiple quenching mechanisms be modelled accurately. The current program included modeling and simulations of quenching via mixing.
- The experimental and modeling work related to chemical effects on PAH and soot formation led to substantial progress toward resolving the longstanding issue within the combustion community related to modeling the effect of aromatic species on soot concentration and the spatial distribution of soot. Enhanced PAH reactions in the chemical kinetic mechanism and improvements in the soot model to track particle size distribution led to substantially improved ability to predict soot concentrations and distributions in all of the co-flow flames.

In addition to these fundamental insights the program also made the following important fundamental contributions:

- The kinetic model with detailed PAH chemistry that was developed in this program is a major contribution from this work because it was a critical element in the advancement of the soot modeling capability. Development of this model was not a part of the original program design, but

became necessary when kinetic model development within the combustion community did not evolve as quickly as anticipated. In addition, the modeling studies have demonstrated that this mechanism captures many key trends in gas-phase emissions from gas-turbine engines.

- The data base from the various experiments made using the same set of test fuels is a unique resource for researchers who are simulating gas turbine combustion because of the breadth of chemical and physical processes encompassed across the experimental devices and because of the wide range of experimental conditions used.
- To our knowledge, no research teams other than this team and the SERDP-funded team led by Venkat Raman (WP-2151) are attempting to simulate speciated emissions from gas turbine engines. So the work is unique in the field.

The key findings and contributions from this program have substantially extended the fundamental knowledge required to evaluate a science-based methodology for selecting alternative fuels based on their emissions characteristics. The next section describes a possible methodology built upon the results of this program.

1.5 Science-based Methodology for Evaluating Alternative Fuels

A science-based methodology for evaluating alternative fuels based on their emissions and performance would utilize many of the same experiments included in the current program as well as the modeling tools. One possible conception of the overall program is illustrated in the figure below, which is the approach that was developed for the National Jet Fuels Combustion Program. Members of this SERDP project team (Mel Roquemore, Tim Edwards and Med Colket) had leadership roles in the development of the methodology. This science-based methodology is built around the development of advanced combustion models that engine manufacturers (OEMs) can use to simulate the performance of their engines running alternate source fuels. They compare the modeling results to priority data and decide if additional testing and development are required. The present focus of the modeling effort for the National Jet Fuel Combustion Program (NJFCP) is prediction of fuel-dependent effects on lean blow-out and cold ignition. Development of the advanced combustion models and the requisite chemical kinetic models for prediction of emissions would be conducted using a process very similar to that used in the SERDP program that is the subject of this report.

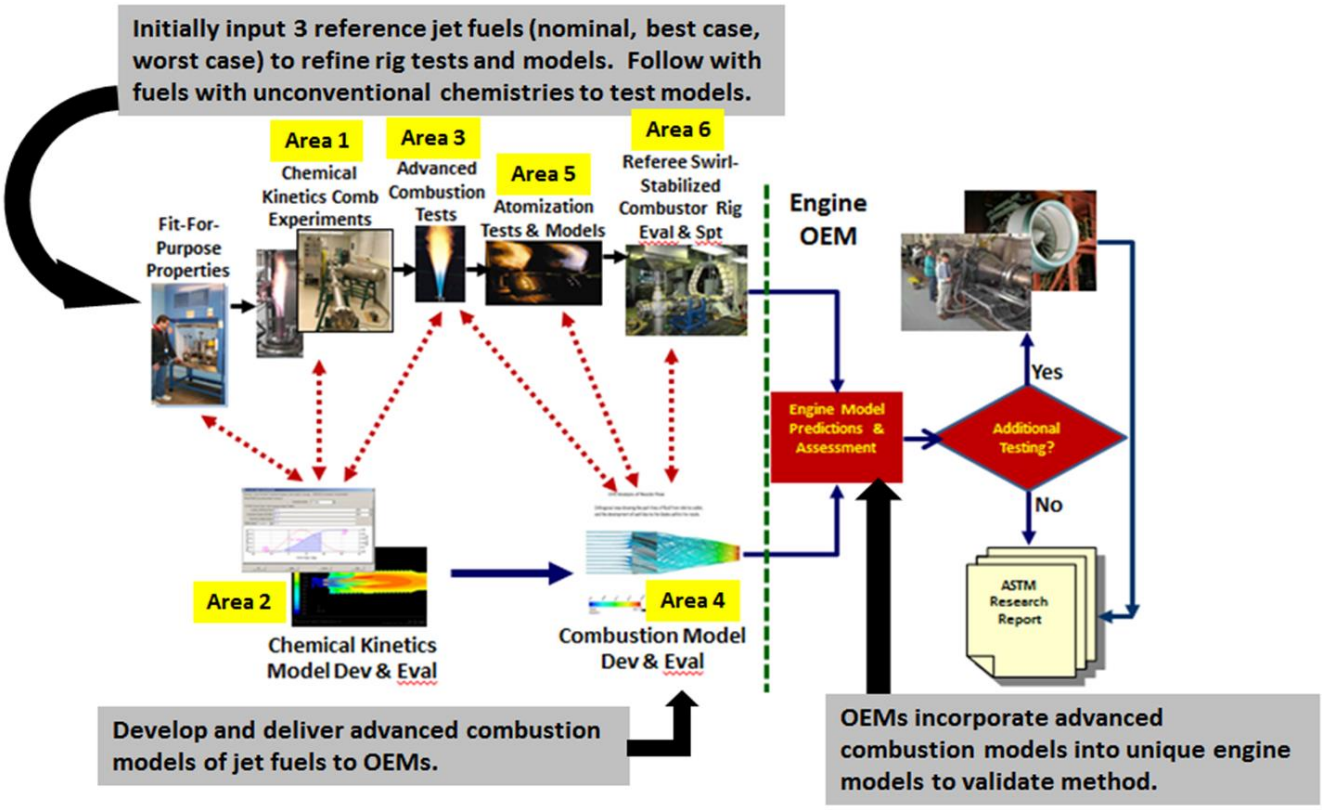

Figure 1.1. National Jet Fuel Combustion Program Organization Chart

Key fundamental advances required for successful development of the advanced combustion models include:

- Demonstrate the capability of formulating chemical kinetic models (detailed/skeletal/reduced) that can be used to make accurate estimates of emissions (soot, hazardous air pollutants, etc.)

from combustion devices burning "practical" liquid hydrocarbon fuels with a broad range of physical and chemical properties.

- Quantify the impact of reducing the number of species in chemical kinetic models on the accuracy associated with emissions.

- Identify and quantify the liquid fuel parameters that have the largest impact on emissions and provide insights into how fuels could be optimized to give low emissions in combustion systems.

- Develop and evaluate a tool that offers the potential of being used to optimize combustion system design and fuel characteristics for low emissions.

- Develop models that are applicable to combustor relevant higher pressures and temperature conditions for practical alternative jet fuels similar to those developed on the Navy's Mobility Fuels program or used in the NJFCP.

- Demonstrate models' ability to capture variations in emissions with changes in engine power levels (P3, T3, flow-rates, etc.)

- Develop and demonstrate a new, innovative approach that can be used to estimate soot emissions, with a better than the current-state-of-the-art accuracy, when burning fuels with a broad range of physical and chemical properties in different combustion systems.

1.6 Contents of Final Report

The contents of the Final Report include our final results from experimental and simulation work at the end of the project as well as summaries of key intermediate results that illustrate how the work progressed over the five years of the project. As the project evolved, we gained new insights and encountered challenges that led us to improve, and in some cases, to redirect our efforts. In several cases, we reran complete sets of experiments and simulations. For the most part, the results from the earlier sets of experiments are not represented in this report. However, these intermediate experimental results are documented in our two interim reports dated October 2012 and June 2014 on Project WP-2145 page on the SERDP website.

2 INTRODUCTION

2.1 Motivation for Program

Gas turbine engines (GTEs) consume about 73% of the total fuel purchased by the DoD and are the major source of carbon monoxide (CO), unburned hydrocarbons (UHC), oxides of nitrogen (NOx), and PM2.5 emissions (soot) produced at military airbases. SERDP has recognized the impact of GTEs on the environment and has sponsored several fundamental programs with a long-term goal of reducing emissions by advancing the scientific base needed to develop improved computational tools for designing low volatile and nonvolatile PM2.5 particulate combustors burning JP-8 fuel. Indeed, several nonvolatile PM2.5 soot models have been successfully tested on the SERDP Soot Science Program. Recently, the DoD established goals for transitioning from petroleum derived JP-8 fuel to synthetic derived alternative JP-8, that will consist of blends of petroleum JP-8 and synthetic fuels and fully synthetic fuels. This presents new challenges for designing low emissions combustors burning alternative fuels. First, the alternative fuels, that could be in the DoD inventory in the next ten to twenty years, are in the early stages of being defined and second; there is very little fundamental data on potential alternative fuels. This program seeks to address these challenges by establishing a scientific base for modeling all emissions from GTEs burning alternative fuels and providing a methodology for selecting future alternative fuels based on their emissions characteristics.

2.2 Program Objectives

The overarching goal of the program is to enhance the accuracy of prediction of emissions of total unburned hydrocarbons (UHC), hazardous air pollutants (HAPs), non-volatile particulate emissions (PM) and carbon monoxide (CO) emissions by establishing well validated science-based emission models and a methodology that can be used to design for low HAPs, total UHC, CO, NOx and PM emissions in retrofit, growth or new military combustion systems burning alternative fuels. The specific objectives of this program are to: (1) establish a science base needed to develop accurate models for total UHC, HAPs, PM and CO emissions from military gas turbine engines burning alternative fuels and (2) establish a science-based methodology for selecting practical alternative fuels that minimize emissions.
The major deliverables of this work are:

a) Fundamental insights into the effects of fuel composition and volatility obtained from coupled modeling and experimental efforts in six different reactors/combustion systems: shock tube, well-stirred reactor, co-flow jet diffusion flames, a model combustor, a “referee” combustor and a small gas turbine engine.
b) An extensive validation database from the same six devices for use by other researchers in future development of chemical mechanisms for alternative fuels.
c) A methodology for evaluating alternative fuels based on emissions.
d) A series of archival papers to place the emissions/fuels models and the validation data into the open literature and to disseminate the fundamental insights derived from this work.

2.3 Background

2.3.1 Linear Behavior of UHC Emissions at Low Power

Herndon et al. (2009) demonstrated an unexpected characteristic of the composition of UHC emissions when comparing different aircraft. They found that the concentrations of many hydrocarbons were linearly related to each other, regardless of engine design, over a range of operating conditions corresponding to low power conditions. Such a correlation is shown in Figure 2-1.This surprising relationship was observed just a few years ago and to our knowledge this relationship has not been explained, nor have reasons been given why the correlation fails for some UHCs, e.g., butenes, pentenes, alkylated aromatics, naphthalene (Herndon, et al., 2009).

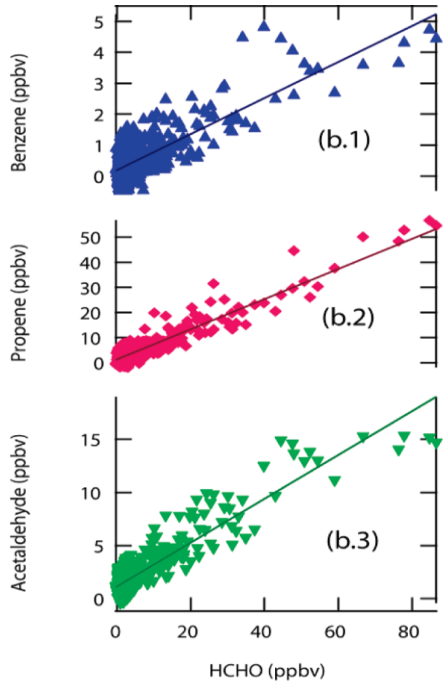

Figure 2-1. UHC emission data for a broad range of engines at Oakland airport. (Herndon et.al., 2009).

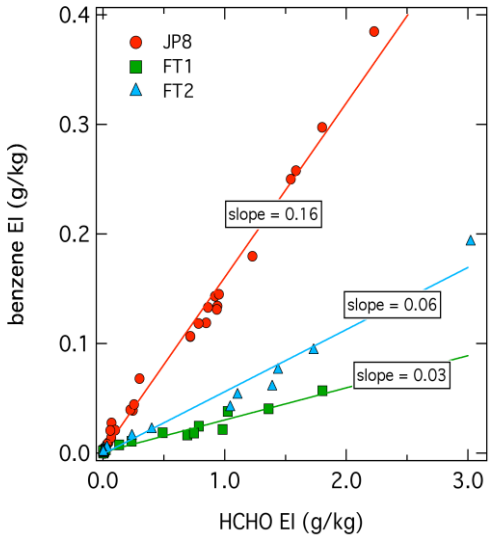

Figure 2-2. Variable Benzene to Formaldehyde ratios for JP-8 and two FT fuels (Miake-Lye, 2010).

What adds to this puzzle is that similar measurements in the exhaust of engines fueled by the FT fuels results in some different correlations (Miake-Lye, 2010), as shown in Figure 2-2. This figure shows a relative change in benzene, but the data shows shifts in many other species as well (propenes, butenes, alkylated aromatics, naphthalene). As some of the compounds may be HAPs (e.g., benzene, formaldehyde, acetaldehyde, etc.) or may be converted to HAPs in the atmosphere, this change in speciation may well have an impact on the urban atmosphere. Hence, it is prudent to develop an understanding of the mechanisms by which these changes occur as well as an understanding of the likely impact on the atmosphere.

Fundamental combustion science provides some insights into possible reasons behind these trends and will be explored as part of the work. Figure 2-3 shows the overall process of combustion for a hydrocarbon fuel (see e.g., Glassman, 1987 or Turns, 1996). When sufficient oxygen is present, at stoichiometric or fuel-lean conditions, combustion of the fuel proceeds initially via radical driven processes that form unsaturated compounds. These compounds are oxidized to form intermediates that contain a carbonyl group such as formaldehyde and acetaldehyde. These compounds continue to react releasing CO. Thus, formaldehyde is a good marker for the extent of reaction. If the fuel-air ratio is much greater than the stoichiometric requirement, that is, fuel-rich region, the oxidation of the fuel cannot be completed. The unsaturated intermediates build to sufficient levels that their recombination reactions dominate over oxidation which leads to the formation of polycyclic aromatic hydrocarbons (PAH) and eventually to soot particles.

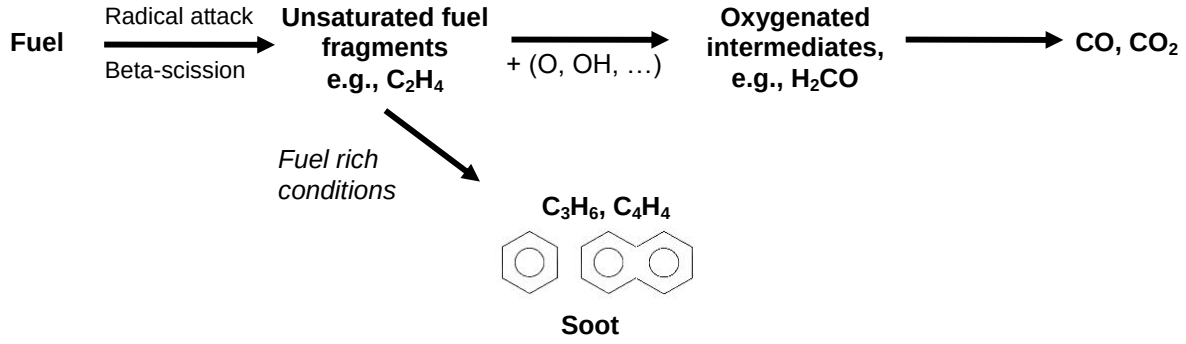

Figure 2-3. General reaction scheme for high temperature hydrocarbon oxidation for fuel-lean and fuel-rich conditions.

Although the primary combustion zone of a gas turbine combustor is overall fuel-rich, locally it will have a wide range of local air-fuel ratios. Therefore, the primary zone will have regions that proceed down the oxidation path forming oxygenated intermediates and CO. There will also be regions that have high fuel-air ratios in which large concentrations of unsaturated intermediates, PAH and soot exist. The mixing of secondary air and liner cooling air can contribute to local quenching of the reaction process. When a fuel-rich region is quenched by cooling air, it will lead to UHC emissions that are dominated by unsaturated intermediates such as ethylene, butadiene, and benzene. When a fuel-lean region is quenched, the UHC emissions will contain more CO and oxygenated intermediates, such as aldehydes.

2.3.2 Unburned Fuel contribution to UHC Emissions

In the course of conducting our work on this program, the potential for unreacted fuel to contribute to the total UHC emissions became evident. As will be shown later in this report, the data from the T-63 engine shows clear evidence of fuel that had completely escaped the combustion process. When aircraft emissions regulations were first instituted in the 1970's, the detailed speciation of UHC constituents was not a concern. In the early 1990s, Spicer et al. (1992, 1994) provided the first detailed organic species composition data, and this compositional "fingerprint" included a set of longer chain hydrocarbon species that overlapped with species in the fuel composition. However, no attempt was made at that time to connect

the measured species with the details of the combustion process.

The linear behavior discussed in 2.3.1 above helped to draw additional attention to the organic speciation of the emissions, and resulted in an update of the EPA SPECIATE profile for aircraft engine emissions (Knighton et al, 2009). However, this linear behavior was based on a variety of species measured primarily with a Proton Transfer Reaction Mass Spectrometer (PTR-MS: Knighton et al., 2007), which is not sensitive to paraffins and other important simple-HC fuel species. Thus, linear scaling was developed based on partially reacted fuel components, which excludes many species that represent the basic fuel constituents themselves.

An important question is, do the fuel constituents that are emitted in the exhaust follow the same linear scaling as the partially oxidized species? As will be discussed later in this report, at idle conditions, the fuel constituents in the exhaust appear in proportions that are commensurate with the proportions in the fuel itself. This suggests that some fuel is passing through the engine without being affected by combustion kinetic processes. So, it is important to understand whether this class of compounds in the exhaust emissions behave the same or differently compared to those partially reacted species that have been shown to have a linear scaling.

As discussed in 2.3.1, a combination of kinetics and fluid mechanics (quenching) come together to produce the organics described by the linear scaling. For the fuel compounds, their undisturbed proportions suggest that fuel is passing through the engine totally unaffected by chemical kinetics. Thus, their behavior and dependence of engine power may not be identical to those species that are controlled by both kinetics and fluid mechanics. This general area has not been explored to date and may suggest that there is more than one class of organic emissions.

The updated SPECIATE profile was developed based on the linear scaling argument, and it was assumed that all organic species, including fuel constituents, scaled with the same power dependence. This was assumed due to a lack of detailed power dependence of the fuel constituents. The present study will provide additional data on the fuel constituents and provide more insight on low power organic emissions behavior. This may result in a second update of the SPECIATE profile and a better representation of aircraft organic emissions when aircraft emissions assessments are performed for the EPA.

More specifically, this avenue of research will more completely explore the UHC emissions and will provide better insight into how chemical kinetics and/or fluid mechanics can affect these emissions in different ways for different species. Since all organic species are not equally important from environmental and human health (e.g. HAPs) perspectives, it is important to understand if different classes of organic species behave differently. And, further, it is important to have a fundamental understanding of how combustor processes (chemistry and flow) can affect combustion efficiency and overall engine emissions performance. Such a fundamental understanding will allow for improved combustor designs and emissions performance for future engine technology.

2.3.3 Emissions Trends at High Power

In general, as engine power increases, the emissions indices of CO and UHC, where emission index is g of emission per kilogram of fuel, decrease dramatically. These trends for CO and UHC are illustrated in Figure 2-4 and Figure 2-5, respectively, with data taken during a study of two FT fuels. The decrease in the emission indices of CO and UHC is generally attributed to increasing temperatures and pressures in the combustor as the fuel flow increases with power. As power increases emissions of NOx and particulate matter increase. Bulzan et al. (2010) report that for the FT fuels that they studied, NOx emissions were

"fairly similar for all of the fuels (p.5)." However, for particulate matter, substantial differences were identified among the fuels. The variation in black carbon (soot) in shown in Figure 2-6.

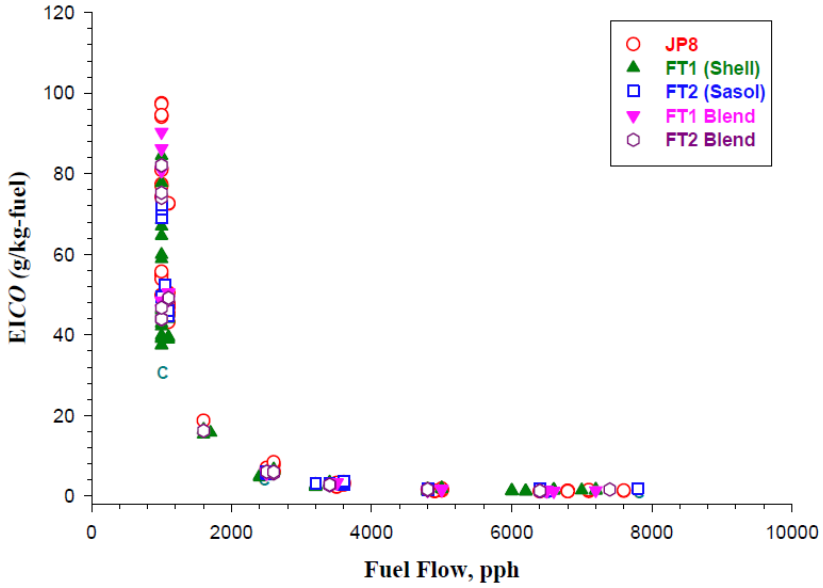

Figure 2-4. Variation of Emission Index of CO with engine power for JP-8, two FT fuels and two JP-8/FT blends. (Bulzan et.al., 2010).

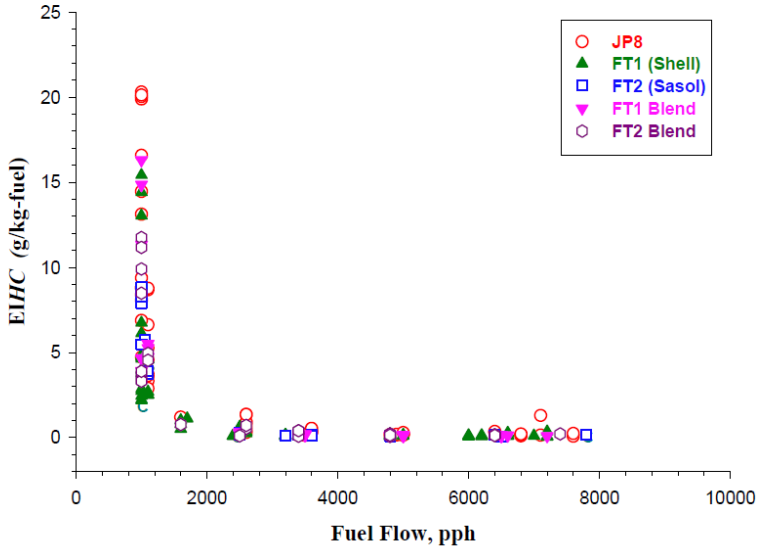

Figure 2-5. Variation of Emission Index of UHC with engine power for JP-8, two FT fuels and two JP-8/FT blends. (Bulzan et.al., 2010).

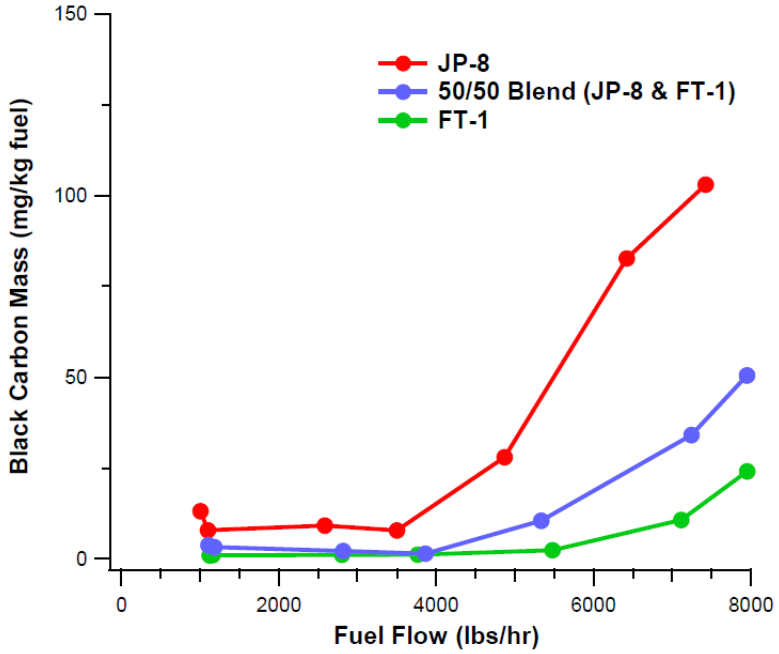

Figure 2-6. Variation of Emission Index of black carbon portion of PM with engine power for JP-8, two FT fuels and two JP-8/FT blends. (Bulzan et.al., 2010).

2.4 Overall Research Approach

Our overall research approach involves mutually supportive, tightly coupled experimental and computational efforts. Our team designed and conducted a series of well-controlled laboratory experiments that systematically progress in complexity in a way that permits collective analysis of the data to develop a fundamental understanding of the production of emissions from burning alternative fuels under a wide range of conditions. Experimental facilities being used in the program include: well-stirred reactor experiments that highlight chemical kinetics; shock tube experiments with kinetics at realistic pressures; premixed and non-premixed jet flame experiments with kinetics and molecular diffusion at pressure; a model combustor that include kinetics, diffusion, flame stretch, laminar and turbulent flows, vaporized and liquid fuel, and a recirculation zone; and a "Referee Combustor", developed at WPAFB in collaboration with GTE manufacturers, that provides the composite effects of all the processes occurring in a gas turbine combustor operated at pressure including spray atomization, vaporization, diffusion, turbulent mixing, stretch, kinetics, and turbulent/chemistry interactions.

The approach of conducting experiments that systematically progress in complexity was extended by adding emissions experiments with a T-63 engine. In support to the SERDP program, the Air Force initiated a study of the emissions from a T-63 engine using the alterative binary fuel blends designed for the SERDP program as well as JP-8 and several practical alternative fuels. Thus, the test devices in this program systematically range from laboratory burners and single swirl cup rigs, to full engine tests. The

T-63 engine studies were conducted early in the program to allow a comparative analysis of emissions from an actual engine and those from fundamental laboratory burner experiments.

In parallel to the experimental efforts, computations were performed for each of the experiments, except the Referee Combustor and the T-63 engine, using the two computational tools. The well-stirred reactor and shock-tube are modeled using the commercial CHEMKIN/SHOCKIN software package. A novel Navier-Stokes based CFD code called UNICORN was used to simulate the co-flow flames and the model combustor at Penn State. The modeling studies resulted in a hypothesis for the linear behavior of cross-plotted UHC emissions from actual engines. A new set of laboratory experiments were conducted to test this hypothesis.

A final key element of our overall approach is a carefully selected fuel set that encompass the range of compositional variation expected among aviation fuels from alternative sources. The fuel set also includes a fuel with a high final boiling point to investigate the effect of volatility on emissions.

3 EXPERIMENTAL FACILTIES AND METHODS

Experimental studies in this program were conducted in a shock tube, a well-stirred reactor, laminar non-premixed and partially premixed flames, a model combustor, a "referee" combustor, and a small gas turbine engine, the T-63. Each of these experiments and the associated the experimental procedures and diagnostic methods are described in a separate subsection. The final sub-section provides details on the fuel set that was selected for the project along with the rationale for selecting the fuels.

3.1 Shock Tube Studies

3.1.1 Shock Tube Facilities

3.1.1.1 UDRI Heated Shock Tube Facility

Effects of fuel composition reaction intermediates were investigated using the University of Dayton Research Institute's (UDRI) high-pressure single-pulse reflected shock tube. The entire tube structure was fabricated out of 304- stainless steel (1.27 cm in thickness) and has provided excellent structural strength and corrosion resistance. It consists of a driver section (7.6 cm ID × 94 cm long), a driven section (5.08 cm ID. × 275 cm long) and a test section (5.08 cm ID × 91.44 cm long), which houses the test gas. All the above mentioned sections are equipped with a high temperature pressure gauge (Omegadyne PX1004). The driven section also includes a 30.5 cm ID × 61 cm long dump tank which attenuates the reflected wave and prevents further heating of the test gas. A pneumatically activated ball valve separates the driven section from the test section. The pneumatic valve is controlled by a dedicated fire control system. For this study, copper diaphragms (8, 10 and 12 mil) were burst using an electrical diaphragm bursting system whose activation is regulated according to the pneumatic ball valve status. The driver and the driven section (including the test section) have two dedicated evacuation systems composed of two vacuum pumps, and a turbomolecular pump for the driven and test section only.

A separate Sample Preparation Unit (SPU) was used to pre-vaporize the fuel in order to ensure that a homogeneous gaseous mixture was introduced into the test section. The SPU included an injection port, a custom-made glass sample receiver, a 15 L silico-steel chemically inert gas handling canister (Restek TO-Can), a high temperature pressure gauge (Omegadyne PX1004), and a stainless-steel manifold for gas/sample inlet into the canister/test section connected to a dedicated vacuum pump.

In order to study low vapor pressure fuels, the shock tube and the SPU were wrapped in a custom designed heating jacket and the system was maintained at 145 °C. The heating jacket has a 2.5 cm thick insulation and also heating elements, control and measuring thermocouples. The control thermocouples are linked to a temperature control system which consists of 12 micro-controllers (Fuji, model PXR3) and a thermal cutoff option. Schematics of complete UDRI heated shock tube and the Sample Preparation Unit are shown in Figure 3-1 and Figure 3-2 respectively.

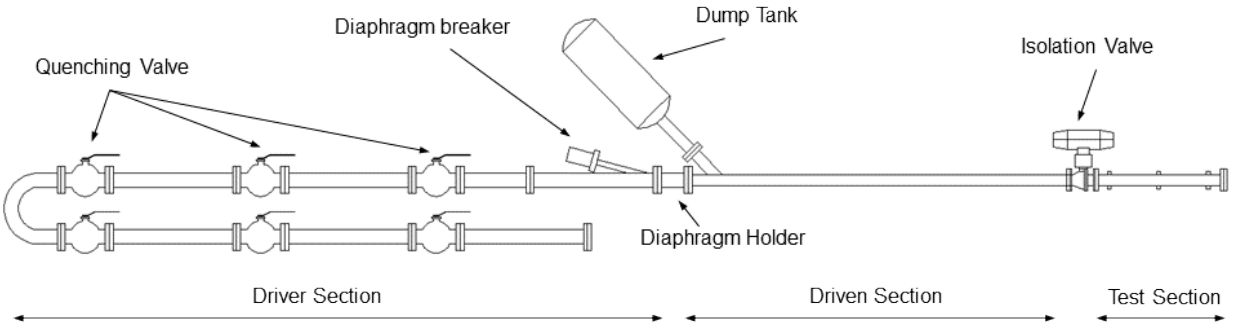

Figure 3-1. Schematic of the heated shock tube.

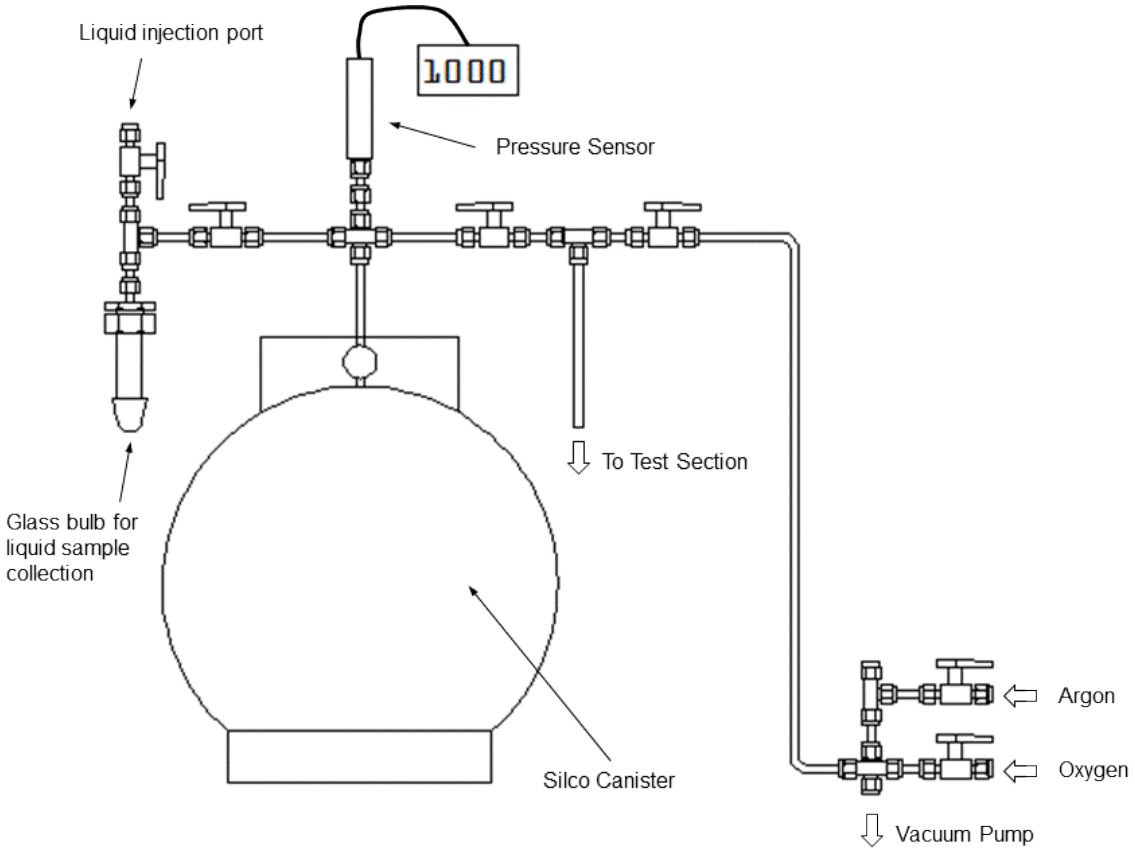

Figure 3-2. Schematic of the sample preparation unit (SPU).

3.1.2 Experimental Methods

3.1.2.1 Heated Shock Tube Operation

A copper diaphragm appropriate for the test conditions must be inserted between the driver and driven sections before each experiment. The tube is then evacuated using a turbo-molecular pump backed by a mechanical vane pump for the driven and test sections (pressure~ $1x10^{-6}$ torr) and a set of mechanical vane pumps for driver and breaker sections (pressure~ $1x10^{-3}$ torr). The fuel mixtures, Argon (Airgas, UHP grade) were made manometrically using the pressure reading from the high temperature pressure transducer located at the SPU. A certain amount of liquid fuel is injected through the fuel injection port into the glass sample receiver. Fuel vaporizes and a predetermined amount of Argon is introduced in the SPU from a separate Argon tank.

The test section is then filled with the fuel mixture containing the fuel and argon, from the dedicated SPU, through a delivery valve connecting the SPU with the test section. The oxidizer, Oxygen, is filled from a separate oxygen tank (Airgas, research grade) connected with the SPU, through the supply lines connected with the same delivery valve. The fuel mixture with oxygen is kept in this configuration for about half-an hour. This allows the fuel-argon mixture to mix thoroughly with the oxygen inside the test section via diffusion. The gas leak rate is maintained below 0.01 torr per minute across all sections and valves of the shock tube in the current study. The gases were metered based on calculated partial pressure using strain gage panel meter (Omega, DP25B-S) with a readout resolution of 0.1 Torr and 0.1 Psi for driven/test section and driver section, respectively.

The fire control system closes the pneumatic test section valve, approximately 0.5 seconds after the rupture of diaphragm and subsequent shock initiation. This seals the combustion products in the test section.

3.1.2.2 Diagnostic Techniques

The incident/reflected shock wave events were monitored using a four-channel digital oscilloscope (Tektronix, DPO2000). Incident velocities were measured by dividing the distances between the three high temperature piezoelectric pressures transducers spaced over the last 81 cm of the side wall by the arrival time of the shock wave past the transducers. Figure 3-3 displays the definition of the so-called "incident times," *i.e.*, the time taken by the incident shock waves to travel from a side pressure transducer to the end wall of the test section. Linear regression correlation between the incident shock velocity and axial distance was used to calculate an extrapolated incident shock velocity at the end wall of the test section. Figure 3-4 shows an example of the linear correlation with uncertainties for each average velocity and their extrapolation to the end wall velocity. Uncertainty of the average velocity was based on the uncertainty in distance measurements (between piezoelectric pressure transducers: 0.001 m) and the maximum rise time of the piezoelectric pressure transducers signal (1 μs).

An in-house MATLAB based code was used to compute the incident shock velocity (V_{SHOCK}) and pre-ignition temperature (T_5) and pressure (P_5), corresponding to the post-reflected shock conditions. The relationships used to compute T_5 and P_5 are based on the one-dimensional ideal shock equations implemented in the SHOCK application within CHEMKIN-PRO (Reaction Deign, 2011). The information provided to the code was the measured incident times, the initial temperature and uncertainty (416.15 ± 4 K), initial pressure (P_1 ± 0.1 Torr), and the composition of the test gases in terms of molar fraction of fuel

components, oxygen and argon. The code also performed an uncertainty analysis on the pre-ignition conditions (incident shock velocity, temperature and pressure).

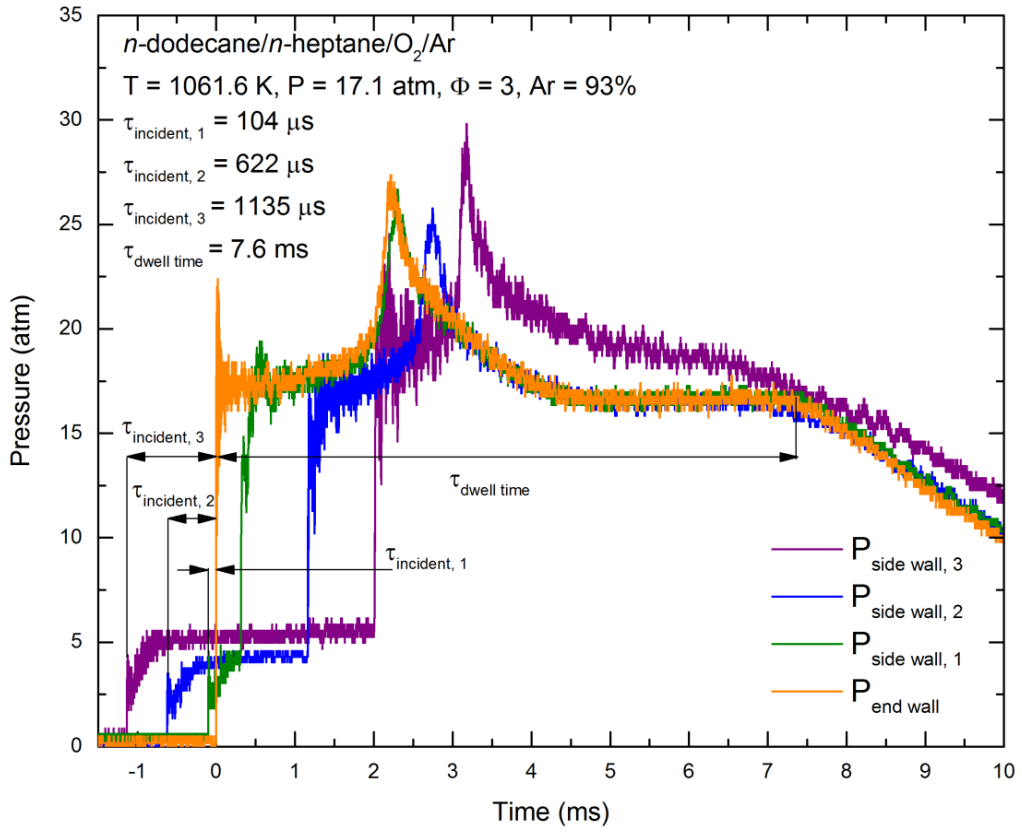

Figure 3-3. Example of time interval measurements of the incident shock wave passage and total experimental observation time (dwell time).

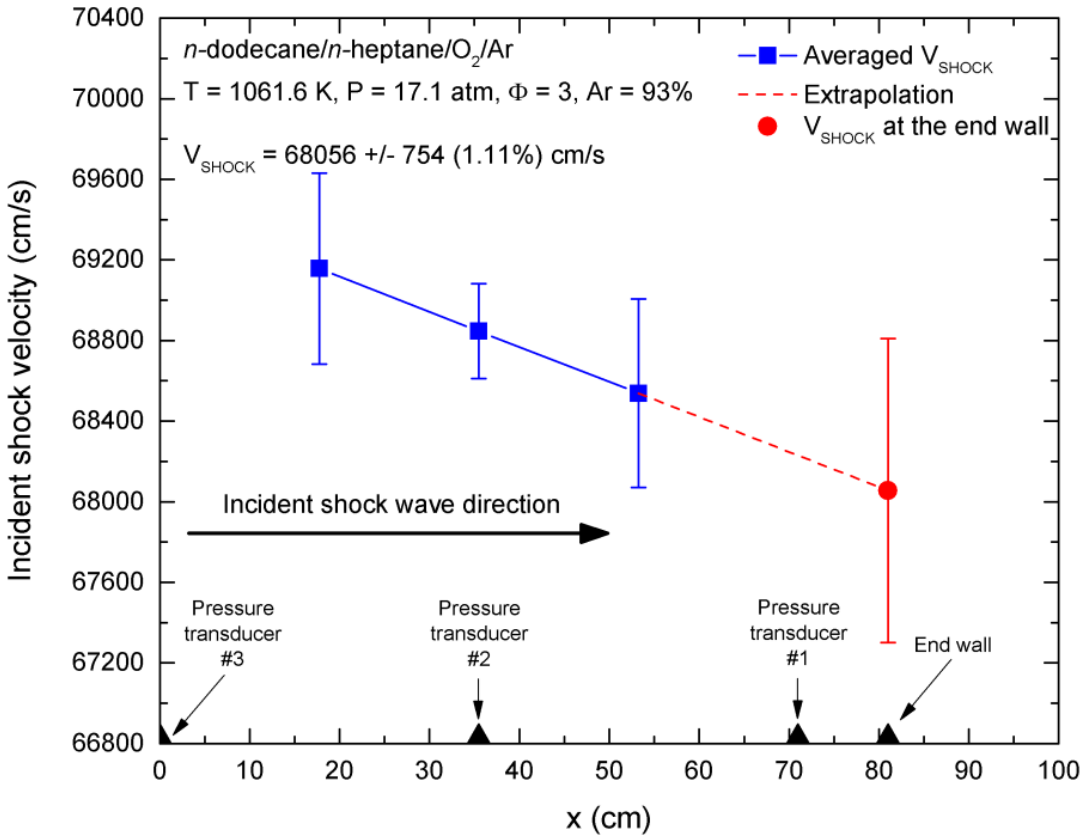

Figure 3-4. Example of linear regression analysis used to calculate the incident shock velocity at the end wall of the test section.

The ignition delay times were measured using the chemiluminescence emission from excited OH* and the pressure time history recorded at the test section end wall. A photomultiplier tube (Hamamatsu, H5783-04) fitted with a 20-nm band pass interference filter centered at 307 nm was used to detect OH A-X chemiluminescence. Photo detectors viewed emission through an optical cable connected to a fused quartz window mounted at the test section end plate. Ignition delay time was defined as the time interval between the arrival of the incident shock wave at the test section end wall and the onset of ignition. Arrival of the incident shock wave was recognized as the first spike in pressure signal, whereas the onset of ignition was defined as the maximum slope of the pressure and OH* emission rise extrapolated to the pre-ignition baseline, as shown in Figure 3-5.

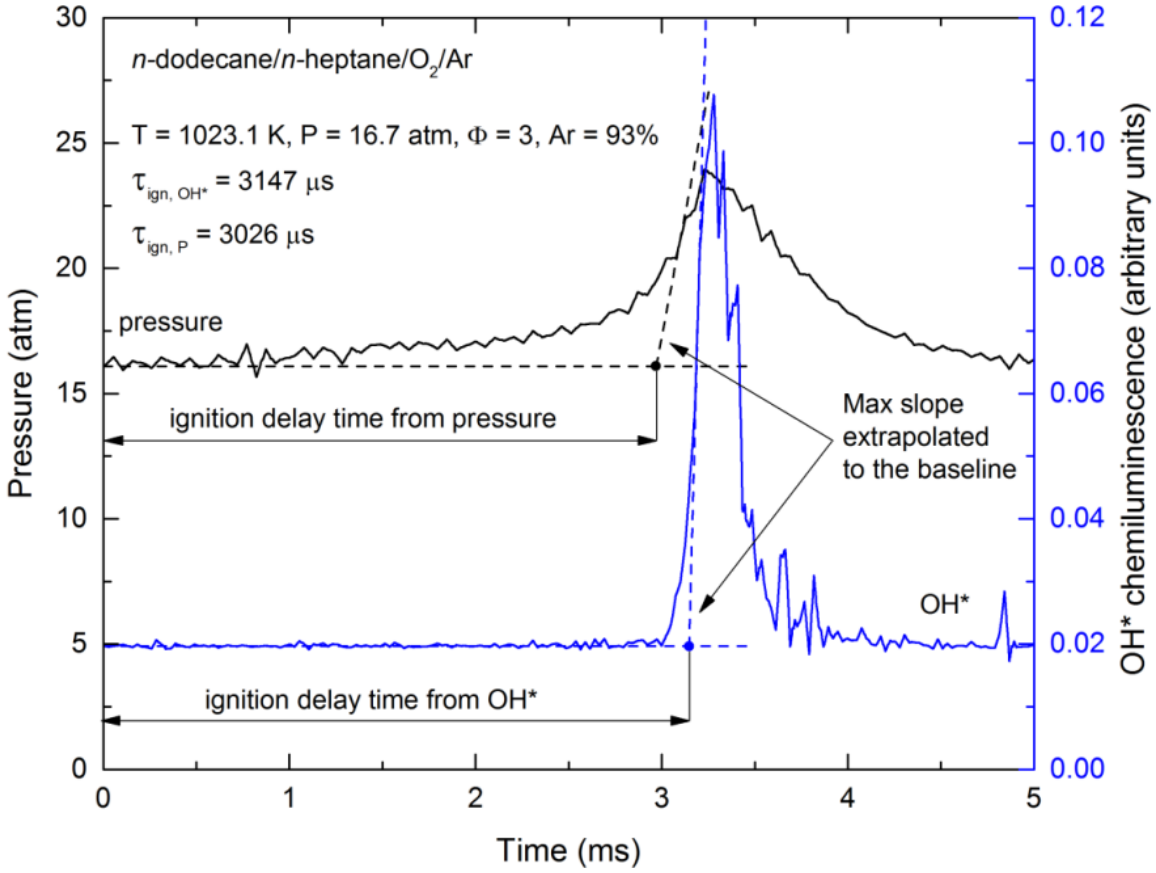

Figure 3-5. Ignition delay time measurement.

3.1.2.3 Combustion Products Sampling and Characterization

The method for sampling combustion products was an enhanced version of the procedure previously developed by our group (Sidhu et al., 2001, Kahandawala et al., 2004, Kahandawala et al., 2008). After closure of the pneumatic ball valve, exhaust gases sealed in the test section were collected into a newly developed product sampling unit (PSU), while the test section was purged with dry helium (P ~ 100 psi). The PSU was filled up to 900–1000 Torr. The PSU consists of a 25 L stainless steel (316 SS grade) gas sample cylinder, a pressure gauge (Omega, PX35D0-100AV), a control panel with pressure meters (Omega, DP25B-S; resolution of 1 Torr), flow controller, and a septa port (see Figure 3-6).

The PSU was initially evacuated using a mechanical vane pump (VIOT, VPE3). After vacuum was reached (< 1 Torr), two pre-sampling/pre-analysis internal standards were injected into the PSU, including neon (Airgas, research grade) for the quantification of C_1-C_2 species and deuterated benzene (Supelco, solution in methanol at 2000 μg/mL) for analysis of single ring aromatic species and fuel components.

As the gas was swept from the test section into the PSU, soot was collected onto 47 mm pre-cleaned quartz filters (GE Healthcare Whatman) using an in-line stainless steel high volume particulate sampler (VWR).

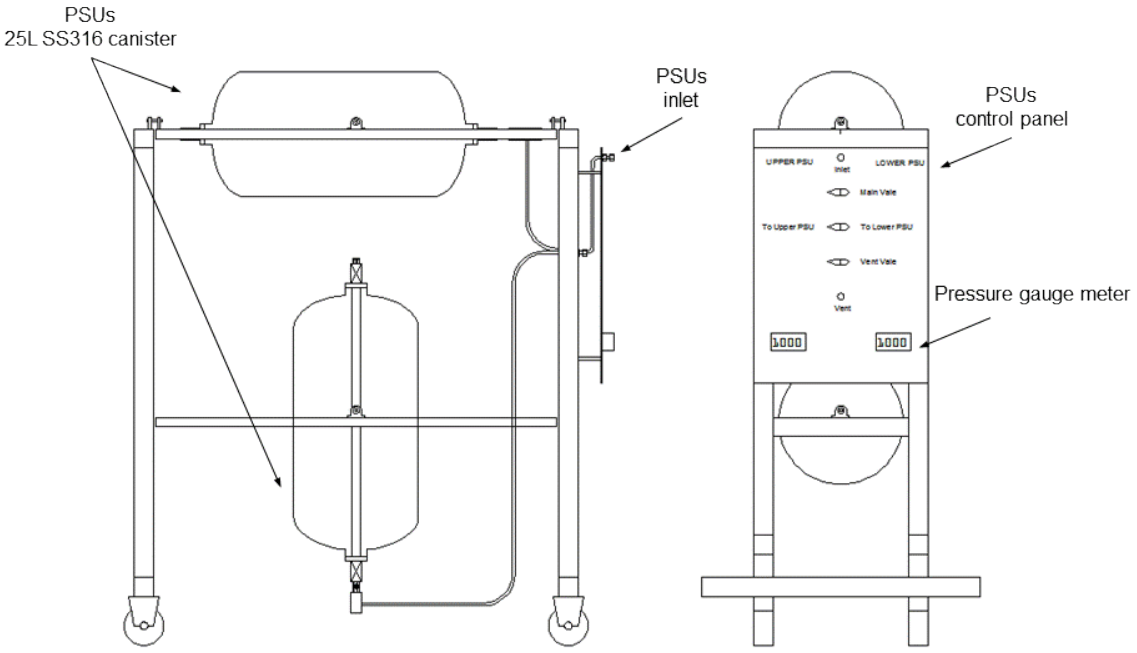

Figure 3-6. Schematic of the product sampling unit (PSU).

Light gases analysis (CO, CO_2 and C_1 to C_2 unburned hydrocarbons) were analyzed by taking a gas sample from the PSU through the septa port and manually injecting it into a GC instrument (Varian 3800) equipped with a thermal conductivity detector (TCD) through a 60/80 Carboxen-1000 metal packed column (Supelco).

Table 3.1 lists the light gases that were measured with their corresponding retention times and relative response factors to neon ($RRF_{x,Neon}$), calculated as the ratio between the response factor of the target species (RF_x) and the response factor of neon (RF_{Neon}) (see 3.1) (Chan, 2004) . A standard mixture of carbon monoxide, carbon dioxide, methane, acetylene, ethylene, and ethane (with 1% concentration balanced in nitrogen: Scott, Lot# 275PLU2SPC02E) was used to obtain calibration curves for the response factor calculation. Peak areas were used as a measure of instrument detection response.

$$RRF_{x,Neon} = \frac{RF_x}{RF_{Neon}} \tag{3.1}$$

Table 3-1. Light gases analytical details.

Target Species	Retention time (min)	RRF to Neon
Neon	0.978	1
Carbon oxide	6.882	0.587 ± 0.064
Carbon dioxide	10.752	0.393 ± 0.043
Methane	13.171	0.767 ± 0.084
Acetylene	15.749	1.213 ± 0.457
Ethylene	17.859	0.743 ± 0.129
Ethane	20.093	0.492 ± 0.054

After volatile species analysis, the PSU was evacuated through three separate sorbent sample tubes, including silica gel coated with 2,4-dinitrophenylhydrazine (DNPH) to capture aldehydes and ketones species (SKC Inc.), coconut charcoal (SKC Inc., Anasorb 2000) to capture single ring aromatic species and fuel components, and XAD-2 polymeric adsorbent (SKC Inc.) to capture semi-volatile compounds. Emission trapping was performed sequentially in the following order: silica gel sorbent tubes, coconut charcoal traps and XAD-2. The PSU pressure at the beginning and end of the trapping process for each sorbent tube was recorded in order to normalize for the entire gas volume sampled in the PSU.

Due to their volatility and instability at high temperatures, carbonyl compounds are usually derivatized with DNPH to improve their stability. Details of the derivatization reactions can be found elsewhere (Dong and Moldoveanu, 2004.). For this study, derivatization occurred during the trapping process using silica gel coated with 2,4-DNPH (SKC, Inc), with a flow rate of 0.15 L min^{-1}, below the maximum recommended by the manufacturer (0.5 L min^{-1}). The extraction technique was developed to study different amounts of solvent volume in combination with gravity feed and agitation extraction techniques.

It was determined that the optimal recovery yields (> 88%) were obtained using the gravity feed technique with a volume of acetonitrile (Spectrum Scientific, HPLC grade) greater than 20 mL. A stock solution of formaldehyde and acetaldehyde in water (Ultra Scientific, 1000 μg mL^{-1}) was used for extraction optimization studies. Samples were later concentrated down to ~1.8 mL using nitrogen blowing (Airgas, industrial grade) to enhance detection limits, and 10 μL of a mixture of deuterated standards: 1,4-dichlorobenzene-d_4, naphthalene-d_8, acenapthene-d_{10}, phenanthrene-d_{10}, chrysene-d_{12}, and perylene-d_{12} (Sigma-Aldrich, solution in methylene chloride of 2000 μg mL^{-1}) was injected as a pre-analysis standard in order to normalize the sample volume. Sample analysis was performed using an Agilent 6890/5973 GC/MS system equipped with a DB-5HT capillary column (30 m x 0.25 mm ID x 0.1 μm film) also from Agilent. Integration of the target species peak areas was computed using ion separation techniques. Quantification of aldehydes species was carried out using computed response factors relative to naphthalene-d8. Table 3-2 reports the list of aldehydes characterized in this work (formaldehyde, acetaldehyde, and propionaldehyde) with their corresponding quantitating ion, retention times and relative response factor to deuterated naphthalene. In this case, relative response factors were calculated as:

$$RRF_{X,IS} = \frac{\frac{Area_X}{Area_{IS}} - y_{intercept}}{\frac{[X]}{[IS]}} \quad (3.1)$$

where $Area_X$ is the peak area of the species *X*, $Area_{IS}$ is the area of the internal standard peak, $y_{intercept}$ is the intercept obtain from the linear correlation among different calibration stock solutions, and *[X]* and *[IS]* are the concentration of the target species and the internal standard, respectively, in the calibration stock solutions.

For the relative response factors calculation, calibration stock solutions of formaldehyde-2,4DNPH (100 μg mL^{-1}), acetaldehyde-2,4DNPH (1000 μg mL^{-1}) and proprionaldehyde-2,4DNPH (1000 μg mL^{-1}) in acetonitrile were obtained from Supelco.

Table 3-2. Aldehydes species analytical details.

Target Species	Quantitating Ion	Retention time (min)	RRF to naphthalene-d_8	y-intercept	Calibration Range (μg/ml)	Recovery (%)
Naphtalene-d_8 (IS)	136	12.17	1	-	-	-
Formaldehyde	210	23.62	0.4273±0.0108	-0.0916±0.0268	1.93–18.89	89.42
Acetaldehyde	224	25.27	0.3724±0.0097	-0.0883±0.0272	2.58–21.36	88.84
Propionaldehyde	238	26.33	0.2555±0.0068	-0.0591±0.0189	1.93–21.36	-

Single aromatic species and residues of fuel components were extracted from the charcoal sorbent tubes according to the NIOSH 1501 and NIOSH 1500 methods, respectively, with the only variation being 1.5 mL of carbon disulfide (Sigma-Aldrich, ≥99.9% Chromasolv grade) instead of 1 mL. The flow rate during trapping was set to 0.1 L min^{-1} as recommended by the manufacturer. Samples were than analyzed with the same GC/MS system, and the ion separation technique was used for the integration of target species peak areas. Relative response factors were calculated with reference to deuterated benzene (benzene-d_6) using formula (3.1). The extraction technique was validated by performing recovery studies. Stock solution for relative response factor calculation and recovery studies was purchased from Supelco. Table 3-3 reports the analytical details for the species characterized with this technique, as well as the recovery percentages.

Semi-volatile species were captured using XAD-2 sorbent traps at a flow rate of 0.25 L min^{-1}. The traps were spiked (prior to sampling) with 10 μL of the same deuterated standard mixture used for aldehydes species characterization. Semi-volatile species were later extracted using 40 mL of methylene chloride (Spectrum Scientific, PestiSolv grade stabilized with amylene) by the gravity feed technique, then concentrated down to ~1.8 mL with nitrogen blowing and analyzed using the GC/MS system configuration mentioned earlier. This extraction technique was previously developed and validated by Kahandawala (2004). The analytical method was updated to utilize the features of programmable temperature vaporizer (PTV) inlet, which allows reaching higher detection limits for the heavier species. The relative response factor for semi-volatiles were calculated with reference to naphthalene-d8 (using equation (3.1)), and are

listed in Table 3-4 with their corresponding quantitating ions. For indene, biphenyl and 2-ethenyl naphthalene, a semi-quantitative approach was used assuming an RRF of unity.

Table 3-3. Aromatic species and fuel component residues analytical details.

Target Species	Quantitating Ion	Retention time (min)	RRF to benzene-d_6	y-intercept	Calibration Range (µg/ml)	Recovery (%)
Benzene-d_6 (IS)	84	1.56	1	-	-	-
Benzene	78	1.57	1.0266±0.0028	-0.0072±0.0767	1.59–619.43	104.59
iso-Octane	57	1.67	0.9057±0.0026	-0.0887±0.0627	1.33–518.02	90.69
n-Heptane	57	1.74	0.2847±0.0131	-0.0143±0.3822	1.50–583.15	111.43
Methylcyclohexane	83	1.90	0.5046±0.0052	-0.0163±0.1135	1.34–522.56	100.47
Toluene	91	2.24	1.0338±0.0069	-0.1600±0.1879	1.57–613.05	108.54
Ethylbenzene	91	3.70	1.0426±0.0118	-0.1972±0.3279	1.59–623.00	97.61
m-Xylene	91	3.87	0.8001±0.0098	-0.0948±0.2663	1.57–612.34	86.83
Styrene	104	4.42	0.7052±0.0100	-0.3530±0.2849	1.64–642.10	70.10
n-Dodecane	57	1.74	0.2721±0.0131	-0.1080±0.3822	17.30–443.60	79.95

Table 3-4. Semi-volatile organic species analytical details.

Target Species	Quantitating Ion	Retention time (min)	RRF to naphthalene-d_8	y-intercept
Naphtalene-d_8 (IS)	136	10.25	1	-
Indene*	116	7.91	1	-
Naphthalene	128	10.29	1.0795+0.0222	0.0023+0.0252
Naphthalene, 2-methyl	142	11.91	0.6254+0.0149	0.0000+0.0169
Naphthalene, 1-methyl	142	12.13	0.6221+0.0120	0.0000+0.0233
Biphenyl*	154	13.06	1	-
Naphthalene, 2-ethenyl*	154	13.69	1	-
Acenaphthylene	152	13.92	1.7964+0.0218	-0.0101+0.0105
Acenaphthene	154	14.35	1.1515+0.0297	-0.0401+0.0337
Fluorene	165	15.53	1.1757+0.0306	-0.0515+0.0347

*semi-quantitative analysis

Non-volatile species deposited on the collected soot filter were extracted using a sonication technique. The soot filter was spiked (prior to extraction) with 3 μL of the same deuterated standard mixture used for aldehydes/semi-volatile species characterization. Three steps were involved in the extraction procedure: 1) filter were summers in 20 mL of toluene (Spectrum Scientific, PestiSolv grade stabilized with amylene) then 2) sonicated in sonic bath at 50 C and subsequently 3) centrifuged at 3000 RPM for 60 minutes. Solvent was later transfer to a new test tube and steps 1-3 were repeated two more times. Later, the collected solvent was concentrated down to ~1.8 mL with nitrogen blowing and analyzed using the GC/MS system configuration mentioned earlier. A semi-quantitative analysis was used assuming an RRF to naphthalene-d8 of unity.

Mass of the collected particulate matter (PM; *i.e.*, soot) samples was determined via the temperature programmed oxidation (TPO) or carbon burn-off method with a LECO Model RC 412 multiphase carbon determinator. In this method, the mass of collected PM was determined by measuring the CO_2 generated during oxidation of soot.

3.1.2.4 Experimental Condition

The experiments covered pre-ignition temperatures in the range of 950–1500 K, at a pressure of 15–16 atm, and at an equivalence ratio of 3, with argon as diluent gas at a fixed concentration of 93% (mol). The reaction time was kept constant at 7.4–7.7ms (see Table 3-5).

Table 3-5. Experimental matrix.

***n*-Dodecane (mol %)**	***n*-Heptane (mol %)**	***iso*-Octane (mol %)**	**Methylcyclohexane (mol %)**	***m*-Xylene (mol %)**	**Oxygen (mol %)**	**Argon (mol %)**
0.462	0.781	-	-	-	5.747	93.000
0.469	-	0.704	-	-	5.827	93.000
0.480	-	-	0.791	-	5.729	93.000
0.704	-	-	-	0.434	5.862	93.000

Pre-ignition temperature range: 950–1550 K
Pre-ignition pressure: 16.7 ± 0.6 atm
Dwell time: ~7.4–7.7 ms

Select experiments were carried out to investigate the effect of dwell time on emission formation. For this study a pre-ignition temperature of ~1040 K was chosen, and dwell times of ~3.3, ~7.7, and ~11.8 ms were investigated for all surrogate mixtures.

3.2 Well-stirred Reactor Studies

Experiments were conducted in the WSR under fuel-rich and fuel-lean conditions. The studies under fuel-rich conditions were part of the original design of this program and were done to simulate fuel-rich regions in a combustor. The plan for the fuel-lean experiments was created part-way through the program. These experiments were designed to test new insights into processes that lead to UHC formation in GTE that developed during the program (See Section 5.3). During the fuel-lean experiments, the fuel-air mixture is changed in such a way that the reaction stops, leading to a "lean blow out." This lean blowout simulates thermo-physical and chemical conditions that occur during the quenching processes that produce UHC emissions under low power conditions in GTEs.

3.2.1 Fuel-rich Studies

Experiments were performed in the well-stirred reactor (WSR) facility at the Air Force Research Laboratory in Dayton, OH. The toroidal WSR design was derived from the work of Nenniger et al., Zelina and Ballal, and Stouffer (Nenniger et al., 1984; Zelina et al., 1994; Stouffer et al., 2007). A representative cross section drawing of WSR and jet ring is shown in Figure 3-7. Two opposed premixed fuel and air inlets ensure equal flow around the reactor.

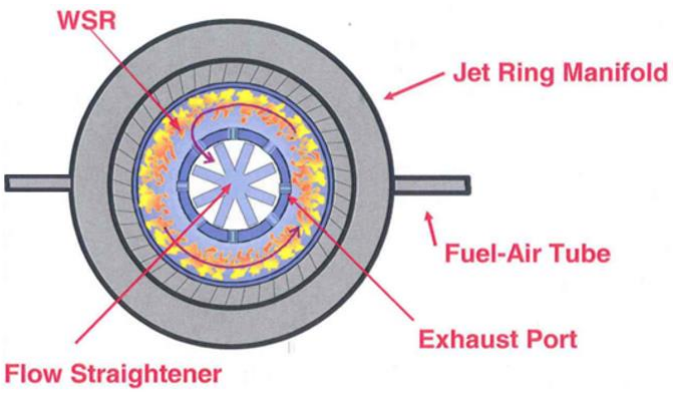

Figure 3-7. Cross-section of the WSR (Stouffer, et. al., 2005, Stouffer, et. al., 2007).

Figure 3-8 illustrates the experimental arrangement for generating and collecting fuel-rich combustion products using a well-stirred reactor. Well-stirred reactors are designed so the fuel and oxidizer are with combustion products at time scales that are shorter than chemical time scales. This rapid mixing allows chemical effects on combustion properties to be studied with minimal influence of mixing effects. In the current work, gaseous or vaporized fuel is premixed with air, and the mixture enters the reactor through a manifold with 48 holes distributed equally around the circumference (Stouffer et al., 2007). The 1.6 mm diameter holes are drilled at 20 degrees with respect to the radius to cause the bulk flow to swirl around the reactor axis. Recirculation zones, which form due to the torodial shape of the reactor and the relatively high velocity of the fuel and air jets, facilitate rapid mixing of reactants and combustion products (Briones et al., 2008).

The reactor is made from refractory material to avoid the need for active cooling. For the fuel-rich tests, the reactor was fabricated from alumina. Peak temperatures within the reactor are between 1550 and

2050 K depending on the fuel composition and the equivalence ratio. The peak temperature (not corrected for radiation losses) was found by traversing a type-B thermocouple through the reaction zone. The residence time within the reactor (i.e., global), which is determined based on the volume (250 mL), mass flow rates and density for the different operating conditions, was varied between 3 – 5 ms by changing the fuel and air flow rates. Combustion products exhaust through a ceramic stack located on top of the well-stirred reactor to the atmosphere. A flow straightener is located at the base of the stack to reduce swirl and eliminate the recirculation zone that forms for swirl numbers greater than 0.4 (Lefebvre and Ballal, 2010). Cold flow tests were performed to verify that no recirculation zones form within the stack and entrain surrounding air.

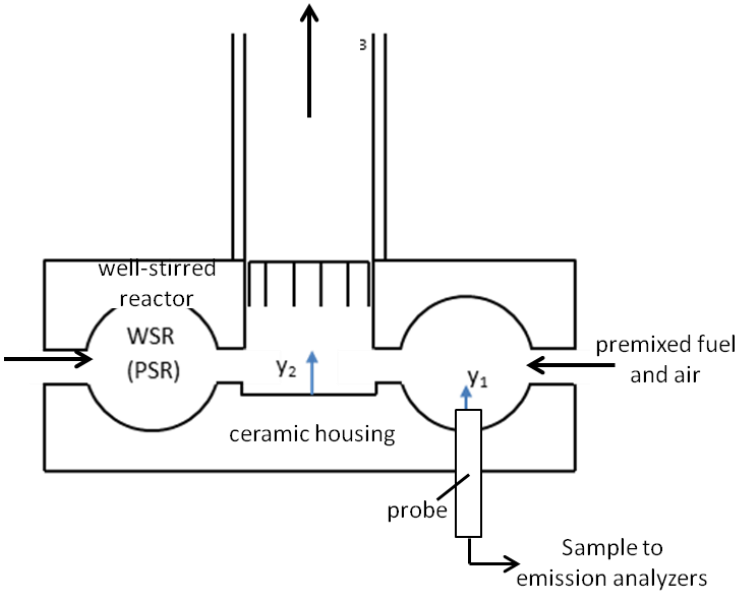

Figure 3-8. Illustration of experimental arrangement for collecting fuel-rich combustion products from well-stirred reactor.

Exhaust samples are pulled from the reactor through an oil-cooled probe, as illustrated in Figure 3-8. The inner diameter of the 25 cm long probe is 8 mm. The oil temperature is set to be less than 420 K at the inlet to the probe. The sample is pulled through heated lines to infrared absorption and Magneto-pneumatic analyzers (Horiba, models VIA-510 and MPA-510) and an FTIR multi-gas analyzer (MKS model 2080) to measure CO and CO_2 and various unburned hydrocarbons, respectively. Measurements are reported on a dry basis.

Spatial gradients in the species concentrations were calculated along the length of the probe using a plug flow reactor model (Reaction Design, 2011) to estimate quenching of exhaust products within the probe. Measured flow rate and temperature profile (within probe) at representative conditions are used as inputs. The temperature profile is estimated by traversing a bare bead thermocouple through the sampling probe while pulling a sample. This approach neglects changes in convective heat transfer as a result of the obstruction within the sampling passage. Notional species concentrations at the inlet to the probe are calculated by modeling the well-stirred reactor as a perfectly stirred reactor and the stack section as a plug

flow reactor. The calculated CO, CO_2, CH_4 and C_2H_2 concentrations change by less than 2.5% along the length of the probe, while the temperature drops from roughly 1400 K to 700 K.

Tests were conducted with ethylene, JP-8 (POSF 6169), Sasol (i.e., Fischer-Tropsch fuel POSF 7629), and a blend of dodecane/m-xylene. The former fuel is relatively simple while JP-8 and Sasol are practical for aviation applications. The dodecane/m-xylene mixture (25/75% by volume) is a surrogate representing the maximum volume of aromatics which are allowed for JP-8. The air flow rate was fixed for each test at 6, 8, or 10 g s^{-1}. Data are reported with respect to the average residence time at a fixed air flow rate, but over the range of equivalence ratios. Fuel flow rates were adjusted to achieve the desired equivalence ratios (i.e., Φ between 1.3 and 2.4). The premixed fuel and air were heated to temperature between 400 and 450 K for the liquid fuels and between 300 and 450 K for ethylene. The preheat temperature for ethylene was adjusted to avoid over heating the reactor.

3.2.2 Fuel-lean Studies

For the work where the reactor was operated under fuel-lean conditions, fused silica (Rescor 750, SiO2) sealed with spring-loaded reactor sections (Blunck, et.al., 2012) was used. This material reduces heat loss through the wall via a low thermal conductivity and a low thermal expansion coefficient (Stouffer, et. al., 2005; Stouffer, et. al., 2007). A low thermal expansion coefficient assists in reducing cracking with fast transients that occur during lean blow off experiments. (Stouffer, et. al., 2007). Properties of the fused silica for the toroidal WSR reduce the need for active cooling around the reactor (Blunck, et. al., 2012). Low thermal conductivity aids in reducing heat loss from the reactor walls (Stouffer, et. al., 2005). A modified Inconel jet ring with 48 fuel/air jets was sealed between the reactor components. A ceramic paper gasket seals were placed between the top reactor half and jet ring to seal the reactor under operating conditions (Cotronics 390, 1/8" thickness), while a mica gasket was used between the bottom reactor half and the jet ring. Figure 3-9 displays the WSR with the ceramic components in red and the jet ring in blue.

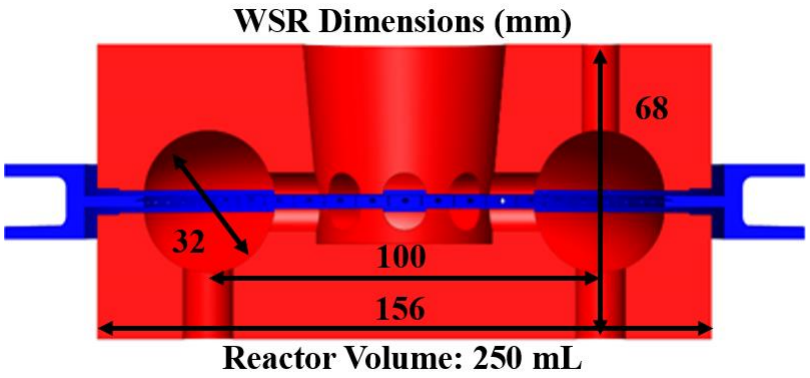

Figure 3-9. A transverse cross-section of the toroidal WSR is shown with dimensions listed in mm. Reactor volume is 250 mL. Reactor components (red) are fused silica and the jet ring (blue) is Inconel.

Premixed fuel and air is injected in the toroid of 250 mL through the jet ring containing 48 jets with 1 mm diameter. Jets are located on the outside of the circumference. Earlier versions of the toroidal WSR used small passages or long narrow straight tubes for injector nozzles. Large pressure losses occurred for those configurations, requiring pressures higher than isentropic chocking conditions to achieve sonic

velocities exiting the jets, thus limiting the operational range because of the potential for auto ignition in the jet ring (Stouffer, et. al., 2005). The feed jets for the current WSR are angled 20 degrees off the radius of the torus causing the bulk flow to move around the reactor (Stouffer, et. al., 2005; Stouffer, et. al., 2002; Vijlee, 2014; Stouffer, et. al., 2007; Nenniger, et. al., 1984). The sonic velocity and angle from the jets provides for recirculation zones around the upper and lower half of the toroid in addition to axially around the toroid.

Continuous high rate mixing between the incoming reactants and the products separates the WSR from other premixed combustion system (Blunck, et. al, 2012; Blunck, et. al, 2015; Stouffer, et. al., 2005; Stouffer, et. al., 2007; Briones, et. al, 2008). Previously, numerical modeling has been performed and found that the WSR operates in the given well-stirred turbulent reaction regime (Briones, et. al, 2008). For a "Perfectly-Stirred Reactor", a homogeneous profile of temperature and species in the reactor will result due to the extreme mixing. However, it is impossible to achieve this condition over the entire combustor due to practical limitations on reaction rates and mixing (Stouffer, et. al., 2007). For example, because of practical limitations of mixing, the area near the fuel and air jets has a higher fraction of incoming reactions than products (Stouffer, et. al., 2007).

The design of the reactor allows for separate nitrogen cooling flow on the outside of the jet ring. Lower temperature along the jet ring combats auto ignition in the jet ring. Previous experiments using the WSR experienced the need for active cooling which was accomplished by increasing the air flow rate during the experiments.

Experiments have also been performed to investigate the mean-temperature distribution along the vertical direction from the wall to the midpoint of the toroid. One experiment used ethylene in fuel-lean conditions. Profiles were generally flat, with larger gradients near the walls for lower residence times due to heat transfer (Stouffer, et. al., 2005). Another experiment investigated temperature distribution while testing ethylene under fuel-rich conditions. This data, with 48 jets, was compared with Nenniger's 32-jet ring design. The temperature measurement near the centerline jet region was relatively lower as compared to the previous design, producing a flatter profile. This was attributed to enhance mixing and yielded and more consistent emissions measurements (Stouffer, et. al., 2005).

Products from combustion exit the reactor via 8 radial ports at the toroid inner diameter and through a 5-cm-diameter ceramic stack above the WSR. Bulk swirl is reduced and local recirculation zones formed because of the large swirl number are eliminated through a flow straightener placed at the exhaust of the toroid and at the base of the stack (Blunck, et. al., 2015).

Instruments and components used for WSR operation and emissions measurements are shown on the schematic in Fig. 3. Liquid fuel is delivered by two syringe pumps (ISCO 500 D) operated in continuous flow mode. The piston flow meter accuracy is +/- 0.5%. Uncertainty of liquid flow measurement including calibration is estimated to be +/- 1.4% (Stouffer, et. al., 2007). The liquid fuel passes through a swirler and enters a heat exchanger, where the fuel reaches a temperature of 473 K at the inlet of the vaporizer. Heated fuel is introduced in the vaporizer with 10-20% of the total combustion air via an air-swirled atomizer nozzle containing heated air at 400 K and mass flow of 60 standard liters per minute (slpm). Remaining air at 489 K and mass flow of 440 slpm is added in the vaporizer as a coaxial stream (Stouffer, et. al., 2007). Upon entering the vaporizer, the air-lines are filtered and monitored along with being controlled using mass flow controllers (Brooks Instruments) (Stouffer, et. al., 2002). Uncertainty for the mass flow controllers is +/- 1.5% (Stouffer, et. al., 2007). Electric, PID-controlled heaters heated the incoming fuel and air streams. Flow rates of the fuel and air, paired with the temperature control of each, are used to control the incoming

fuel-air mixture to the reactor. Flow rates for the experiment are also chosen to ensure turbulent mixing and sonic velocities from the jets into the reactor (Vijlee, 2014). The vaporizer used for the atmospheric WSR has been used in previous tests and was shown to safely and successfully mix the fuel with the air (Stouffer, et. al., 2005; Stouffer, et. al., 2007). This strategy, using premixed and pre-vaporized fuel, eliminated physical complications associated with droplet combustion and established an ideal gas turbine combustor environment without physical complication.

A fixed spark igniter within the reactor initiates combustion. When testing with liquid fuel, the reactor was first brought to a stable thermal condition using a gaseous fuel (usually ethylene). Gaseous fuel flowrate into the WSR was controlled with a series of pressure regulators, to slowly reduce pressure, and mass flow controllers (Brooks Instruments). Introducing gaseous fuel before the liquid fuel allowed the reactor to preheat to prevent fuel condensation within the small jet ring passages. After operational temperatures were reached, the fuel was transitioned smoothly from the gaseous fuel to the liquid fuel (Stouffer, et. al., 2007).

3.2.2.1 Instrumentation

Temperature, pressure, and fuel and air mass flow were controlled using LabVIEW software and National Instruments hardware. Routines were performed within the LabVIEW software to calculate equivalence ratio. Online, Fourier Transform Infrared Spectroscopy (FTIR) based measurements of emissions were recorded using MKS software on a standalone computer and synchronized to the main data acquisition software.

A bare, linear-tracking, custom, type-B thermocouple (0.2mm diameter, platinum – 6% rhodium, platinum – 30% rhodium) without coating was used to measure reactor temperature. Measurements for temperature were taken at 0.25” from the outer wall of the reactor and were not corrected for radiation and other heat losses. Therefore, the gas temperature readings may not be accurate in an absolute sense, yielding lower temperatures than expected, but enable relative comparisons between conditions. A 0–5 psia pressure transducer was used to monitor the slight pressure increase in the reactor. A maximum pressure of 5.5 kPa above ambient conditions was experienced during testing.

Exhaust samples were extracted using an oil-cooled probe (420 K) through a 1.4-mm-diameter orifice. The samples were passed through the probe which quenches the reactions, similar to quenching in a typical combustor (Blunck, et. al., 2012). The probe rested 5 mm above the wall of the lower toroid and is 90 degrees around the axis of the toroid from the thermocouple. Temperatures of the oil were kept constant at 420K while sampling to minimize condensation in the sampling line.

Gaseous emissions were transported through a heated line containing a pump, filter and oven before entering the FTIR. The heated lines and oven were maintained at 420 K by PID controllers. Flow entered and exited the FTIR at a constant temperature of 463K where it was exhausted or sampled via charcoal tubes and gas bags. A sketch of the sampling methodology is shown in Figure 3-10.

The FTIR system utilized in the current lean blow out work was a MKS 2030 High Speed (5Hz) gas analyzer with a gas cell path length of 5.11 m and was used to measure the emissions from the WSR. This FTIR system allows major gaseous species to be detected online, while saving the spectra for later detailed investigation. The Gasoline Ethanol method, within the MKS software package, was employed to analyze the IR spectra and calculate emission concentration values. Measurement accuracy using this FTIR is +/- 2%. Carbon monoxide (CO), carbon dioxide (CO2), water (H2O), nitrogen oxide (NO), nitrogen

dioxide (NO2), acetylene (C2H2), ethylene (C2H4), and formaldehyde (CH2O) are among the many emissions that absorb infrared radiation and can be quantified using the method employed in the FTIR.

Following the FTIR was a valve to capture bag samples and enable offline measurement of C1–C12 species, primarily for C1–C4 hydrocarbons. An Agilent 6890/5973 GC-FID-MS (Gas Chromatography-Flame Ionization Detector-Mass Spectrometry) and Gas Pro Column was utilized to analyze emissions from the extracted samples.

Capturing exhaust emissions through charcoal tubes was also employed as a sampling technique to obtain heavy hydrocarbon species, generally above C4 species. Another valve following the FTIR was used to draw these samples. A pump drew 1-liter exhaust emission samples at a rate of 1 liter per minute. Remaining gases pulled through the pump were exhausted through the hood where the WSR operates. Previous work has been performed using this method to extract hydrocarbons from jet-fuel emissions (Anneken, et. al., 2014). The tube was later extracted with carbon disulfide and the mass of each component was measured using an Agilent 7890 GC-FID and Gas Pro Column.

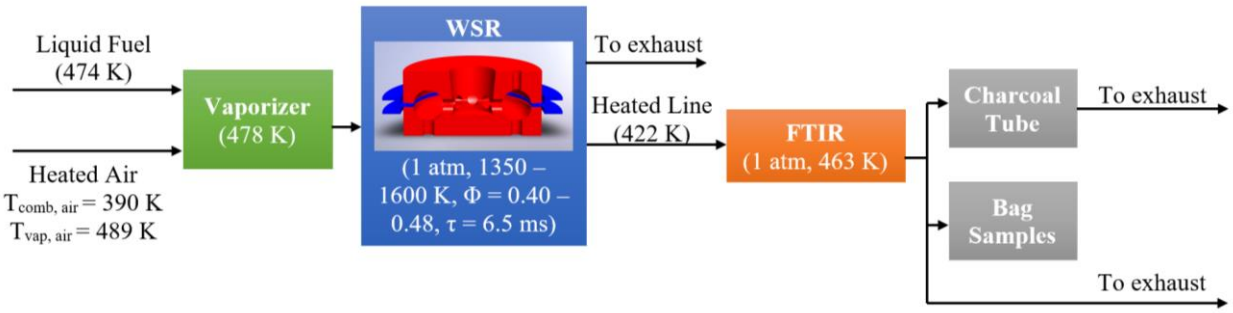

Figure 3-10. Experimental Schematic for WSR Emission Studies. A heated line takes the sample from the reaction region in the WSR to the FTIR. Charcoal tube and bag samples are taken after the FTIR before being exhausted.

3.3 Laminar Co-flow Flame Studies

In order to study the formation of pollutant species range of fuel-air mixtures that occur within the primary zone of a gas turbine combustor, both non-premixed and partially premixed flames are being studied. This section describes the experimental setup, methods and conditions used in these experiments.

3.3.1 Laminar Co-flow Flame Burner

The co-flow burner used in this study is based on the design of Santoro et al. (1983), which has a central fuel jet (I.D. = 11.1 mm) surrounded by a co-flowing air stream (I.D. =101.6 mm). A cross-sectional drawing of the burner is shown in Figure 3-11. The annular region for the co-flow air contains screens, glass beads, and a honeycomb to produce a uniform exit velocity profile. The fuel tube extends 5mm above the top surface of the annulus for air flow. The original design was modified to permit the use of heating tape and insulation around the fuel tube to ensure that the fuel vapor did not condense. This modification included cutting the honeycomb around the fuel tube for installation of insulation. As a result of this modification there is an annular region of insulation, approximately 5mm in width, that penetrates the top

surface of the honeycomb, leading to a larger recirculation region near the fuel tube than is present in the original burner design.

During the experiments, the flame is surrounded by a brass chimney in order to minimize the effect of air currents on the flame. Optical access to the flame is provided by four slits that are approximately 4 mm high and 12 mm long. The chimney has an I.D. of 4.22 inches, and it is 16 inches in length. A perforated ceramic plate and a wire mesh are used to restrict the air flow and generate a pressure slightly above ambient pressure within the chimney. The positive pressure reduces effects of air that can enter the optical slots on the chimney and disturb the flame.

Fuel is vaporized using a design based on the work of Zhu et al. (2004). The vaporizer is built from a 1/4" Swagelok, brass T-fitting filled with fiber glass. The fiber class distributes the liquid fuel and avoids small pools of liquid. The vaporizer is wrapped with electrical heating tape and maintained at a temperature of approximately 350°C. Nitrogen at 200°C serves as a carrier gas for the vaporized fuel and vaporization temperature. Liquid fuel is delivered to the vaporizer by a high pressure, syringe pump. The transfer line carrying the fuel/Nitrogen mixture to the burner is wrapped with heating tape to maintain a temperature of 300°C. For studies of partially premixed flames, heated air is introduced along with the nitrogen.

The original fuel vaporization/delivery system used in the jet flame studies had a single vaporizer and fuel delivery pump, as shown in Figure 3-12 (Y. Wang, 2015). In the later stages of the project, the design was modified to include two vaporizers and two delivery pumps, one for n-dodecane and one for the second fuel component. The design change was made to improve the reliability and durability of the vaporizer system. However, the change to a dual vaporizer system enabled a very rapid switch between pure n-dodecane and the binary mixtures. The rapid switching capability made it possible to use n-dodecane as a base flame to verify that the vaporizer and burner were operating consistently from day-to-day.

The flow rates of premixed air and nitrogen were controlled by mass flow controllers (Brooks Instruments 5850 series). The mass flow controllers are calibrated using a bubble meter. The nitrogen is 99.9% pure industry grade. In the two vaporizer system, the n-dodecane was supplied using a Isco 500D syringe pump and the second fuel component was supplied by a Chemyx Nexus 6000D syringe pump. The fuels in this experiment are industry grade with > 99% purity; the Fisher-Tropsch fuel used is a coal-based Sasol fuel.

The co-flow air is set at a constant flow rate of 4 scfm. The co-flow air is supplied from an air compressor and is filtered. The upstream pressure is set to 80 psi and flow rate is controlled using a metering valve. The flow rate is monitored using a Teledyne Hasting LAFM-5 laminar flow element and a mass flow meter. The flow meter is calibrated using a bubble meter.

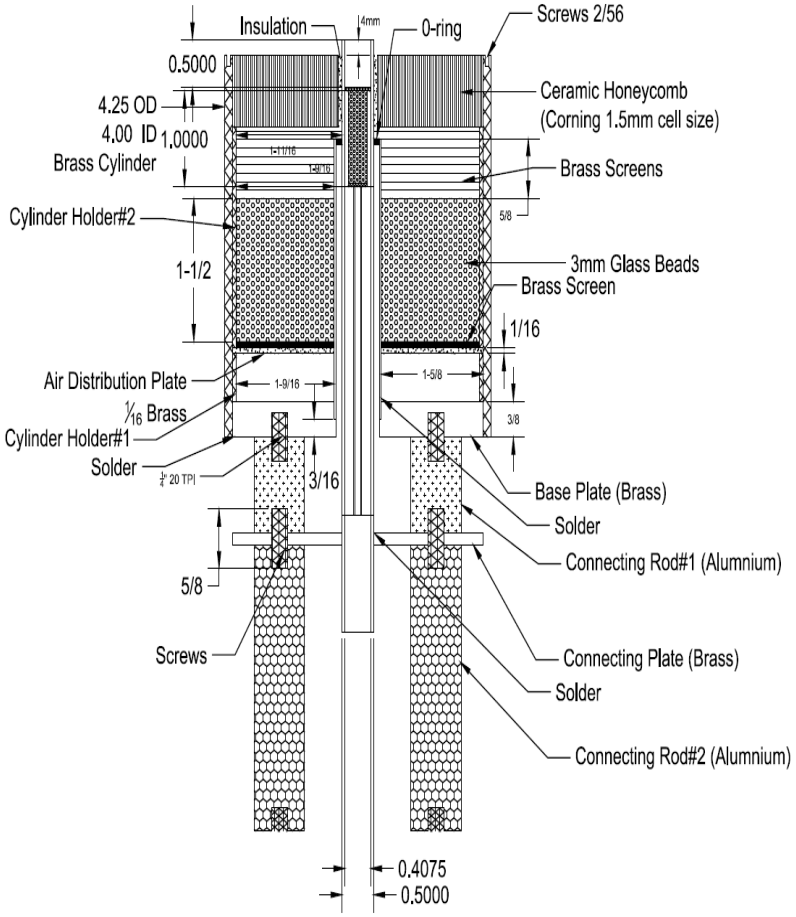

Figure 3-11. Cross-section of burner used in jet flame studies.

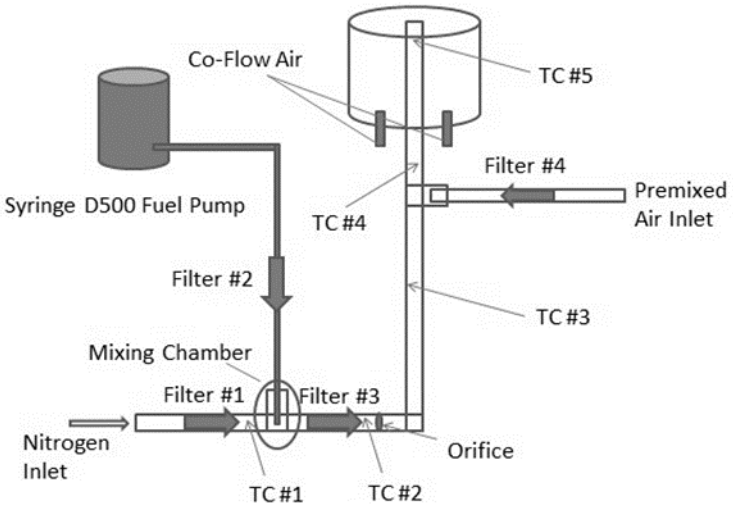

Figure 3-12. Original vaporizer system.

3.3.2 Experimental Methods

Three different laser-based diagnostics methods were applied in the jet flames: laser extinction and planar laser-induced incandescence (LII) for soot measurements and planar laser-induced fluorescence (PLIF) for PAH.

The experimental setup for the laser extinction is shown in Figure 3-13. The laser extinction measurements are conducted using the 514.5 nm line of a 2W Argon-Ion laser (Coherent Innova70). The laser beam was modulated at 1000 Hz using an optical chopper (Stanford Research SR560). A portion of the laser beam was guided on to a photo-diode using a beam-splitter to monitor the incident laser power. The transmitted light was collected by an integrating sphere (LabSphere) which was used to reduce the effects of "beam steering" at higher pressures. The signals from the two photo-diodes are converted to voltages using trans-impedance amplifiers and then fed to a lock-in amplifier. For a complete radial soot profile of the diffusion flame, extinction values are recorded every 250μm, by moving the burner relative to the laser path using the horizontal translation stage. The calculated beam waist for the argon-ion laser was approximately 60μm. The radial extinction profiles were tomographically inverted for calculation of local soot volume fractions. Data is collected at four seconds at 10Hz at each sampling location. For each flame studied, the peak soot volume fraction measured by laser extinction was used to calibrate the LII

Soot distributions within the flames were also measured using laser-induced incandescence (LII). The setup for LII is shown in Figure 3-14. A Nd:YAG laser (Spectra Physics GCR 270-10, 10Hz, 9ns) is used as a light source to irradiate the soot particles. The second harmonic of this laser is used at obtain 532 nm for heating the soot particles. The residual 1024 nm was separated from 532 nm by using a set of dichroic mirrors and the 1064 nm is absorbed using a beam dump. The Gaussian 9 mm beam is expanded into a 55 mm vertical laser sheet using a set of plano-convex cylindrical (f=55 mm) and convex lens (f=400 mm). A combination of a 532 nm half-wave plate and a 532 nm Glan-Thompson prism are used to vary the laser fluence.

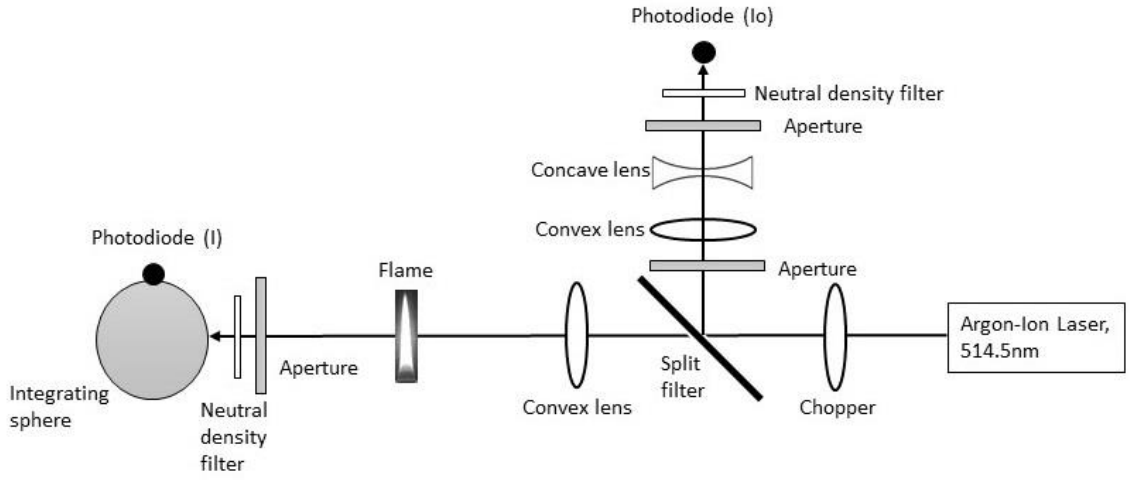

Figure 3-13. Experimental setup for laser extinction.

The incandescence from soot is collected at 90 degrees to the laser sheet by a Princeton Instruments ICCD camera with a sensor size of 512x512 pixels using an f 2.8 105mm UV lens. A narrow band

interference filter centered at 430 nm with 10 nm FWHM is used ahead of the UV lens. This helps to eliminate any interference to LII from PAH fluorescence and the C_2 Swan band fluorescence.

The camera is operated in 'gate' mode triggered by a TTL signal from the laser when the Q-switch of the laser is triggered. A 10 ns gate delay from the start of the laser pulse is used to avoid interference from Elastic/Mie scattering from soot particles. The LII signal collection starts immediately after the laser pulse to prevent particle size dependence of LII signal for each pulse. A gate width of 100 ns has a good signal to noise ratio and is small enough to avoid particle size dependence of the LII signal. The intensifier gain on camera is 140 on a scale from 0-255.

LII signals for each flame condition are summed multiple images collected from consecutive laser pulses to improve the signal/noise ratio and remove the effects of slight unsteadiness and fluctuations present in the flame. The number of images collected was varied from 50 to 100 depending on the signal/nose level; The laser pulse is monitored for shot-to-shot energy variation. These shot-to-shot energy variations are found to be quite small relative to the time-averaged signal. Since laser fluence is in the 'plateau' region, it was not necessary to correct individual LII image for laser fluence variation. A background image of the flame with no laser sheet was collected under the same conditions (gate width, gate delay, gain of intensifier, accumulations) for which LII was collected. The accumulated background image is subtracted from accumulated LII image to correct LII signals for flame luminosity and the dark counts inherited in amplified signal collection system. Corrections are made to the data to account for variation in laser intensity across the sheet.

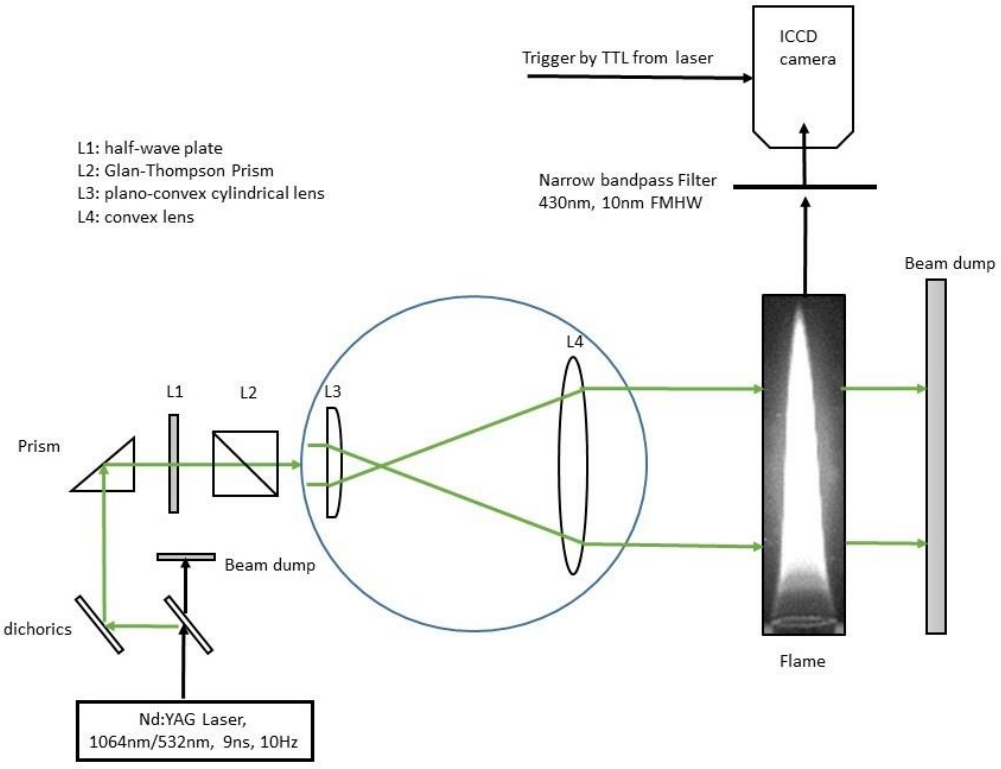

Figure 3-14. Experimental setup for planar laser induced incandescence.

Planar laser induced fluorescence (LIF) is used to get qualitative measurement of aromatic hydrocarbons in the jet flames. PAH molecules exhibit broadband fluorescence over a wide range of

excitation wavelengths (Parado et al., Beretta, et al.). The spectral distribution of the fluorescence signal is dependent on the excitation wavelength. Zizak *et al* (1996) reported that different class of PAH molecules fluoresce at different wavelength depending on the size of the PAH molecule. The variation with PAH size is a result of decreases in the difference of energy levels between the excited state and ground state with increasing size of the PAHs. This variation of fluorescence the size of PAH was used to identify two different classes of PAHs: single/two ring aromatics and molecules having more than three rings. Two sets of wavelength filters are used in front of ICCD camera to achieve this.

The optical arrangement for the LIF experiment is same as the LII setup as shown in Figure 3-14. The second harmonic is replaced with a fourth harmonic generator to produce 266 nm. The energy of laser pulse is kept at 500 μJ to keep it below the threshold for generating LII signals. The lifetime for LIF signal is in the same order as the laser pulse. Therefore, the camera is gated-on for 170 ns total duration and 20 ns before the laser pulse. The number of images collected was varied from 70 to 200 depending on the signal/noise level. Two sets of wavelength filters are used to obtain two different size groups of aromatics. A combination of WG320 and UG11 filters transmit fluorescence in the range from 320 nm to 380 nm, which corresponds to the small aromatics (1 and 2 rings). A combination of GG420 and BG12 filters transmit fluorescence in the range from 480 nm to 520 nm, which corresponds to the large aromatics (3 and 4 rings).

Since the LIF signals are collected from a group of species, it is impractical at this time to calibrate the LIF signal with aromatic species concentration. Consequently, only qualitative concentration results of aromatics are obtained and discussed.

In addition to the laser methods for studying PAH and soot, visible light images were collected to document flame shapes and to determine flame heights.

3.3.3 Experimental Conditions

Three experimental conditions were studied for each of the fuels: non-premixed, phi=6 and phi=2. The fuel flow rate was varied to keep a constant carbon flow for all flames. The nitrogen flow to the vaporizer was 0.2 SLPM for all fuels except for m-xylene/dodecane. For the m-xylene fuel, 0.2 SLPM of nitrogen was not sufficient to eliminate soot breakthrough, so the nitrogen flow was increased to 0.46 SLPM. The main air flow to the burner was held constant at 4 SCFM for all experiments.

Table 3-6. Experimental conditions for jet flame studies.

Fuel	Equivalence ratio (Φ)	Fuel flow rate (ml/min)	Nitrogen flow rate (L/min)
m-xylene/n-dodecane (m-X)	∞ and 6.	0.200	0.2 and 0.48
n-heptane/ n-dodecane (C7)		0.218	0.2
iso-octane/ n-dodecane (i-C8)		0.217	
methylcyclohexane / n-dodecane (MCH)		0.209	
n-hexadecane/ n-dodecane (C16)		0.210	
Pure n-dodecane (C12)		0.211	

3.4 Model Combustor

Most of the studies in the program were aimed at understanding chemical effects so pre-vaporized fuel was used. Studies of the effects of boiling point on emissions require that studies be conducted in systems that include fuel sprays. In order to determine whether changes in boiling point resulting from the use of alternative fuels may affect soot production, studies were conducted in a model combustor.

3.4.1 Model Combustor Test Facility

This section describes the different components and systems associated with the model gas turbine combustor. As shown in the schematic of the model gas turbine combustor in Figure 3-15, the combustor consists of the inner section, where the combustion occurs, and the outer section which provides a co-flow configuration for regenerative cooling. Compressed air from the air delivery system flows through the outer section where it gets preheated. In the process, it cools the combustion chamber and the exhaust line. This preheated air enters a Watlow process systems Model 700, 140 kW electric heater where it can be heated to temperatures of up to 800K. The heated air is choked by a 7.39mm inlet venturi before passing through a 45° flat-vaned swirler. The fuel from the injector mixes with the swirling air and this mixture is ignited at the dump plane. The combustion process occurs in the 45mm diameter, 307 mm long combustion chamber. The combustion products are choked at the 0.4 inches' diameter exit nozzle before entering the exhaust section. The inlet venturi and the exit nozzle isolate the inlet and exhaust streams from the instabilities in the combustion chamber.

This system is capable of running gaseous as well as liquid fuels. The natural gas is introduced upstream of the inlet venturi and can be used to study premixed combustion. For running liquid fuels, the natural gas is used to start the reactor and establish a stable combustion environment before the liquid fuel is introduced in the chamber. Once a stable natural gas flame is achieved, the liquid fuel is brought in at a low flow rate through the injector. The flow of natural gas is decreased gradually and that of liquid fuel is increased. The natural gas is finally cut off completely to achieve a stable flame with the liquid fuel.

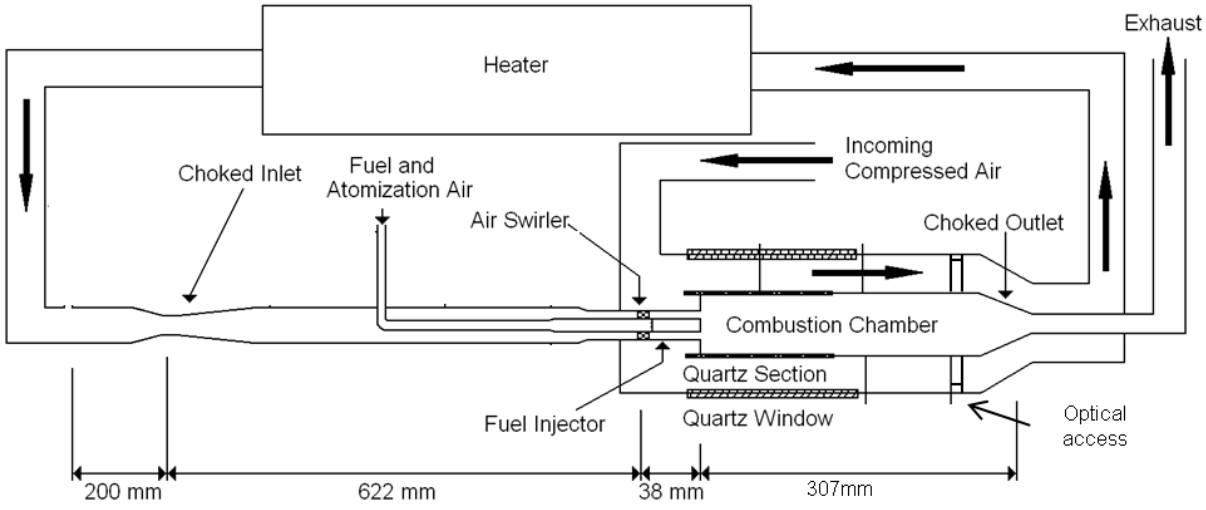

Figure 3-15. Schematic of model gas turbine combustor facility.

The static pressures at different locations in the system are measured using Setra pressure transducers. K-type thermocouples are used to monitor the temperatures in the system. The pressure across the quartz combustion chamber is monitored using a differential pressure transducer. The temperature of the exit nozzle is maintained around 400 °F using cooling air and water. The flow rate of the cooling water is controlled using a Masoneilan valve which is actuated using the building air supply. A control valve diverts part of the exhaust flow into the emission analyzer system. A nitrogen system for purging the combustible mixtures out of the system is included in the system for use in the event of an emergency or the flame blowing out.

The air compressor is capable of delivering air at a maximum flow rate of 50 g/s at 2.41 MPa. A set of four Fox Industries critical venturi orifices with throat diameters of 2.34, 2.84, 4.95, and 7.39 mm are used for metering the air. The required air flow rate is measured by opening one or more of these critical orifices, by controlling the upstream air pressure and by monitoring the upstream temperature. A part of the compressed air is metered using a 1.14 mm diameter jewel orifice and is used for cooling the injector and atomizing the liquid fuel spray.

The liquid fuel is stored in three tanks of about 24-liter capacity located in the fuel shed. A Helium gas cylinder is used to pressurize the liquid fuel to about 3.45 MPa. The fuel flow is metered using an electronically controlled variable-area, cavitating, needle valve (Whitey, Model SS 21RS4) and a Hoffer turbine flowmeter (model MF 1/2x30B). A set of pneumatic valves are used to control the fuel flow.

During transition from natural gas to liquid fuel or liquid fuel shut-off, the pressure in the injector fuel tube can fall below the combustion chamber pressure and there is a possibility of the combustion products flowing back into the injector or blocking the injector holes. This backflow is prevented using the trickle purge system which maintains a minimum pressure in the fuel lines.

A sectional view of the combustion chamber is shown in Figure 3-16. It consists of several modular stainless steel sections. The modularity in the design allows the length of the chamber and location of the diagnostics to be varied. The cooling air flows through the outer section and removes heat from the combustor. This air then enters the heater and is preheated to the desired temperature. The heated air then enters as the combustion air, flows through the swirler and around the injector tube. It atomizes the liquid fuel and mixes with the droplets in the mixing section between the 9.53 mm diameter injector tube and 20 mm diameter inlet tube. This mixture flows into the 45 mm diameter, 307 mm long chamber where combustion occurs. The 2 mm thick, 114 mm long quartz chamber piece allows optical access for viewing the flame. The cooling air in the outer section impinges onto the quartz piece and provides a small pressure differential across this piece, which eliminates the need for a very thick piece of quartz to sustain the combustion pressures and temperatures. The cooling air also impinges on the 19 mm thick external quartz windows. The 114 mm stainless piece located downstream of the optical section houses the ignitor. Two quartz windows, about 12.5 mm in diameter are mounted on the 51 mm section to allow laser diagnostics on the flame. A thermal barrier coating (TBC) of zirconium oxide is provided on these sections to prevent overheating. The 10.16 mm diameter, 30° exit nozzle is located downstream of this section. Cooling air and water are used to maintain the temperature of the nozzle.

Sealing is achieved between the inner and outer sections and from the outside of the chamber using sets two graphite gaskets between each module. The different modules are aligned using steel pins and held together using a hydraulic jack.

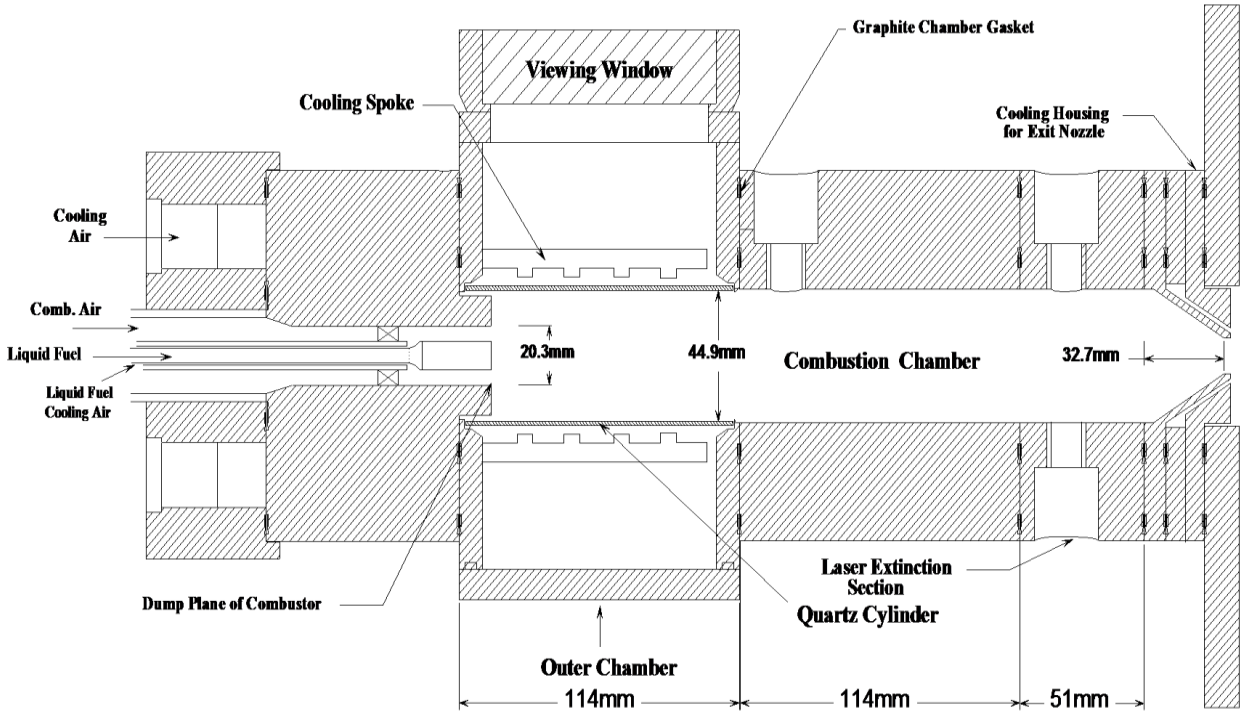

Figure 3-16. Cross-sectional view of combustion chamber.

The air swirler consists of an inner ring and outer ring with eight straight vanes mounted in between at 45° angle. It imparts a swirl motion to the incoming air which improves the mixing of air and fuel. The swirl number for the 45° swirler is found to be approximately 0.69, assuming that the axial and swirl velocities are uniform.

The liquid fuel injection system consists of two concentric tubes, an injector, and a bluff body as shown in Figure 3-17. As described earlier, a part of the main compressed air that is metered and diverted using the 1.14 mm diameter jewel orifice, flows through the annulus between the tubes. This air is used for cooling the liquid fuel thus preventing it from vaporizing before it is injected into the air stream. The injector used in the current study, called the MP liquid fuel injector (named after the designers, Mordaunt and Pal) [41], is attached to the end of the concentric tubes. Liquid fuel delivered under pressure by the liquid fuel delivery system flows through the inner tube and is forced out through 12 radial holes, 0.127 mm diameter, in the injector. The shear flow of the cooling air atomizes these 12 liquid fuel jets and the droplets vaporize in the heated main air flow. The point of injection is 37 mm upstream of the combustor dump plane. A stainless steel bluff body coated with zirconium oxide is attached to the end of the injector. The tip of the bluff body gets aligned with the dump plane and helps in anchoring the flame.

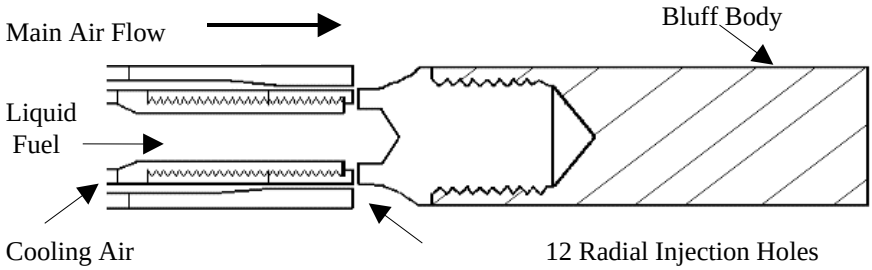

Figure 3-17. Schematic of the liquid fuel injection system. Source, Mordaunt (2005).

3.4.2 Experimental Methods

The extinction set-up for the model gas turbine combustor is shown in Figure 3-18. The extinction measurements were conducted using a Coherent (Innova 70) 2 W, 514.5 nm wavelength argon ion laser. Similar to the set-up for the wick burner studies, the incident beam was chopped and part of the beam was diverted onto a UDT Sensors PIN-10D photodiode to monitor the laser power. Instead of a focused beam, a collimated beam was used because the long path length of 45 mm would require a lens with a very long depth of field, which would be difficult to achieve. The collimated beam was diverted into the extinction section of the combustor using a set of mirrors. The extinction section was fit with two quartz windows mounted in Swagelok fittings and located at diametrically opposite sides of the section. Nitrogen gas at approximately 1 g/s from a purge system impinged on the windows at all times during the test to cool the windows and to prevent soot deposition. The transmitted laser beam was collected onto a second PIN-10D photodiode. An O.D. 1.0 neutral density filter attenuated the beam and kept the measured intensity in the linear region of the photodiode. A 3 mm aperture was located in front of the photodiode to eliminate back reflections from the windows. An Andover Corporation 515FS10-50 514.5 nm narrow bandpass filter mounted in front of the photodiode blocked the broadband flame radiation from reaching the photodiode. Any interference from scattered or stray beams was minimized by placing PVC piping coated with black paint along the whole beam path.

The output signals from the photodiodes were processed through trans-impedance and lock-in amplifiers to minimize interference from extraneous radiation, and data were acquired using a National Instruments® data acquisition system and a custom-written LabVIEW® program. The beam attenuation, I_t/I_0, was calculated from the photodiode signals: I_t being the intensity of the beam transmitted through the flame; and I_0 the intensity of the incident beam.

Extinction measurements in the model gas turbine combustor were made at only one location in the combustor (248 mm downstream of the dump plane), and the average extinction coefficient was calculated from the measured transmittance. The resulting soot volume fraction is an average line-of-sight volume fraction.

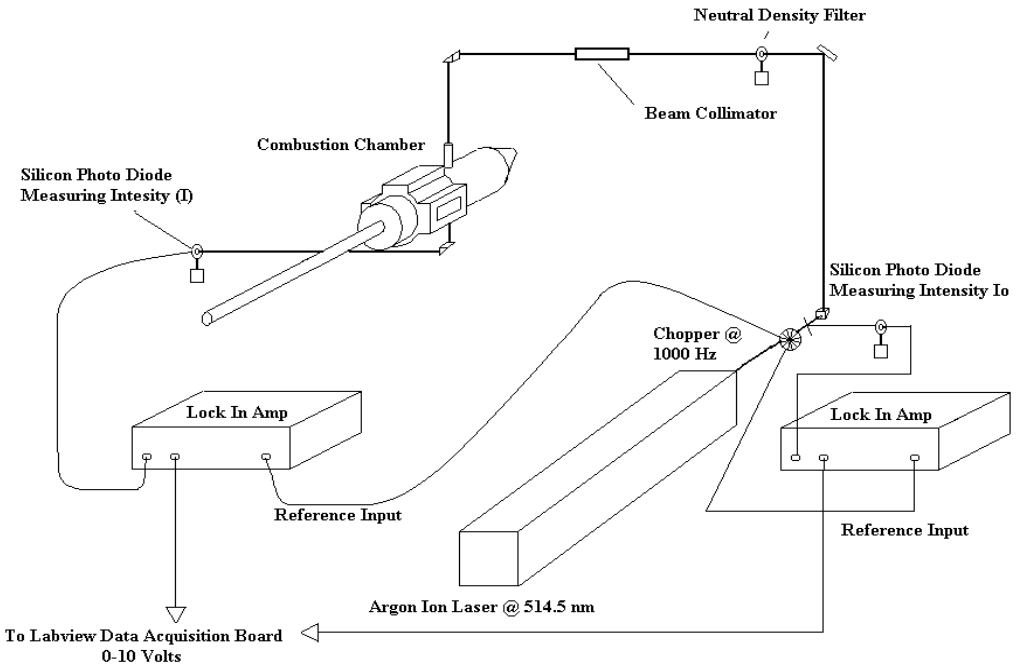

Figure 3-18. Optical setup for laser extinction on the model gas turbine combustor.

3.4.3 Experimental Conditions

The combustor was operated with a constant inlet air temperature for all tests. This was achieved by maintaining a temperature of 560 ± 10 K upstream of the critical venturi. A 10.2-mm-diameter exit nozzle was used to choke the exhaust and obtain a mean operating pressure of 0.51 MPa. The air flow rate was set to 32 g/s and the equivalence ratio was varied from $\varphi = 1.0$ to $\varphi = 1.8$ in intervals of 0.1 by varying the fuel flow rate. The equivalence ratios reported are not local values but global average values determined by the flow rate of the air and fuel. The uncertainty in the equivalence ratio measurement is ±2.6%.

3.5 Referee Combustor Studies

3.5.1 Referee Combustor Facilities

The single cup combustor facility is located at AFRL and was designed to study gas turbine combustion emissions, stability, LBO, ignition, and acoustics. A brief discussion of the rig will be presented here, and further details may be found in Stouffer et al. (2016) and Corporan et al. (2015). Figure 3-19a shows a picture of the combustion rig, which consists of a pressure vessel surrounding a plenum-fed combustor. The pressure vessel, shown in Figure 3-19b, allows optical access to four sides of the combustor through 20x15 cm fused silica windows. The air system currently allows operation with up to 0.91 kg/s air flow at pressures up to 5 atm and maximum supply temperatures of 811 K. A special emphasis was placed on the control of the various combustor parameters. Proportional-Integral-Derivative (PID) control loops were used extensively to achieve fine control of the various parameters. The total air flow rate was measured by the use of Coriolis mass flow meters which are accurate to ±0.35 %. The air mass flow was controlled by regulating the air pressure upstream of two control valves (coarse and fine) in parallel. The coarse control valve was manually controlled while the fine valve was controlled with PID feedback from the mass flow meter. During operation the pressure drop across the control valves was sufficient to operate in a choked condition so that the average mass flow rate to the combustor was independent of downstream pressure fluctuations. The back pressure on the combustor was maintained using the same approach as the air flow control with two control valves installed in parallel downstream of the combustor. A 250 kW electric heater was used to heat the air, and was also PID-controlled to maintain a steady temperature for the experiments.

The facility has an advanced fuel system based on two identical subsystems, which can either allow on-line blending of different fuels through a single injector, or staged fuel injection to feed two different fuel injectors (pilot and main) at different delivery pressures and flow rates. Further versatility is provided by the ability to introduce additives to the fuel by the use of high pressure syringe pumps. Early experiments used the entire facility fuel system; however, we realized that for conditions near lean blowout we could use the additive syringe pumps to supply and control the fuel flow. The two sets of syringe pumps provided controlled fuel flow, while the fuel flow rate was determined by the use of a Coriolis meter installed upstream of the fuel nozzle. The fuel temperature at the nozzle was also controlled to a constant value by the use of a heat exchanger fed by a process water heating system.

The combustor, shown in Figure 3-20a, was designed in consultation with turbine engine manufacturers for the purpose of studying fuel effects on combustion processes using a representative combustor incorporating many of the features of a state of the art combustor. The combustor has a hybrid fuel nozzle configuration similar to that described by Mansour (2000) incorporating a single central pilot injector nozzle surrounded by five main injection nozzles. The injector nozzle is surrounded by three co-annular air swirlers, shown in Figure 3-20b. For the current study only the central pilot injector nozzle was used. The top and bottom walls of the combustor are constructed from Haynes 188 alloy and have effusion cooling passages as well as two stages of dilution holes and mounting bosses for igniters. The combustor effusion cooling flow was a significant fraction (~63 %) of the total flow to help prevent combustor damage and geometry change during an extended experimental campaign. Note that optical access is provided by two large side windows composed of fused silica. Ignition for the combustor is provided by an APU igniter mounted in the liner connected to an aircraft engine exciter that provided a spark at approximately 10 Hz.

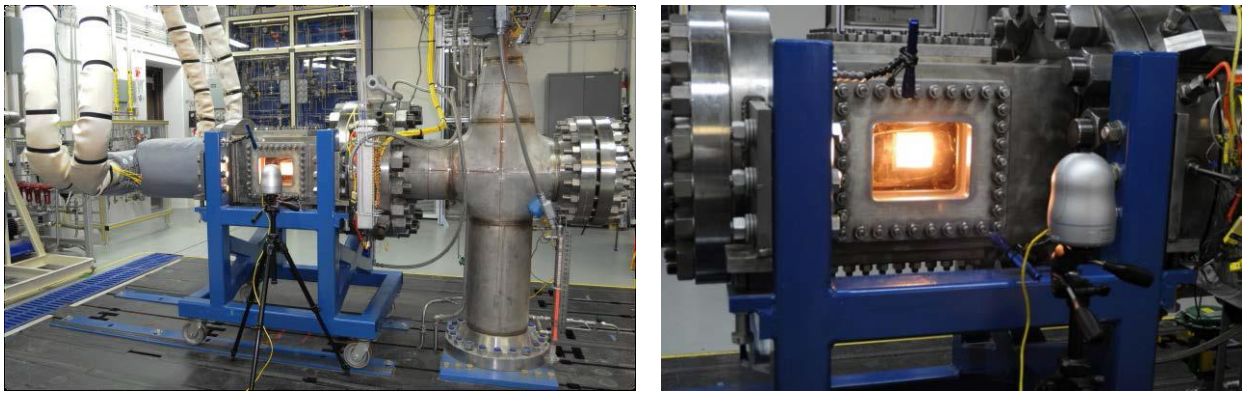

Figure 3-19. (a) Combustor Rig (b) Close-up of Pressure Vessel.

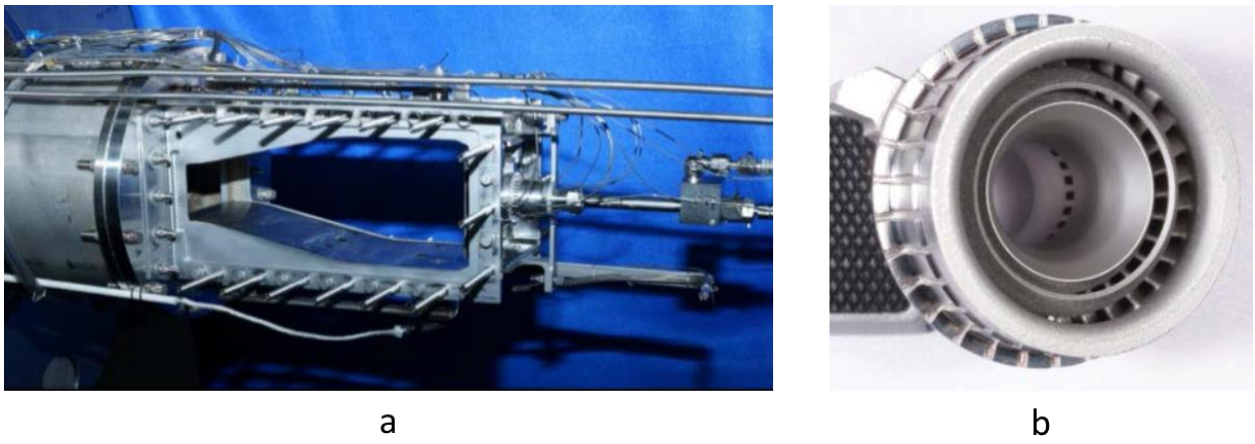

Figure 3-20. (a) Swirl Stabilized Single Cup Combustor (b) Close-up of Fuel Nozzle.

3.5.2 Experimental Methods

Three oil-cooled (150°C) stainless steel probes (Figure 3-21), installed approximately 30 cm from the combustor dome, were used to capture combustion products for transport to the instruments. The probes had a 15.9 mm outside diameter and a 1.0 mm diameter orifice and were installed 3.8 cm apart. These could be isolated via remotely operated ball valves for individual sampling to assess compositional uniformity profile in the exhaust plane or if sampling from any combination of probes was desired. After extraction,

the exhaust sample was split into two streams to provide undiluted (gaseous) and diluted (PM) samples for emissions measurements. Heated lines (150°C for gaseous and 75°C for PM), approximately 25 m long were used to transport the samples to instruments located in a mobile emissions laboratory outside of the test cell.

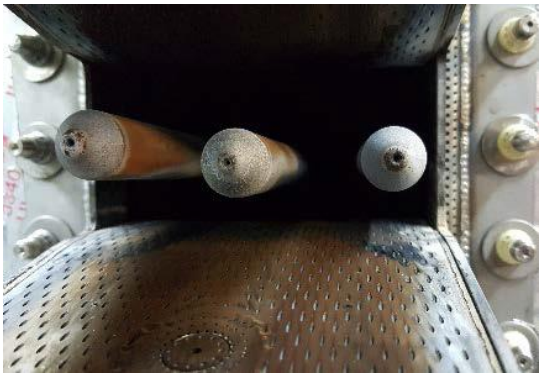

Figure 3-21. Close up of the Emission Probes (Note: During Measurements the Probes Tips are Further Downstream).

The PM samples were diluted with nitrogen through a Dekati diluter installed approximately 4 m from the probe tips to minimize losses through transport lines and to reduce sample temperature and particle concentrations to allowable instrument levels. PM emissions were characterized using conventional aerosol instruments. A TSI Model 3775 Condensation Particle Counter (CPC) quantified the concentration of particles per unit volume (particle number) and a TSI Model 3936 Scanning Mobility Particle Sizer (SMPS) with a nano-differential mobility analyzer (nDMA) and 3776 CPC measured the particle size distribution (PSD) for electrical mobility diameters between 5-150 nm. Due to the very low equivalence ratios and clean-burning fuels (except the Jet A and n-C12/m-xylene), the combustor produced extremely low particle concentrations, which resulted in inconsistent particle size distributions. As such, these will not be discussed further. For all tests, the particle numbers were corrected for nitrogen dilution based on the raw and diluted CO2 measurements. Undiluted CO, CO2, NO, NO2 and several hydrocarbon species were measured and/or monitored with a MKS 2030 FTIR-based analyzer. A non-disperse infrared analyzer (NDIR) CAI model 602P measured the diluted CO2 in the PM sample.

Sampling of aromatic compounds and C6-C20 hydrocarbons was performed via adsorption using charcoal tubes (Supelco ORBOTM – 32). An undiluted sample at a constant flow rate of 1.0 SLPM was drawn through the tube for a predetermined amount of time (typically five minutes). The tube consisted of two adsorbent beds separated by a short section of urethane foam. The front charcoal bed (100 mg) was used for sample collection and the back charcoal bed (50 mg) to capture any sample breakthrough. Samples in each bed were prepared for analysis by placing in gas chromatograph (GC) vials. Compound extraction was performed via addition of 1.0 mL of carbon disulfide (CS2) and agitation. An internal standard (n-C20) was added to each vial prior to GC analysis via mass spectrometry (MS) or flame ionization detection (FID) analysis. Aromatic concentrations were measured via GC/MS using Select Ion Monitoring (SIM) mode for a characteristic ion for each specific compound. The analysis was performed using an Agilent GC/MS, GC/FID Model 6890/5973.

Sampling of gaseous C1-C4hydrocarbons was performed via collection of undiluted exhaust gas in 3LTedlar bags directly downstream of the FTIR. The concentration (ppmV) of C1-C4species was quantified via GC/FID analysis based on total area response to carbon number using gaseous calibration standards.

3.5.3 Experimental Conditions

The operating points for the combustor are summarized in Table 3-7. Steady operation points were obtained by setting the air mass flow, temperature and pressure at a constant level required to achieve the desired combustor ΔP, which was measured between the plenum and a pressure tap located at 3.1 cm downstream of the deflector plate at the exit of the flow swirler. The location of the combustor ΔP pressure tap also served as the combustor pressure location. After setting the air flow rates and pressures, the fuel flow rate and the supply temperature were then adjusted slowly to achieve the desired equivalence ratio.

Table 3-7. Experimental conditions for the AFRL single cup rig.

Air Flow (kg/s)	0.392
Air Temperature (K)	394
Fuel Nozzle	Pilot Only
Fuel Temperature (K)	322
Combustor Pressure (kPa)	207
ΔP (% of Plenum Pressure)	3 %

3.6 T-63 Engine Studies

Emissions measurements were taken from an Allison T63-A-700 turboshaft engine. One study focused on the characterization of gaseous emissions while another examined the chemical composition of emitted soot particles. Two fully formulated fuels and four surrogate mixtures were evaluated in this effort, with selected properties shown in Table 3-8. The fuels included a petroleum-derived JP-8 and an *iso*-paraffinic kerosene derived from coal via Fischer-Tropsch FT synthesis produced by Sasol (Corporan et al., 2011). The FT fuel is a highly branched *iso*-paraffinic fuel with negligible normal and low cycloparaffin content. The surrogates were comprised of binary fuel blends and were selected to independently assess the effect of various hydrocarbon classes on emission propensity. All surrogates used *n*-dodecane as the base component, while the second compound was interchanged with *m*-xylene, methylcyclohexane, *iso*-octane and *n*-heptane, which represent aromatic, cycloparaffin and paraffinic hydrocarbon classes, respectively. The percentage of carbon from *n*-dodecane to the total number of moles of carbon was constant for each of the mixtures (i.e., 70.8%) to provide a basis of comparison.

Table 3-8. Composition of fuels tested.

Name	Component	Volume (%)	Mass Fraction	Hydrogen Content (%)	H/C Ratio
m-X	*m*-xylene	25.0	0.277	13.8	1.90
	n-dodecane	75.0	0.723		
MCH	methylcyclohexane	28.4	0.289	15.1	2.12
	n-dodecane	71.6	0.711		
i-C_8	*iso*-octane	30.6	0.289	15.5	2.19
	n-dodecane	69.4	0.711		
C_7	*n*-heptane	31.3	0.292	15.6	2.20
	n-dodecane	68.7	0.708		
JP-8	aromatics	16.7		13.9	1.92
	n-paraffins	19			
	iso-paraffins	31			
	cycloparaffins	34			
	naphthalenes	1.4			
SPK	aromatics	0.2		15.5	2.19
	iso-paraffins	99.8			

3.6.1 T-63 Engine Facilities

Experiments were carried out in the Engine Environment Research Facility (EERF) at the Wright Patterson Air Force Base (WPAFB). The engine facility allows for remote control of the engine operating power. Conditions tested were ~ 2% (low speed idle), ~ 7% (high speed idle), ~ 20% (intermediate) and ~ 85% (cruise) of the maximum rated power (282 hp). The sampling methods applied are similar to previous investigations (Corporan et al., 2004a; Corporan et al., 2004b; Corporan et al., 2005; Corporan et al., 2011; DeWitt et al., 2008). Products were extracted from the engine exhaust by an oil cooled (150 °C) probe and

transported to analytical instruments housed in the mobile Turbine Engine Research Transportable Emissions Laboratory (TERTEL) parked outside the EERF.

3.6.2 Experimental Methods

Various instruments provide online and offline characterization of gaseous and particulate emissions. Gaseous emissions and particle size distributions (PSD) were collected at all four settings, but soot samples were collected only at low speed idle, intermediate and cruise conditions. Samples were extracted from the engine exhaust via oil cooled (150°C) probes and transported ten meters through stainless steel tubing to analytical instruments housed in the Propulsion Directorate's Turbine Engine Research Transportable Emissions Laboratory (TERTEL). The tubing was heated to avoid condensation of volatile organic compounds and water vapor, and to reduce the loss of soot onto the tube walls. Gaseous and particulate emissions were measured from two sampling lines: one raw and one diluted (N_2 dilution at the probe tip). Sample dilution is used for aerosol measurements to inhibit particle interactions during transport and to prevent saturation of measurement instrumentation. A non-dispersive infrared (NDIR) analyzer (California Analytical, 602P) was used to determine the dilution ratio (DR) using the diluted and raw CO_2 concentrations. The total particle counts and particle size distributions (5-230 nm) were measured in a diluted sample using a condensation particle counter (CPC, TSI, 3022A) and a scanning mobility particle sizer (SMPS; TSI, 3936), which consisted of an electrostatic classifier (TSI, 3080), long differential mobility analyzer (DMA; TSI, 3081) and condensation particle counter (CPC; TSI, 3025A). Major and minor gaseous emissions were quantified in the raw gas sample. A Fourier-transform infrared gas analyzer (MKS, MultiGas 2030) measured the concentration of several major and minor gaseous species, including CO_2, CO, NO_x, CH_4, C_2H_2 and C_2H_4. A flame ionization detector (California Analytical, Model 600) measured total unburned hydrocarbons (THC). Trace and specific hydrocarbon species were measured via two separate methodologies. Charcoal tubes (Supelco, ORBO – 32 small) collected low molecular weight (MW) aromatics (e.g., benzene) and dinitrophenylhydrazine tubes (DNPH; Supelco, LpDNPH H30) were used to sample aldehydes. The tubes were held in the raw exhaust line with Teflon ferrules. The outlet of the tube was connected to plastic quarter inch tubing connected to a flow control device and a vacuum pump. The flow controller was set to extract sample raw gas at the rate of 0.5 to 1.0 liters per minute. A stopwatch was used to time the sampling and determine the volume sampled from the system. The tube was exposed to the exhaust flow for a period of time and was then removed from the flowpath, capped and put away for analysis.

The analysis of the ORBO tubes was performed by breaking the glass tube and pouring the charcoal from the front section of the tube into a 2 mL GC vial. The back portion of charcoal was transferred into a second GC vial. Each vial was filled with 1.0 mL of carbon disulfide, accurately added with a 1000 µl syringe, and then an internal standard solution containing *n*-eicosane (*n*-C20) at a concentration of 50 µg/mL. These samples were analyzed using GC-FID and GC-MS analysis for identification and quantification of individual hydrocarbon species. During analysis, identification of unreacted fuel compounds, in addition to the target HAPs, is feasible by comparing the extracted compounds from charcoal samples to standards where liquid jet fuel (same as used in engine operation) is injected directly onto charcoal tube and extracted using the same methodology. Table 3-9 shows the hazardous air pollutants measured in combustion emissions.

Table 3-9. Hazardous air pollutants measured in combustion emissions.

Benzene	isopropylbenzene
Toluene	phenol
Ethylbenzene	naphthalene
M,p-xylene	2-methyl naphthalene
o-xylene	1,3-dimethyl naphthalene
styrene	

A raw aerosol sample was also taken from the heated line by a cascade impactor (MSP, nano-MOUDI II, 125B) (Marple et al., 1991; Marple & Olson, 1999) for the characterization of soot particles. Particle samples were deposited onto silicon frame windows (Silson, 5.0 mm square) on three different stages that span an aerodynamic range of 10–100 nm. The chemical composition of the samples was probed by micro-FTIR spectroscopy, which couples an optical microscope to a Fourier transform infrared spectrometer (Bruker, model IFS 66/S). Mid-infrared vibrational spectra (500-6000 cm^{-1}) were measured for the samples collected.

Emission Index (EI) values, defined as the amount of the combustion product formed normalized to the mass of fuel burned, were used for data comparison. This approach provides normalization when comparing engine operation with different fuels and at varying power settings. Emission index values for gas-phase compounds (mass emitted/kg fuel consumed) were calculated with a method similar to that used by Spicer et al. (2009), where the mass of fuel burned is calculated assuming all fuel carbon is emitted as CO_2, CO and UHC:

$$EI_x\left(\frac{mass\ i}{kg\ fuel}\right) = \frac{(mass\ specie\ i\ emitted)MW_i \times 10^3}{(MW_C + \alpha\, MW_H)\cdot([CO_2] + [CO] + [UHC])} \qquad (3.1)$$

where MW_i is the molecular weight of specie *i*, MW_C and MW_H are the molecular weights of carbon and hydrogen, α is the hydrogen to carbon ratio of the fuel, and $[CO_2]$, [CO] and [UHC] are the concentrations of CO_2 (background corrected for atmospheric concentration), CO and UHC in the exhaust, respectively. Particle Number Emission Indices were calculated using the methodology included in current draft of the SAE Aerospace Information Report (AIR) 6037, which is consistent with the method used in similar studies (Timko et al., 2010):

$$EI_{PN}\left(\frac{\#}{kg\ fuel}\right) = \frac{PN\ x\ 10^6(0.082 \times T_{sample})}{(MW_C + \alpha\, MW_H)\cdot([CO_2] + [CO] + [UHC])(P_{sample})} \qquad (3.2)$$

where PN is the dilution correction particle number (number particles per mL of sample gas), and T_{sample} and P_{sample} are the temperature and pressure at the inlet of the CPC.

3.7 Test Fuel Matrix

The selection of fuels for the program represented a significant challenge since potential future alternative fuels are just beginning to be defined. Also, there can be significant variations between the fuel chemistry and physical properties of a typical JP-8 and alternative fuels. Substantial differences exist among different alternative fuels as well. For example, synthetic paraffinic kerosene (SPK) varies substantially in the fraction of n-alkanes, lightly branched alkanes and heavily branched alkanes. Variations in the distillation curves also exist. In contrast, coal-derived fuels contain very large fractions of cycloparaffins. Because of the wide range of possible fuels, we chose to study binary fuel blends that encompass a wide range of possible compositions consistent with the types of hydrocarbons expected from synthetic jet fuels and the current specifications for jet fuels containing synthetic hydrocarbons (ASTM D7566).

Our overall strategy for studying effects of composition was to use fuel mixtures containing components from just two of the four classes of compounds that are expected to comprise future jet fuels, i.e., normal paraffin, iso-paraffin, cycloparaffin, and aromatics. We believed that this approach would be the most effective in allowing us to identify the effects of specific types of chemical compounds on emissions. To formulate the fuel matrix, we first had to select a base fuel into which the compounds representative of the chemical classes will be blended.

Because the program focuses on prediction of emissions, any fuels used in the study must have well developed chemical models. Therefore, the fuel matrix was constructed using components with chemical kinetic models that were available at the time the program was initiated, or that were expected to be developed under SERDP, AFOSR, and NASA programs. The components for which satisfactory kinetics currently existed at the start of the program were: selected n-alkanes, heavily-branched iso-alkanes, and single ring aromatics. Mechanisms for cycloalkanes and lightly-branched alkanes were still under development but were expected to be ready for use by the time they were needed. The most highly developed of all of these mechanisms is that for normal alkanes. Therefore, the fuels were used n-dodecane as the major component in all of the fuels tested.

The base fuel has a composition of 25% m-xylene/75% dodecane by volume. This composition was chosen because 25% represents the maximum volume fraction of aromatics permitted by JP-8 specifications. To investigate the effects of alternative fuels, we designed three other fuels in which the carbon content of the m-xylene was replaced by a normal paraffin, a branched paraffin and a cyclo-paraffin. The molecules selected were: n-heptane, iso-octane, and methylcyclohexane. The fuel matrix is presented in Table 3-10. The iso-octane/dodecane fuel corresponds to the presence of iso-alkanes from FT and gas-to-liquid (GTL) fuels. The methylcyclohexane is representative of cycloparaffins found in coal derived fuels, and m-xylene represents the aromatic species in coal-derived fuels. For all fuels, we chose to keep the carbon fraction of the dodecane and the additive constant. The H/C ratios do vary among the fuels, which also simulates the behavior of real fuels.

In addition to studying chemical effects, we also investigated the effect of fuel volatility on emissions. The hypothesis behind these tests is that changes in volatility may affect the vaporization of fuel droplets in a way that would increase emissions. The expected trends is that increasing boiling point of the fuel would lead to increased emissions of UHC and soot. These studies were conducted in a model combustor at Penn State and in the Referee Combustor at WPAFB. The two fuels used for these tests were

n-heptane/n-dodecane and n-hexadecane/n-dodecane. The shown in Table 3-10 the boiling point of the n-heptane and n-hexadecane differ by nearly 200°C.

Table 3-10. Matrix of binary fuel blends; major component in mixtures is n-dodecane (BP=216°C).

Second component in mixture with n-dodecane	**Boiling Point at 1 atm**	**Volume fraction in mixture**	**Mole fraction in mixture**	**%H in mixture**	**H/C ratio of mixture**
m-xylene	139°C	25.0%	38.2%	13.7%	1.90
n-heptane	98°C	31.3%	41.4%	15.6%	2.20
iso-octane	99°C	30.6%	38.2%	15.5%	2.19
methylcyclohexane	101°C	28.4%	41.4%	15.1%	2.12
n-hexadecane	286°C	28.4%	23.6%	15.3%	2.16

4 MODELING AN D SIMULATION METHODS

4.1 Chemical Mechanisms

The first reaction mechanism utilized in these studies was developed in a prior SERDP project (Roquemore and Litzinger, 2011). This mechanism utilized two surrogate fuels, n-dodecane and m-xylene, to represent Jet-A kinetics. SERDP v1.0 n-dodecane/m-xylene two-fuel surrogate kinetic model was developed in collaboration with Professor Hai Wang of USC and his research staff, as well as Professor Ken Brezinsky of University of Illinios - Chicago (UIC) and his research staff, and followed the same methodology as previous versions of the SERDP two-component reaction models. Specifically, reactions associated with m-xylene oxidation and decomposition, as well as its decomposition products, were taken from the published mechanism of m-xylene oxidation of Gudiyella et al. (2011) in K. Brezinsky's laboratory. Reactions associated with n-dodecane, and its decomposition products, were taken from the "JetSurf, version 1.0" reaction set assembled by Sirjean et al. (2009). Lastly, the reaction set associated with small species chemistry (e.g., hydrogen, carbon monoxide, carbon dioxide, hydrocarbons with four or fewer carbon atoms) were those of the USC Mechanism, version 2.0 (Wang, et al, 2007).

To ensure consistency in nomenclature among the three mechanisms, tabulations of each species present in the three mechanisms, along with its atomic formula and thermochemical property data (heat of formation, entropy) were created. Entries with different names that had identical atomic populations and thermochemical values were considered to determine if they were equivalent species. For such cases, careful review of the conversion was required to ensure accuracy and proper identification of equivalent species. Due to broader validation of the USC mechanism and its thermodynamics, species, and thermochemical properties, those associated with the USC mechanisms superseded the UIC-based compounds when duplication occurred.

After species name conflicts had been rectified, the reactions associated with each of the above mechanisms were assembled into one large reaction set. The next step was to eliminate redundant reactions that were created as a result of the combination of the three mechanisms. Due to the large number of reactions comprising the merged reaction set, the CHEMKIN-II kinetic mechanism interpreter code was used to identify any unintentionally duplicated reactions. As with species conflicts, for any reaction duplication issue, the USC-based reaction and rate data were maintained and the UIC-based reaction was removed from the larger kinetic mechanism. The final two-component model comprises 1682 reactions amongst 243 species.

A change as made to the m-xylene reaction set to account for pressure effects. Davis et al. (1996) discussed the importance of fall-off formulations for aromatic unimolecular reactions at atmospheric pressure. Accordingly, the UIC-based Arrhenius rate data for the reaction of m-xylene undergoing a H-homolysis reaction to form the m-xylyl and hydrogen radicals was replaced with a Troe-style fall-off rate expression.

An additional modification to the m-xylene reaction system was made after simulating the transient propagation of a lean premixed flame into a decreasing equivalence ratio environment. Analysis of the simulations revealed an interesting issue; namely, that at some compositions the m-xylene was decaying faster than the n-dodecane, which did not appear reasonable. Additionally, the m-xylene not only decayed faster than the n-dodecane, it exhibited an anomalous "tail" at times greater than 50 msec. in which its concentration increased from essentially zero to small but finite concentrations.

Several perturbation simulations were performed in which the initial values of n-dodecane were varied (i.e., eliminated, halved, doubled) and all simulations that included n-dodecane yielded m-xylene profiles that exhibited the "tails" mentioned above, but interestingly, the pure m-xylene did not.

Discussions with several team members led to the discovery of the following 'concerted' reaction in the m-xylene sub-model as the source of the unexpected behavior:

$$\text{m-Xylene} + C_2H_4 = \text{Methyl-Styrene} + CH_4$$

(A 'concerted' replacement reaction, in this case, is a reaction in which a methyl group and a vinyl group are exchanged on the m-xylene molecule.) The original published m-xylene mechanism (Gudiyella, et. al., 2011, Gudiyella, 2012) included the above reaction, citing the work of Tokmakov and Lin (2004) as the basis for the reaction and rate parameters used in the m-xylene model. A review of the Tokmakov and Lin reference did not find a concerted reaction analysis, but instead an analysis of elementary type radical-stable species reactions involving, for example, vinyl and benzene. Accordingly, the above reaction was replaced with the following elementary reactions:

$$\text{m-Xylyl} + C_2H_4 = \text{Methyl-Styrene} + H$$

and

$$\text{m-Xylene} + C_2H_3 = \text{Methyl-Styrene} + CH_3$$

After the original reaction was replaced with the above two reactions (the only changes made to the model), the same analysis described above was duplicated. While the presence of various levels of n-dodecane still had an impact on the overall rate of m-xylene decomposition (through the increase in the radical pool and subsequent radical attack reactions on m-xylene), the rate of m-xylene decay was reduced. With the updated reactions, the m-xylene decomposition is then slower than the n-dodecane decomposition, which is consistent with the relative slow decay of aromatic compounds and no anomalous "tails" were observed in the m-xylene profiles. Indeed, the new profiles relax to the pure m-xylene decay profiles at times greater than 100 milliseconds, suggesting that the same thermally driven reactions are present in each system.

In addition to modifications made to the m-xylene parent fuel reaction set, additional modifications were made to the reactions involving m-xylene decomposition products. Specifically, as analysis with the SERDP-PAH kinetic models continued, several issues with respect to the m-xylene sub-mechanism's impact on PAH production were recognized. First, the inability of the reaction system to predict the known (e.g., from experiments) large production of polycyclic aromatic hydrocarbons (PAHs) was confirmed; second, it became apparent that methylstryrene was produced in large concentrations under fuel-rich conditions, yet there were no sink paths for the molecule; and third, there were no PAH forming steps from bi-m-xylyl whereas, in the analogous case of toluene decomposition, bibenzyl provided a significant route for PAH production.

As discussed above, one reaction modification was the elimination of the concerted m-Xylene reaction with two elementary reactions involving methyl-styrene. This change produced a significant drop in the predicted methylstyrene concentration, which had accounted for as much as ~ 10% of the mass in some simulations. Nevertheless, since there are other pathways for methylstryrene production and since the

mechanism had no loss processes, we included decomposition steps and PAH growth steps based on the presence of this molecule (denoted MCSTYREN in the mechanism). These new reactions are documented in Table 4-1.

Table 4-1. Added Reaction steps to account for mass growth, decomposition and oxidation of methylstyrene (MCSTYREN).

Reactants		Products				A	n	E	Comments
MMCSTYRYL	H	MCSTYREN				1.54E+13	-1	-6880	!analogous to MACSTYRL +H reaction
MACSTYRYL		MMCSTYRYL				5.00E+11	0	10000	!estimate
MBCSTYRYL		MMCSTYRYL				5.00E+11	0	10000	!estimate
MCSTYREN	O2	MMCSTYRYL	HO2			3.00E+14	0	42992	!analogous to toluene reactions
MCSTYREN	OH	MMCSTYRYL	H2O			1.62E+13	0	2770	!analogous to toluene reactions
MCSTYREN	OH	MBCSTYRYL	H2O			1.33E+08	1.4	1450	!analogous to toluene reactions
MCSTYREN	H	MMCSTYRYL	H2			1.26E+14	0	8359	!analogous to toluene reactions
MCSTYREN	H	C6H5C2H3	CH3			1930000	2.2	4163	!analogous to toluene reactions
MCSTYREN	O	C6H5C2H3	2H	CO		1.3E+13	0	3795	!assume rapid break-up of OC6H4(C2H3)CH3 and then C5H4-1CH2
MCSTYREN	O	CO	H	C4H4	n-C4H5	1.30E+13	0	3795	!assume rapid break-up of OC6H4(C2H3)CH3
MCSTYREN	CH3	MMCSTYRYL	CH4			3.16E+11	0	9500	!analogous to benzyl reactions
MMCSTYRYL	H	C6H4C2H3	CH3			1.50E+66	-14	64580	!analogous to benzyl reactions
MMCSTYRYL	O	C6H4C2H3	2H	CO		4.00E+14	0	0	!analogous to benzyl reactions
MMCSTYRYL	HO2	C6H4C2H3	2H	OH	CO	1.00E+12	0	0	! Divide by 5 as chain branching
MACSTYRYL	C2H2	A2CH3-1	H			3.80E+07	1.62	4438.34	! from Mueller A1C2H2 + C2H2
MBCSTYRYL	C2H2	A2CH3-2	H			3.80E+07	1.62	4438.34	! Requires isomerization 5 - 6 C-membered ring
MMCSTYRYL	MMCSTYRYL	DIVINYLANTHRA	2H2			1.00E+11	0.4	0	! Low estimate of recombination (some reversetakes place)
MMCSTYRYL	MCSTYREN	DIVINYLANTHRA	2H2	H		5.00E+12	0	20000	!estimate
C6H6CHCH	C2H2	A2	H			3.80E+07	1.62	4438.34	! from Mueller A1C2H2 + C2H2

The columns (in Tables 4-1 and 4-2) labeled A, n, E, are for the traditional parameters in the extended Arrhenius expression for the rate constant: $k = A\ T^n \exp(-E/RT)$ where T is temperature in Kelvin (K), R is the universal gas constant (cal/mole/K), and A has units in cc, moles, sec and E has units of cal/mole. To accommodate these steps, divinylanthracene (DIVINYLANTHRA] was added to the reaction set, and thermodynamic properties were computed from the THERM code (Bozzelli and Ritter, 1994).

In addition, a series of alternative PAH forming reactions were developed, based on analogy to the toluene system and based on the new reaction pathways involving 5-membered rings suggested recently (2015) by Wornat. The series of reactions are:

Table 4-2. Added reactions to account for PAH formation.

Reactants		Products			A	n	E	Comments
MDICPCH2	H	DIMSTILBENE	H2	H	5.00E+13	0	5000	! Colket and Seery
DIMSTILBENE	H	DIMPHENAN	H2	H	2.50E+14	0	16000	! Analogous to stillbene+H+>A4+h2, Colket and Seery
DIMPHENAN	H	A4	2H2	H	1.26E+14	0	8359	! Assume fast step to A4, rate after Colket and Seery (H+Benzyl)
INDENE	H	INDENYL	H2		3.03E+08	1.7	5590	! Analogous to C5H6+H
INDENE	CH3	INDENYL	CH4		1.80E-01	4	0	! Analogous to C5H6+H
INDENYL	C2H2	A2CH2-1			3.80E-45	17.1	22460	! 1/3 of 1st step in rate for C5H5 + C2H2
INDENYL	C2H3	A2CH2-2			3.80E-45	17.1	22460	! 1/3 of 1st step in rate for C5H5 + C2H2
A2CH2-1	C2H2	PHENYLENE	H		2.00E+11	0	0	! Reaction based on work by Wornat, rate is a guess
A2CH2-1	C2H4	PHENYLENE	H	H2	2.00E+11	0	0	! Reaction based on work by Wornat, rate is a guess
PHENYLENE	H	PHENYLENYL	H2		3.03E+08	1.7	5590	! Analogous to C5H6+H
PHENYLENE	CH3	PHENYLENYL	CH4		1.80E-01	4	0	! Analogous to C5H6+H
PHENYLENYL	C3H4	A4	H2	H	2.00E+11	0	0	! Reaction based on work by Wornat, rate is a guess

For these reactions, several additional species were added, including dimethlystilbene (DIMSTILBENE), dimethylphenanthrene (DIMPHENAN), Phenylene and Phenylenyl. As described above, the thermodynamic properties were also calculated using THERM.

Continued re-examination of the m-xylene sub-mechanism was made in an effort to find 'dead-end' species that are produced yet for which there are no further reaction pathways. We identified the following

molecules: indene (C9H8), methyl-indene (C9H7CH3), and methyl-indenyl (C9H6CH3), with relatively high mass levels. For reference, indene is a 6 member aromatic ring fused to a dehydrogenated 5 member ring. The conversion to higher PAH masses was not occurring, presumably because the mass could not move beyond these species. Methyl-indene is analogous to methylcyclopentadiene fused to a benzene ring. By error, we had neglected to include the conversion of methylene-indene to naphthalene. Based on the known isomerization of methylcyclopentadienyl to benzene (+H), the conversion of methyl-indenyl to naphthalene should occur readily. We adopted the reaction rate given by Ritter (1990) for the reverse process of the single ring enlargement.

This simple addition to the reaction mechanism of this single reaction made a very significant increase in production of the higher molecular weight PAH, for the m-xylene/dodecane system. Typical increases were about a factor of two for many of the major species, such as pyrene (a four-ringed aromatic).

A variety of other checks and balances were made to ensure that the additional reactions did not negatively impact the overall reaction model and that the additional reactions added to the SERDP mechanism did not adversely affect the model's results for global parameters like ignition delay. Conversely, rich PSR (Glarborg et al., 1986) calculations were made at both atmospheric and elevated conditions for pure m-xylene-air systems employing both the original SERDP-PAH mechanism and the updated SERDP-PAH mechanism. The new mechanism not only slightly increased PAH formation above 127 amu, but it also enabled continued pyrene production as the equivalence ratio is increased. Whereas the original mechanism yielded a pyrene peak at an equivalence ratio of 2.5 before falling at richer conditions, the updated mechanism exhibited continued pyrene growth at equivalence ratios above 3.

In addition to this base SERDP mechanism for the binary fuel, n-dodecane/m-xylene, we expanded this SERDP mechanism (revised as described above) based on work performed in a companion program funded by ONR (Colket, et al, 2013). This expanded mechanism included a greater number of parent hydrocarbons. The cyclic reactions were also adopted from JetSurf. The iso-octane reactions were adapted from the primary reference fuel (e.g., for gasoline) reaction model developed by Lawrence Livermore National Laboratories (LLNL) (Curran, et al, 2002). The iso-dodecane reaction model was developed collaboratively by UTRC and Advanced Fuel Research, Inc. (AFRI), based on analogous pathways/reactions from the LLNL iso-octane model. UTRC developed the n-hexadecane reactions. Propyl-benzene reactions were adopted from the mechanism developed by Combustion Science and Engineering (Gokulakrishnan, 2011). The species list from this full mechanism now includes:

- n-alkanes: n-heptane, n-decane, n-dodecane, n-hexadecane
- iso-alkanes: iso-octane, iso-dodecane
- cyclo-alkanes: methyl-, ethyl-, propyl-, and butyl-cyclohexane
- aromatics: meta-xylene, propyl-benzene

This expanded chemical kinetic reaction model (SERDP-2015) comprises 590 species and 3302 reactions, approximately double the size of the base SERDP mechanism.

As part of this program, it was desirable to have a valid reaction kinetics model for the formation of polycyclic aromatic hydrocarbons (PAH). The expanded mechanism described above served as the kinetic reaction set to which three different PAH formation mechanisms were appended:

a) SERDP-based PAH reactions: The PAH related chemistry and kinetics developed in previous SERDP-funded program were added.
b) Mueller/Pitsch-based PAH reactions: Reactions associated with two ring and larger aromatic species were taken from this reaction mechanism and added to the SERDP parent fuel reaction set. These PAH related reactions are further discussed in Mueller and Pitsch (2013).
c) DLR-based PAH reactions: Slavinskaya and colleagues developed an ethene mechanism that they extended to include PAH formation pathways. The PAH specific reactions from this mechanism were extracted and added to the SERDP parent fuel reaction set (Dworkin, et al, 2011).

Because the Mueller/Pitsch mechanism included reactions involving n-heptane, iso-octane, and m-xylene, calculations involving the entire mechanism were also made and used for comparison to the SERDP-based parent fuel reaction set.

4.2 UNICORN

UNICORN-2D code is a time-dependent, two-dimensional mathematical model developed for the simulation of unsteady reacting flows. We used this code for the simulation of various flames considered in this project. Seven chemical-kinetics mechanisms are used for representing various fuels used in this study.

1. GRI Version 3.0 mechanism developed by Gas Research Institute, which consists of 53 species and 650 elementary-reaction steps. This is used for the simulation of methane flames.
2. SERDP-2011-PAH mechanism developed during the current program is an extension of our previous mechanism SERDP-2011. PAH chemistry has been added to this mechanism. The final mechanism consists of 329 species and 3936 one-way reactions.
3. A semi-detailed chemical-kinetics model (CRECK-0810) developed by Ranzi et al. for the combustion of JP-8 surrogates. It consists of 206 species and 11302 reactions. A vast number of these reactions (4993) are lumped (or global) reactions involving four are more product species. Note that the computation of source terms in the species conservation equations becomes significantly more cumbersome due to the presence of lumped reactions.
4. Ranzi et al. (2001) developed a semi-detailed chemical-kinetics model including low-temperature fuel cracking and high-temperature combustion kinetics of cracked products. This mechanism should give better predictions for the unburned hydrocarbons (UHCs) in the engine exhaust as a fraction of the cracked products escape from the complete-combustion regions and show up in the exhaust. This mechanism consists of 465 species and about 30,000 reactions. Note that UNICORN code has been extended for the first time for mechanisms as large as this. A significant code restructuring was needed for accomplishing this task.
5. One of the objectives of this research is to evaluate chemical kinetics mechanisms available in the literature and select the best for the combustion of the various fuels considered. Literature search pointed to Pitsch's JP-8 mechanism, which has been used, especially in the Europe, for generating flamelet libraries. This mechanism consists of 394 species and 3984 reactions. A new UNICORN code incorporating Pitsch's mechanism has been developed.

6. The UTRC team extended SERDP-2011 mechanism for addressing combustion of iso-octane, mch and hexadecane. This new mechanism is referred to as SERDP-2014 mechanism. It consists of 522 species and 6398 reactions. A new UNICORN code has been developed for this mechanism.
7. Toward the end of this program, the UTRC team modified the SERDP chemical kinetics for the growth of PAH species, which was critical for modeling soot in aromatic fuels. The modified mechanism is referred to as SERDP-2015 mechanism and it consists of 587 species and 6624 reactions. A new UNICORN code was prepared for computing multidimensional flames efficiently with this mechanism.

Soot in UNICORN code is modeled using the following three approaches.

1. Two-equation approach: Soot in the flowfield is simulated assuming it as a gaseous species while solving the flow equations and as mono-sized particles while calculating the formation and growth processes. As a result, two conservation equations--one for the soot volume fraction and the other for the soot number density are added to the Navier-Stokes flow equations. Soot nucleation, agglomeration and oxidation processes are modeled following Lindstedt approach (Lindstedt, 1994). This method is very robust and gives reasonably accurate solutions. Due to the large number of chemical-kinetics models and fuels used in this study, most of the soot predictions were made using the two-equation approach.
2. Method-of-moments approach: This method considers moments of the soot particle size distribution (PSD). The mass of a soot particle in a particular class (i^{th}) is expressed as im_0, where m_0 is the mass of a single carbon atom. Various soot moments are then obtained through multiplying the population balance equation (also known as Smoluchowski master equation) with the corresponding moments of the soot particles. Only six moments are considered in this research. Consequently, six transport equations for the soot moments are solved along with the species, velocity and energy conservation equations. Various nucleation, surface-growth, surface-condensation and oxidation models are used for obtaining the source terms in the soot momentum equations. The method-of-moments approach requires only a fraction of the computational resources that are required for solving the gas-phase fluid dynamics; however, it faces serious disadvantages while closing the soot momentum equations. To achieve closure of the momentum equations, the fractional-order moments have to be determined in terms of the integer-order moments that are solved through conservation equations. Following the work of Frenklach (1987 and 1994) logarithmic interpolations are used for obtaining fractional-order moments from the integer-order ones. Due to this interpolation procedure, solution for the momentum equations tends to diverge, especially when the flow is dynamic or quite different from the final solution. Because of these problems, method-of-moments approach has been used in a limited number of simulations.
3. Sectional method: The PSD of soot particles in the presence of nucleation, surface growth, surface condensation, oxidation and coagulation is described using the general population balance equation (Kumar and Ramakrishna, 1996). As the numerical solution for the continuous PSD demands significant computational resources, researchers use sectional approach for solving discretized PSD. The continuous PSD is divided into 40 bins (or sections) and the soot particles within each section are described with average properties for size, mass, etc. Note that if the entire PSD is

divided into one section then sectional model becomes equivalent to two-equation model. On the other hand, the accuracy of the section method increases with the number of bins. Once the soot particles in a section are characterized with average properties then standard soot nucleation, surface growth, surface condensation and oxidation models (such as in Mouis et al. 2012) may be applied. Particle coagulation and agglomeration are evaluated within the sections and between the two adjacent sections using particle dynamics. This approach in conjunction with the SERDP-2015 chemical-kinetics provided the best soot predictions.

We have also developed specific versions of UNICORN code for addressing unique burners in the program for improving efficiency and accuracy of the simulations. Well-Stirred-Reactor (WSR) at Wright Laboratories is one of the burners considered for understanding the production of UHCs in engine emissions. Significant parts of the flames in Well Stirred Reactor represent distributed reaction zones. Typically, CHEMKIN (software sold by Reaction Design) is used for computing the concentrations of the species that come out of the WSR. Due to the licensing cost of CHEMKIN it has been decided to develop an in-house code for doing WSR calculations. Moreover, it is always beneficial to have an in-house code as it can be easily modified to suit our tailored needs. Using the successful strategies established with UNICORN multi-dimensional codes, UNICORN-0D code has been developed for doing WSR calculations. The convergence performance of UNICORN-0D code is excellent. Besides computing species profiles of WSR exhaust gases, it can also compute ignition delay times and blowout limits. The UNICORN-0D code developed during this project is fully functional.

Studies on practical combustors such as CFM-56 were performed toward the end of the project in the 4^{th} and 5^{th} years. Flowfields in these combustors are three dimensional and turbulent. Keeping this in mind we have developed a 3D version of the UNICORN code. The uniqueness with UNICORN codes is that chemical kinetics models are completely integrated for obtaining the best computational efficiencies. In the past we used a smart code for incorporating a given chemical kinetics mechanism into a 2D UNICORN code. We have completed writing the 3D version of this smart code. This code was used to simulate the model combustor at Penn State.

4.3 CHEMKIN

The kinetic mechanism, described Section 4.1, was used in conjunction with several programs associated with the Chemkin-II suite of kinetic software (Kee, et al., 1980). Specifically, the standard Chemkin codes PREMIX (Kee et al., 1985) and OPPDIF (Lutz, et al, 1997) were used to generate simulations of laminar, freely propagating flames and aerodynamically strained opposed jet flames, respectively. Additionally, a UTRC modified version of the Chemkin-II PSR code (Glarborg et al., 1986) was used to simulate the chemistry occurring in gas turbine combustors via a network of PSRs. This modified code is referred to as NETPSR (Bhargava, et al., 2000).

The PREMIX code is capable of predicting temperature and species profiles in two laminar premixed flame configurations. One configuration is the burner-stabilized flame with a known mass flow rate. The second flame configuration (and the configuration used in these studies) is the freely propagating adiabatic flame. In this case there are no heat losses (by definition) and thus the temperature profile is computed directly from the energy equation. Flame speed depends, in part, on the transport of heat, and predicting the

temperature distribution is an integral part of the flame speed calculation. The code discretizes the conservation equations associated with the flame (i.e., continuity, energy, and species) by making finite difference approximations to reduce the boundary value problem to a system of algebraic equations representing the convective, diffusive, and reactive components of the governing equations. In the freely propagating flame, the flame speed is a system eigenvalue and is determined as part of the solution.

The OPPDIF code computes the diffusion flame between two opposing nozzles. It utilizes a similarity transformation procedure to reduce the two-dimensional axisymmetric flow field to a one-dimensional problem. Furthermore, by assuming that the radial component of velocity to be linear in radius, the dependent variables become functions of the axial direction only. OPPDIF solves for the temperature, species mass fractions, axial and radial velocity components, and radial pressure gradient, which is an eigenvalue in the problem. As PREMIX, OPPDIF utilizes conventional finite differencing techniques to solve the associated system governing equations.

The NETPSR code is an extension of the Perfectly Stirred Reactor (PSR) code created at Sandia National Laboratories (Glarborg, et al, 1988). The NETPSR code enables assessing the effects of detailed chemistry in a combustor volume, by dividing the combustor volume into an interconnecting set (network) of single PSRs. Typically, a network is designed to simulate the mixing and flow characteristics of the experiment, as closely as possible. It is an alternate method (to CFD) for modeling combustor characteristics. Detailed chemistry assists in predicting NOx, CO, UHC and particulate emissions from a combustor, but implementing full detailed kinetic behavior in CFD (for high Reynolds numbers, flows and complex geometries of interest to PW) is not feasible in the near future. Standard PSR methods cannot accurately model flow and mixing characteristics. Nevertheless, by segmenting the combustor into regions that exhibit different residence times and different mixtures of fuel, air and/or constituents from adjoining segments, such networks can provide a reasonably realistic prediction of emissions.

A schematic of a single PSR is provided in Figure 4-2. The key assumption for this reactor is that the mixing within the volume is so intense that the concentrations of species and the temperature are uniform everywhere within the volume and that these conditions characterize the exit flow conditions. Methods for obtaining the solution for a single PSR are provided in Glarborg et al. (1988). The overall combustor is assumed to be divided into segmented volumes (in a series and/or parallel network), each of which represents a single PSR volume. The NETPSR code simulates this ensemble of reactors. In general, the NETPSR code treats an arbitrary ensemble of coupled PSR volumes that interchange mass and accounts for detailed combustion chemistry not (or barely) possible in a CFD model.

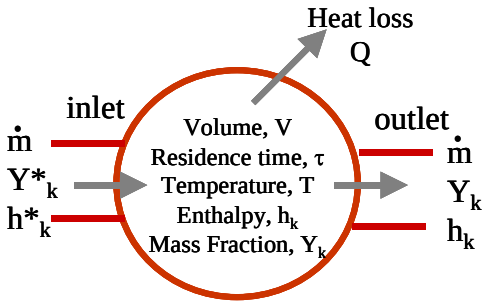

Figure 4-1. Chemkin II – PSR Model.

4.4 SHOCKIN

The PYTHON-based code SHOCKIN is currently being used as a new approach for ignition delay time simulation. SHOCKIN is an in-house program recently developed by our group that takes experimental pressure profile as an input and accurately models the gas dynamics effects associated with the shock tube experiments. During each time step, for a control mass of gas-mixture, SHOCKIN uses Cantera 2.1.1 package to model the combustion of the reacting system (with constant volume (V) and internal energy (U) constraints). In the next step, the system is isentropically brought to a measured experimental pressure at a frozen composition (see Figure 4.2). Li et al. (2008) used a similar strategy in the development of the CHEMSHOCK shock tube modeling code. SHOCKIN approach was validated using a previously-validated "optimized USC Mech II" model in a shock tube combustion experiment on ethylene (Flora et al., 2011).

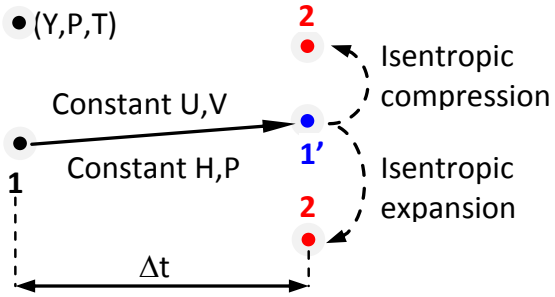

Figure 4.2. Schematic illustration of the computational method used by SHOCKIN for each time step Δt. From point 1 to 1' the mixture reacts at constant U, V. Subsequently, the mixture composition is frozen and isentropically expanded or compressed to match the experimental pressure at the point 2.

5 FUNDAMENTAL PROCESSES LEADING TO ENGINE EMISSIONS

5.1 Introduction

As described briefly in the introduction, emissions from gas turbine engines depend not only on the fuel, but also on the engine operating condition, as well as the combustor configuration. Fortunately, pre-2008, most engines relied on a similar (combustor) architecture or rich-quench-lean (RQL) and hence had similar emission characteristics.

The early portion of the modeling work in this program has focused on the linear relationship amongst hydrocarbons under low power conditions. The effort concludes that the emissions derive from the quenching of premixed flames at the lean flammability limit. This work has resulted in one manuscript submitted for publication (Zeppieri and Colket, 2014) and three follow-on efforts submitted for presentations describing validation of proposed concepts in a well-stirred reactor (Blunck, et al, 2015), extension to quenching into a progressively leaner and leaner laminar flame (Katta, et al 2014), then a finally a turbulent flame, propagating into non-flammable regions (Hassanaly, et al, 2015). A portion of the original work is provided below, and more information on each of the efforts is provided in appendices.

It should be recognized that these are not the only emissions from engines. In addition there are CO emissions, also produced at low power and soot, NOx and polycyclic aromatic hydrocarbon (PAH) emissions that are produced primarily at high power. PAH production will be discussed in this report, but the discussion of the remainder of the emissions will be deferred primarily until the final report.

5.2 Reaction Models for the Formation of Polycyclic Aromatic Hydrocarbons

The portion of the SERDP reaction mechanism (Roquemore and Litzinger, 2011) describing the formation and decay of the polycyclic hydrocarbons (PAH) was constructed from the work of Wing Tsang at NIST (funded by SERDP) and additions from the work of Colket and Seery (1993) for the role of alkylated aromatics and expanded by the SERDP team to include steps specific to m-xylene. As this model seems to inadequately compute PAH levels in the co-flow flame, we conducted a review of recently proposed PAH mechanisms and performed a comparative kinetics analysis. We selected two other reaction sets for comparisons. One was created at Stanford under an earlier SERDP program and recently modified and used by Mueller and Pitsch (2013) for simulations of soot production in a combustor. The mechanism was provided by Prof. H. Pitsch. The second one was developed by Slavinskaya (DLR) and the model is described by Dworkin, et al (2011). The latter is based on ethylene chemistry, so we needed to add the base SERDP mechanism with specific steps for heptane, m-xylene, etc., to run comparative simulations. For the Mueller model, we could run simulations both using their full model and with our light hydrocarbon chemistry as the base. Simulations for each of the four models (SERDP, SERDP/DLR, Mueller, SERDP/Mueller) have been performed using several fuels and for

- 1 atm, 400K, phi = 2. 2.5, 3, tau – above extinction
- 20 atm, 730K, phi = 2. 2.5, 3, tau = .75, 1.5, 3 msec

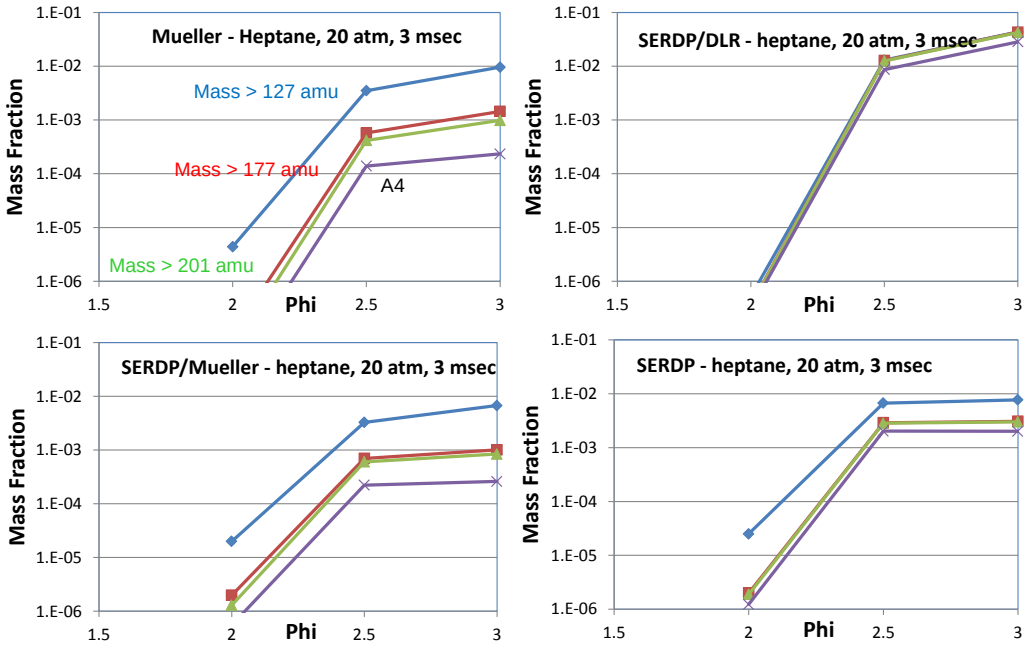

Figure 5-1. Comparison of predictions of different PAH mechanism from heptane.

Several sets of simulations are shown here. For each figure, four curves are presented, one for total mass of all aromatic species above 127 amu (naphthalene and above), one for total mass of all aromatic species above 177 amu (phenthrene/anthracene and above), one for total mass of all aromatic species above 201 amu (pyrene and above), and one for pyrene (A4) at mass 202 amu. In several of the plots the curves overlap, but in all cases, this series is listed from highest to lowest. The first represents mass of all species with 2 aromatic rings and above, the second, 3-rings and above, and the third, 4-rings and above. In addition, computations were performed for each of the primary fuels of this study. Data is shown here in Figure 5-1, Figure 5-2, and Figure 5-3 for heptane, iso-octane and m-xylene, respectively. Simulations were also obtained with methylcyclohexane (MCH), but not shown here, as the base Muller mechanism does not include MCH.

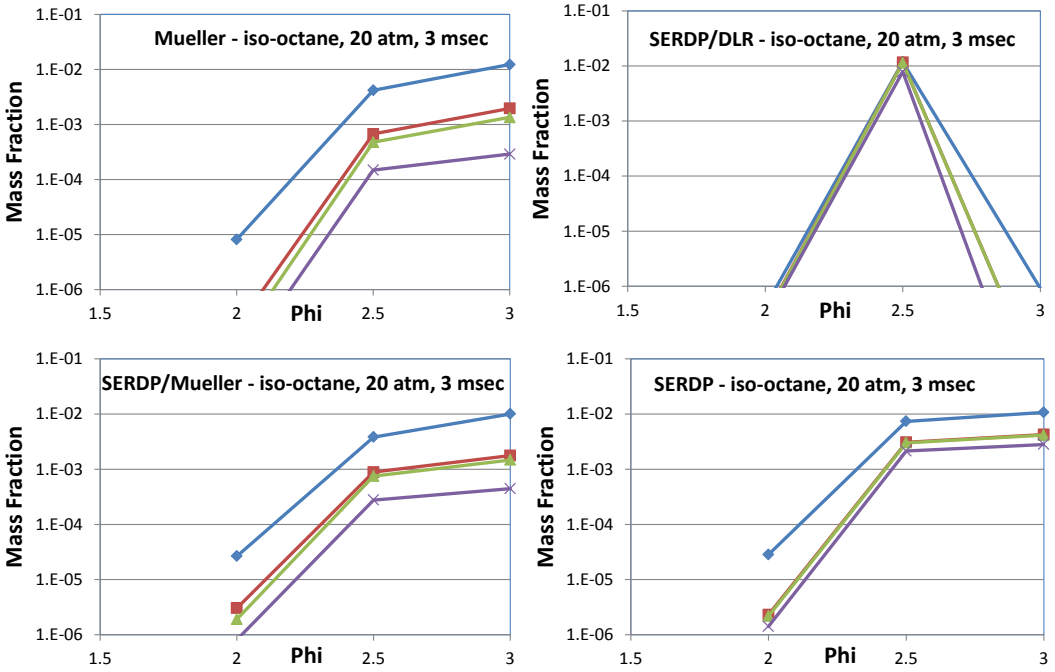

Figure 5-2. Comparison of predictions of different PAH mechanism from iso-octane.

In summary of this analysis, we find that (1) an upper limit of PAH formation near saturated values are attained in many cases, (2) the SERDP mechanism produces the largest PAH concentrations at less rich conditions, (3) the DLR mechanism produces the largest amounts of PAH and moves mass towards the largest species fastest, (4) the DLR PAH mechanism inhibits very fuel-rich iso-octane combustion, and (5) the Mueller mechanism produces a more distributed range of PAH, which is probably most realistic.

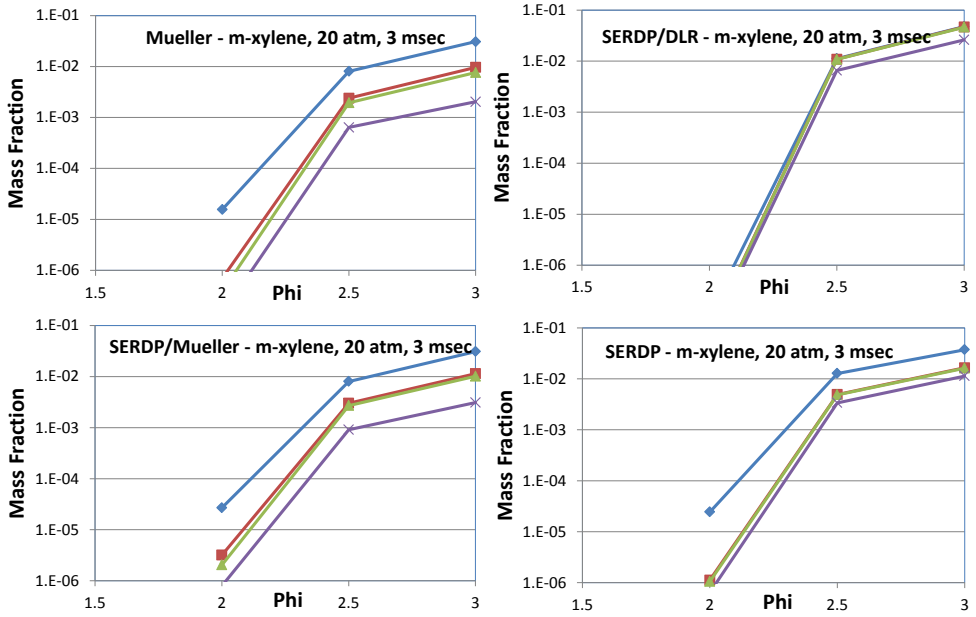

Figure 5-3. Comparison of predictions of different PAH mechanism from m-xylene.

5.3 Model Predictions of Linear Scaling of UHC Emissions at Low Power

Emissions from aircraft turbine engines can impact air quality on the local, regional, and global levels. Locally, potentially noxious emissions impact the lives of airport workers and those living in the vicinity of the airport. Additionally, emissions of ozone precursors (organic species and nitrogen oxides) may influence photochemical pollutants in the vicinity of airports. At the larger regional and global levels, emissions may impact the chemistry of the upper troposphere and stratosphere (Spicer et al., 1994). The impact of these emissions generated from aircraft consuming logistics fuels (i.e., Jet-A) is understandably complicated. Furthermore, as oil prices and demand continue to rise along with global warming concerns, motivation for development and utilization of alternative aviation fuels will continue.

The impact of emissions from these alternative fuels is less understood than that associated with Jet-A. Recent studies and programs have been initiated to better understand the impact and nature of these different aircraft fuels on engine operation, emissions (e.g., organic, volatile, non-volatile), and performance (Kinsey, 2009; Anderson et al., 2011, Spicer et al., 1992 and 1994). One of the key findings that emerged from these studies, which was discussed in the introduction, is a linear relationship among many of the hydrocarbon emissions and also partially oxidized compounds (e.g., formaldehyde, acetaldehyde). While this linear relationship appears to hold for various engine designs as well as over the lower portion of the engine's operational envelope, the slopes of the lines shift somewhat when various alternative fuels are used. The shift in the slopes has potential impact on local air quality.

Hence, this work seeks to understand the physical and chemical mechanisms by which the linearity amongst hydrocarbon (HC) emissions occurs. With such understanding, it is anticipated that changes in HC emissions due to conversion to alternate fuels can be estimated, followed by projection of the impacts on atmospheric chemistry.

5.3.1 Exploratory Investigations

A variety of simulations were initially explored in an attempt to uncover the basis for the linear relationships amongst exhaust species. Initially, most were unsuccessful. Instead of reproducing the sequence of our modeling efforts, it is clearer to provide the following description: The speciation of hydrocarbon emissions is intimately linked to the preferential (selective) sequence of formation of certain compounds during fuel pyrolysis and oxidation. This linkage is illustrated by examining hydrocarbon speciation in fundamental combustion configurations.

It is instructive to first examine the general history of a higher hydrocarbon fuel as it decomposes into hydrocarbon intermediates (e.g., products 1 and 2 in the figure), next to CO, and finally to H_2O and CO_2. A schematic plot depicting this sequence is depicted in Figure 5-4.

In a first specific example, a freely propagating premixed laminar flame at equivalence ratio of 0.6 has been computed using initial approximating conditions of an engine at a 5% power level. The structure within this flame was examined, with a focus on the reaction zone wherein the parent fuel has decomposed into intermediate hydrocarbon species, and before the species are oxidized completely to carbon oxides. The fuel was assumed to be the SERDP surrogate of the n-dodecane/m-xylene blend, and the reaction mechanism was that described in Section 4.1.

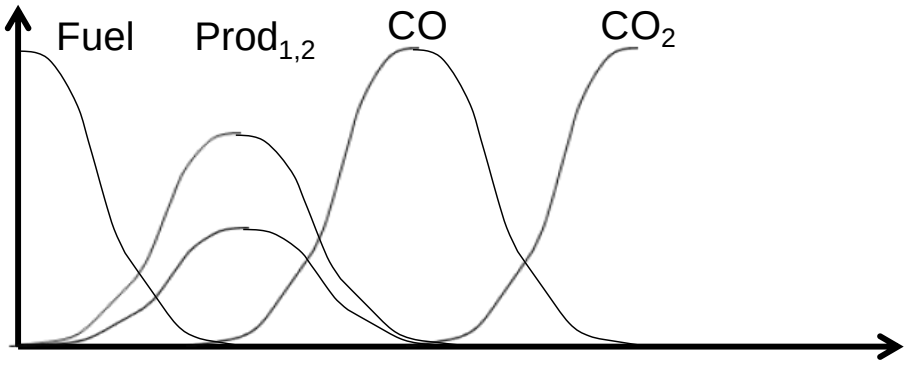

Figure 5-4. Schematic depicting the sequence of hydrocarbon oxidation.

Plots of the hydrocarbon emission indexes (EI, or grams of hydrocarbon per kilogram of parent fuel) as functions of formaldehyde EI at various positions within this premixed flame are given in Figure 5-5. As can be seen, the data sets are generally nearly linear. While not shown here, the slopes are similar to those slopes observed experimentally (this will be discussed later). The data in Figure 5-5 start from the unreacted state (origin) and progress to the fully burned state. Hence, all hydrocarbon trends start at the origin, rise to their peak values as the fuel is consumed and then fall back towards the origin as the hydrocarbons (and formaldehyde) are consumed and oxidized. Note however, this emission "trajectory" may be different than gas turbine combustor emissions due to the fact that the premixed flame contains no mechanism of suppressing/quenching reaction.

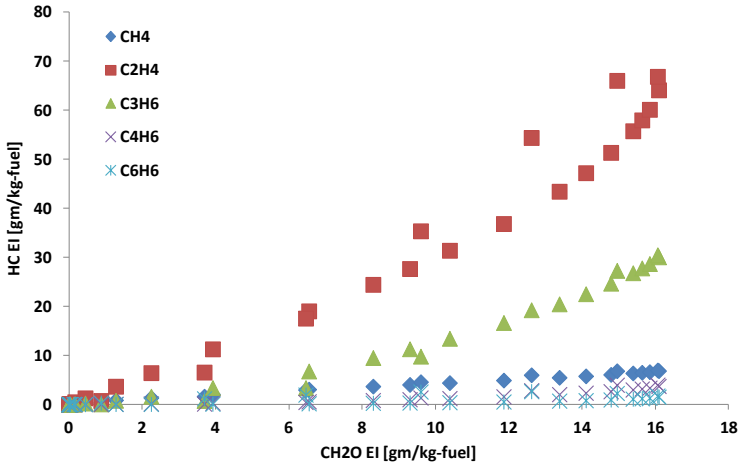

Figure 5-5. Selected hydrocarbon EI vs. formaldehyde EI profiles for a premixed flame at Phi=0.6.

Opposed-jet flames have also been simulated. In one simulation, air with added raw fuel (equivalence ratio of 0.6) was opposed with prescribed (stirred) reactor products, at the same equivalence ratio. (For reference, the fluid dynamic stagnation plane is located at ~ 0.7 cm. from the left jet.) This configuration may be recognized as a strained premixed flame, whereas the freely propagating flame is unstrained.

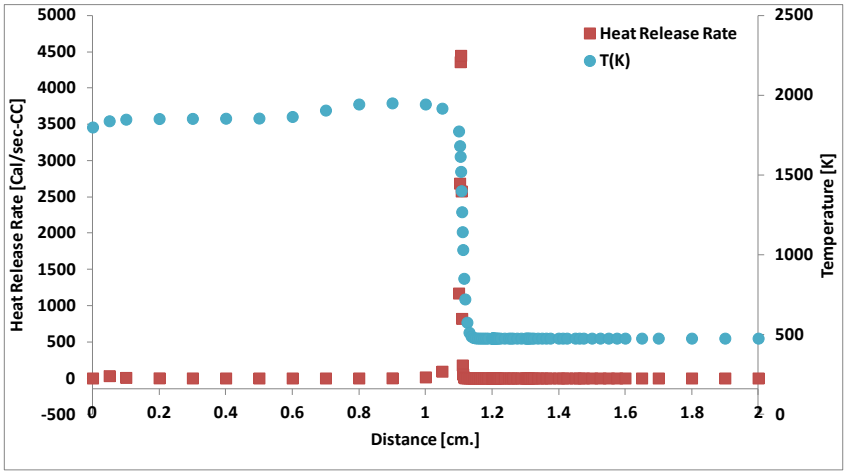

Figure 5-6. Heat release and temperature profiles of opposed-jet (strained) flame.

The heat release profile for this flame is shown in Figure 5-6 and demonstrates that the reaction is limited to a very thin region associated with the temperature spike.

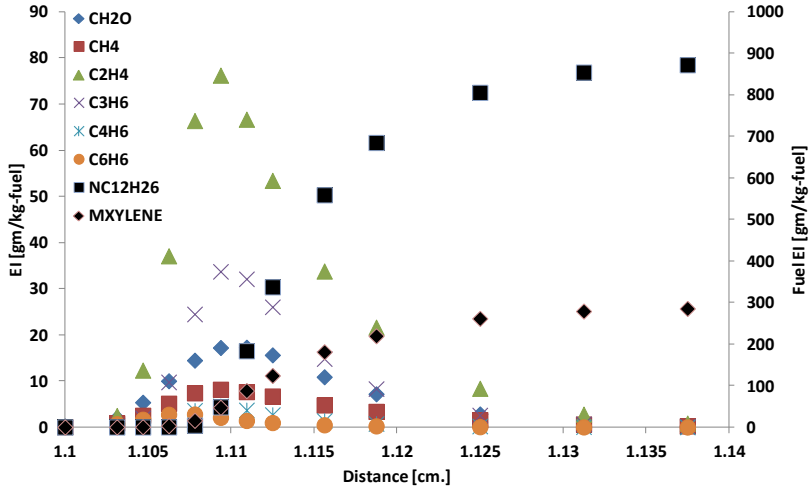

Figure 5-7. Select hydrocarbon EI profiles for opposed-jet flame.

The EI values associated with the selected hydrocarbons in this heat release zone are shown in Figure 5-7, with an expanded distance scale. Note that outside of this heat release zone, the EI values are essentially zero. (Only parent fuel reactants, n-dodecane and m-xylene, exist outside of this region.) This region of "active" hydrocarbon EI values corresponds to the fuel chemistry within the zone. As in the case of the premixed flame, hydrocarbon EI values rise as fuel is consumed, pass through a maximum as the parent fuels are fully reacted and then decay to zero as they are oxidized. When these EI values are plotted as functions of the formaldehyde EI values through the reaction zone, linear scaling trends are once again obtained, as shown in Figure 5-8. The slopes associated with these trends are in agreement with those obtained from the premixed flame simulations.

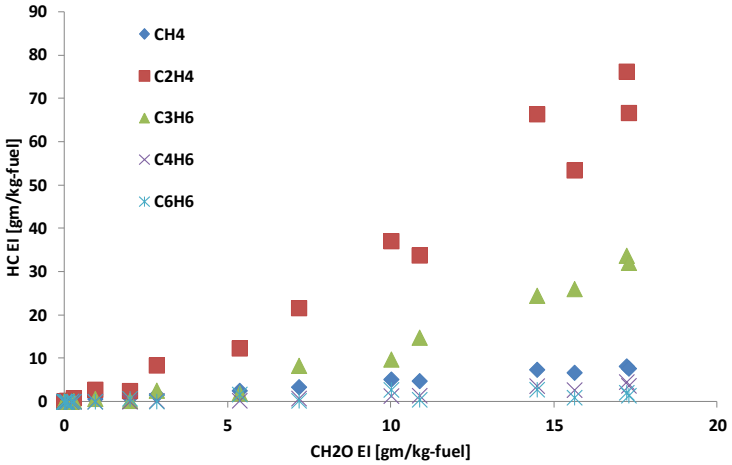

Figure 5-8. Hydrocarbon EI vs. formaldehyde EI for opposed-jet flame.

5.3.2 Quench Requirements to Freeze Hydrocarbon Emissions

The analysis in the prior section establishes that hydrocarbon emission indices are approximately linear within the structure of premixed flames. Similar results at different equivalence ratios have been obtained, although the slopes are slightly different. In order for such emissions to transit the combustor volume and maintain these constant ratios, the gases must be quenched to suppressed further reaction.

To consider required quench times, the residence times in the freely propagating and opposed-jet fames have been computed and are given in Figure 5-9. The total times through the reaction zones in the flames are approximately 200 microseconds, which is at least a factor of 20 times less than the residence time in the combustor. To quench this reaction zone, one may speculate that a quench time much shorter than the dwell time in the reaction zone of the flame will be required.

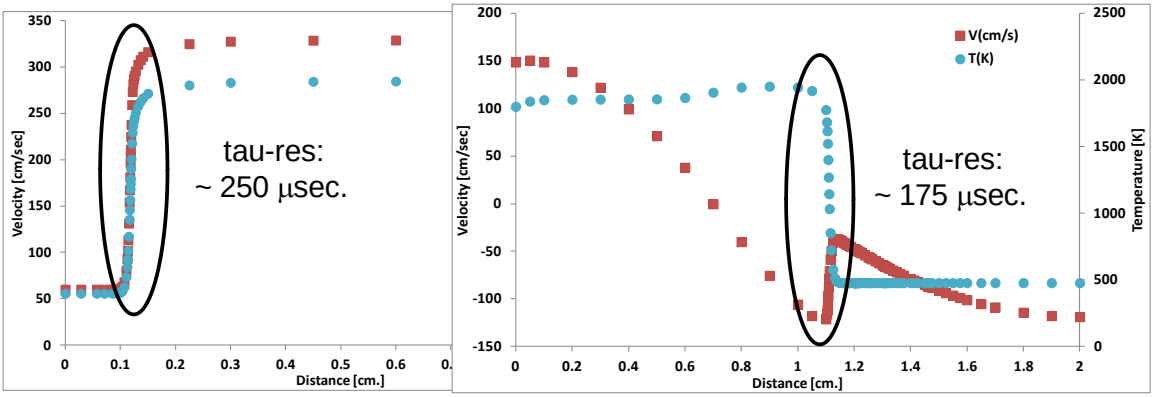

Figure 5-9. Residence time comparisons of unstrained and strained premixed flames.

5.3.3 NETPSR Reactor Analysis

In addition to the flame analysis, we have performed a large series of simulations using the NETPSR code at UTRC. Initially, we attempted to simulate the bulk characteristic of the burner flows and residence times.

Most of these efforts were unsuccessful. One approach, not inconsistent with the above discussion on flame structure and quenching requirements, was successful and is described below.

The successful network model is shown in Figure 5-10. Key features are (1) a partially burned lean (phi = 0.6) mixture, to start the process, (2) extra unreacted fuel is added immediately afterwards along with additional air to make a new mixture at a new (but specified) equivalence, but insufficient time to react completely, and (3) rapid quenching due to quickly added air, with insufficient time to complete reaction of the partially burned mixture with added fuel, and finally (4) a burn-out reactor, to allow the system to relax, if reaction kinetics are still occurring.

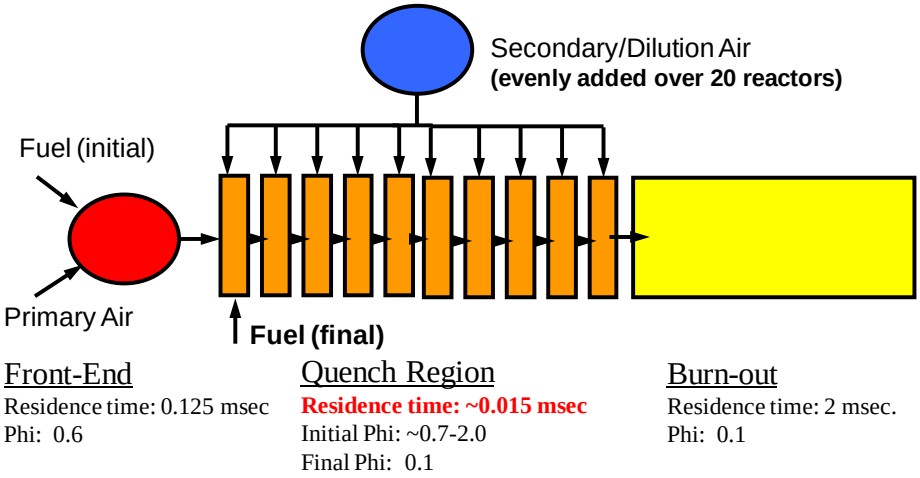

Figure 5-10. Schematic of reactor series (T_3 = 477K, P_3 = 4.08 atm).

This model produces linear relationships between the different hydrocarbon species (and hydrocarbon oxygenates as well) when the added fuel/air mixture results in overall lean conditions, as shown in Figure 5-11. In this figure, emission indices of methane (CH_4), ethane (C_2H_4), acetaldehyde (CH_3CHO), propene (C_3H_6) and 1,3-butadiene (C_4H_6) are shown plotted against that of formaldehyde (HCHO). The more spread out points (mostly on the lower branch), are obtained when the added fuel in the first quench reactor (2^{nd} reactor in Figure 5-10) raises the equivalence ratio in the reactor just a little (usually lean conditions), and the denser points are obtained for large amounts of additional fuel added (up to very fuel-rich conditions). In all cases, extra air is added to always lean out the mixture to an overall equivalence ratio of 0.1 at the entrance of the burn-out zone. Hence the added air in the quench zone changes for each of these cases.

For both the very lean cases and the very fuel-rich cases, the hydrocarbons are nearly linearly proportional; yet the proportionality constants are different. We will argue that it is the slope of the first few (sparse) points that are responsible for the universal (linear) results, as changes in our assumptions will alter the fuel-rich branch, while the fuel-lean branch remains unaltered.

A critical feature of this network is that the residence time in the first quench volume must be very short (< 1 microseconds) with a total quench time of the quench reactor sequence of ~15 microseconds. Otherwise sufficient reactions will occur, leading to heat release and an acceleration of the reaction chemistry towards products. In such cases, the linearity amongst hydrocarbon species as observed in Figure 5-11 will not exist.

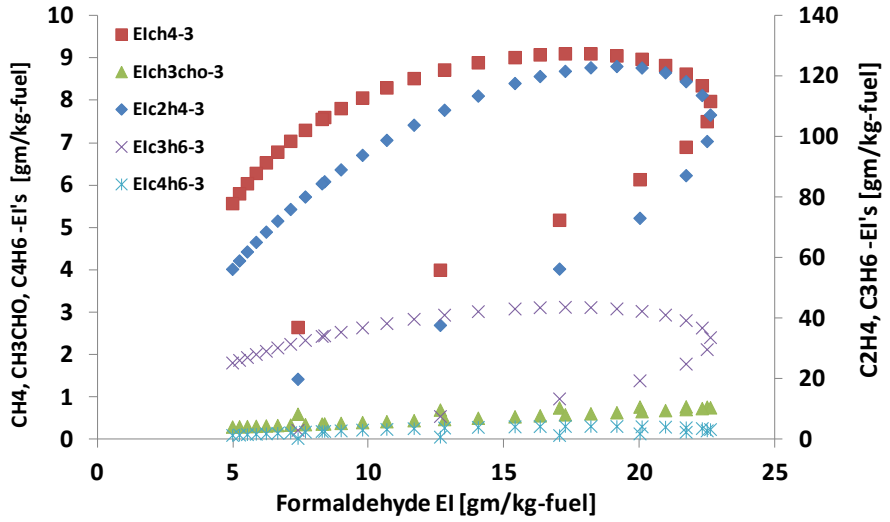

Figure 5-11. Trends in emission indices for a variation in equivalence ratio of 1st quench reactor.

In most cases, the constant (relative to the formaldehyde level) is higher for the fuel-rich cases. However, this is not a general rule. For the case of acetaldehyde (CH_3CHO) in Figure 5-11 and for benzene (C_6H_6) in Figure 5-12, the rich results have lower slopes than for the lean conditions. Under lean conditions for CO a linear relationship is not observed (Figure 5-12). Also shown in Figure 5-12 are data showing that concentrations of the original fuel fragments (n-dodecane and m-xylene) increase dramatically, with increasing fuel-richness in the 2nd reactor.

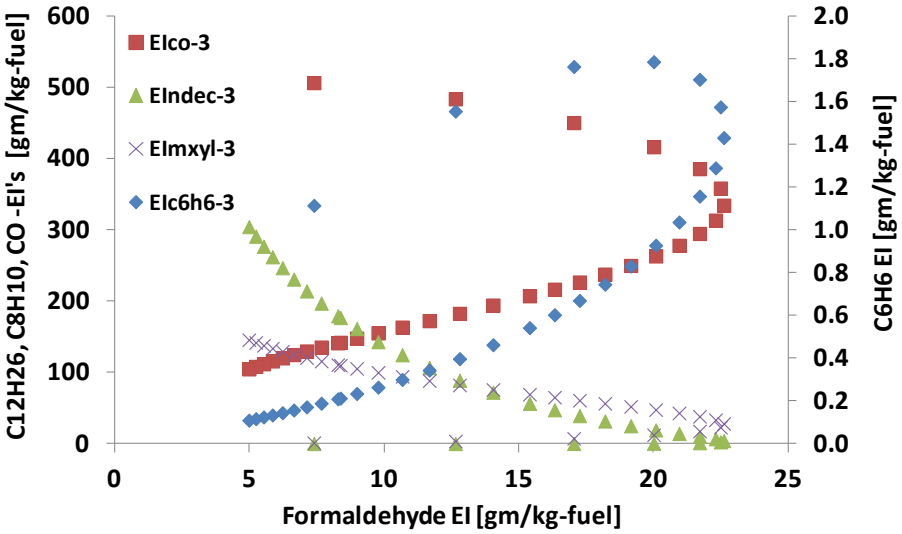

Figure 5-12. Trends in indices for variations in equivalence ratio of 1st quench reactor.

This network configuration has been explored over a broad range of conditions to test the generality of any conclusions. First, we have perturbed the quench rate to evaluate the consistency of the solutions.

As shown in Figure 5-13, the linear relationship between ethylene and formaldehyde predicted values are insensitive to the assumed quench rate. The quench was extended by diverting some of the fuel to the 3rd, 4th and 5th reactors in a proportional manor (resulting in extended quench times from ~0.8 microseconds to ~3 microseconds). There is a hint that a (higher) constant ratio exists for the rich side (top portion of the curve). The lean side (lower branch) is invariant.

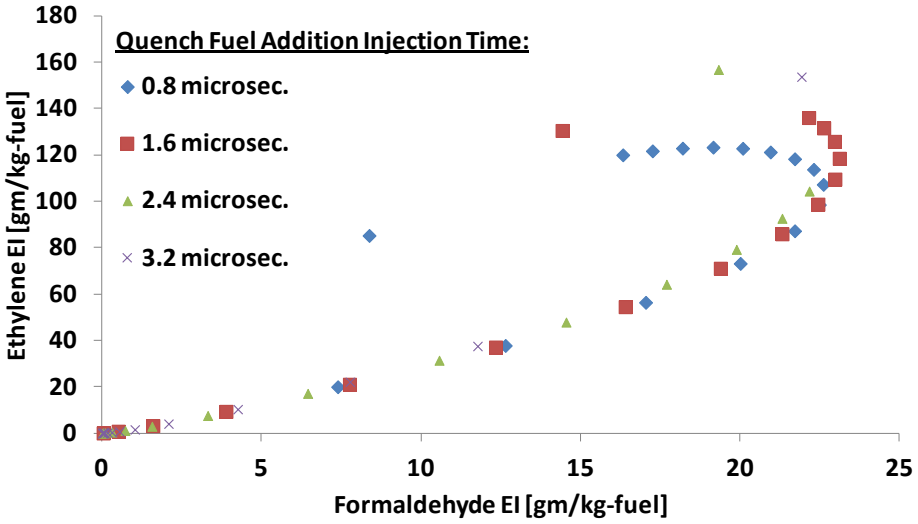

Figure 5-13. Trends in indices for variations in quench times.

In Figure 5-14, ethylene emission indices (as a function of the formaldehyde EI) are plotted for different assumed values of the initial equivalence ratio (phi). The (lower-branch) ethylene solutions appear to be invariant; however, note that for these cases, the very first reactor (in Figure 5-10) can start at substantially fuel-rich conditions, yet the initial slope with small amounts of fuel addition is unchanged.

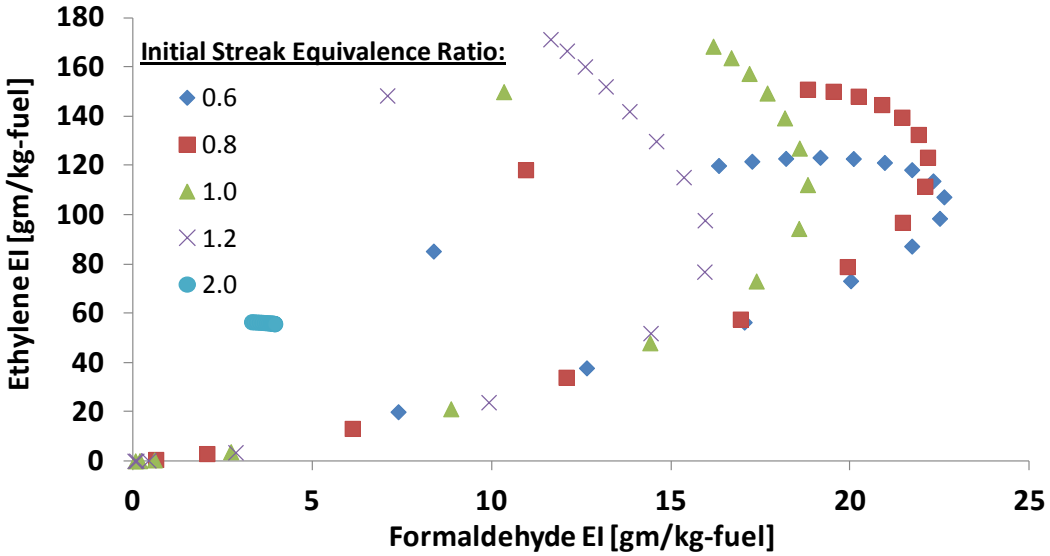

Figure 5-14. Variations in ethylene emission indices for different initial equivalence ratios.

In summary, we find that linear relationships occur for quenching of both fuel-lean and fuel-rich gases, but that the ratios are different for the fuel-lean and fuel-rich sides; that ethylene emission indices are relatively invariant to a wide variety of assumptions on the fuel-lean side, when just small amounts of additional fuel is added (usually fuel-lean); and that unburned fuel fragments increase significantly with increasing fuel-air ratio in the quenched gases.

5.3.4 Quantitative Comparisons

An important aspect in arguing whether or not the above modeling results provide an insight into the linearity amongst hydrocarbon exhaust emissions is a quantitative comparison. A first observation is that the peak formaldehyde (EI) levels observed in the above reactor and flame analyses are ~ 20, whereas the engine emission data are O(1). We believe that this difference is a simple matter of dilution within the combustor. In fact, most of the fuel must still be burning to completion with negligible hydrocarbon emissions; otherwise the burner efficiencies would be very low. A partially burned fraction of up to 5% of the fuel appears at least plausible. This would explain the difference in the magnitudes in the emission indices.

A second question will be on the slopes of the lines. Are the model predictions in fact consistent with the experimental observations? A summary of various hydrocarbon emission indexes (HCEI) vs. that of formaldehyde for the network reactor solutions, the freely propagating opposed jet flame and the strained premix flame (as well as other conditions) are compared in Table 5-1 against the experimentally observed values for various engine exhaust streams. Considering the range in model configuration, the uncertainties in the detailed reaction model and the surrogate definition, this comparison is very encouraging. The results support arguments of very rapid decay of the primary fuel into fragments of hydrocarbon products (depending on the chemistry to the primary fuel), followed by a 'relatively' slow oxidation of the hydrocarbon intermediates.

Table 5-1. Comparison of various predicted HCEI ratios against Formaldehyde Emission Indexes (EI) with engine exhaust data.

	Model Predictions					Engine Data	
	PSR Network	Opposed Jet	Opposed Jet	Pre-mixed	Pre-mixed	Spicer	Aerodyne
	(Lean Side)	(Burned (0.6) vs. Fuel/Air	(Fuel/Air (1.0) vs. Fuel/Air	Phi = 0.6	Phi = 1.0	(JP-5/CFM-56/idle)	(AAFEX/JP-8)
CH4	0.44	0.49	0.72	0.42	0.76	0.43	-
C2H4	3.27	4.25	3.93	3.2	4.2	2.69	1.33
C3H6	0.61	1.63	1.59	1.45	1.66	0.79	0.51
C4H6	0.06	0.23	0.14	0.14	0.15	0.3	-
C6H6	0.17	0.18	0.09	0.05	0.1	0.32	0.16

There are of course differences between the predicted values and the experiments. We attribute these differences to three probable causes: (1) the fuel surrogate is inadequate as it was selected for soot emissions, not for gaseous emissions; (2) the reaction kinetics model has weaknesses; and (3) simplified model scenarios examined incompletely describe the complex turbulent reacting flow phenomena in real

combustors, with liquid fuel. Resolving the last of these will be challenging within the scope of the present program, but substantial progress can still be made with the first two issues.

5.3.5 Predictions for Different Surrogate Fuels

The network model was extended to explore whether predictions differ if different fuels were used. Experimentally, in engine exhaust tests with various alternative fuels, it had been observed that many of the major species followed the same hydrocarbon fingerprint as with petroleum jet fuels. Some minor differences were observed with light hydrocarbon species but much larger differences were observed with the aromatic species. The differences correlate with levels of aromatics in the parent fuel.

In an attempt to replicate these experimental observations, predictions were made with pure n-dodecane, and two other 'fuels', one with added m-xylene and the other with added methylcyclohexane. Emission indices for several hydrocarbons are plotted against that of formaldehyde for each of the three fuels in Figure 5-15. As can be seen in the plots, several of the major species (ethylene and propene) are virtually identical for the lower portion of the curves. These are the linear sections and correlate with overall lean conditions in the volume with added unreacted fuel/air mixture just before the rapid quench (first orange box in Figure 5-10). This result is consistent with the experimental observations and our speculation that the hydrocarbon emissions are a result of rapidly quenched (lean) pockets of gas.

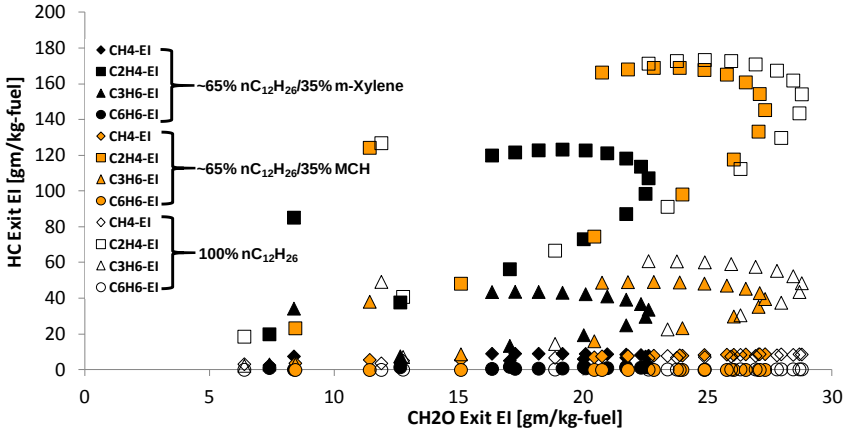

Figure 5-15. Emission indices of several hydrocarbons (HCEI) for three fuels.

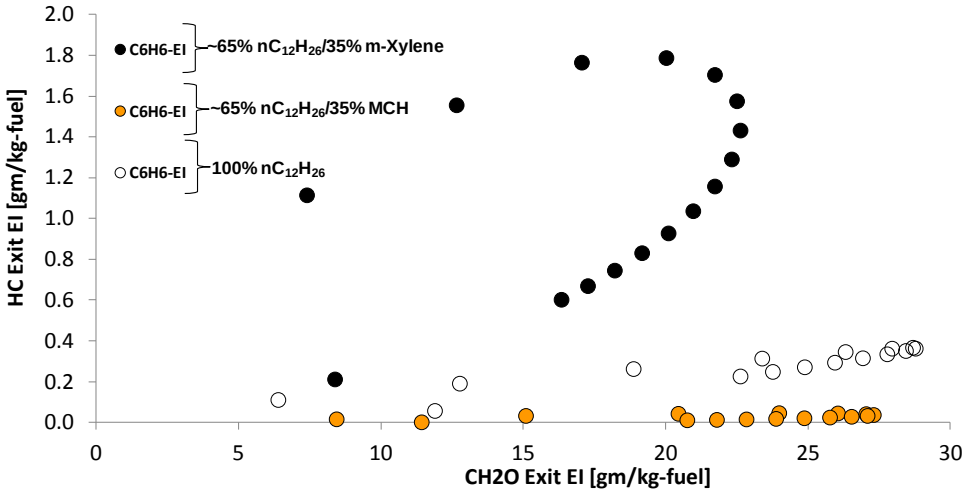

Figure 5-16. Predicted emission indices of benzene for three different fuels.

To compare the predicted benzene profiles, we present an expanded scale in Figure 5-16. It is clearly shown that there are substantial differences between the pure n-dodecane fuel and that with mixed m-xylene. As observed in the experimental data, benzene levels are noticeably higher with the fuel having the high aromatic content. The low benzene prediction with added methylcyclohexane in the fuel is a surprise and we are exploring the mechanistic processes that produce this modeling result.

We also considered methane for which we observed differences (not shown here). The results with n-dodecane and n-dodecane with added m-xylene had virtually identical slopes, but the data with added methylcyclohexane exhibited a slightly higher slope (~10%) than for the other fuels. Again this is an issue worth further exploration.

5.3.6 Impact of Engine Cycle on Emissions Trends

To explore the generality of our modeling results, the computations were also run for a range of low power conditions. (High power conditions result in very high combustion efficiencies and virtually no unburned hydrocarbon emissions.) The results for the lean side emissions are shown in Figure 5-17. As can be observed, the data all result in the same slope as obtained for the idle conditions, which was assumed for all of the conditions in the other analyses. This result provides further support for the arguments presented here, as the experimental data were obtained not only for different engines at different locations, but also at different engine power levels.

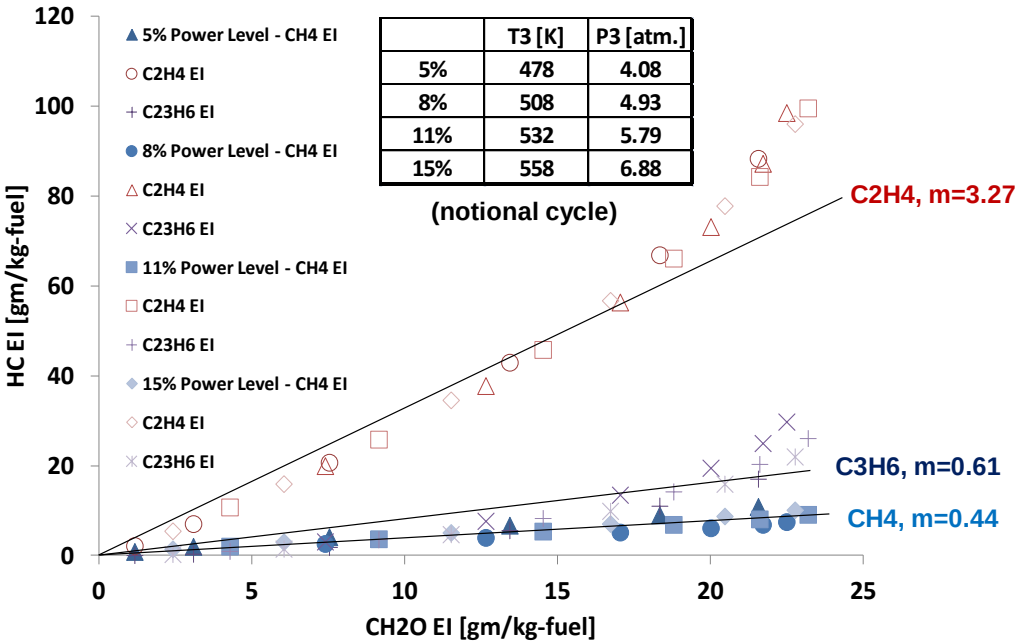

Figure 5-17. Prediction of hydrocarbon emissions from the network reactor code.

5.4 Computational Study of Formation of UHC Emissions in Opposed-jet Flames

A fundamental study on nonpremixed flames is carried out in this project for understanding the HCs generated in the flame zone. It is believed that small fractions of the HCs produced in the flame zones are transported through the combustor and eventually show up as UHCs in the exhaust. Calculations for the opposing-jet flames formed between air and HC fuels are made using UNICORN-2D code and the resulted speciation profiles along the stagnation line for different fuels are compared. The opposed-jet flame is selected for the initial alternative fuels HC emissions study because it has quenching characteristics, at high strain rate, that are similar to those expected in practical gas turbine combustors. Thus, this study is conducted to provide insights into the similarity and differences between HC emissions in gas turbine engine and in an opposed jet flame.

The chosen burner configuration consists of two opposing jets of diameters 10 mm each. The separation distance between the exit planes of these two jets is 10 mm. The bottom jet consists of HC fuel and the upper jet consists of air. The temperatures of the fuel and air jets are set as 300 K. Velocities of the fuel and air jets are varied for obtaining different strain rates on the flames. For eliminating the disturbances that might arise because of the ambient air entrainment, both the fuel and air jets are surrounded by a low-speed (0.1 m/s) nitrogen flow. Simulations for the flowfield between the upper and lower jet exits are performed using a 301x41 variable grid system, which yields a uniform spacing of 33 mm in the axial direction (across the flame surface) and expanding spacing with a minimum of 100 mm in the radial direction (along the flame surface).

Calculations for the opposing-jet nonpremixed flames formed with various HC fuels and at different stretch rates are performed. Fuels used in this study are methane, acetylene, ethylene, ethane, propane, n-heptane, iso-octane, n-decane, n-dodecane, and JP-8. Note that JP-8 fuel is modeled as a surrogate mixture

of 77% n-dodecane and 23% m-xylene. For each fuel, calculations are started with an air-jet velocity of 0.25 m/s and then gradually increased until the flame extinguishes. In order to keep the flame close to the mid-section between the fuel and air jets, the momentums of the fuel and air jets are kept equal while changing the velocities. Opposing-jet flames are typically characterized with global or airside strain rates. Global strain rate (k) is defined as

$$\textit{Global Strain Rate} \quad k = \frac{2|V_2|}{L}\left(1+\frac{|V_1|}{|V_2|}\sqrt{\frac{|\rho_1|}{|\rho_2|}}\right)$$

Here, V_1 and V_2 represent the velocities of the fuel and air jets, respectively and r_1 and r_2 represent the densities of the respective jets. L is the separation distance between the fuel- and air-jet exits. Airside strain rate (k_a) is the maximum local strain rate that air jet encounters while entering the flame zone. As the air jet moves closer to the stagnation point, local strain rate increases. However, due to volumetric expansion, local strain rate starts to decrease as air enters the reaction zone, resulting in a local peak value in strain rate. This value is obtained through plotting local strain rate along the stagnation line (centerline) for each case.

Results obtained for all the fuels and at all strain rates are shown in Figure 5-18. Here, variations in the peak temperatures of the flames are plotted with respect to global (Figure 5-18a) and airside (Figure 5-18b) strain rates. The highest strain rate for each fuel represents the value at which flame extinguishes. Among all fuels, acetylene forms the most stable flames (global extinction strain rate ~ 2000 s^{-1}) with peak temperatures (> 2100 K) that are well above those of the flames formed with the other fuels. For showing the differences in the flame responses to the strain rate for different fuels, results of the acetylene flames are not considered in Figure 5-18. As expected, flame temperature decreases with strain rate. When the flames are weakly stretched temperature of the ethylene flame was highest and that of the JP-8 flame was the lowest. The differences in the temperatures of the weakly stretched flames more or less correspond to the maximum strain rate that flame can withstand. Ethylene flame extinguished when the global stain rate reached ~1345 $s,^{-1}$ while JP-8 flame extinguished when the global strain rate reached a value of ~ 83 $s.^{-1}$ An exception to this behavior is observed for methane fuel. Even though the weakly stretched methane flame has a peak temperature that is between those of the ethylene and ethane flames, it extinguished at a global strain rate that is much lower than those of ethylene and ethane. To see whether the spread in the extinction strain rates of various fuels is due to the type of strain rate considered in Figure 5-18a, variations in peak temperatures are plotted with respect to airside strain rate in Figure 5-18b. In general, airside strain rates are slightly lower than the global strain rates. Other than that the flame responses to strain rate are similar when plotted against global or local strain rate values.

It is possible that the combustion inefficiency observed in the aircraft gas turbine engines could result from the premature extinguishment of a small fraction of flamelets. Therefore, it is important to know how the UHCs found in the engine exhausts are generated in flames near extinction conditions. Distributions of temperature and various UHCs along the centerline are shown in Figure 5-19 for methane flame at a global strain rate of 448 s^{-1}. As shown in Figure 5-18, further increase in strain rate extinguishes this flame. Distribution of temperature gradient is also shown in Figure 5-19a for understanding the underlying chemical activity. The stagnation point (where the velocity is zero) is marked with a black bold line and the flame location based on CH peak is marked with a red arrow in Figure 5-19b. Fuel and air are entering the reaction zone from the left and right sides of the flame location, respectively. A list of various UHCs found

in aircraft engine exhaust has been compiled by Spicer et al. (1994) and Knighton et al. (2009). There are about 50 UHCs in those lists. For the purpose of simplicity, only the first 12 UHCs (ethylene, formaldehyde, acetylene, propene, acetaldehyde, acrolein, butene, butadiene, benzene, ethane, propanal, and pentene) in the list of Knighton et al. (2009) are considered in the present study. Note that species glyoxal, methylglyoxal and butanal are not considered due to their unavailability in the chemical-kinetics mechanism adopted for this study. Variations of these 12 HC species along the centerline for the 448-s^{-1}-methane flame are shown in Figure 5-19b. Note that as the concentration of propanal is < 0.01 ppm it is not shown in Figure 5-19b.

As expected, the majority of the HC species are present on the fuel side of the flame. Concentrations of some of the HCs (ethylene, acetylene and ethane) generated in simple methane flame are higher than those found in the engine exhaust (Spicer et al., 1994, Knighton et al., 2009). It is interesting to note that these HCs survive and diffuse into the cold fuel (z < 4.7 mm). The major difference in the environments that HCs encounter in the nonpremixed flames and engine exhaust is the availability of oxygen. The HCs generated in the former survive due to lack of oxygen. Temperature and species distributions in the near-extinction propane flame are shown in Figure 5-20. The global strain rate for this flame was 377 s^{-1}. Unlike in the methane flame, the propane flame shows an inflection region in temperature profile on the fuel side. Rate of increase in temperature, on the fuel side in the case of propane flame, increases initially and then decreases before increasing again. Such endothermic reactions become more pronounced as the carbon content in the fuel increases. Flame structures plotted in Figure 5-21 and Figure 5-22 for fuels heptane and JP-8, respectively, show more pronounced inflections in temperature profiles. All the 12 considered HCs are produced in the heptane and JP-8 flames and are diffusing into the cold fuel.

In general, the concentrations of HC species produced in the reaction zones of the nonpremixed flames are higher than those found in engine emissions. However, there are some exceptions. For example, maximum concentration of propanal in propane, heptane and JP-8 flames is ~ 1 ppm, whereas, data of Spicer et al. shows ~ 17 ppm propanal in engine emission. More interestingly, acetaldehyde found in engine emissions is about 25 times more than that produced in JP-8 nonpremixed flame. Formaldehyde is also produced less (by ~ 50%) in nonpremixed flames than in engine emissions.

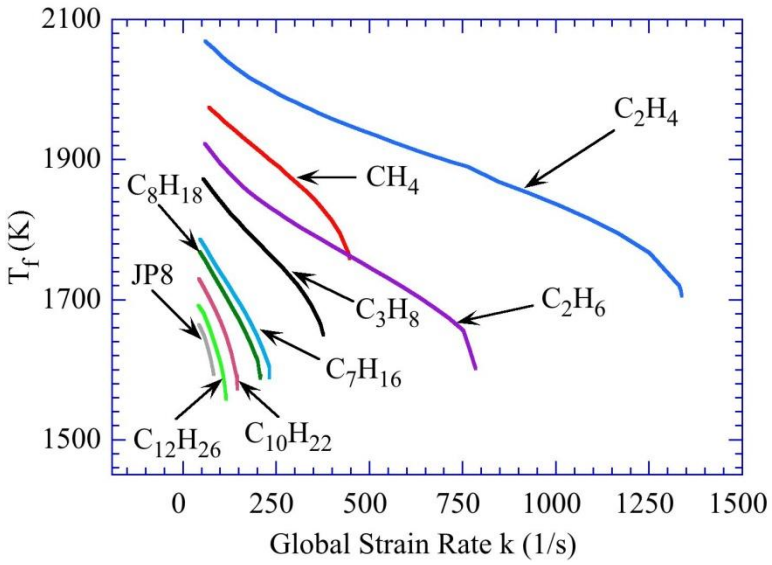

(a)

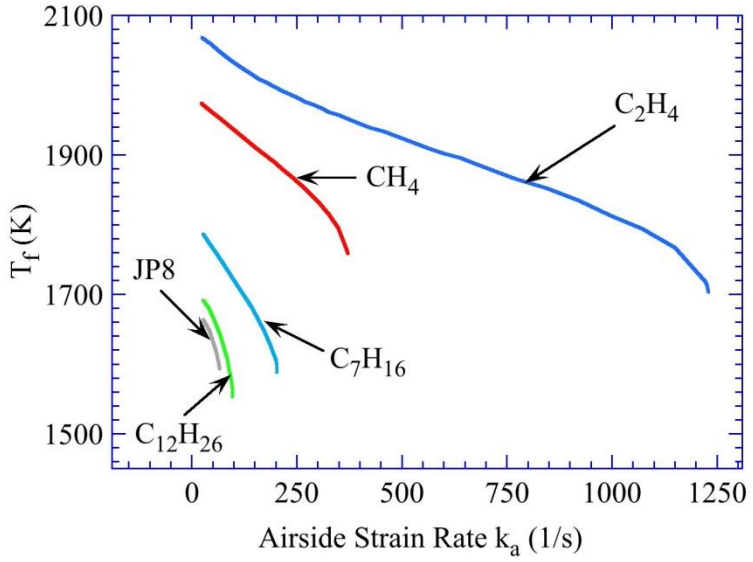

(b)

Figure 5-18. Peak temperatures of the opposing-jet nonpremixed flames formed between air and hydrocarbon fuels at different strain rates. (a) Data are shown with respect to global strain rate and (b) data are shown with respect to airside strain rate.

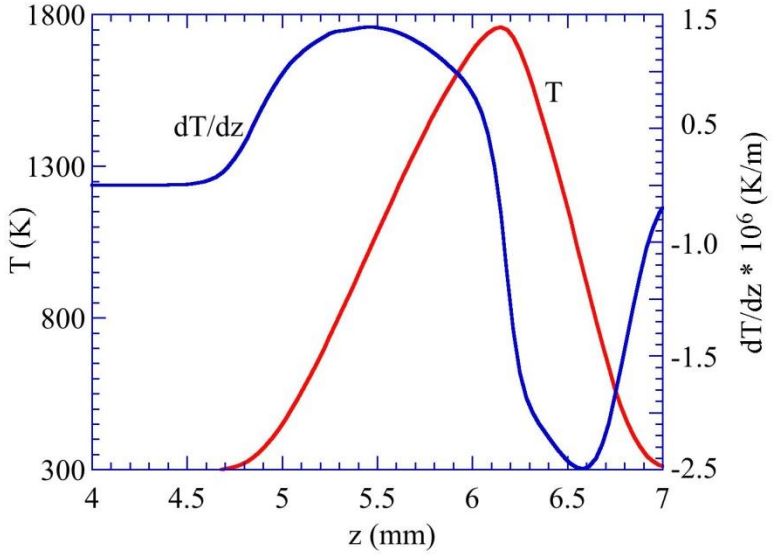

(a)

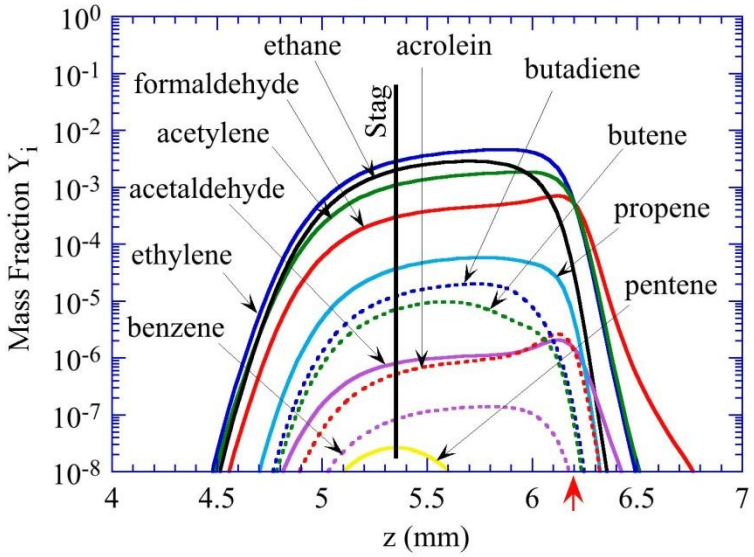

(b)

Figure 5-19. (a) Flame structure and (b) various hydrocarbon species produced in a near-extinction opposing-jet flame formed between air and methane. Global strain rate is 448 s^{-1}.

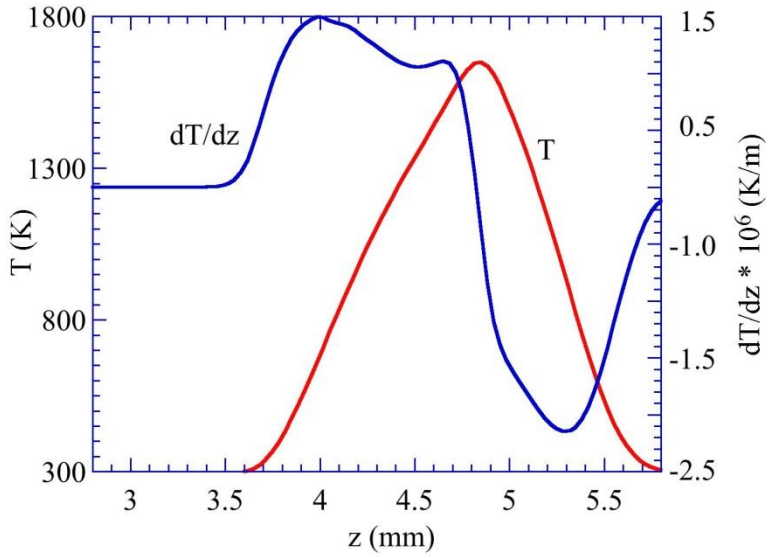

(a)

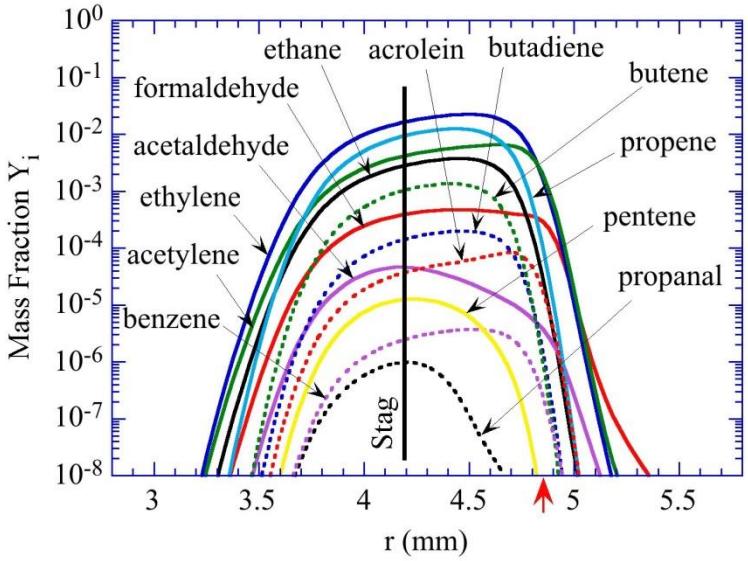

(b)

Figure 5-20. (a) Flame structure and (b) various hydrocarbon species produced in a near-extinction opposing-jet flame formed between air and propane. Global strain rate is 377 s^{-1}.

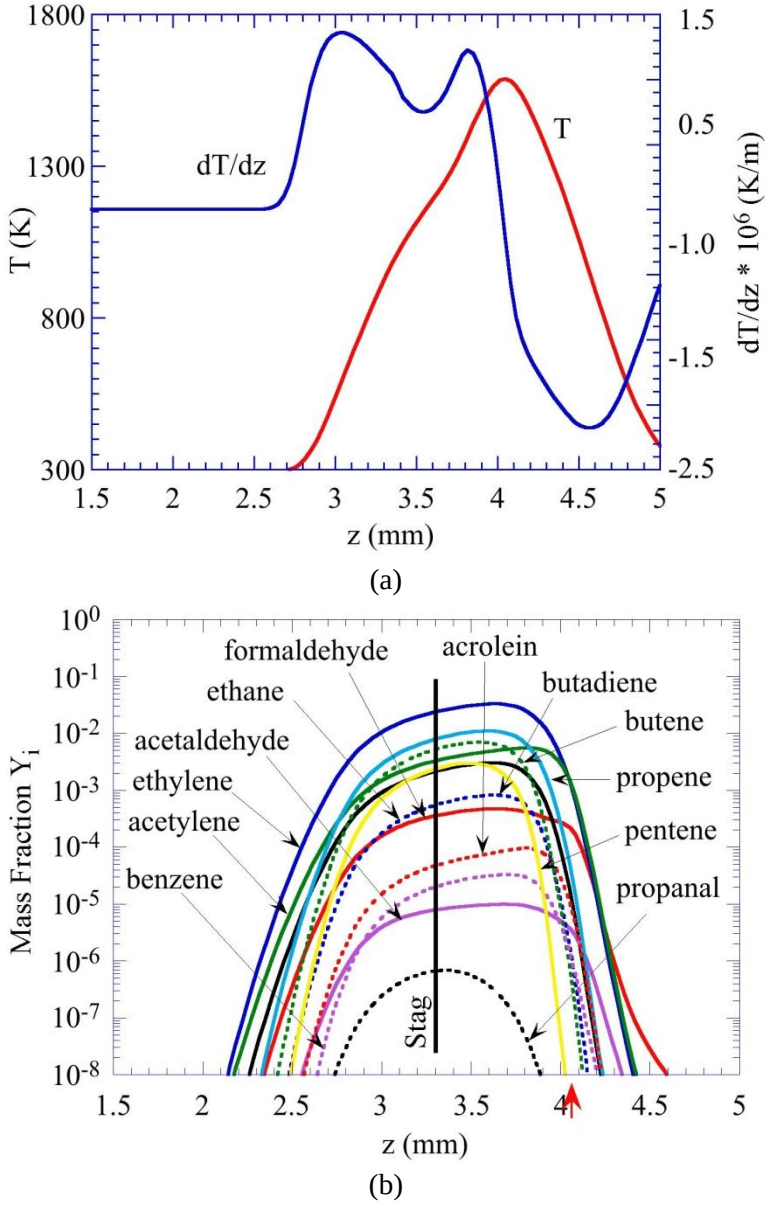

Figure 5-21. (a) Flame structure and (b) various hydrocarbon species produced in a near-extinction opposing-jet flame formed between air and heptane. Global strain rate is 233 s^{-1}.

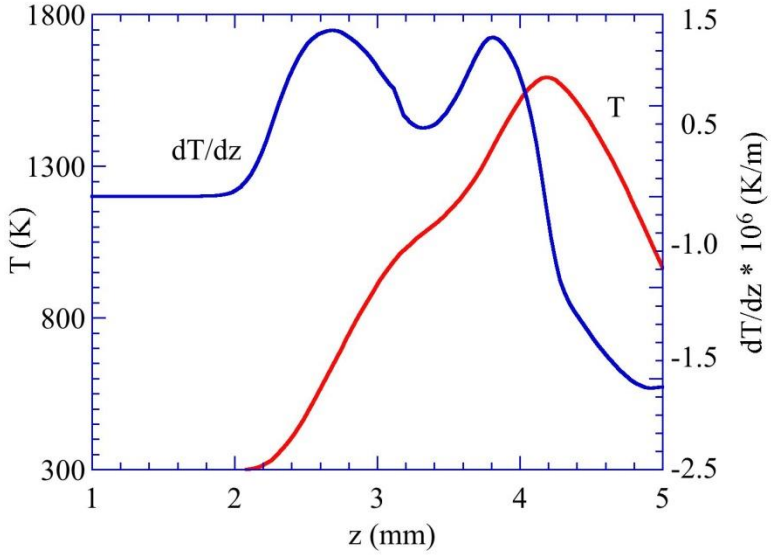

(a)

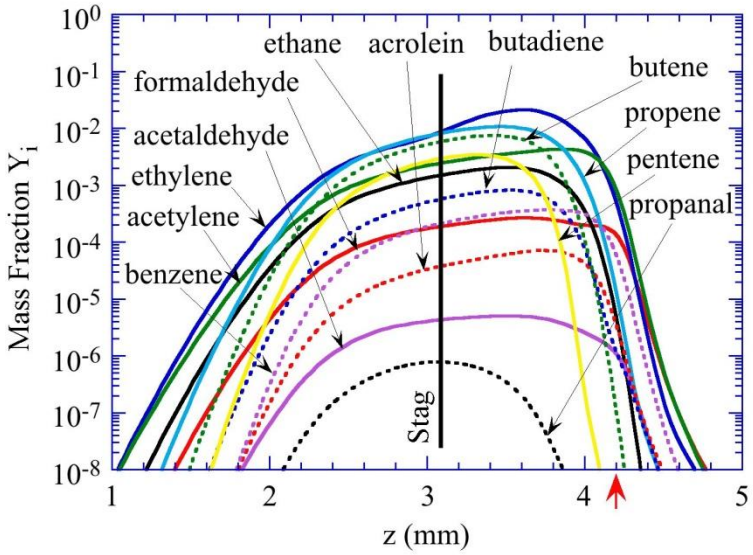

(b)

Figure 5-22. (a) Flame structure and (b) various hydrocarbon species produced in a near-extinction opposing-jet flame formed between air and JP-8. Global strain rate is 83 s^{-1}.

5.5 Primary Flame Zone Structure - the role of preferential diffusion

The primary zone of a gas-turbine engine typically consists of recirculation zones (RZs) that are established with bluff-bodies and swirling fuel and/or air jets. While the RZs serve as flame holders, the swirling jets in these engines help the combustion processes to take place in compact, stable, and efficient way and in breaking up of the liquid fuels. On the other hand, formation of pollutant emissions such as soot, carbon monoxide (CO), nitric oxide (NO), and unburned hydrocarbons (UHC) in the combustor also

depends strongly on the flames established in the primary zone. Therefore, it is necessary to understand the primary zone flame structures not only for improving the stability of the combustor but also for reducing the pollutant emissions. Experimental or numerical studies focusing on understanding the primary zones of the modeled gas-turbine engines are limited due to the complexity in the geometry and operating conditions such as pressure. Alternatively, researchers are obtaining detailed flowfields and chemical structures of the RZs in simple bluff-body burners with a hope that the fundamental understanding gained on these RZ-supported flames can be extrapolated to the primary zones of a gas-turbine engine. For example, Air Force centerbody burner was designed to establish different sooting structures, Cambridge swirl burner was designed to stabilize stratified flames over a range of flow rates and Sidney bluff-body burners were designed to produce benchmark data for model validation.

Recent experiments of Barlow et al. (2011) in a bluff-body stabilized, turbulent lean premixed CH_4/air flames revealed that atom balances (atomic mass fractions) were not conserved across the flame brush going from reactants to products. Through the measurements of temperature and major species (CO_2, O_2, CO, N_2, CH_4, H_2O, and H_2) they computed C/H atom ratios at different locations in the flame and found that its values can exceed that of the original fuel by more than 10 percent. Conducting some well-planned experiments on laminar and turbulent burners they hypothesized that H_2 and H_2O diffusive preferentially ahead of CO_2 and CO toward the reactants and are subsequently transported (through advection) downstream and away from the local flame brush. They also concluded that RZ causing preferential transport effect to be amplified.

The physics leading to a biased distribution of C and H atoms may also take place in the primary zones of a gas-turbine engine and may play a role in the amount of soot and UHCs produced. The importance of the findings of Barlow et al. (2011) warrants further verification/validation. Therefore, reacting flows in Sandia bluff-body burner are simulated using a detailed CFD code and investigated the reasons for increase in local C/H atom ratio. Calculations for the Air Force centerbody burner are performed and the distributions of C/H atom ratio in the RZ-supported nonpremixed flames are obtained.

UNICORN-2D was used for simulating combusting flows in the bluff-body burners. GRI Version 3.0 (Smith, et al.) developed by Gas Research Institute (consisting of 53 species and 650 elementary-reaction steps), was incorporated into UNICORN. Mixture viscosity and thermal conductivity were then estimated using the Wilke and Kee expressions, respectively. Temperature-dependent molecular diffusion was assumed to be of the binary-diffusion type, and the diffusion velocity of a species was calculated using Fick's law of mass diffusion and the effective-diffusion coefficient of that species in the mixture. While the thermal diffusion (Soret effect) was ignored, the final diffusion velocity of each species is obtained by adding a constant (independent of species) correction velocity that was obtained from the mass-conservation equation. Note that Soret effect was purposefully ignored in this work for identifying the preferential-diffusion effects in bluff-body flames.

The bluff-body burner of Sandia consists of a 12.5-mm diameter centerbody and a single annular non-swirling premixed flow of 5-mm thickness. A large annular co-flow (diameter of 19.2 cm and velocity of 0.4 m/s) of air was used to prevent environmental entrainment and to provide known boundary conditions. Velocity of the fuel flow was varied from 1.3 m/s to 7.7 m/s. A perforated plate was mounted in the annular gap 35-mm upstream of the exit plane to act as a turbulence generator. However, since the Reynolds number based on the bluff-body diameter and cold flow properties of the reactants is only 6400 for the highest velocity case (7.7 m/s), simulations for the combusting flow in this burner are performed assuming that the flow is laminar. Note that the intention of the present study is not for directly comparing

the simulations with the experiments; but, rather, for exploring the preferential diffusion effects on C/H-atom distribution (which is a laminar transport phenomenon) in the RZ-supported flames.

Calculations for the Sandia bluff-body burner were made using UNICORN code after constructing a nonuniform 301x501 computational mesh system over a 50-mm x 200-mm physical domain in the radial and axial directions, respectively. This gave a 40-μm resolution in the radial and axial directions in the neighborhood of the reaction zone. Premixed mixture of methane and air at an equivalence ratio of 0.77 was used as fuel. Flat velocity profiles were used for the main fuel jet and for the coannular air jet. While the inlet temperatures of the fuel and air jets were set as room temperatures, the bluff-body was treated as an adiabatic wall. Flow values at the exit boundary were obtained using linear interpolations of the corresponding values from the interior points. Results obtained for the fuel-jet velocity of 6.4 m/s are shown in Figure 5-23. Similar to that seen in the experiments (Barlow et al., 2011), a steady premixed flame, anchored to the outer edge of the bluff-body, is established. The flame surface (identified from the heat-release-rate contour in the right half of Figure 5-23) is curved inward toward the centerline first and then expanded away from the centerline in the downstream locations. A recirculation zone of ~ 10 mm height is established behind the bluff-body. Note that even though the flow became unsteady in the downstream locations (> 50 mm), the flame and RZ near the bluff-body remained steady. It is known that combustion stabilizes the RZ of a bluff-body. In the absence of any flow instabilities it is expected that a 3D unsteady simulation would also result in a flame that is identical to the one shown in Figure 5-23. Distribution of the C/H atom ratio, evaluated from all the 53 species in the local mixture, is shown on the right half using rainbow color scheme. Note that the experimental data reported in Barlow et al. (2011) considered only the major species (CO_2, O_2, CO, N_2, CH_4, H_2O, and H_2). Sampling of these major species from the simulated flame data yielded C/H atom ratios that are lower by ~ 1.2%-suggesting a negligible influence of minor species on C/H atom ratios. Distributions of H_2O (broken lines) and CO_2 (rainbow colors) are shown in the left half of Figure 5-23.

For the methane-air combustion system in the absence of preferential diffusion one should expect a constant C/H atom ratio of 0.25. However, due to preferential diffusion, C/H atom ratio on the reactants side of the flame surface (200-w/cm^3 contour) decreased below 0.25 and on the products side it increased above 0.25 (Figure 5-23). More interestingly, C/H atom ratio increased significantly near the flame surface close to the bluff-body. This confirms the findings of Barlow et al. (2011). Based on the limited experimental data available to them, Barlow et al. (2011) speculated that the observed increase in C/H ratio was due to the presence of RZ near the bluff-body. Even though the region where C/H atom ratio increased significantly falls within RZ, Figure 5-23 also suggests that there are some other regions in RZ where C/H atom ratio did not increase that much. The low-speed flow in RZ provides longer residence times for the fluid elements and, thereby, causes chemical reactions to progress further and enhances molecular diffusion. The former effect would increase (or decrease) the species concentrations at the RZ center where velocity approaches zero and the latter effect would make the species to distribute uniformly within RZ. Species distributions, obtained from the computed data (such as Figure 5-23), showed neither an increase nor a decrease in their concentration at the RZ center, nor uniformity within the RZ. These observations made from computational data raises a question “is RZ responsible for the increase in C/H atom ratio?”

In order to understand the effect of fuel-jet velocity on C/H atom distribution in bluff-body supported flames, calculations for Sandia burner with fuel-jet velocities ranging from 2 m/s to 7 m/s were performed. Steady RZs were established for all the velocities and, as expected, the length of the RZ increased with velocity. Results obtained for 3.8-m/s and 6.4-m/s fuel-jet velocities are compared in Figure 5-24. Here,

distributions of CO_2 and H_2O concentrations and C/H atom ratio are plotted with respect to temperature at different heights above the bluff-body. Note that temperature is nearly uniform within the RZ (Figure 5-23). Data obtained for an unstrained laminar 1D flame at an equivalence ratio of 0.77 (Barlow et al., 2011) are included in Figure 5-24(e & f) for comparison purpose. Note that the 1D data were calculated using Chemkin with GRI 3.0 (Smith et. al.) chemical-kinetics and including multi-component transport and Soret effects (Barlow et al., 2011).

Four characteristics heights above the burner surface were considered in the plots shown in Figure 5-24. Data along a radial line 0.5 mm above the bluff-body were used for describing the flame characteristics near the bluff body. Data along the radial lines passing through the RZ centers (located 2.7 mm and 3.3 mm above the burner surface for the 3.8-m/s and 6.4-m/s-velocity cases, respectively) were used for identifying the effects of residence time (note that residence time would be maximum at the RZ center in a steady flowfield). Data along the radial lines passing through the top edges of the RZs (located 7.2 mm and 10.2 mm above the burner surface for the 3.8-m/s and 6.4-m/s-velocity cases, respectively) were used for identifying the effects of RZs. And, finally, data along the radial line (h = 12. 5 mm) away from the RZs were used for characterizing the trailing flame structure. The following observations were made from Figure 5-24:

1. At any characteristic height in the flame C/H atom ratio increases with jet velocity. This was also observed in the experiments of Barlow et al. (2011).
2. Deviation of C/H atom ratio from that of 1D flame was highest near the bluff-body surface and then the difference gradually diminishes in the downstream locations. However, at peak temperature locations, the C/H atom ratio continues to be significantly higher than the corresponding value of the 1D flame.
3. Maximum CO_2 and minimum H_2O (at a given temperature) are found near the bluff-body surface. Distributions near the RZ center where residence time would be longest did not depict any unique behavior such as reaching a maxima or minima. This suggests that the lower velocities within the RZ did not influence the species distributions.

UNICORN code has been validated previously in predicting structures of various premixed and nonpremixed flames. However, for making sure that the preferential diffusion effects predicted in Sandia burner were neither due to systematic errors in the modeling nor due to the non-equilibrium chemical kinetics (residence-time effects), calculations for the 6.4-m/s-fuel-jet-velocity case are repeated after setting the diffusion coefficients of all the species equal and identical to that of O_2. The predicted flame structure in the absence of preferential diffusion is shown in Figure 5-25. A comparison of streamlines in Figure 5-23 and Figure 5-25a suggests that the RZ structure did not change with the imposition of equal-diffusivity condition. As expected, in the absence of preferential diffusion, H_2O contours (broken lines in the left half of Figure 5-25a) are closely following the CO_2 contours (color separations in the left half of Figure 5-25a). The C/H atom ratio has become 0.25 (original ratio in methane fuel) everywhere in the flame (right half of Figure 5-25).

Radial distributions of C/H atom ratio and H_2O and CO_2 concentrations with respect to temperature at two heights from the bluff-body surface are shown in Figure 5-25b. Note that 3.3-mm location is very close to the bluff-body surface where maximum deviations in C/H atom ratio from the unstrained 1D flame data were observed in the detailed simulations (Figure 5-23 and Figure 5-24f) and 12.5-mm location is

downstream of RZ and in the trailing flame. At both locations C/H atom ratio became equal to 0.25, even though, H_2O and CO_2 concentrations at 12.5-mm location are slightly lower than those at 3.3-mm location. This variation in species concentrations resulted from the non-unity Lewis number (ratio between heat and mass transports). Enforcing diffusion coefficient of every species equal to that of O_2 eliminated preferential diffusion in the simulations shown in Figure 5-25, however, it retained Lewis number that is slightly greater than unity. Due to this species distributions plotted with respect to temperature deviated slightly. This was confirmed in a simulation (not shown) performed after adjusting the thermal conductivity of the mixture in such a way that the Lewis number also becomes unity. Simulations shown in Figure 5-25 confirm that the variations observed in Figure 5-23 and Figure 5-24 are due to preferential diffusion of the species and RZ by itself doesn't change the C/H atom ratio.

For understanding the effects of flame stretching on C/H atom ratio, a pseudo 1D flame is considered. Premixed flames formed between the two opposing jets (separated by 10 mm) of methane-air mixtures at an equivalence ratio of 0.77 are evaluated at different stretch rates. The double flame structure along the centerline is typically considered as a 1D-flame problem and is modeled using codes such as CHEMKIN. However, for eliminating the code-variation factor in the present study, UNICORN code is used for computing the 2D structures of the flames at different stretch rates. Results obtained for a weakly (60 s^{-1}) stretched case and a moderately (280 s^{-1}) stretch rate case are shown in Figure 5-26. Here, stretch rate is calculated as twice the jet velocity divided by the jets separation distance. For comparison purpose, data reported by Barlow et al. for the unstretched 1D flame are also included. Also, the 2D color plots of temperature for the two stretch-rate cases are included as insets. Peak temperature decreased from 1944.6 K to 1854.9 K when the stretch rate was increased from 60 s^{-1} to 280 s^{-1} while the weakly stretched flame has recovered nearly 99.86% of the adiabatic temperature of 1947.2 K-suggesting that it is nearly equivalent to an unstretched flame. The C/H atom ratio plotted with respect to temperature for this flame (Figure 5-26) reasonably matched with that of the 1D unstretched flame, especially in the high temperature region. The lower C/H atom ratios of the weakly stretched flame (compared to 1D flame) in the lower-temperature region could be, in part, due to the two-dimensional effects that were ignored in the 1D simulation and, in part, due to the differences in the diffusion models used in UNICORN code and Chemkin (mixture average vs multi-component). Nevertheless, the most notable outcome of this study on opposing jet flames is that the higher C/H atom ratios observed in bluff-body-supported flames (Figure 5-23 and Figure 5-24) are not due to flame stretch and, hence, not due to non-equilibrium chemistry.

The higher C/H atom ratios in bluff-body supported flame (Figure 5-23), especially near the base region, may be explained using Figure 5-27; in which, radial distributions of various species concentrations (normalized with their peak values) and velocity are shown. Flame identified from maximum heat release rate is located at r = 6.07 mm. Due to preferential diffusion H_2O is transported farther into the reactants side (r > 6.07 mm) of the flame surface compared to that of CO_2. Due to the presence of bluff-body, axial velocity (U) is nearly zero on the products side (r < 6.07 mm) of the flame surface and rapidly increases to the fuel-jet value (6.4 m/s) on the reactants side. A combination of this velocity gradient with the higher diffusion of H_2O makes the convective flow on the reactants side to carry more H_2O than CO_2. As a result, H_2O is siphoned out of the products and caused the C/H ratio to increase significantly. Due to entrainment (cf. streamlines in Figure 5-23) in the downstream locations, higher outward diffusion of H_2O is somewhat compensated by the inward convective flow and, thereby, reduced the variation in the C/H atom ratio. The major difference between the 1D flame (example, along the centerline in opposing-jet configuration of Figure 5-26) and the 2D bluff-body-supported flame is that the former doesn't have a convective flow

parallel to the flame surface. As the bluff-body-supported flame experiences convective flow parallel to the flame surface at all heights, more H_2O than CO_2 was always taken out of the flame surface-resulting higher C/H atom ratio in the high-temperature regions at all heights (Figure 5-24). Finally, an increase in the fuel jet velocity increased the removal of H_2O from the flame surface and, thereby, increased the C/H atom ratio (Figure 5-24). Convective flow also affects H_2 and other lighter species; however, due to their significantly lower concentrations, their impact on C/H atom ratio was minimal. Note that RZ doesn't change the velocity gradient near the flame surface and is not causing any increase in C/H atom ratio. On the other hand, higher C/H atom ratios have developed in regions that are beyond RZs (Figure 5-23 and Figure 5-24) and nothing significant in species concentrations or C/H atom ratio developed at the RZ centers.

RZs are crucial in stabilizing not only the premixed flame but also the nonpremixed flames. We have studied several ethylene nonpremixed flames in a centerbody burner in our previous SERDP project. It would be interesting to see the types of distributions one gets for C/H atom ratios in these RZ-supported nonpremixed flames. Attached and lifted-flame configurations of centerbody burner are considered for this purpose. Computed flame structure, for the former case, is shown in Figure 5-28 (a) and that for the lifted case is shown in Figure 5-28 (b). The ethylene-air combustion was modeled using the detailed chemical kinetics developed by Wang and Frenklach (consisting of 99 species and 1066 elementary-reaction steps). Centerbody burner used in these simulations consists of a 46-mm-diameter plate mounted symmetrically in a 80-mm-diameter chimney. A 7.6-mm-diameter hole was made at the center of the plate through which ethylene fuel was injected. Air diluted with nitrogen was flowed through the annular gap between the plate and chimney.

C/H atom ratio distributions in the centerbody flames for the attached and lifted conditions are shown in the right halves of Figure 5-28 (a) and (b), respectively. Note that soot was simulated in these flames and was included in the calculation of C/H atom ratios. The inner and outer RZs associated with the centerbody burner are visualized with streamlines (right halves of Figure 5-28 (a) and (b). H_2O (solid lines) and CO_2 (rainbow colors) distributions are shown in the left halves. Contours of a low heat release rate (5 w/cm^3) are used for identifying the reaction zones. Note that the flame in Figure 5-28 (b) was lifted and anchored to the outer RZ at a location of about 13 mm above the centerbody plate. C/H atom ratios in both these flames are significantly higher along the flame surfaces. RZs in neither flame seem to be enhancing the C/H atom ratios. Especially, the higher C/H atom ratio near the flame edge in the lifted-flame case shown in Figure 5-28 (b) did not advect to the centerbody surface even though a strong RZ was present there. Lack of enhancement in C/H atom ratio near the centerbody plate confirms that RZ doesn't play a significant role in distributing the species preferentially. However, the calculations performed for the Sandia and Air Force burners suggest that C/H atom ratio could significantly increase behind a bluff-body. The significance of preferential diffusion on UHCs will be studied during the remaining project period.

Calculations for the Sandia bluff-body burner are made for higher velocities (Reynolds numbers) using a nonuniform mesh system of 301x501 points distributed over a physical domain of 50-mm x 200-mm in the radial and axial directions, respectively. This gave a 40-μm resolution in the neighborhood of the reaction zone. Premixed mixture of methane and air at an equivalence ratio of 0.77 is used as fuel. Velocities for the fuel jet and co-flowing air are set equal to 15.0 m/s and 0.4 m/s, respectively. Flame computed for this high fuel-jet velocity became unsteady with vortices shedding along outer surface of the RZ. Instantaneous and time-averaged flames are shown in Figure 5-29. Flame is stably anchored to the outer edge of the bluff-body. A pseudo RZ is evident in the time-averaged visualization of the flow field (Figure 5-29b). Distributions of the C/H atom ratio are shown on the right halves using rainbow color

scheme. The C/H atom ratio increased significantly near the flame surface close to the bluff-body even for this high-velocity case.

Variations in the C/H atom ratio with respect to temperature at 2 and 6.5 mm above the bluff-body are shown in Figure 5-30a and Figure 5-30b, respectively. Distributions of the simulation at two instants and that of the time-averaged data are shown in these figures. Note that temperature is nearly uniform within the RZ (Figure 5-29). Data obtained for an unstrained laminar 1D flame at an equivalence ratio of 0.77 are also included in Figure 5-30 for comparison purpose. The C/H atom ratio increased significantly from its stoichiometric value of 0.25, especially near the bluff body. These profiles also qualitatively match with those measured by Barlow et al. (2011).

Finally, turbulent calculations for the Cambridge swirl burner are made using UNICORN-2D code and activating k-e turbulence model. This burner consists of two annular channels through which fuel/oxidizer mixtures can flow, and a large (382 mm diameter) co-flow of filtered air to prevent the entrainment of ambient air. The diameter of the bluff-body is 12.7 mm and the thicknesses of the two annular fuel jets are 6.35 mm each. Velocity of the inner jet is 18.7 m/s and that of the outer jet is 8.31 m/s. Both fuel jets are operated at 0.75 equivalence ratios. The same grid system of 301x501 points is used for this turbulent simulation. Photograph of the actual flame is shown in Figure 5-31(a) and the iso contours of temperature are shown in Figure 5-31 (b). Calculations have predicted the flame structure reasonably. Calculated and measured axial velocities obtained in the recirculation zone are compared in Figure 5-32 at four different heights. More interestingly, the C/H atom distribution behind the bluff body (Figure 5-33) is predicted reasonably. These calculations suggest that non-uniform distribution of species is prevalent in the turbulent-flame cases also.

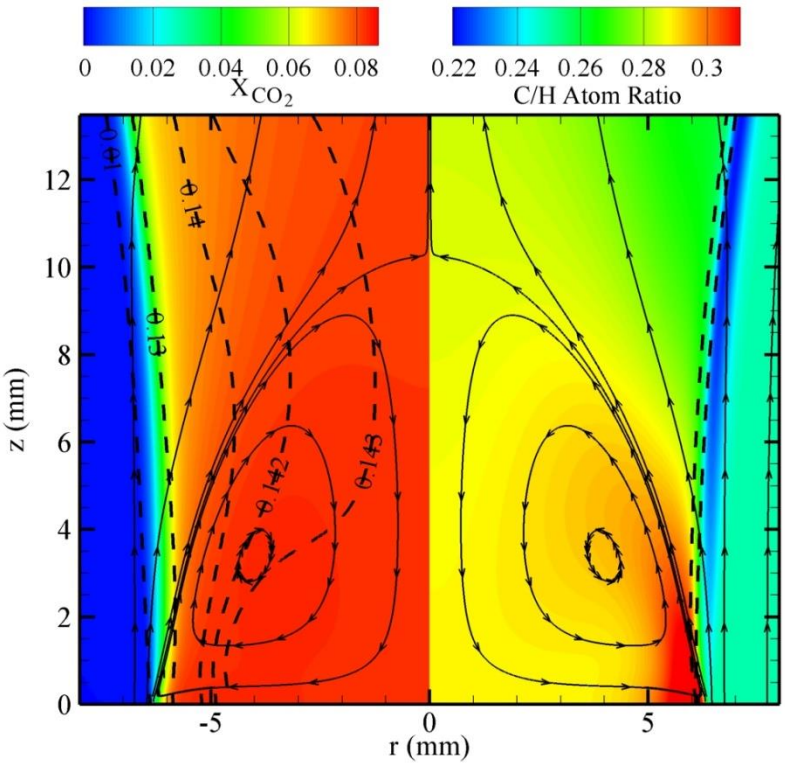

Figure 5-23. Premixed flame stabilized on a 12.7-mm diameter bluff-body burner. Iso-concentration contours of H_2O (broken lines) and streamlines are superimposed on CO_2 distribution in the left half. Streamlines and contours (broken lines) representing a heat-release-rate value of 200-w/cm^3 are superimposed on C/H-atom-ratio distribution in the right half.

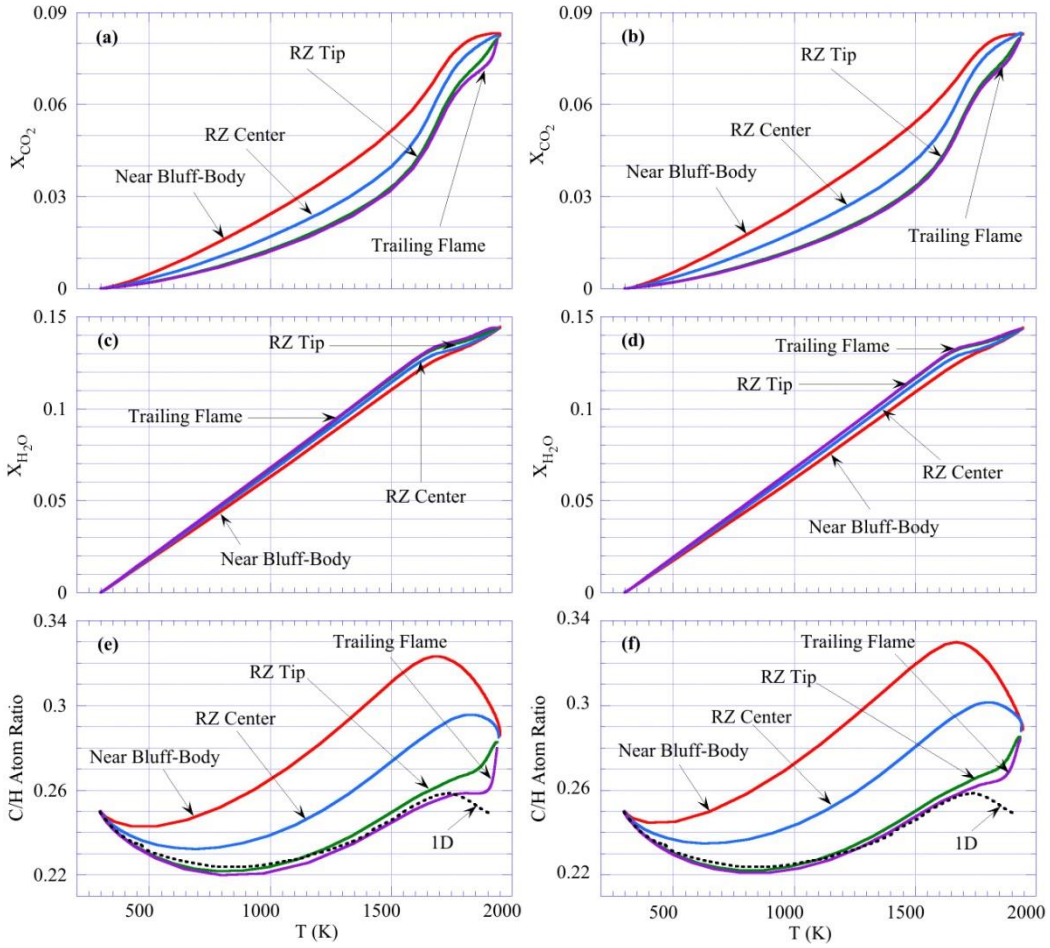

Figure 5-24. Distributions of CO_2 and H_2O concentrations and C/H atom ratio with respect to temperature (along a radial line) at different heights above the burner surface. (a), (c) and (e) are for 3.8-m/s fuel-jet velocity and (b), (d) and (f) are for 6.4-m/s fuel-jet velocity. Results for an unstrained laminar 1D flame are included in (e) and (f).

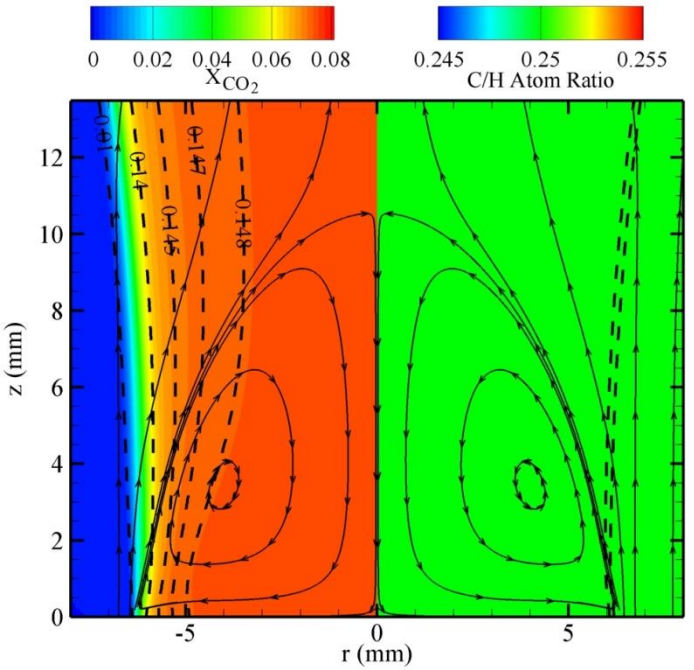

(a)

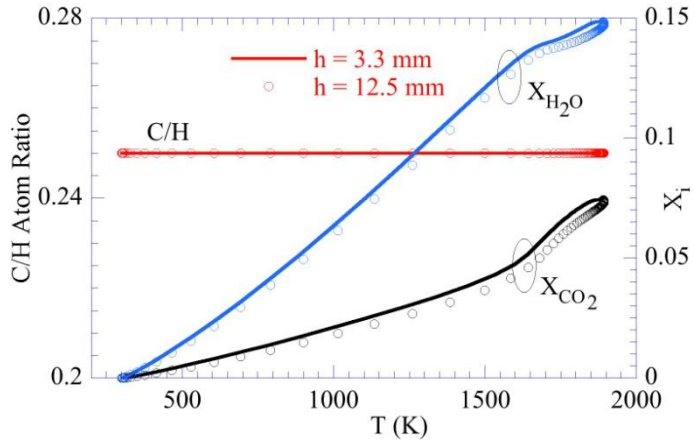

(b)

Figure 5-25. Results of the simulation performed for the flame shown in the previous figure after assuming diffusion coefficients of all the species are equal. (a) Iso concentration contours of H_2O (broken lines) and streamlines are superimposed on CO_2 distribution in the left half. Streamlines and contours (broken lines) representing a heat-release-rate value of 200-w/cm^3 are superimposed on C/H-atom-ratio distribution in the right half. (b) Distributions of C/H atom ratio and H_2O and CO_2 concentrations with respect to temperature (along a radial line) in the recirculation zone (h = 3.3 mm) and in the downstream flame (h = 12.5 mm).

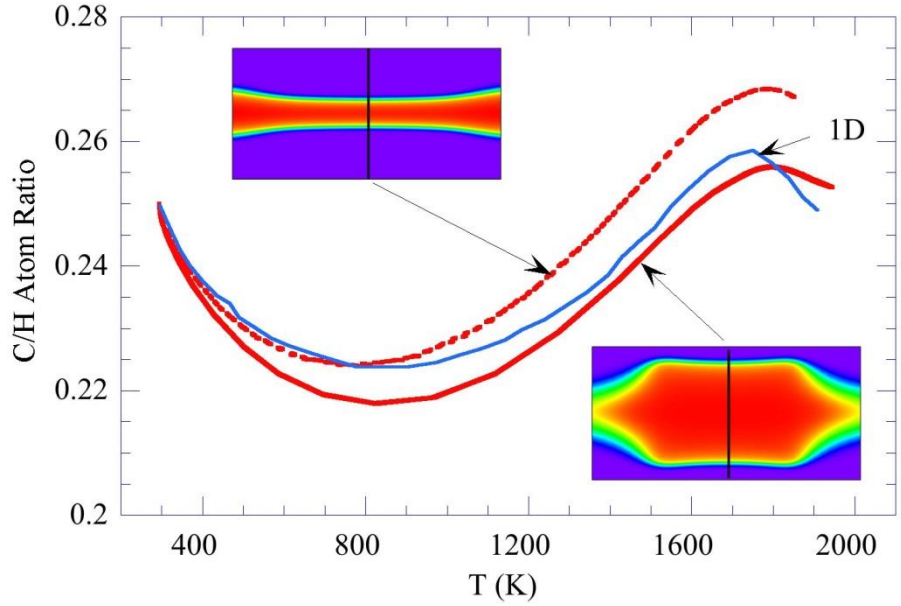

Figure 5-26. Opposing jet premixed flames simulated with UNICORN code. C/H-atom-ratio distributions with respect to temperature along the centerline for weakly (60 s^{-1}) and moderately (280 s^{-1}) stretched flames are compared with the data obtained for an unstretched 1D flame.

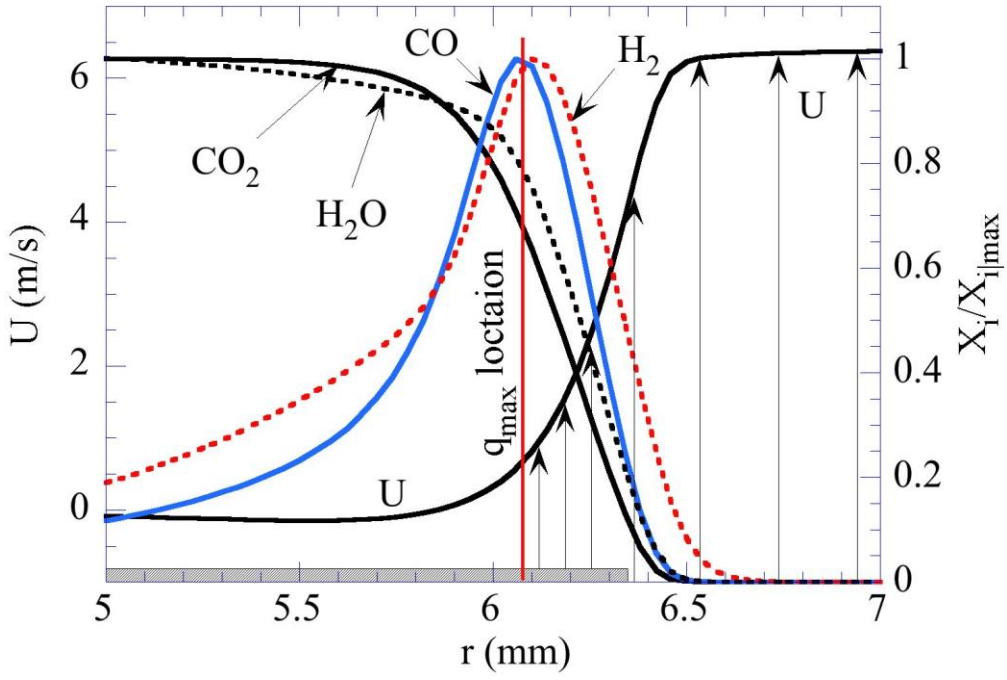

Figure 5-27. Normalized species concentrations and axial velocity near the bluff-body surface (z = 0.5 mm). Flame location is identified based on maximum heat release rate.

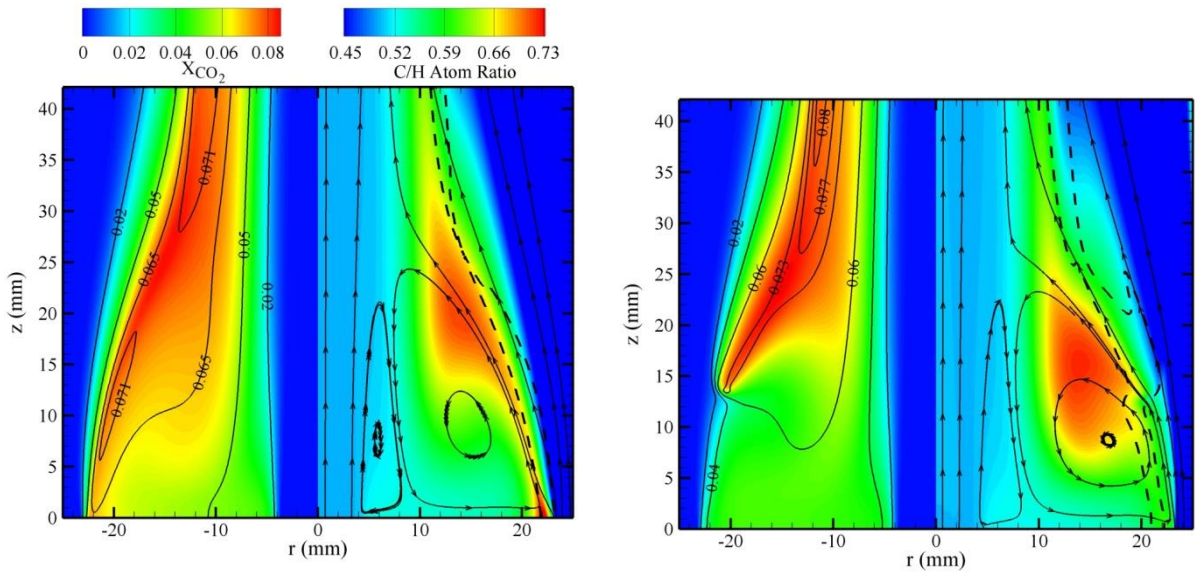

Figure 5-28. Non-premixed flames stabilized in a 46-mm-diameter centerbody burner. (a) Attached-flame and (b) Lifted-flame modes. Iso-concentration contours lines of H_2O are superimposed on CO_2 distribution (color plot) in the left half. Streamlines and 5-w/cm3-heat-release-rate contour (broken lines) are superimposed on C/H-atom-ratio distribution in the right half.

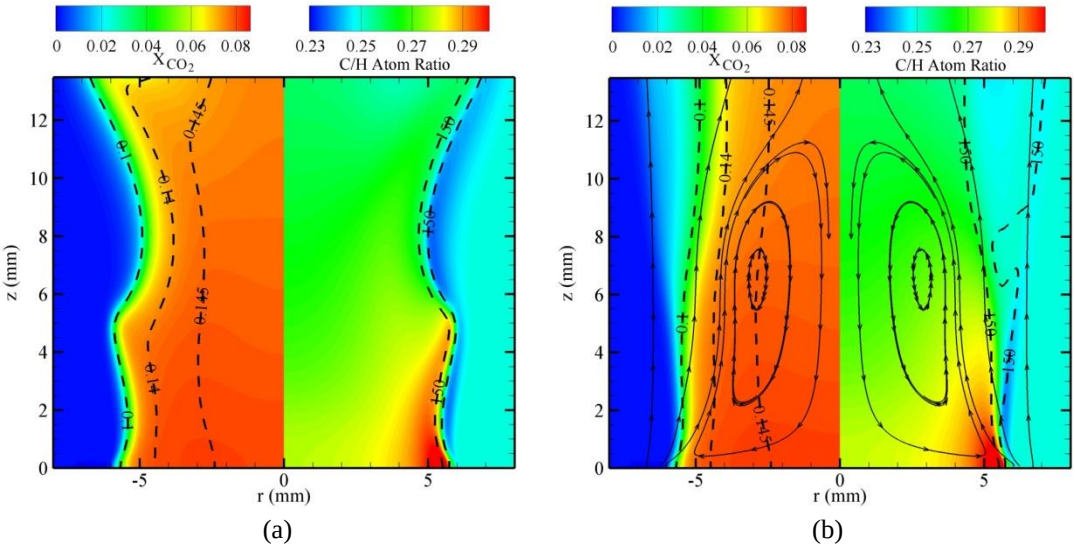

Figure 5-29. Premixed flame stabilized on a 12.7-mm diameter bluff-body burner. Iso-concentration contours of H_2O (broken lines) are superimposed on CO_2 distribution in the left halves. Heat-release-rate contour (broken lines) of 150-w/cm^3 are superimposed on C/H-atom-ratio distribution in the right halves. (a) Instantaneous, (b) time-averaged flames. Streamlines are superimposed on time-averaged image.

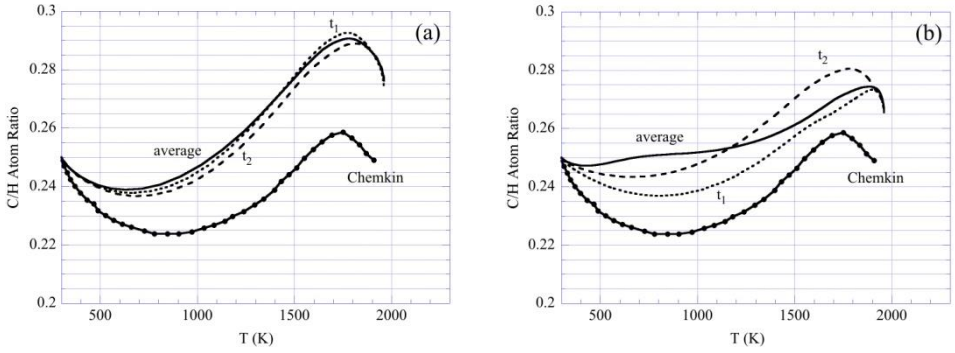

(a) (b)

Figure 5-30. Distributions of C/H atom ratio with respect to temperature (along a radial line) at (a) 2 mm and (b) 6.5 mm above the burner surface. Results for an unstrained laminar 1D flame obtained with Chemkin are included.

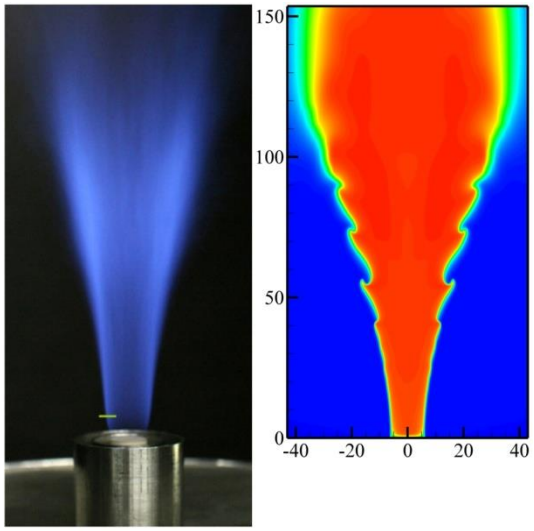

(a) (b)

Figure 5-31. Turbulent flame obtained in (a) experiment and (b) calculations for the Cambridge burner operating with non-swirling fuel jets.

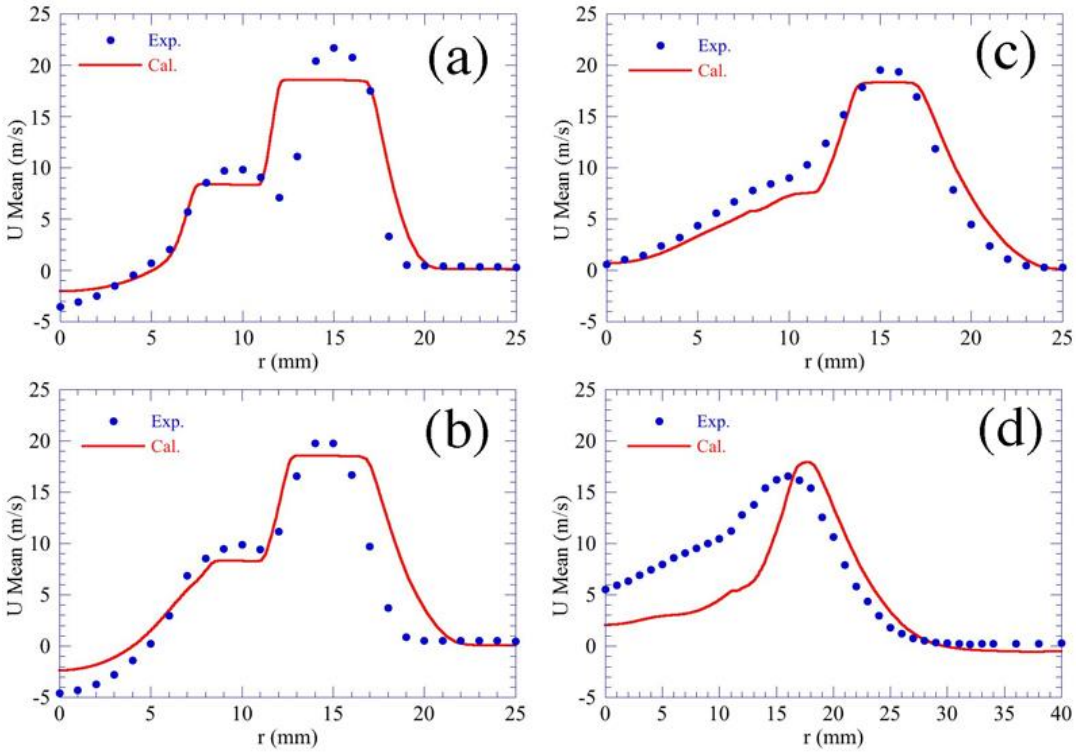

Figure 5-32. Comparison between computed and measured axial velocities obtained at four different heights in the recirculation zone.

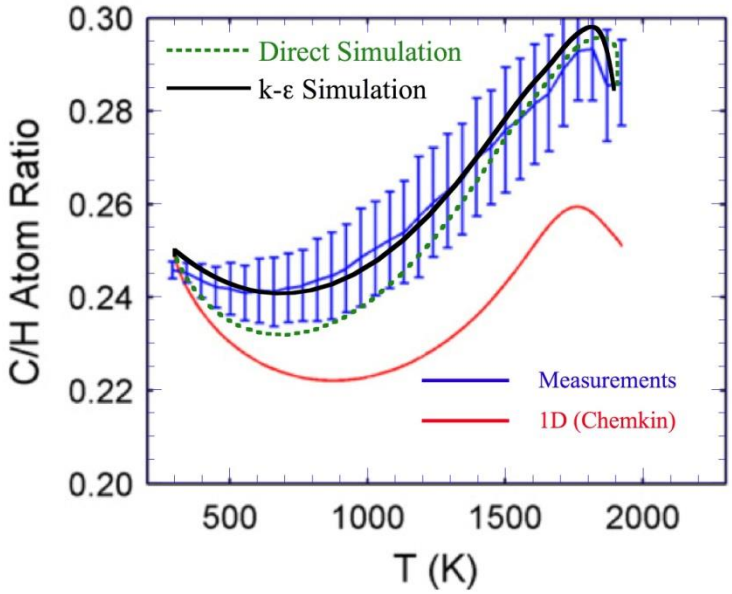

Figure 5-33. Computed and measured distributions of C/H-atom ratio with respect to temperature near the bluff-body surface (x = 2 mm). Direct simulation is obtained without using any turbulence model.

5.6 Flame-Turbulence Interaction

Opposed jet flames have been used for many years (including our previous and current SERDP programs) to understand the flame-turbulence interaction under a variety of situations and for different fuels. These studies have been critical in gaining an understanding of vortex-flame interactions associated with turbulent flames. However, these studies offered few clues on how the width of a turbulent flame could become significantly larger than that of a laminar flame established under similar velocity conditions. In an attempt to further understand turbulent flames, an opposed jet flame is used in a non-traditional way and the vortex-flame interactions during the turbulent transition process are studied. The flame is made to interact with a series of multiple mushroom vortices generated from the collision of fuel and air jet vortices. The version of the UNICORN code, that incorporates 13 species and 74 reactions among the constituent species, has been used for the simulation of unsteady flames resulting from multi-vortex/flame interactions in opposing-flow hydrogen jet diffusion flames.

The opposing-jet-flow burner designed by Rolon is used for the investigations of vortex-flame interactions. It is shown in Figure 5-34, and is described in detail in Rolon et al (1995). A flat flame is formed between the fuel and air jets having velocities of 0.69 and 0.5 m/s, respectively. The hydrogen-to-nitrogen ratio used for the fuel jet is 0.38. Wrinkled flames are established by shooting vortices simultaneously from the fuel and air sides. The collision of these vortices at the flame surface, in general, imposes unsteady stretch on the flame. Such a collision involving stronger vortices may also quench the flame locally and generate multiple vortices. Studies are performed to investigate various types of vortex-vortex/flame interactions by incorporating different sizes of fuel- and air-side injection tubes and varying the injection durations. Fuel- or air-side vortices were generated by injecting a specified amount of fuel or air through the respective syringe tube and then through an injection tube. The diameters of the injection tubes were changed for introducing different size vortices. The z-r coordinate system used for the simulation of flames associated with the Rolon burner is shown in Figure 5-34. Calculations for these axisymmetric flames are made using a non-uniform 801 x 501 mesh system distributed over a physical domain of 40 x 40 mm. This resulted in a mesh spacing of 0.05 mm in both the axial (z) and the radial (r) directions in the region between the two nozzles.

Prior to the injection of vortices, a flat flame is simulated for the conditions described earlier. The computed steady-state flame in the form of iso-temperature distributions is shown in Figure 5-34, along with the schematic diagram of the burner. Note that the gravitation force in this simulation is neglected. The slight upward curvature of the flame surface develops as a result of the lower density of the hydrogen fuel. Apparently, the velocity difference used for the fuel and air jets (0.69 m/s vs 0.5 m/s, respectively) did not provide a perfect balance of momentum for the two jets; resulting in a slight shift in the flame location from the center toward the air jet (lower nozzle).

The objective of this work is to extend the vortex-flame interaction studies into the turbulence region. To accomplish this, the injection velocities and mass of the fuel and air were gradually increased. This resulted in a rapid extension of flame at the vortex center. However, it did not cause the whole flame extinguishment. Instead, the laminar flame gradually transitioned into a near-turbulent flame. Results of a calculation made with an 18 m/s fuel injection and a 15 m/s air injection are shown in the right half of Figure 5-35. The Reynolds number calculated for the 18-m/s jet is 2500. The temperature field time averaged over a 12.5-ms period is shown. For comparison purpose the laminar base flame is shown on the left half of Figure 5-35. The high stretch rate in the case of 18 m/s fuel injection caused the flame to

extinguish at the center. On the other hand, the rest of the opposing jet flame became broadened. It is obvious that the turbulence generated at higher velocities helped the flame to survive and to become broader. However, this time-averaged view of the flame doesn't shed any light on how exactly the interaction between turbulence and flame increases the width of the flame. In the following paragraphs, different visualization techniques are used to aid in gaining a better insight into how the turbulence-flame interaction results in a thicker flame.

In Figure 5-36 through Figure 5-39 the weak turbulence-flame interaction is illustrated at the same time but viewed using different parameters. In Figure 5-36, the instantaneous velocity field is superimposed on the temperature distribution plotted in rainbow colors. The instantaneous location of stoichiometry (obtained from the mixture fraction) is shown in red. Velocity field in Figure 5-36 suggests the existence of some turbulence (fluctuations) and recirculation zones. It also explains some observed features in temperature such as local flame broadening (due to decrease in velocity) and accumulation of hot gasses in the recirculation zone. Length of the flame surface (identified from stoichiometry) is significantly longer compared to that in the laminar case. Regions with oxygen-rich mixtures are observed at r ~ 8 and 11 mm. Oxygen in these regions is eventually consumed, which leads to an increase in overall combustion. However, the instantaneous velocity or temperature fields don't provide insights into the processes that led to broadening of the flame.

Vorticity corresponding to the velocity field in Figure 5-36 is shown in Figure 5-37. An extended rainbow color scheme is used for identifying the low-vorticity regions. While white and red regions represent vorticity away from the sheet, blue and green regions represent vorticity into the sheet. The presence of positive-vorticity regions next to the negative-vorticy regions suggests the development of mushroom vortices. Oxygen-rich pockets seem to be associated with the vortices rotating in counterclockwise direction.

Distribution of scalar dissipation rate obtained from mixture fraction is shown in Figure 5-38. In general, scalar dissipation rate is higher on the oxygen-rich side of the stoichiometry. As expected, flame temperature increased where scalar dissipation rate is lower. Details of the flow structure show up in the particle-tracking technique. Instantaneous locations of the particles are shown in Figure 5-39 along with the OH-concentration distribution. White color particles are injected from the air nozzle while black-color particles are injected from air jet. As expected, OH is mostly located on the air side of stoichiometry. Several mushroom vortices could be identified in Figure 5-39. Particle tracking not only provided details of the vortices that were identified from the other visualization methods but also revealed the underlying vortices in the recirculation zone that were not found in Figure 5-36--Figure 5-38. Knowing detailed fluid structures aids in understanding how the flame becomes broadened in turbulent flow.

Figure 5-39 shows that vortices are initially (close to r = 0) filled with either black or white particles and mixing of these particles becomes more pronounced as they propagate radially. It is important to note that white particles represent pure oxygen initially and then a mixture of oxygen and products once they enter into the flame zone. Similarly, black particles represent pure fuel or a mixture of fuel and products. Fuel and air jets are colliding at z ~ 17 mm and generating vortical structures. Oxygen and fuel are carried into the flame by these vortices. As the trapped fluid in the vortices roll with time the mixing of oxygen and fuel increases. Layers of black particles surrounding the layers of white particles may be found in these vortices.

The instantaneous images of particle locations reveal the level of mixing between fuel and air; however, it doesn't provide insight into how the flame width is being increased. Indeed, to provide insight

into this process time evolving visualizations are necessary. Particle tracking along with the temperature evolution of the vortices and flame are shown in Figure 5-40 starting from the time the two high-speed air and fuel jets start interacting. The high stretch rate developed along the stagnation line when both the fuel and jets met extinguished the flame locally (Figure 5-40a). The mushroom vortex formed out of the jet collision travelled radially and stripped off a small flamelet as marked with an arrow in Figure 5-40b. Edge of the flame is then drawn into the vortex through the wake region (Figure 5-40c). While the flame edge continued to roll into the vortex, hot products from the flame are also sucked into wake of another mushroom vortex as seen in Figure 5-40d. Propagation of flame and hot products in the wakes of vortices are evident in Figure 5-40e and Figure 5-40f. A new vortex then punches through the flame and creates a local quenching in Figure 5-40g. Similarly, Figure 5-40h and Figure 5-40i show flame quenching and entrainment, respectively. Following the sequential images in Figure 5-40 one could recognize two significant processes during turbulence-flame interactions. First one is the quenching process, which was also revealed during the single vortex-flame interaction studies. Fast moving vortices increase local stretch rate on the flame surface and cause extinction when the stretch rate increases beyond the limiting value, which is often termed as unsteady-stretch limit. Interestingly, while this quenching process decreases the overall burning in the turbulent flames, the actual burning in a turbulent flame is significantly increased beyond that taking place in a laminar flame. The second observation made from Figure 5-40 might explain enhancement in burning. One can see repeated occurrences of entrainment of hot gasses (or portions of the flames) into the wakes of the mushroom vortices. Such entrainment not only increases burning of the gasses due to the prevailing weaker stretch rates in the wake regions but also enhances flame propagation as the flames are sucked into the mushroom vortices.

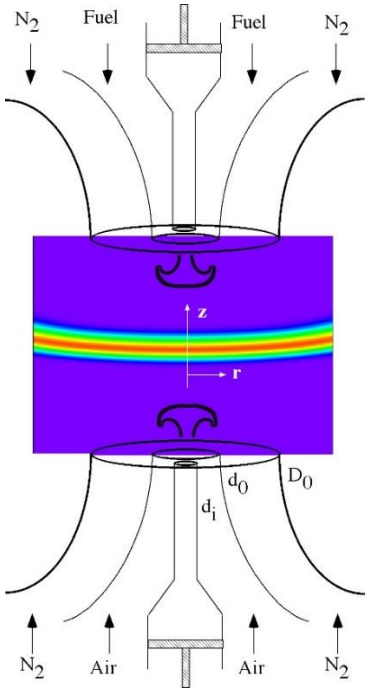

Figure 5-34. Schematic diagram of opposing-jet-flow burner used for the investigations of vortex/flame interactions. Nitrogen-diluted hydrogen fuel and air introduced from upper and lower nozzles, respectively.

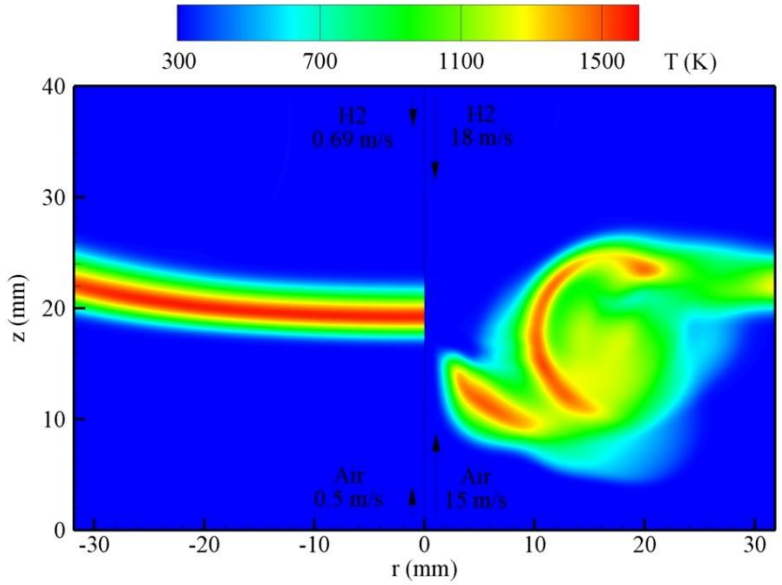

Figure 5-35. Laminar and near-turbulent opposing jet flames are shown in the left and right halves, respectively. Temperature distributions are plotted. Time-averaged temperature over a period is used for the near-turbulent case.

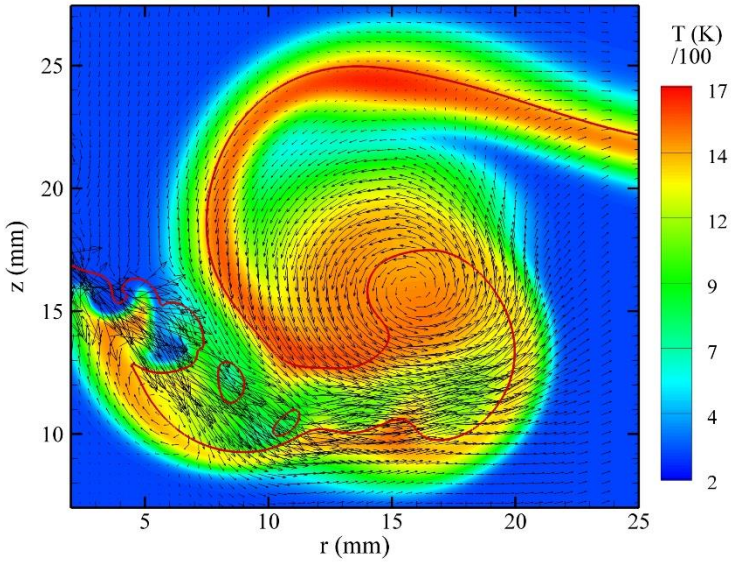

Figure 5-36. Instantaneous flame visualized with temperature and velocity fields.

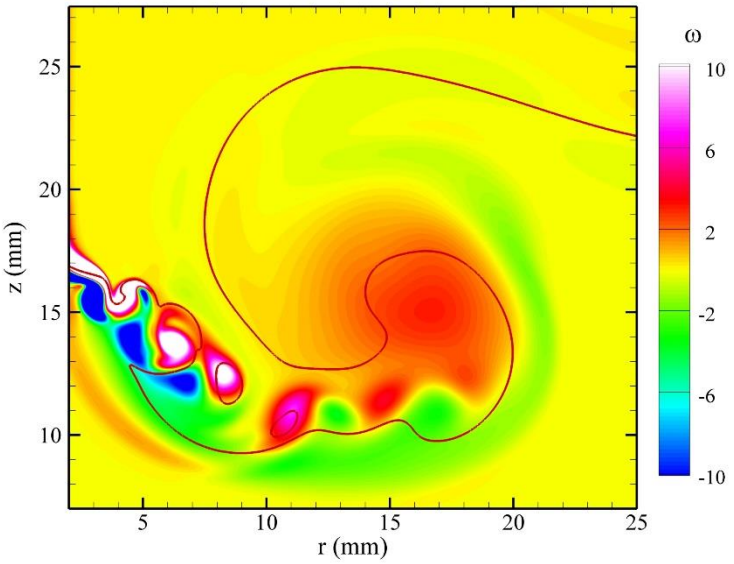

Figure 5-37. Instantaneous flame visualized using vorticity.

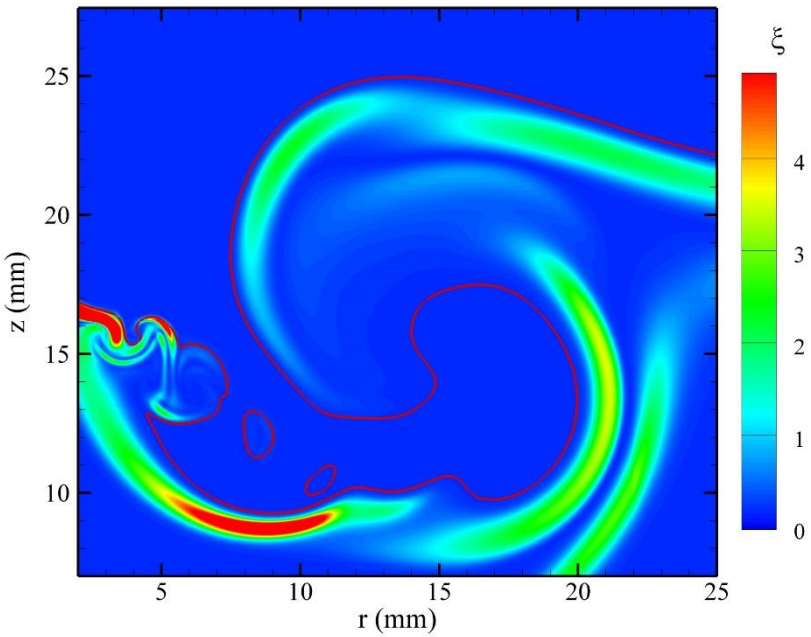

Figure 5-38. Instantaneous flame visualized using scalar dissipation rate.

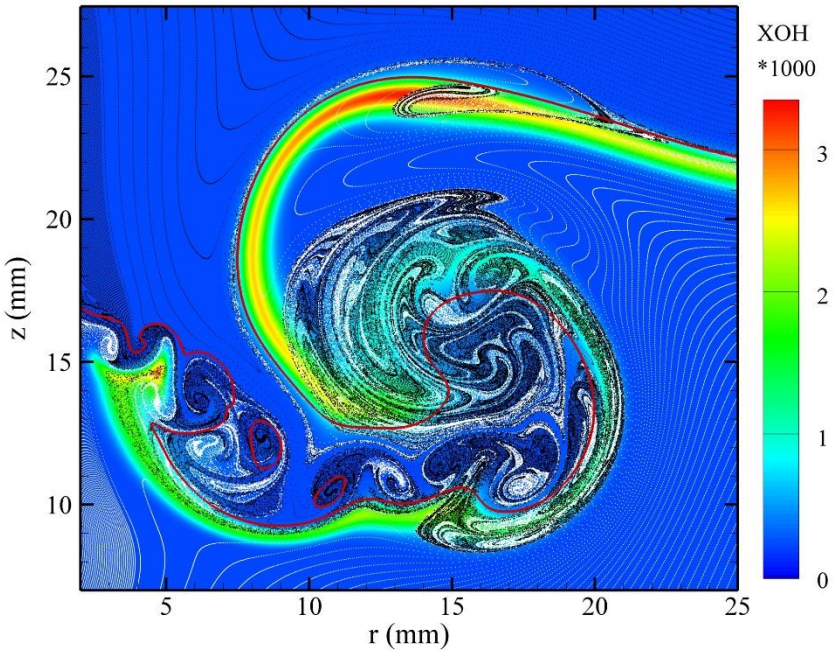

Figure 5-39. Instantaneous flame visualized using OH concentration and particle-tracking technique.

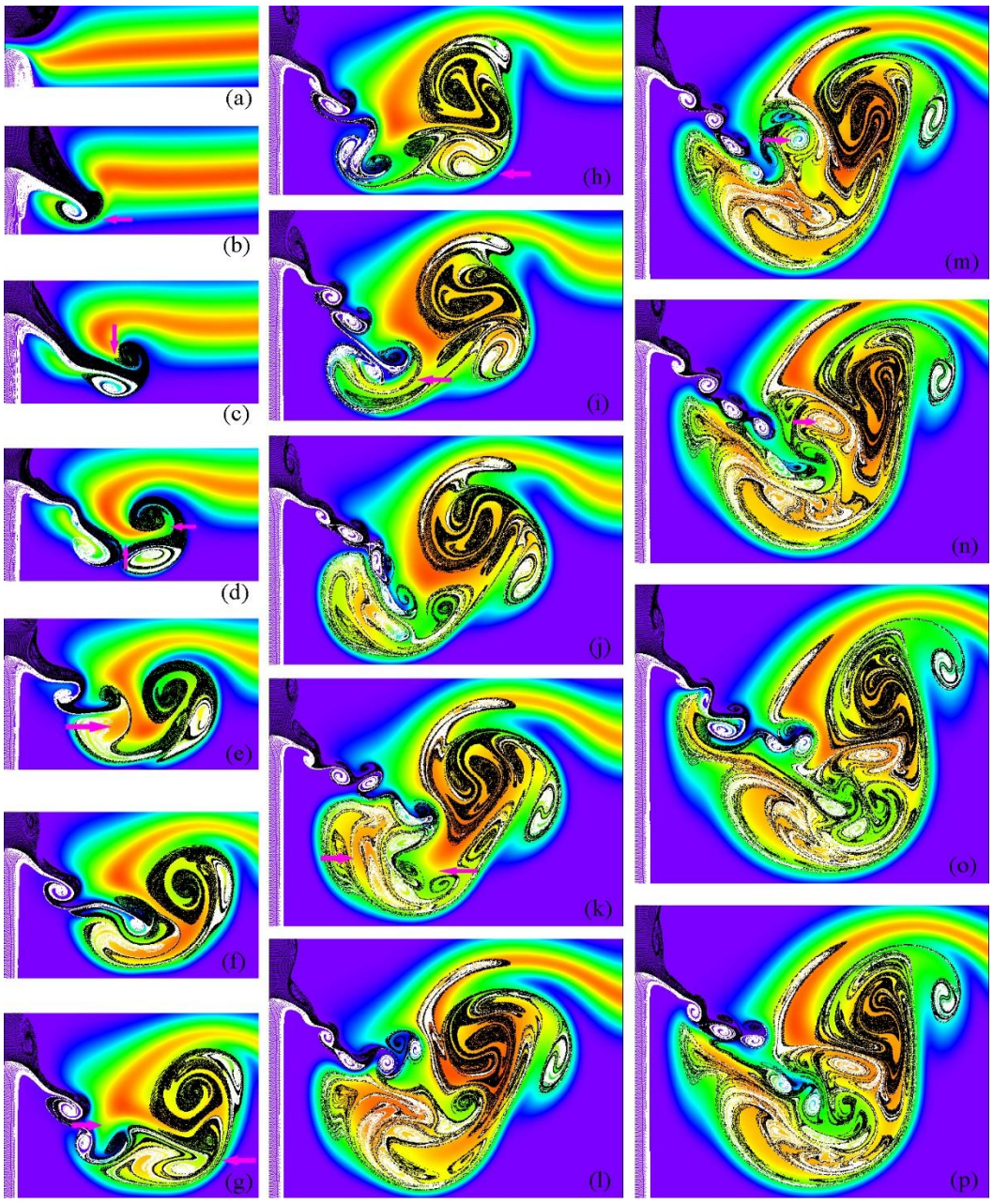

Figure 5-40. Evolutions of the vortices and temperature field in a flame transitioning to a turbulent one.

5.7 Flame Propagation through Stratified Mixtures

It is believed that the unburned hydrocarbons (UHCs) observed in the aircraft exhaust are resulting from premature quenching of flamelets and consequent fuel heating. A corresponding "thought" experiment was designed for studying the distributions of species in aircraft emissions. In this experiment, the possibility of lean quenching and then heating the remaining fuel for the production of emissions in combustors is theoretically studied through performing a series of calculations for the tube shown in Figure 5-41. Initially, the tube is filled with a premixed mixture of fuel and air in such a way that the equivalence ratio varies from stoichiometric to zero. An ignition source is provided on one side of the tube where fuel and air are at stoichiometry. In a narrow tube, the flame established at the ignition source quickly becomes a propagating planar flame and travels through the leaner mixtures. Flame velocity decreases in lean mixtures and eventually the flame gets extinguished when the equivalence ratio of the local mixture falls below the quenching limit. Simulations for this experiment were made using the UNICORN code. For validation purposes, experiments of Kang and Kyritsis (2005 and 2007) that are similar to the one described in Figure 5-41 are simulated.

Kang and Kyritis (2005 and 2007) filled their 10-cm-long tube through injecting stoichiometric methane-air mixture from one side of the tube and air from the other side. After certain amount of time the mixture in the tube establishes stratification from stoichiometric to zero (pure air). The local equivalence ratio and the flame propagation velocity were measured in the 4.5-cm-long visual section at the center of the tube. Various distributions for equivalence ratios in the visual section were obtained through changing the airflow rate. Four stratification distributions studied in the experiment are shown in Figure 5-42. The profiles within the visual section were matched with the measurements. Linear distributions are assumed between the ignition location and the beginning of the visual section and between the end of the visual section and end of the tube. The flame is initiated at the ignition location through increasing the local temperature of the gas to 1800 K briefly for a period of 2 ms. The flame propagates from one end of the tube to the other. The equivalence ratio distributions upstream of the flame front at different instants for case 3 are shown in Figure 5-43. The location of the flame front is marked with vertical lines. The times of flame-front arrival are also shown in Figure 5-43. Surprisingly, the stratification in the tube upstream of the flame front was affected neither by the presence of flame nor by the delay in the flame's arrival.

Flame propagation velocities are calculated from the locations of the flame at different times (the way they were obtained in the experiment) and plotted in Figure 5-44 for the four stratification cases considered (Figure 5-41). Measured flame speeds are also shown in Figure 5-44 using symbols. Note that only flame speeds in the visual section of the experiment are shown in Figure 5-44. Recalling that the lean flammability limit for methane-air mixtures is about 0.5, Figure 5-44 shows that flame has actually propagated into mixtures that are well below this limit. In fact, flame velocity gradually decreased to a very low value (close to zero). Calculations have reasonably predicted the flame propagation in the stratified mixtures. The discrepancy between the measurements and calculations (Figure 5-44) could be due to 1) the assumptions on equivalence ratio distributions within the invisible sections of the tube and 2) the heat losses from the tube. Nevertheless, comparisons in Figure 5-44 suggest that the flame in Figure 5-41 has been reasonably modeled.

For understanding the generation of UHCs, calculations for the flame in Figure 5-41 have been repeated after replacing the methane fuel with a mixture of 58.6% n-dodecane and 41.4% n-heptane. Note that this mixture is one of the fuel blends selected for studying emissions in a suite of burners in our SERDP

program. For making sure that the chemical kinetics used for n-dodecane and n-heptane yields correct flame speed, calculations are first made without any stratification. The initial 90% of the 100-cm-long flame tube is filled with stoichiometric n-dodecane-air mixture and the remaining tube section is filled with nitrogen as shown in Figure 5-45a. The history of the flame propagation is shown in Figure 5-45b through plotting temperature distribution along the centerline of the tube at different instants. Flame front location can be identified in this figure from the intersection of the blue (cold) and red (hot) regions. Constant-slope interface suggests that flame has propagated at a constant velocity of 34.2 cm/s. This is comparable to the laminar flame speeds of 38 cm/s for n-heptane. Flame speeds measured by Kumar and Sung (2007) for n-dodecane with preheating suggest that they are about 10% lower than those of n-heptane flame. Consequently, flame speed for the n-dodecane-n-heptane mixture could be estimated as ~36 cm/s.

The flame is extinguished at x = 90 cm when the local mixture became pure N_2. Flame extinction resulted in heat conduction near the flame front as seen in Figure 5-45b. The temperature of the gases in the products region decreased while that of the fresh mixture (N_2 in this case) increased. Calculations for the flame propagation and extinction in fuel-lean mixture are performed after specifying fuel stratification in the tube as shown in Figure 5-46. Equivalence ratio of the n-dodecane-n-heptane-air mixture is decreased from stoichiometry to zero in the tube section between 10 and 90 cm while it is maintained at unity in the initial 10-cm section. The last 10-cm section of the tube was filled with nitrogen. A flame was initiated in the tube at x = 0.2 cm. As the flame moved through the stratified fuel-air mixture, its propagation speed decreased (Figure 5-46b). The interface between red and blue regions curved away from the tube exit. Moreover, as expected, the temperature of the flame decreased as it moved through the fuel-lean mixtures. Eventually the flame was extinguished at x ~ 42 cm. Local equivalence ratio at this location was 0.6. Heating up of the unburned fuel-air mixture (x > 42 cm) and cooling of the burned gases (x < 42 cm) are evident in Figure 5-46b. The species generated during the heating of the unburned fuel are investigated for understanding the characteristic emissions from n-dodecane-n-heptane fuel blend.

Temperature and species mass fractions are averaged along the centerline of the tube at every instant and plotted in Figure 5-47. Variations in averaged temperature and CO and C_2H_4 mass fractions with respect to time are shown in Figure 5-47a. Correlations between averaged mass fractions of various species and ethylene are shown in Figure 5-47b—Figure 5-47h. The average temperature increases as the flame consumes more and more unburned fuel-air mixture (Figure 5-47a) and then becomes nearly constant as the flame is extinguished (~ 130 ms). During the flame propagation phase while the mass of CO decreased the mass of ethylene remained very low. The wiggles in Figure 5-47a are developed as the flame moved from one grid point to the other.

Figure 5-47 (a) suggests that mass of ethylene increases significantly once the flame is quenched. In the preheat zone of the premixed flame, n-dodecane and n-heptane decompose and forms various HCs including ethylene. Subsequent oxidation reactions in the high temperature of the flame consumes these HCs. However, in the thought experiment studied here, see Figure 5-41, the energy from the burned gases continues to heat the fuel even after the flame is quenched. Such heating produced HCs and since there is no flame for consuming these HCs, they ended up as UHCs in the system. Correlations between product species (CO and CO2) and ethylene are shown in Figure 5-47b and those between UHCs and ethylene are shown in Figure 5-47c—Figure 5-47g. Even though there are tens of UHCs in the model, only ones that are present in significant quantities in the aircraft emissions are shown in these figures. The correlations between PAH species ($C_{10}H_8$ and $C_{16}H_{10}$) and ethylene are shown in Figure 5-47h. Interestingly, not only are there correlations between UHCs and ethylene but also the ones between products (CO and CO2) and

ethylene are nearly linear. However, the PAH species are decreasing during this fuel-heating process. This could be due to the incomplete chemical kinetics for the PAH formation in the model.

Figure 5-41. Flame system used for studying UHCs.

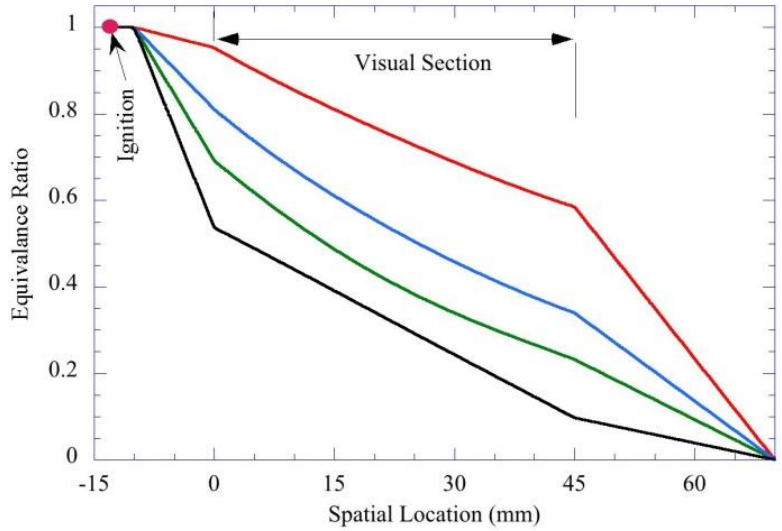

Figure 5-42. Initial equivalence ratio distributions used for the simulation of stratified-combustion experiment of Kang and Kyritsis (2005, 2007).

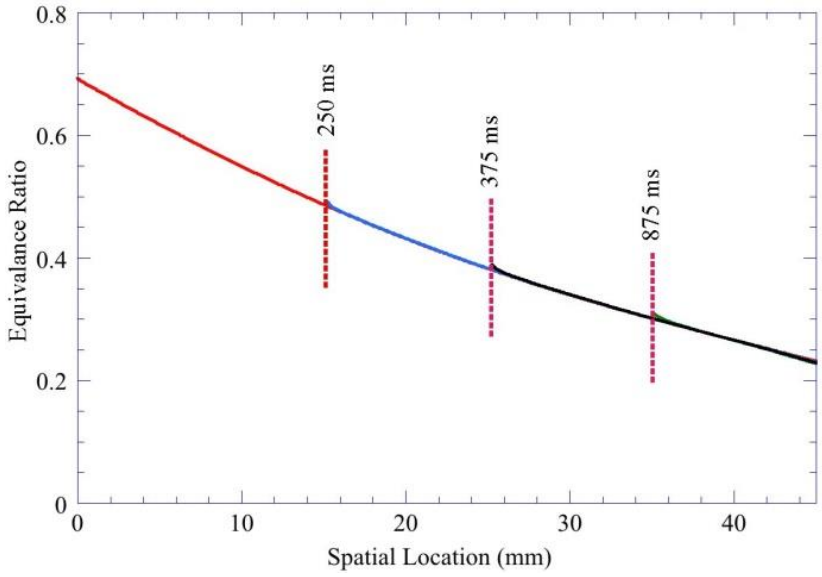

Figure 5-43. Effect of diffusion on equivalence-ratio distribution as flame propagates through tube.

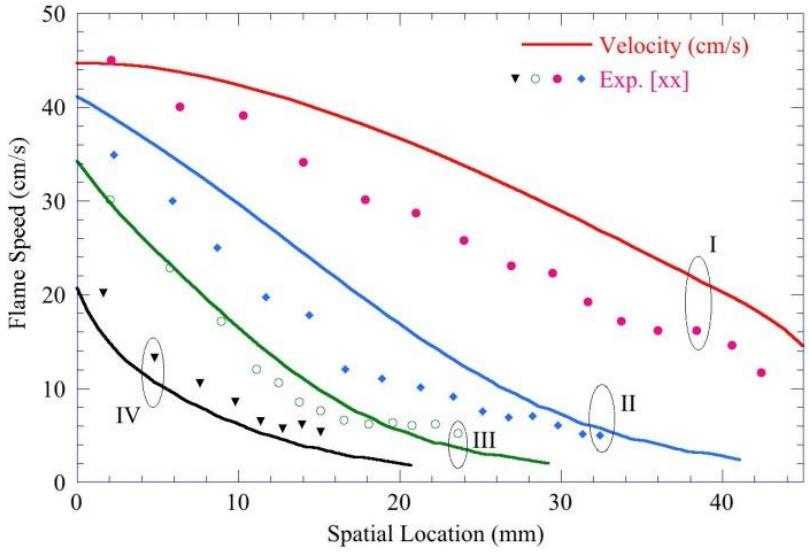

Figure 5-44. Computed and measured flame speed for different equivalence ratio distributions.

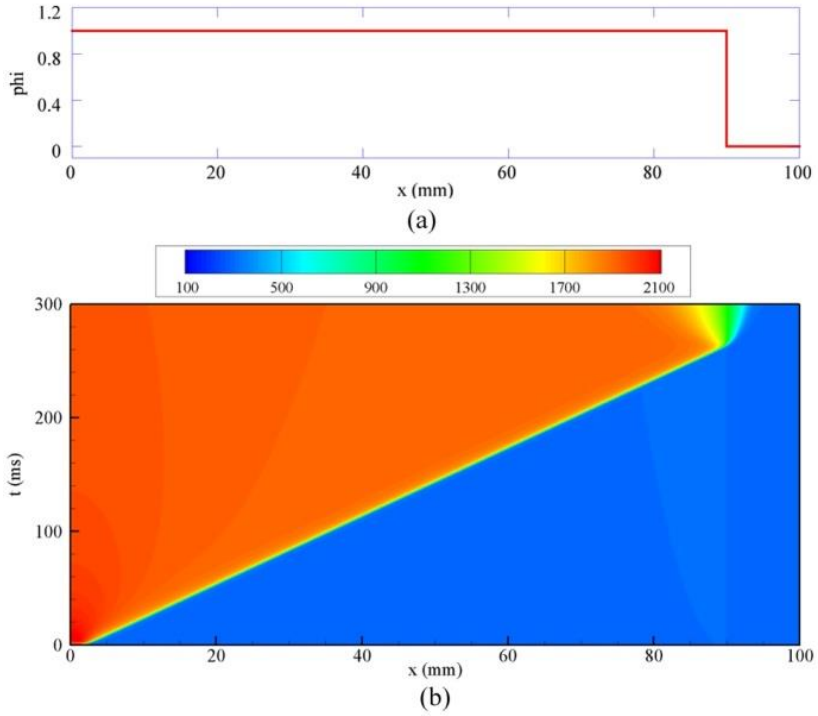

Figure 5-45. Propagation of n-dodecane flame through constant phi. (a) Initial phi distribution, (b) temperature at mid-section at different times.

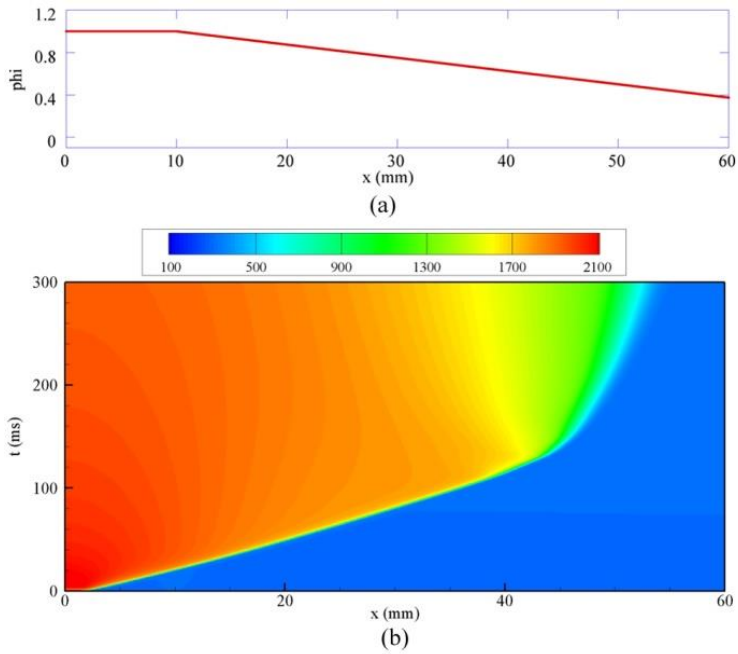

Figure 5-46. Propagation of n-dodecane flame through linearly varying phi. (a) Initial phi distribution, (b) temperature at different times.

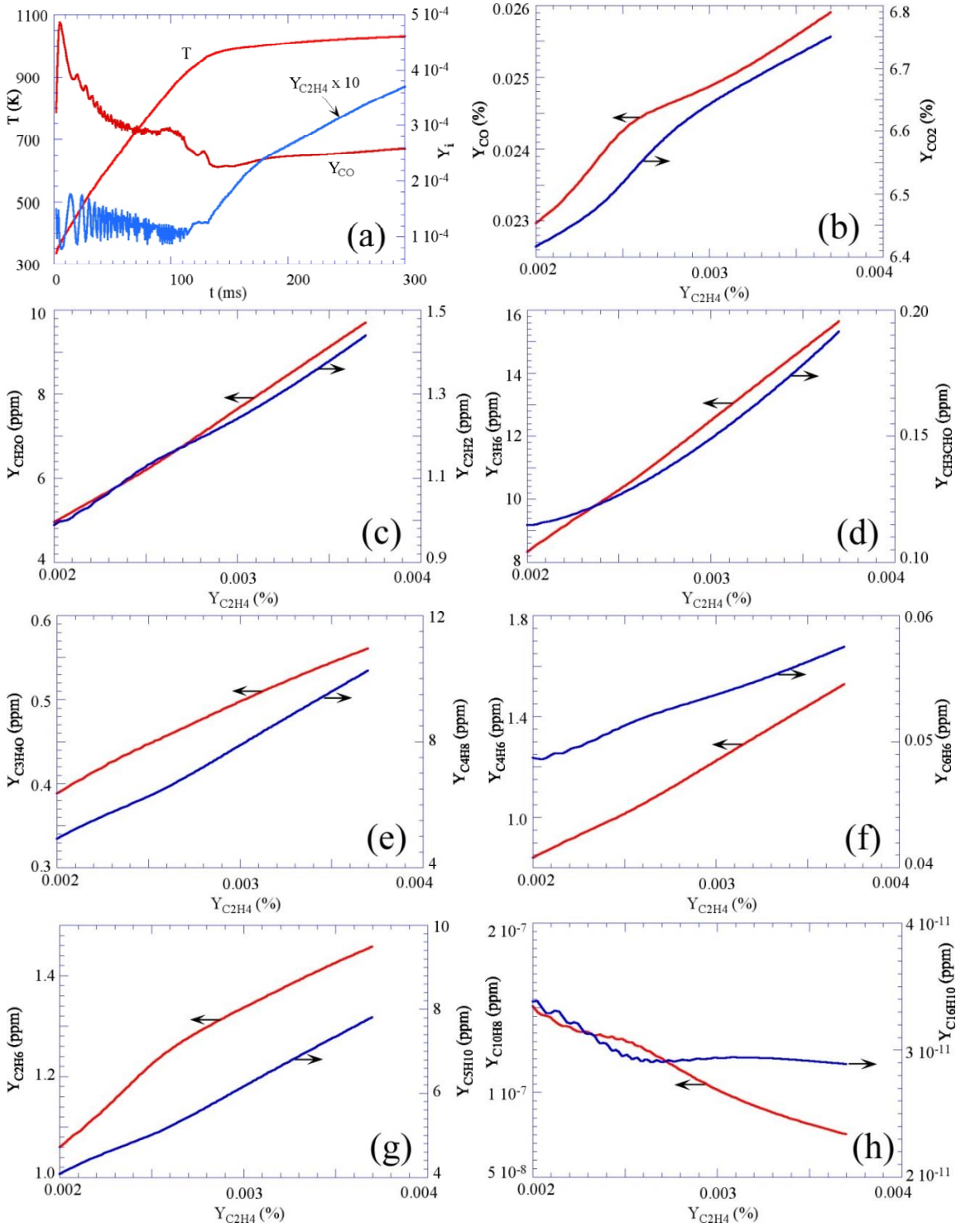

Figure 5-47. (a) Variations in averaged temperature and species mass fractions as the flame propagated through the stratified mixture. (b)-(h) Correlations between mass fractions of various species and ethylene after the flame is extinguished.

5.8 Simulation of Emissions from Low-Temperature Combustion in Opposed-Jet Flames

Negative temperature coefficient (NTC) region of ignition delay time observed in heavy hydrocarbon fuels such as n-heptane and JP-8 could lead to self-sustained "cool" flames with peak temperatures ~ 700 K. "Cool" flames that were accidentally discovered 200 years ago intrigued researchers all these years and became more interesting after their identification in the Flame Extinguishment (FLEX) Experiment of NASA experiments. "Cool" flames and low-temperature chemistry play critical roles in the control of engine ignition timing, unintended engine failure, knocking, emissions, and fire safety. They may also be important during high-altitude relighting of an aircraft engine. The chemistry associated with "cool" flames is typically studied using experimental approaches such as heated burners and jet-stirred reactors. The heated burner experiments in combination with emission spectroscopy measurements have identified that the bluish chemiluminescence associated with "cool" flames is due to formaldehyde. However, the complicated wall-flow interactions in these burners make it difficult to establish a "cool" flame in a controlled manner with well-defined boundary conditions. Realizing these difficulties researchers started looking into ways for establishing a "cool" flame in a well-controlled, laboratory burner.

Recently, Won et al. (2015) reported an experimental study on self-sustained "cool" diffusion flames established in an opposing-jet burner. They issued heated fuel (n-heptane/N_2 mixture) from the top nozzle and air from the bottom nozzle. As they could not find an operating condition for stabilizing a "cool" diffusion flame, they have looked into alternative ways for stabilizing the flame. They came up with an idea of adding ozone to air stream for promoting the low-temperature chemistry and, thereby, increasing the stability limits of a "cool" flame. Even though, this idea worked and authors were able to characterize a "cool" diffusion flame, the primary purpose of establishing a self-sustained "cool" flame was lost. Addition of ozone complicates the overall chemical kinetics and it will be very difficult to differentiate the issues with the ozone chemistry from those of the low-temperature chemistry of n-heptane (or any fuel with NTC characteristics) using the data obtained from these flames. Moreover, the difficulty authors encountered in establishing a self-sustained "cool" diffusion flame with n-heptane and air could be due to the limitations of their experimental facility or they might not have explored some other possibilities due to lack of CFD tools.

Even though, Won et al. (2015) could not establish an opposing jet "cool" diffusion flame (without adding ozone) experimentally they have studied the characteristics of such flames numerically using a one-dimensional code. Following the traditional practice they used a global strain rate for describing the flame and ignored not only the flow rates that are essential for establishing the flame in the laboratory but also the gravitational forces that are important in the low-velocity regimes in *only* which "cool" flames can be stabilized. Consequently, while the one-dimensional analyses of Won et al. (2015) are useful in understanding the structure of a hypothetical "cool" diffusion flame, they cannot shed any light on whether such flames can be established in a laboratory or not.

A numerical study is conducted to investigate the possibility of establishing a self-sustained "cool" diffusion flame in a laboratory opposing-jet burner through systematically changing the geometry and boundary conditions. The well-tested, time-dependent, UNICORN code is used for simulating the reacting flows associated with the opposing-jet burner.

The ignition delay times calculated by Farouk and Dryer (2014) for a stoichiometric mixture of n-heptane and air at 1-atm pressure are shown in Figure 5-48. They used a mechanism that has been reduced from the detailed mechanism of Curran et al (2008). The reduced mechanism has shown to reproduce the

ignition delay times predicted by the detailed mechanism over a wide range of temperatures and pressures. The reduced mechanism has also predicted the first and second stage burnings of a droplet under microgravity conditions. We have incorporated this mechanism into UNICORN code for predicting multi-dimensional flames burning n-heptane. For stability and efficiency of the calculations, chemical mechanisms in UNICORN code are implicitly integrated with the flow solvers. For making sure that such integration was performed accurately, the ignition delay times for the n-heptane/air mixture at different temperatures are calculated using UNICORN code and the results are plotted in Fig. 5-59 using symbols. Recently, we have also performed 2D calculations for the burning of the droplets in microgravity using UNICORN code and predicted the two-stage burning pattern. These calculations and the agreement shown in Figure 5-48 suggest that UNICORN code with Farouk's chemical kinetics is capable of predicting flames formed in the NTC region.

Each ignition delay time shown in Figure 5-48 is obtained using UNICORN code after spontaneously increasing the temperature of a pocket of fuel/air mixture to a specified initial value. Note that in each calculation fuel pocket initially goes through "cool" ignition and then goes through "hot" ignition. The actual changes in temperature and heat release rate (HRR) of the fuel pocket from time zero up to "hot" ignition are shown in Figure 5-49. These calculations were performed for an initial temperature of 600 K. Ignition took place at 471.2 ms. For showing the details of the "cool" and "hot" ignitions, two time scales are used in Figure 5-49. Results on a single time scale are shown in the inset. From t = 0 to ~400 ms, temperature of the fuel pocket increased just by 10 K. "Cool" ignition took place at ~ 419.3 ms and temperature increased to ~ 880 K. Significant amount of heat was released (HRR reached 215 w/cc) during the "cool" ignition process. After "cool" ignition temperature increased further, rather gradually, to ~ 950 K in 40 ms. "Hot" ignition took place at ~ 471.2 ms. The amount of heat released during "cool" ignition and the time delay between the "cool" and "hot" ignitions (~ 52 ms) suggest a possibility for establishing a self-sustained "cool" flame.

Researchers routinely use opposing-jet burners similar to that shown in Figure 5-50 for establishing a normal diffusion flame. The possibility of establishing a "cool" diffusion flame in this burner is investigated numerically. Fuel and air are flowed on to each other through 10-mm diameter nozzles that are separated by 10 mm. Low-speed (5 cm/s) co-annulus flows of nitrogen are used for shielding the fuel and air jets from the room air. Liquid n-heptane is pre-vaporized by adding heated nitrogen. The fuel mass fraction in the n-heptane/N_2 mixture is set as 0.8 and the temperature of the mixture at the nozzle exit is set at 400 K. Note that this dilution and temperature are typically used in establishing diffusion flames with pre-vaporized liquid fuels. The axisymmetric flowfield between the fuel and air nozzles is simulated using a 401x51 grid system.

Typically, a flame in the opposing-jet burner is established by flowing fuel and air at given flow rates and igniting the mixing layer with an igniter. After performing several calculations with different velocities (stretch rates), 4 cm/s and 7 cm/s velocities are chosen for fuel and air jets, respectively, for establishing a "cool" diffusion flame. Traditional ignition sources such as hot spots (spark igniters in the experiments) won't work for "cool" flames as the high temperatures used in these sources for accelerating ignition processes establish normal flames directly. On the other hand, using a low-temperature source for ignition won't work due to long ignition delay times at those temperatures. Note that it is not possible to obtain a "cool" flame from a normal flame through varying the jet velocities or mole fractions of the fuel and oxygen as the environment in which a normal flame would not survive is also unfavorable for a "cool" flame.

Flames can also be initiated through increasing the temperature of the air jet. The possibility of igniting a "cool" flame in the opposing-jet burner (Figure 5-50) using heated air is investigated through simulating reacting flows for different air temperatures. The entire flow between the fuel and air nozzles is solved. In each case, heated air gradually mixed with the fuel that is coming in the opposite direction and formed layers of fuel-air mixtures with equivalence ratio increasing from 0 to ∞. Similarly, temperatures of these layers decrease from the specified air-jet temperature to that of the fuel (400 K). A flame is expected to form if the temperature/equivalence-ratio condition of a layer favors ignition. Simulations did not support ignition anywhere in the burner for air-jet temperatures $\leq$ 724 K. However, a "cool" diffusion flame was formed when the air temperature was increased to 725 K. While "cool" diffusion flame continues to form for air temperatures up to 1152 K, the local temperature/equivalence-ratio condition did not favor a "hot" ignition. When the air-jet temperature was increased to 1153 K, "hot" ignition took place and a normal diffusion flame is formed. Results of these heated-air-jet simulations are shown in Figure 5-51.

Temperature and HRR distributions along the centerline of the burner are plotted in Figure 5-51 for air-jet temperatures of 724 K, 725 K, 1152 K and 1153 K. Locations of the stagnation planes (u = 0) for different cases are shown with vertical lines. The stagnation planes in the 724-K and 725-K cases are identically located. Note, fuel jet is at z = 0 and air jet is at z = 10 mm. Even though notable amount of heat is released on the airside of the stagnation plane in the case of 724 K, ignition did not take place. One-degree rise in air temperature (725-K case) provided "cool" ignition at z = 4.8 mm with a peak HRR of ~ 18 w/cc. Interestingly, "cool" flame is formed on the fuel side of the stagnation plane—not where heat was getting released in the 724-K case. Formation of a "cool" flame did not change the location of the stagnation plane, suggesting that the volumetric expansion from heat release is equally distributed on both sides of the stagnation plane. Increasing air temperature to 1152 K did not affect the HRR associated with the "cool" flame. However, stagnation plane shifted closer to the fuel jet. One-degree rise in air temperature (to 1153 K) provided "hot" ignition on the airside of the stagnation plane and extinguished the "cool" flame. Significant endothermic reactions (with negative HRR) are found to take place once the normal flame is formed. Interestingly, the peak HRR associated with the normal flame is only ~ 50% more than that of the "cool" flame. The low flow rates associated with this numerical experiment are limiting the HRR values.

Simulations performed with heated air jets suggest that a "cool" flame or a normal flame can be established independently through setting a specific temperature for the air jet. Nevertheless, flames in these simulations are continually supported by the heated air. A truly self-supported diffusion flame is then established by reducing the temperature of the air jet back to 300 K. Simulations for a self-supported "cool" diffusion flame are made using the solution obtained for the 725-K case in Figure 5-51 as initial condition and setting the air-jet temperature to 300 K. The resulted self-supported "cool" diffusion flame is shown in the left half of Figure 5-52. Temperature distribution and streamlines between the fuel and air nozzles are shown. The velocities of the fuel and air jet are 4 and 7 cm/s, respectively and the temperatures are 400 and 300 K, respectively. The global stretch rate computed based on jet momentums and nozzle separation is 24.38 s^{-1}. Fuel consists of 80% n-heptane and 20% nitrogen by mass. The computed "cool" flame in Fig. 5-63 (left half) is flat, steady and stable. Peak temperature (~ 730 K) is on the fuel side of the stagnation plane. For simplicity, these calculations were made after neglecting the gravitational forces. Typically, these forces are ignored in the simulations of normal diffusion flames formed between the opposing jets of fuel and air. Our earlier studies have shown that only the flame edge and exhaust gases are affected by the gravitational force. However, as the velocities used for "cool" flame are quite small, gravity may have an influence on these flames.

For understanding the effect of gravity on "cool" flame, calculations are repeated after including the gravitational forces acting in the downward direction. That means, fuel is moving vertically upward and air is moving vertically downward as shown in Figure 5-50. Resulted "cool" flame is shown in Figure 5-52 in the right half. Gravitational force made the heavy n-heptane fuel jet to spread more while moving upward, which caused the "cool" flame to shift slightly toward the fuel nozzle. "Cool" flame in the center region ($0 < r < 5$ mm) remained flat even under gravitation force. However, buoyancy caused the edge of the "cool" flame to curve upward. Comparing the "cool" flames shown in the left and right halves of Fig. 5-63 suggests that gravitational force may influence the structure of a "cool" flame to some extent but it doesn't destabilize it. Interestingly, calculations performed with gravitational force acting in the upward direction (this is equivalent to placing fuel on the top and air in the bottom in Fig. 5-61), resulted in extinction of the "cool" flame. While flowing down toward the stagnation plane, fuel did not decelerate as quickly and pushed the stagnation plane closer to the airside nozzle. This increased the stretch on the “cool” flame and extinguished it. Further calculations performed after decreasing the fuel jet velocity and increasing the air jet velocity yielded stable "cool" flame even for the top-fuel-bottom-air configuration.

A self-sustained normal diffusion flame is established through performing calculations staring from the solution obtained for the 1153-K case in Figure 5-51 and resetting the air jet temperature to 300 K. Note that the flow conditions (velocities, temperatures and mass fractions) are identical to those used for establishing the "cool" diffusion flame (Figure 5-52). Structures of the "cool" (left halves) and normal (right halves) diffusion flames are compared in Figure 5-53. Temperature and streamlines are shown in Fig. 5-64(a), H_2 concentration and heat release rate are shown in Figure 5-53(b), and C_2H_4 and OH concentrations are shown in Figure 5-53(c). Gravitational force is ignored in both these simulations. As described earlier, radiation from gaseous species was included in these calculations. Parametric studies performed after turning off the radiation suggested that it has insignificant effects on the structures of the “cool” and normal flames. The following differences between "cool" and normal diffusion flames may be noted:

1. "Cool" diffusion flame forms very close to the stagnation plane, but on the fuel side; whereas normal diffusion flame forms well away (> 2 mm) from the stagnation plane, but on the airside.
2. Volumetric expansion in the “cool” flame is weak and occurs on both sides of the stagnation plane.
3. Peak heat release rates in “cool” and normal diffusion flames are comparable (30 Vs 35 w/cc). Endothermic reactions (negative HRR) are insignificant in “cool” flames. On the other hand, they dominated the normal flame structure on the fuel side.
4. Cracked fuel species such as C_2H_4 and H_2 are distributed on both sides of the “cool” flame, whereas they are present only on the fuel side of the normal diffusion flame.
5. Concentration of OH radicals is five orders lower in the “cool” flame compared to that in the normal flame.

While some of the observed differences such as locations of the stagnation planes between the “cool” and normal flames can be explained from the respective densities, differences in OH concentrations and HRR are directly related to the respective flame temperatures. Detailed structure of the “cool” diffusion along the centerline is shown in Figure 5-54. Axial distributions of axial velocity, temperature and stretch rate are plotted in Figure 5-54(a). An inflection in stretch rate profile forms on the airside just before temperature starts rising ($z = 7.2$ mm). The stretch rate at this inflection point (k_{air}) could be used for characterizing a “cool” diffusion flame. It is ~ 13.0 s^{-1} for the “cool” flame established in this study.

Distributions of reactants, combustion products, fuel fragments and oxygenated species are shown in Figure 5-54(b) and (c). Distributions of the low-temperature intermediate species are shown in Figure 5-54(d). Significant amounts of H_2O and CO are produced in the "cool" flame. H_2O is the most dominant product species. Interestingly, CH_2O is the second most formed product species. Among the cracked fuel species, C_2H_4 is being produced the most. The ketohydroperoxides that form during the low-temperature fuel cracking [Fig. 5-65(d)] are distributed on both sides of the stagnation plane. They are consumed partially at the stagnation plane as the temperature increases due to the formation of "cool" flame. Fig. 5-65 suggests that "cool" flame produces a large number of species in significant concentrations. Moreover, these product species are distributed over a wide distance (~ 4 mm). The low temperatures (< 740 K) of "cool" flames help the diagnostics and sampling techniques in measuring these species.

Extinction characteristics of the "cool" diffusion flame are studied through changing the velocities of the fuel and air jets in Figure 5-50. For each set of conditions entire flame between the fuel and air nozzles is calculated for capturing the flame extinguishment that might occur at radial locations away from the centerline. Stable "cool" flames are established for different conditions. Interestingly, similar to a normal diffusion flame, "cool" flame also extinguished first at the centerline when the fuel and air velocities are increased. The peak temperature (T_{peak}), maximum in heat release rate (HRR_{max}) and the airside stretch rate (k_{air}) along the centerline obtained for each set of velocity conditions are plotted in Figure 5-55. T_{peak} is found to decrease monotonically as the stretch rate on the flame is increased. HRR_{max} increased with stretch rate up to a value of 31 w/cc and then decreased. "Cool" flame extinguished when the stretch rate was increased beyond 14.7 s^{-1}. Peak temperature for the highly stretched stable "cool" flame was found to be ~ 704 K.

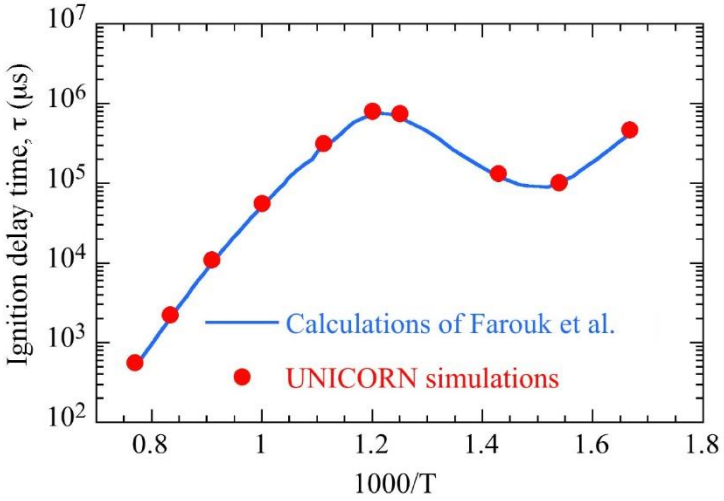

Figure 5-48. Ignition-delay times calculated for stoichiometric n-heptane-air mixture at 1-atm pressure by Farouk et al [4]. Results from the simulations of UNICORN code integrated with the reduced mechanism of Farouk et al. are shown with symbols.

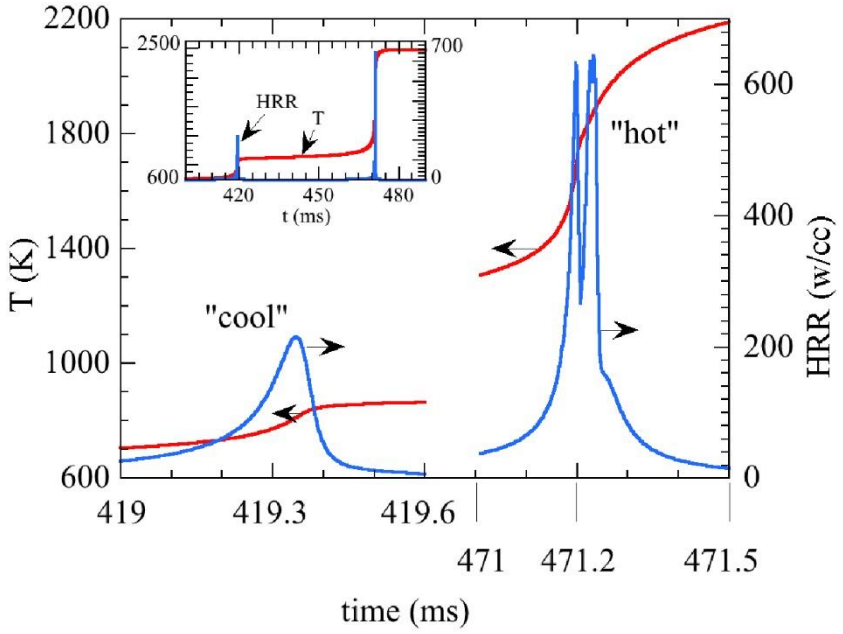

Figure 5-49. History of temperature and heat release rate recorded during the ignition process of a fuel pocket with 600 K initial temperature. Time scales are broken into two parts for providing details during the "cool" and "hot" ignition events. Plot using the time scale covering both the ignition events is shown in the inset.

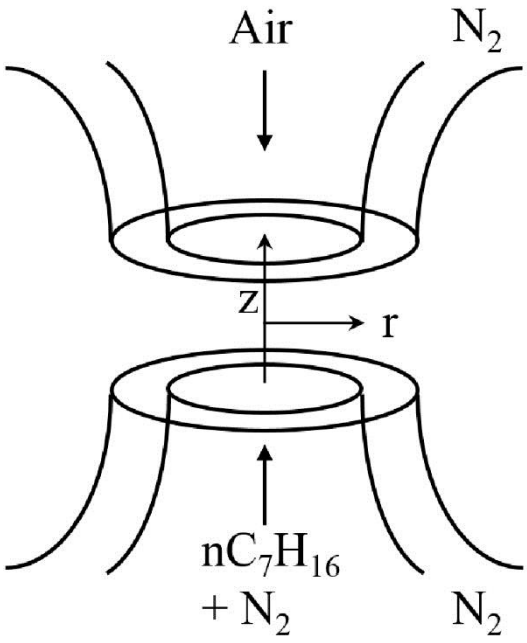

Figure 5-50. Schematic diagram of the opposing-jet-diffusion-flame burner used in the simulations for forming a "cool" diffusion flame.

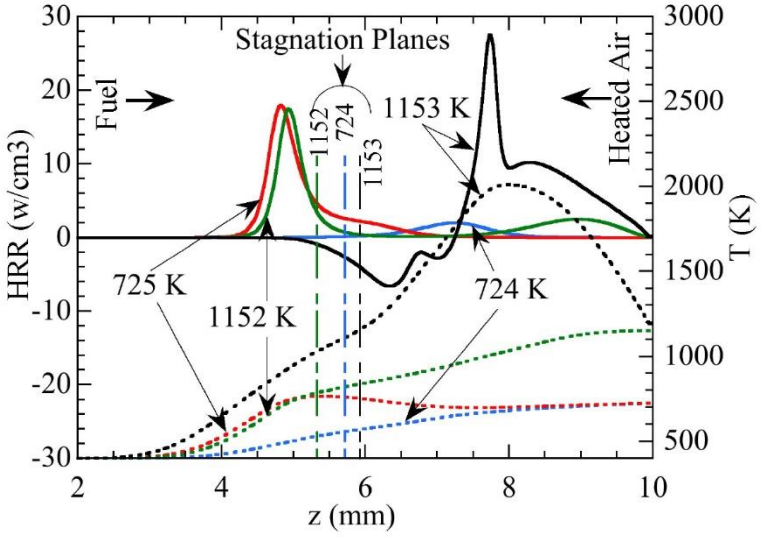

Figure 5-51. Steady-state distributions of heat release rate and temperature along the centerline of the opposing-jet-diffusion-flame burner obtained for different air temperatures. Locations of the stagnation planes are marked with dashed lines with corresponding colors. Note, stagnation planes for 724-K and 725-K cases are identically located.

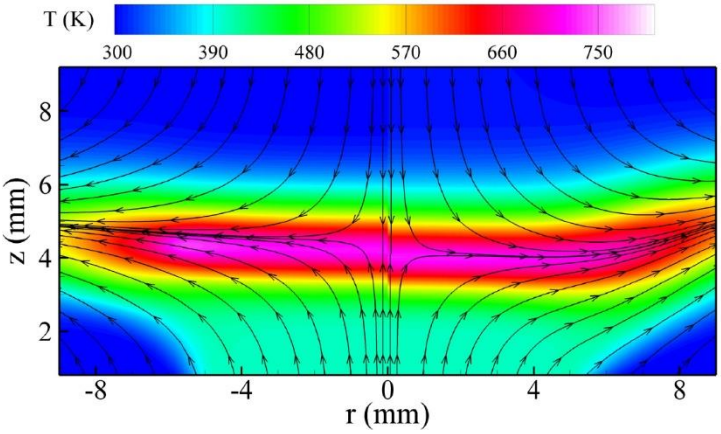

Figure 5-52. “Cool” flame obtained without (left half) and with (right half) gravitational force. Temperature distributions and streamlines obtained between the fuel and air nozzles are shown.

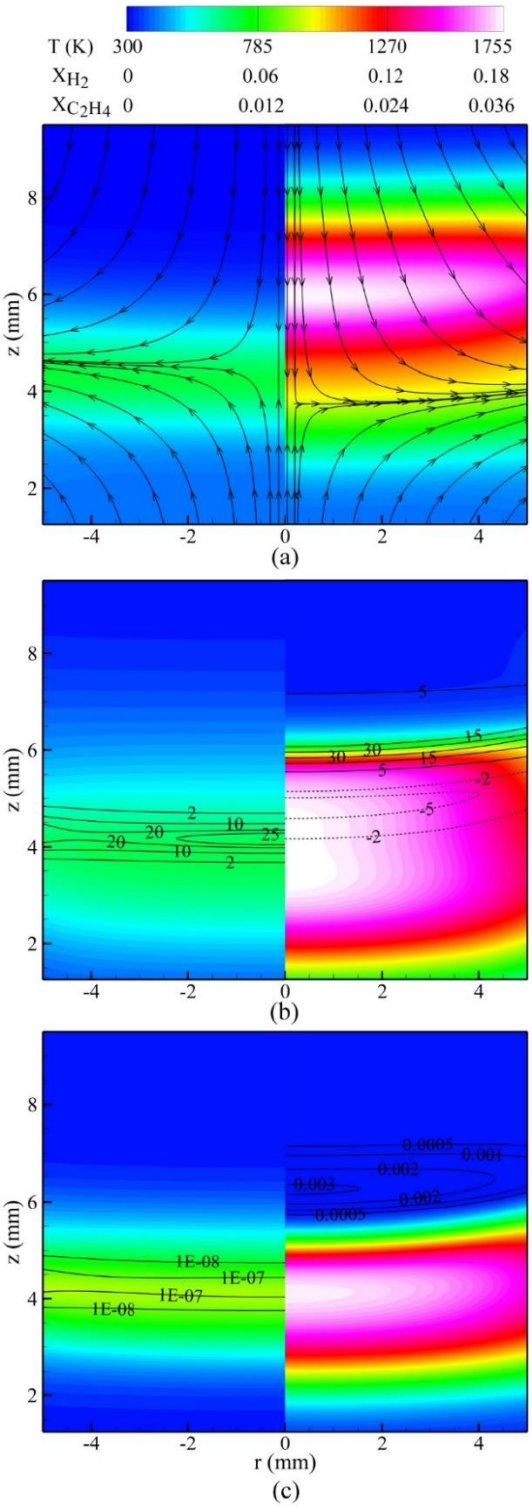

Figure 5-53. Two types of diffusion flames formed in opposing-jet burner under identical conditions. "Cool" flame is shown in the left halves and normal flame is shown in the right halves. (a) Temperature distributions and streamlines, (b) H_2-concentration distributions and iso-heat-release-rate contours, and (c) C_2H_4-concentration distributions and iso-concentration contours of OH radicals between the fuel (z = 0) and air (z = 10 mm) nozzles.

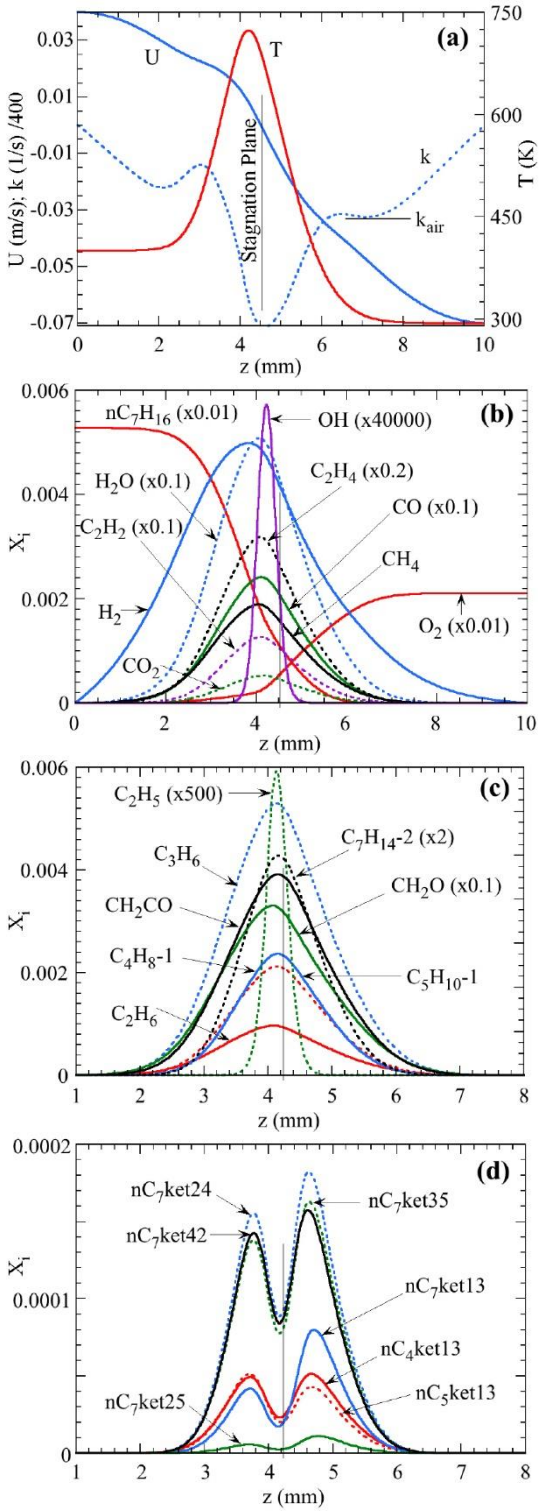

Figure 5-54. "Cool" diffusion flame structure along the centerline. Distributions of velocity, temperature and stretch rate are shown in (a) and those of reactants, products, intermediate species and low-temperature intermediates are shown in (b), (c) and (d), respectively.

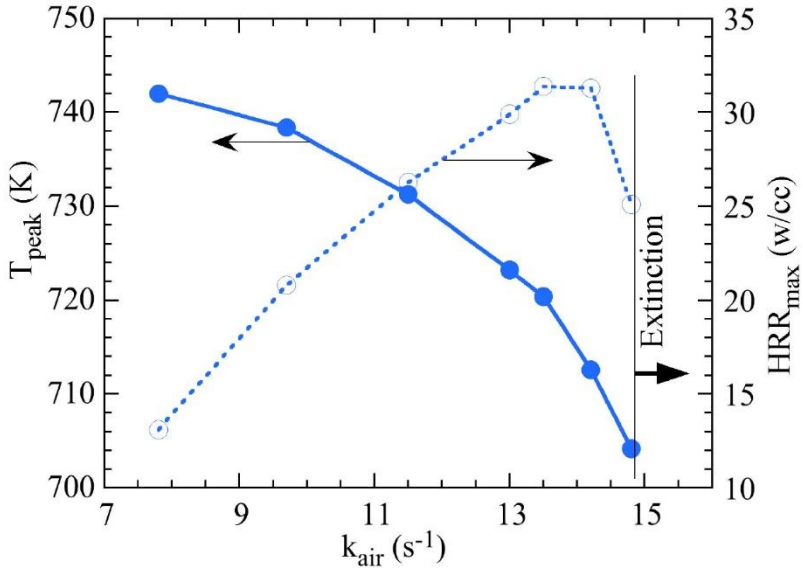

Figure 5-55. Variations in peak temperature and maximum HRR of a "cool" diffusion flame subjected to increasing stretch rate. Flame extinguished for stretch rates > 14.7 s^{-1}.

6 SHOCK TUBE STUDIES

This section of the report summarizes the results from the shock tube studies. Experimental results are presented for ignition delay times and reaction products for all of the binary fuel blends. Results of simulations conducted using the chemical kinetic model developed during the program are used to interpret the results and to assess the ability of the kinetic model to simulate reaction products that are founds in GTE emissions. Fuel chemistry effects are then illustrated by a comparison of ignition delay and combustion products for the four binary fuel blends tested.

6.1 Ignition Delay Times

Ignition delay is a measure of the time required to build up radical concentrations to support an explosion in reactions and heat release, whereas speciation of products provide a measure of reaction pathways. Both are required to have confidence in any chemical reaction mode. Consequently, ignition delay is a primary metric for the quality of any chemical kinetic model. Hence, as part of this program, ignition delays were measured over a range of temperatures under fuel-rich conditions to assess to capability of the reaction model. Verifying performance of the model against ignition delay times was important because the fuel-rich condition used in this study was outside of the range used in much of the data used to develop the kinetic parameters for elementary reactions in model.

6.1.1 Experimental Results

Ignition delay times of the binary mixtures were measured under fuel-rich conditions (Φ = 3) at pressures of 16.7 ± 0.6 atm and over a temperature range of 950–1550 K. Uncertainties are estimated to be 1.09–1.20% for T_5 and 4.0–3.9% for P_5. The uncertainty in incident shock velocity (V_{shock}) is the main source of uncertainty for pre-ignition conditions. Higher uncertainty exists for higher V_{shock} values primarily due to the fact that faster incident shock waves record shorter time intervals between consecutive pressure transducers; thus, the propagation of uncertainties had higher impact on the uncertainty of V_{shock}. At higher pre-ignition temperatures the uncertainty of T_5 increased, whereas the uncertainty of P_5 decreased; this is mostly related to the operational conditions used to achieve higher post-reflected shock temperatures while maintaining a constant post-reflected shock pressure.

Figure 6-1 shows the ignition delay times measured for all four binary fuel blends. The measurements from pressure and OH* emission agree quite well (within 20%) of their mean value; according to Hall et al. (2005) , a 20% agreement is acceptable considering the experimental scatter of shock tube ignition delay experiments. Although the sudden rise in pressure signal is used as an indication of ignition, it is only observable for highly concentrated mixtures (Burcat et al., 1971, Burcat and Radhakrishnan, 1985). It is observed that data for the fuels tested show an Arrhenius-like dependence of pre-ignition temperature on ignition delay over the tested temperature range.

The SERDP kinetic model developed in this program was used to model the ignition delay times, which are compared to the experimental data in Figure 6-1. Three computational approaches were used to predict the ignition delay: the closed homogeneous batch reactor (CHBR) model provided by CHEMKIN-PRO (Reaction Design, 2011) with constant internal energy and volume assumption (constant U, V), constant

enthalpy and pressure assumption (constant H, P), and the SHOCKIN (Flora et al., 2011) model that includes the experimental pressure profile in the kinetics calculations to account for any non-ideal gas dynamic effects. The adiabatic and constant volume assumption is used for each time step in SHOCKIN simulations. The temperature inflection point was chosen to determine onset of ignition. Figure 6-1 clearly shows that the SHOCKIN model predicts ignition delay for all binary fuel blends over the entire temperature range quite well. However, the model slightly overestimates experimental values at temperatures below 1100 K for n-dodecane/n-heptane. The constant U, V assumption estimates larger ignition delay times at lower pre-ignition temperatures for n-dodecane/n-heptane (T_5 < 1250 K), n-dodecane/methylcyclohexane and n-dodecane/m-xylene (T_5 < 1150 K) whereas for n-dodecane/iso-octane overestimates over all temperature range. The constant H, P assumption estimates similar values to the constant U, V model for the n-dodecane/n-heptane and n-dodecane/methylcyclohexane mixtures; but values are larger for the former assumption for n-dodecane/iso-octane (over entire temperature range) and n-dodecane/m-xylene mixtures (< 1200 K).

Comparison of the ignition delay (experimental and kinetic modeling) for all tested fuels is shown in Figure 6-2. It can be seen that all experimental ignition delays fall within bands of ± 35% over the all temperature range. However, slight differences in reactivity among the binary fuel blends can be observed at pre-ignition temperatures below 1100 K and above 1400 K. In the lower temperature range, it appears that the presence of m-xylene reduces the mixture reactivity and leads to slightly larger ignition delay times; the n-dodecane/n-heptane and the n-dodecane/iso-octane blend have indiscernible differences in this temperature range. At pre-ignition temperatures higher than 1400 K, the iso-octane fuel blend had the slowest ignition, followed by n-dodecane/methylcyclohexane, n-dodecane/n-heptane and n-dodecane/m-xylene. In the range of 1100–1400 K all the binary fuel blends behave similarly. These small differences are reflected in the activation energies of the exponential correlations, as shown in Table 6-1. The table shows that combining n-dodecane with 25% (liquid volume) m-xylene caused slightly higher activation energy (102 kJ mol^{-1}) than the other paraffinic mixtures, whose activation energy is within 3.9% of their average.

Modeled ignition delay times for the CHBR model (constant U, V) show comparisons that are similar to the experimental results, with the exception of the iso-octane fuel that reported slightly longer ignition delay times than the n-dodecane/m-xylene blend at temperatures below 1100 K. Additionally, the modeling for n-dodecane/n-heptane mixture exhibits two zones with different activation energies; this is also observed in the experimental results. Transition between the two zones appears to occur around 1150–1200 K. Similar behavior was not observed for the other binary fuel blends, and might be characteristic of a normal-alkane mixture oxidation; the presence of another hydrocarbon class appears to inhibit this peculiar effect.

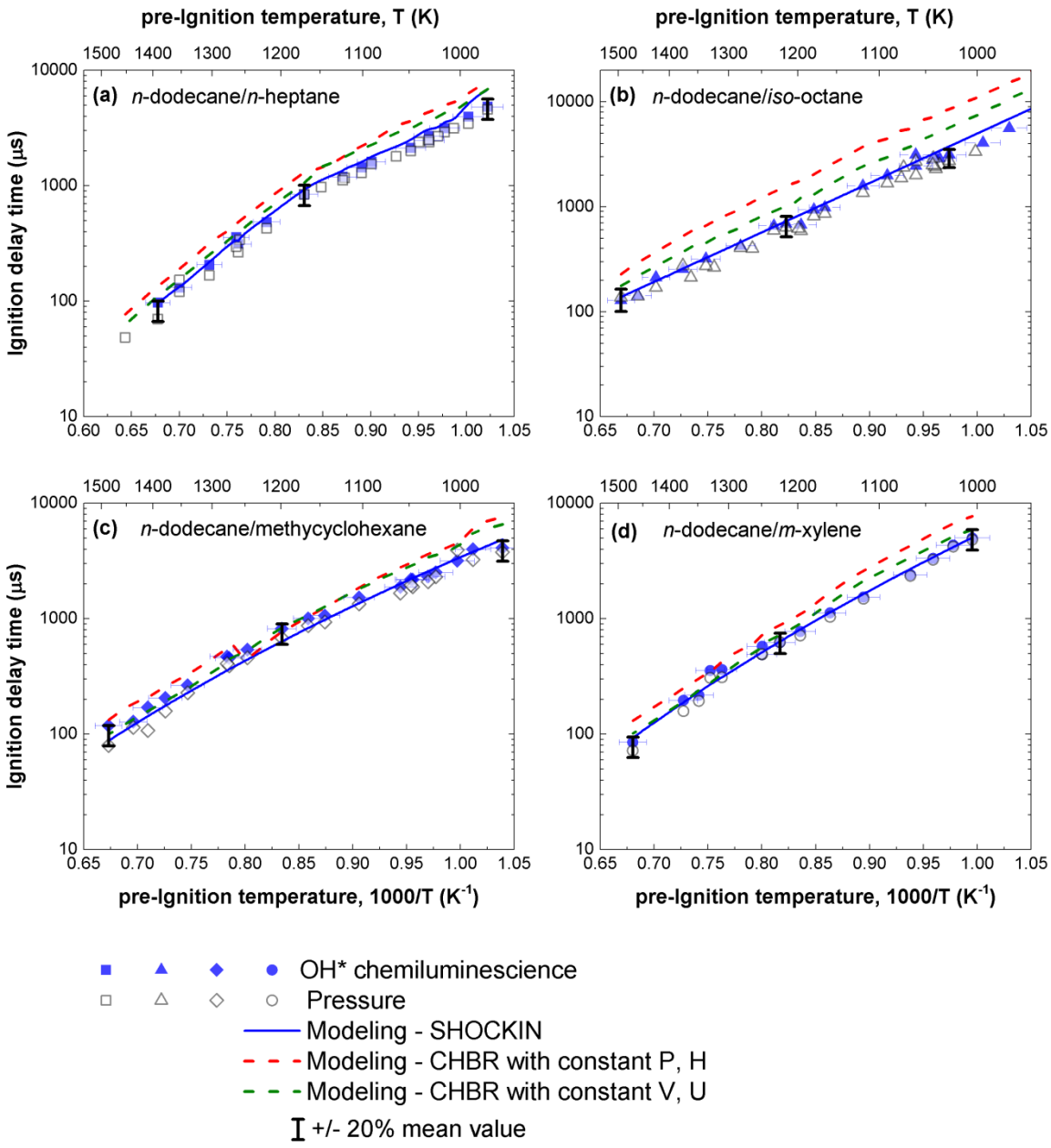

Figure 6-1. Ignition delay measurements for (a) n-dodecane/n-heptane blend, (b) n-dodecane/iso-octane blend, (c) n-dodecane/methylcyclohexane blend and (d) n-dodecane/m-xylene blend. Filled symbols are measurements from OH* emissions whereas open symbols are from the pressure profiles recorded at the end plate of the test section.

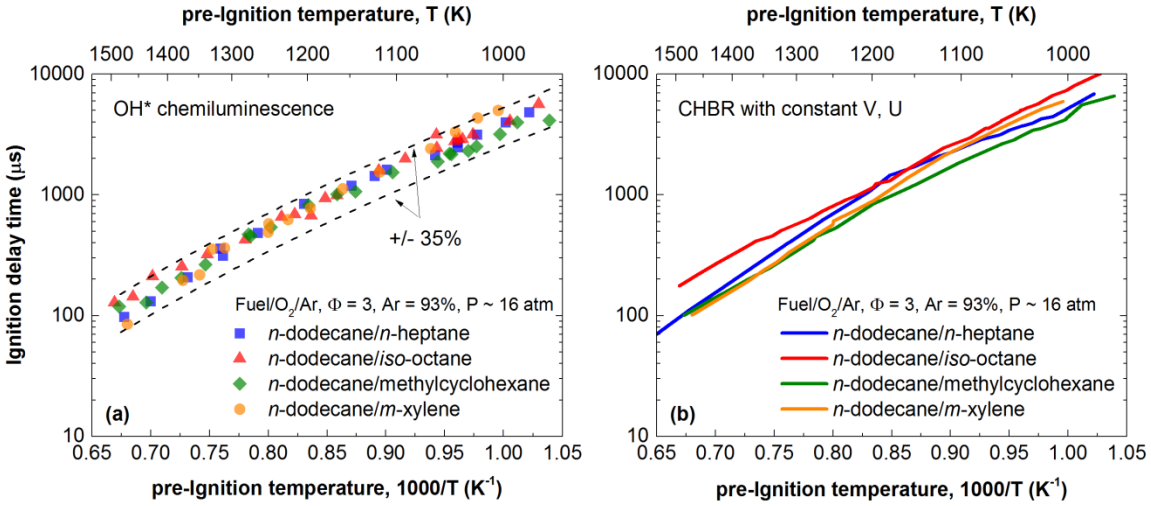

Figure 6-2. Comparison experimental (a) and modeled (b) ignition delay times for ■: n-dodecane/n-heptane; ▲: n-dodecane/iso-octane; ◆: n-dodecane/methylcyclohexane; ●: n-dodecane/m-xylene.

Figure 6-3 compares the ignition delay of binary fuel blends studied here with other fuels previously investigated under similar conditions by UDRI. The comparison includes single component fuels such as *n*-dodecane (Flora et al., 2011), *m*-xylene (Saxena et al., 2011), methylcyclohexane (Nagulapalli et al., 2015) , a blend of *n*-heptane/toluene (80/20 % by liquid volume) (Kahandawala et al., 2008) and two practical fuels – JP-8 (POSF 3773) (Balagurunathan, 2012) and S-8 (POSF 4820) (Balagurunathan, 2012). Table 6-1 lists the Arrhenius correlation parameters (pre-exponential factor and activation energy) for these fuels. Comparison of the experimental ignition delay shows that all the fuels (excluding *m*-xylene) fall within the ± 35% error band. *m*-Xylene shows the lowest reactivity with the longest ignition delay and highest activation energy (102 kJ mol^{-1}). Methylcyclohexane exhibits the lowest activation energy (76.5 kJ mol^{-1}), while the activation energy calculated for the practical fuels (89 and 86 kJ mol^{-1} for JP-8 and S-8, respectively), *n*-dodecane (81 kJ mol^{-1}) and *n*-heptane/toluene (84 kJ mol^{-1}) are similar to the surrogate mixture values. These results further validate the previous conclusions regarding the controlling role of normal alkanes during the pre-ignition chemistry of mixtures in which they are present in significant quantities (Dagaut and Cathonnet, 2006, Balagurunathan et al., 2011).

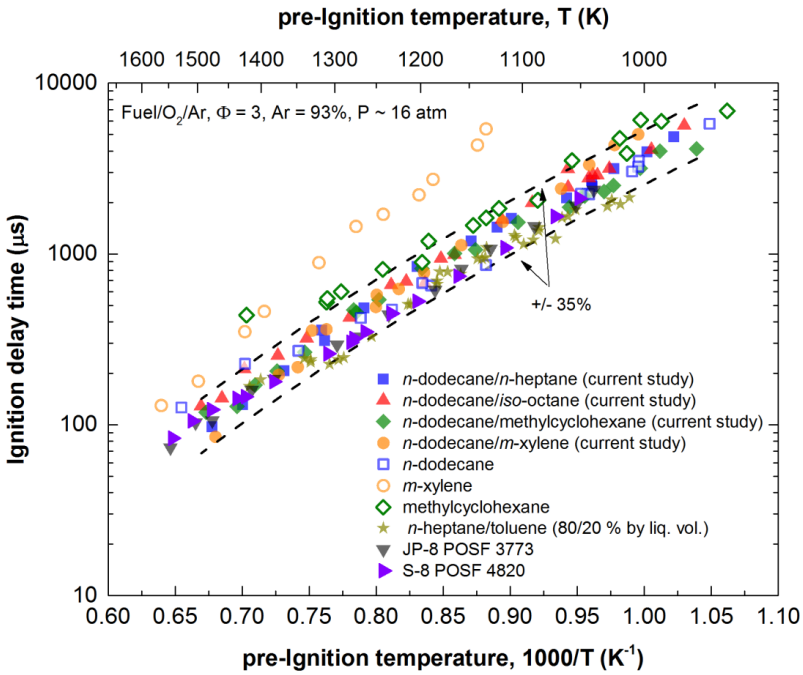

Figure 6-3. Comparison of experimental ignition delay times measured under similar experimental conditions: □: *n*-dodecane (Flora et al., 2011); ○: *m*-xylene (Saxena et al., 2011); ◇: methylcyclohexane (Nagulapalli, 2015); ★: *n*-heptane/toluene (Kahandawala et al., 2008); ▼: JP-8 POSF 3773 (Balagurunathan, 2012); ▶: S-8 POSF 4820 (Balagurunathan, 2012).

Table 6-1. Ignition delay time correlations for the binary fuel blends studied in this work and for other surrogate and practical fuel investigated at the UDRI shock tube facilities under similar experimental conditions.

Fuel	Temperature range (K)	A	E_a (KJ/mol)
Fuel/O_2/Ar, Φ=3, Ar = 93%, P ~ 16 atm $\tau_{ign} = Ae^{\frac{E_a}{RT}}$			
n-dodecane/*n*-heptane (current study)	978–1554	$10^{-1.20 \pm 0.13}$	92.6 ± 2.8
n-dodecane/*iso*-octane (current study)	970–1494	$10^{-0.94 \pm 0.07}$	87.7 ± 1.6
n-dodecane/methylcyclohexane (current study)	962–1485	$10^{-0.85 \pm 0.10}$	84.0 ± 2.3
n-dodecane/*m*-xylene (current study)	1004–1470	$10^{-1.59 \pm 0.14}$	102.5 ± 3.0
n-dodecane	953–1527	$10^{-0.70 \pm 0.09}$	80.8 ± 2.0
m-xylene	1133–1563	$10^{-2.09 \pm 0.13}$	126.3 ± 3.2
methylcyclohexane	941–1421	$10^{-0.30 \pm 0.15}$	76.5 ± 3.0
n-heptane/toluene (80/20% by liq. vol)	1011–1417	$10^{-0.91 \pm 0.01}$	83.8 ± 1.3
JP-8 POSF 3773	1039–1546	$10^{-1.12 \pm 0.05}$	89.1± 1.1
S-8 POSF 4820	1051–1542	$10^{-1.00 \pm 0.05}$	86.1 ± 1.3

6.1.2 Chemical Kinetic Analysis

In order to better understand the differences and similarities in reactivity among the binary fuel blends, brute force sensitivity calculations of the ignition delay were performed. The CHBR model (constant U, V) was chosen for these computations because the CHBR model is less computationally expensive than SHOCKIN and the constant U, V assumption estimated ignition delay better than the constant P, H assumption. Since CHEMKIN-PRO does not offer the possibility to perform sensitivity analysis targeting specific parameters (*e.g.*, ignition delay), an in-house code was developed to perform the task. Cantera 2.1.1 (Goodwin et al.) was used, and the code was developed using Python (Python Software Foundation). Cantera allows the reaction rates (forward and backward) to be multiplied by a user-defined factor in order to investigate any impact this could have on target variables. For this study the sensitivity analysis for ignition delay was performed similar to that of Curran et al. (1998): the reaction rate (forward and backward) of each reaction is multiplied by a factor of two, and then the change in ignition delay is calculated. A positive sensitivity coefficient corresponds to a lower reactivity (longer ignition delay), and a negative coefficient indicates a faster ignition. Pre-ignition temperatures of ~1000 K, ~1250 K and ~1470 K were chosen to represent the low, mid and high temperature chemistry. Sensitivity analysis results are shown and compared for the binary fuel blends in Figure 6-4–Figure 6-6. For each simulation the top 15 reactions with the highest absolute sensitivity coefficient were considered.

In addition to the sensitivity analysis, a local rate of production analysis was carried out with an emphasis on formation/consumption of the radical pool during the pre-ignition period. Half of the ignition delay time was chosen to compute the analysis based on the conclusion of Saylam et al. (2007) that the

reactions relevant to the auto-ignition chemistry are highly active at this time. Results of the rate production analysis are shown in Figure 6-7,

Figure 6-8, and Figure 6-9 for pre-ignition temperatures of ~1000 K, ~1250 K and ~1470 K, respectively. The computations were carried out using the CHBR model (constant U, V). The percentages on each arrow are calculated using the equation (6.1), and indicate the amount of the particular species $[X]_i$ that is produced or consumed by the particular reaction *i* with respect to the total amount being produced or consumed.

$$\%_{[X]_i} = \frac{[X]_i}{\sum_j^{N\ reactions} [X]_j} \cdot 100 \qquad (6.1)$$

The sensitivity analysis results show that the majority of reactions having higher impact on the reactivity for the fuels fall within C_1–C_4 chemistry at all temperatures, with few exceptions at the lowest temperatures. This is consistent with the conclusions reported by You et al. (2009) for the combustion of normal alkanes at high temperatures (T > 1100 K), in which the kinetics of fuel cracking is fast and could be decoupled from the oxidation kinetics of fuel fragments. Thus, the entire pre-ignition chemistry of a large alkane can be reduced to the oxidation kinetics of C_1–C_4 hydrocarbons. Based on the experimental and modeling results, it appears that this can also be extended to other hydrocarbon classes such as branched alkanes, cycloalkanes and aromatics.

At low temperature the recombination of HO_2 radical producing molecular oxygen and hydrogen peroxide is the most important termination step for all the binary fuel blends (see Figure 6-4). This reaction impoverishes the HO_2 radical pool and, therefore, the mixture reactivity. In regards to chain branching, hydrogen peroxide decomposes into two hydroxyl radicals (the only consumption pathway for H_2O_2 (> 90%) common to all of the binary fuel blends). The HO_2 and H_2O_2 molecules are stable enough below 1000 K to participate as chain carriers and significantly impact the chemistry at those conditions (Gardiner, 2000). It is shown in Figure 6-7 that HO_2 is mostly formed during the oxidation of C_2–C_4 alkyl radicals and formyl radical reaction with molecular oxygen. The surrogate mixtures exhibit slight differences for HO_2 production: the channel forming the hydroperoxy radical from formyl radical has a lower impact (6.5%) on the total formation for the n-heptane/n-dodecane fuel compared to the other binary fuel blends (12–16%). Also, the *n*-dodecane/methylcyclohexane mixture shows additional channels producing HO_2, including the oxidation of C_4H_7 (10.8%) and the decomposition of $CH_3CcC_6H_9OOH$ (6.7%).

The OH radical is one of the main chain carrier species during hydrocarbon oxidation Saylam et al. (2007). Under these low temperatures and fuel-rich conditions, it is mostly produced by the decomposition of H_2O_2 (40–49%) and reaction between hydroperoxyl radical and methyl radical (19–30%). As shown in the sensitivity analysis results in Figure 6-4, these are the major reactions in reducing the ignition delay time at those temperatures (T < 1000 K) for all surrogate fuel mixtures.

Formaldehyde (CH_2O) production during the ignition delay period of hydrocarbon oxidation is significant (Gardiner, 2000). As Figure 6-7 suggests, formaldehyde is not directly involved in chain branching, but its reactions (with OH, HO_2, CH_3, and *m*-xylyl) produced species such as the formyl radical which eventually lead to chain branching. The methoxy radical (CH_3O) decomposition and oxidation are the major pathways forming formaldehyde, which eventually is consumed into formyl radical through H-abstraction with OH (17–32%), HO_2 (17–44%), CH_3 (5–17%) and *m*-xylyl radical (~55%) when *m*-xylene was present in the parent fuel blend.

It appears that the pre-ignition chemistry of the *iso*-octane surrogate is particular sensitive to reactions involving the methyl radical (CH_3). The reactions $CH_3+HO_2 <=> CH_3O+OH$ and $CH_3+CH_3 (+M) <=> C_2H_6 (+M)$ have the highest absolute sensitivity coefficient for this mixture among all the surrogate mixtures. Since the re-combination of CH_3 radical slows the self-ignition propensity of the mixtures, it might cause the model to overestimate the ignition delay for the *n*-dodecane/*iso*-octane binary fuel mixture.

There is a significant change in the pre-ignition chemistry from 1000 K to 1250 K. Sensitivity analysis results presented in Figure 6-5 show that the reaction between HO_2 and allyl radical (aC_3H_5) (producing hydroxyl radical, vinyl radical and formaldehyde) is the most negatively (higher reactive) sensitive reaction under those conditions for all the surrogate mixtures. Other reactions with high impact on ignition delay are 1) H-abstraction of ethylene through OH forming vinyl radical and water, 2) the addition of molecular oxygen to atomic hydrogen to form OH and O radicals, and 3) the oxidation of formyl radical to form HO_2 and CO (particularly in the case of n-dodecane/iso-octane). On the other hand, the decomposition of formyl radical into CO and H appears to reduce the reactivity of the mixtures.

At mid-temperatures (~1250 K) the vinyl radical plays a significant role for all the surrogate mixtures.

Figure 6-8 shows that it is mostly produced by H-abstraction of ethylene with OH (19–32%) and CH_3 (6–13%), and from the reaction between aC_3H_5 and HO_2 (42–52%). Vinyl radical is mostly converted into CH_2CHO (54–55%) and HCO (18–38%), whose oxidation with molecular oxygen would produce hydroperoxyl radical. The production of HO_2 has shifted toward the HCO oxidation (30–38%).

At high temperatures the model predictions are in good agreement with experimental results. The reaction $H+O_2<=>O+OH$ is the most sensitive chain branching reaction, and is common among all the surrogate mixtures. The vinyl radical formation from ethylene and its oxidation into vinyloxy radical (CH_2CHO) have a high impact on the mixture reactivity; an increase in their reaction rates lead to shorter ignition delay times. The n-dodecane/iso-octane mixture reported lower sensitivity coefficients for those reactions compare to the other surrogate mixtures; this is reflected in the modeled ignition delay times shown in Figure 6-2 (i.e., n-dodecane/iso-octane exhibited the longest ignition delay at higher pre-ignition temperatures).

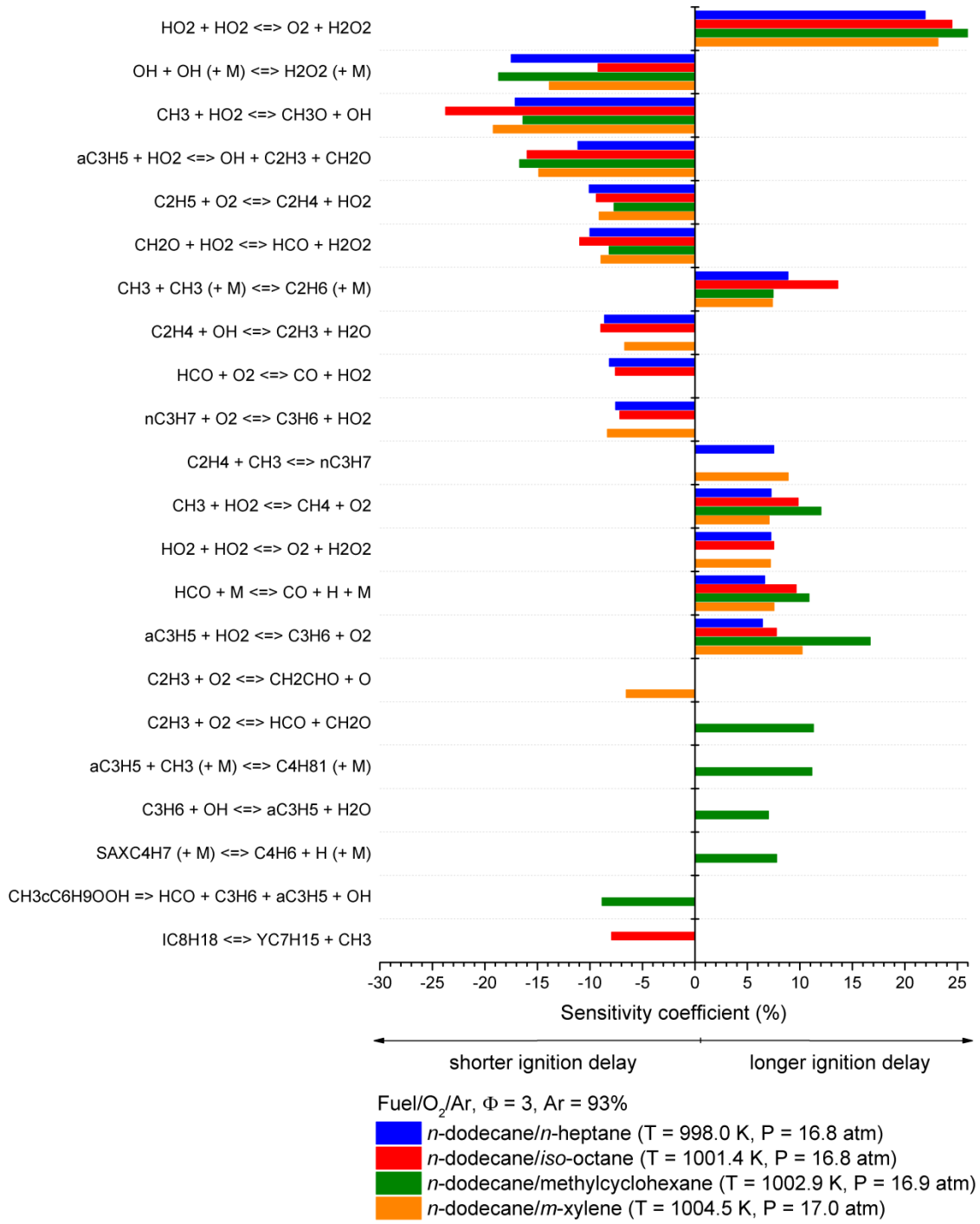

Figure 6-4. Sensitivity analysis results comparison targeting ignition delay time at T ~ 1000 K, P ~ 16.9 atm at Φ = 3, Ar = 93%. For each surrogate fuel, the 15 top reactions with the highest absolute sensitivity coefficient were considered.

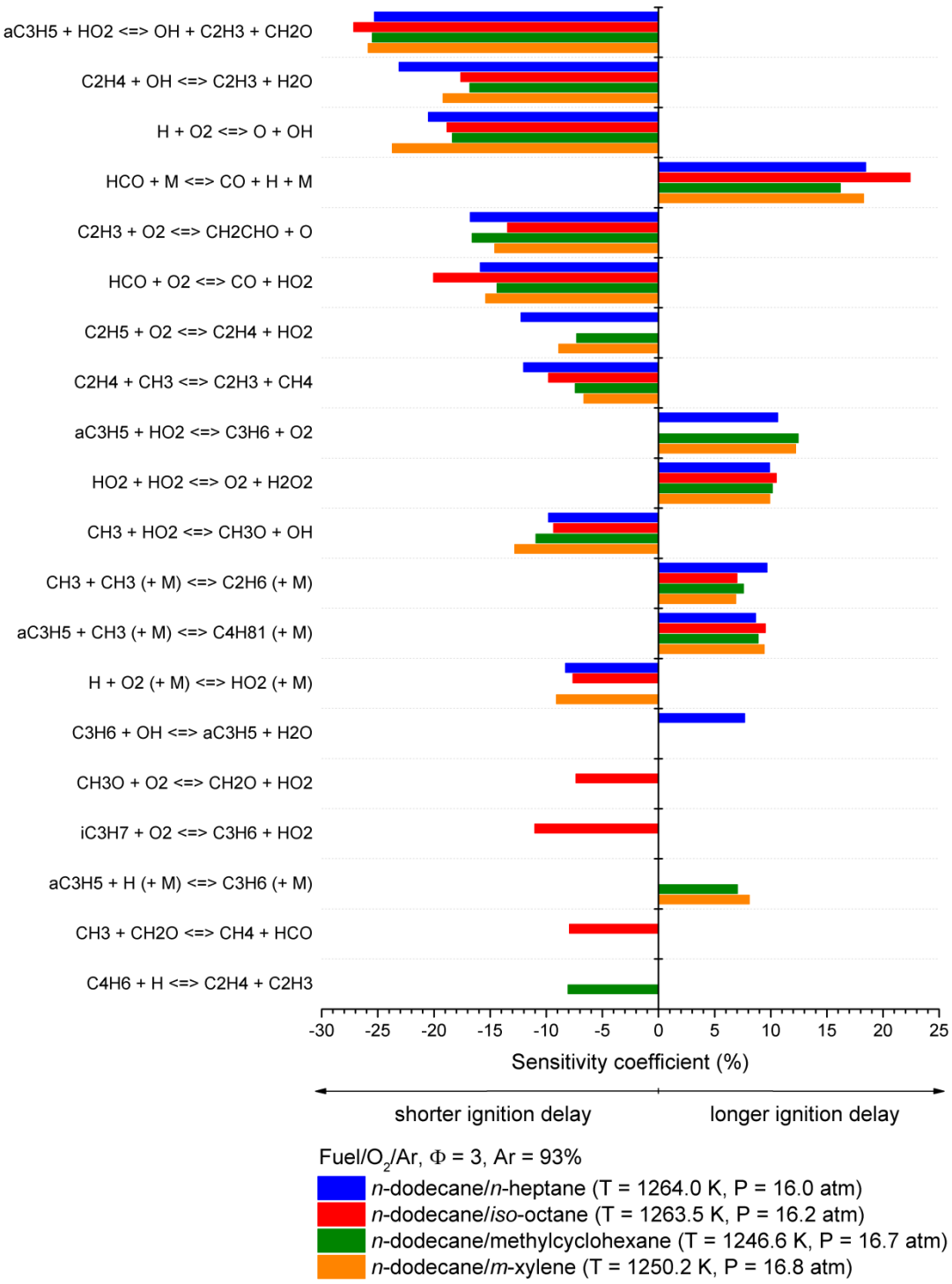

Figure 6-5. Sensitivity analysis results comparison targeting ignition delay time at T ~ 1250 K, P ~ 16.5 atm at Φ = 3, Ar = 93%. For each surrogate fuel, the 15 top reactions with the highest absolute sensitivity coefficient were considered.

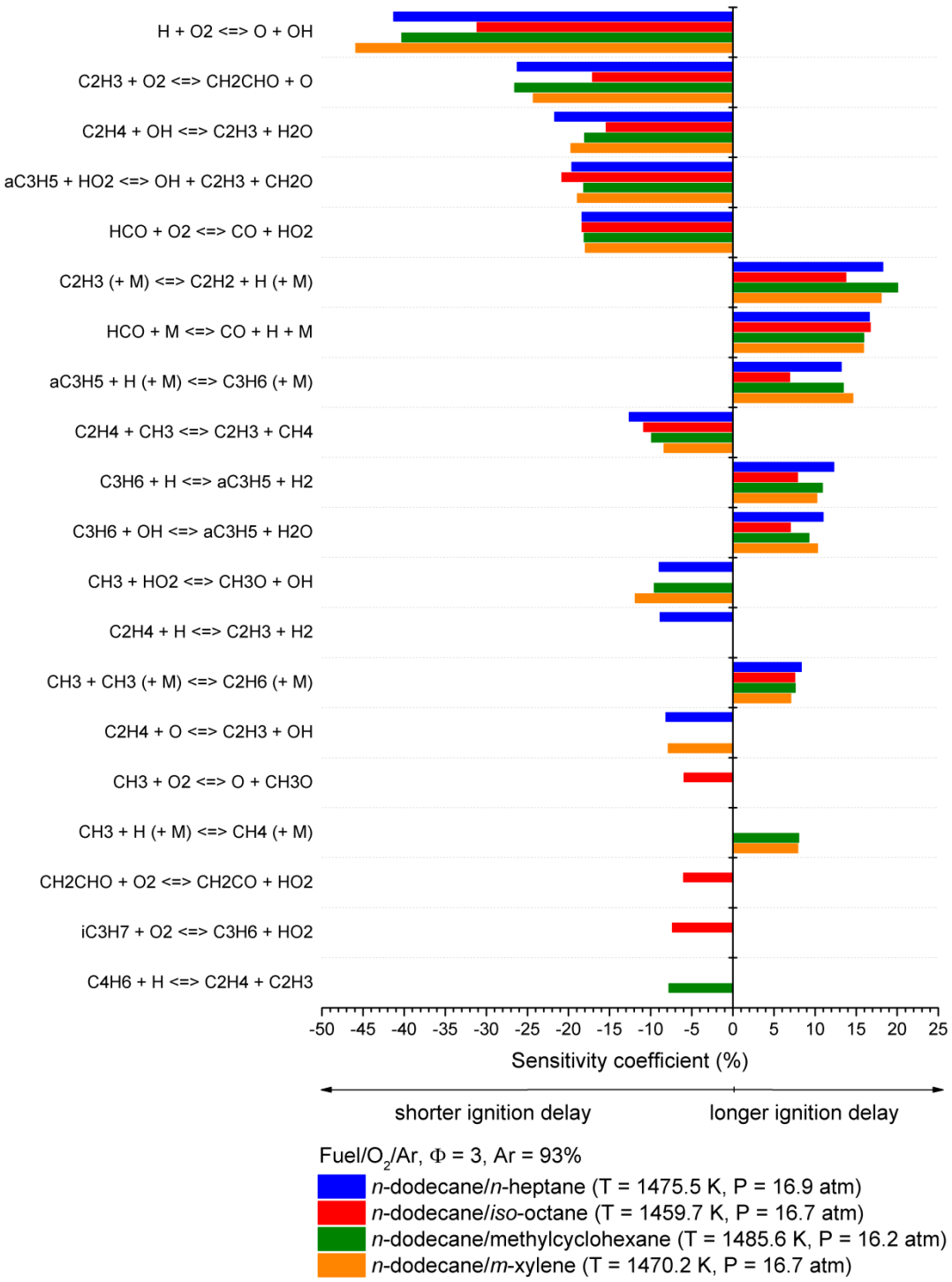

Figure 6-6. Sensitivity analysis results comparison targeting ignition delay time at T ~ 1470 K, P ~ 16.5 atm at Φ = 3, Ar = 93%. For each surrogate fuel, the 15 top reactions with the highest absolute sensitivity coefficient were considered.

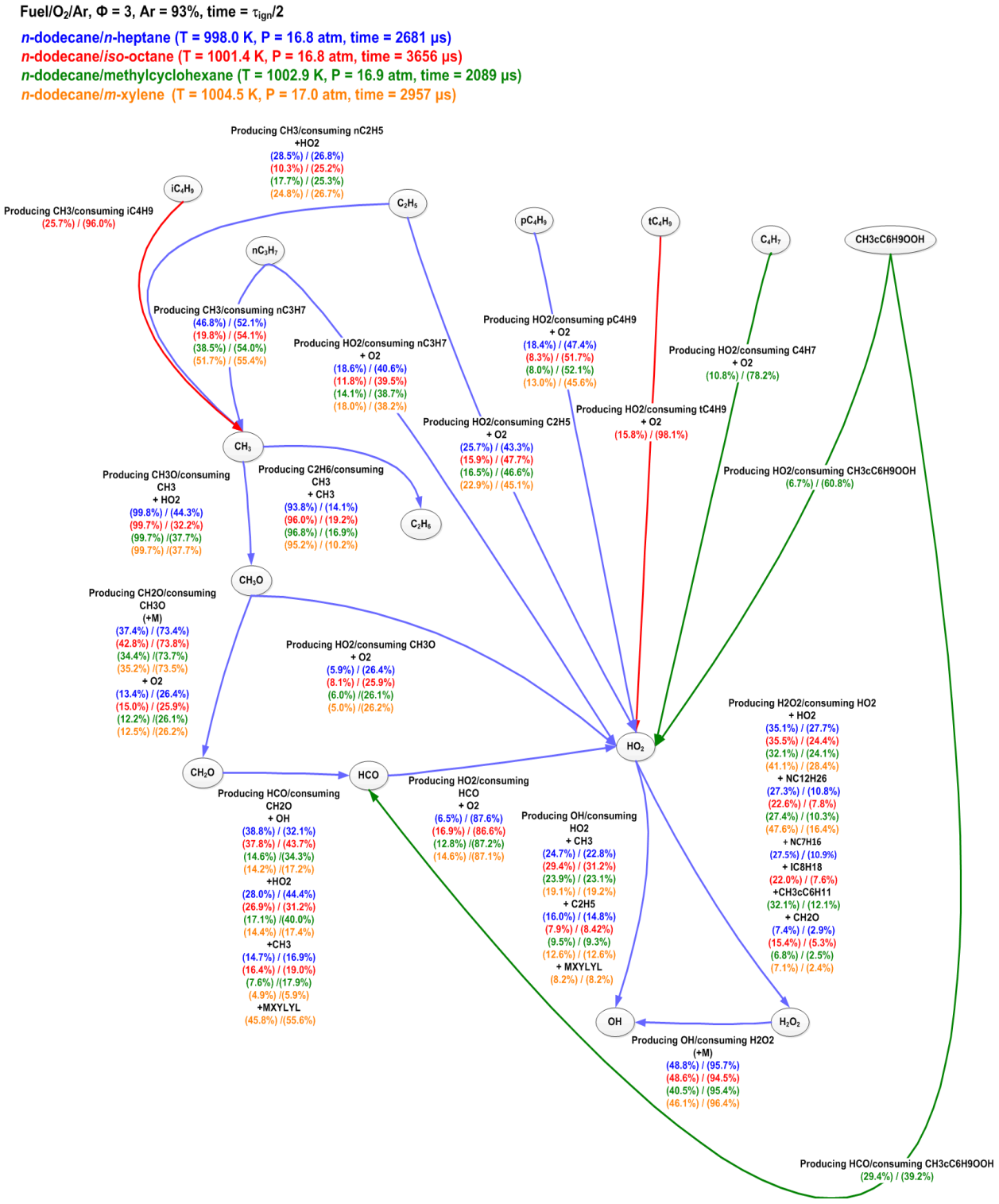

Figure 6-7. Local rate of production analysis at T ~ 1000 K and time equals to half of the ignition delay for all the surrogate mixtures. The CHBR model with constant U, V assumption was used.

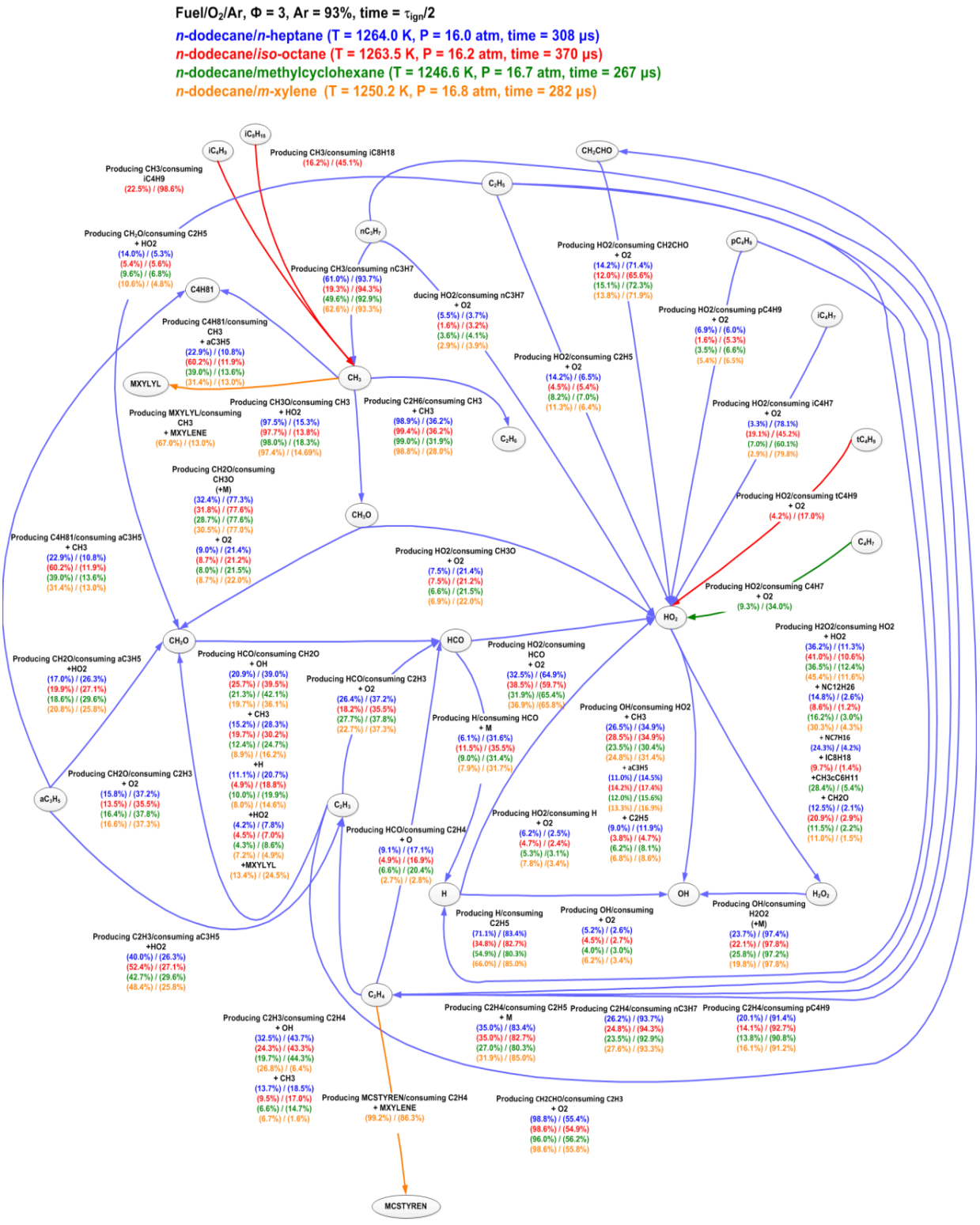

Figure 6-8. Local rate of production analysis at T ~ 1250 K and time equals to half of the ignition delay for all the surrogate mixtures. The CHBR model with constant U, V assumption was used.

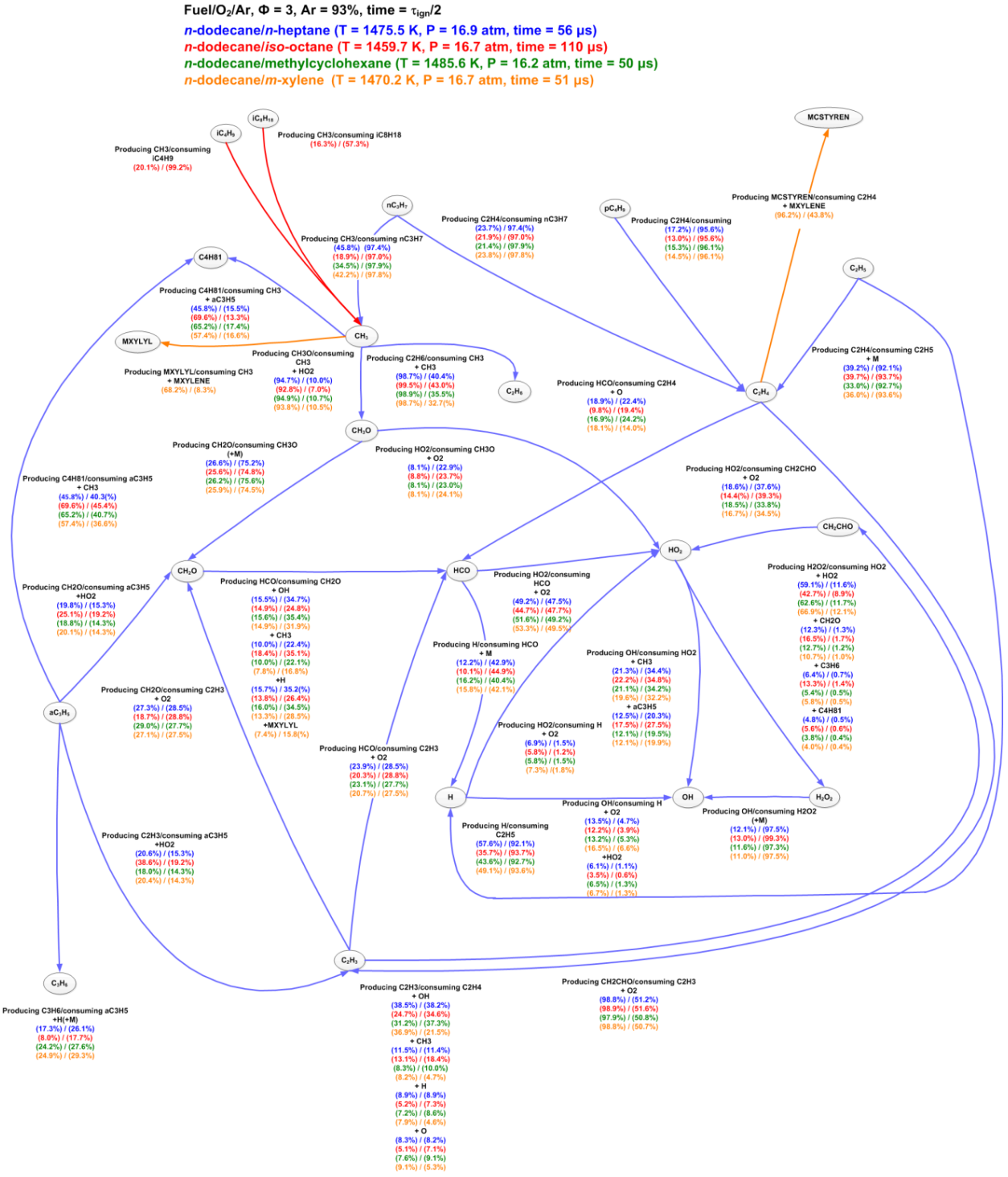

Figure 6-9. Local rate of production analysis at T ~ 1470 K and time equals to half of the ignition delay for all the surrogate mixtures. The CHBR model with constant U, V assumption was used.

Figure 6-10 shows the main radicals (OH, HO_2, and O) in which molecular oxygen is transferred. These results have been computed using the CHBR model (constant U, V) at half of the ignition delay time. The consumption percentage has been calculated according to equation (6.1). At a pre-ignition temperature near 1000 K most of the molecular oxygen (70–90%) is consumed through C_1-C_4 alky radical and formyl radical oxidation to produce HO_2 radical. For the n-dodecane/methylcyclohexane fuel, however, there is also a significant conversion into OH radical compared to the other surrogates. As the pre-ignition temperature increases, the reaction consuming molecular oxygen tends to forms more OH and O radicals, reducing the production of HO_2. According to the SERDP model, the binary fuel blends show similar conversion percentages and the differences in composition do not appear to affect this aspect of the oxidation kinetics for fuel-rich conditions.

Further attention was paid to the decomposition channels of n-dodecane in order to investigate whether the presence of additives (n-heptane, iso-octane, methylcyclohexane or m-xylene) affects the n-dodecane consumption pathways. Figure 6-11 shows decomposition reactions, including H-abstraction by HO_2, OH, H, O, O_2, CH_3, and unimolecular decomposition. It can be observed that the consumption pathways are clearly affected by the pre-ignition temperature, with the H-abstraction by OH radical being dominant at the lower temperature (~1000 K), and H-abstraction by atomic hydrogen and unimolecular decomposition leads the n-dodecane consumption at higher temperatures (> 1250 K). However, the presence of the additives has no effects on the consumption of the n-dodecane since the surrogates reported very similar consumption percentages.

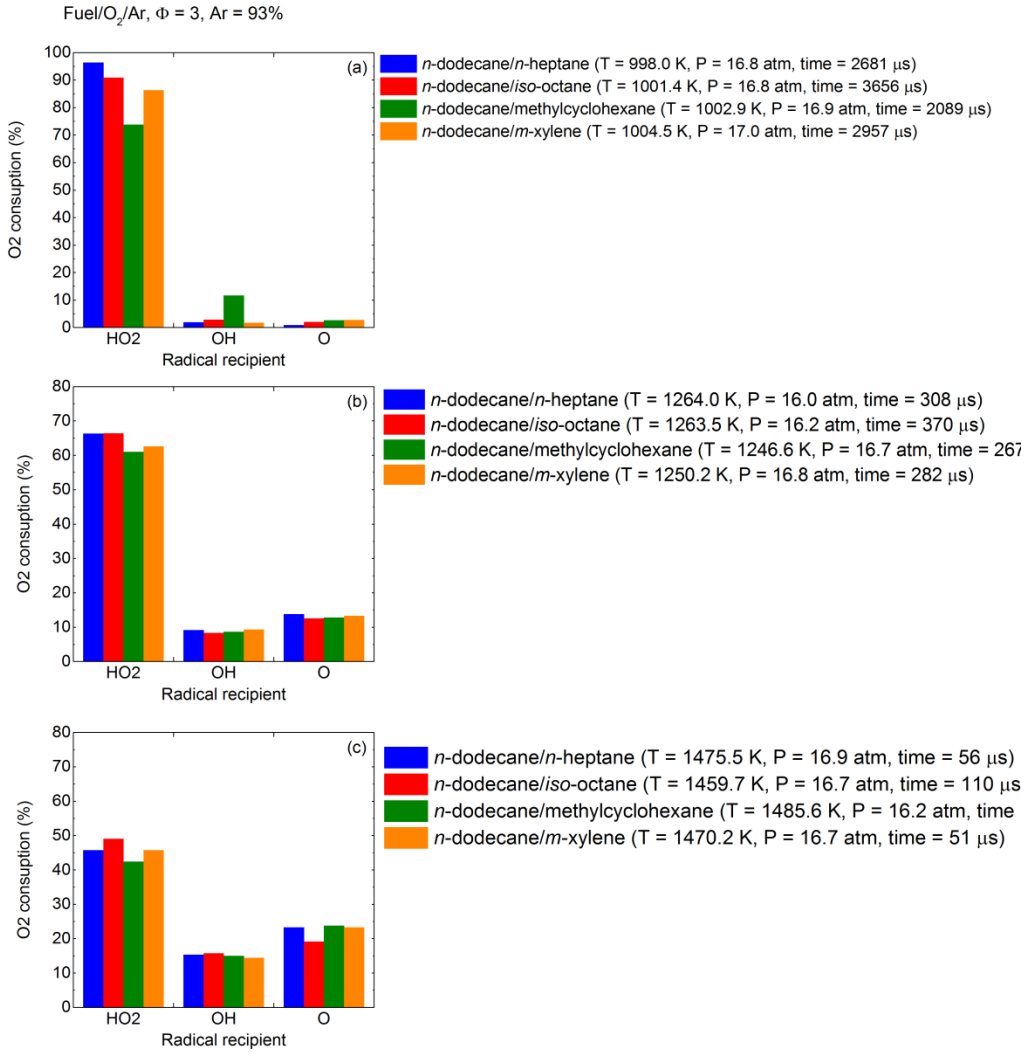

Figure 6-10. Comparison of the molecular oxygen conversion among the surrogate mixtures at time equal to half of the ignition delay; (a) T ~ 1000 K, (b) T ~ 1250 K, (c) T ~ 1470 K. Computation performed using the CHBR model with the constant U, V assumption.

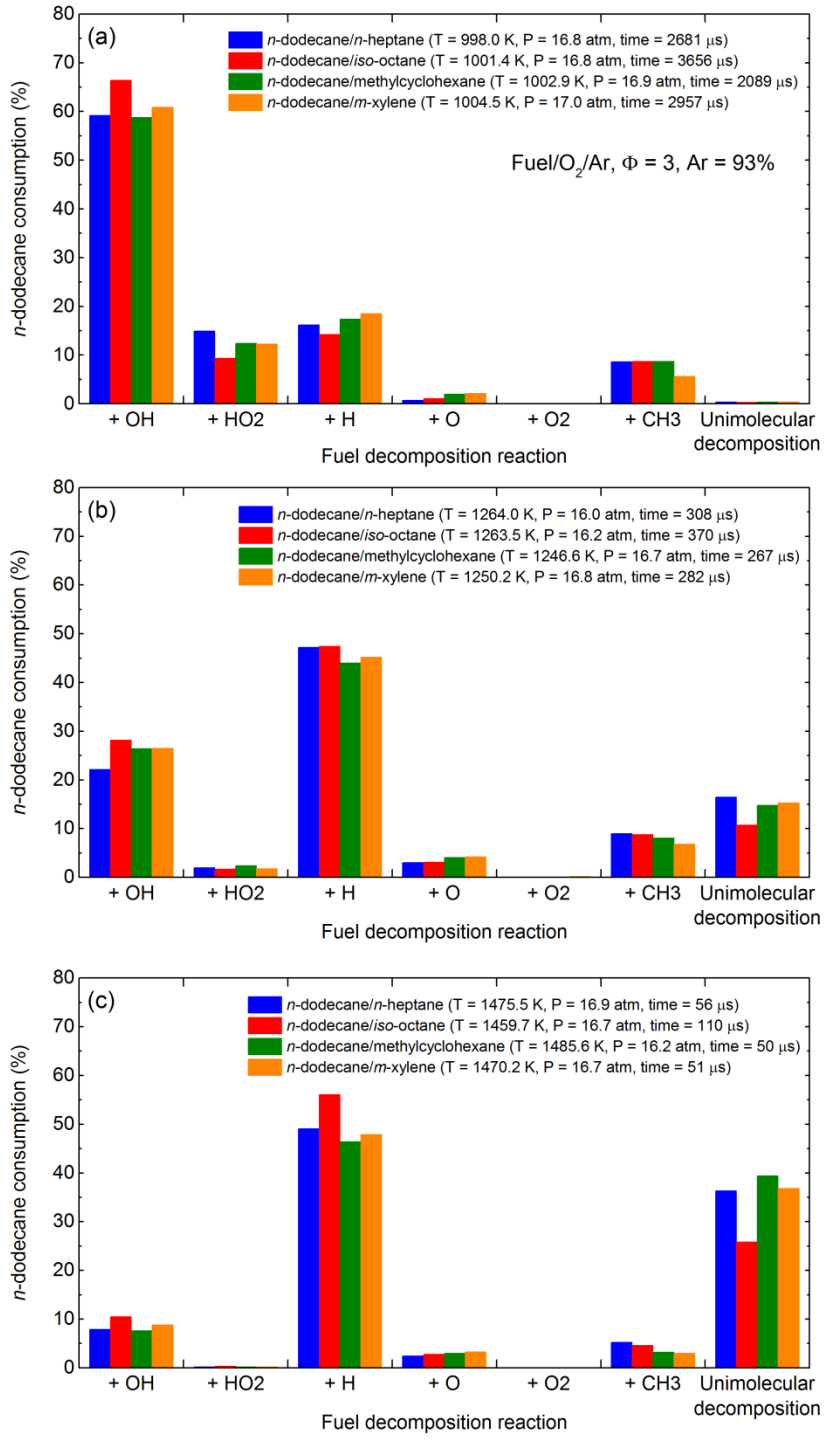

Figure 6-11. Comparison of n-dodecane decomposition pathways among the surrogate mixtures at time equal to half of the ignition delay; (a) T ~ 1000 K, (b) T ~ 1250 K, (c) T ~ 1470 K. Computation performed using the CHBR model with the constant U, V assumption.

6.2 Emissions

6.2.1 Experimental Results

Select pollutants were characterized from the fuel-rich combustion of the binary fuel mixtures. An equivalence ratio (Φ) of 3 was chosen to represent fuel-rich conditions. For all experiments discussed in this subsection, the dwell time was kept in the range of 7.5–8.0 ms. Dwell time was identified by the arrival of the rarefaction fan to the end wall of the test section, causing the pressure and temperature to rapidly decrease. The cooling rate calculated for the experiments reported in this study were in the range of $6 \cdot 10^5$–$1.3 \cdot 10^6$ K s^{-1}, which are large enough to quickly freeze the chemical reactions (according to Yasunaga and Tranter 2013). Emissions are reported in terms of carbon yield based on the initial mass of carbon in the fuel.

Carbon recoveries were calculated, and are displayed in Figure 6-12. The pre-ignition temperature differences between consecutive experiments were kept below 60 K in order to assure a good reproducibility for better interpretation of the results. For the n-dodecane/n-heptane, the overall carbon recovery yields are in the range of 69–101%, with the lowest values at the lower temperatures. The lower recoveries are possibly due to analytical limitations: many species that are likely abundant at lower temperatures were not characterized (mostly C_3–C_5). Light gases are shown to be the dominant products over the temperature range studied. Carbon monoxide reported the largest emissions, followed by C_2H_2 and similar amounts of CH_4 and CO_2. Soot emissions also become significant at higher temperatures for the n-heptane blend; the other three fuels also showed soot emissions increasing at higher temperatures. For the case of *n*-dodecane/*iso*-octane, 35 experiments were carried out; carbon recoveries were in the range of 51–98%. Similar to the n-dodecane/n-heptane blend, light gases (C_1-C_2) are the dominant source of combustion products. For the *n*-dodecane/methylcyclohexane, carbon recoveries from 20 experiments were in the range of 64–94%, with the lower temperature having the poorest recoveries. Carbon recoveries of 15 experiments for *n*-dodecane/*m*-xylene were in the range of 50–95%.

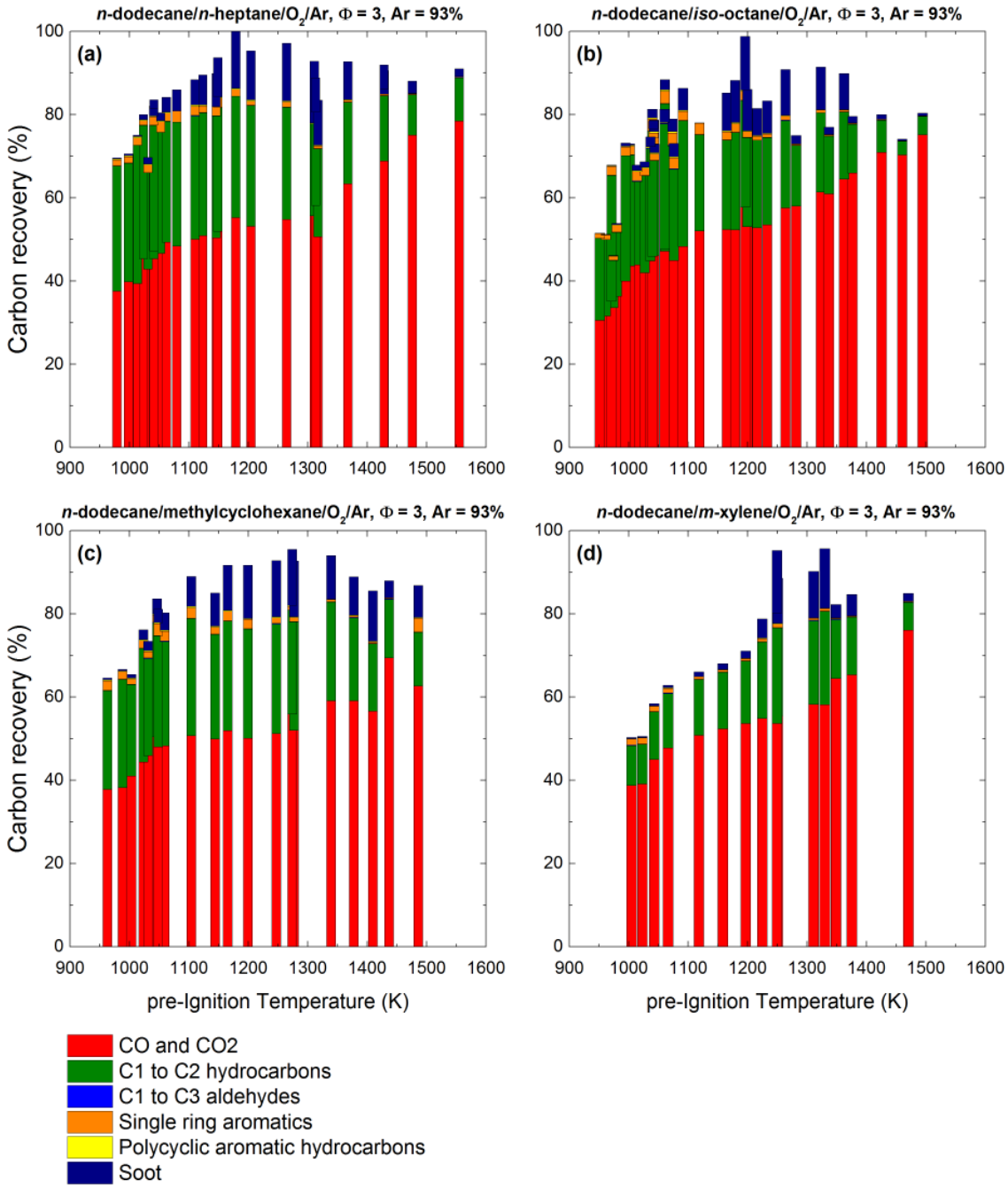

Figure 6-12. Experimental carbon recoveries measured for (a) n-dodecane/n-heptane blend, (b) n-dodecane/iso-octane, (c) n-dodecane/methylcyclohexane, (d) n-dodecane/m-mxylene. All the experiments were at an equivalence ratio of 3, argon concentration of 93% (mol), pre-ignition pressure of ~16 atm, and dwell time of ~7.5–8.0 ms.

Emissions were simulated using the three modeling approaches. The total simulation time used for the CHBR models was not kept constant, rather it was matched to the calculated for each experiment as the sum of the predicted ignition delay and the experimental post-ignition time. The latter was defined as the

difference between the experimental dwell time and ignition delay, and was adopted to ensure that the mixture ignites and has enough time to burn, especially at lower temperatures where kinetic models usually overestimate ignition delay times. Figure 6-13 shows an example of the temporal variation in pressure, temperature and density obtained for the three computational approaches. The sharp rise in temperature clearly identifies the ignition event. The SHOCKIN approach predicts the ignition delay and gas-dynamics occurring during the pre- and post-ignition (*e.g.*, quenching fan that reduces temperature and pressure, freezing the reactions) well. Between the two CHBR approaches, the constant U, V assumption provided better predictions during the pre-ignition event; the constant P, H assumption predicted the post-ignition region and are in good agreement with the SHOCKIN results. In this regard, the post-ignition profiles for temperature and density agree well.

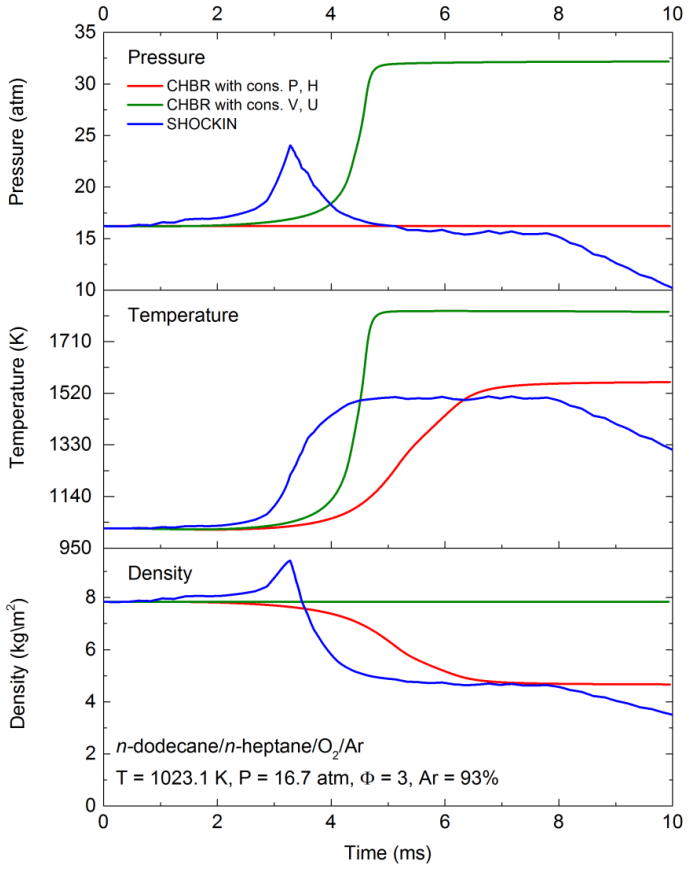

Figure 6-13. Example of time history profiles for pressure, temperature and density from the application of the three computational approaches.

A common conclusion can be inferred for all the surrogate mixtures from the simulated emission results: SHOCKIN and CHBR models with constant P, H assumption predicted similar emission values and trends over the whole temperature range, whereas the CHBR with constant U, V assumption poorly reproduced emissions. These results reflect the conclusions previously discussed for the simulated time history profiles of pressure, temperature and density.

Figure 6-14 shows the comparisons of CO and CO_2 yields for the tested surrogate mixtures. All binary fuel mixtures show similar trends of CO and CO_2; CO emissions increased over the tested pre-ignition temperatures from 28–35% to 70–77%. A rapid increase was observed between 950 and 1090 K, followed by a very small increase (1090–1310 K) and a further rapid increase at higher temperatures. While the *m*-xylene fuel blend had a similar trend for CO, lower yields were measured at the pre-ignition temperatures below 1200 K. Carbon dioxide yields have a bell-shaped trend for all paraffinic blends, with peaks around 1260–1280 K, whereas the *m*-xylene fuel blend showed constant yields below 1250 K of values larger than those for the n-heptane/n-dodecane fuel. Above 1250 K the *m*-xylene fuel blend shows CO_2 yields similar to the other surrogates. Figure 6-14 also displays comparison between simulated emissions using SHOCKIN. CO yields are well predicted for all binary fuel blends above 1250 K, but are overestimated below 1250 K. Similar to experimental results, modeled CO yields for the *m*-xylene fuel blend are lower than values for n-heptane/n-dodecane below 1250 K. Model estimates for carbon dioxide predicted similar trends previously discussed, with a bell-shaped curve peaking at 1250–1280 K.

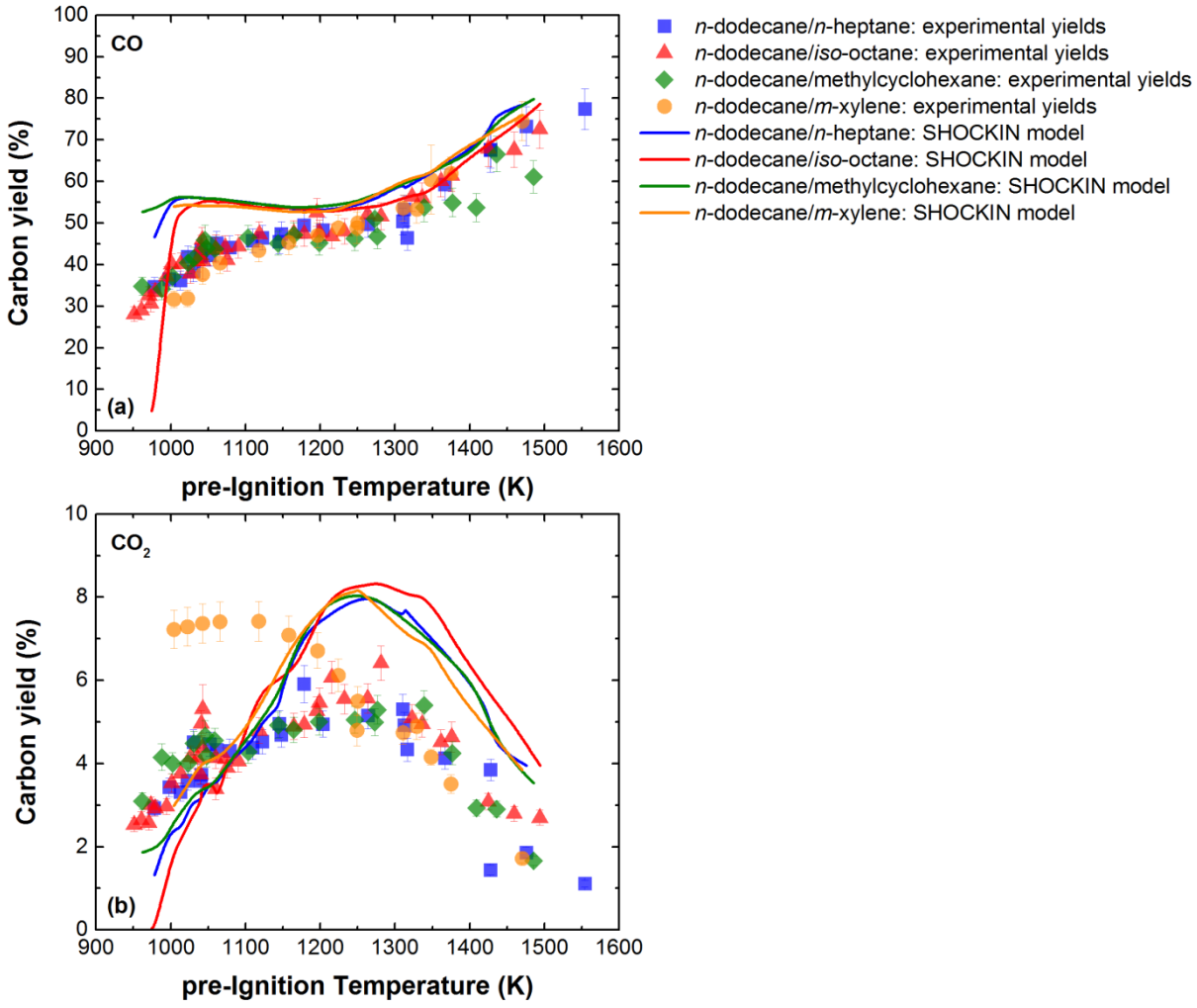

Figure 6-14. CO (a) and CO_2 (b) emissions comparisons among the binary fuel blends.

Figure 6-15 compares the measured and predicted formaldehyde and acetaldehyde emissions. Similar formaldehyde emissions were measured among the paraffinic mixtures: an initial rise from 0.005% to 0.1% from 950 to 1040 K, followed by fast decrease to 0.02% (between 1040 K and 1190 K) and similar values at higher temperatures. The *m*-xylene blend had the lowest emissions of formaldehydes with a maximum of 0.65% at 1040 K. Acetaldehyde yields show a rapid decrease in trend for all binary fuel blends above 990 K, with the largest values at lower temperatures (starting at 0.12%). Below 990 K — mostly measured for the *n*-dodecane/*iso*-octane mixture — values decline with decreasing temperature, with a minimum of 0.03% at 950 K.

The poor prediction formaldehyde points to possible problems with the low temperature reactions within the kinetic mechanism, especially for the iso-octane fuel, for which the predicted carbon yields are more than one order of magnitude higher. For the n-heptane fuel, the prediction is high by about a factor of 4 and for the methylcyclohexane fuel the predictions are within a factor of 2 of the measurements. For acetaldehyde the comparisons between the model and experiment are better than for formaldehyde. The difference is a factor of two or less. Challenges in making the aldehyde measurements may also be contributing to the disagreement. Quantitative measurements of aldehydes are very difficult because of loss (due to reaction or decomposition) during transport to the detection system and accurate calibration of the various compounds. This is particularly true for the smallest aldehyde, e.g., formaldehyde which has two reactive H-atoms and can even trimerize under large concentration conditions.

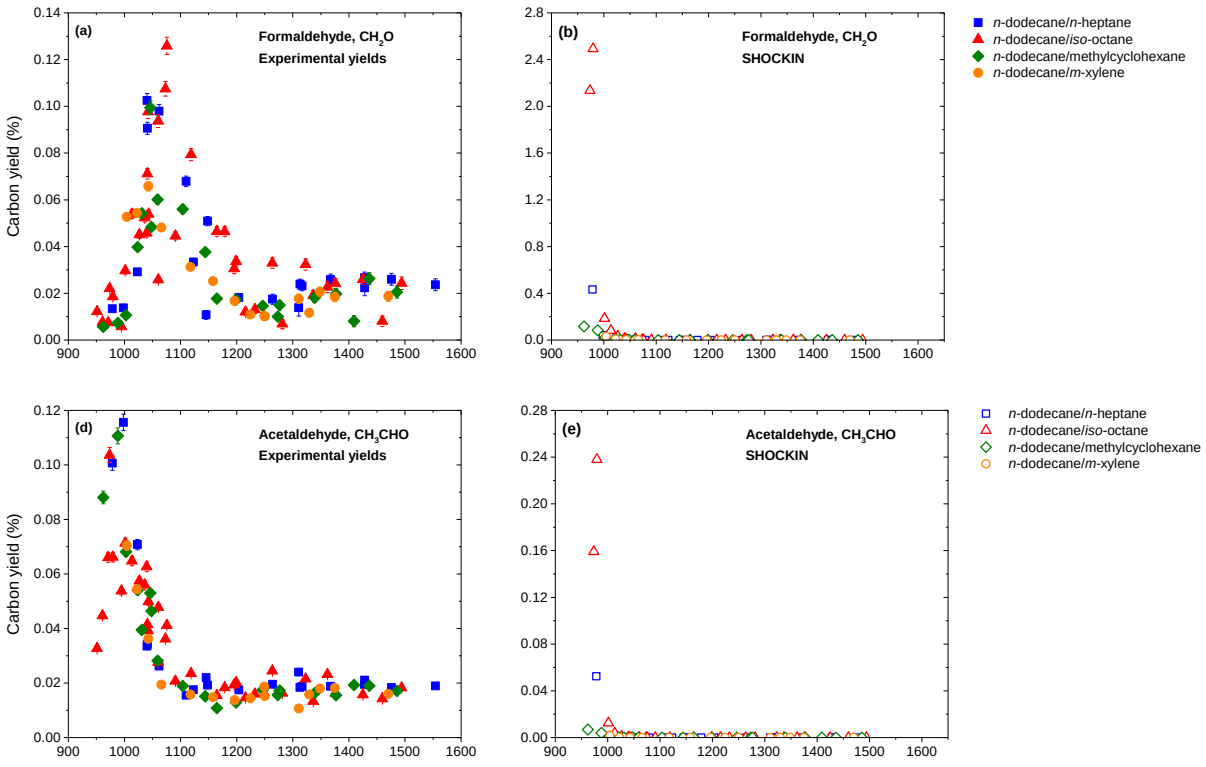

Figure 6-15. Comparison of measured and predicted formaldehyde and acetaldehyde emissions.

Figure 6-16 shows comparisons of methane and ethane emissions. The paraffinic blends show similar trends and yields for both species. Methane yields appear to have a bell-shaped curve with a peak of 7–10% at 1060 K. The *iso*-octane fuel blend has slightly higher emissions of methane for 960–1122 K, whereas the methylcyclohexane blend has slightly lower yields this range. For temperatures above the methane peak, all paraffinic fuels has similar methane yields. The *m*-xylene fuel has very low methane yields in the range of 1000–1250 K, with values being similar to those of the n-heptane/n-dodecane fuel at higher temperatures. Simulated results do not show the bell-shaped curve observed for the experimental data but a decreasing trend instead. At lower temperatures (< 1070 K) the model overestimated, but good agreement was found at higher temperatures. Relative differences among the fuels were well predicted. Ethane was the light gas hydrocarbon with the lowest yields (< 0.7%); it showed an exponential decaying trend over the entire pre-ignition temperature range for all fuel mixtures. The *iso*-octane blend has the higher values of ethane emission, particularly at 950–1215 K. The n-heptane/n-dodecane and methylcyclohexane blends show similar ethane yields, whereas the *m*-xylene blend has slightly lower values. Experimental trends were reflected by the model results; however, the computed yields were underestimated.

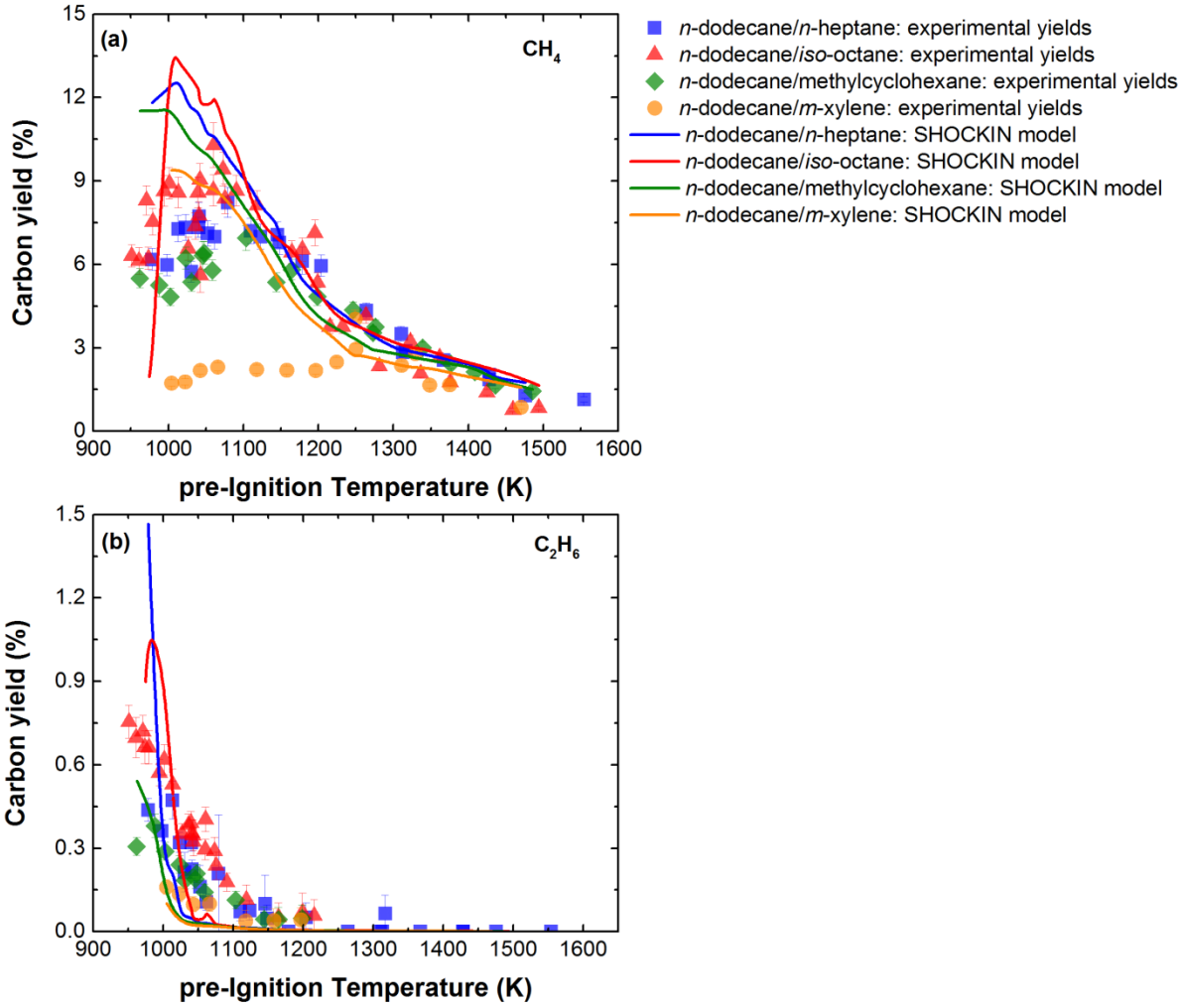

Figure 6-16. Methane (a) and ethane (b) emissions comparisons among the binary fuel blends.

Figure 6-17 reports experimental and predicted emission yields for acetylene and ethylene. Acetylene is the most abundant hydrocarbon in the exhaust gas, with values as high as ~20%. All four fuel blends have a bell-shaped curve for acetylene (peak at 1230 K). The *iso*-octane blend showed slightly lower yields compared to the n-heptane/n-dodecane. Similarly, the methylcyclohexane blend had lower acetylene yields up to 1230 K. The presence of *m*-xylene appeared to significantly reduce the emission of acetylene below 1250 K. At higher temperature all fuels showed similar acetylene yields. Although kinetic modeling results reflected the experimental trends, the model overestimated acetylene yields above 1300 K for all fuel blends. Ethylene yields (experimental and simulated) has a continuous decay over the pre-ignition temperature range. Experimental yields decreased from 12% to below 2% over the range. The paraffinic blends showed very similar ethylene emissions, whereas the *m*-xylene blend has lower yields. Similar to acetylene, modeling predictions captured the experimental trends but underestimated the yield values.

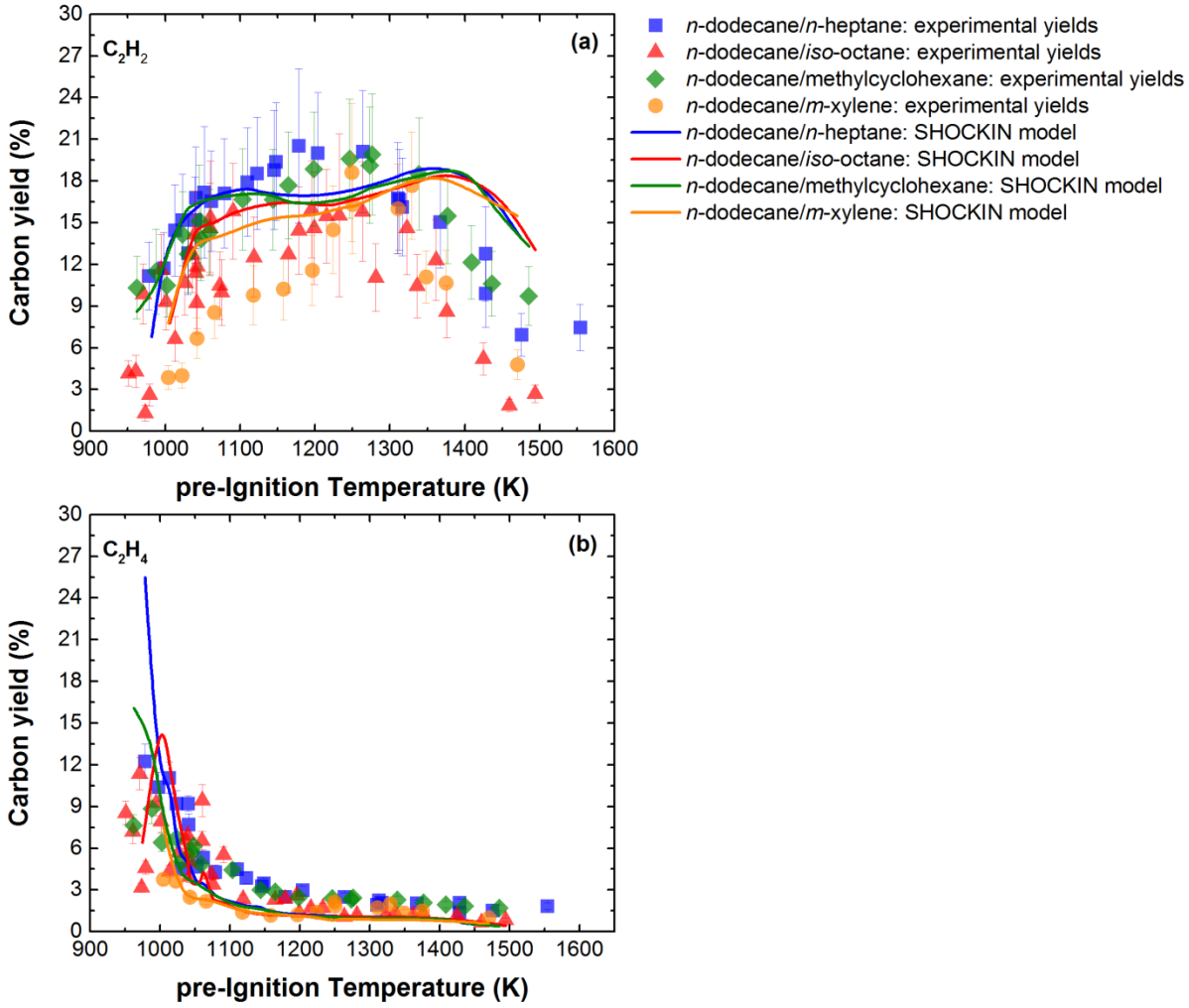

Figure 6-17. Ethylene (a) and acetylene (b) emissions comparisons among the binary fuel blends.

Figure 6-18 reports the emission yields for single aromatic species, including benzene and toluene. For the paraffinic fuels, benzene yields were very similar and showed a bell-shaped curve with peaks of 2.5–2.8% at 1070 K. Benzene yields for the *m*-xylene fuel were significantly smaller than those of the n-heptane/n-dodecane below 1200 K. Model results for benzene yields predicted similar trends but with peak temperatures at 1140 K and 1070 K for the paraffinic and *m*-xylene fuels, respectively. Benzene yields were significantly overestimated for all fuel mixtures over the entire temperature range. Moreover, model values for the *m*-xylene mixture are higher than those for paraffinic mixtures, which was not observed experimentally. Measured toluene yields showed a decrease with increasing temperature for all the binary fuel blends. The paraffinic fuels has similar yields whereas the *m*-xylene mixture formed higher toluene yields at the low temperatures (T < 1063 K). Predicted toluene yields reflected the experimental observations, with values and trends in reasonable agreement.

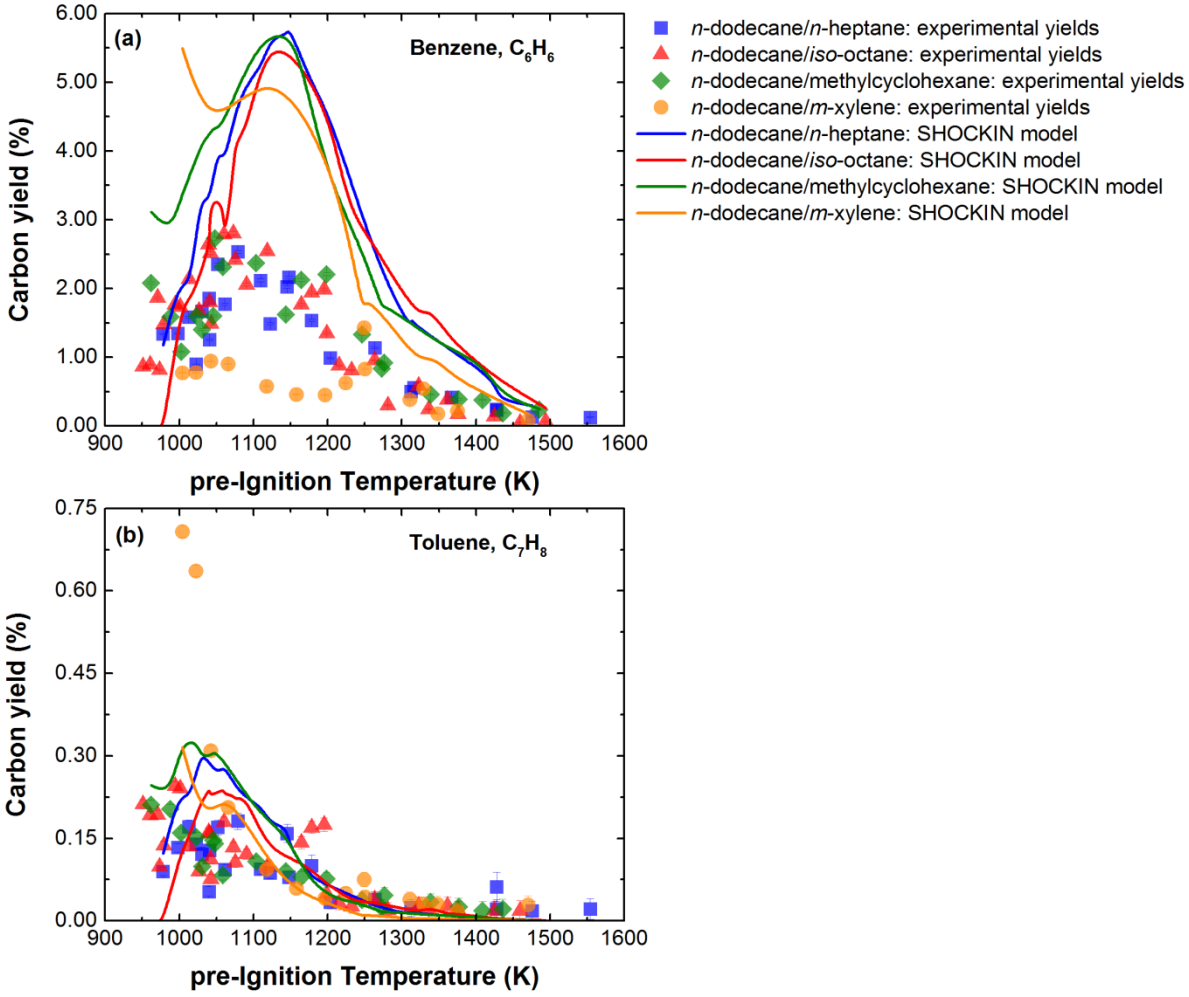

Figure 6-18. Benzene (a) and toluene (b) emissions comparisons among the binary fuel blends.

Naphthalene yields (experimental and modeled) are displayed in Figure 6-19. All paraffinic mixtures has similar values, both experimental and modeling, with a bell-shaped trend peak of ~0.1% at ~1160 K. The model overestimated the naphthalene yields by one order of magnitude over the entire temperature range. The *n*-dodecane/*m*-xylene mixture has lower experimental yields than the other binary fuel blends; however, the opposite was predicted by the kinetic model.

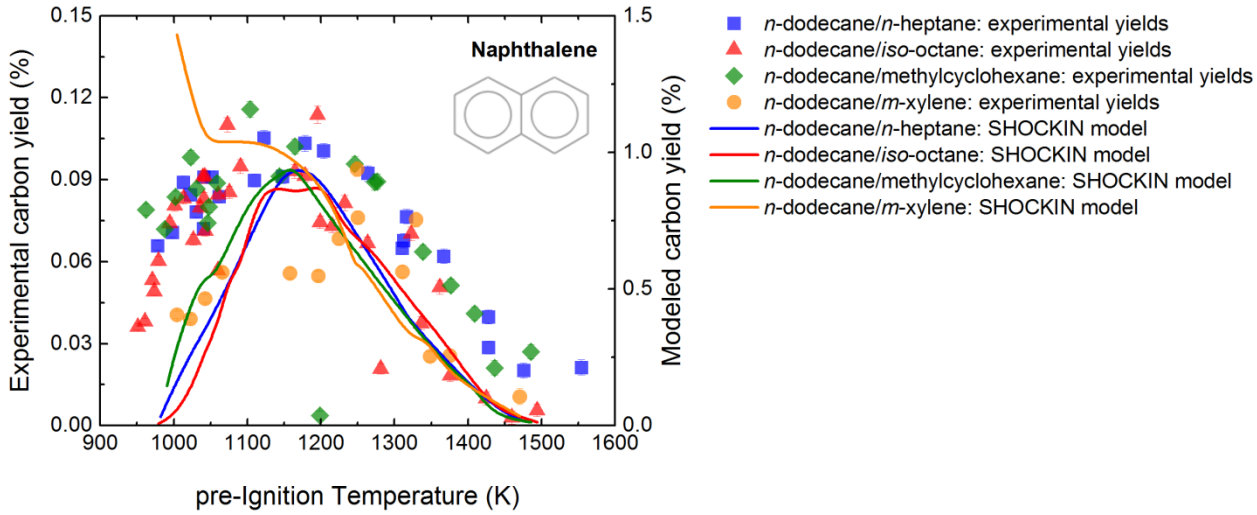

Figure 6-19. Naphthalene emissions comparisons among the binary fuel blends.

Figure 6-20 display additional semi-volatile organic compounds that were characterized. These species include indene, fluorene, 2-methytl naphthalene, 1-methyl naphthalene, biphenyl and 2-ethenyl naphthalene. Indene has the highest yields. Bell-shaped trends were common among all these species for all fuel mixtures. Additionally, the paraffinic fuels has similar values for all these species but lower yields were measured for the *n*-dodecane/*m*-xylene mixture. For the paraffinic blends, indene peaks at 0.05% around 1160 K. Fluorene shares the same peak temperature with lower yields of 0.02%. 1- and 2-methyl naphthalene has similar peak temperatures (1050 K), with the former having slightly lower yields (~0.01%) than the latter (0.017%). For the *m*-xylene blend, 1- and 2- methylnaphthalene decreased over the whole temperature range from 0.01% at low temperatures to 0.0003% at high temperature. Biphenyl yields are very similar among the paraffinic blends: peak yields of 0.02% occur at ~1060 K. The *n*-dodecane/*m*-xylene blend has significantly lower biphenyl yields but similar peak temperature. Similar observation can be seen for 2-ethenyl naphthalene, with lower peak yields of ~0.01%. Kinetic modeling was available for most of the discussed PAHs except for 2-ethenyl naphthalene. For indene and fluorene modeling results underestimated experimental values by an order of magnitude; however, dependency on pre-ignition temperature was reasonably captured but with peak at ~1150 K. Also, model results for the *n*-dodecane/*m*-xylene blend were larger than those computed for the n-heptane/n-dodecane fuel. Simulated yields for 2- and 1- methyl naphthalene are in reasonable agreement with experimental results, with the peak at ~1150 K. Model estimates of biphenyl yield were an order of magnitude lower than experimental values; however, the pre-ignition temperature dependence was well captured.

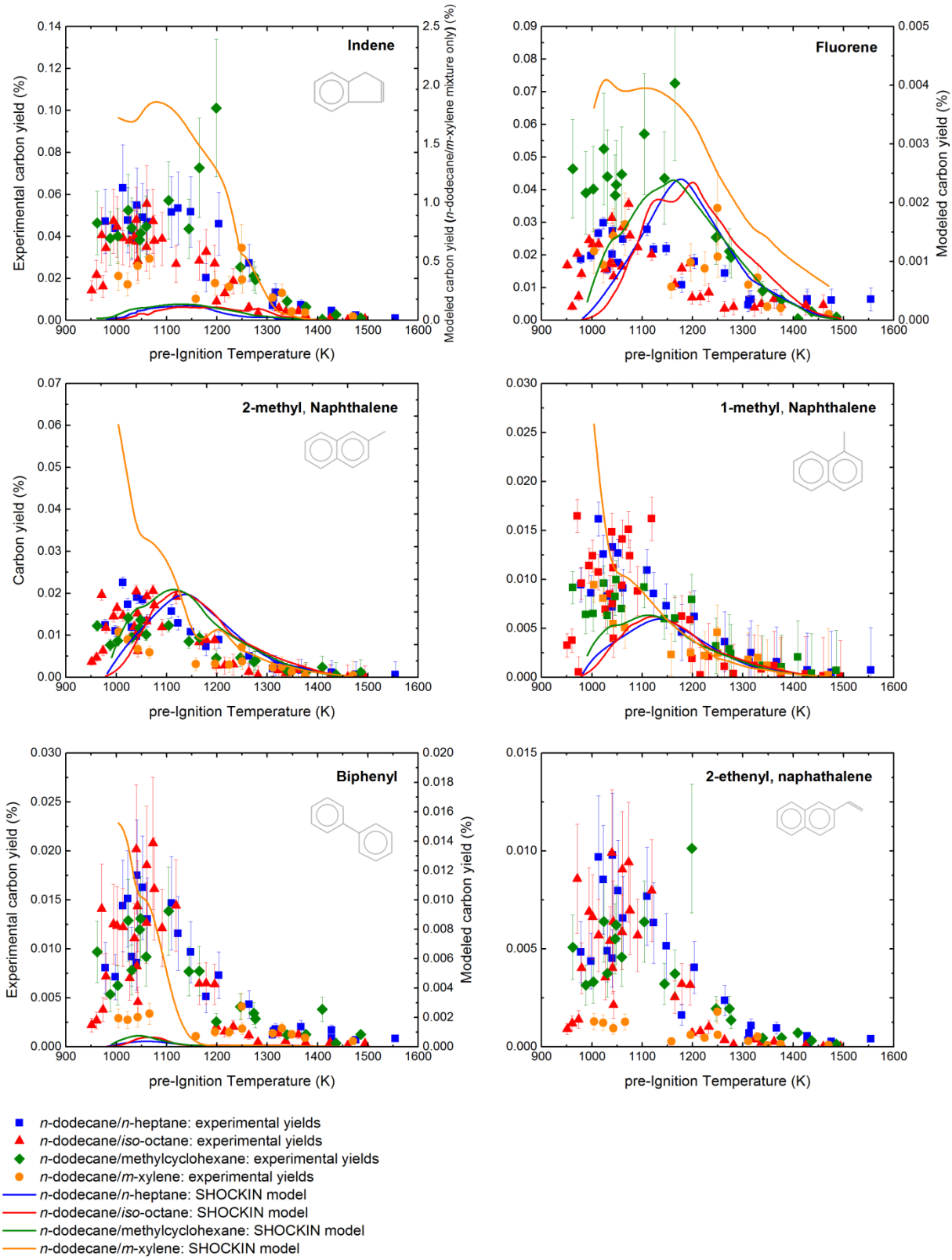

Figure 6-20. Semi-volatile emissions comparisons among the binary fuel blends.

Figure 6-21 to Figure 6-23 show non-volatile species extracted from the collected soot filters. The extraction and analysis techniques allowed to characterized species with molecular weight as high as 326 amu (Rubicene). Bell-shaped trends were common among all these species for all fuel mixtures; however, differences in the peak temperatures existed between the paraffinic mixtures and the *n*-dodecane/*m*-xylene mixture. Particularly, paraffinic mixtures has peak temperatures at ~1100 K whereas the fuel with *m*-xylene showed maxima at ~1250 K. Additionally, the paraffinic fuels has similar values for all these species but higher yields than were measured for the *n*-dodecane/*m*-xylene mixture. Model results were available for phenanthrene and pyrene only. Simulated results for phenanthrene display a bell-shaped trend with peak at ~1250 K for the paraffinic fuels, and a decaying trend for the n-dodecane/m-xylene mixture. Pyrene simulations show bell-shaped trends for all the fuels with peak at ~1250K. Simulations predicted carbon yields three order of magnitude higher than experimental results.

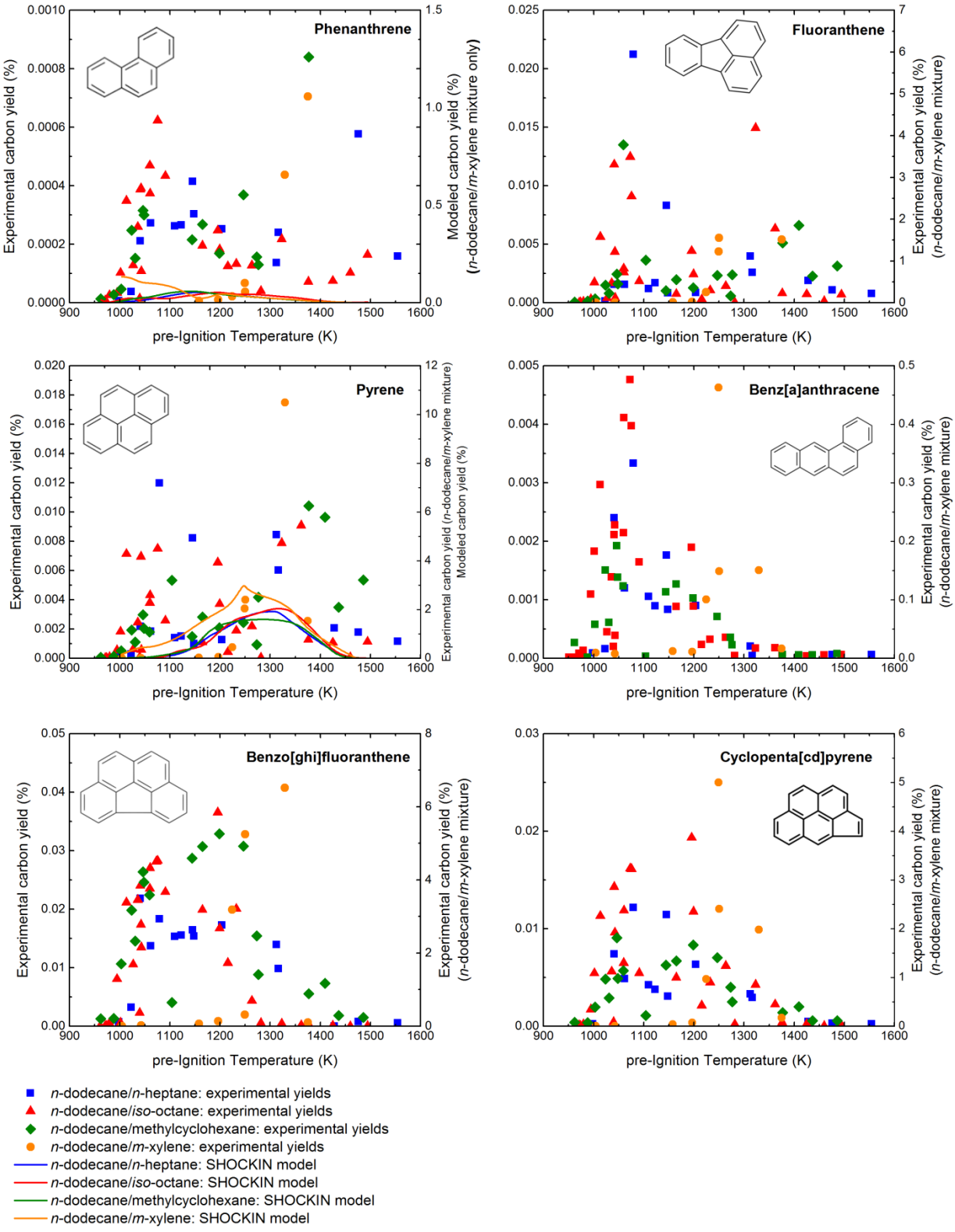

Figure 6-21. Non-volatile emissions comparisons among the binary fuel blends.

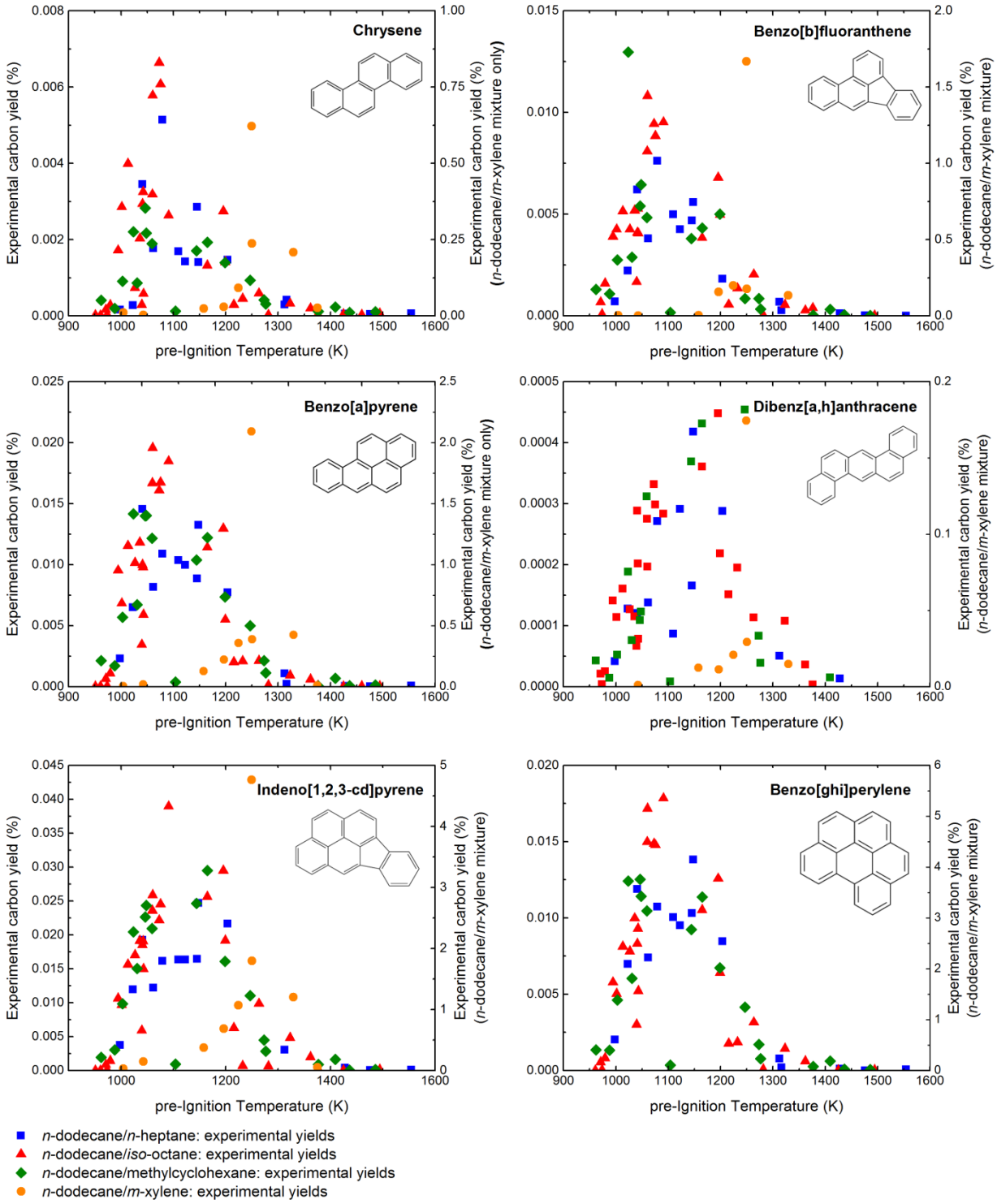

Figure 6-22. Non-volatile emissions comparisons among the binary fuel blends.

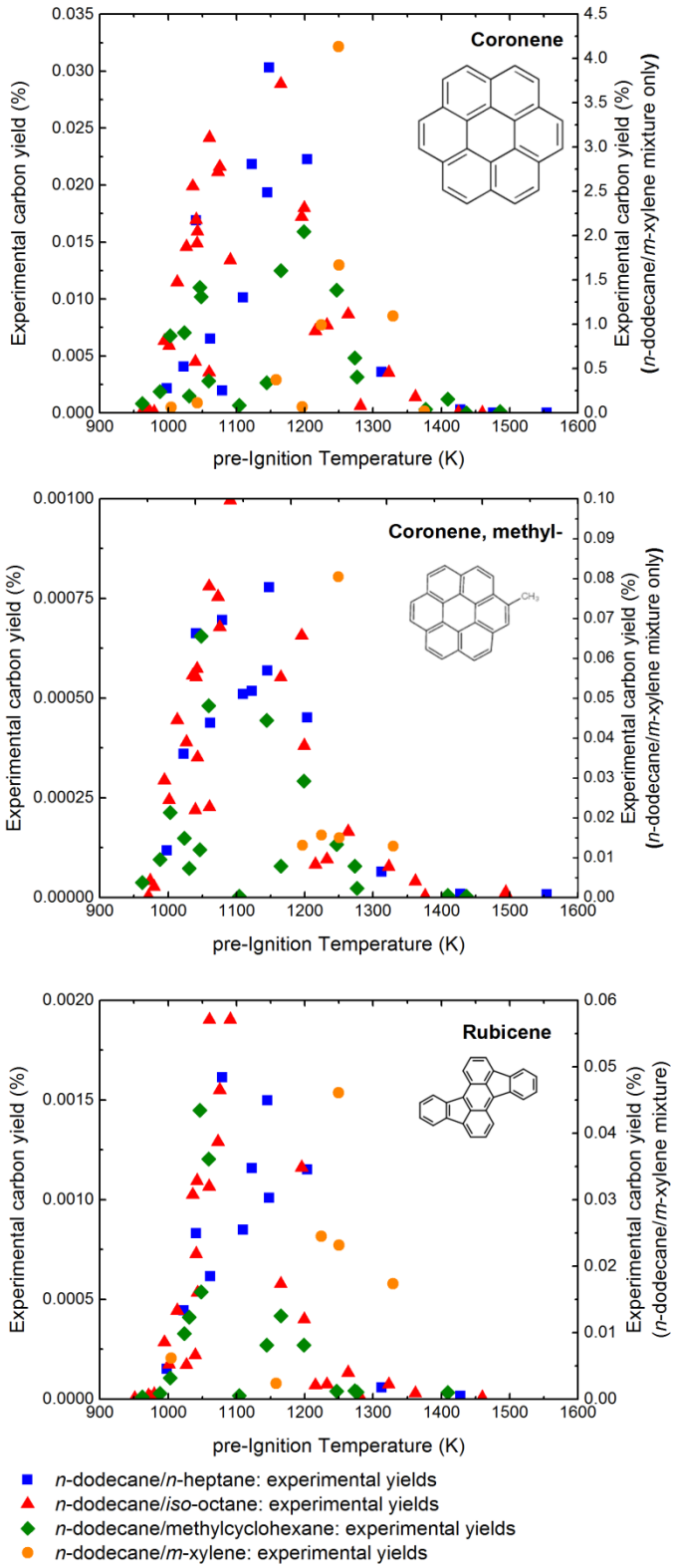

Figure 6-23. Non-volatile emissions comparisons among the binary fuel blends.

Soot yields measured for the fuel mixtures are shown in Figure 6-24. A modified Gaussian expression was used to fit the experimental values; curve fit parameters for each fit are reported in Table 6-2. A typical bell-shaped trend was obtained for all the binary fuel mixtures, and is the result of competition between kinetic and thermodynamic factors. At low temperatures the pyrolysis pathways are rate controlling. As the temperature increases, growth reaction rates increase, leading to the maxima observed. As the temperature further increases, both the decreasing stability of soot pre-cursor and increasing rates of the oxidation reactions limit the formation of soot. This is also reflected in the fractions of volatile and elemental carbon collected on the soot filters (see Figure 6-24): elemental and volatile carbon increases and decreases, respectively, as the pre-ignition temperature increases up to 1400 K; the trend is reversed at higher temperatures.

The paraffinic binary fuel mixtures have similar soot yields, with peak values of 11.5–13.5% at 1246–1263 K. The *iso*-octane mixture shows slightly lower yields than the other paraffinic mixtures, particularly in the peak region of 1150–1350 K. The *m*-xylene blend produced significantly lower soot yields than the paraffinic mixtures below 1250 K but similar yields at higher temperature. This result was unexpected since it is known that the presence of aromatics in the parent fuel leads to an increased amount of soot formation.

A similar investigation was carried out by Darius *et al.* (2009) who used shock tube experiments combined with laser diagnostic techniques to study soot formation from the oxidation of *n*-decane and a kerosene surrogate (80% *n*-decane and 20% *n*-propylbenzene), at an equivalence ratio of 5, pressures above 11 bar and pre-ignition temperatures between 1450 K and 2360 K. It was observed that the addition of *n*-propylbenzene had a weak effect on soot formation (*i.e.*, similar yields for *n*-decane and *n*-decane/*n*-propylbenzene). Kahandawala *et al.* (2009) also reported soot yields from fuel-rich combustion ($\Phi = 3$) of 2-methylheptane and an *n*-heptane/toluene mixture (80/20%). That study showed the addition of toluene produces slightly higher soot yields at temperatures below 1150 K.

Figure 6-25 displays the volatile and elemental carbon collected on the soot filters. Elemental carbon shows similar soot yield trends, while the volatile carbon yields peak at ~1070 K for the paraffinic blends and at ~1250 K for the *n*-dodecane/*m*-xylene mixture. The *m*-xylene blend has lower yields of volatile carbon compared to the paraffinic fuels. This could be due to slower formation of soot-precursor species in the *n*-dodecane/*m*-xylene blend causing a lower emission of soot below 1250 K. Additionally, a careful examination of the experimental procedures for shock tube and product sampling operations did not reveal any possible source of artifacts in the observed soot emissions. Moreover, same experimental procedures were used for all the fuel blends. Further investigation is needed in the low temperature region in order to better understand the cause of lower emission yields measured for the *n*-dodecane/*m*-xylene blend.

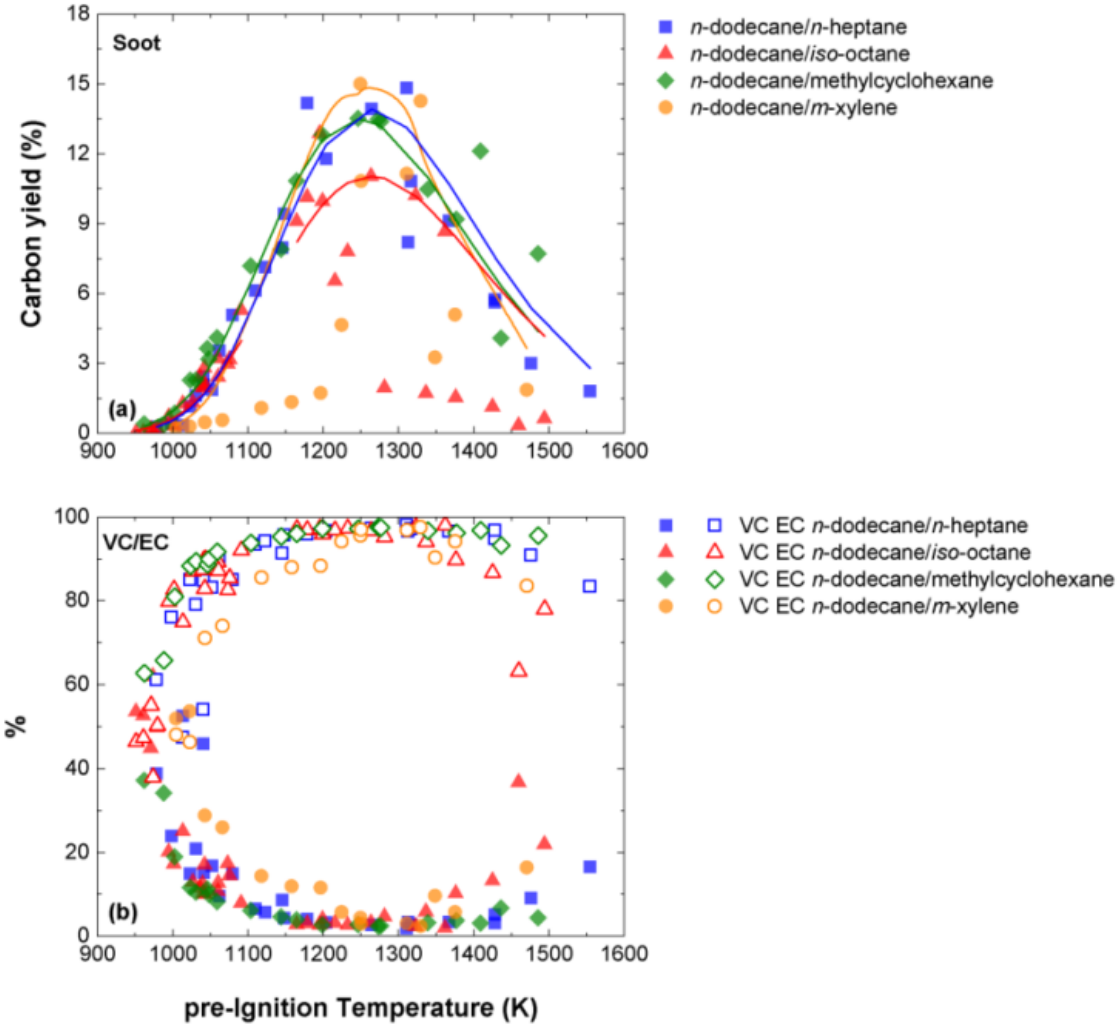

Figure 6-24. Soot yields (a) and mass percentages (b) measured for volatile and elemental carbon collected on the soot filters.

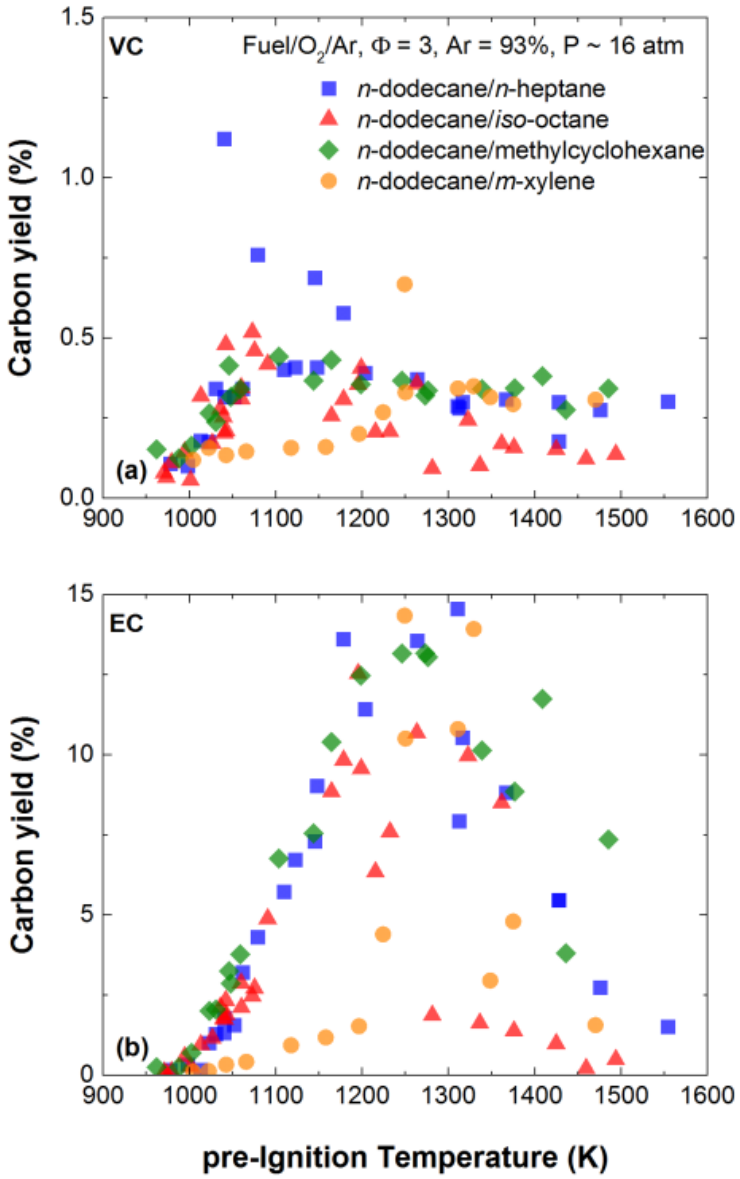

Figure 6-25. Volatile (a) and elemental (b) carbon collected on the soot filters expressed in terms of carbon yields as function of the pre-ignition temperature.

Table 6-2. Modified Gaussian expressions used to interpolate soot yields measurements vs. pre-ignition temperature.

Fuel	Temperature range (K)	T_{opt} (K)	Y_{max} (%)	A
Fuel/O_2/Ar, Φ=3, Ar = 93%, P ~ 16 atm $Y = Y_{max}\, e^{A\left(\frac{T_{opt}-T}{T}\right)^2}$				
n-dodecane/*n*-heptane	978–1554	1264.0	13.9	-46.12
n-dodecane/*iso*-octane	970–1494	1263.5	11.0	-40.74
n-dodecane/methylcyclohexane	962–1485	1246.6	13.5	-43.58
n-dodecane/*m*-xylene	1004–1470	1246.5	15.0	-62.50

Figure 6-26 combines measurements of soot and its precursors for the n-heptane/n-dodecane fuel; acetylene, benzene and soot yields are reported on the left axis, while naphthalene is scaled accordingly on the right axis. The figure is used to show whether a potential growth pathway for soot formation can be inferred. Specifically, acetylene, naphthalene and soot show very similar trends and peak temperatures over the temperature range. However, the peak temperature of benzene is about 200 K colder. This might suggest that the formation of benzene occurs in the early stages of formation reactions and is followed by the growth to higher PAHs, eventually leading to the formation of soot. Moreover, it is evident that acetylene acts as a building block for the growth pathways. Figure 6-27 and Figure 6-28 report carbon yields of benzene, naphthalene and soot as function of acetylene yields. The former considers only yields below the soot maxima (1263 K) while the latter reports measurements at higher temperatures. It is observed on the left side of the soot-bell curve that naphthalene and soot yields exponentially increase with increasing acetylene yields, but there is no clear trend for benzene yields. This suggests that acetylene might not be directly involved in the formation of benzene, as proposed by Frenklach *et al.* (1985) and Bittner and Howard (1981). However, acetylene might directly contribute to further growth of PAHs and soot formation through addition reactions, as suggested by the HACA mechanism (Frenklach et al., 1991). At temperature above the soot peak (1263 K), benzene, naphthalene and soot appear to exponentially decrease with the decreasing of acetylene. This particular observation might reflect the earlier conclusion: a lower pool of assisting growth species (*e.g.*, acetylene) leads to a lower formation of PAHs and soot. Oxidation reactions of larger PAHs and soot can also play a significant role at these temperatures, and the results displayed in Figure 6-28 might be a combination of the two processes. These conclusions can be extended to all fuel mixtures tested in this work since they all have similar trends for those species.

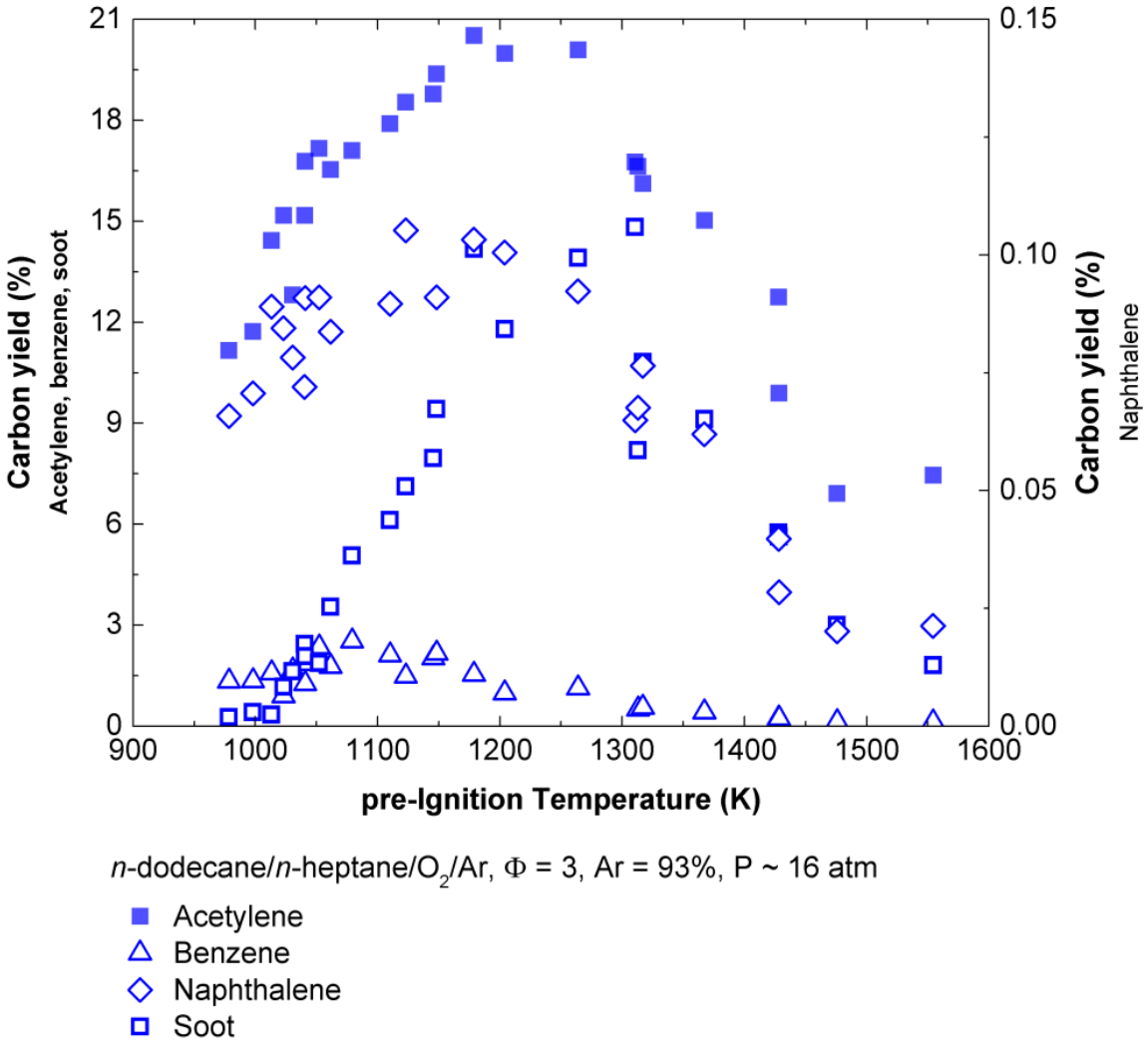

Figure 6-26. Measured particulate matter pre-cursors including acetylene, benzene, naphthalene and soot for *n*-dodecane/*n*-heptane mixture.

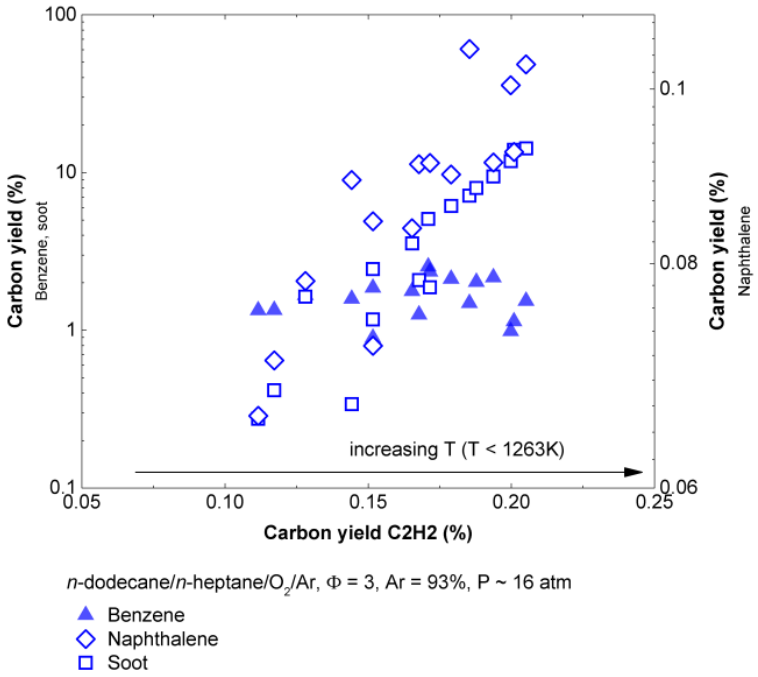

Figure 6-27. Carbon yields of benzene, naphthalene and soot as functions of acetylene yields for the base binary fuel blends over the temperature range of 978–1263 K.

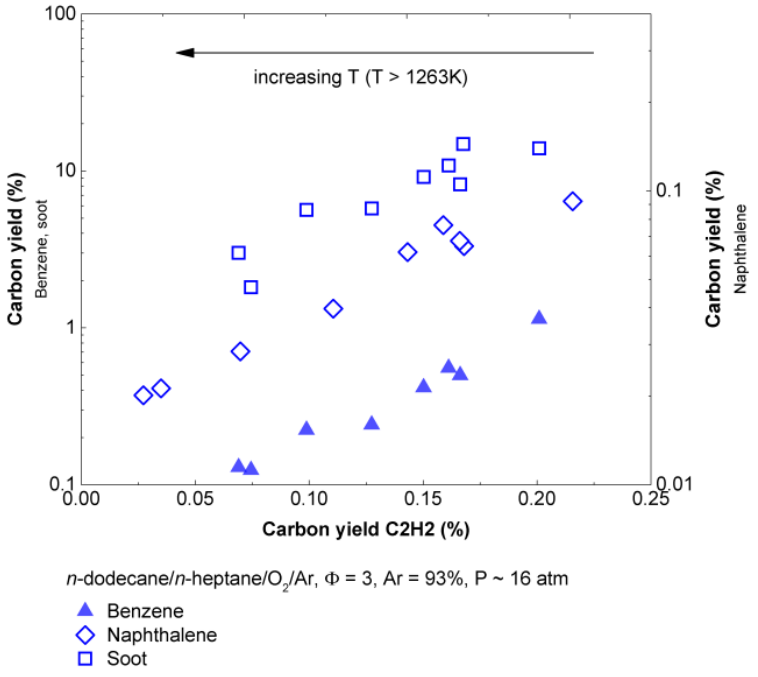

Figure 6-28. Carbon yields of benzene, naphthalene and soot as functions of acetylene yields for the base binary fuel blends over the temperature range of 1263–1554 K.

The major observation that can be inferred from these experimental and kinetic modeling results is that the paraffinic binary fuel mixtures shared similar concentrations of intermediates for the tested experimental conditions. This similarity can be attributed to the common presence of *n*-dodecane in

relatively large quantities being able to control the formation of intermediates. The recent MURI program introduced the concept of distinct chemical functionalities (*n*-alkyl, *iso*-alkenyls and benzyl-type) (Dooley et al., 2012), where the combustion of surrogate mixtures reproduce the combustion of target real fuel well if the surrogate formed similar chemical functionalities observed or predicted for the real fuel. For this study, the fuel-rich oxidation of *iso*-octane or methylcyclohexane coupled with *n*-dodecane produced similar chemical functionalities (as defined by Dooley *et al.* (2012)), leading to similar intermediates. However, the presence of an aromatic leads to differences at low temperatures: lower emission yields are observed for the *m*-xylene blend compared to the paraffinic binary fuel mixtures. For certain species this experimental observation was also supported by the kinetic mechanism predictions. However, aromatic species formed from the *m*-xylene mixture were always overestimated by the model calculation, leading to poor agreement with experimental observations. Experimentally, non-volatile species measured for the *m*-xylene blend were several order of magnitude larger than similar emission observed for the paraffinic species.

6.2.2 Chemical Kinetic Analysis

In a similar manner to what was carried out for the kinetic mechanism analysis in the pre-ignition region, global rate of production calculations were performed for selected species to better understand the main chemical pathways responsible for their production/destruction. The global rate of production analysis was computed at pre-ignition temperatures of ~1000 K, ~1250 K and ~1470 K to represent the low, mid, and high temperature chemistry, respectively. Based on the performance of all three computational approaches, the CHBR with constant P, H assumption was used for these calculations. Results are displayed from Figure 6-29–Figure 6-35 for the top 15 reactions responsible for the production/consumption of the selected species. The computed rate of production coefficients are expressed in terms of carbon yields with respect to the initial mass fraction of carbon in the system (*i.e.*, the amount of carbon converted into a particular species by a reaction).

Figure 6-29 reports the rate of production coefficients for carbon monoxide. The major reaction pathways forming CO for all fuel mixtures include the H-abstraction of formyl radical (HCO) by atomic hydrogen, molecular oxygen and water, formyl radical decomposition and H-abstraction from ketene (CH_2CO). As the pre-ignition temperature increases, the HCO decomposition and H-abstraction of ketene dominate the production of CO. Consumption of CO is mostly attributed to oxidation with OH to produce carbon dioxide. As previously stated, all fuel mixtures had very similar production and consumption coefficients for carbon monoxide over the entire temperature range, reflecting experimental observations.

Rate of production analysis for carbon dioxide is shown in Figure 6-30. Similar coefficients resulted from similar reactions. Oxidation of carbon monoxide by hydroxyl radical, hydroperoxyl radical and molecular oxygen are the major common pathways producing CO_2. As pre-ignition temperature increases, oxidation of carbene (CH_2) with molecular oxygen becomes more important. The *m*-xylene blend shows an additional pathway forming CO_2 (especially at the low temperatures), which is the reaction of $C_6H_4CH_3 + O_2 => C_5H_4CH_2 + CO_2 + H$. This global reaction might be responsible for higher emission of CO_2 at the lower temperature, as observed experimentally.

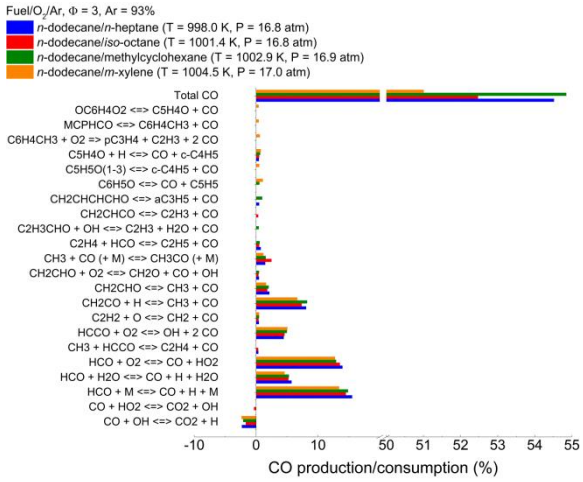

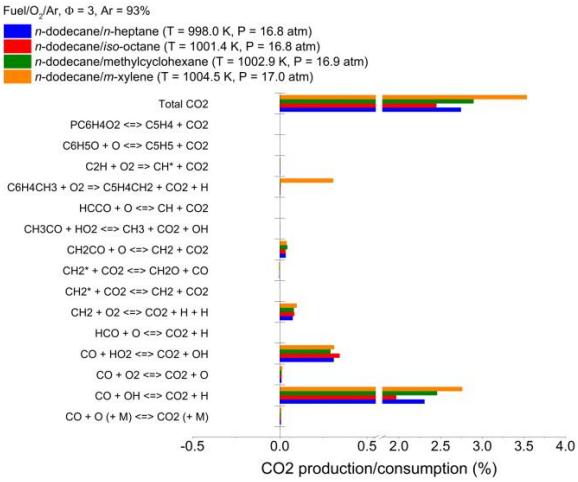

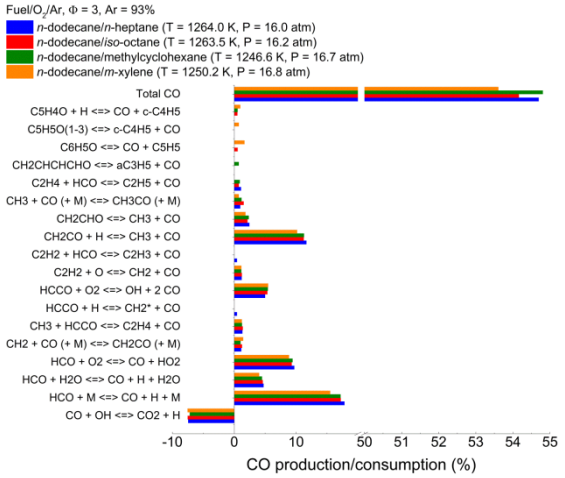

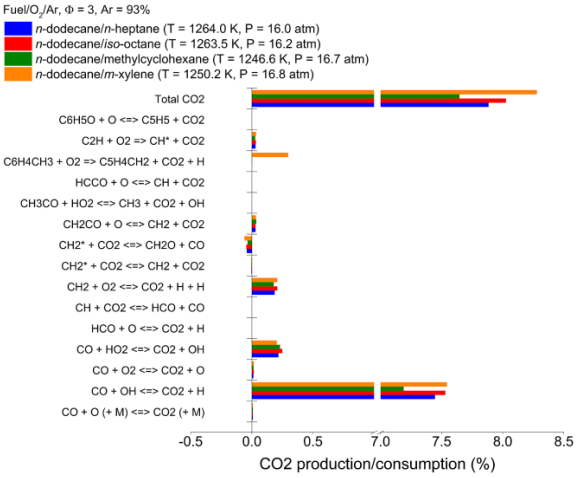

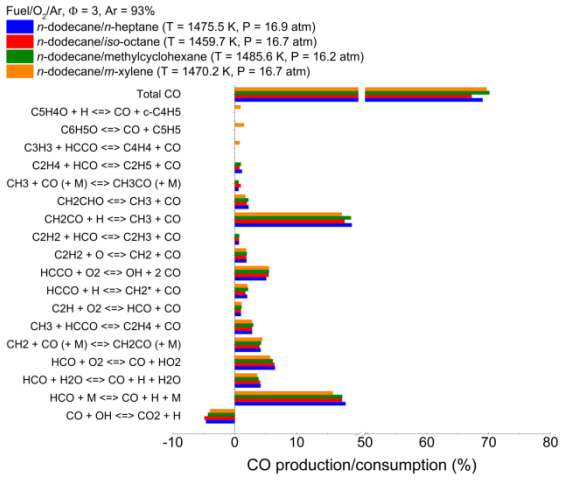

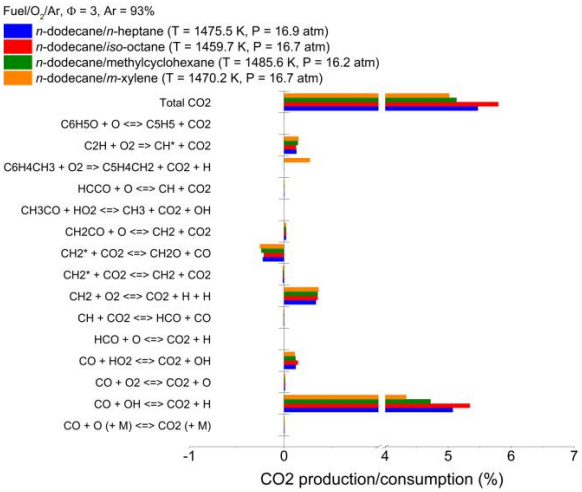

Figure 6-29. Global rate of production analysis for carbon monoxide (CO).

Figure 6-30. Global rate of production analysis for carbon dioxide (CO_2).

Rate of production analysis for methane is shown in Figure 6-31. The main production channels at low temperatures include the reactions of methyl radical with formaldehyde producing formyl radical and

methane, and the H-abstraction of ethylene by methyl radical forming vinyl radical and methane. Other formation channels include addition reaction of methyl radical with hydroperoxy radical and atomic hydrogen. Also, the decomposition of *m*-xylene through H-abstraction by CH_3 forms significant quantities of methane. At a pre-ignition temperature of 1250 K, the reaction of $CH_3CHO + CH_3 <=> CH_3CO + CH_4$ significantly contributes to methane production. At higher temperatures the addition of atomic hydrogen to methyl radical is the dominant pathway forming methane, followed by the H-abstraction of ethylene by methyl radical and the reaction between formaldehyde and methyl radical. These pathways are common to all tested binary fuel mixtures. Methane is mostly consumed through H-abstraction by O, OH, and H. The H-abstraction by H and OH become the preferred consumption channels with increasing temperature for all fuel mixtures.

According to the SERDP model, ethane is almost entirely formed through methyl radical recombination for all fuel mixtures, as shown in Figure 6-32. Larger quantities of carbon are converted into ethane for *n*-dodecane/*iso*-octane. Ethane is consumed through H-abstraction by O, OH, and H, with atomic hydrogen being dominant at higher temperatures. Although the measured ethane yields appeared quite small compared to the other light hydrocarbons, Figure 6-32 shows that it is an important intermediate since a large amount of the initial carbon are involved in ethane oxidation chemistry.

Acetylene is a key intermediate under fuel-rich combustion since it is considered a soot precursor. Acetylene was the most abundant hydrocarbon measured during the fuel-rich combustion of all binary fuel mixtures. Figure 6-33 reports the rate of production coefficients calculated for acetylene. At all temperatures, the major producing pathway is the decomposition of the vinyl radical. At low temperatures other common pathways include the oxidation of the vinyl radical by molecular oxygen, propene radical (CH_3-CH=CH*) and the H-catalyzed decomposition of propyne (pC_3H_4). Common consumption pathways at lower temperature include the oxidation by atomic oxygen. The *n*-dodecane/*iso*-octane blend shows consumption through oxidation by OH, whereas the *n*-dodecane/*m*-xylene mixture presents consumption by reaction with m-xylyl. These two pathways might explain lower acetylene yields measured and calculated for those mixtures. At higher pre-ignition temperatures acetylene yield is very similar among the fuel mixtures (experimentally and computationally). As a result, the rate of production analysis shows common pathways, which include the H-catalyzed decomposition of H_2C_4O, and unimolecular decomposition of H_2CC. Acetylene is consumed at higher temperatures through reactions with CH_3, C_2H, O, OH and H. The SERDP mechanism shows that the HACA-type reaction related to PAH growth does not represent significant consumption pathways for acetylene since the results from the rate of production analysis do not include these reactions.

Ethylene rate of production analysis results are presented in Figure 6-34. The major production channel at all temperatures is through decomposition of ethyl radical for all fuel mixtures. Other common production pathways include the decomposition of C_3-C_4 hydrocarbons such as nC_3H_7, pC_4H_9, C_4H_8 and C_3H_6. The two latter species are very significant at lower temperatures. Ethylene is mostly consumed through H-abstraction to form vinyl radical. For the *n*-dodecane/*m*-xylene blend, ethylene is also consumed through the reaction with *m*-xylene, especially at lower temperatures. This reaction might be responsible for lower emission yields measured at lower temperatures for the *m*-xylene blend: since ethylene is an important precursor for acetylene (through formation of the vinyl radical), lower formation of soot precursors might be expected.

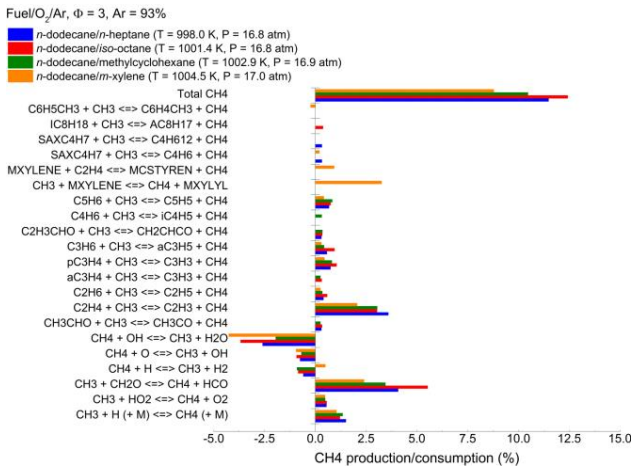

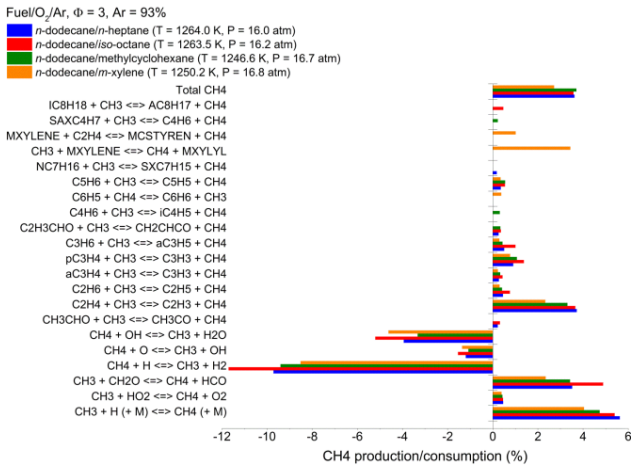

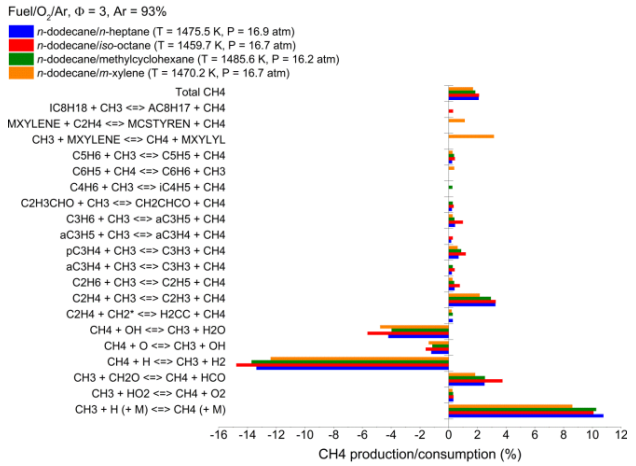

Figure 6-31. Global rate of production analysis for methane (CH_4).

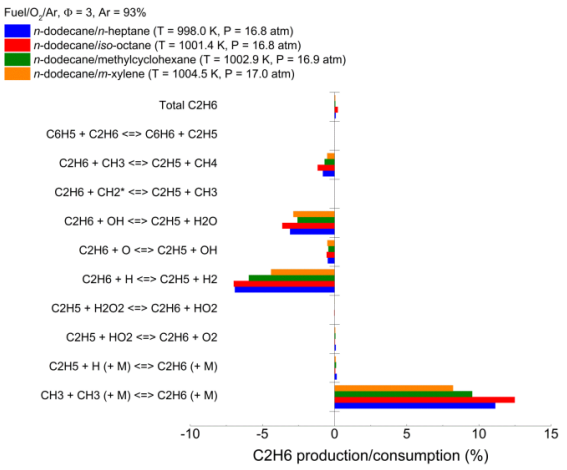

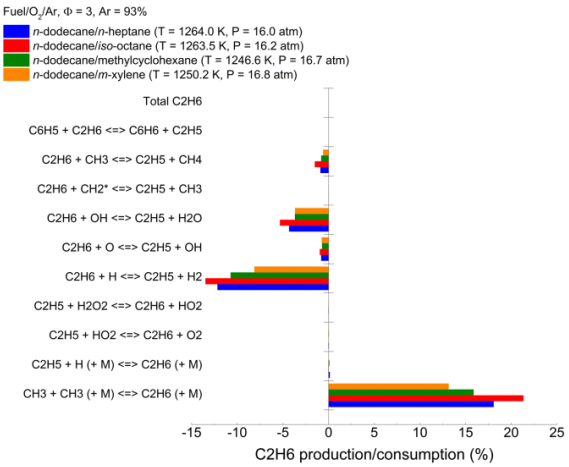

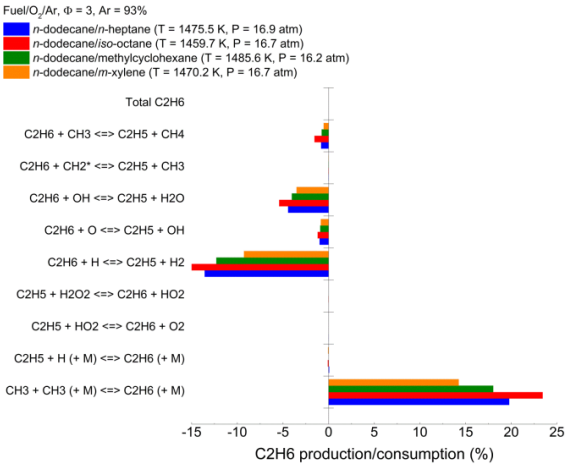

Figure 6-32. Global rate of production analysis for ethane (C_2H_6).

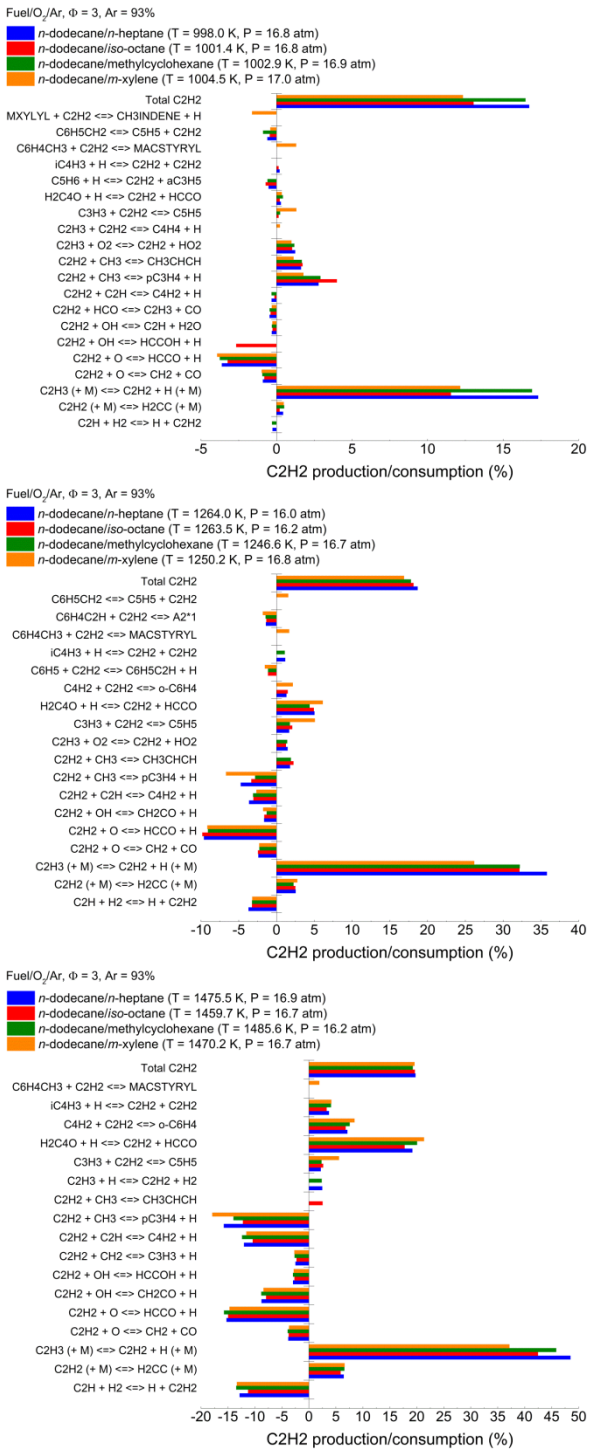

Figure 6-33. Global rate of production analysis for acetylene (C_2H_2).

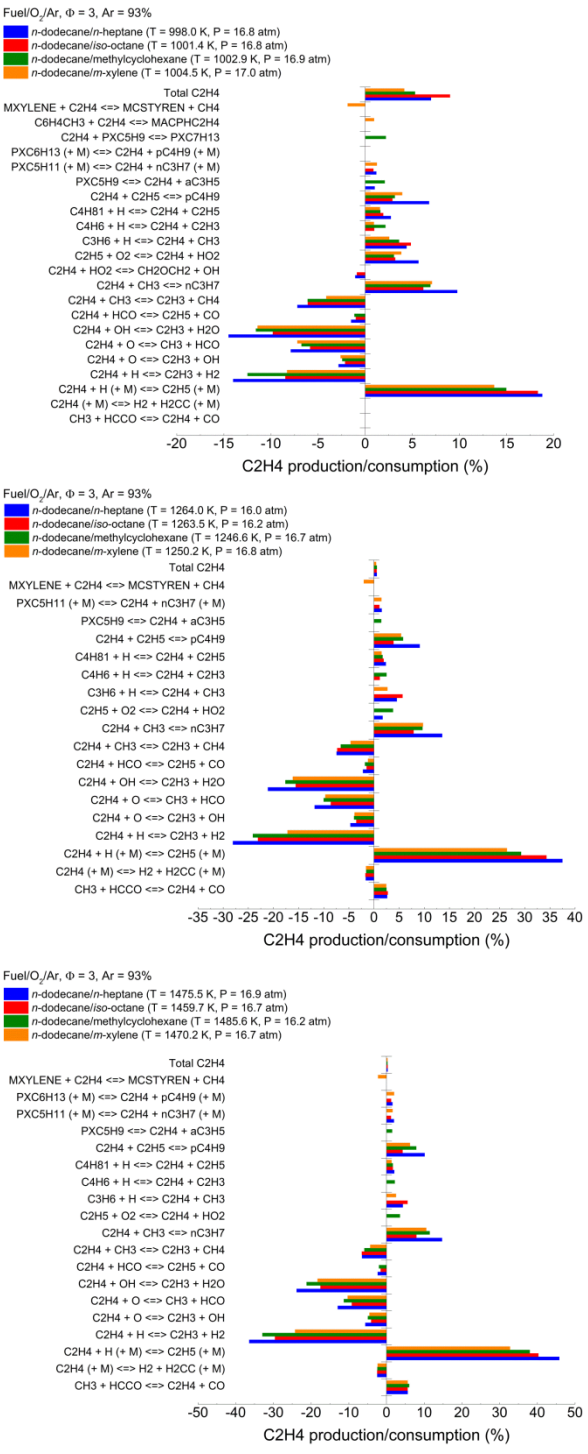

Figure 6-34. Global rate of production analysis for ethylene (C_2H_4).

Formation of the fist aromatic ring is an important step towards soot production. In the SERDP mechanism benzene formation mostly occurs by propargyl radical recombination for all the fuel mixtures, especially at pre-ignition temperatures above the soot peak (~1250 K). At lower temperatures the

decomposition of $C_6H_6CH_3$ into methyl radical and benzene appear to be the most significant production channel for benzene, especially for the *n*-dodecane/*m*-xylene blend. Among the consumption channels, the addition of methyl radical to benzene producing $C_6H_6CH_3$ appears to have similar impact of its reverse reaction mentioned earlier. The H-catalyzed dissociation of benzene into phenyl radical and methyl radical is also a critical consumption pathway for benzene. This latter is the initiation step for further aromatic growth, as described in the HACA mechanism.

Rate of production analysis for toluene is displayed in Figure 6-36. It is shown that the presence of *m*-xylene leads to several reaction pathways forming toluene, with similar impact on its production. Also, among the fuel mixtures the *n*-dodecane/*m*-xylene blend reported the highest rate of production coefficient. At the low temperature, toluene is produced by addition of atomic hydrogen to benzyl radical ($C_6H_5CH_2$), the decomposition of $C_6H_6CH_3$, and the reaction between benzyl radical and formaldehyde to form toluene and methyl radical. Decomposition of *m*-xylene by reaction with atomic hydrogen also produces toluene. Consumption pathways at the low temperatures include H-catalyzed decompositions into benzyl radical and molecular hydrogen, and into benzene and methyl radical. At higher pre-ignition temperatures, production channels include the decomposition of $C_6H_6CH_3$ and the addition of methyl radical to benzyl radical. The reaction $C_6H_5CH_3$ (toluene) + H <=> C_6H_5 + CH_3 produces toluene for the paraffinic mixtures but consumes it for the *n*-dodecane/*m*-xylene blend. The reason behind this behavior might be that at high temperatures (T > 1250 K) the kinetic mechanism predicted lower benzene yields than the paraffinic mixtures (see Figure 6-18). Lower concentration of benzene might shift the equilibrium of that reaction toward toluene consumption. Other consumption pathways at higher temperatures include H-catalyzed decomposition and unimolecular decomposition above 1470 K.

The only complete chemistry for PAH growth implemented in the SERDP mechanism is for naphthalene. As shown in Figure 6-37, at low temperature naphthalene is merely produced by addition of propargyl radical to benzyl radical. This is actually a three step sub-mechanism where the addition of propargyl radical to benzyl radical forms benzofulvyl radical and a H-atom. The benzofuvyl radical dissociated into benzofulvene, which via H-atom catalyzed isomerization produces naphthalene (Marinov et al., 1998). This pathway appears to be common to all fuel mixtures; however, the *m*-xylene blend has the highest rate of production coefficients. At a pre-ignition temperature of ~1250 K, which corresponds to the experimental peak in soot yield, there are additional significant production channels typical of the HACA mechanism. One is the addition of molecular hydrogen to the allylic radical of naphthalene, A2*1. The latter is produced through an acetylene addition reaction as $C_6H_4C_2H+C_2H_2$=A2*1. The addition of molecular hydrogen to A2*1 resulted in higher rate of production coefficients than the propargyl addition reaction for all fuel mixtures. At higher temperatures, naphthalene is produced by both HACA growth reactions and the addition propargyl radical, with equal rates. For the *n*-dodecane/*m*-xylene blend, the addition of molecular hydrogen to the allylic radical A2*1 follows the reverse pathway consuming naphthalene, whereas the addition of propargyl radical to benzyl radical dominates the naphthalene production. At all temperatures, the consuming channel for naphthalene that is not part of the HACA framework are negligible compared to the production channels, they mostly include oxidation reactions by hydroxyl radical for all binary fuel mixtures.

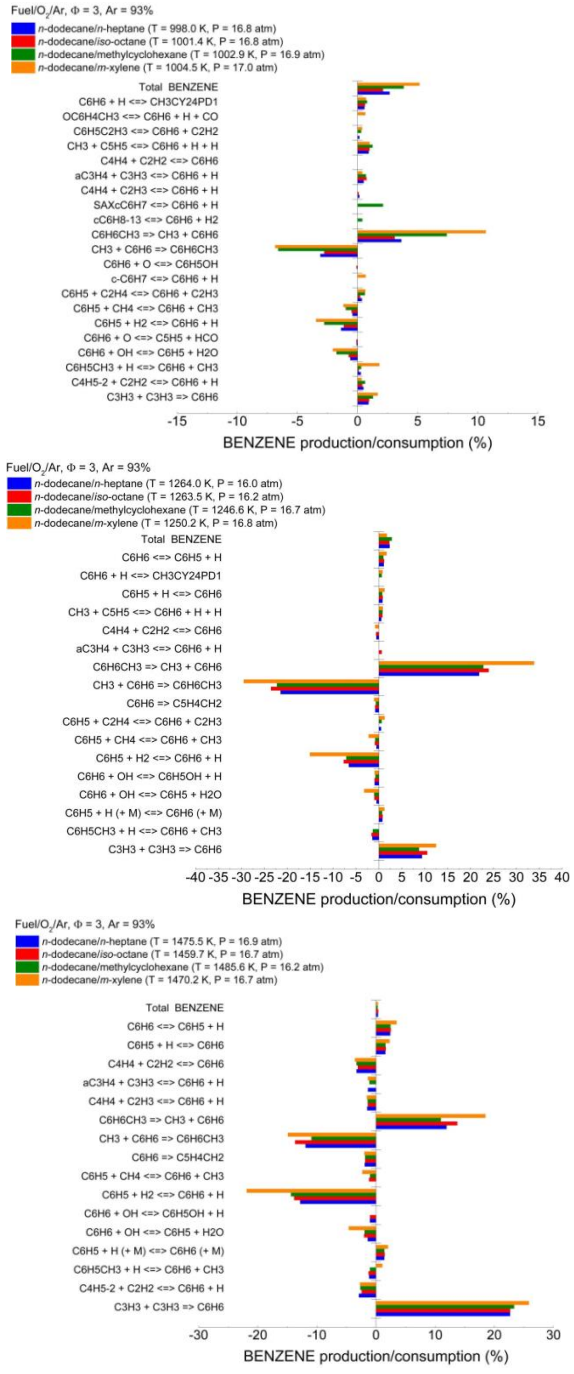

Figure 6-35. Global rate of production analysis for benzene (C_6H_6).

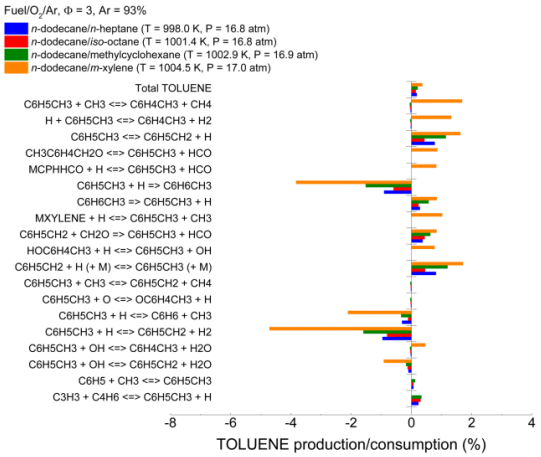

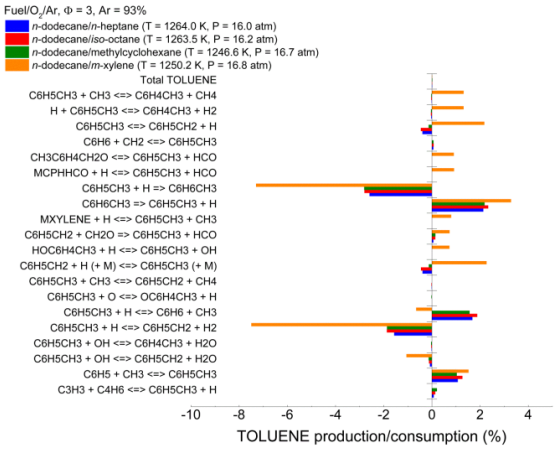

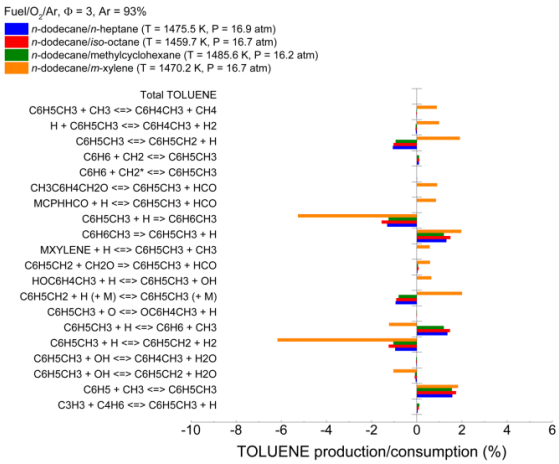

Figure 6-36. Global rate of production analysis for toluene ($C_6H_5CH_3$).

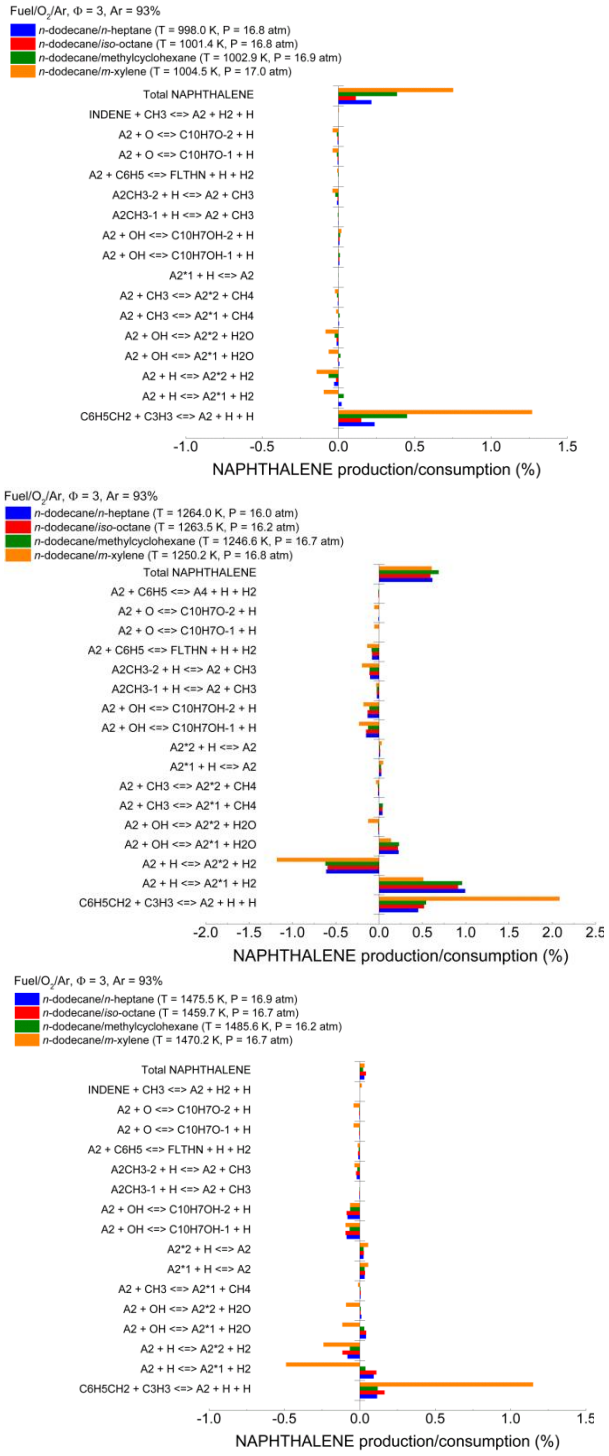

Figure 6-37. Global rate of production analysis for naphthalene ($C_{10}H_8$).

6.2.3 Effect of Dwell (Reaction) Time

In the previous section, emissions from the four fuels measured at a dwell times of ~7.7 ms were discussed; the major observation was that the paraffinic mixtures have very similar emission yields, which was supported by kinetic modeling results. It is important to understand whether observed behavior is affected by changing the dwell (reaction) times, especially for the m-xylene fuel that did not show the expected effect on soot.

To investigate the effect of dwell time, emissions were measured at three different dwell times for a selected temperature condition. The dwell times tested include ~3.3 ms, ~7.7 ms and ~11.7 ms; the pre-ignition temperature was selected in order to have the shortest achievable dwell time (3.3 ms) close to the ignition event.

The experimental pressure profiles recorded for this particular study are displayed in Figure 6-38. Reproducibility of the post-reflected shock zone, ignition and post-ignition region for each experiment are seen at the different dwell times for each fuel. Arrival of the quenching wave was observed by the linear decrease in pressure.

Table 6-3 lists the experimental condition and ignition delay times measured for each experiment; the scatter (< 0.7%) among the experimental pre-ignition temperatures are well within the uncertainties related to the temperature values (~1.6%). Figure 6-39 displays the ignition delay measurements (symbols) for all the fuel mixture and dwell times (straight lines): the dwell times were always larger than the ignition delay, therefore, emissions were sampled post-ignition.

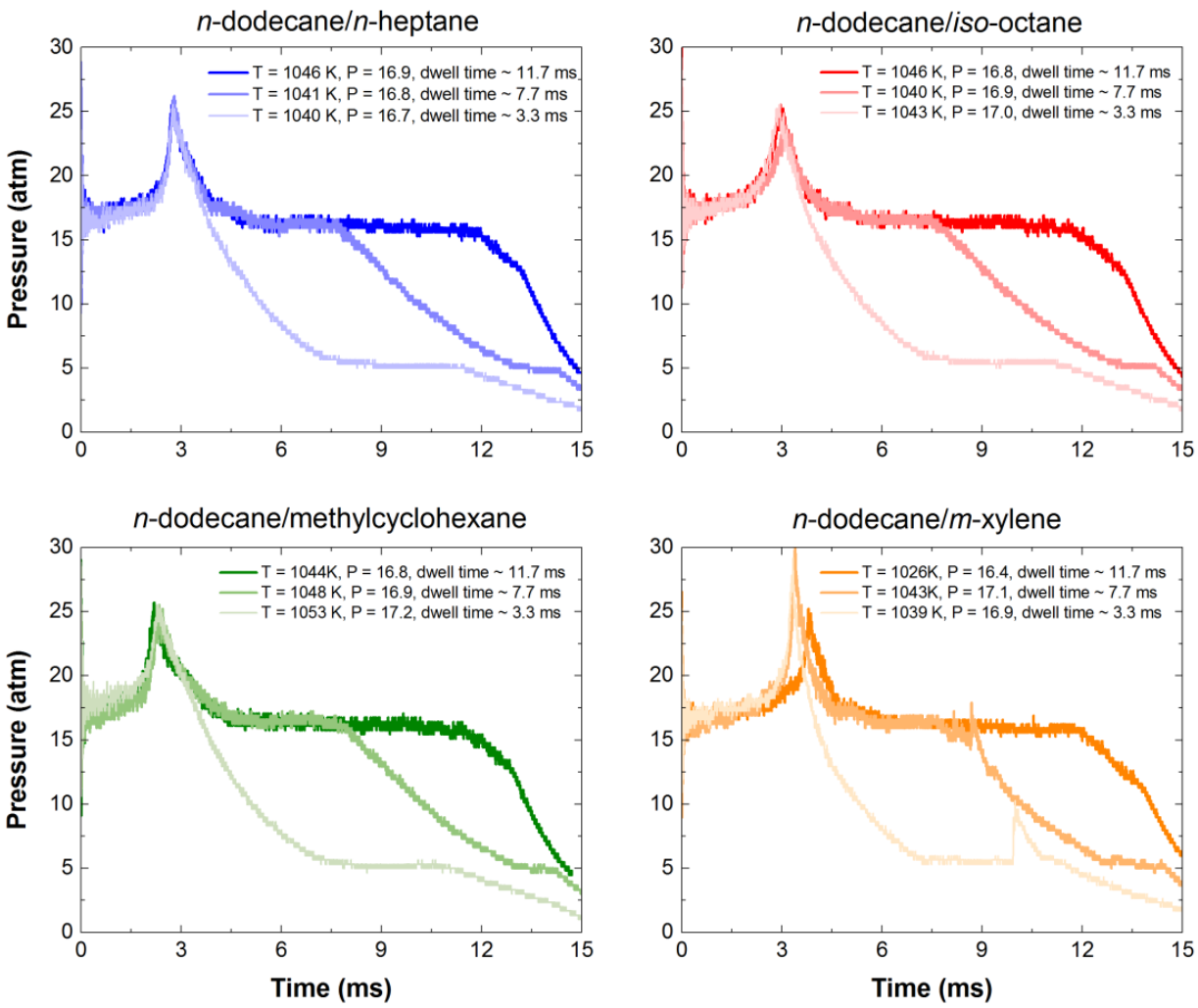

Figure 6-38. Experimental pressure profiles showing the different swell times obtained maintaining similar pre- and post- ignition conditions.

Table 6-3. Experimental condition and ignition delay measurements for the quenching effects studies.

Fuel composition	□dwell (ms)	T_5 (K)	P_5 (atm)	τ_{ign}, OH* (μs)
n-dodecane/*n*-heptane	3.3	1039.5	16.7	2636.9
	7.7	1040.8	16.8	2690.9
	11.7	1046.3	16.9	2667.3
n-dodecane/*iso*-octane	3.3	1042.7	17.0	2428.8
	7.7	1039.6	16.9	2881.8
	11.7	1045.7	16.8	2848.0
n-odecane/methylcyclohexane	3.3	1052.7	17.2	2158.0
	7.7	1048.0	16.9	2181.4
	11.7	1044.3	16.8	1876.5
n-dodecane/*m*-xylene	3.3	1039.0	16.9	3221.3
	7.7	1042.7	17.1	3320.3
	11.7	1025.8	16.4	3730.9

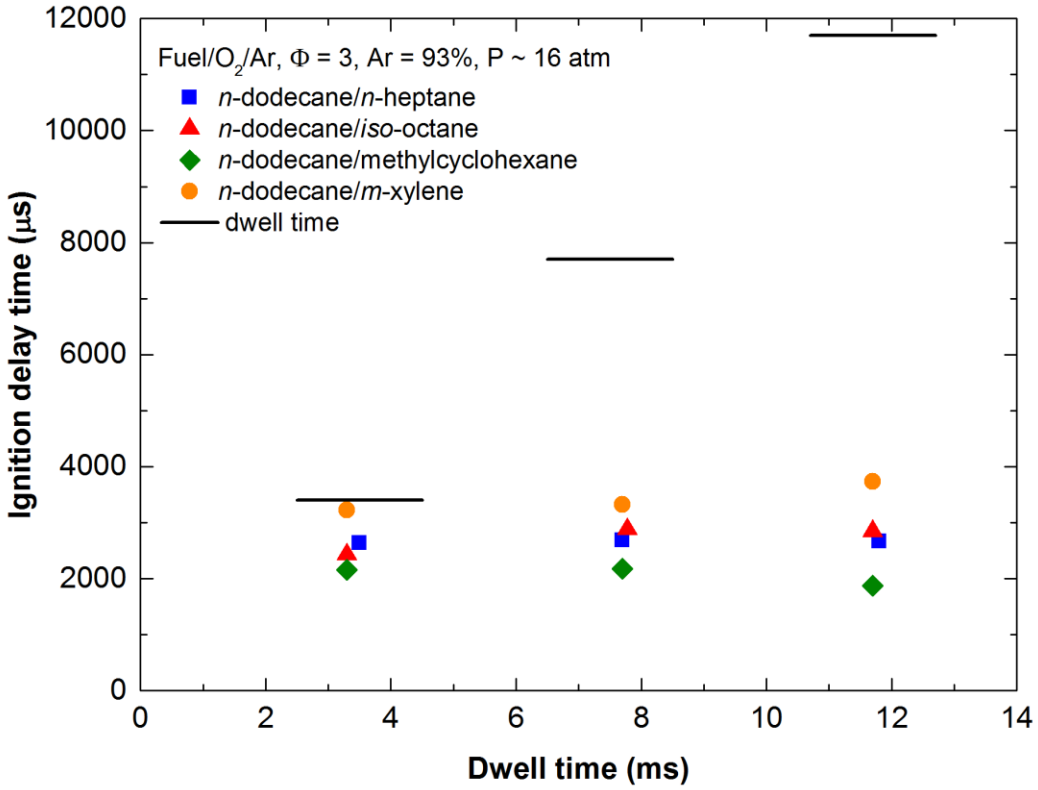

Figure 6-39. Ignition delay times and dwell times for each of the experiments.

Temporal profiles for C_1-C_2 light gases (including CO, CO_2, and C_1-C_2 hydrocarbons) are reported in Figure 6-40. Temporal profiles calculated by SHOCKIN are also displayed as dashed lines; profiles were computed using the experimental pressure signals with the longest dwell times. Carbon monoxide yields (see Figure 6-40) increased with longer reaction time for all fuel mixtures. Slight differences were observed for the *m*-xylene mixture: lower yields are observed at 3.3 and 7.7 ms. Kinetic modeling estimated lower CO yields for *n*-dodecane/*m*-xylene and constant trends of CO yields above ~6 ms. Similar to CO results, carbon dioxide yields increased with longer dwell times for the paraffinic fuels with similar yields. The *n*-dodecane/*m*-xylene blend has higher values than the paraffinic blends, with an initial increase during the first 7.7 ms followed by a decrease at the longer dwell time. Model predictions had similar values of CO_2 yields at reaction times longer than 6 ms, with an increasing trend. Methane time-history yields are shows in Figure 6-40. It appears that methane emission decreases with longer dwell times for the paraffinic mixtures. However, for the *m*-xylene blend, methane yields decreases in the first 7.7 ms followed by an increase at longer reaction times. Modeling predictions do reflect the difference existing among the fuel mixtures, but show constant trends after ~4 ms. Production of acetylene (see Figure 6-40), appears to be prominent at short reaction times, then decreases at longer dwell times. The paraffinic mixtures had similar temporal evolution yields of acetylene; the *n*-dodecane/*m*-xylene blend shows an initial consumption during the first 7.7 ms followed by a production trend during longer reaction times. Modeling prediction for acetylene shows an initial production phase during the 4–7 ms, followed by a slow consumption trend. Similarly to the experimental measurements of acetylene yields, modeling prediction were lower for *n*-dodecane/*m*-xylene mixture over the whole dwell time range. Ethylene and ethane showed similar temporal trends both experimentally and by modeling predictions (see Figure 6-40). In fact, both species appear to be consumed over the course of the reaction time. In addition, all the fuels show similar emission yields. The modeling predictions show differences in the earliest reaction times (up to 6 ms), mostly due to small changes in ignition delay times.

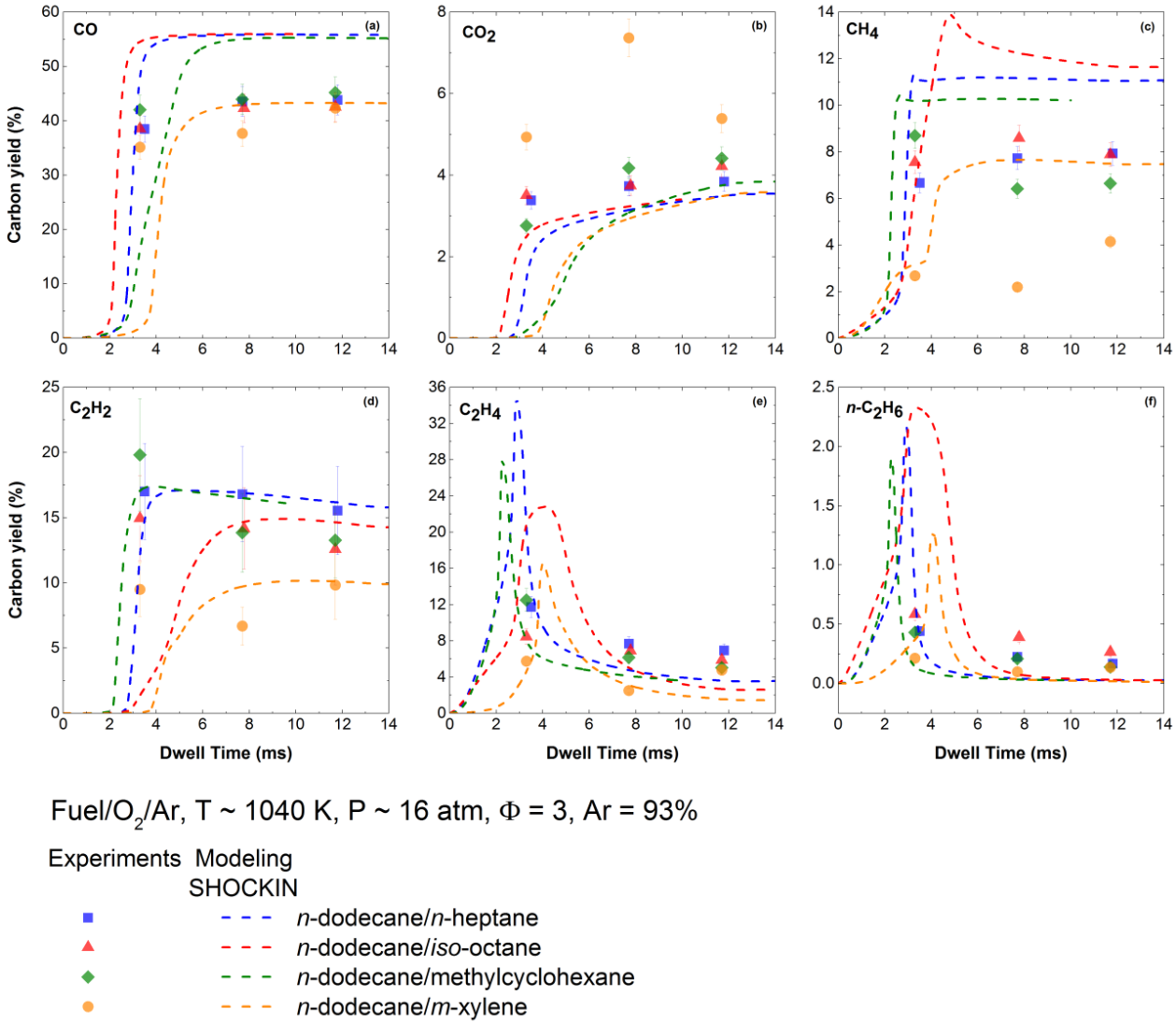

Figure 6-40. Time-dependent emission yields for CO, CO_2 and C_1-C_2 hydrocarbons.

Temporal evolution of aldehydes yields are displayed in Figure 6-41. Only experimental values are reported since the poor agreement with modeling predictions. The n-heptane/n-dodecane fuel has the highest yields of formaldehydes whose values increased at increasing reaction times. A similar trend was reported by the *n*-dodecane/*iso*-octane mixture but with lower yields. The fuels with methylcyclohexane and *m*-xylene show an initial production of formaldehyde in the first ~7.7 ms, followed by a consumption trend during longer reaction times. In the case of acetaldehyde (Figure 6-41), all fuels agree, having similar yields and trends, with values decreasing over the reaction times.

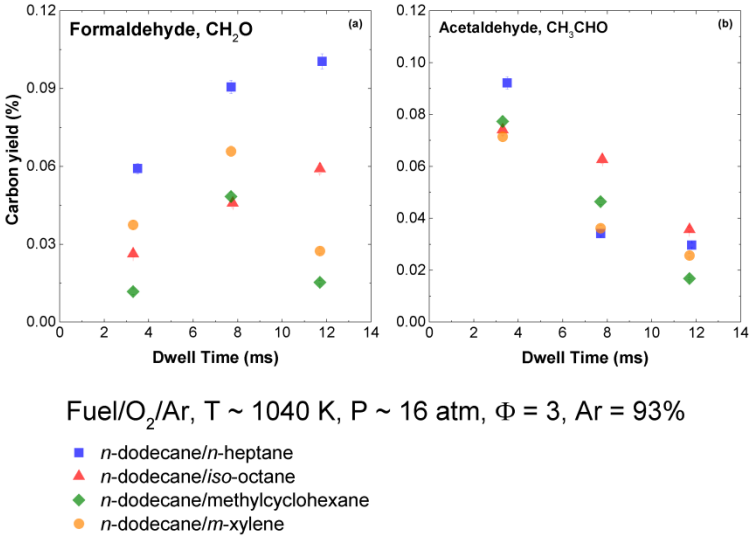

Figure 6-41. Time-dependent emission yields for aldehyde species.

Temporal yield profiles for single rings aromatic species, including benzene and toluene, are shown in Figure 6-42. The mixture with methylcyclohexane had the highest benzene yields at the shortest dwell time, and linearly decreased at longer reaction times. A similar trend was observed with the n-heptane/n-dodecane fuel with lower yields. The *iso*-octane mixture, initially produced benzene until ~8 ms and then consumed it at longer dwell times. Finally, the *m*-xylene mixture showed a linear trend over the entire observed dwell time, reporting the lowest yields at the shortest reaction time. The yield profiles predicted by the kinetic model showed a continuous production of benzene over the entire reaction time, with the methylcyclohexane mixture having the lowest yields, followed by the n-heptane/n-dodecane fuel, *iso*-octane and *m*-xylene.

Toluene yield profiles are displayed in Figure 6-42. The n-heptane/n-dodecane fuel and *iso*-octane blend had similar yields with a quasi-constant trend over the entire reaction time. The *n*-dodecane/methylcyclohexane and *n*-dodecane/*m*-xylene blends had similar trends, with an initial consumption during the first 8 ms followed by a production in the next 4 ms. Among the fuel mixtures, similar yields of toluene were measured at ~7.7ms, whereas the mixture with *m*-xylene had the highest yields at ~3.3 ms, followed by the methylcyclohexane and *iso*-octane blends and the n-heptane blend. At ~11 ms the methylcyclohexane blend had the highest toluene yields, followed by *m*-xylene, *iso*-octane and *n*-heptane mixtures. A different behavior was predicted by the kinetic mechanism, where a continuous increasing trend was reported.

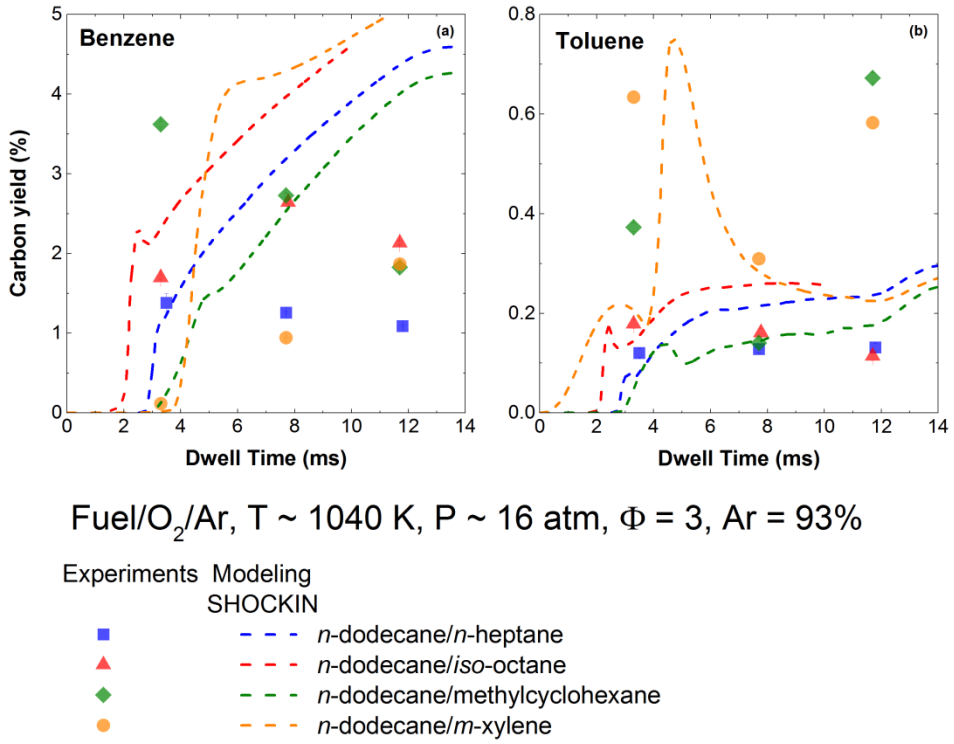

Figure 6-42. Time-dependent emission yields for benzene and toluene.

Temporal profiles of semi-volatile polycyclic organic hydrocarbons are displayed in Figure 6-43. Kinetic model estimates are shown only for naphthalene. Indene appears to be consumed during the post-ignition time for the paraffinic mixtures but the *m*-xylene blend shows production. All the other PAHs had similar temporal evolution. Particularly, the n-heptane/n-dodecane fuel and *iso*-octane mixture show similar yields and similar time-history: initial formation up to ~7.7 ms followed by slow consumption rates. The *m*-xylene and methylcyclohexane mixtures had similar trends but with slightly different yield values: high values at the shortest dwell times, decreasing at longer reaction times.

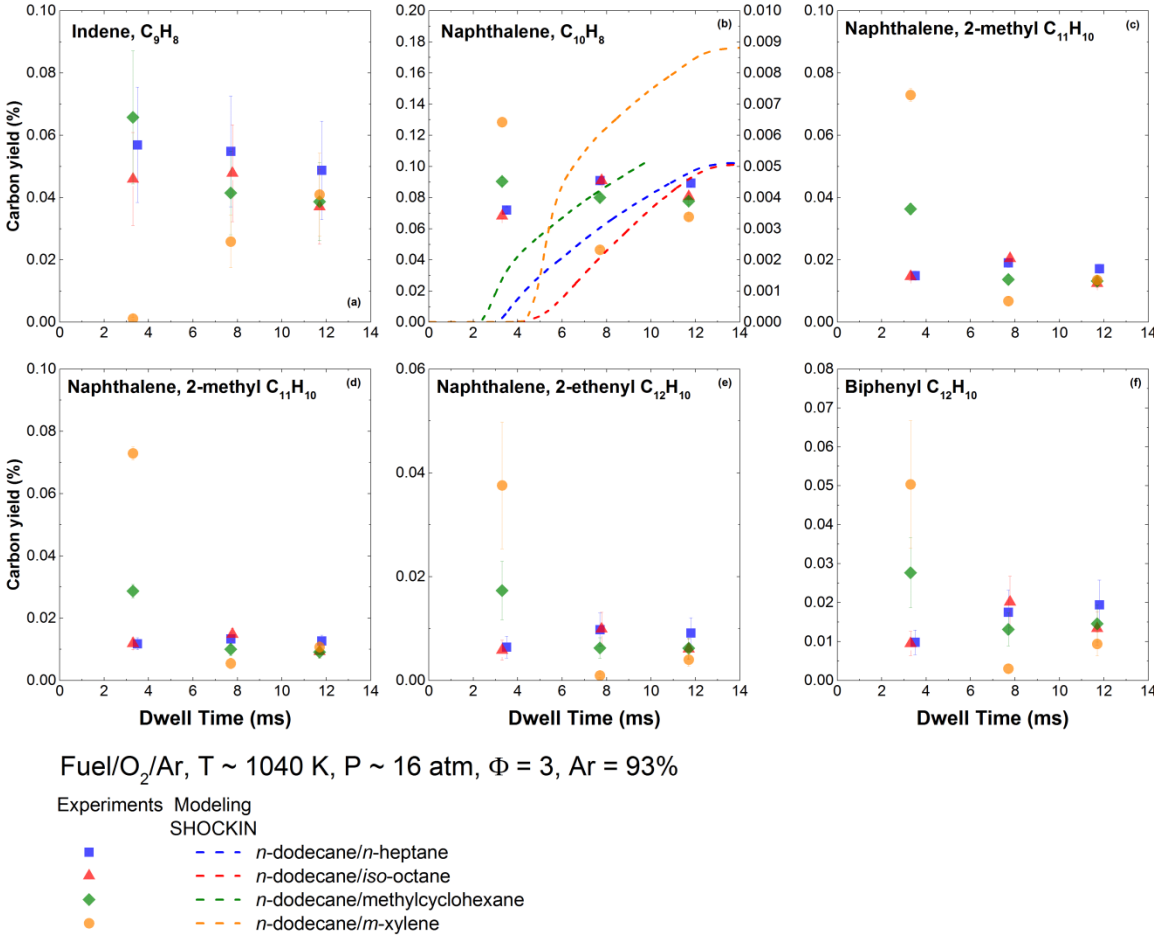

Figure 6-43. Time-dependent emission yields for semi-volatile organic compounds (SVOC).

Figure 6-44 reports the temporal profile of soot yields for all binary fuel mixtures. Soot appears to be produced over the entire reaction time, indicating a continuous growth under those pre-ignition temperatures conditions. However, for the *m*-xylene blend, it appears that soot is not produced during the initial 7.7 ms; at longer reaction times soot is formed with carbon yields similar to those reported by the paraffinic blends. This is reflected in another panel of Figure 6-44, where volatile and organic carbon fractions collected on the soot filter are displayed: the volatile carbon decreases in favor to an increase of the elemental carbon. For the *m*-xylene blend there is a slow consumption/formation of volatile/elemental carbon during the first 7.7 ms, followed by a rapid formation of elemental carbon (thus, a rapid consumption of volatile carbon) at longer reaction times. This is consistent with the temporal profiles for polycyclic aromatic hydrocarbons discussed earlier.

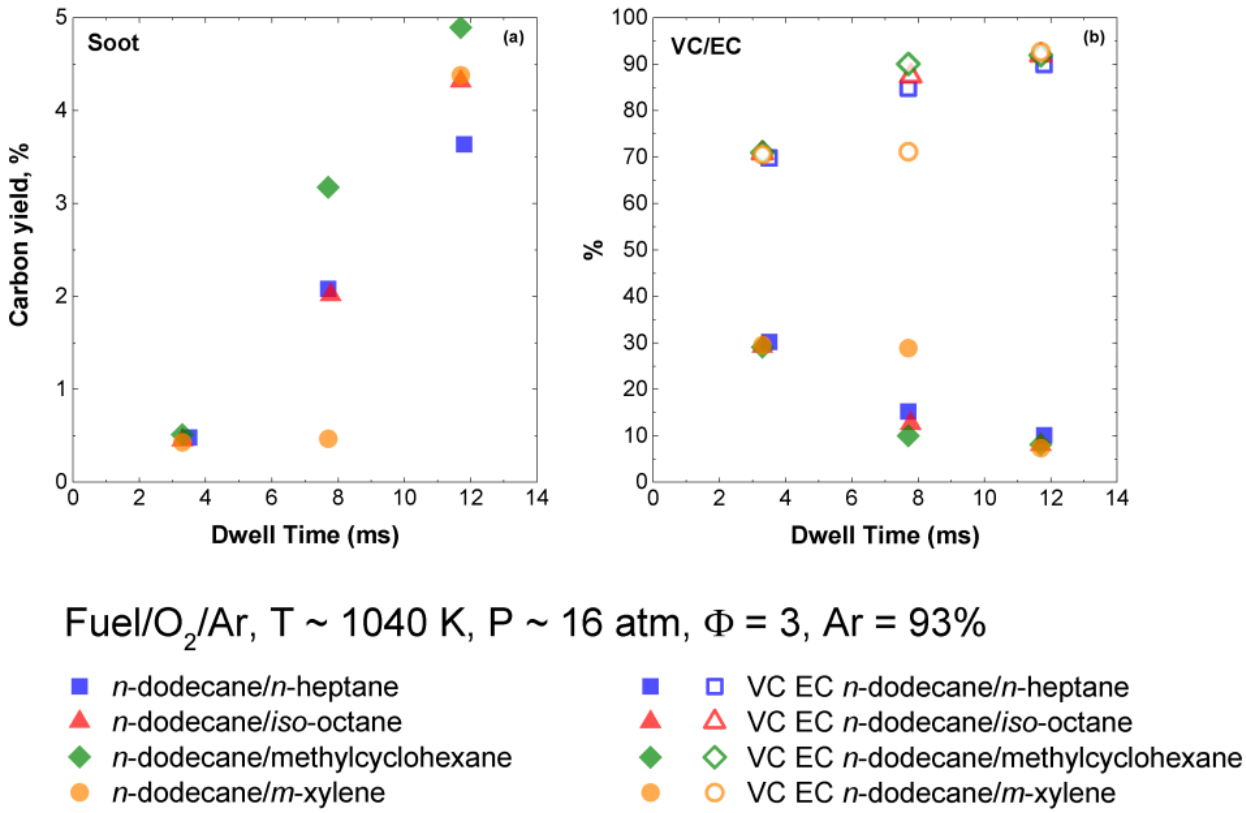

Figure 6-44. Time-dependent emission yields for the particulate matter (PM).

7 WELL-STIRRED REACTOR STUDIES

Experiments were conducted in the WSR under fuel-rich and fuel-lean conditions. The studies under fuel-rich conditions were part of the original design of this program and were done to simulate fuel-rich regions in a combustor. The fuels studied under fuel-rich conditions included the m-xylene/dodecane, MCH/dodecane, and heptane/dodecane fuel mixtures as well as JP-8 (POSF 6169), Sasol (*i.e.*, Fischer-Tropsch fuel POSF 7629). JP-8 and Sasol represent a conventional and alternative fuel, respectively. These fuels were included to allow for comparisons to the results from the T-63 engine.

The plan for the fuel-lean experiments was created part-way through the program. These experiments were designed to test new insights into processes that lead to UHC formation in GTE that developed during the program (See Section 5.3). During the fuel-lean experiments, the fuel-air mixture is changed in such a way that the reaction stops, leading to a "lean blowout" (LBO). This lean blowout has simulates thermo-physical and chemical conditions that occur during the quenching processes that produce UHC emissions under low power conditions in GTEs. Simulation of LBO experiments is presented in Section 7.3.

7.1 Fuel-rich Studies

7.1.1 m-xylene/n-dodecane, JP-8 and Sasol Fuels

Emission indices of methane, formaldehyde, acetylene with respect to ethylene for JP-8 (top), Sasol (middle), and m-xylene/dodecane (bottom) fuels are reported in Figure 7-1. Production of acetylene (relative to ethylene) is greater than the production of methane. Methane production is greater than formaldehyde, irrespective of fuel. Little difference is observed between the data as the residence time is varied. This trend results from differences in the chemical kinetic pathways for these fuels. The slope of the correlation between ethylene and other unburned hydrocarbons is the greatest for EI_{C2H4} <10. This range corresponds to an equivalence ratio, which is less than 1.7. The decrease in the slope for EI_{C2H4} >10, which corresponds to equivalence ratios greater than 1.7, is attributed to the production of other (larger) unburned hydrocarbons being favored. A linear correlation between unburned hydrocarbons is not observed over the entire range of equivalence ratios tested. It is noteworthy that the range of fuel-to-air ratios (i.e., equivalence ratio) over which emissions were reported when a linear trend was observed was relatively narrow for the T-63 study (see section 11.2).

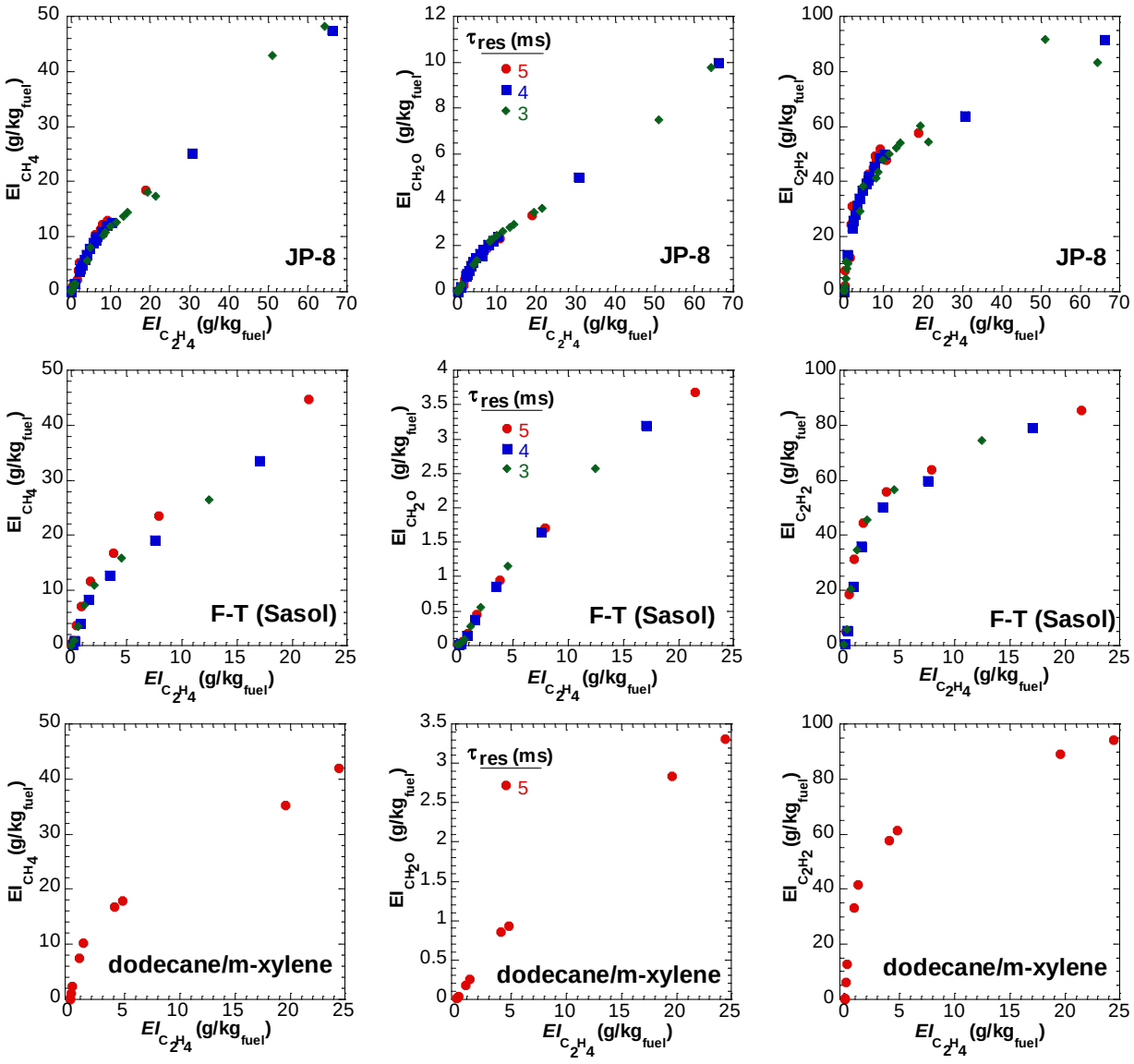

Figure 7-1. Emission indicies of methane, formaldehyde, acetylene with respect to ethylene for JP-8 (top), Sasol (middle), and dodecane/m-xylene (bottom) fuels.

Figure 7-2 reports emission indices of acetylene and methane with respect to formaldehyde (left and middle panels) and methane (right panel) for ethylene/air reactions. Emission indices were correlated with respect to unburned hydrocarbons other than ethylene to avoid complexities of interpreting measurements of a fuel and a product. The slopes of correlations between emission indices tends to be the greatest for lower equivalence ratios and decreases for larger equivalence ratios, similar to the trends observed for liquid fuels. Sensitivity to residence time is observed when emission indices of unburned hydrocarbons are plotted with respect to emission indices of formaldehyde. No such sensitivity is observed for the correlation between methane and acetylene. These observations indicate that the time-scale of formaldehyde production and consumption is sensitive to the residence time within the reactor for ethylene/air reactions.

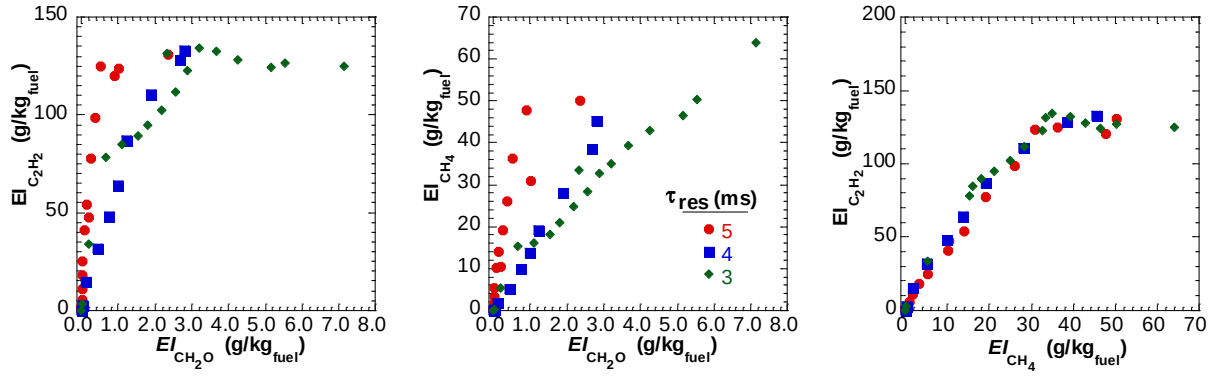

Figure 7-2. Emission indicies of actylene and methane with respect to formaldehyde (left and middle) and methane (right) for ethylene/air reactions.

No such sensitivity was observed for the liquid fuels, as shown in Figure 7-2. A linear correlation between unburned hydrocarbons is not observed over the entire range of equivalence ratios tested, similar to the results for the liquid fuels. It is arguable that a linear type trend is observed between emission indices of methane and acetylene for $EI_{CH4} < 30$.

Emission indices of ethylene (1st column), acetylene (2nd column), formaldehyde (3st column), and methane (4th column) for varying equivalence ratios are reported in Figure 7-3. Results for JP-8, Sasol, and dodecane/m-xylene fuels are shown in the top, middle, and bottom panels. Little variation is observed between the emissions as the residence time is changed. Changes in emission indices are modest for $1.3 \leq \Phi \leq 1.4$ and increase linearly (on the log scale) for $1.4 \leq \Phi \leq 1.7$. The slope of the relation between emission indices of the unburned hydrocarbons and equivalence ratio reduces for $\Phi \geq 1.7$. The slope variation about $\Phi = 1.7$ is attributed to a change in the reaction pathways to the production of larger unburned hydrocarbons. A similar plot of emission indices with respect to equivalence ratio for ethylene/air reactions is show in Figure 7-4. Similar trends are observed as those for liquid fuels, except for the sensitivity to residence time for emission indices of ethylene and formaldehyde.

Figure 7-5 shows the emission indices reported in Figure 7-1 rescaled so that peak ethylene values were less than 5 g/kg_{fuel}. This scaling is similar to that used for the linearity study of the T-63. The objective was to explore whether a linear correlation is observed over a limited range, similar to those for an engine. Values corresponding to $\Phi < 1.35$ were not included in the plot, but this does not change the observations. A linear trend is observed between ethylene, and methane and formaldehyde for JP-8 and dodecane/m-xylene. A similar trend is not apparent for acetylene emissions. Further investigation is required to assess the chemical processes responsible for the linear trend in the well-stirred reactor and to determine any similarities to the processes responsible for the trends observed in emissions from engines.

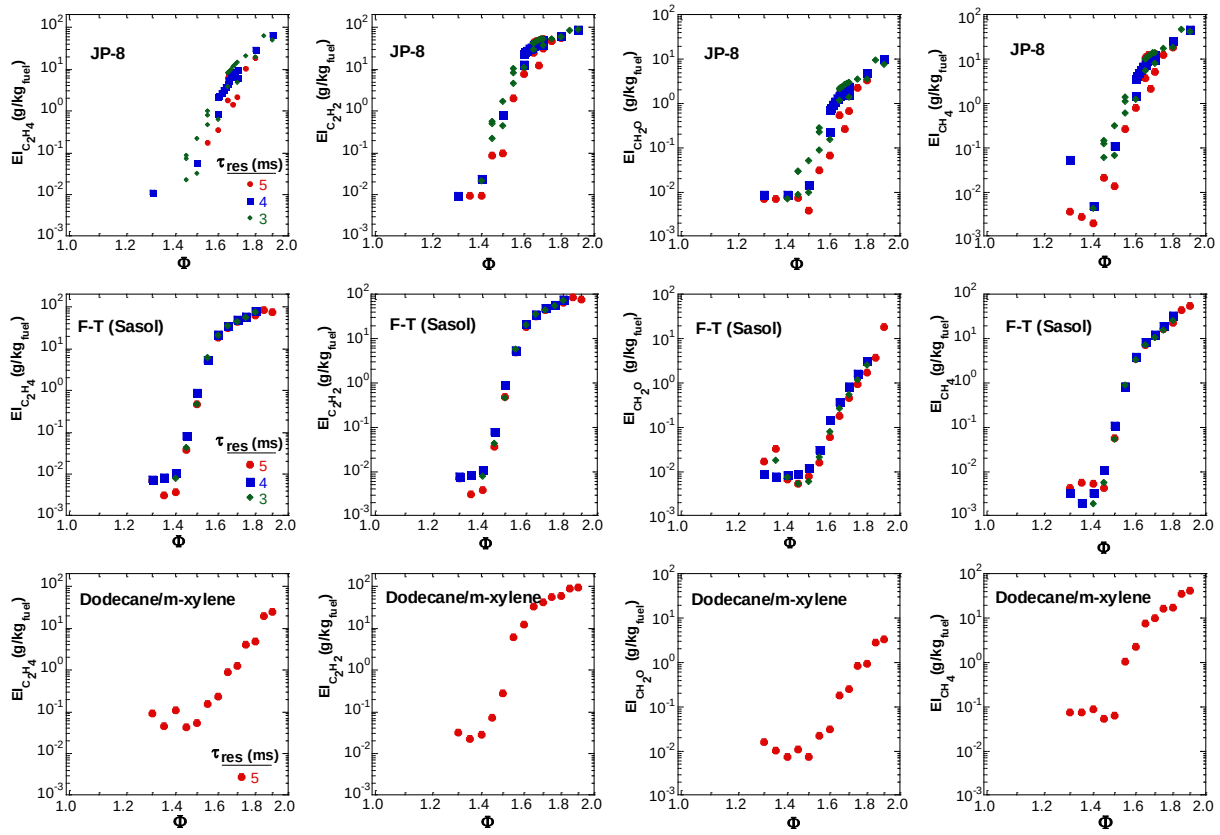

Figure 7-3. Emission indicies of ethylene (1st column), acetylene (2nd column), formaldehyde (3st column), and methane (4th column) for varying equivalence ratios for JP-8 (top), Sasol (middle), and dodecane/m-xylene (bottom) fuels.

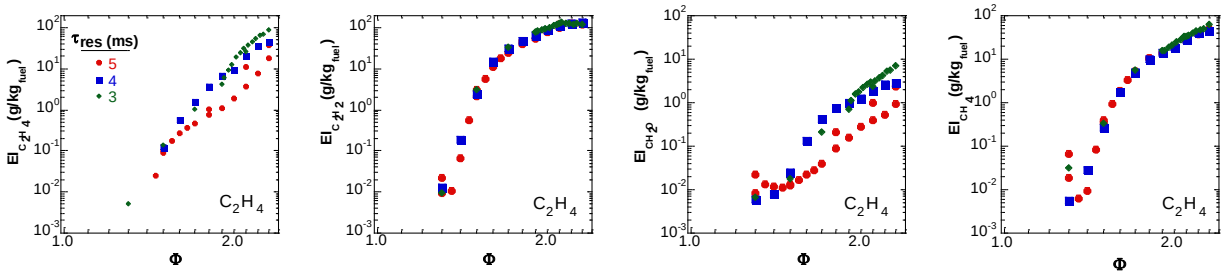

Figure 7-4. Emission indicies of ethylene (1st column), acetylene (2nd column), formaldehyde (3st column), and methane (4th column) for varying equivalence ratios for ethylene air reactions.

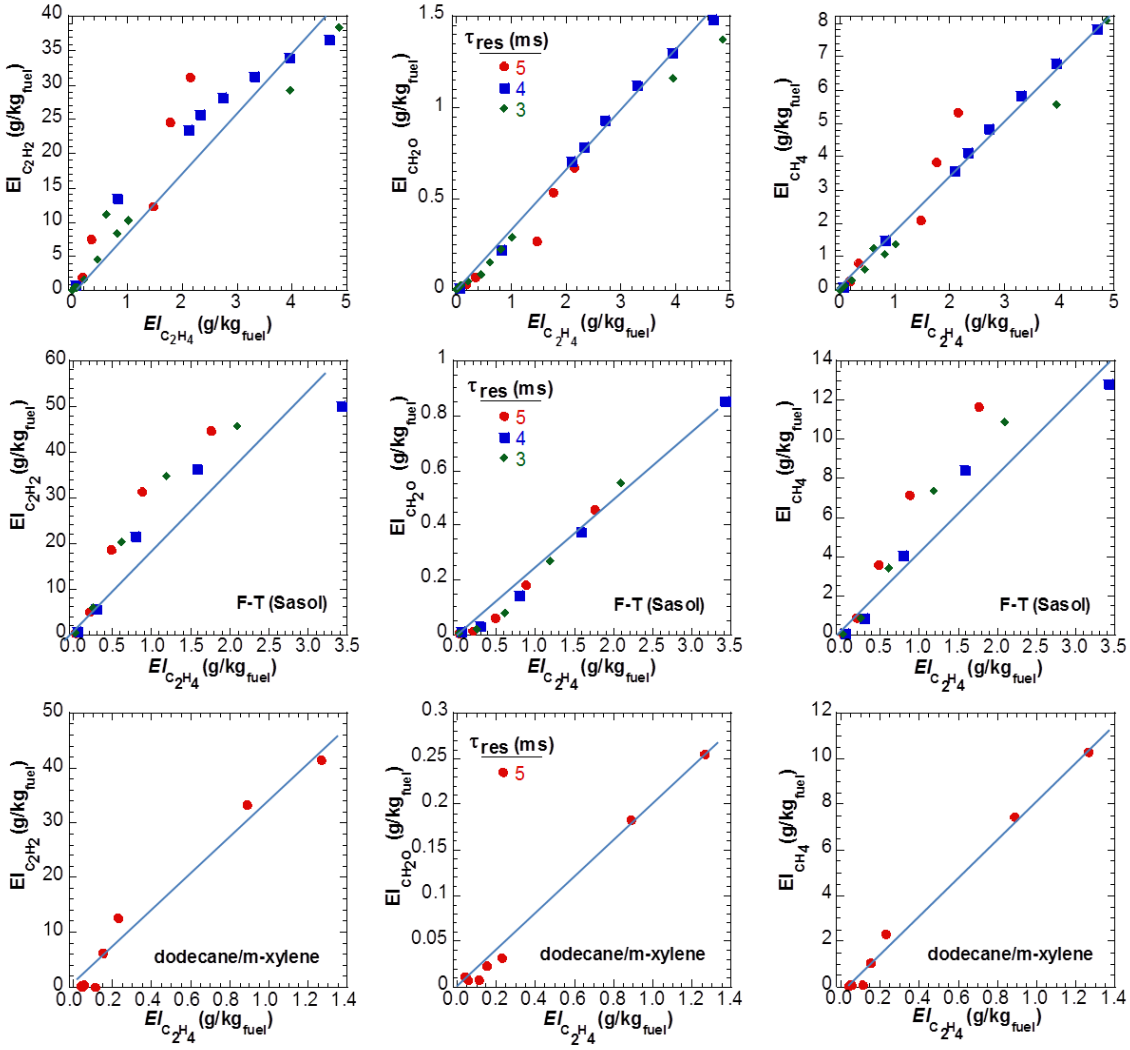

Figure 7-5. Emission indices of methane, formaldehyde, acetylene with respect to ethylene for JP-8 (top), Sasol (middle), and dodecane/m-xylene (bottom) fuels. The scale of the plots are reduced relative to Figure 2.

7.1.2 Heptane/Dodecane Experiments

Emissions data was acquired for n-heptane/n-dodecane over a range of equivalence ratios from 1.4 to 1.92 at a residence time of approximately 5 ms. Figure 7-6 shows the emissions indices (g/kg_{fuel}) of methane, ethylene, acetylene, and formaldehyde plotted vs equivalence ratio in the fuel-rich region. The trends are all similar to those shown in Figure 7-3 for m-xylene/n-dodecane. Overall the EI of the four compounds increases as equivalence ratio increases. The slope of the EI vs. phi curve is shown to be linear for all four of the compounds between 1.4< phi < 1.7. At higher equivalence ratios the slope of the EI curve is shown to decrease at higher equivalence ratios for the acetylene, and ethylene, while the curve remains linear for the lower concentration formaldehyde and methane.

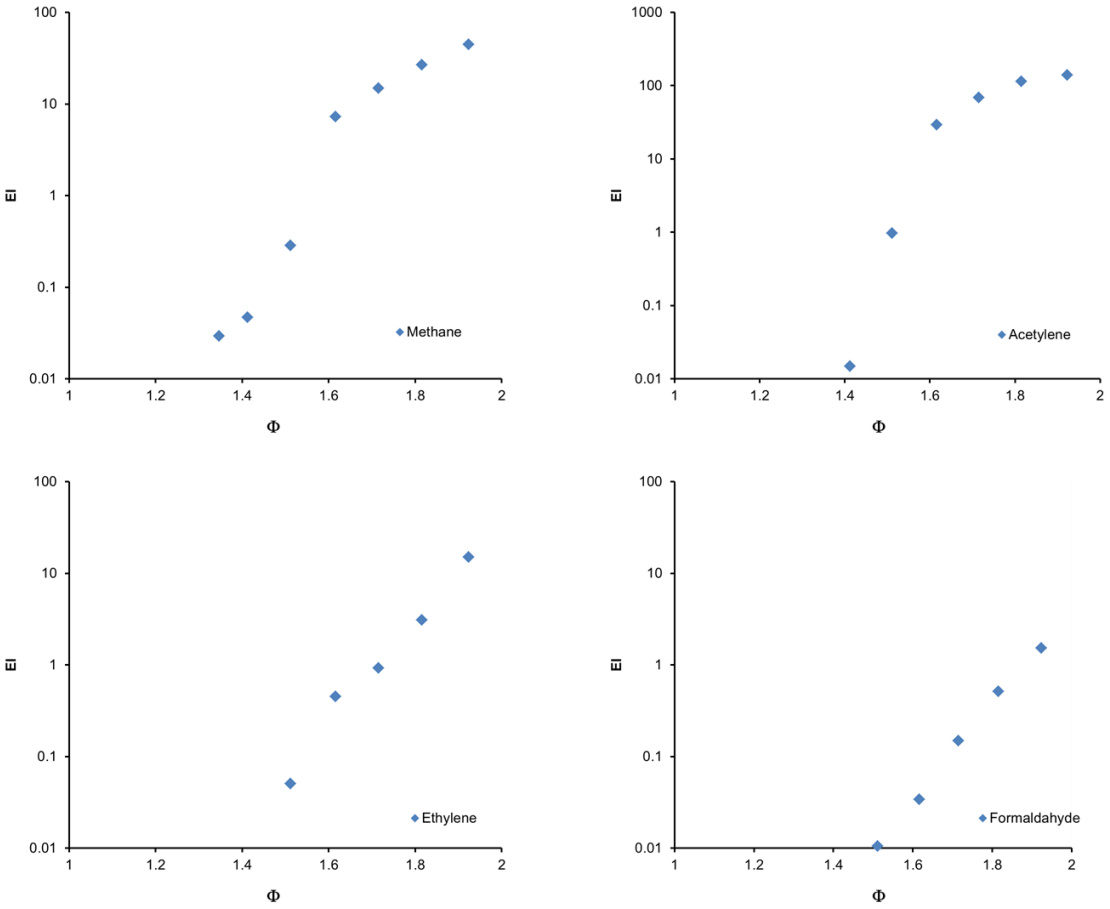

Figure 7-6. Emission Indices of Methane, Acetylene, Ethylene and Formaldehyde for the n-Heptane/n-Dodecane Surrogate.

The formaldehyde, methane and acetylene emission indices are shown plotted against the ethylene in Figure 7-7. The concentration of acetylene was shown to be highest followed by methane, and ethylene and formaldehyde. In general, a linear curve of EI for the other three compounds vs. EI(C_2H_4) was not observed over the whole range of equivalence ratios. It could be argued that at low EI(C_2H_4) values (EI(C_2H_4) <1) the trend is linear, however there were only two valid (above detectable limit) measurement points for C_2H_4 in this range.

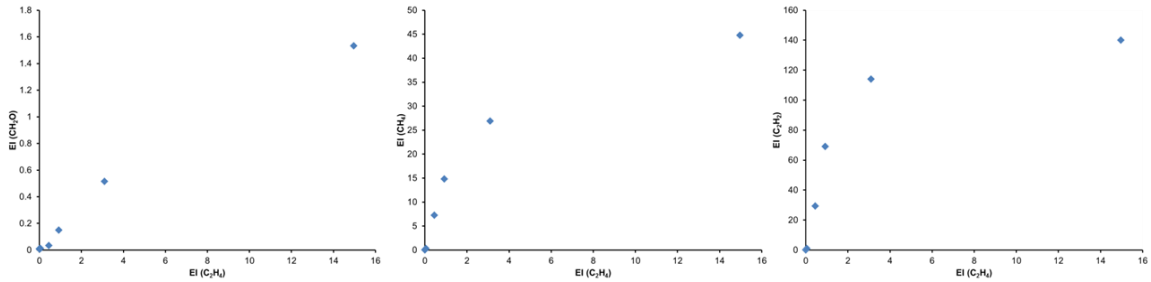

Figure 7-7. Emission Indices of Formaldehyde, Methane and Acetylene vs. Emission Indices for Ethylene for the Heptane/Dodecane Surrogate.

7.1.3 Methylcyclohexane/n-Dodecane Experiments

Emissions data was acquired for n-heptane/n-dodecane over a range of equivalence ratios from 1.4 to 1.92 at a residence time of approximately 5 ms. Overall the EI of the four compounds increases as equivalence ratio increases. Over the entire measurement range the concentration of acetylene was shown to be highest followed by methane, and ethylene and formaldehyde. The trends are all similar to those shown previously for m-xylene/n-dodecane and n-heptane/n-dodecane. The slope of the EI vs. ϕ curve is shown to be linear for all four of the compounds between $1.4<\phi< 1.7$.

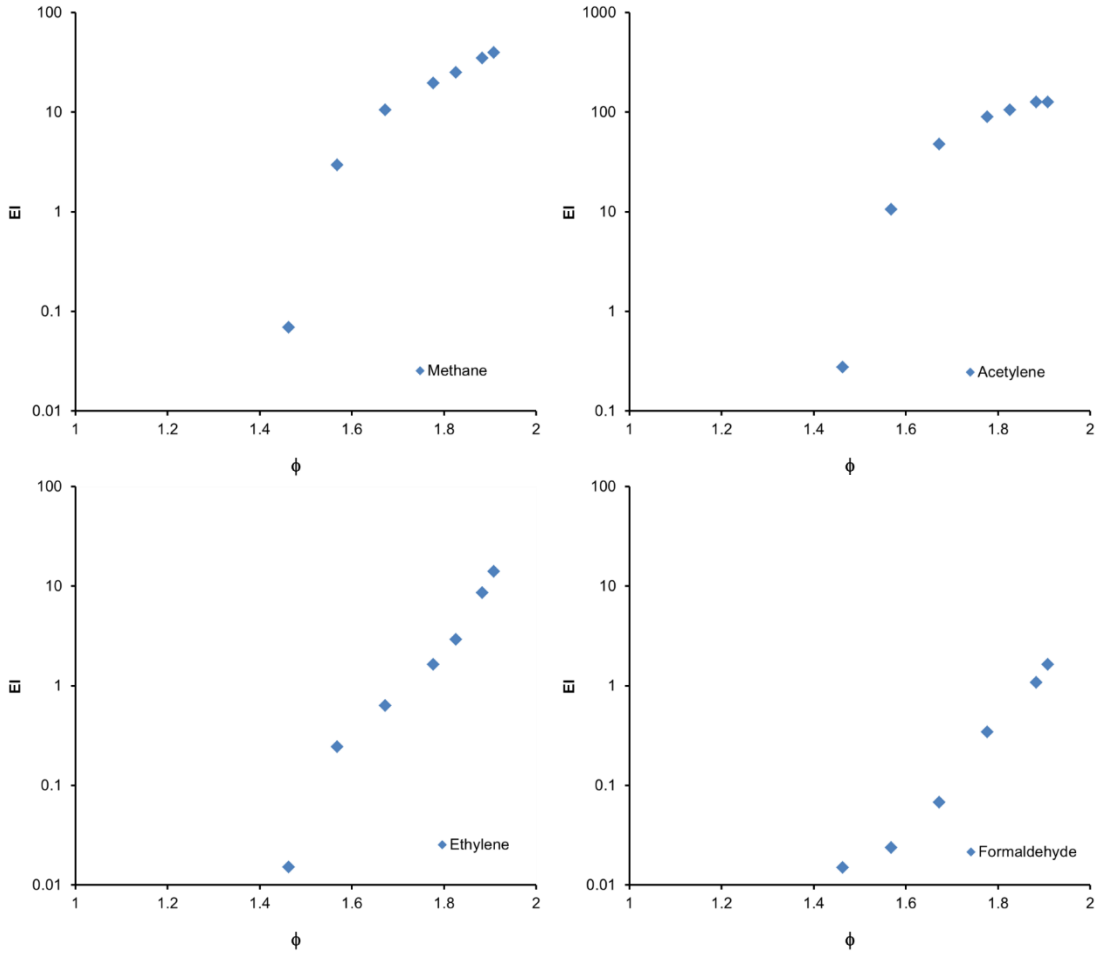

Figure 7-8. Emissions from the WSR on the Approach to Lean Blowout.

7.1.4 Discussion of Results for Fuel-rich Mixtures

Increasing the equivalence ratio (*i.e.,* fuel-to-air ratio) tends to shift production of unburned hydrocarbons from molecules with smaller carbon numbers toward those with larger numbers. This is evident by the slope of the concentration relative decreasing with increases in equivalence ratio for molecules with small carbon numbers. Conversely, the slope of the correlation increases for larger equivalence ratios for molecules with larger carbon numbers. Production of combustion products tends to be insensitive to the residence time within the reactor over the time-scale (*i.e.,* 3-5 ms) of the measurements, with the exception of formaldehyde for ethylene/air reactions. The time-scale of formaldehyde production

and consumption was sensitive to the residence time within the reactor, as shown in Figures 7-2 and 7-4. Increasing the residence time increased the emission indices of formaldehyde. Further work is required to determine whether this sensitivity is specific to ethylene or relatively simple unburned hydrocarbon fuels.

The sensitivity of emissions to changes in the peak temperature and concentration of aromatics was assessed using calculations. Including up to a 3% heat loss in the calculations had little influence on species concentrations. The temperature of the reactions decreases by approximately 2.5% for this heat loss. Changing the aromatic concentration from 18% to 28% (by volume) had a negligible effect on the temperature or species concentrations of emissions from the well-stirred reactor. One exception is the concentration of benzene, which increased with increase in the volume of aromatic in the fuel. This is in agreement with trends observed in emissions measurements for gas turbine engines.

7.2 Lean Blowout Experiments

An initial series of lean blow experiments was conducted in the reactor that was used for the fuel-rich studies. Those results are summarized in the Appendix to this report. Subsequent to the initial series of LBO experiments, the reactor was upgraded to improve the reliability and durability of the reactor under the conditions experienced during LBO. These upgrades are described in Section 3.2.2.

After the upgrades to the reactor, it was used in a new series of experiments to determine the conditions at LBO and to elucidate the controlling combustion kinetics near 1 atm in the range of 1350–1550 K. A high speed 5 Hz FTIR, paired with the use of gas bag and charcoal tube sampling were used to determine emissions from the reactor. The combination of both online and offline measurement techniques provided a means to capture a wide range of hydrocarbons. CO_2 and CO are shown to be the major carbon-containing emissions from the given fuel surrogate mixtures. Experimental results for emissions and combustion performance were determined at a constant air flow rate of 600 g/min. Bulk residence time with the given experimental conditions was determined to be approximately 6-7 ms, which is in the typical range of gas turbine engines of 5-10 ms (McAllister, Chen, Fernandez-Pello, 2011).

Each lean blowout experiment was initiated at an equivalence ratio of > 0.48 where measured formaldehyde levels dropped to 0 ppm. Equivalence ratios were reduced by keeping air constant and decreasing fuel flow until lean blow off where the flame extinguished. At most points test points throughout each experiment, the reactor was held at constant flow and thermal conditions for more than 12 minutes. FTIR measurements, recorded continuously at 5 Hz, were averaged over the 12 second running average period for each sample, while gas bags and charcoal tubes were taken at the last point of the sampling process for each equivalence ratio. This holistic sampling process captured major and minor species throughout the duration of the experiment, while ensuring steady state conditions for the bag and charcoal tube samples.

For points at or near LBO, the reactor could not be held constant for 12 minutes because of the tendency to blow out. At these near-LBO conditions, a non-equilibrium condition between the wall and gas temperatures may be responsible for some scatter in the WSR temperature data. Once blow out occurred, the reactor was re-ignited by reducing air and fuel flow rates. Once steady state conditions were reached at the start of the blow out test, a second test was conducted in a similar fashion. As was experienced in previous experiments, hysteresis does occur when approaching LBO if there is insufficient time for the reactor to reach a steady-state temperature at each condition. Leaner conditions can be reached if the reactor walls are relatively hot, resulting from a rapid decrease in equivalence ratio. If LBO is approached more

slowly, the walls have sufficient time to cool to the local gas temperature and, therefore, LBO is experienced at higher equivalence ratios (Vijlee, 2014). Increments in fuel flow rate were small while decreasing the fuel flow, thus reducing the chance for hysteresis. Previous literature showed variance in blow off temperature of +/- 50 K (Vijlee, 2014) and blow off equivalence ratio near 2% (Blunck, et. al, 2015).

7.2.1 Discussion of Reactor Temperature and LBO Results

Temperatures at the experimental conditions were well below the maximum operating temperature of the ceramic to achieve the durability required for testing with one build of the reactor and to prevent cracking. Incoming fuel and air to the jet ring was held at a temperature of 460 K, which is in the typical combustor range of 200–900 K (McAllister, Chen, Fernandez-Pello, 2011). Figure 7-9 displays the relationship of reactor temperature to equivalence ratio. Each point represents the average of all the samples for the given equivalence ratio, with the maximum standard deviation shown on one of the points. As leaner conditions were approached, the reactor blew out at the minimum reactor temperature indicated. Temperature is observed to linearly decrease with decreases in equivalence ratio, with all fuels approaching lean blow out around 1400 K. Lean blow out was measured to be 0.425, 0.422, 0.420, 0.414, and 0.415 for the m-xylene/n-dodecane (m-X), iso-octane/n-dodecane (i-C8), methylcyclohexane/n-dodecane (MCH), n-heptane/n-dodecane(n-C7), and pure n-dodecane (n-C12), respectively. Reactor temperatures at LBO were measured to be approximately 1415 K, 1405 K, 1402 K, 1401 K, and 1392 K for the m-X, i-C8, MCH, n-C7, and n-C12 fuels, respectively.

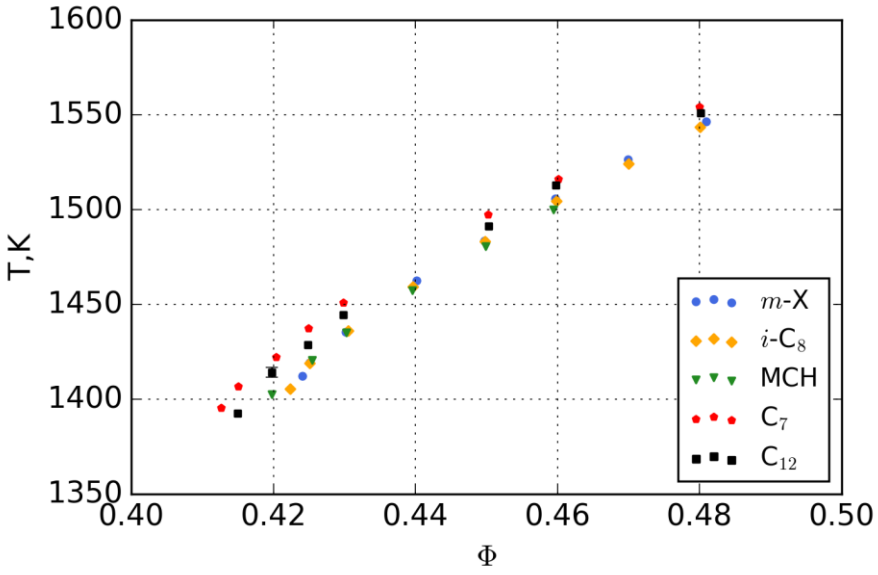

Figure 7-9. WSR reactor temperature effects with equivalence ratio. Temperature trends to decrease when decreasing equivalence ratio, thus reducing fuel flow. (P = 1 atm, τ = 6-7ms).

Variation in equivalence ratio at LBO with respect to H/C ratio is shown in Figure 7-10. In a constant enthalpy well-stirred condition, equivalence ratio at blowout tends to increase with a decrease in H/C ratio. i-C8 at near-LBO conditions was measured at a higher equivalence ratio, creating an outlier to the overall trend. The cause of the LBO at higher equivalence ratio of the i-C8 fuel could be attributed to the iso-paraffinic structure in the i-C8 surrogate mixture, which contributes to reactions that scavenge radicals.

Heat release rate as a function of equivalence ratio is shown in Figure 7-11. Heat release rate can be determined by multiplying mass fuel flow rate by the heat of combustion (in this case, Lower Heating Value, LHV)). LHVs were measured using ASTM Standard D4809. A decrease in heat release is expected as there is less fuel reacting in leaner conditions. Similar heat release rates between the fuel surrogates was experienced, as they have similar LHVs and flow rates.

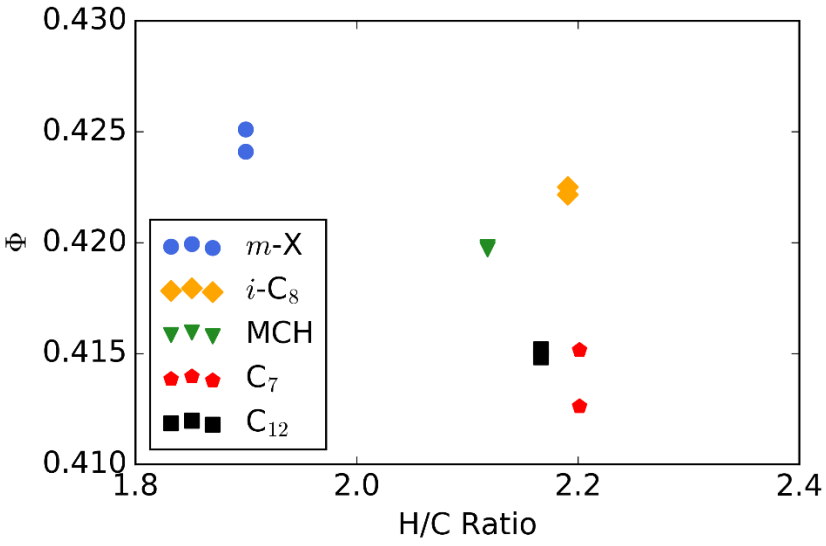

Figure 7-10. WSR LBO effects with H/C number of the given surrogate fuel mixture is listed for each fuel and its respective color. (P = 1 atm, τ = 6.5ms). For a constant enthalpy system, decreases in H/C ratio trend to increase the state of LBO, thus reducing resistance to LBO.

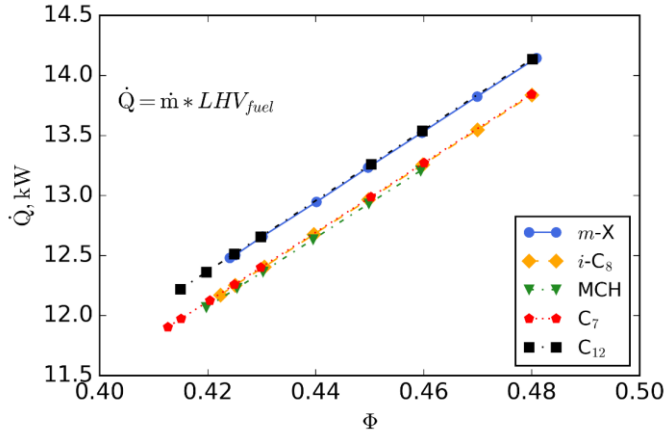

Figure 7-11. WSR heat release rate with equivalence ratio. Decreases in fuel flow trends to reduce energy released in the combustion process. Fuel mass flow rates were multiplied by their corresponding heat of combustion to determine heat release rate. (P = 1 atm, τ = 6-7ms, $\dot{V}_{fuel}$ = ~22-26 mL/min).

7.2.2 Discussion of Major and Minor Emissions

In addition the temperatures and lean blow out limits between fuel surrogate mixtures, emissions were measured to identify differences among the fuels. Emissions data from the FTIR are represented in a similar manner to the temperature measurements in Figure 7-9. Carbon dioxide (CO2) was measured and compared as a function of equivalence ratio, shown in Figure 7-12. The decrease in concentration for CO2 was expected as leaner conditions were approached. A decrease in CO2 towards leaner conditions decreases combustion efficiency as more CO and other hydrocarbon intermediates are produced. Figure 7-12 also displays carbon monoxide (CO) concentration with varying equivalence ratio. CO tended to increase as equivalence ratio decreased. Concentrations of CO increased by 2.5 times from the beginning of the test at the higher equivalence ratios to LBO. At the leaner conditions and towards blow off, CO yield was consistent for all surrogates around 6,000 ppm. The increased yield of CO is expected because CO is only partially oxidized during the short residence time in the reactor, particularly as lean blow off is approached.

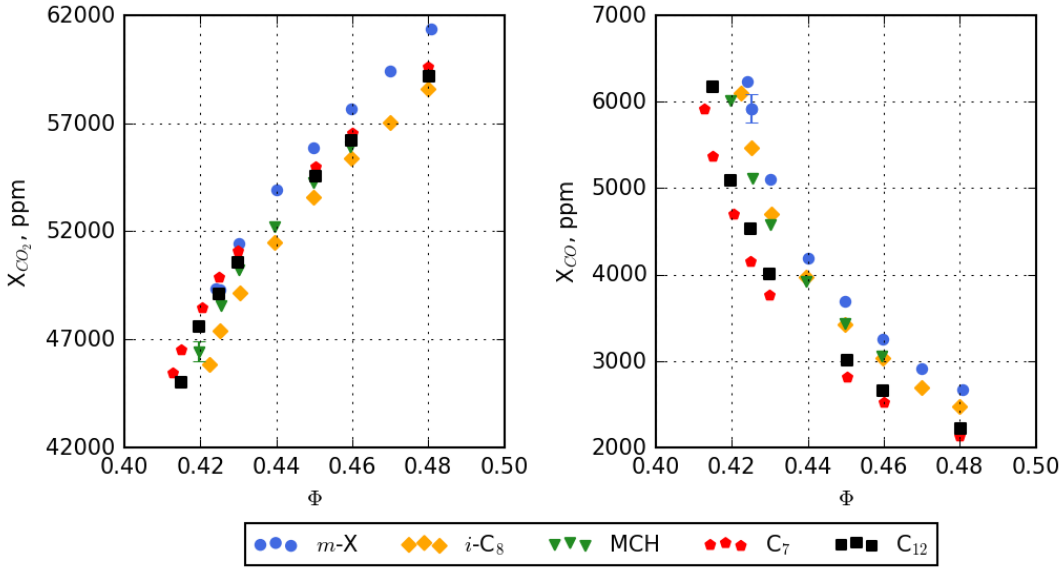

(a) (b)

Figure 7-12. Carbon dioxide (a) and carbon monoxide (b) concentration (ppm) a function of equivalence ratio at atmospheric conditions and a residence time of approximately 6.5 ms. Temperatures for these experiments are reported in Figure 7-10.

As leaner conditions are approached, other hydrocarbon species are formed due to the reduction of heat release which lowers reactor temperature and slows reaction rates. Formaldehyde, acetylene, ethane, ethylene and methane are the minor species with the highest concentration observed during the LBO experiments. These species increase as leaner conditions are approached. In Figure 7-13, formaldehyde, a marker for incomplete combustion and other intermediates production, increases dramatically as equivalence ratio is decreased.

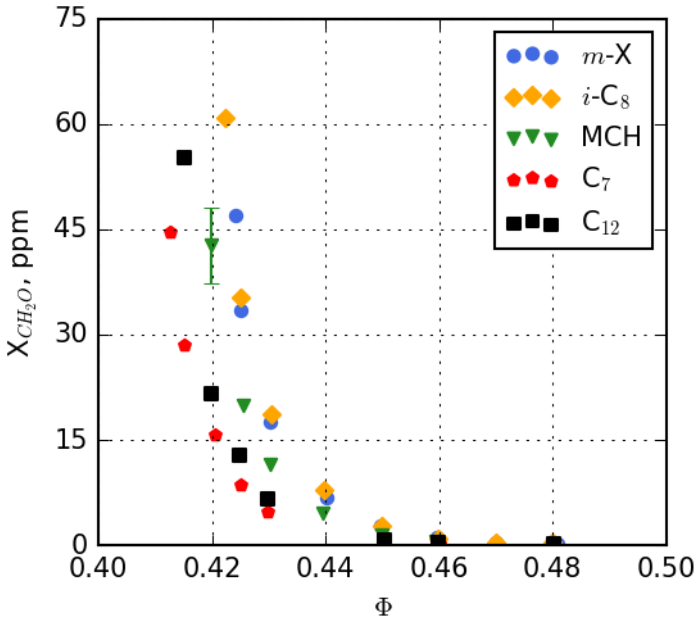

Figure 7-13. Formaldehyde concentration (ppm) as a function of equivalence ratio at atmospheric conditions and a residence time of approximately 6.5 ms. Measurements from methane were recorded from the FTIR.

Figure 7-14 shows the methane concentration as a function of equivalence ratio and cross-plotted against formaldehyde. Both charts provide a means to analyze emissions produced as leaner conditions approach, and can yield a possibility to qualitatively compare emissions produced by the varying fuel surrogates. Yields at lean blowout are approximately 25-35 ppm. Methane emissions scale between the fuel surrogate mixtures as a function of formaldehyde. Ethane yields a similar trend to methane, as shown in Figure 7-15, where peak concentrations at lean blow out vary between approximately 4-8 ppm. The linear behavior in the cross-plots against formaldehyde is consistent with the behavior of emissions from actual aircraft engines at low power (see Section 2.3.1, Linear Behavior of UHC Emissions at Low Power).

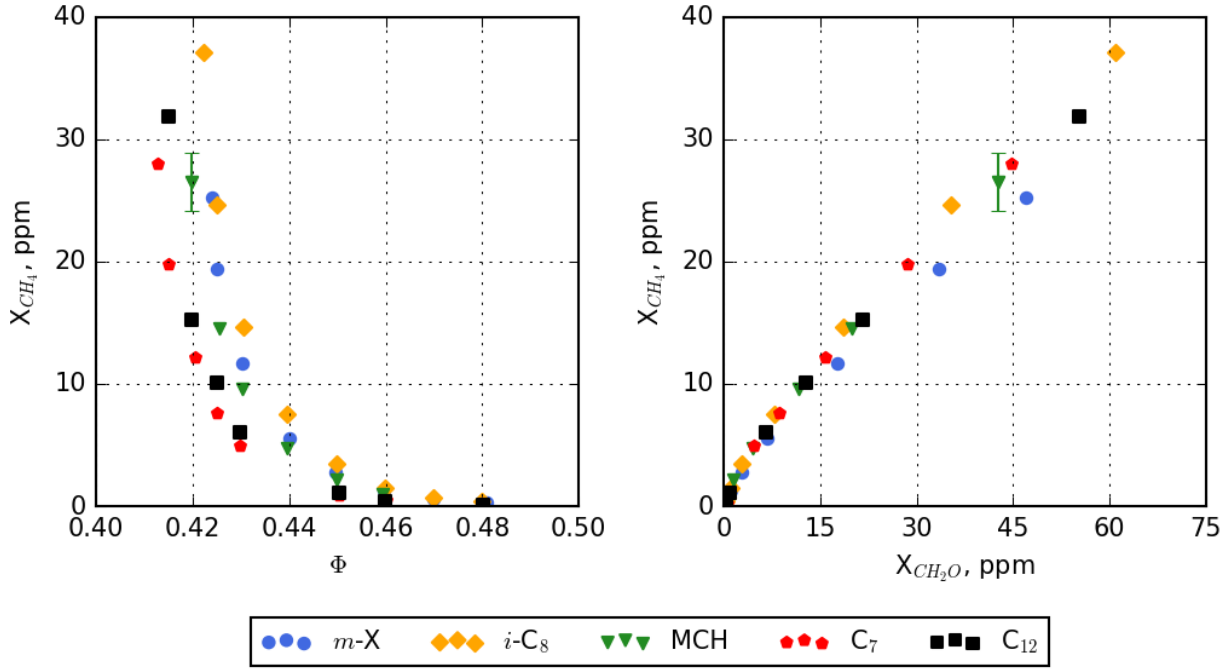

(a) (b)

Figure 7-14. Methane concentration (ppm) as a function of equivalence ratio (a) and as a function of formaldehyde concentrations (b) at atmospheric conditions and a residence time of approximately 6.5 ms. Measurements from methane were recorded from the FTIR.

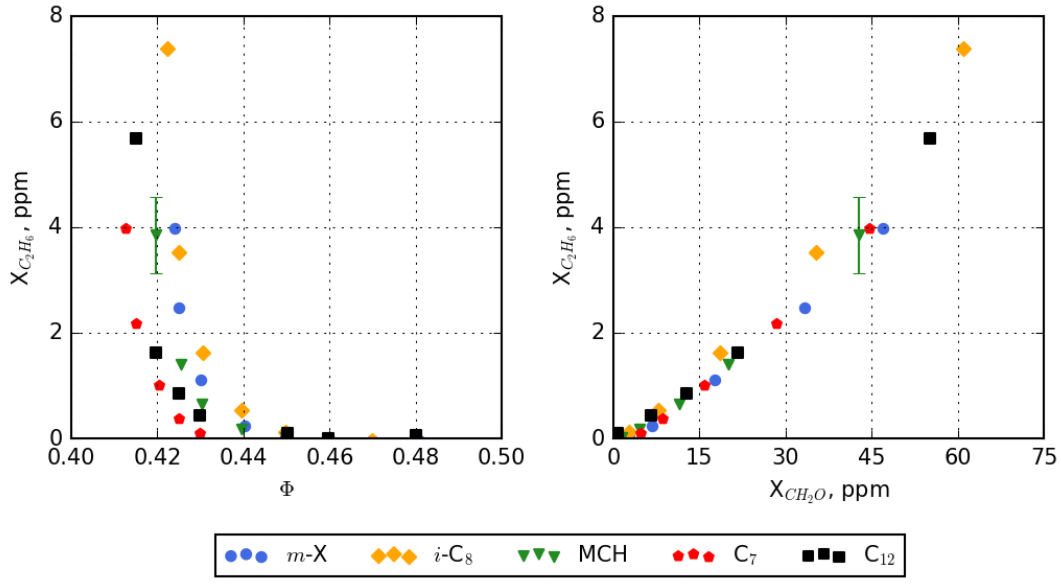

(a) (b)

Figure 7-15. Ethane concentration (ppm) as a function of equivalence ratio (a) and as a function of formaldehyde concentrations (b) at atmospheric conditions and a residence time of approximately 6.5 ms. Measurements from ethane were recorded from the FTIR.

Figure 7-16 and Figure 7-17 display ethylene and acetylene as a function of equivalence ratio and formaldehyde. Both species are produced in increasing amounts as leaner conditions are approached. Linear trends of the species are also observed when they are cross-plotted against formaldehyde.

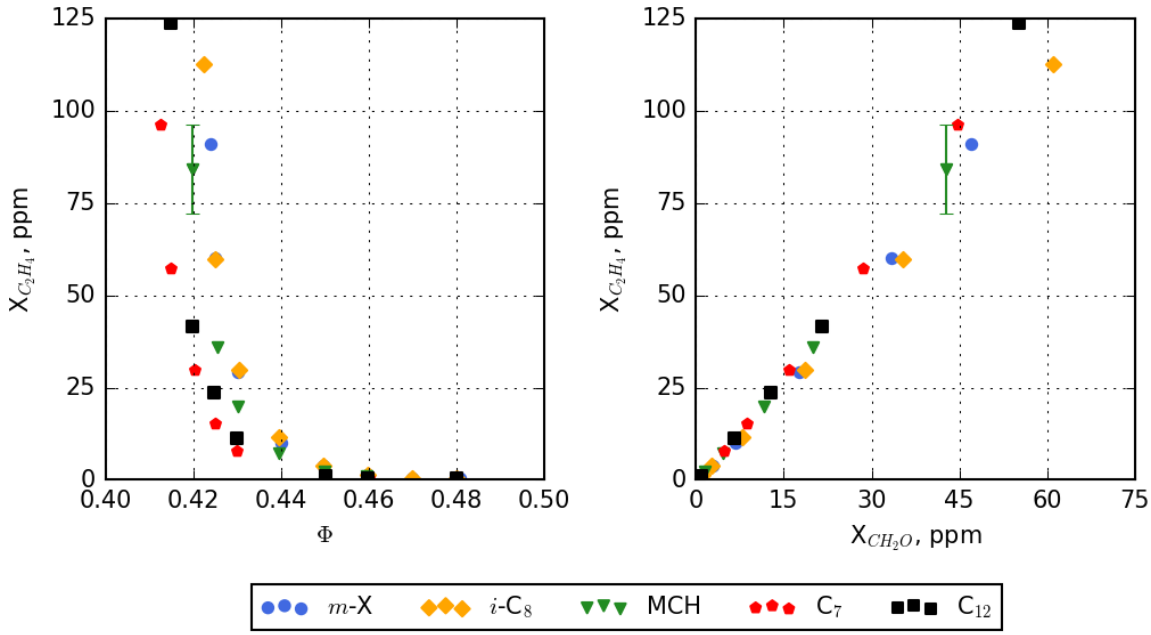

(a) (b)

Figure 7-16. Ethylene concentration (ppm) as a function of equivalence ratio (a) and as a function of formaldehyde concentrations (b) at atmospheric conditions and a residence time of approximately 6.5 ms. Measurements from ethylene were recorded from the FTIR.

Both online and offline emissions analysis provide data on heavier hydrocarbon emissions as well as HAPs. Propene, measured by both the FTIR and gas bag sampling technique, is shown in Figure 7-18 and Figure 7-19. Concentrations near lean blow out vary around 10-25 ppm. Both techniques capture the same qualitative trend among the fuel surrogates and yield similar values.

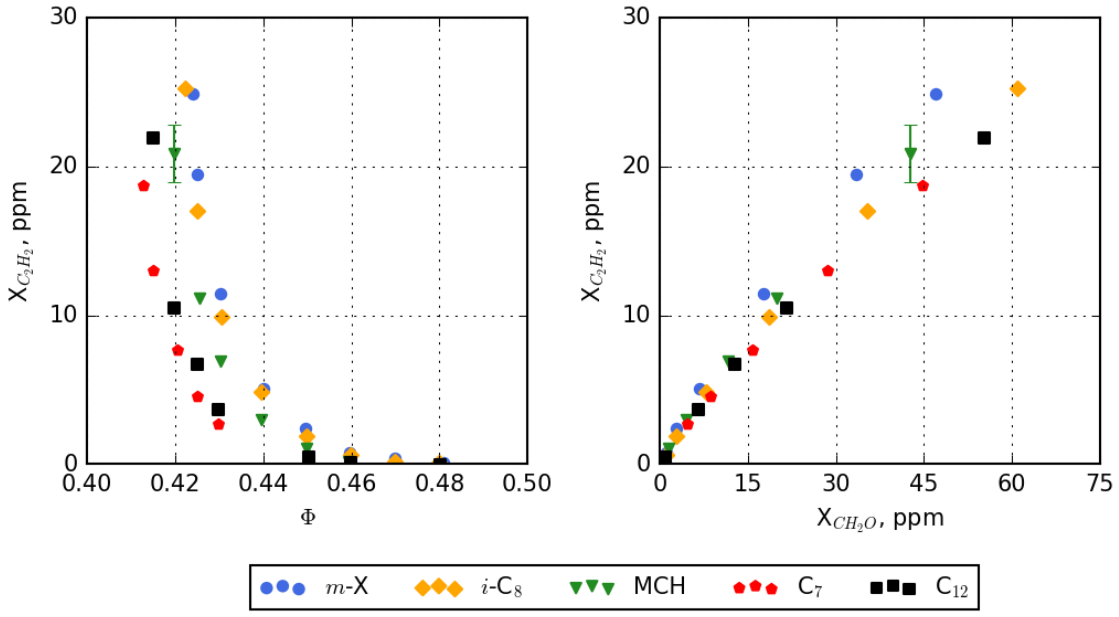

(a) (b)

Figure 7-17. Acetylene concentration (ppm) as a function of equivalence ratio (a) and as a function of formaldehyde concentrations (b) at atmospheric conditions and a residence time of approximately 6.5 ms. Measurements from acetylene were recorded from the FTIR.

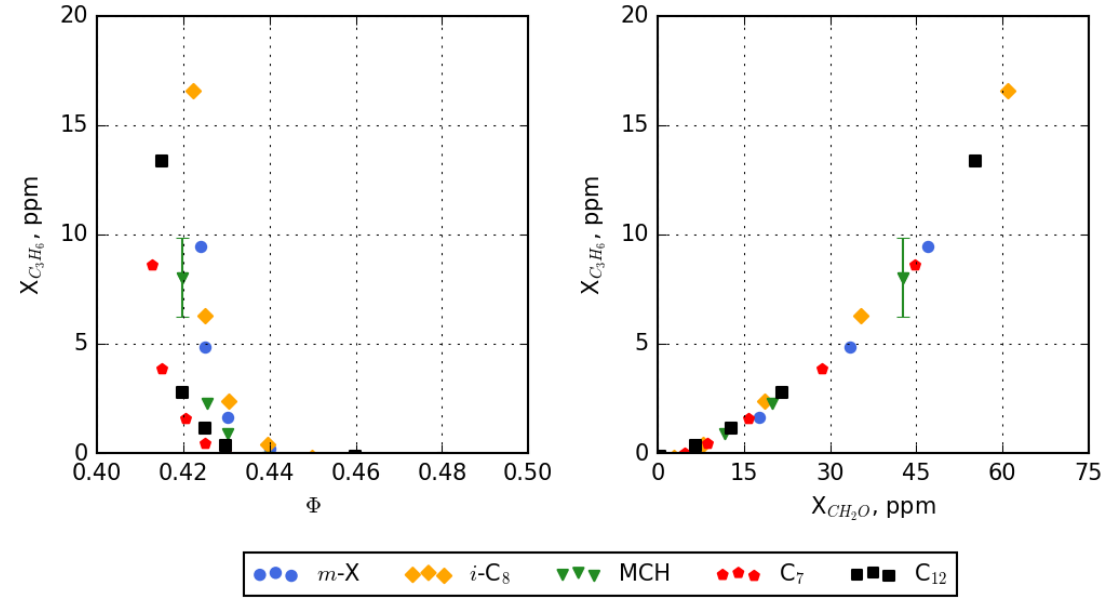

(a) (b)

Figure 7-18. Propene concentration (ppm) as a function of equivalence ratio (a) and as a function of formaldehyde concentrations (b) at atmospheric conditions and a residence time of approximately 6.5 ms. Measurements from propene were recorded from the FTIR.

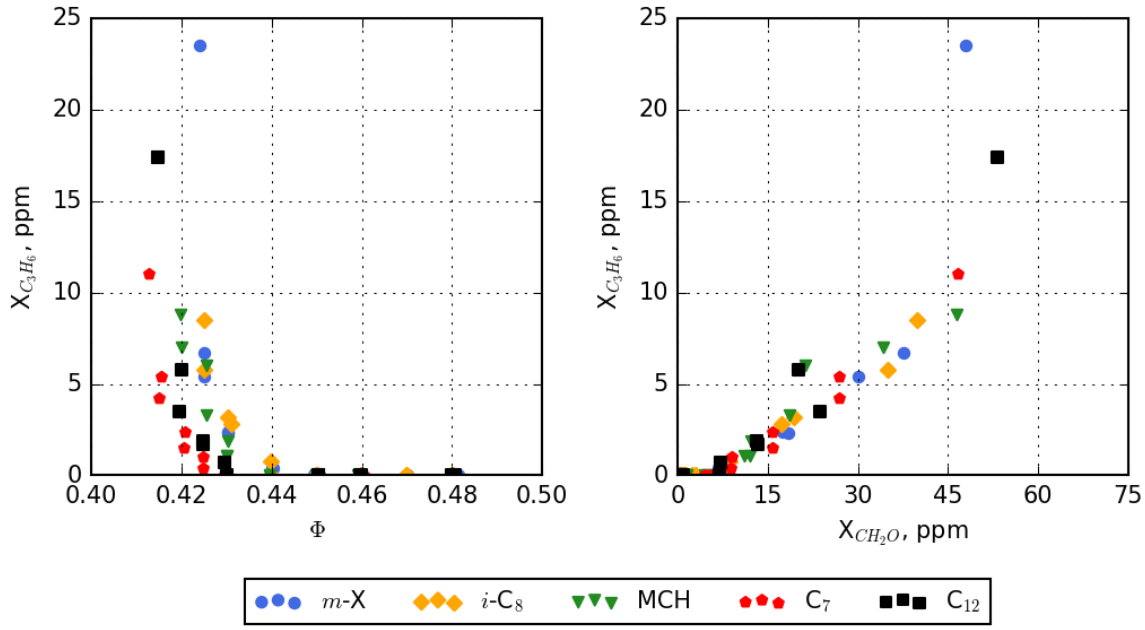

(a) (b)

Figure 7-19. Propene concentration (ppm) as a function of equivalence ratio (a) and as a function of formaldehyde concentrations (b) at atmospheric conditions and a residence time of approximately 6.5 ms. Measurements from propene were recorded from the gas bag sampling technique.

7.2.3 Discussion of HAPs During LBO Testing

1,3 butadiene is shown the following figures (Figure 7-20, Figure 7-21, and Figure 7-22) as a function of equivalence ratio and formaldehyde, similar to previous emissions. Increased levels of 1,3 butadiene are observed across the three sampling techniques as lean blow out is approached. This yields promising results for the online sampling techniques of the FTIR relative to the other offline measurements. The one caveat to this is that the charcoal tube sampling is the detection of both butene and 1,3 butadiene and not solely to 1,3 butadiene. Regardless, experimental trends to the creation of this species as lean low out is approaching is important to know in low power conditions.

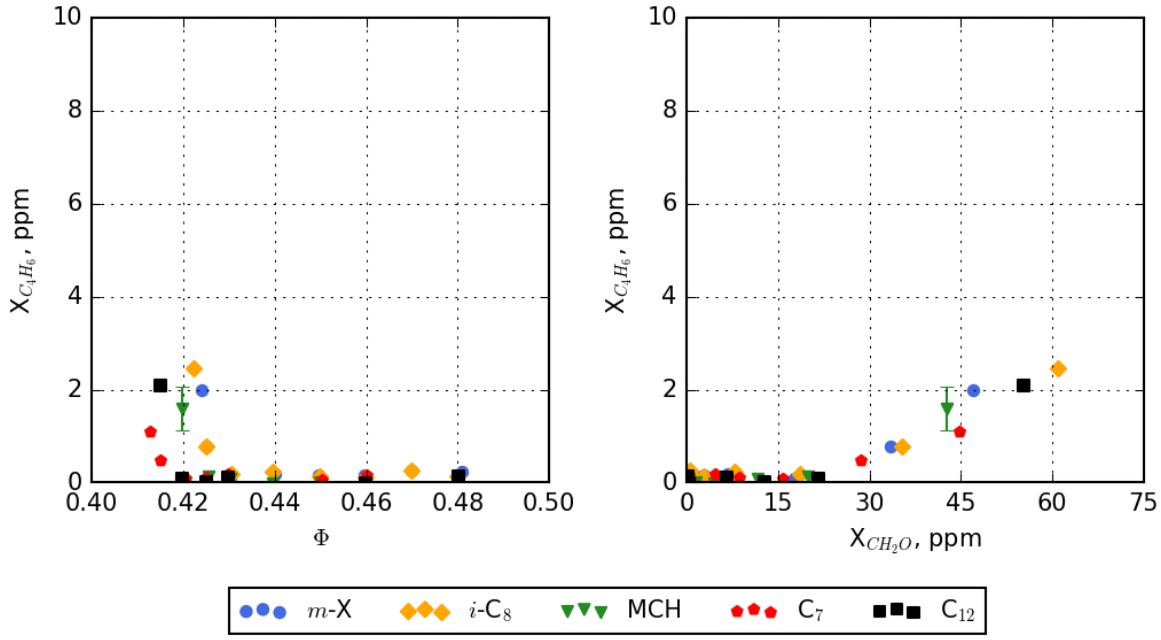

(a) (b)

Figure 7-20. 1,3 butadiene concentration (ppm) as a function of equivalence ratio (a) and as a function of formaldehyde concentrations (b) at atmospheric conditions and a residence time of approximately 6.5 ms. Measurements from 1,3 butadiene were recorded from the FTIR.

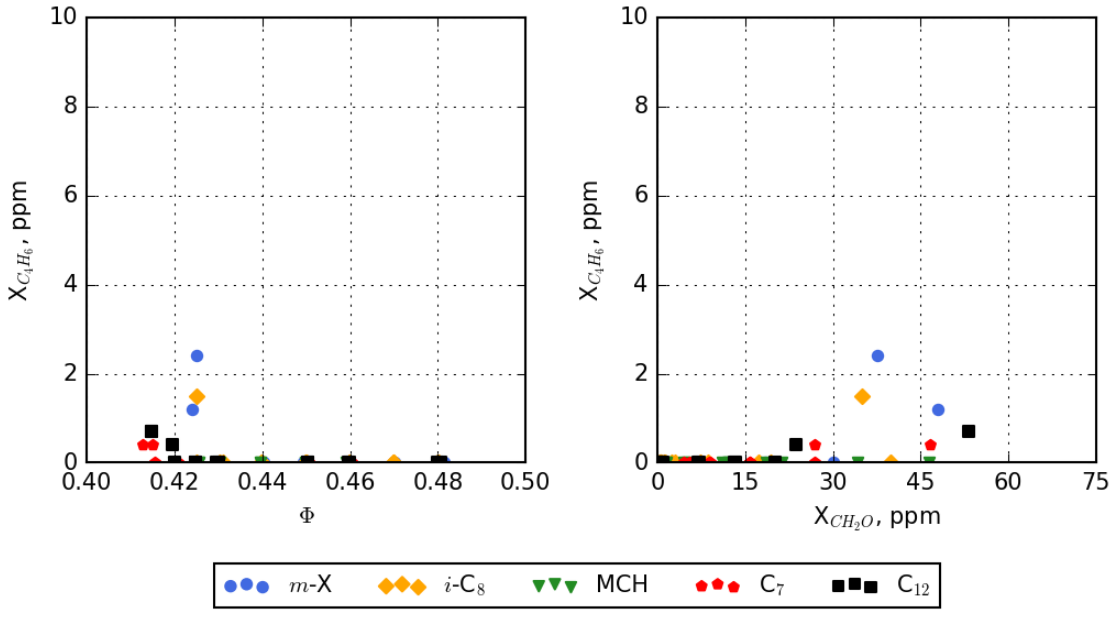

(a) (b)

Figure 7-21. 1,3 butadiene concentration (ppm) as a function of equivalence ratio (L) and as a function of formaldehyde concentrations (b) at atmospheric conditions and a residence time of approximately 6.5 ms. Measurements from 1,3 butadiene were recorded from the gas bag sampling technique.

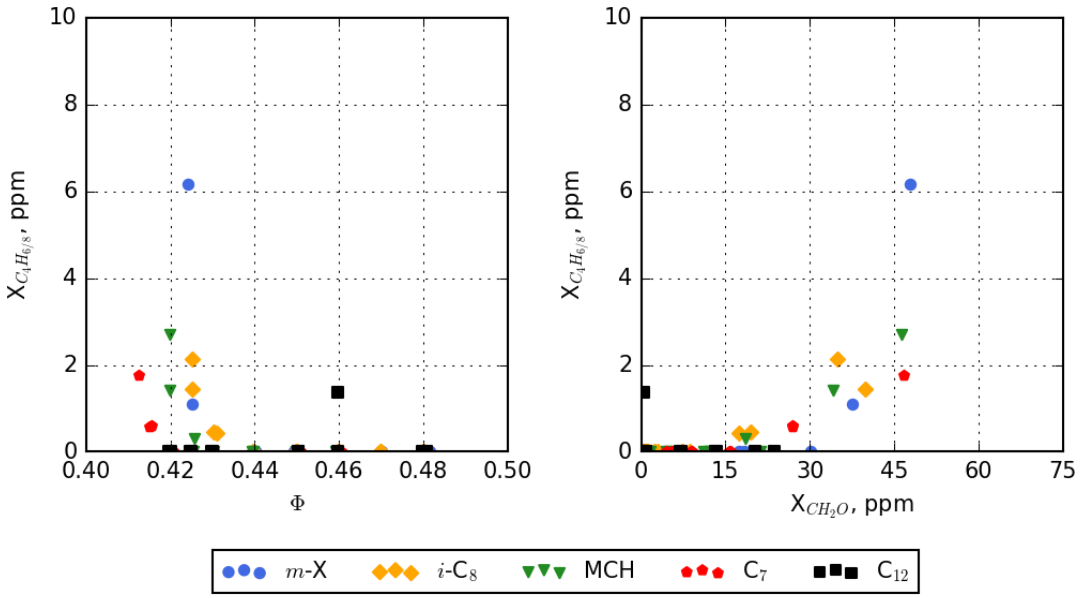

(a) (b)

Figure 7-22. Butene and 1,3 butadiene concentration (ppm) as a function of equivalence ratio (a) and as a function of formaldehyde concentrations (b) at atmospheric conditions and a residence time of approximately 6.5 ms. Measurements from butene and 1,3 butadiene were recorded from the charcoal tube sampling technique.

Other HAPs were also measured during the experiments. Acetaldehyde, shown in Figure 7-23 and measured using the FTIR, increases towards leaner conditions to a yield of approximately 10 ppm. Methanol, in Figure 7-24, shows similar trends qualitatively and quantitatively with acetaldehyde with formaldehyde production. Figure 7-25 shows the isobutylene production measured using the FTIR. Isobutene is only produced by the iso-octane/n-dodecane fuel as expected based on the structure of the fuels. The production of iso-olefins would be expected from alternative fuels that contain iso-paraffins.

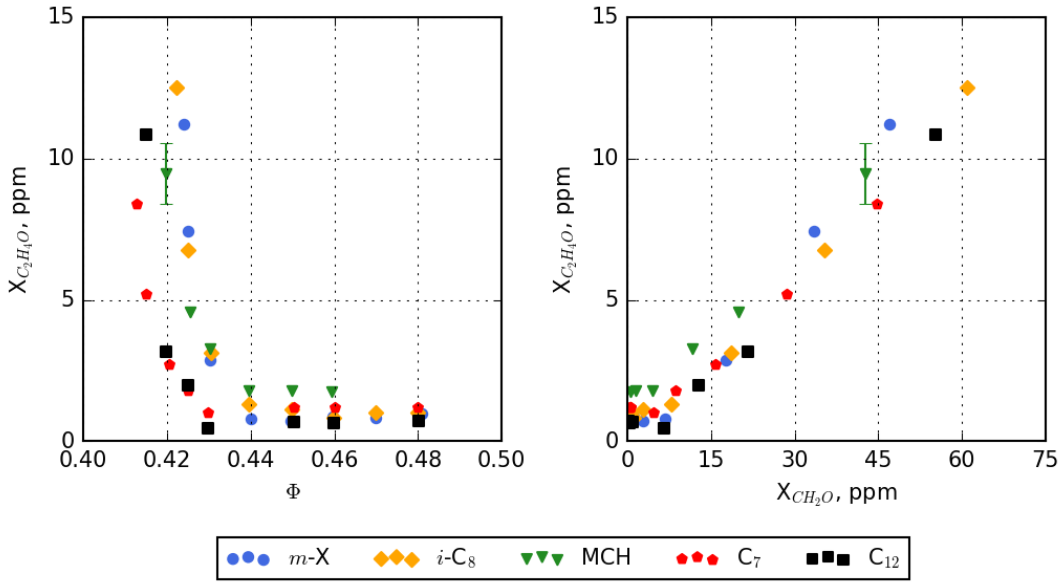

(a) (b)

Figure 7-23. Acetaldehyde concentration (ppm) as a function of equivalence ratio (a) and as a function of formaldehyde concentrations (b) at atmospheric conditions and a residence time of approximately 6.5 ms. Measurements from acetaldehyde were recorded from the FTIR.

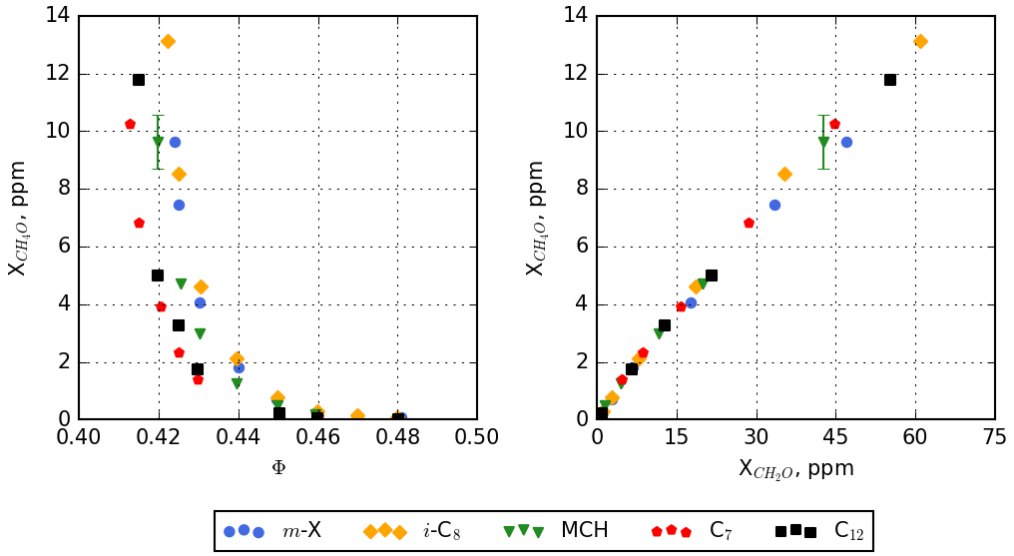

(a) (b)

Figure 7-24. Methanol concentration (ppm) as a function of equivalence ratio (a) and as a function of formaldehyde concentrations (b) at atmospheric conditions and a residence time of approximately 6.5 ms. Measurements from methanol were recorded from the FTIR and deviate slightly out of the calibration range of 0-10 ppm towards lean blowout conditions.

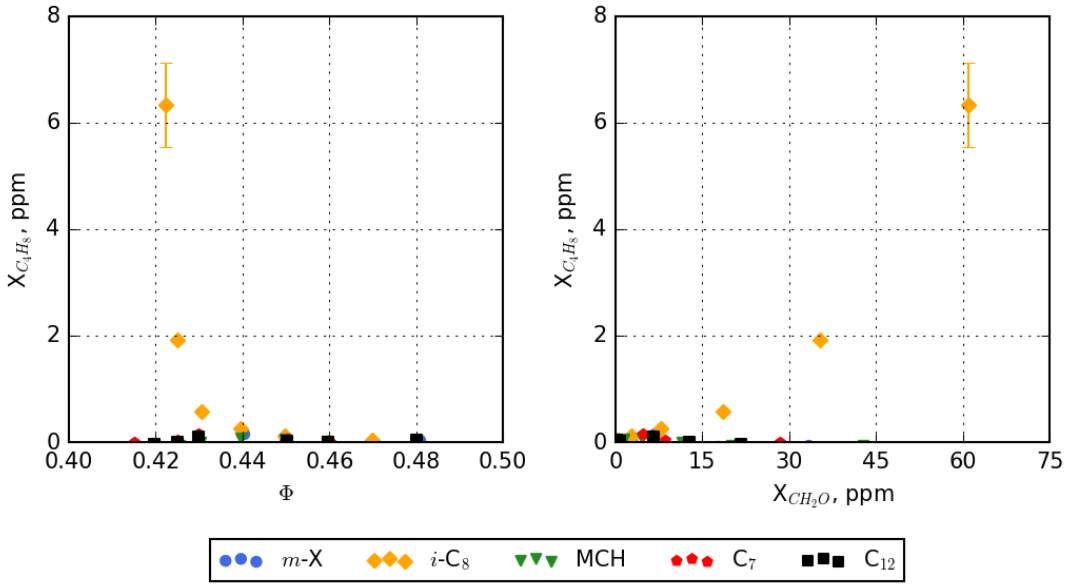

Figure 7-25. Isobutene concentration (ppm) as a function of equivalence ratio (a) and as a function of formaldehyde concentrations (b) at atmospheric conditions and a residence time of approximately 6.5 ms. Measurements from isobutene were recorded from the FTIR.

Benzene, toluene, and m-xylene are shown in Figure 7-26, Figure 7-27, and Figure 7-28, respectively, based on analysis of the product samples captures on charcoal tubes. These HAPs also show demonstrate differences based on fuel composition. Towards leaner conditions, the m-xylene/n-dodecane

fuel yielded approximately 4 ppm of benzene and the methylcyclohexane fuel produced a maximum of approximately 2 ppm. The other two fuels containing only normal and iso-paraffins produced more less than 1/10th the amount of benzene. The cross-plot against formaldehyde makes the differences in benzene production among the fuels even more clear than the plot against equivalence ratio.

Both toluene and m-xylene are observed experimentally with the m-xylene/n-dodecane fuel. These two HAPS are not produced by any of the other fuels, which are purely paraffinic fuels. This trend is as expected because of the fact that aromatic species will not form from paraffins under fuel-lean conditions and because toluene can form from m-xylene in a hydrogen displacement of the methyl group.

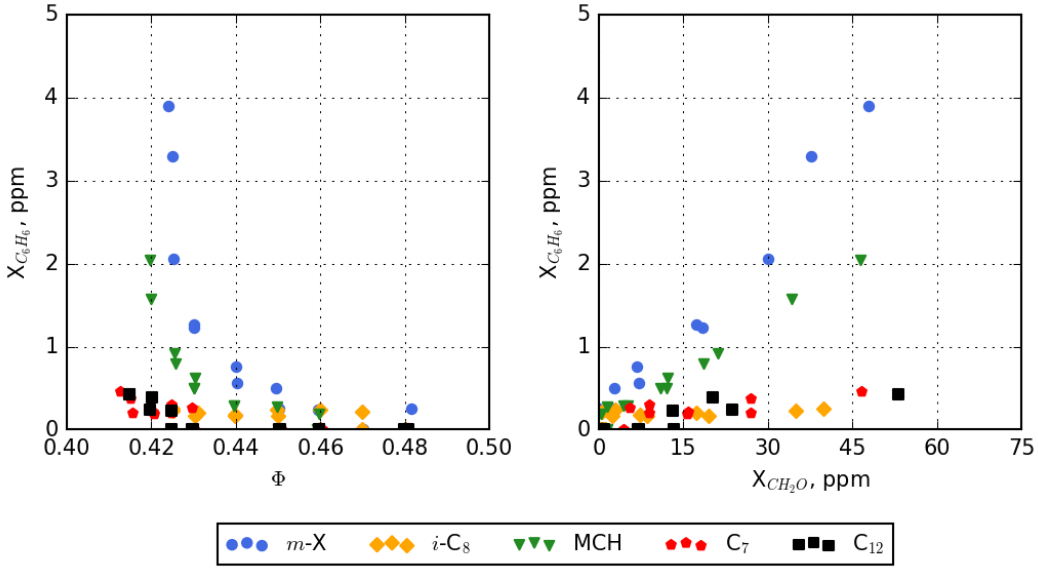

Figure 7-26. Benzene concentration (ppm) as a function of equivalence ratio (a) and as a function of formaldehyde concentrations (b) at atmospheric conditions and a residence time of approximately 6.5 ms. Measurements from benzene were recorded from the charcoal tube technique.

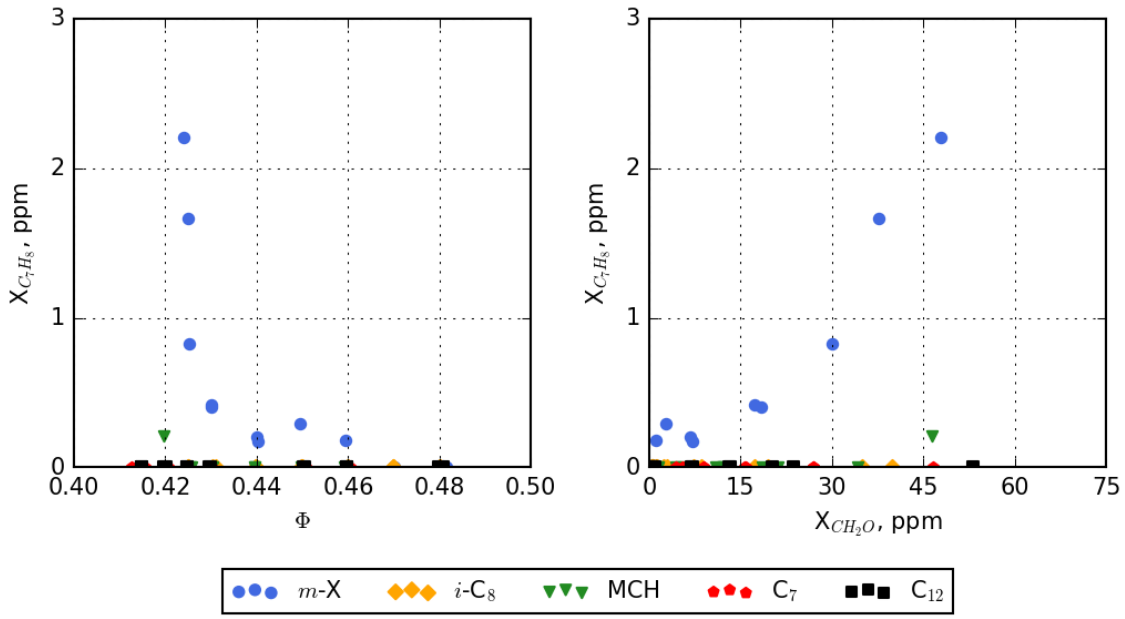

Figure 7-27. Toluene concentration (ppm) as a function of equivalence ratio (a) and as a function of formaldehyde concentrations (b) at atmospheric conditions and a residence time of approximately 6.5 ms. Measurements from toluene were recorded from the charcoal tube technique.

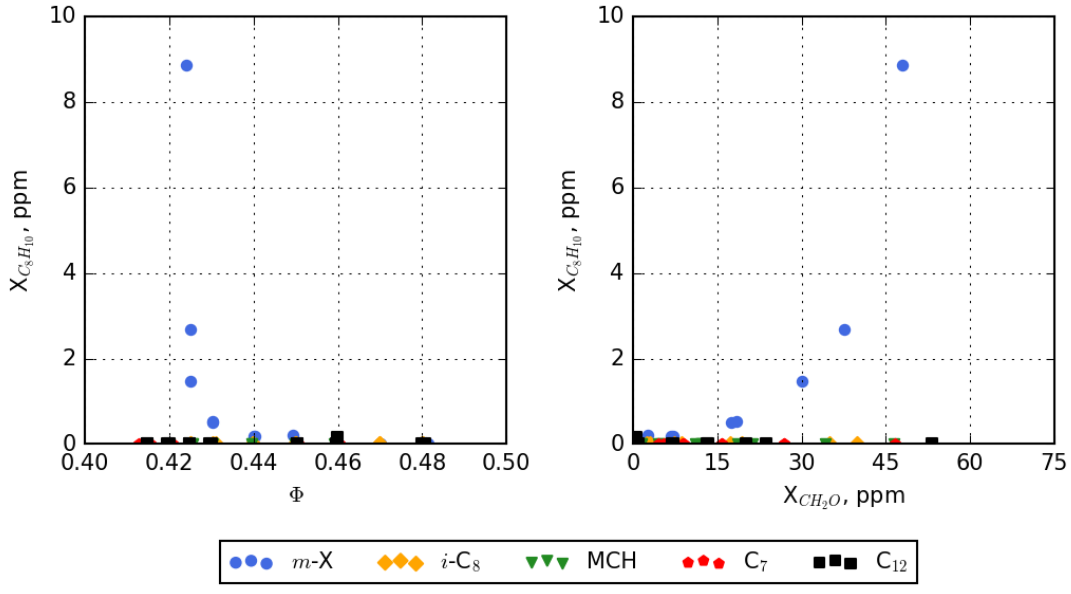

(a) (b)

Figure 7-28. p&m-xylene concentration (ppm) as a function of equivalence ratio (a) and as a function of formaldehyde concentrations (b) at atmospheric conditions and a residence time of approximately 6.5 ms. Measurements from p&m-xylene were recorded from the charcoal tube technique.

7.3 Modeling of Lean Well-Stirred Reactor Experiments

The AFRL well stirred reactor (WSR) experiments near lean blowout (LBO) were modeled utilizing the Chemkin PSR software (Glarborg, et al, 1986; and Kee, et al, 1980). The experiments were conducted by maintaining a constant air flow and slowly decreasing fuel flow until blowout. To replicate these experiments, a series of discrete reactor simulations were performed in which each successive simulation was slightly leaner than the previous run. As the equivalence ratio was reduced, the peak reactor temperature was also reduced. Consequently, the bulk gas density increased and the bulk residence time in the reactor also increased. The assigned temperatures were based on the experimental data and are shown in Figure 7-29.[2]

The initial series of lean blowout experiments showed that blowout occurred in the vicinity 1300-1350 K. When adiabatic simulations were made, the computational blowout temperature was approximately 1250 K, as shown in Figure 7-29 and Figure 7-30. Both the adiabatic and fixed temperature computational profiles approach and converge in the vicinity of the blowout condition. The corresponding evolution of reactor species profiles for both sets of simulations generally exhibited strong similarities and trends as shown in Figure 7-31.

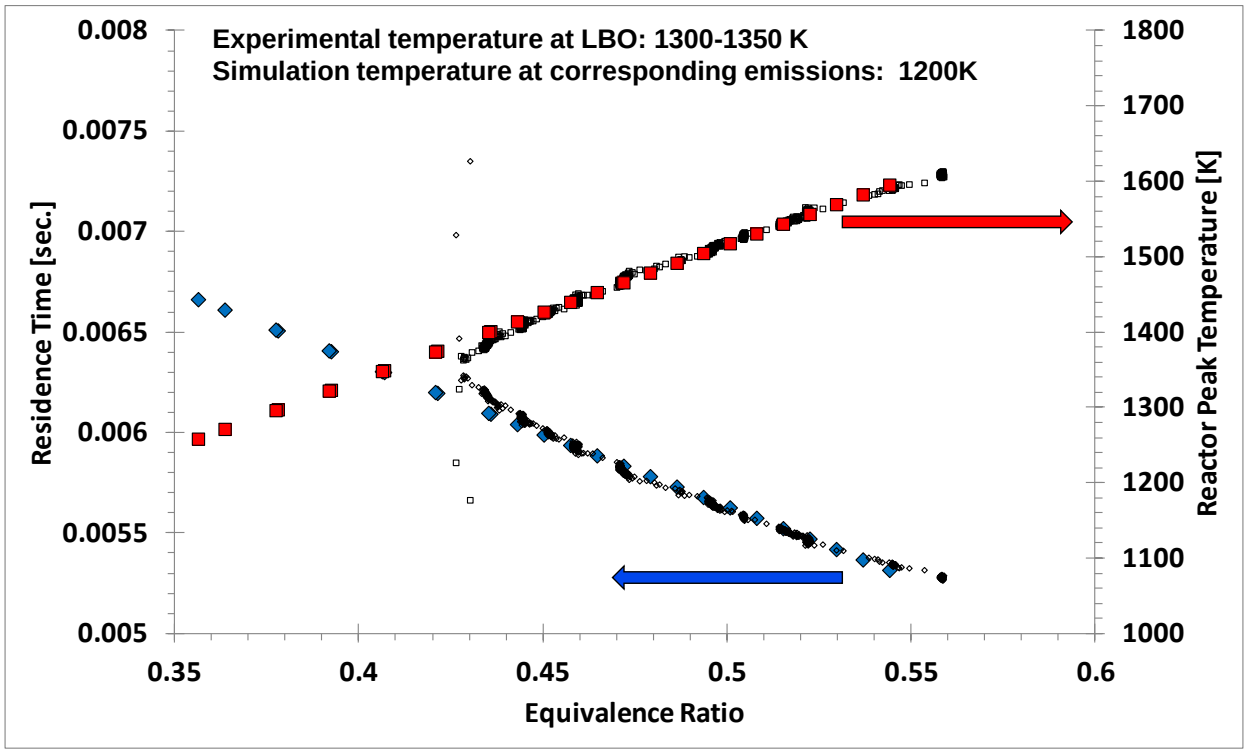

Figure 7-29. Progression of Reactor Equivalence Ratio, Temperature, and Residence Times (Large symbols: Simulations, Small symbols: Experiments).

[2] The initial series of experiments showed lower temperatures at lean blowout than the final series of experiments (~1400K) due to differences in initial reactor and higher heat losses in the reactor that was used in the initial series of experiments.

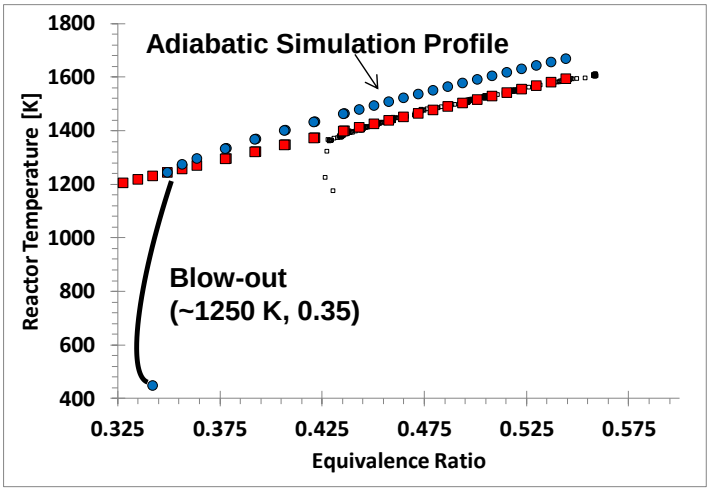

Figure 7-30. Temperature Profiles as LBO is approached (Large symbols: Simulations, Small symbols: Experiments).

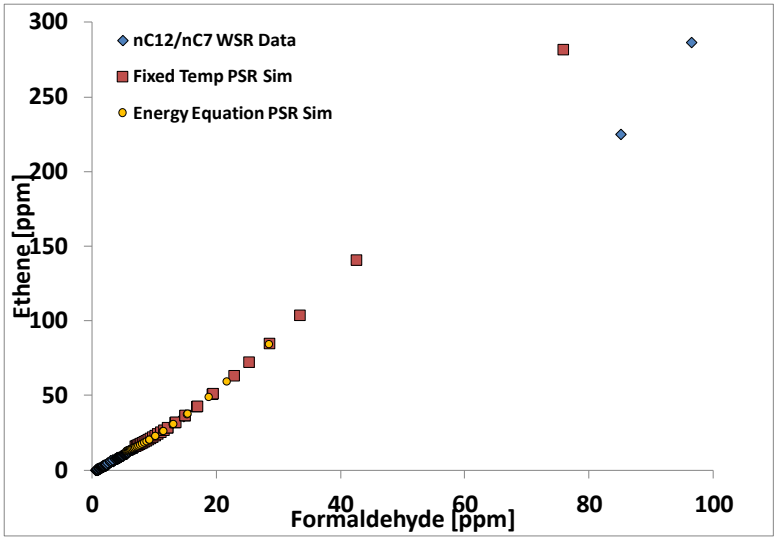

Figure 7-31. Ethene Emissions as Function of Formaldehyde Emissions as LBO is Approached.

The peak experimental formaldehyde mole fraction during approach to LBO was approximately 100 ppm. The corresponding formaldehyde (near LBO) mole fraction value from the adiabatic simulation was 30 ppm. The constant temperature simulation near 1200 K yielded a formaldehyde reactor mole fraction of 80 ppm. Due to the improved agreement with the experimental data, the simulation values obtained from the fixed temperature profiles will be summarized. An improved method of estimating reactor blowout based on global PSR performance was developed utilized a non-adiabatic analysis. Essentially, a heat-loss term was introduced into the energy equation as simulations progressed. This term was taken to be a fixed fraction of the chemical energy (i.e., fuel flow x fuel LHV) injected into the reactor. The fraction was calibrated at a stable operating point and then adjusted as equivalence ratio was decreased. Shown in Fig. 7-15 is a plot of the new modeling technique compared to the previous adiabatic and fixed temperature profiles. The introduction of heat loss improves the LBO simulations. Furthermore, because

the non-adiabatic simulations yielded essentially the same reactor temperatures as the fixed temperature simulations (Fig. 7-12), the emissions profiles are identical, up to the point of reactor blow out in the non-adiabatic cases.

Interestingly, previous analysis based on the fixed temperature simulations indicated that, at these lean conditions, the chemistry for several major hydrocarbon species was very sensitive to the reaction:

$$H + O_2 = O + OH$$

This sensitivity is due to the chain-branching nature of this reaction coupled with the decreased molecular oxygen consumption rate. As oxidation rates slow down, fuel pyrolysis chemistry continues to produce these hydrocarbon species. Since they are not being quickly oxidized, their concentrations build within the reactor.

Analysis associated with these new non-adiabatic simulations reveal that the system chemistry is even more sensitive to:

$$CO + OH = CO_2 + H$$

The sensitivities for several major compounds for the n-dodecane/n-heptane fuel at 1246 K (i.e., near blowout) are shown in Fig. 7-16. The importance of both of the above reactions is clearly indicated. This additional sensitivity in the non-adiabatic cases is due to the fact that in these simulations, unlike the fixed temperature simulations where the system temperature is independent of reaction, the energy equation is being solved and is coupled to the conversion of the fuel chemical energy into gas thermal energy. The driving force for this energy conversion is the oxidation of CO to CO_2. Since the actual experiments also require conversion of fuel chemical energy to sustain the high reactor temperatures, this non-adiabatic analysis seems to be more physically and chemically consistent with the experiments.

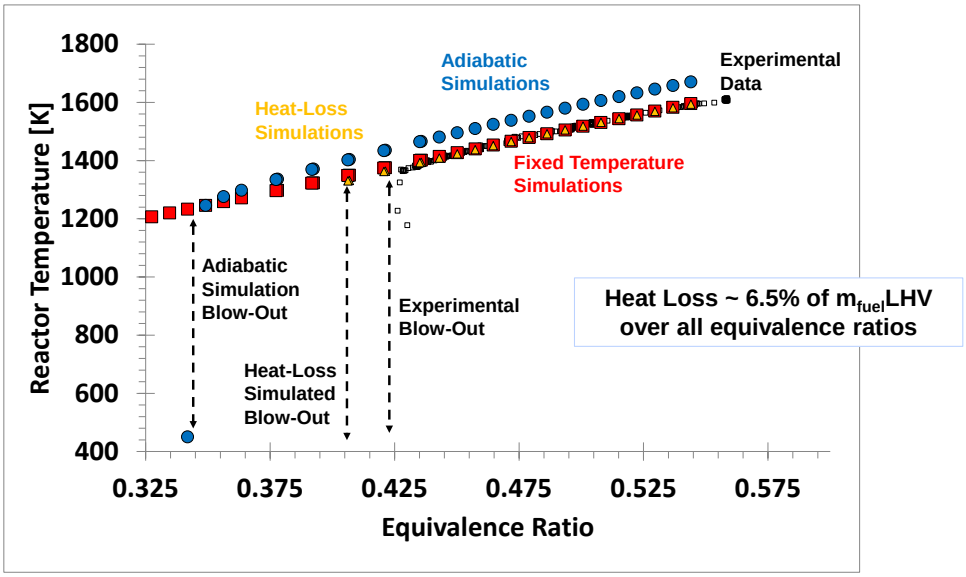

Figure 7-32. Comparison of LBO Temperature Profiles: Experimental, Adiabatic, Fixed-Temperature, and Non-Adiabatic for JP-8/Air System.

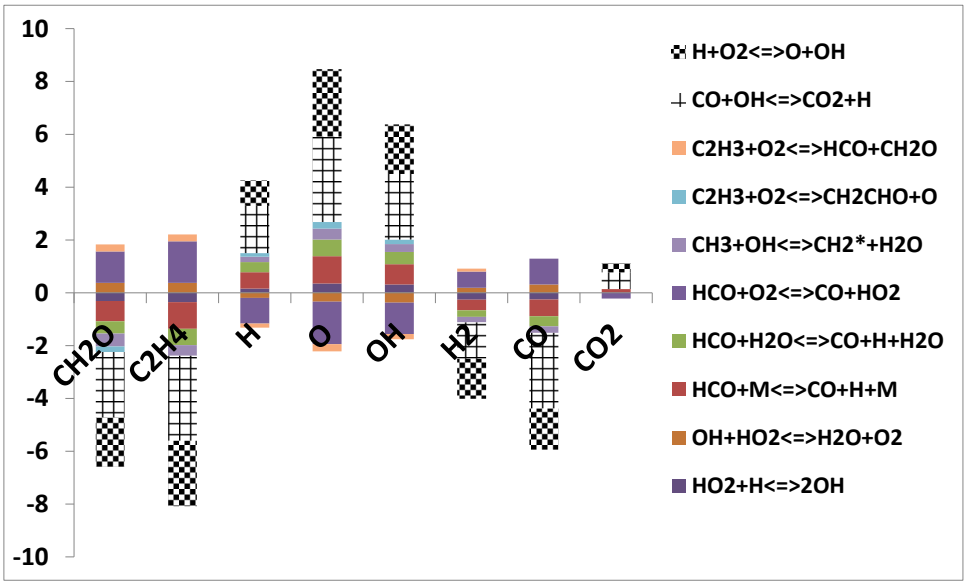

Figure 7-33. Non-Adiabatic Simulations Major Species Sensitivities to System Reactions (1250 K).

7.3.1 Kinetic Mechanisms and Surrogate Formulations

Six different fuels were studied in the WSR experiments: JP-8, a nC12/nC7 blend, a nC12/MCH blend, and pure nC12. All six experiments were simulated with the kinetic mechanism developed under the current program. The JP-8 experiments were simulated using two different fuel formulations: the binary n-dodecane/m-xylene blend developed in earlier SERDP studies and a four component blend developed under ONR funding. Fuel blends and surrogates modeled using this expanded mechanism are documented in Table 7-1. Additional simulations were made with this mechanism in which iso-octane and m-xylene were separately added to n-dodecane. All the different simulations conducted are summarized below.

Table 7-1 Different Fuel Blends and Surrogates Used with SERDP Kinetic Mechanism.

Fluel Blend	Gaseous Mole %	Fuel
SERDP JP-8	**64.38**	**nC12**
	35.62	**m-Xylene**
ONR-Blend JP-8	**40.5**	**nC16**
	36.9	**m-Xylene**
	18.8	**iso-C12**
	3.8	**nC12**
nC12/nC7	**58.62**	**nC12**
	41.38	**nC7**
nC12/iso-C8	**58.65**	**nC12**
	41.35	**nC7**
nC12/MCH	**58.64**	**nC12**
	41.36	**nC7**
nC12/m-Xylene	**58.6**	**nC12**
	41.4	**nC7**

In addition to the two JP-8 simulations made with the SERDP mechanism, five additional university kinetic mechanisms (and surrogates) were acquired and utilized to simulate the JP-8 LBO experimental data. When using these mechanisms, the surrogate JP-8 formulation utilized in the simulations were those recommended by the mechanism creators. The different mechanisms, number of species and reactions in each mechanism, and surrogate parent fuel compounds and quantities are shown below. (For reference, the UTRC surrogates discussed above are the last two mechanisms in the table.) Furthermore, all the mechanisms were used in conjunction with the same reactor condition profiles discussed above.

Table 7-2 Experimental matrix for n-Dodecane/m-Xylene study.

Mechanism	Species	Reactions	Surrogate Fuel	Mole %
Dooley-Dryer	1599	6633	Toluene	17%
			Iso-Octane	45%
			n-Decane	38%
CREK	233	7005	Iso-Octane	10%
			Methylcylcohexane	20%
			m-Xylene	15%
			n-Dodecane	30%
			Tetralin	5%
			n-Hexadecane	20%
Dagaut	209	1673	n-Decane	74%
			Propylcylcohexane	15%
			Propylbenzene	11%
CSE	834	3208	n-Dodecane	38%
			Iso-Octane	37%
			Propylbenzene	25%
Pietsch/Stanford	394	1992	n-Dodecane	48%
			Methylcylcohexane	27%
			m-Xylene	25%
UTRC	243	1682	n-Dodecane	64%
			m-Xylene	36%
	557	3660	n-Dodecane	4%
			n-Hexadecane	41%
			Iso-Dodecane	19%
			m-Xylene	37%

7.3.2 JP-8 Results from WSR and Analysis

Only four species were sampled real-time from the AFRL JP-8 experiments: formaldehyde, methane, ethene, and acetylene. Thus, comparisons between experimental and simulation profiles for these four compounds will be discussed first. Shown in Figure 7-34 are the comparisons of ethene mole fraction as a function of formaldehyde mole fraction.

The maximum experimental values at LBO are ~175 ppm and ~400 ppm for formaldehyde and ethene, respectively. The CSE mechanism best simulates the ethene versus formaldehyde trend, followed by the Dooley-Dryer (above) and CRECK (below) mechanisms. The Stanford/Mueller/Pitsch mechanism and the UTRC-ONR formulation yield similar ethene-formaldehyde relationships as blowout is approached. The sensitivity to surrogate fuel formulation can be observed by comparing the UTRC-SERDP and UTRC-ONR trends.

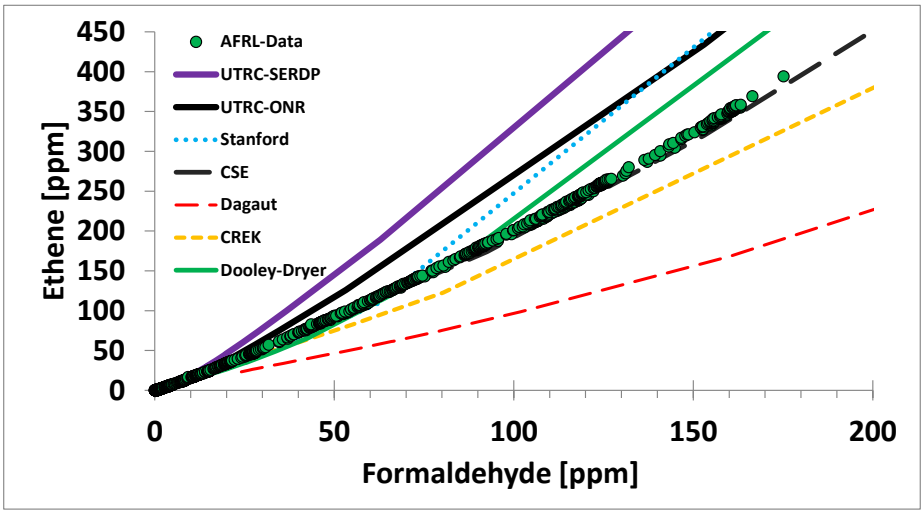

Figure 7-34. Ethene as Function of Formaldehyde for Both Experiment and Simulations.

Although both have essentially the same amount of aromatic (m-xylene, ~36% mole fraction), the SERDP blend has a large normal alkane (nC12) that comprises the other two-thirds of the mixture, but the ONR formulation has 20% of the fuel comprised as an iso-alkane species. Since iso-compounds tend to make less ethene than normal-alkanes, the enhanced ethene formation with the SERDP blend seems consistent with this finding. Surprisingly, even though the Dagaut formulation had nearly 75% n-alkane (nC10), it yielded the lowest values of ethene near blowout.

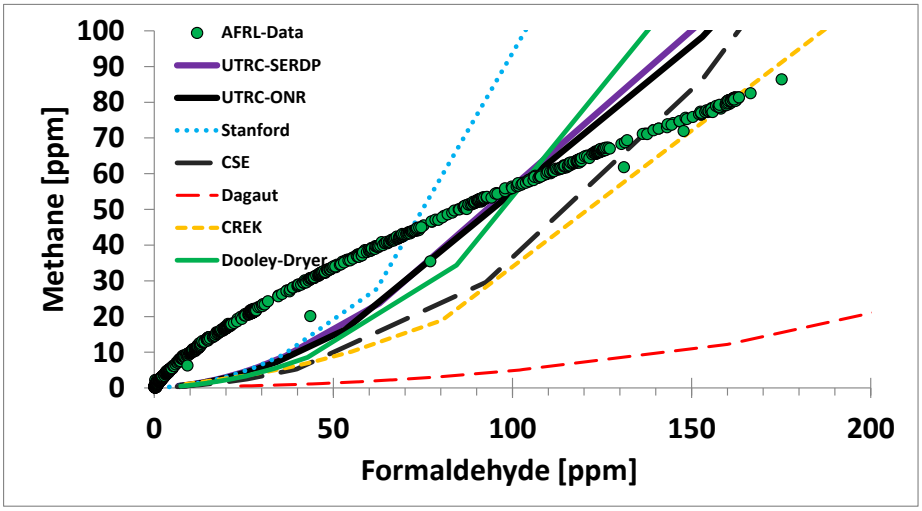

Figure 7-35. Methane as Function of Formaldehyde for Both Experiment and Simulations.

Figure 7-35 compares methane mole fractions to formaldehyde. One interesting feature of these curves is that as blowout is approached, the experimental methane trend has a negative concavity, whereas all the simulation trends exhibit positive concavity. Also, close to blowout (i.e., formaldehyde values near 100 ppm), the simulations all reveal more sensitivity of methane to formaldehyde than is experimentally observed. The trends from the two different UTRC formulations do not reveal a large methane sensitivity to the JP-8 surrogate definitions used. Most of the simulations were comparable in terms of methane

selectivity. The Stanford/Mueller/Pietsch mechanism showed a slightly larger sensitivity of methane to formaldehyde formation. Once again, the Dagaut mechanism yielded the lowest levels of methane formation versus formaldehyde formation.

Next, comparisons between acetylene mole fractions and formaldehyde are given in Figure 7-36. Though not as dramatic as the methane profiles, there is again a difference in concavity between the experimental and simulation profiles. Both UTRC formulations and the Dooley-Dryer mechanism yield values that are slightly higher than the experimental data at blowout. Similarly, the CREK mechanism yields values slightly lower than the experiment at blowout. Since once again the Dagaut mechanism is under-predicting acetylene formation, one explanation is that the mechanism may have some underlying discrepancies within the formaldehyde formation/consumption pathways in the model.

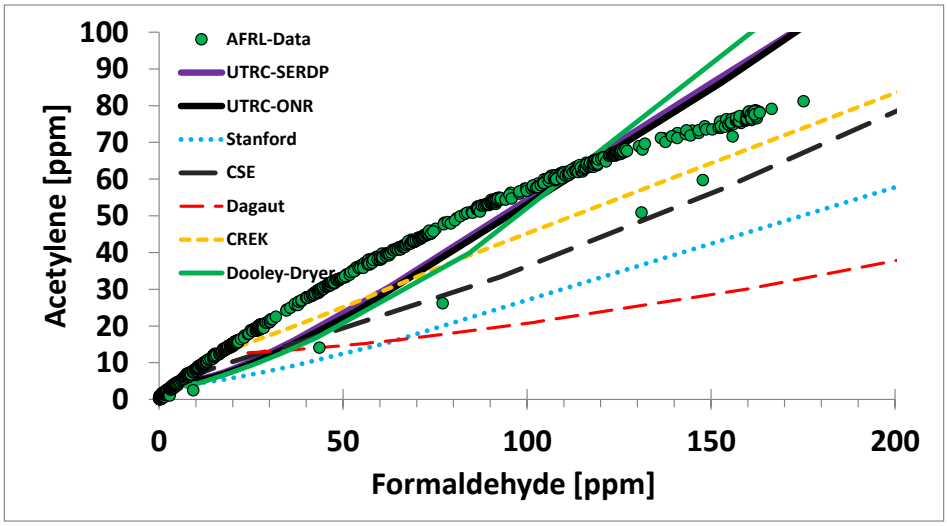

Figure 7-36. Acetylene as Function of Formaldehyde for Both Experiment and Simulations.

7.3.3 Predictions of HAPs from JP-8

Based on the reasonable agreement between these simulations and experimental data for the above four compounds, a preliminary extension to other intermediate compounds, especially those that are other important HAPS precursors or HAPS themselves, can be made and is discussed below.

One intermediate that is a strong HAPS precursor is propene and its trends versus formaldehyde are shown in Figure 7-37. Based on the simulations, the propene mole fractions at blowout should be comparable to those of methane and acetylene. 1-Butene is another HAPS precursor whose trends can be observed and its profiles are given in Figure 7-38. Both the UTRC and CRECK surrogates/mechanisms yield the highest sensitivities of 1-butene to formaldehyde. Even at these highest levels, 1-butene is predicted to be significantly lower than propene levels at blowout. Furthermore, note the two different UTRC formulations reveal a slight difference in 1-butene sensitivity. The SERDP binary fuel formulation, with its higher levels of n-alkane percent in the parent fuel generates nearly twice as much 1-butene as does the four component fuel blend. The additional fuel present in the four fuel blend, iso-dodecane, do not yield large amounts of 1-butene. Hence, these results seem consistent. While iso-alkanes do not yield large amounts of 1-butene, they do lead to large amounts of iso-butene, another HAPS precursor compound. Thus, shown in Figure 7-39 is iso-butene sensitivity to formaldehyde mole fractions. As expected, the four

binary fuel mixtures with iso-alkanes present in the surrogate (Dooley-Dryer, CSE, CRECK, and UTRC-ONR) yield the highest levels of the iso-butene compound. Conversely, the other three blends that have no iso-alkanes form no iso-butene at any reactor condition.

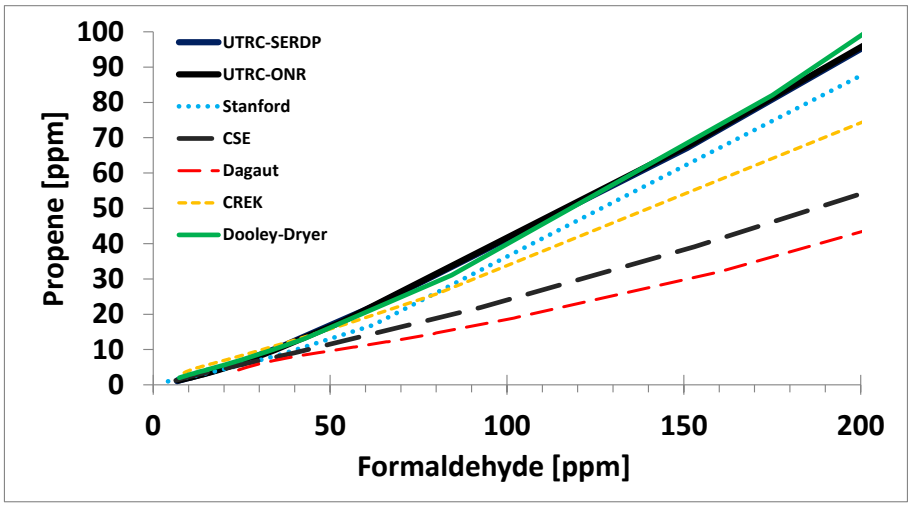

Figure 7-37. Simulations of Propene as Function of Formaldehyde.

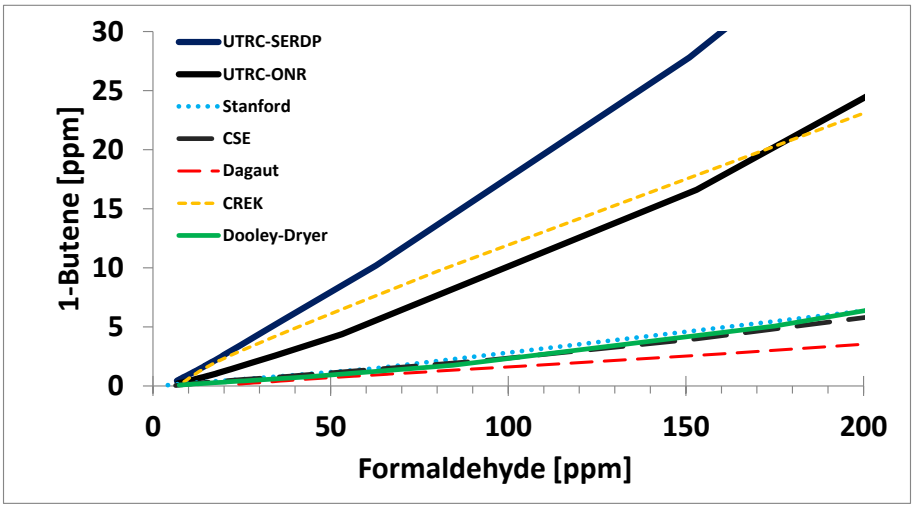

Figure 7-38. Simulations of 1-Butene as Function of Formaldehyde.

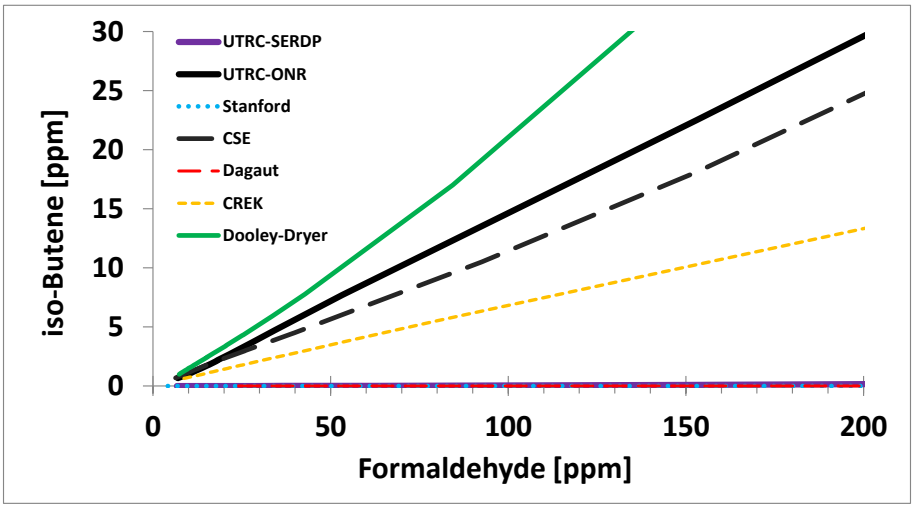

Figure 7-39. Simulations of Iso-Butene as Function of Formaldehyde.

The last two compounds to be discussed, 1,3-butadiene and benzene, are HAPS and their trend profiles are shown in the Figure 7-40 and Figure 7-41, respectively. Interestingly, the levels of both compounds are very close to each other. The model with the highest emissions levels at blowout (Stanford/Mueller/Pitsch) would put both 1,3-butadiene and benzene emissions at approximately half the levels of methane, acetylene, and propene. Both UTRC JP-8 surrogate fuel formulations show nearly identical sensitivity profiles for both 1,3-butadiene and benzene. Since both blends have the same amount of m-xylene in the surrogate definition, the identical levels of benzene formation are not surprising.

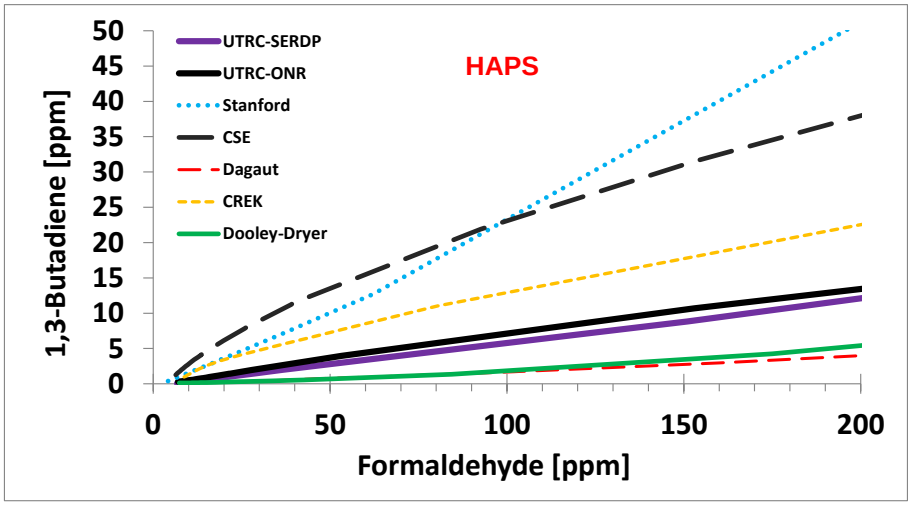

Figure 7-40. Simulations of 1,3-Butadiene as Function of Formaldehyde.

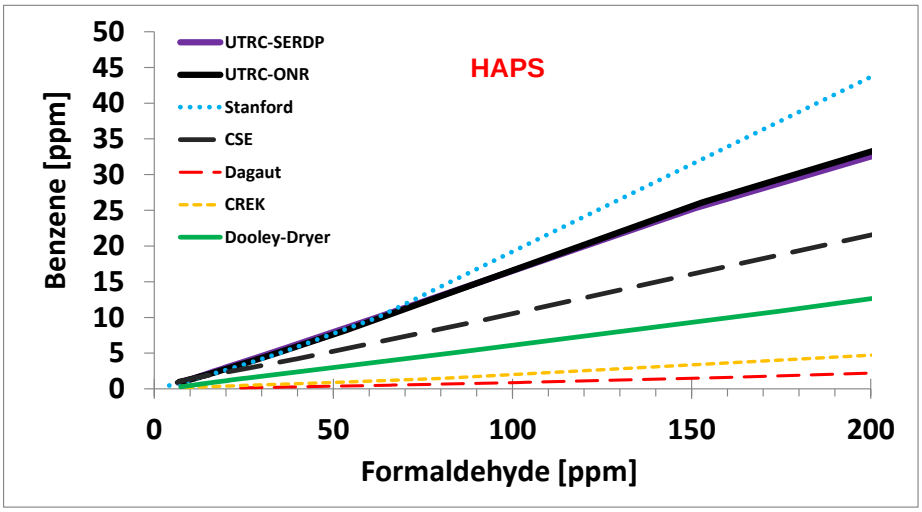

Figure 7-41. Simulations of Benzene as Function of Formaldehyde.

7.3.4 Simulation of Emissions for LBO Experiments for Binary Fuel Blends

7.3.4.1 "Absolute" Emission Profiles

Comparisons between predictions and experiments for pure n-dodecane and the four binary mixtures used in this study will be now be discussed. All experimental results presented in this section are taken from experiments conducted after the reactor material was changed to enhance repeatability of the data.

Figure 7-42 compares the experimental and simulation ethene emissions as functions of equivalence ratio for the various tested fuels. Best results were obtained when solving the coupled species-energy equation (solid lines). At large equivalence ratios, the simulations generate higher emissions of ethene than the experiments. As blowout is approached, the emissions levels rise for both the experiments and simulations. The simulations reasonably capture the magnitude of the increases in the experimental emissions, albeit at shifted equivalence ratios. Specifically, the emissions from the simulations peak in the 0.34-0.375 equivalence ratio range versus the experimental 0.425 range. Also, these coupled species-energy conservation simulations yield reactor blowout at lower levels of emissions than for the experimental emissions.

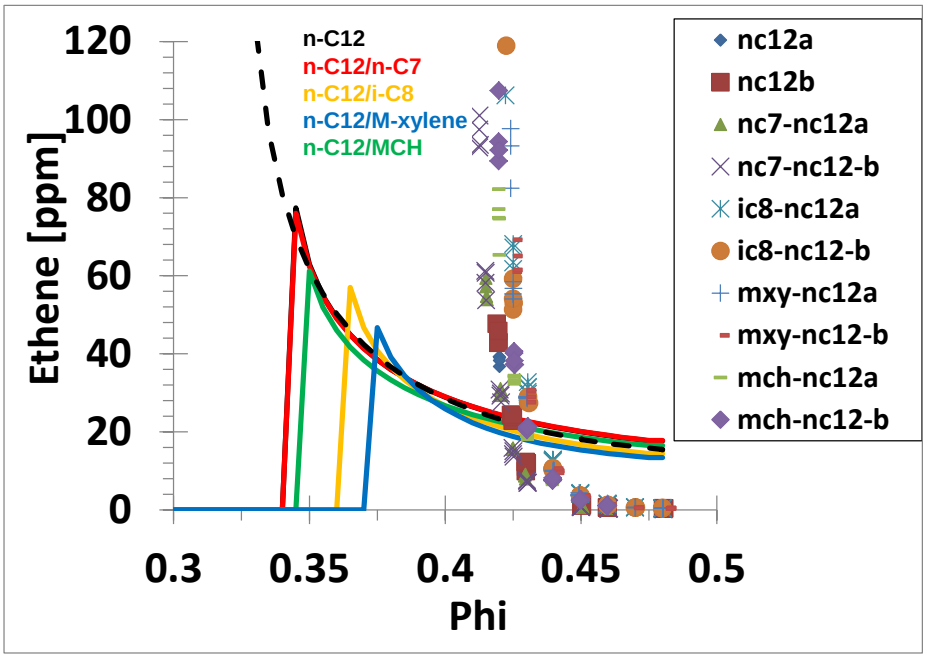

Figure 7-42. Comparison of Experimental and Simulation Ethene Profiles as Functions of Equivalence Ratio and Fuel Compositions (Dashed line represents simulation results at fixed temperature).

The dashed line in Figure 7-42 represents the ethene emissions associated with the fixed temperature profile calculations and shows that at slightly leaner than blowout equivalence ratios the ethene emissions match the experimental values.

The experiments demonstrated a small fuel effect: the two normal alkane fuel blends (n-dodecane and n-dodecane/n-heptane) have slightly leaner blowout equivalence ratios (depicted as the near vertical drop to the baseline) than the other fuel blends. However, since the simulation equivalence ratio range for all the fuel blends is exaggerated relative to the experimental range, the other blend simulations do not generate as high ethene values before blowout.

Comparison of the simulations and experimental results for emissions of methane, acetylene, and formaldehyde, are shown in Figure 7-43, Figure 7-44, and Figure 7-45, respectively. These comparison also show that the coupled species-energy conservation simulations yield emissions that are comparable to the experimental values at lower equivalence ratios and that the simulations blow-out before these levels match the experimental values. However, the fixed temperature profiles generate emissions that match the levels observed in the experiments at equivalence ratios below the blowout equivalence ratios.

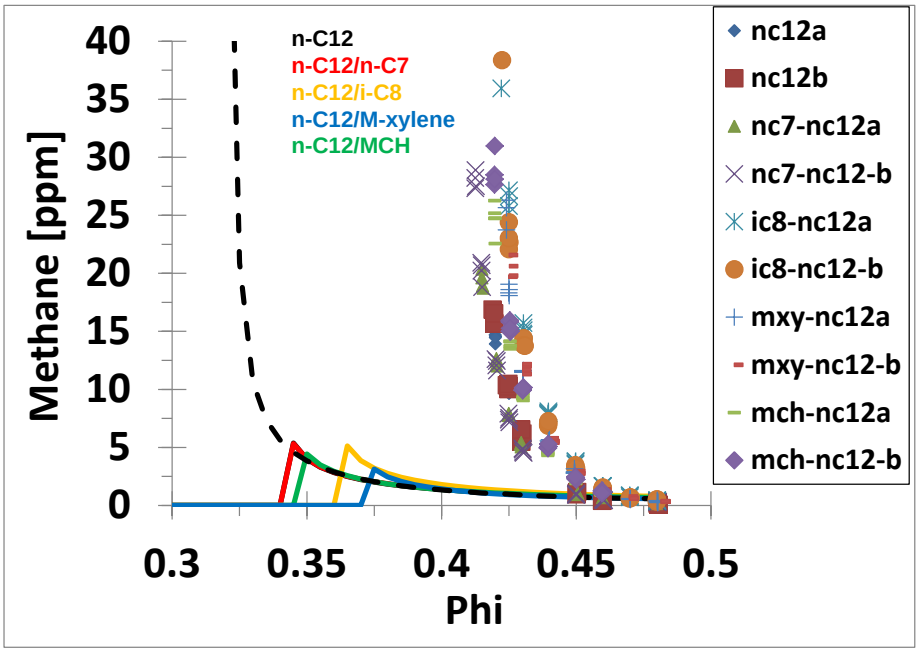

Figure 7-43. Comparison of Experimental and Simulation Methane Profiles as Functions of Equivalence Ratio and Fuel Compositions.

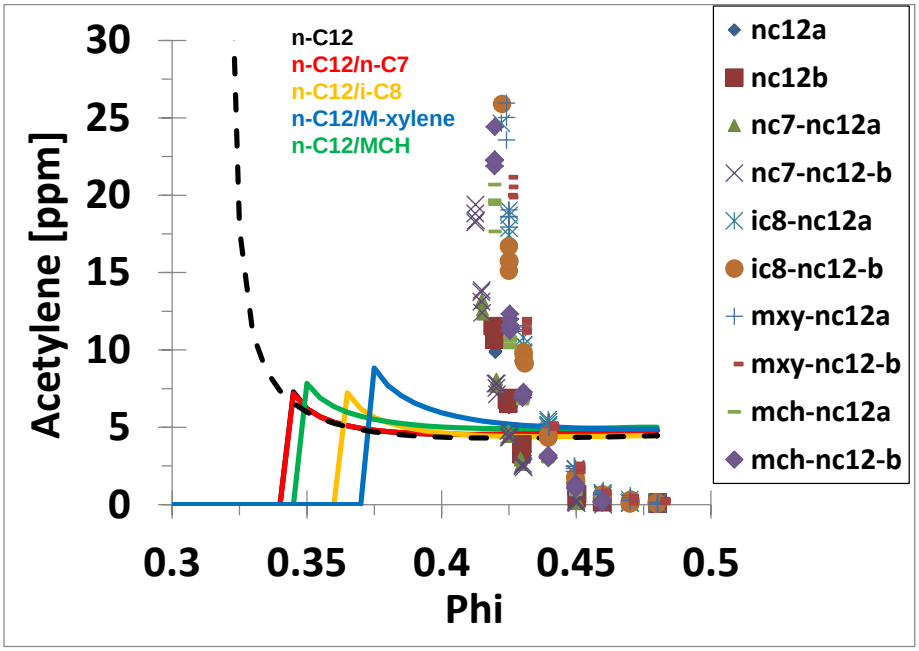

Figure 7-44. Comparison of Experimental and Simulation Acetylene Profiles as Functions of Equivalence Ratio and Fuel Compositions.

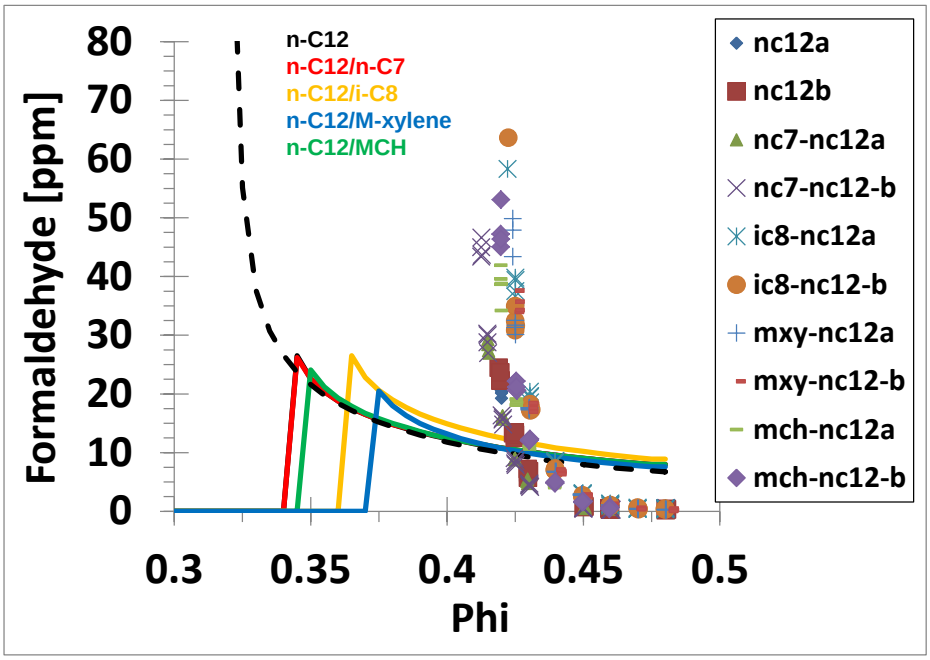

Figure 7-45. Comparison of Experimental and Simulation Formaldehyde Profiles as Functions of Equivalence Ratio and Fuel Compositions.

Interestingly, the comparison of CO emissions as blowout is approached is slightly different than the hydrocarbon emission profiles. This comparison is shown in Figure 7-46. Whereas the coupled species-energy conservation simulation hydrocarbon emissions are below the experimental blowout emission values and the fixed temperature simulations yield experimental emissions levels, the CO emissions for the coupled simulations are very close to the experimental values and the values from the fixed temperature solutions markedly exceed the experimental CO emissions. This finding is consistent with the results of the sensitivity analysis and illustrates the importance of CO oxidation on system heat release and LBO.

Analysis of the fixed temperature simulations reveal the notion of threshold temperature necessary to completely oxidize the formaldehyde generated in the system. Furthermore, this notional threshold temperature appears to be a function of the particular fuel composition. Evidence for this conclusion is shown in Figure 7-47.

The figure illustrates both formaldehyde production and consumption rates and formaldehyde mole fraction levels as functions of reactor temperature. As shown, above a specific temperature, formaldehyde production and consumption is identical. Consequently, formaldehyde reactor concentrations are essentially zero. However, below this temperature, production exceeds consumption and formaldehyde mole fractions rapidly grow as the reactor temperature is reduced from this threshold temperature. Furthermore, for the n-dodecane/n-heptane blend, comparison of this threshold temperature (~1200 K) to the corresponding reactor blowout temperature (~1255 K) suggests a reason why the coupled species-energy simulations do not generate emission levels that are as high as the experimental values. Since the reactor blowout temperature exceeds this threshold temperature, formaldehyde production and consumption rates are essentially in equilibrium and cannot rise sufficiently before blowout occurs. This finding is applicable to all the fuel blends simulated.

Figure 7-48 continues this analysis of reactor emissions when the reactor temperature is below this threshold temperature condition. Essentially, near this threshold temperature where formaldehyde levels begin to grow (~1200 K), the molecular oxygen consumption rate is abruptly decreased. In contrast, both fuel consumption rates are not dramatically decreased. Consequently, as the system oxidation rates are decreasing, allowing formaldehyde concentrations to grow, the fuel pyrolysis rates are much less affected and ensuing hydrocarbon emissions are directly related to the fuel pyrolysis chemistry. This pyrolysis chemistry and ensuing emissions are a direct consequence of fuel composition. As above, these findings of fuel pyrolysis chemistry driving near-LBO emissions are applicable to all the simulated fuel blends.

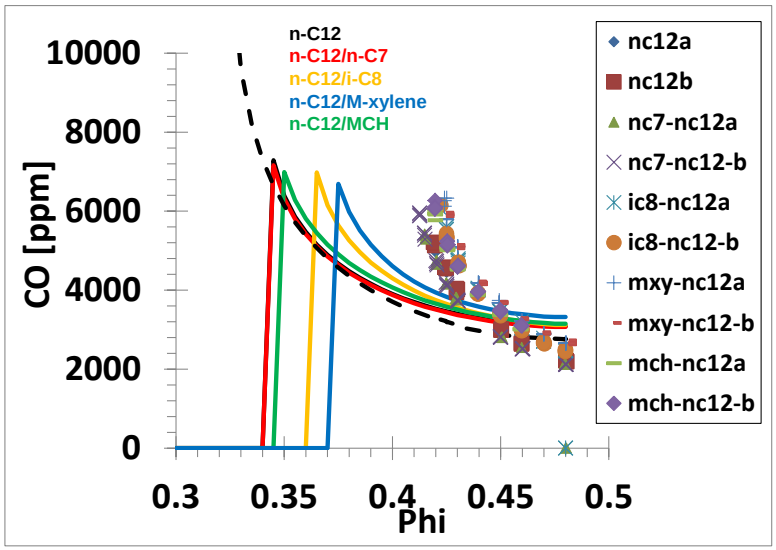

Figure 7-46. Comparison of Experimental and Simulation CO Profiles as Functions of Equivalence Ratio and Fuel Compositions.

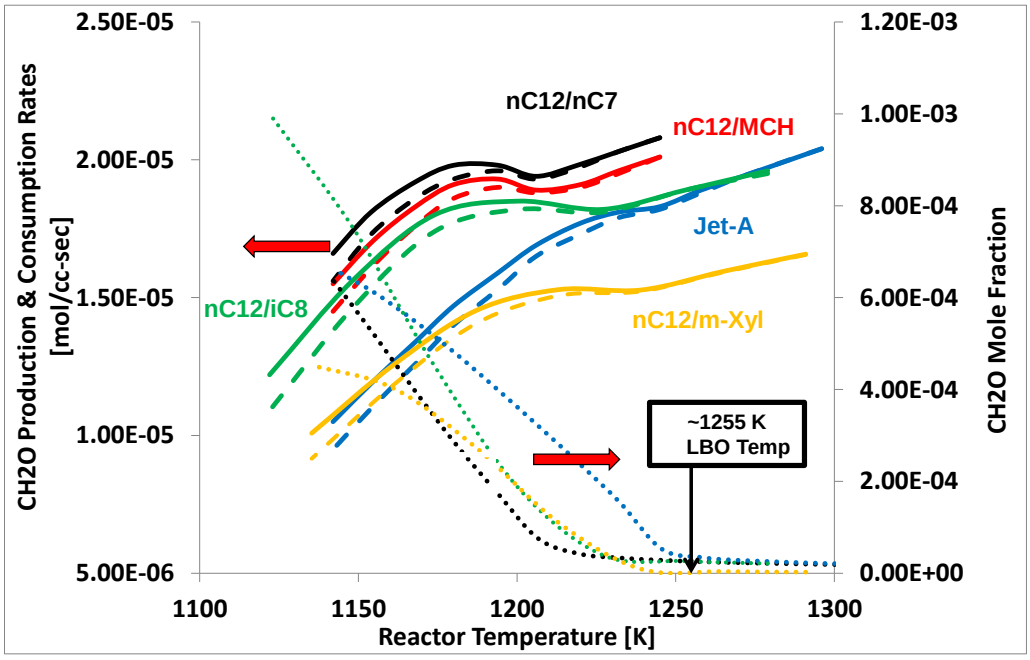

Figure 7-47. Formaldehyde Production (solid) and Consumption (dashed) Rates and Formaldehyde Mole Fraction Levels (dotted) as Functions of Reactor Temperature for All Tested Fuels (simulations).

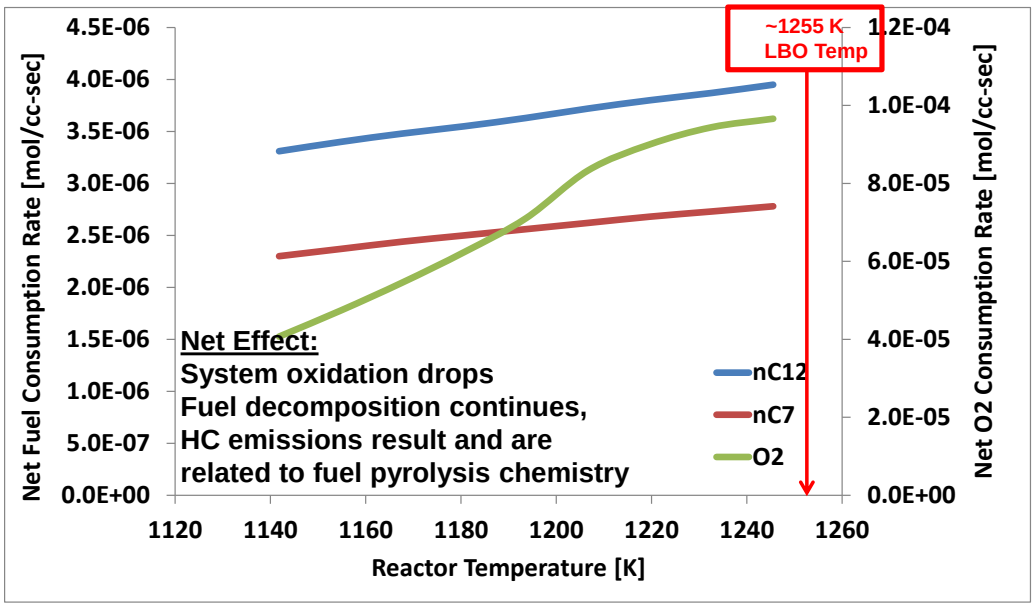

Figure 7-48. Net Fuel and O2 Consumption Rates for the n-Dodecane/n-Heptane Fuel Blend.

7.3.4.2 Cross-plotted Emission Profiles

Although the analysis presented in the prior section revealed that the experimental and modeling emissions data are offset with respect to equivalence ratio, when the emission data are cross-plotted

parametrically against a concurrent emittant (e.g., formaldehyde), the experimental and simulation trends agree quite well, as was demonstrated in the analysis of the JP-8 data. Plots for ethene emissions as functions of formaldehyde emissions are shown in Figure 7-49. The simulation (fixed temperature profile) trends and the experimental trends are in good agreement. Similar results are obtained for the methane and acetylene profiles.

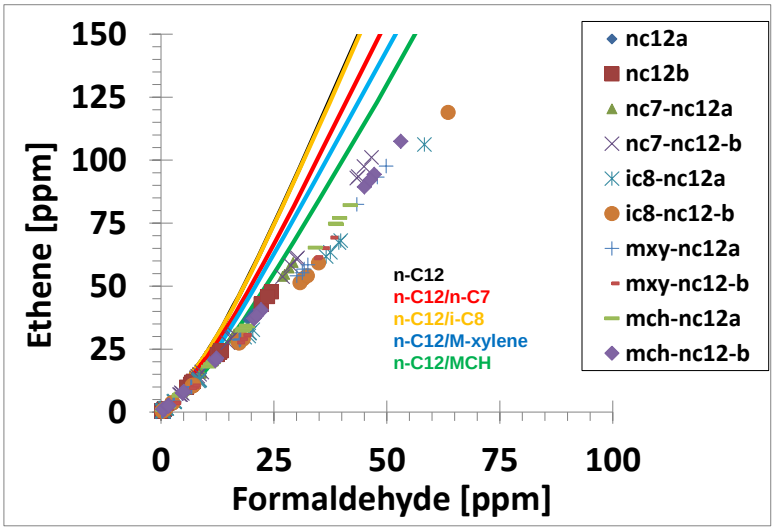

Figure 7-49. Comparison of Experimental and Simulation Ethene Profiles as Functions of Formaldehyde Emissions and Fuel Compositions.

The effect of fuel composition on hydrocarbon emissions is also reasonably captured. For instance, hydrocarbon fragments that are expected to preferentially form due to parent fuel structure show similar trends. Specifically, it is expected that iso-butene and toluene would preferentially form from the binary fuel blends of iso-octane/n-dodecane and m-xylene/n-dodecane, respectively. Figure 7-50 and Figure 7-51 present results that demonstrate for these expected relationships between fuel composition and emissions. The kinetic mechanism and simulation approach is capable to capturing HAPs emissions as well. This capability is demonstrated in Figure 7-52 for 1,3-butadiene emissions.

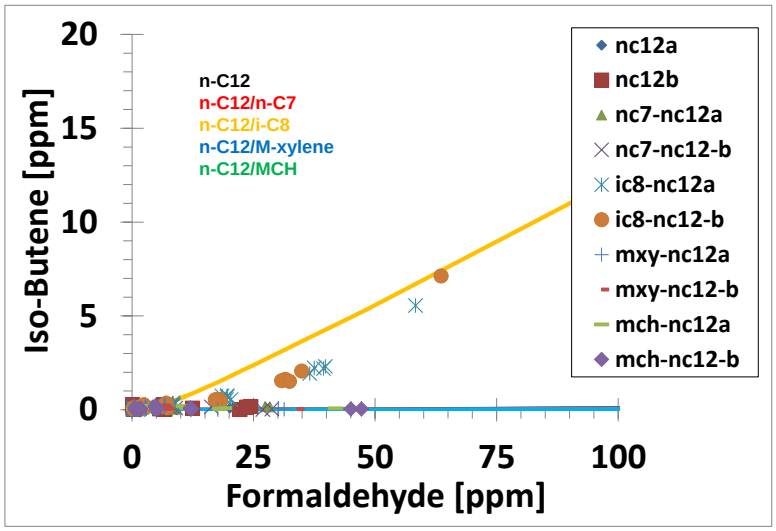

Figure 7-50. Comparison of Experimental and Simulation iso-Butene Profiles as Functions of Formaldehyde Emissions and Fuel Compositions.

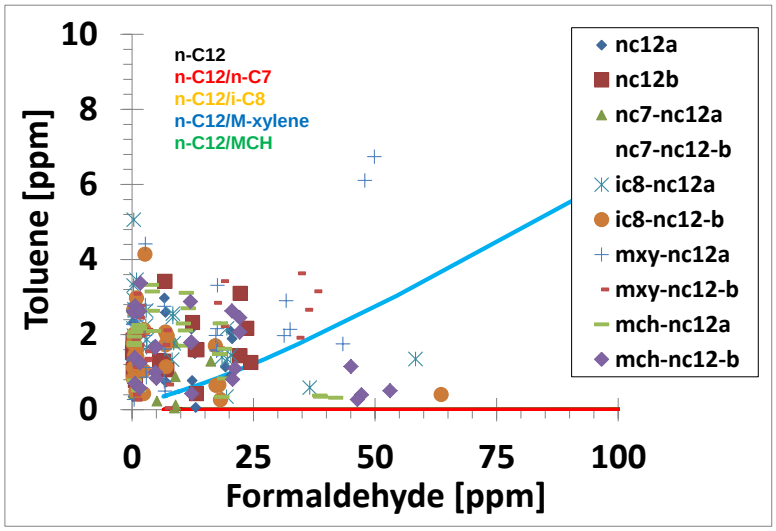

Figure 7-51. Comparison of Experimental and Simulation Toluene Profiles as Functions of Formaldehyde Emissions and Fuel Compositions.

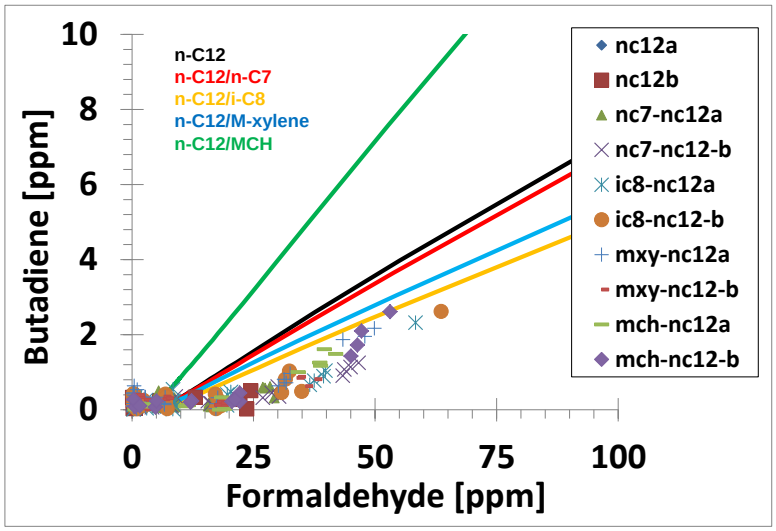

Figure 7-52. Comparison of Experimental and Simulation 1,3-Butadiene Profiles as Functions of Formaldehyde Emissions and Fuel Compositions.

7.3.4.3 Understanding the Impact of Fuel Composition on WSR LBO Performance

The objective of this analysis was to test the hypothesis that the reactor LBO is governed by the interactions between the unreacted flow potential core exiting the reactor ring jets and the recirculated burned gases comprising the bulk of the reactor. Essentially, the analysis approach involved computing the ignition delay times of various gas packets whose mixtures ranged from all burned gas to all unburned gas and comparing this time to the nominal convection time of the unburned gases through the potential core region of the ring jets. The hypothesis was that for equivalence ratios above the blowout equivalence ratio, there would always exist a parcel whose ignition time was faster than the convection time through the potential core, but at blowout equivalence ratios and below, the ignition times would be longer than the convection time. The rationale for the hypothesis was that shear layer between the jets and main reactor burned gases serves as the stabilizing force for reactor operation. Further, that as the unburned gases exit the jet and roll up with the burned gases there will exist an eddy that can ignite within the time that parcel is within the vicinity of the jet potential core.

Estimation of the relevant characteristic times is as follows. The jets have a diameter of one millimeter. Previous analysis (Briones et al., 2008) of the reactor has estimated the length of the potential core region to be on the order of three to five jet diameters. The Mach number of the jet exit flow is on the order of 0.7 to 0.8. Thus, the appropriate characteristic time through the potential core is on the order of 20 microseconds (i.e., L/V). The relevant ignition times were computed as functions of equivalence ratio and the ratio of burned gas and unburned gas mass fractions. The burned gas properties were assumed to be the corresponding equilibrium conditions based on considered equivalence ratio. The parcel temperature and composition were the mass-weighted sums of the burned and unburned gases. Based on these initial conditions and the SERDP chemical kinetic mechanism, constant volume ignition times [Lutz et al.] were computed for the various mixtures. Shown in Figure 7-53 are the ratios of ignition delay times associated with several mass weighted mixtures of unburned-burned gases at several equivalence ratios for the five fuel blends tested and a constant weighted estimate of the unburned gas transit time through the potential

core (more will be said on the constant below). The dashed line represents conditions in which these times are equal; that is, the characteristic Damkohler number is one. As anticipated, the higher equivalence ratio systems (Φ=0.5, 0.48) yield wider mixture ranges whose ignition times are greater than the convective time and these ranges are in the vicinity of 10% unburned gas and 90% burned gas. Furthermore, as the equivalence ratio is reduced, the range of mixtures that yield sub-unity Damkohler numbers shrinks and by an equivalence ratio of 0.38, all fuel blends produce no mixtures whose ignition times are faster than the modified convective times and would thus be considered "blown out."

The one unresolved aspect of this analysis is characterizing the mixture fraction range which corresponds to the actual mixtures found in the ring jet shear layers. If there is a characteristic mixture within the shear layer, that finding would better define the appropriate blowout conditions. (It is believed that CFD analysis of the WSR could answer this question.)

To gain some insight into better characterization of the blowout process, a slightly modified analysis was utilized. In this modified approach, correlations of equilibrium temperatures as functions of equivalence ratio and ignition delay times as functions of initial temperature were generated for each of the five tested fuel blends, as shown in Figure 7-54 and Figure 7-55, respectively.

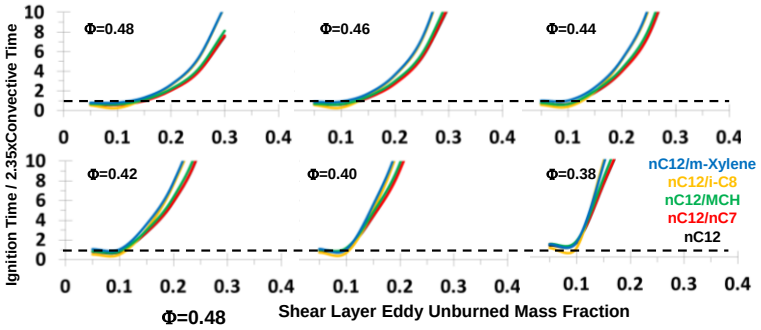

Figure 7-53. Comparison of Potential Core Convection Time and Ignition Times as Functions of Equivalence Ratio and Mixture Fraction for n-Dodecane/Air Mixtures.

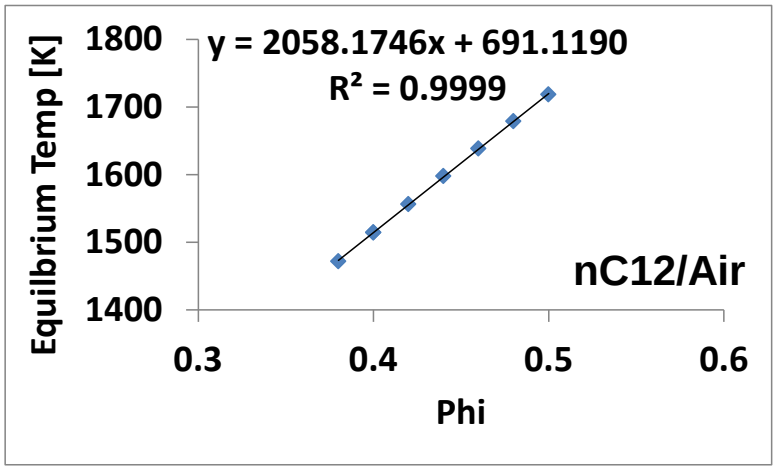

Figure 7-54. Equilibrium Gas Temperatures as functions of Equivalence Ratio (and resulting correlation) for n-Dodecane/Air Mixtures.

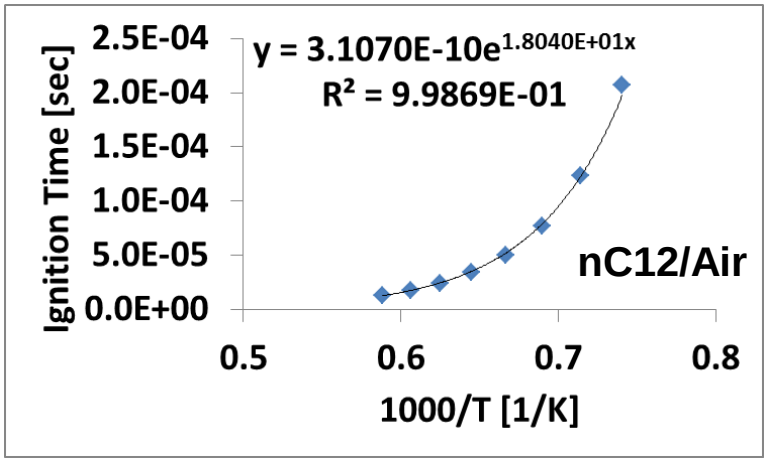

Figure 7-55. Ignition Delay Times as functions of Initial Mixture Temperature (and resulting correlation) for n-Dodecane/Air Mixtures.

With these correlations, an iterative procedure was generated in which a limiting ignition time was chosen (based on the potential core convective time) and the corresponding initial temperature determined from the correlation in Fig. 7-36. Then, knowing this initial temperature, the corresponding equivalence ratio was determined from Fig. 7-35. Any equivalence ratio below this value would generate an equilibrium temperature that would not be able to yield a mixture whose ignition delay time was equal to the limiting time. Thus, an unambiguous blowout equivalence ratio was determined. For this analysis, a factor of 2.35 was used on a core convective time based on three jet diameters (~ 11 μsec), so that the limiting ignition time was 25.92 μsec. (This time was chosen to "anchor" these modeling results to the experimental blowout equivalence ratio for the nC12/air fuels. Furthermore, this time is well within the range of shear layer mixing times (1-80 μsec) deduced from the above CFD analysis of Briones et al.)

The final results of this analysis are given in Table 1 and the comparison of these blowout equivalence ratios to the experimental and PSR blowout based equivalence ratios are shown in Fig. 7-37. As indicated, these critical Damkohler number values agree quite well with the experimental blowout values and yield results whose equivalence ratios are not as low as the perfectly mixed PSR blowout equivalence

ratios (Glarborg et al., 1986). Whereas the HC emissions at near-LBO conditions are more strongly coupled to the fuel composition, due to the importance of fuel pyrolysis chemistry, it would appear that the equivalence ratio at LBO is less sensitive to fuel compositional effects. This conclusion is consistent with the earlier analysis that indicated LBO is more affected by global heat release rates.

Table 7-3. Limiting Equivalence Ratios, Ignition Temperatures and Times.

	Phi	T-eq [K]		Ign. Temp [K]	Ign. Time [sec]
nC12	0.4203	1550.00		1550.00	2.592E-05
nC12/nC7	0.4198	1548.32		1548.32	2.592E-05
nC12/iC8	0.4335	1575.82		1575.82	2.592E-05
nC12/MCH	0.4250	1559.38		1559.38	2.592E-05
nC12/mXyl	0.4377	1592.00		1592.00	2.592E-05

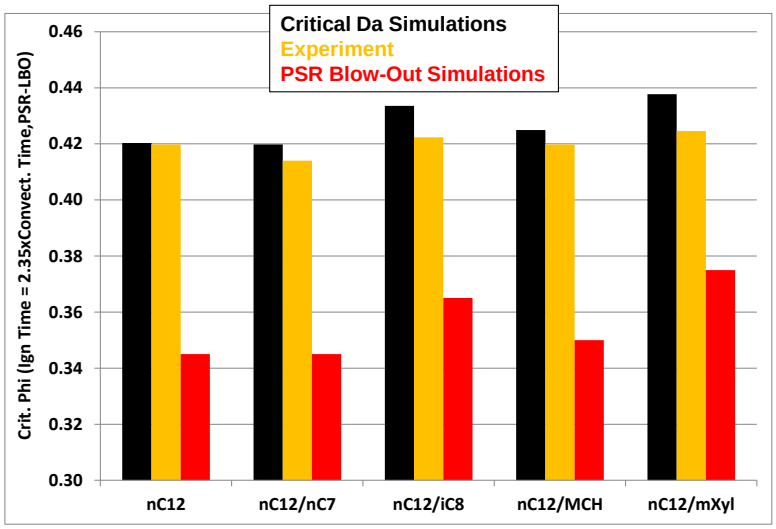

Figure 7-56. Critical Blowout Equivalence Ratios for the Five Tested Fuel Blends.

7.4 UNICORN Modeling Results for m-xylene/dodecane

We have developed UNICORN-0D for calculating chemical kinetics that is taking place in WSR. Several calculations for m-xylene/n-dodecane mixtures are performed with UNICORN-0D integrated with SERDP-2011-PAH mechanism and compared with the measurements. Results obtained for the SERDP mixture (77% n-dodecane and 23% m-xylene) are shown in Figure 7-57 through Figure 7-62. Calculations are initially performed using adiabatic environment. Computed temperatures are consistently well above the measured values as shown in Figure 7-57. Note that the radiation correction applied to the thermocouple measurements (TC Data) did not result temperatures as high as those predicted with adiabatic constraint. Since the WSR rig is not well insulated it is expected that there will be some heat losses through the reactor walls. Even though such heat losses generally depend on the reactor temperature (or in other words equivalence ratio) it will be a cumbersome process for determining the amount of heat loss through trial-and-error process for each equivalence-ratio case. Alternatively, calculations are performed assuming that a fixed percentage of heat generated through combustion is lost through radiation for each equivalence-

ratio case. Results obtained with a 3% heat loss (shown in Figure 7-57) agree reasonably with the corrected TC data.

Computed concentrations for the major species are compared with the probe measurements in Figure 7-58. Results obtained with adiabatic constraint are shown with solid lines and those obtained with 3% heat loss are shown with broken lines. Interestingly, heat loss from WSR did not impact the major species (CO_2, CO and H_2O) significantly. On the other hand, comparisons with measurements are not that satisfactory for CO and CO_2 and reasonable for H_2O and O_2. The discrepancy between the calculations and measurements are observed in other studies and could be associated with the probe measurement technique. Comparisons between computed and measured concentrations for some minor species are shown in Figure 7-59. Reasonable comparisons are obtained for CH_4, CH_2O, C_2H_2 and C_2H_4. Adding heat loss did not affect these species also that much. Data in Figure 7-59 are re-plotted in terms of emission index (EI) and with respect to EI of C_2H_4 in Figure 7-60, Figure 7-61, and Figure 7-62. The computed and measured correlations between EI-C_2H_4 and EI-C_2H_2 are qualitatively in good agreement (Figure 7-60). EI-C_2H_2 increased more than EI-C_2H_4 initially and then reached a plateau for higher EI-C_2H_4 values. The initial rise in the calculated and measured EIs could be fitted with a straight line, suggesting that for small values these two species possess a linear relationship. The behavior of calculated EI-CH_2O with respect to EI-C_2H_4 also qualitatively agrees with that observed in the measurements. EI-CH_2O is increasing linearly with EI-C_2H_4 initially, then remained nearly unchanged for intermediate values if EI-C_2H_4 and then increased again for larger EI-C_2H_4 values. Experimental data showed these trends even though, the mid plateau region is not that obvious from these limited measurements. Note that computed values of EI-C_2H_4 are higher than the measurements and those of EI-CH_2O are lower. The computed and measured correlations between EI-CH_4 and EI-C_2H_4 are shown in Figure 7-62. These species show a linear relationship between them not only for lower values but also for higher values (with a different slope).

Sensitivity of mixture composition on combustion is studied through varying the m-xylene-to-n-dodecane ratio in the fuel. The concentration of m-Xylene is increased by 5% in one case and decreased by 5% in the other case and the results are compared with the base case of 23% m-xylene. Surprisingly, changing the m-xylene by ±5% variation in m-xylene did not show any differences in the temperature (Figure 7-63) or in the species concentrations (Figure 7-64 through Figure 7-66) with an exception to benzene. Concentration of benzene increased with the level of m-xylene in the fuel for all equivalence ratios. This suggests that soot might also increase with m-xylene. This agrees with our previous findings on soot in m-xylene-added ethylene flames.

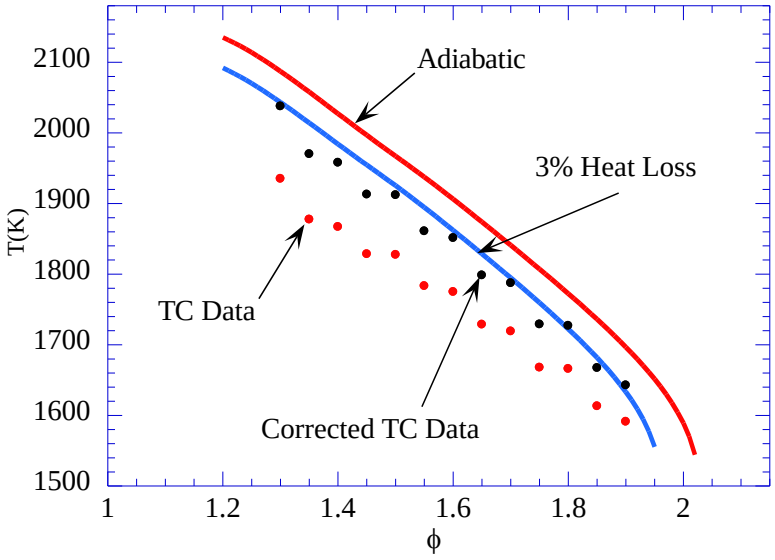

Figure 7-57. Measured and computed temperatures obtained for WSR operating at different equivalence ratios.

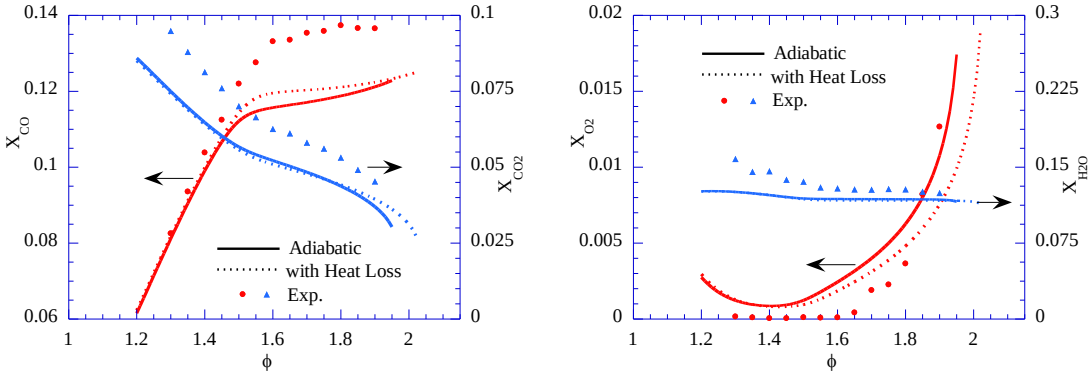

Figure 7-58. Measured and computed concentrations of major species obtained in WSR.

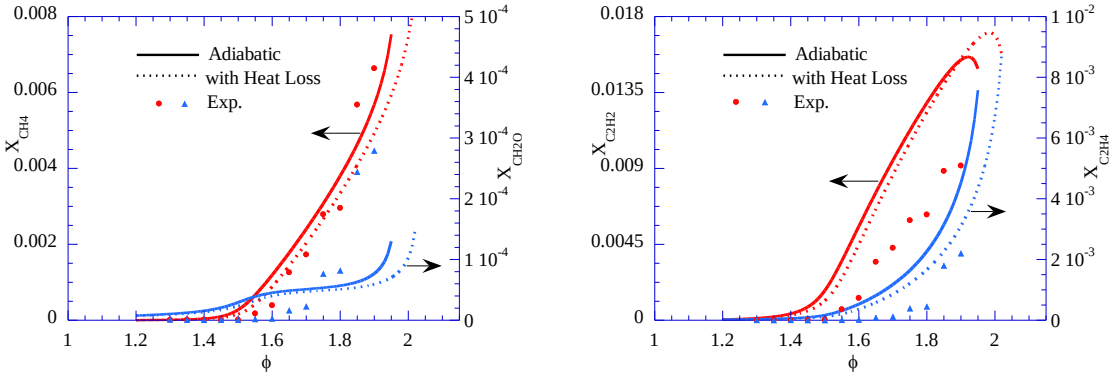

Figure 7-59. Measured and computed concentrations of minor species obtained in WSR.

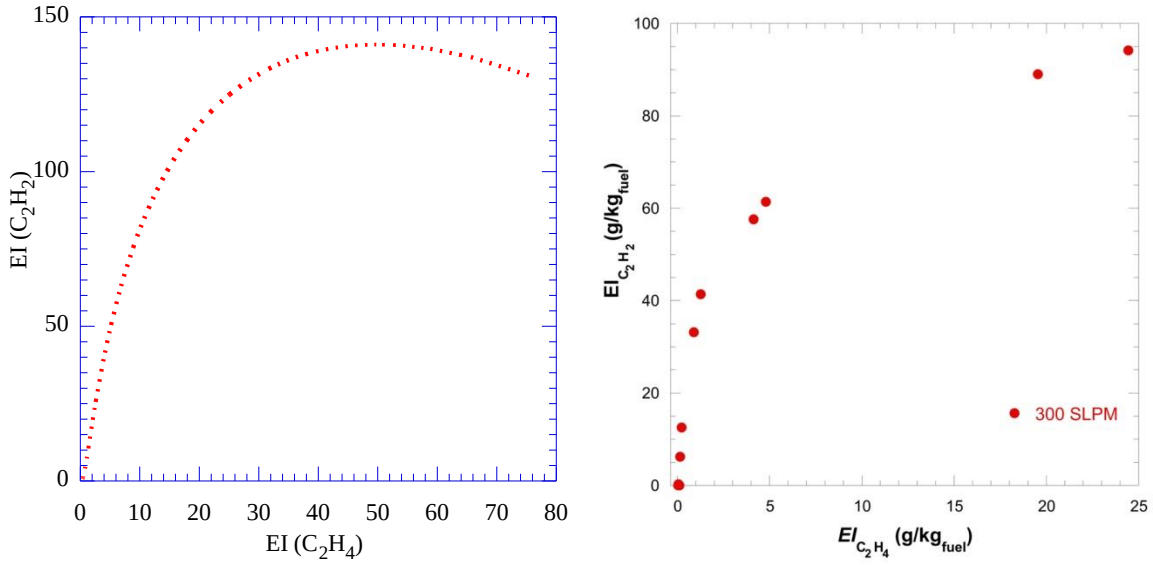

Figure 7-60. Correlations between emission indices obtained for acetylene and ethylene in WSR (a) computed and (b) measured distributions.

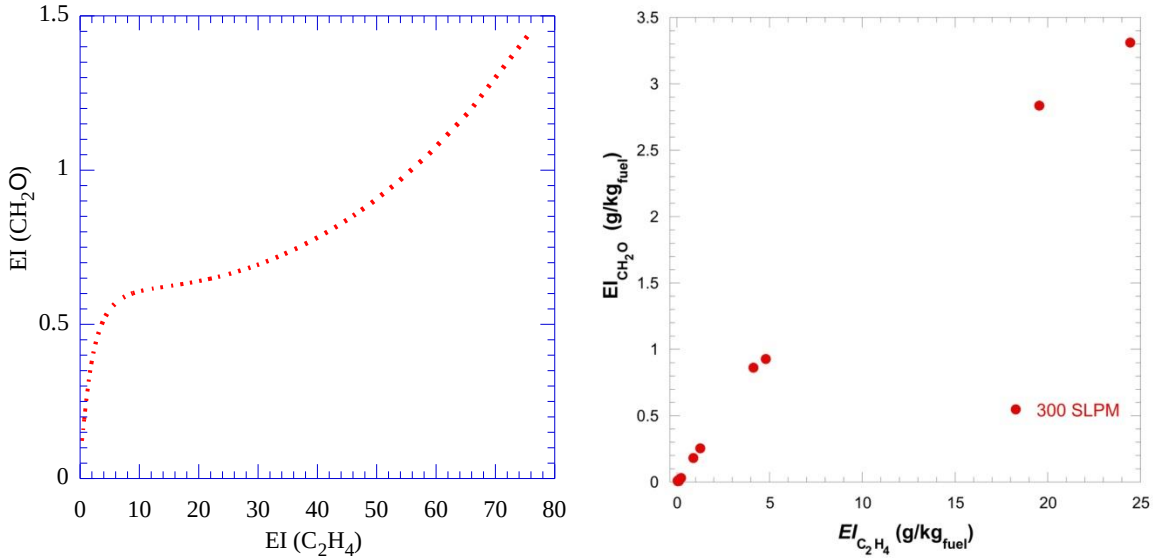

Figure 7-61. Correlations between emission indices obtained for formaldehyde and ethylene in WSR (a) computed and (b) measured distributions.

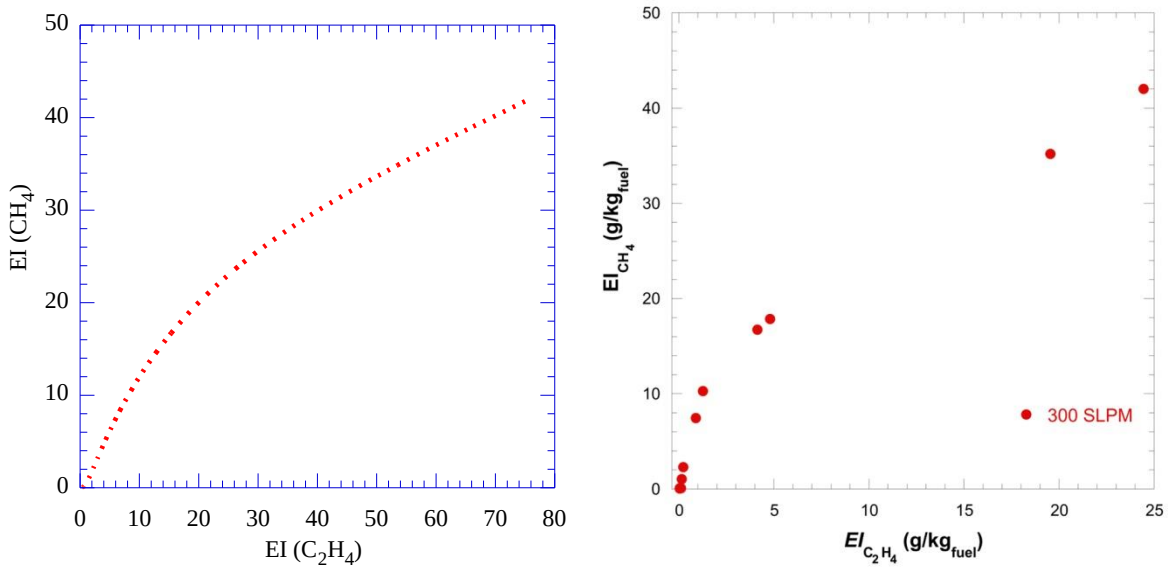

Figure 7-62. Correlations between emission indices obtained for methane and ethylene in WSR (a) computed and (b) measured distributions.

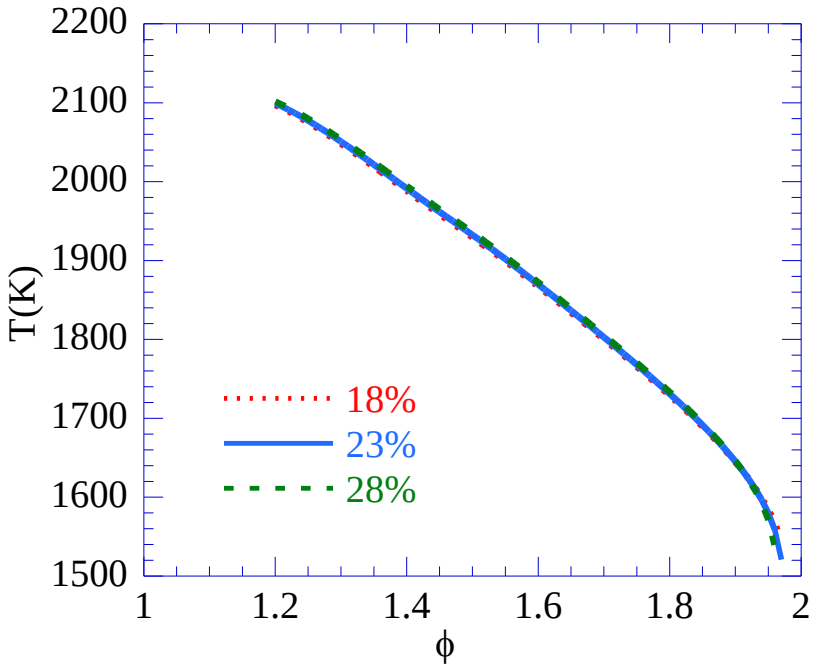

Figure 7-63. Temperature sensitivity in WSR to mixture composition for m-xylene and n-dodecane components.

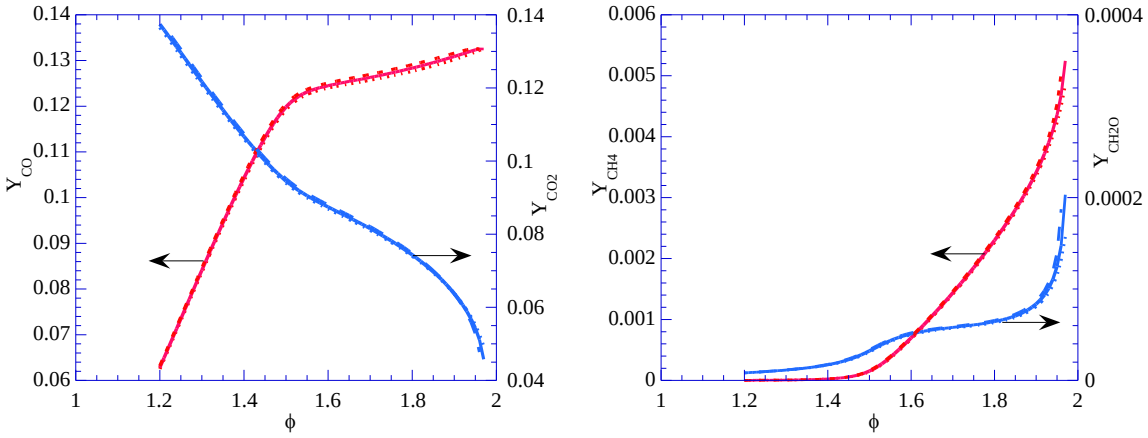

Figure 7-64. Changes in major species concentrations in WSR due to variations in composition for m-xylene-n-dodecane mixtures.

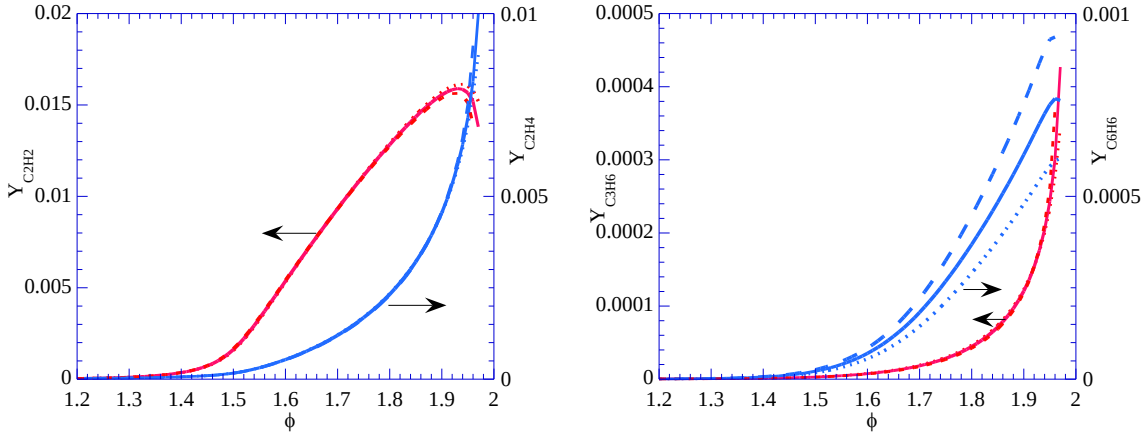

Figure 7-65. Changes in UHC in WSR due to variations in composition for m-xylene-n-dodecane mixtures.

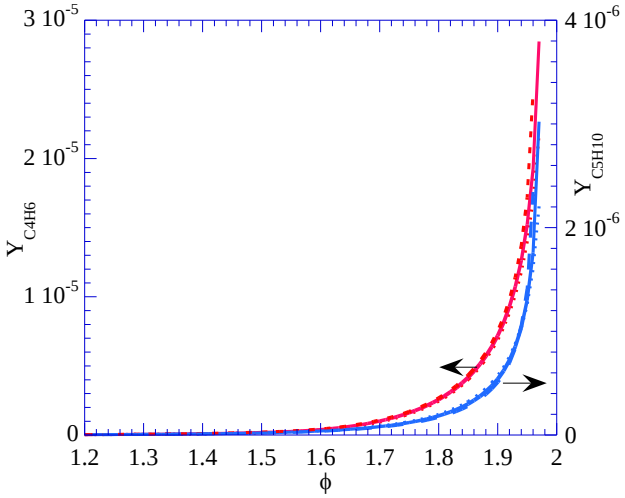

Figure 7-66. Changes in UHC concentrations in WSR due to variations in composition for m-xylene-n-dodecane mixtures.

8 LAMINAR CO-FLOW FLAME STUDIES

This section presents experimental results for PAH and soot for all four fuels in the test matrix: n-heptane/n-dodecane, iso-octane/n-dodecane, m-xylene/n-dodecane, and methylcyclohexane/n-dodecane, plus pure n-dodecane. The experimental results include visible light images to establish flame height, laser-induced fluorescence for PAH species, and laser-induced incandescence for soot. Two flame conditions were studied: a non-premixed co-flow flames (phi[3] = infinity) and partially premixed jets with phi=6. For all flames, nitrogen required for operation of the fuel vaporizer is present in the fuel jet. All results were obtained at atmospheric pressure. The results are presented and discussed in two groupings: non-premixed fuel jets and partially premixed fuel jets.

8.1 Fuel Composition Effects in Non-premixed Co-flow Flames

Non-premixed co-flow flames have similar combustion and reaction characteristics to non-premixed regions in the primary zone of gas turbine combustors. Because fuel is not mixed with any air, it reacts via pyrolytic chemistry to form PAH and soot.

8.1.1 Visible Light Images and Flame Heights

Figure 8-1 presents images of the non-premixed flames for the four fuel mixtures and pure n-dodecane. For standard test conditions with 0.2 slpm of nitrogen flow in the fuel vaporizer system, the non-premixed flame of the m-xylene fuel was "sooting", which means that soot was breaking through the tip of the flame. All other flames are "non-sooting," in that no soot escapes from the tip of the flame. Because the m-xylene flame was sooting at 0.2 slpm, a second experimental condition was established with higher nitrogen flow that brought the flame to a non-sooting condition. The flow rate of nitrogen in this case was 0.48 slpm, which was the minimum flow rate required to stop soot from breaking through the tip of the flame.

Flame heights were determined from the images as the distance between the exit of the fuel tube and the tip of the flame. The variation in the intensity of the visible light near the tip of the flame is caused by small fluctuations (~2mm) in flame height over the course of the exposure time. For the purposes of measuring flame height, the tip was defined by the region of higher luminosity.

Flame heights are similar for the paraffinic fuels, close to 60mm. For the m-xylene fuel at 0.2 slpm nitrogen flow, which is smoking, no flame height can be defined. For the m-xylene fuel at 0.48 slpm nitrogen, the flame height was larger than for the paraffinic fuels. The larger flame height is a consequence of the higher soot levels in this flame, which take a longer time to fully oxidize.

[3] When applied to gas turbine combustion, the equivalence ratio, phi, indicates the relative amount of oxygen present in the fuel-air mixture. Phi is a non-dimensional quantity that compares the amount of oxygen in the fuel-air mixture to the amount required for stoichiometric combustion. Phi=1 indicates that a mixture has a stoichiometric amount of oxygen. Phi < 1 is a "fuel-lean" mixture, which has more than the amount of oxygen required for stoichiometric combustion whereas a phi > 1 is a "fuel-rich" mixture, which has less than the amount of oxygen required for stoichiometric combustion. Phi=infinity indicates a mixture with no oxygen present.

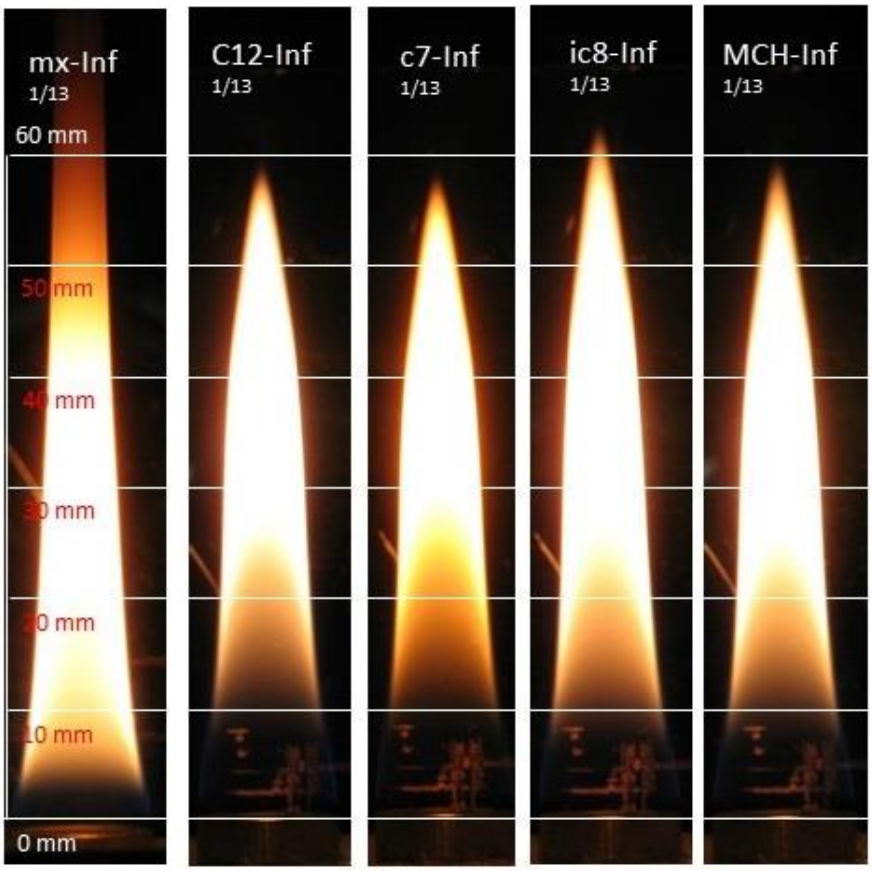

Figure 8-1. Visible light images of non-premixed co-flow flames (phi = infinity) with 0.2 slpm nitrogen.

Table 8-1. Flame heights for non-premixed co-flow flames.

Fuel	**Flame height (mm)**
m-xylene fuel (mx)	undefined
n-dodecane fuel (C12)	59.0
n-heptane fuel (c7)	59.0
iso-octane fuel (ic8)	60.5
methylcyclohexane fuel (MCH)	60.0

8.1.2 Spatial Distribution of Aromatic Species and Soot

Figure 8-2 presents 2-D images of the LIF signals from small and large aromatic species for non-premixed conditions. The aromatic data are from the laser-induced fluorescence measurements with excitation at 266 nm and collection at two wavelength ranges to differentiate between small aromatic species (1 and 2-rings) and large aromatic species (3 or more rings). In Figure 8-2, a different mapping to the color scale was used for the m-xylene fuel data and the paraffinic fuels in order to allow details of the aromatics distribution to be clearly seen for all fuels.

Only the m-xylene fuels shows LIF from small aromatic species near the tube exit. This fluorescence is from the m-xylene in the fuel. As the fuel heats up and reacts, the LIF from the m-xylene decreases rapidly. The formation of aromatic species from the reaction products of m-xylene and n-dodecane is evident from the annular regions of LIF signal that are present very near the fuel tube exit. LIF signals for small aromatic species for the paraffinic fuels have similar spatial distributions. The LIF from small aromatic species for the paraffinic fuels begins at a larger distance from the burner exit than for the m-xylene fuel. This larger distance is caused by the time required for the paraffinic fuels to react to form intermediate species, which then combine to form the first aromatic ring. The iso-octane and methylcyclohexane fuels have similar levels of LIF from the small aromatic species and both are larger than the signals from the n-heptane fuel and the pure n-dodecane. The iso-octane and methylcyclohexane fuels also show LIF from small aromatics closer to the exit of the fuel tube than the n-heptane and pure n-dodecane, indicating that the fuels containing branched and cyclo-paraffins form the first aromatic ring faster the fuels containing normal alkanes.

The spatial distribution of LIF from large aromatic species has a similar character for all of the fuels tested. The LIF signal first becomes visible in an annular region. The distance from the exit of the fuel tube to the height of the first LIF signals from large aromatic species varies with fuel composition. This distance is smallest for the m-xylene fuel, the iso-octane and methylcyclohexane fuels have the next shortest distance, followed by pure n-dodecane and the n-heptane fuel. For all fuels, the radial width of the LIF signal increased with height above the fuel tube exit. The point at which the LIF from large aromatics is detected on the centerline varies with fuel type in a similar manner to the variation in the distance between the burner exit and the first detected LIF signal from large aromatics. The maximum height at which LIF from large aromatic species is detected is similar for all fuels.

Figure 8-3 shows the soot distributions for the test fuel mixtures and pure n-dodecane. In order to show structure of the soot field most clearly, different color scales are used for the m-xylene fuel and the paraffinic fuel. For the m-xylene fuel, the maximum on the color scale is 18ppm and it is 8ppm for the paraffinic fuels. The spatial distributions of soot for the four paraffinic fuels are quite similar. Soot is detected first a thin annular region starting at 15 to 20mm above the fuel tube exit. At higher heights, the radial width of the soot field increases toward the centerline until LII from soot is detected on the centerline at around 30mm. Above this height, the soot concentration increases along the centerline until it decreases to zero at the flame tip.

Soot in the m-xylene flame also appears first in a thin annular region, which begins much closer to the fuel tube exit than for the paraffinic fuels, consistent with the detection of large aromatic species closer to the fuel tube exit, as shown in Figure 8-2. Soot is detected on the centerline at heights similar to the paraffinic fuels. However, the peak soot levels for the m-xylene flame remain in a thin annular region, unlike the paraffinic fuels. The relative ordering of peak soot levels are m-xylene fuel, followed by methylcyclohexane and iso-octane fuel, then pure n-dodecane and finally the n-heptane fuel.

Figure 8-4 presents the centerline profiles for small aromatics, large aromatics, and soot for the four fuel mixtures. The spatial relationship among the aromatic species and soot also represents a temporal relationship because the centerline is a streamline. Thus, the profiles show that the small aromatics form first, followed by the large aromatics and finally soot. There are regions of overlap between small and large aromatics and large aromatics and soot.

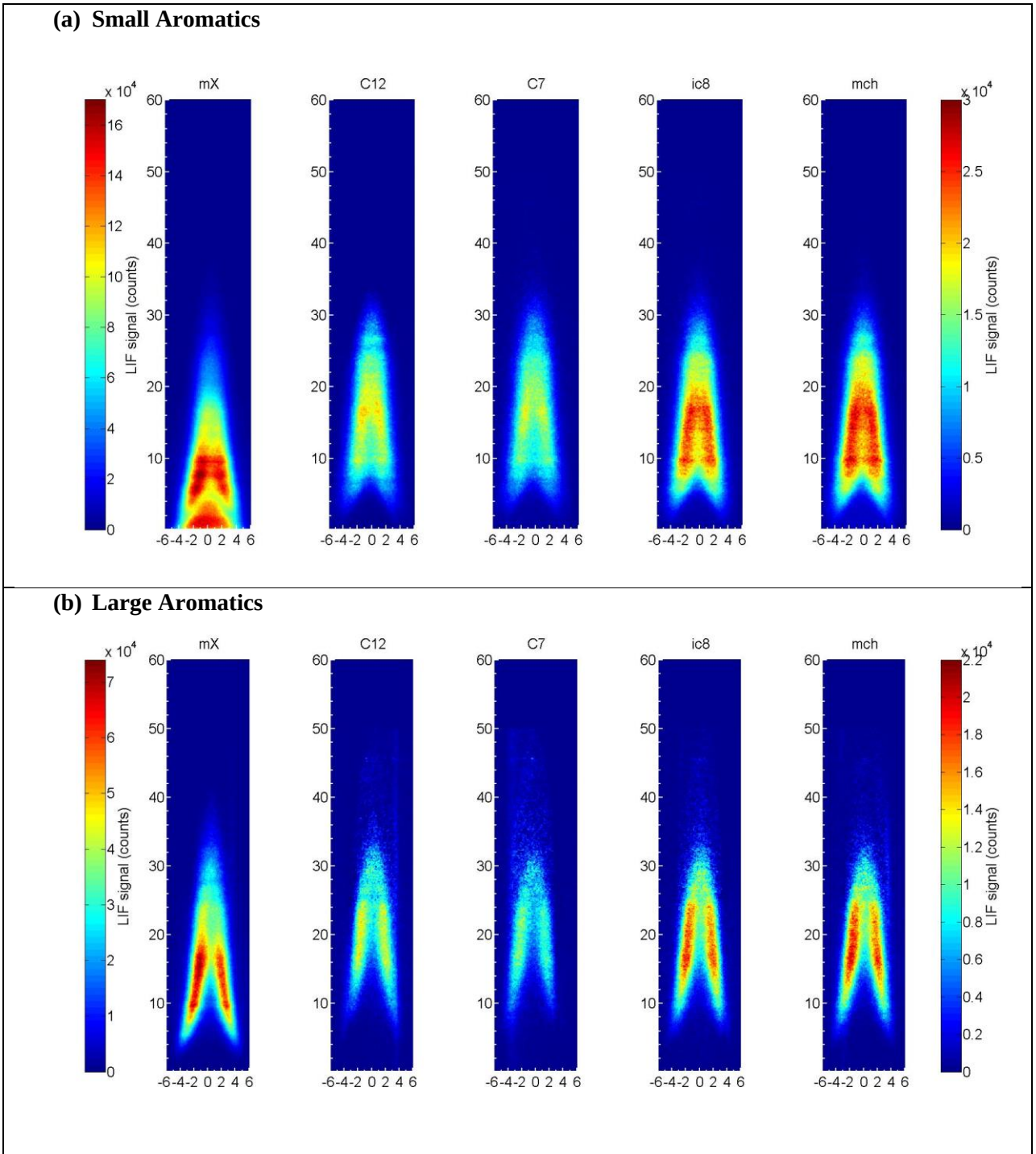

Figure 8-2. Aromatic species distributions for non-premixed co-flow flames with 0.2 slpm nitrogen. Note that the m-xylene fuel (m-X) is on a different scale than the paraffinic fuels.

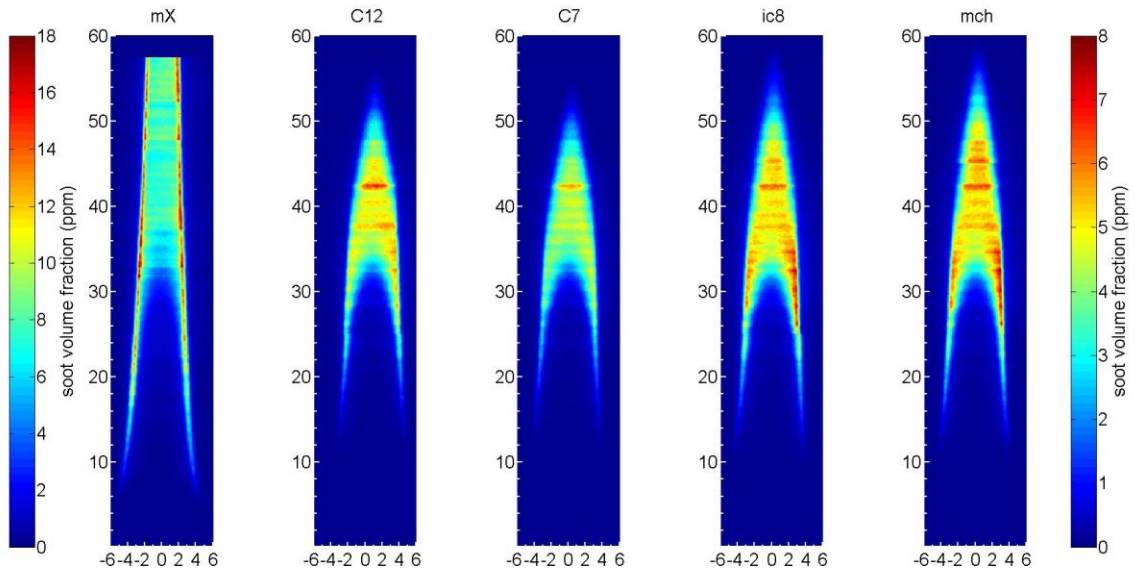

Figure 8-3. Soot species distributions for non-premixed co-flow flames with 0.2 slpm nitrogen. Note that the m-xylene fuel (m-X) is on a different scale than the paraffinic fuels.

Small Aromatics

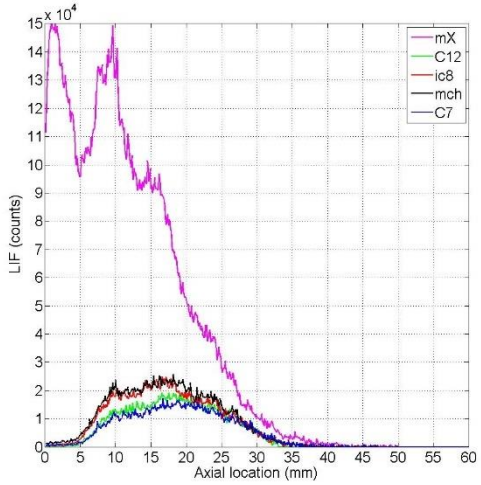

Large aromatics

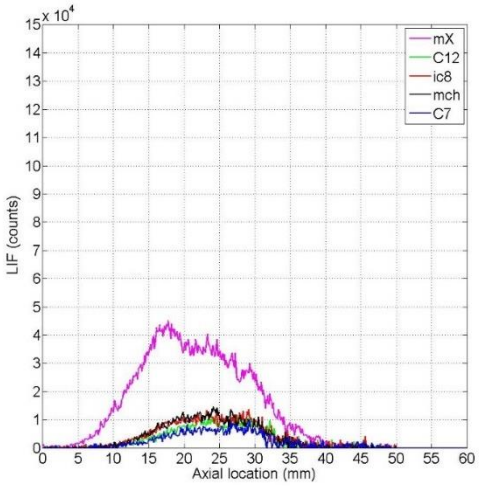

Soot

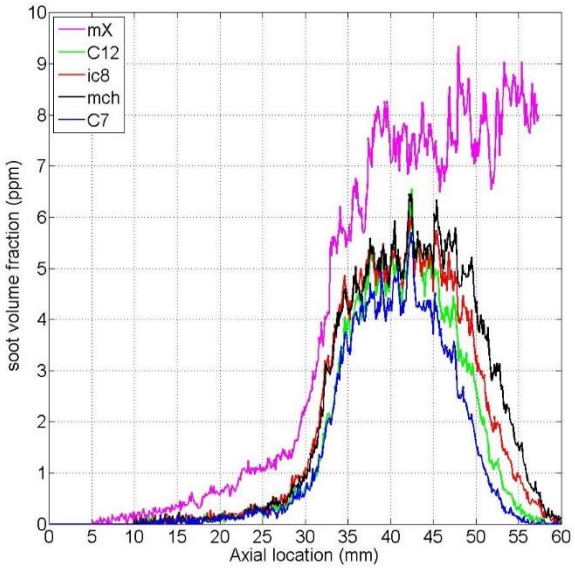

Figure 8-4. Centerline profiles for small aromatics, large aromatics and soot for non-premixed flames with 0.2 slpm of nitrogen.

Figure 8-5 compares the planar distributions of LIF from small aromatics and large aromatics and LII from soot for the m-xylene flames at the two nitrogen flow rates (0.2 and 0.48 slpm). In this Figure, different scales have been used for each plot to show the details of the spatial distribution as clearly as possible. The higher nitrogen flow rate moves the point at which large aromatics and soot are first detected away from the burner. The increased nitrogen flow rate changes the structure of the soot field dramatically, making its general character much closer to that of the paraffinic fuels. Figure 8-6 shows that the centerline soot profile the two m-xylene flames is nearly identical up to a height of approximately 50mm. Above this height, the amount of soot in the 0.2 slpm flame remains approximately constant whereas the amount of soot in the 0.48 slpm flame decreases. This difference between the centerline soot profiles suggests that there is a difference in relative oxidation rates in the two flames at higher heights along the centerline.

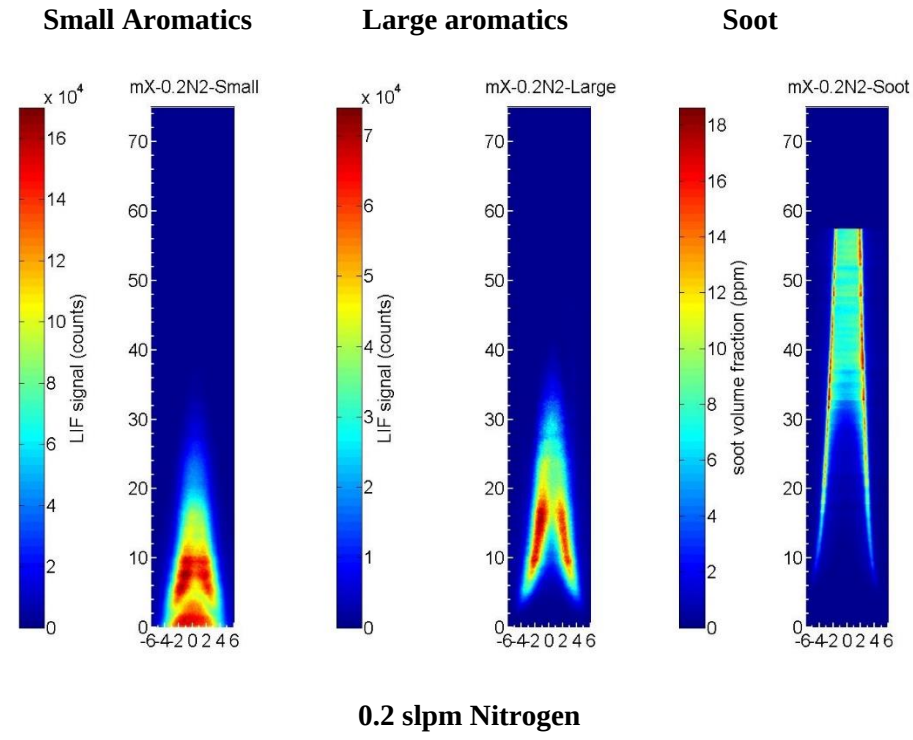

Figure 8-5. Comparison of aromatic species and soot in non-premixed flames of m-xylene fuel with 0.2 and 0.48 slpm of nitrogen. Note that each 2-D plot has a separate scale.

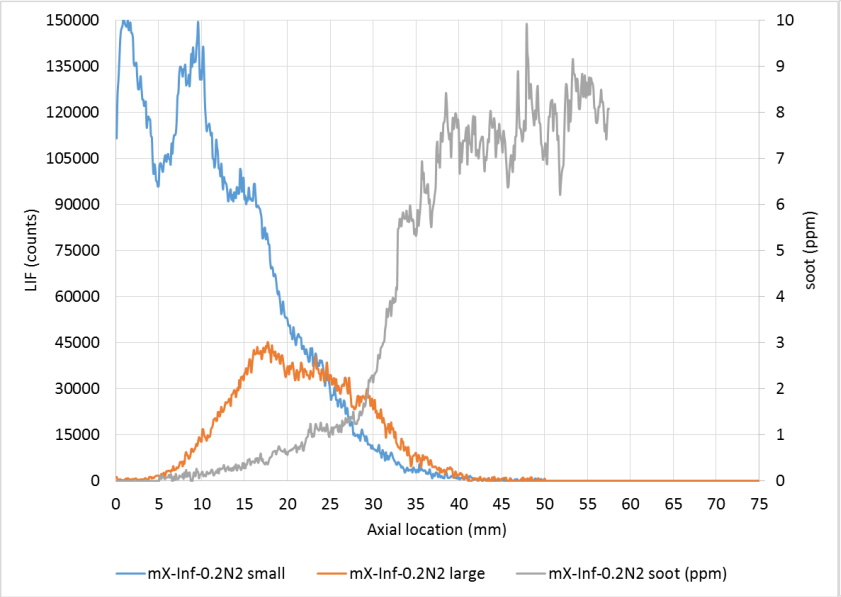

(a) 0.2 slpm Nitrogen

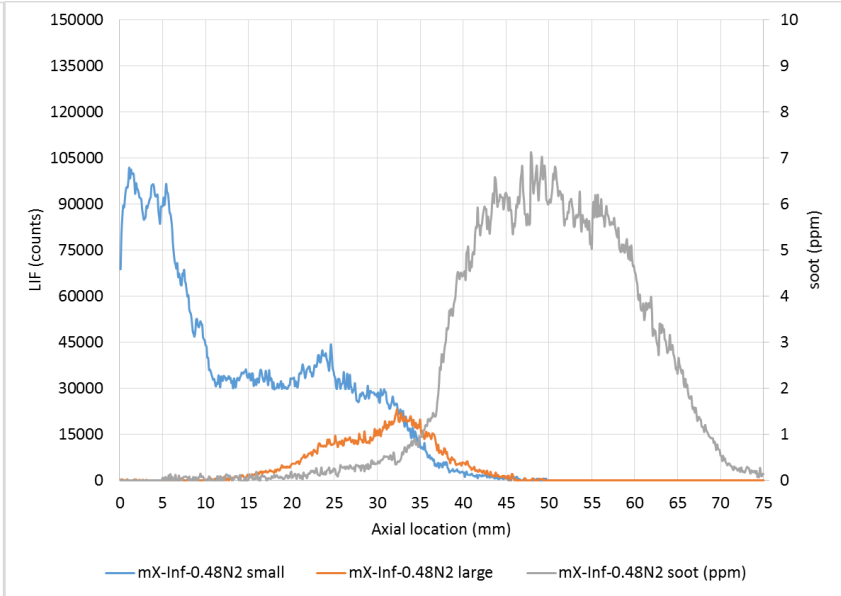

(b) 0.48 slpm Nitrogen

Figure 8-6. Comparison of centerline profiles of aromatics and soot in the non-premixed m-xylene flames with 0.2 and 0.48 slpm of nitrogen.

8.2 Fuel Composition Effects in Partially-premixed Co-flow Flames

Partially-premixed co-flow flames have similar combustion and reaction characteristics to partially-premixed regions in the primary zone of gas turbine combustors. In this study, a fuel-rich equivalence ratio was used so that effects of fuel composition on reactions leading to PAH and soot could be studied. .

8.2.1 Visible Light Images and Flame Heights

Figure 8-1 Figure 8-7 presents images of the partially-premixed flames for the four fuel mixtures and pure n-dodecane. Comparing these images to the non-premixed flames in Figure 8-1 shows that addition of air to the fuel lowers the luminosity from the flames, indicating a decrease in soot because the adiabatic flame temperatures are not affected by the addition of the air to the fuel. The heights of the flames also decrease due to the shorter amount of time required to oxidize the smaller amounts of soot. Flame heights were determined from the images as the distance between the exit of the fuel tube and the tip of the flame and are presented in Table 8-2. The heights of all of the flames are similar, 45 to 54mm, which was not the case for the non-premixed co-flow flames.

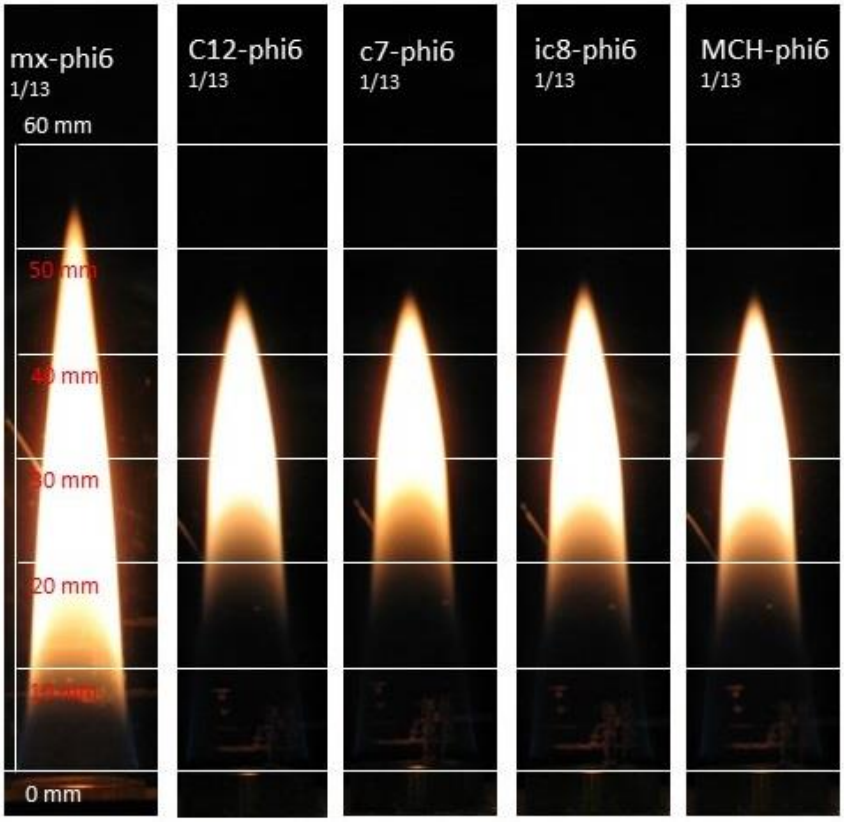

Figure 8-7. Visible light images of non-premixed co-flow flames (phi = 6) with 0.2 slpm nitrogen.

Table 8-2. Flame heights for partially-premixed co-flow flames.

Fuel	Flame height (mm)
m-xylene fuel (mx)	54.0
n-dodecane fuel (C12)	45.0
n-heptane fuel (c7)	45.0
iso-octane fuel (ic8)	46.0
methylcyclohexane fuel (MCH)	46.0

8.2.2 Spatial Distribution of Aromatic Species and Soot

Figure 8-8 presents 2-D images of the LIF signals from small and large aromatic species for partially-premixed jets with a fuel jet of phi=6. In this figure, different mappings to the color scale were used for the m-xylene fuel and the paraffinic fuels in order to allow details of the aromatics distribution to be clearly seen for all fuels. As was the case for the non-premixed co-flow flames, only the m-xylene fuel has LIF from small aromatic species near the tube exit, which is the result of fluorescence from the m-xylene in the fuel. The pattern of fluorescence is similar to that for the non-premixed m-xylene flame. However, the region of LIF from small aromatics forming higher in the flame has lower signal levels compared to the non-premixed flame. For the paraffinic fuels, the addition of air to the fuel jet substantially reduced the spatial extent over which LIF from small aromatic species was detected. For the paraffinic fuels, the maximum LIF signal is located in a small region along the centerline at a height of approximately 25mm.

The LIF signals from large aromatic species are also presented in Figure 8-8. For the paraffinic fuels, there is some interference from LII in the upper portions of the image, in spite of the fact that the incident laser energy was very low. Comparing the LIF from large aromatic species for the non-premixed and partially premixed jets of the paraffinic fuels shows a substantial reduction in the spatial extent over which LIF from large aromatics is observed. This reduction is most likely due to a reduction in the concentration of the large aromatic species. The spatial extent of the large aromatics for the m-xylene fuel was not reduced so substantially by the addition of air to the fuel jet. However, peak signal level did drop substantially from 70000 to 16000.

The LII images from partially-premixed flames for the fuel mixture plus n-dodecane are presented in Figure 8-9 for 0.2 slpm. The effect of air addition is most dramatic on the m-xylene flame. The addition of air lowers soot concentration sufficiently that the flame is no longer sooting, which make a large difference in the soot distribution at higher heights. For the paraffinic fuels, the addition of air to the fuel jet lowers the amount of soot, but does not have much of an effect the soot distribution within the flame. The relative ordering of the flames in terms of the amount of peak soot remains the same as for the non-premixed flames, namely m-xylene fuel, followed by methylcyclohexane and iso-octane fuel, then pure n-dodecane and finally the n-heptane fuel.

Figure 8-10 presents the centerline profiles for small aromatics, large aromatics, and soot for the four fuel mixtures. The overall trends are similar to those observed for the non-premixed flames, but the LIF signal levels are substantially lower for the partially-premixed flames.

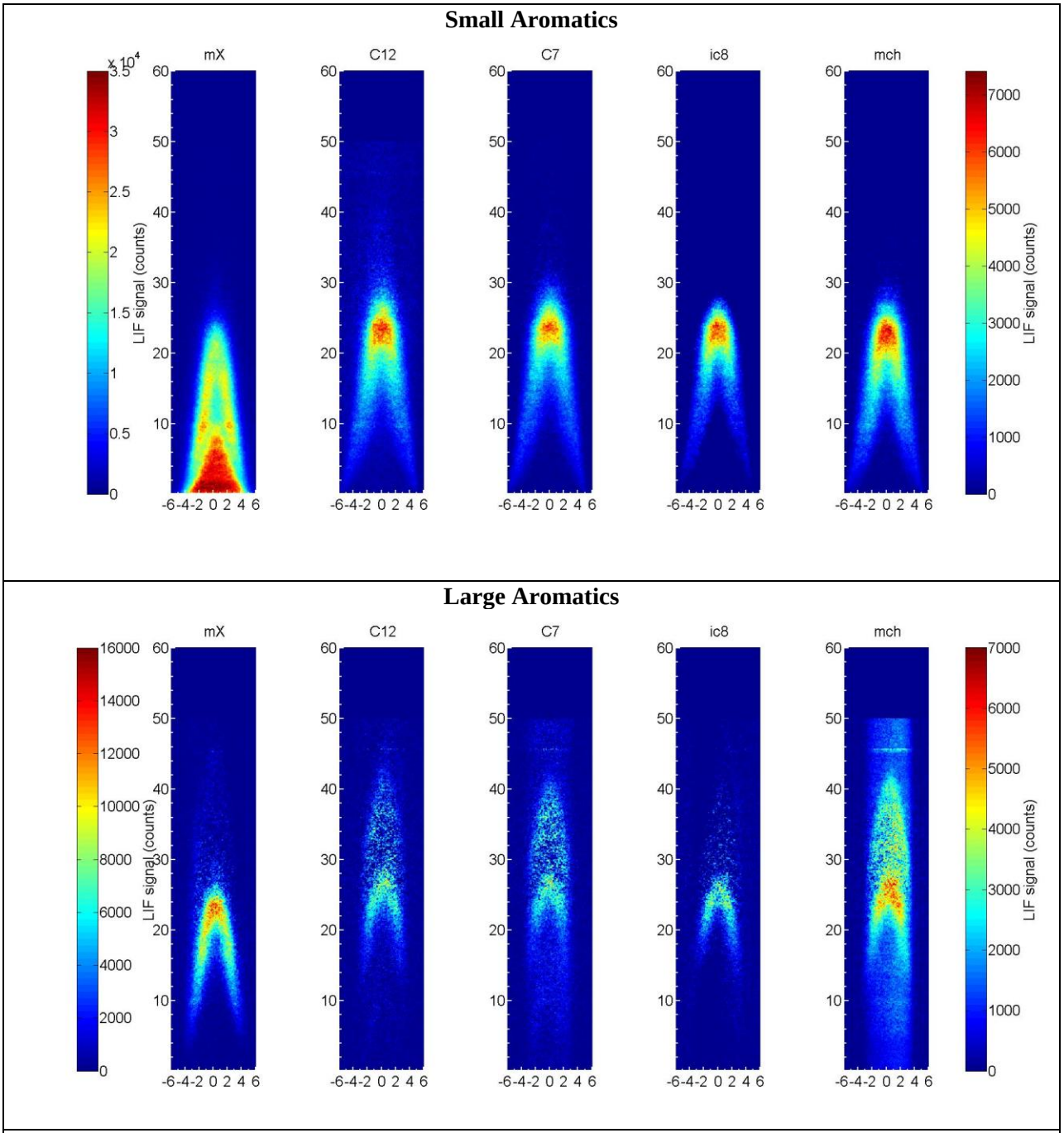

Figure 8-8. Aromatic species distributions for partially-premixed co-flow flames (phi = 6) with 0.2 slpm nitrogen. Note that the m-xylene fuel (m-X) is on a different scale than the paraffinic fuels.

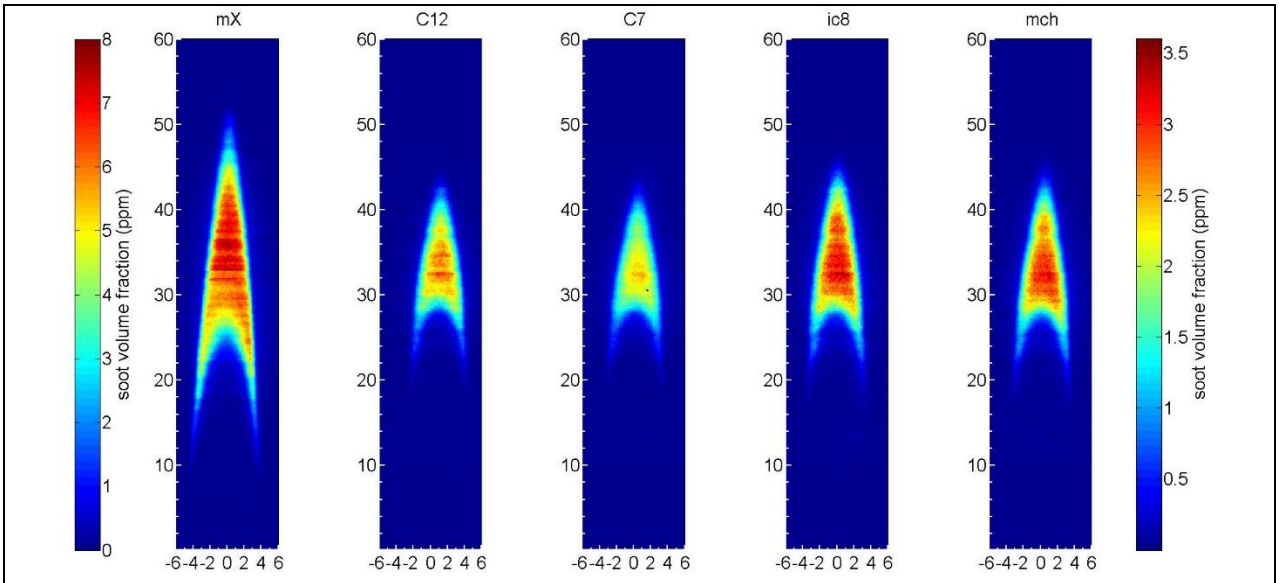

Figure 8-9. Soot distributions for partially-premixed co-flow flames (phi = 6) with 0.2 slpm nitrogen. Note that the m-xylene fuel (m-X) is on a different scale than the paraffinic fuels.

Small Aromatics

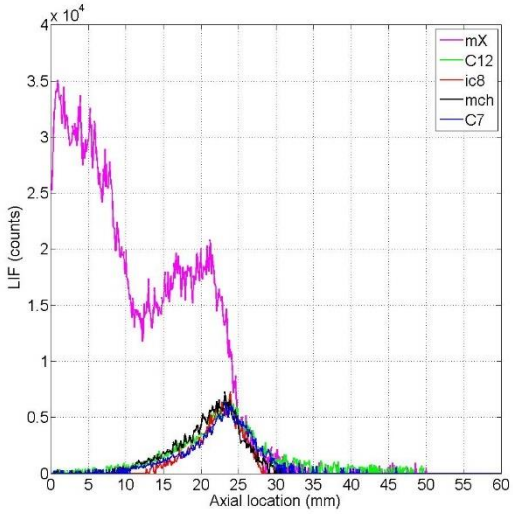

Large aromatics

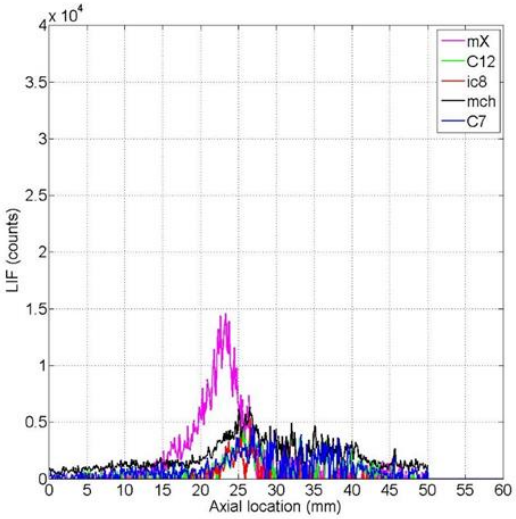

Soot

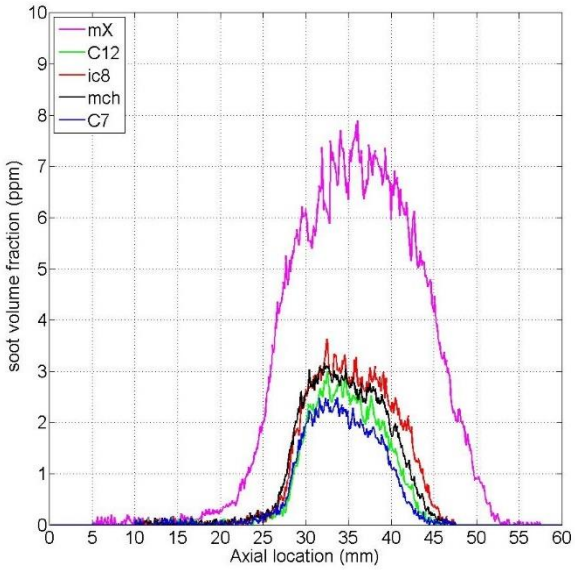

Figure 8-10. Centerline profiles for small aromatics, large aromatics and soot for partially premixed fuel jet at phi=6.

8.3 Simulation of Fuel Effects in Co-flow Flames

8.3.1 Initial Studies using 2-Equation Soot Model

Initial simulations of the effects of fuels on co-flow flame structure were conducted for the four binary fuel mixtures used in this program. The simulations used chemical kinetics developed in this program (SERDP 2014) and a 2-Equation Soot model based on the work of Lindstedt, which treats soot as a gas-phase species. (For additional discussion of this soot model, see Section 4.2.)

Flow rates for the liquid fuel in the central jet and the air in the outer channel were fixed at 0.2 sccm and 113.27 slpm, respectively. The fuel in the central jet was heated and mixed with nitrogen flowing at 200 sccm. The temperature of the gaseous fuel-nitrogen jet exiting from the central tube was maintained at 473 K. Fuels used in this study were prepared through blending n-dodecane with n-heptane, iso-octane, mch or m-xylene. The compositions and velocities of the fuel jets used in the calculations at the tube exit are given in Table 8-3.

Table 8-3. Details of the fuel jet at burner exit.

Case	$Y_{n\text{-}dodecane}$	Y_{add}	Y_{N2}	T_{fuel} (K)	V_{fuel} (m/s)
n-heptane blend	0.260	0.108	0.632	473	0.0718
iso-octane blend	0.264	0.106	0.630	473	0.0652
mch blend	0.259	0.105	0.636	473	0.0654
m-xylene blend	0.149	0.057	0.794	473	0.1476

Soot distributions computed for the four fuel blends are shown in Figure 8-11. Rainbow color palette with blue and red representing 0 and 4.5 ppm, respectively is used. Photographs of the flames in the experiments taken directly using a digital camera are superimposed on the computed soot fields. As the radiation from soot particles is captured in these photographs, brightness represents soot volume (assuming temperature is constant). Also note that while the computed images represent slices of the flame in the longitudinal direction, photographs represent radiation from the whole flame integrated in the direction perpendicular to the plane of symmetry. Overall, reasonable comparisons between computations and measurements were obtained. Calculations have predicted the flame heights (based on soot) reasonably. Except for m-xylene flame (Figure 8-11d) the computed locations at which appreciable amount of soot developed near the flame base matched well with the measurements. While experiments have indicated that no soot is escaping through the flame tip calculations for the n-heptane, iso-octane and mch cases allowed soot leakage. This could be due to insufficient soot oxidation in the model. On the other hand, soot model has correctly computed the consumption of soot in m-xylene flame.

Computed soot profiles along the centerline are compared with the laser-induced-incandescence (LII) measurements in Figure 8-12. While the experimental data (Figure 8-12) were normalized to the respective flame heights measured from photographs, the computed data (Figure 8-12a) were normalized with respect to the flame heights obtained from peak OH concentration. In general, the computed soot profiles matched well with the measurements, especially with regard to the heights at which soot started to increase. Considering the fact that the current state-of-the-art soot models still require significant improvements, the comparisons for the soot volume fraction between the computations and measurements are reasonable. The biggest discrepancy, however, is observed for the m-xylene flame.

Even though the soot predictions seem reasonable for individual flames (both distributions and magnitudes), the current soot model failed to capture certain trends in the sooting behaviors when changes in fuel compositions are considered. For example, soot produced by the n-heptane flame in the experiments is lower than that produced by either the iso-octane or mch flame. On the other hand, calculations have predicted slightly higher soot in n-heptane flame. Similarly, while the experiments suggest that m-xylene in the fuel makes the flame sooty, calculations have predicted less soot in m-xylene flames compared to that in the other flames. While the relative location at which soot started forming in m-xylene flames was advanced in the experiments, it was delayed in the computations. For understanding these discrepancies, detailed flame structures must be investigated.

Distributions of the computed temperature and acetylene concentrations along the centerline in n-heptane and m-xylene flames are compared in Figure 8-13.Two important differences may be noted. Formation of acetylene is delayed and the temperature of the flame is increased in the m-xylene flame. Recalling the fact that the soot inception and growth models used in the present calculations depend on acetylene concentration, the nearly identical shapes and magnitudes of acetylene (except some shift) in both the flames cannot explain the 50% decrease in soot in m-xylene flame. Careful observation of the acetylene profiles indicates that there is a small acceleration in its formation in n-heptane flame, which is missing in the m-xylene flame. It is speculated that this initial rise in acetylene produced more soot precursors, which eventually increased the soot.

The soot nucleation, growth and oxidation rates in n-heptane and m-xylene flames are compared in Figure 8-14 Figure 8-14 and Figure 8-15. Distributions of OH radical (important for soot oxidation) and soot nucleation rate for n-heptane flame are shown in Figure 8-14a in the left and right halves, respectively. Distributions of soot growth and oxidation rates are shown in the left and right halves of Figure 8-14b, respectively. Corresponding distributions for the m-xylene flame are shown in Figure 8-15a and b respectively. As suspected from the acetylene distributions, soot nucleation rate near the base region for m-xylene flame is significantly lower than that in the n-heptane flame. Delayed nucleation reduced the growth rate as well in the m-xylene flame. Even though soot oxidation rates are lower in m-xylene flame all the soot was oxidized due to the small amount of soot production.

The delay in the formation acetylene in m-xylene flame and the associated delays in soot nucleation may be understood better by looking at the fuel breakdown process. The two components in each blend decompose and form lower hydrocarbons such as propane, ethylene and methane. Distributions of the parent fuels as they decompose along the centerline of the jet diffusion flames in are shown in Figure 8-16. The distance in each flame is normalized to its height measured from peak OH location. It is interesting to note how the consumption of one fuel component affects the other. N-dodecane is the common fuel component in all these flames. Even though MCH (C_7H_{14}) is consumed little faster than n-heptane it did not make any difference to the consumption n-dodecane in these two flames. On the other hand, iso-octane consumption accelerated consumption of n-dodecane. Most interestingly, presence of m-xylene limited the consumption of n-dodecane significantly. This delay in fuel consumption caused delay in the production of acetylene in m-xylene flame as seen in Figure 8-13. The fuel consumption profiles in Figure 8-16 shed light on the locations where soot precursor particles are generated, but they do not offer any explanation to why the n-heptane flame in the experiment produced more soot than the iso-octane or MCH flame and why the m-xylene flame is so sooty.

Improvements of the soot model were explored to address the challenge of the under-prediction of soot in the m-xylene flames. The results of those investigations are summarized in the next section.

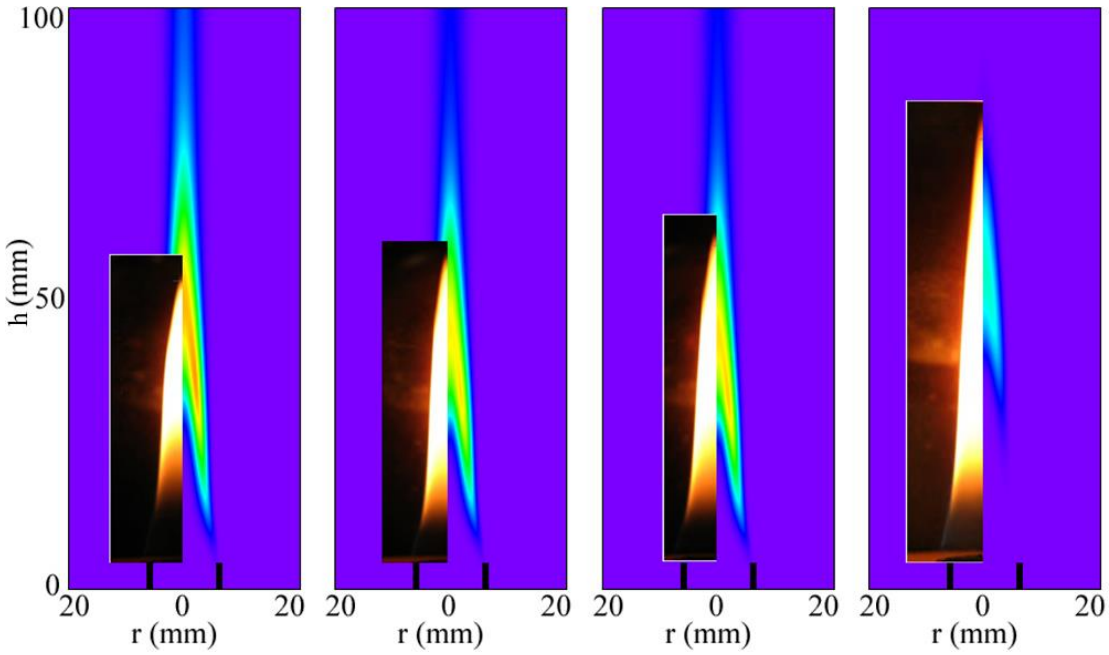

Figure 8-11. Jet diffusion flames obtained with (a) n-heptane-n-dodecane, (b) iso-octane-n-dodecane, (c) mch-n-dodecane, and (d) m-xylene-n-dodecane fuel blends. Direct photographs of the flames are superimposed on computed soot volume fraction (red represents maximum value of 4.5 ppm).

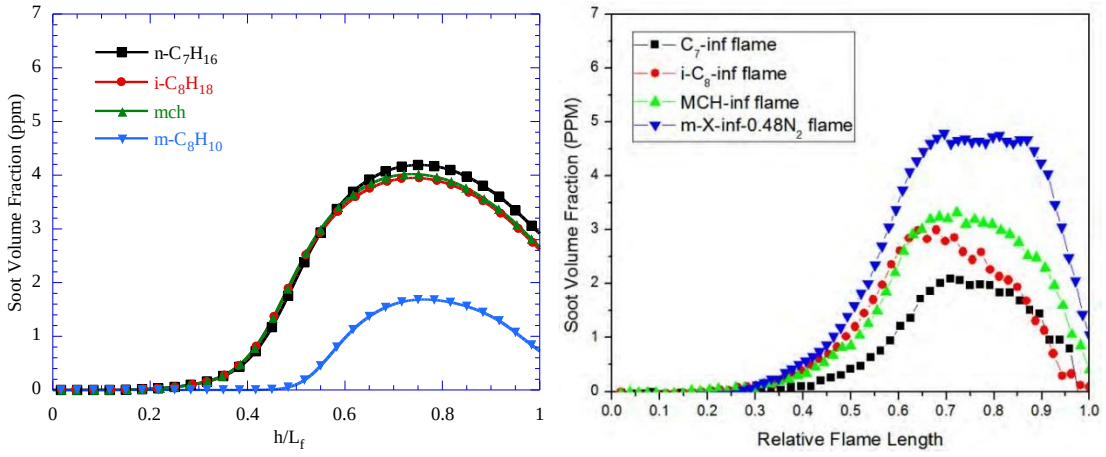

Figure 8-12. Computed (a) and measured (b) soot volume fractions along the centerline for various jet diffusion flames.

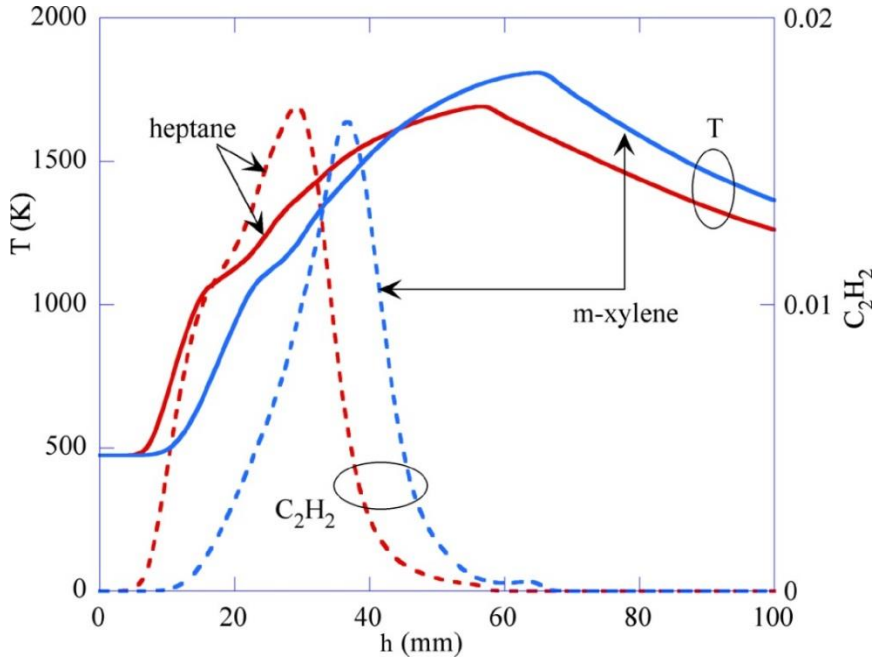

Figure 8-13. Distributions of temperature and acetylene concentration along the centerline in n-heptane and m-xylene flames.

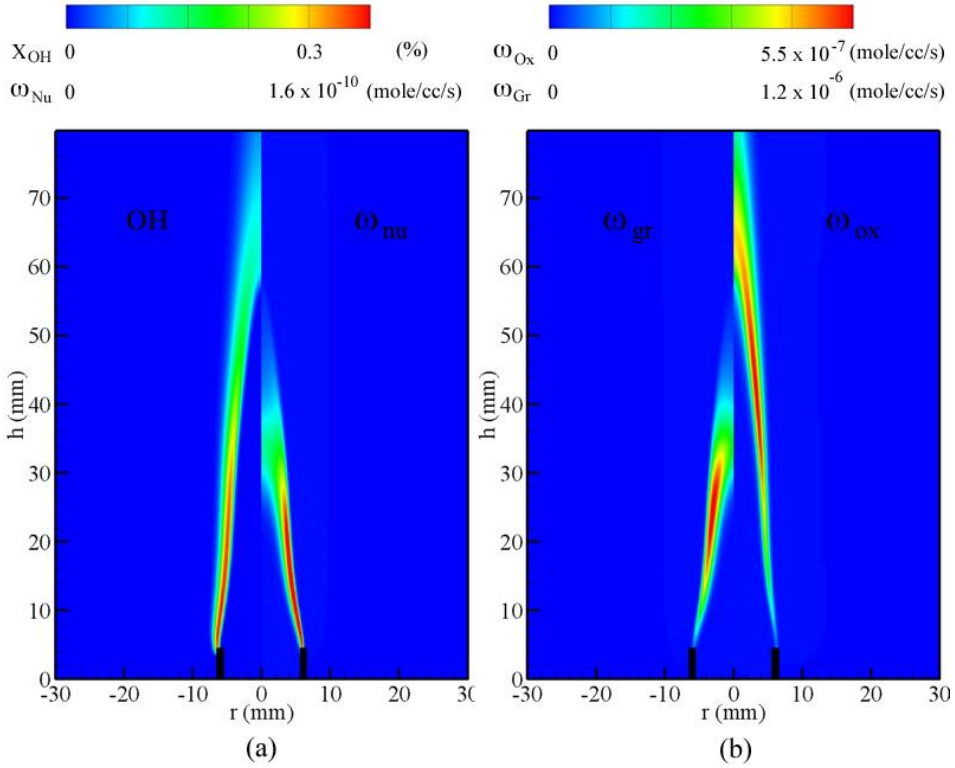

Figure 8-14. Distributions of (a) OH (left) and soot nucleation rate (right) and (b) soot growth rate (left) and soot oxidation rate (right) in n-dodecane-n-heptane flame.

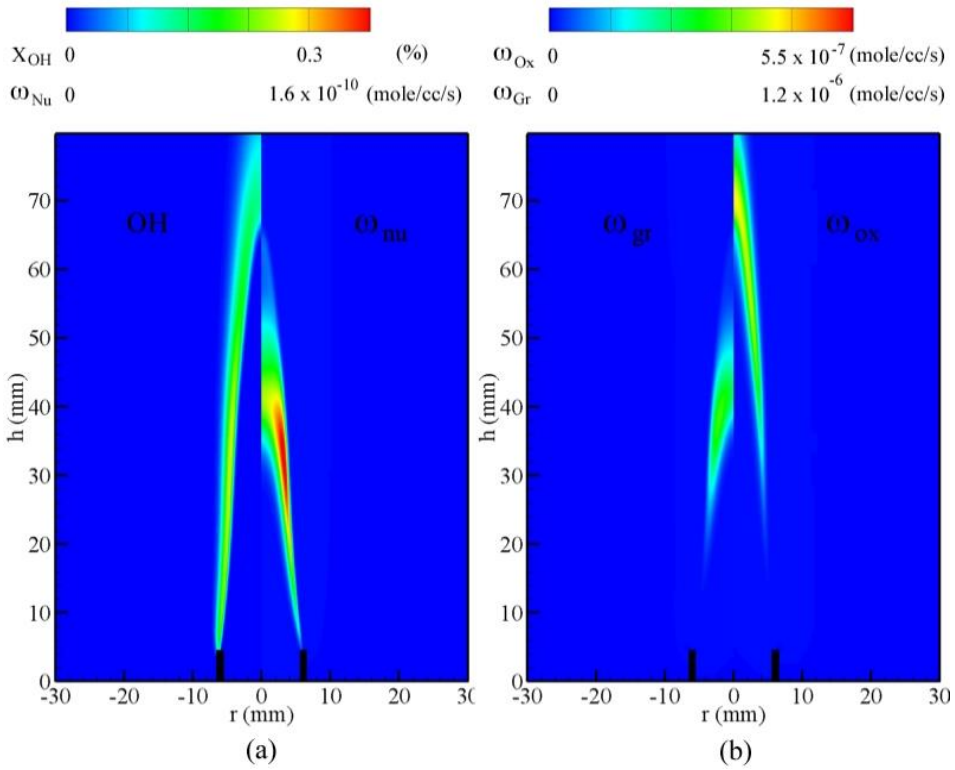

Figure 8-15. Distributions of (a) OH (left) and soot nucleation rate (right) and (b) soot growth rate (left) and soot oxidation rate (right) in n-dodecane-m-xylene flame.

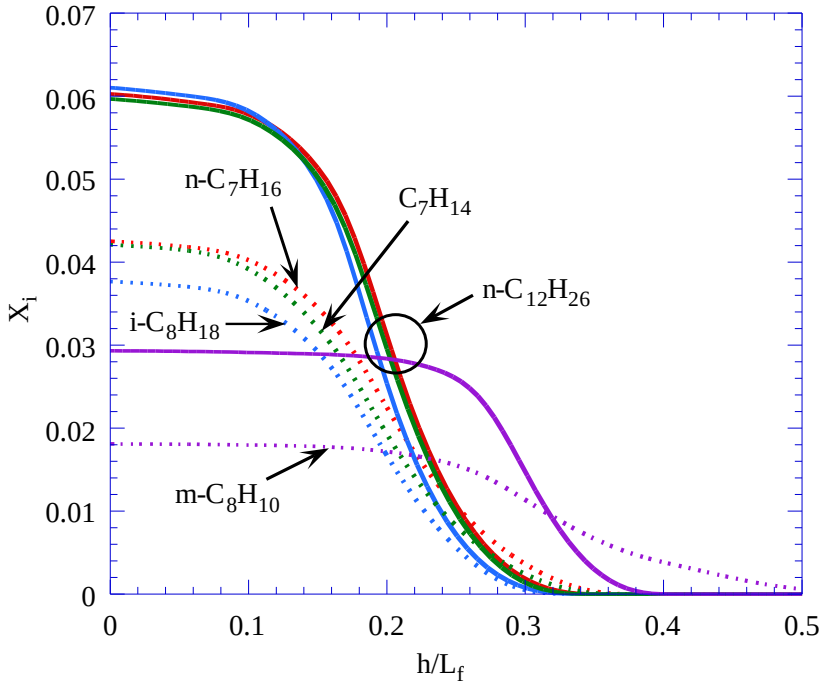

Figure 8-16. Distributions of fuel components along the centerline in n-heptane (red), iso-octane (blue), mch (green) and m-xylene (purple) flames.

8.3.2 Improved Soot Model in UNICORN Code

For much of this program, we have faced a long-standing issue of accurately predicting soot in flames with aromatic fuels such as m-xylene. Researchers around the world including us were having trouble in obtaining the high amounts of soot emissions that were observed experimentally in laminar jet flames burning JP-8 or alternative fuels containing aromatics. CFD simulations were underestimating soot in these flames by more than 200%. Everyone (including us) thought there is something fundamentally missing in the chemical-kinetics models for these fuels for not yielding enough PAH species that allow enhancements to soot formation and growth. We have undertaken an extensive effort to identify this problem. Using UNICORN code and incorporating five state-of-the-art full chemistry models (described in Section 4.2) we have computed jet flames burning various alternative fuels. We have also used all the three soot-modeling approaches (2-equation, method of moments and sectional) that are currently available. We have examined not only the soot yields but also the predicted concentrations of all the PAH species in the gas-phase-kinetics models. Results from this comparative study provided a rather surprising conclusion. The vast number of calculations made with the combinations from gas phase chemistries and soot models yielded more or less the same amounts of soot as the chemical pathways used in these mechanisms for the production/destruction of PAH species were nearly the same. This conclusion should not be that surprising as all the current gas-phase chemistries and soot models were developed from the same fundamental belief that flames from aromatic fuels produce more soot than those from paraffin fuels. After spending several months analyzing the simulation results and the measured soot distributions we have realized that the soot in the flames formed with aromatic fuels is actually not getting oxidized as quickly as that was happening in the flames with paraffin fuels. This lower oxidation rate left more soot in the flames and made it look like as if the flame was producing more soot. Immediately after realizing the disguised cause for large amounts of soot in aromatic flames, we have constructed a new gas phase chemical kinetics (SERDP-2015) and modified the soot sectional method for allowing decrease in oxidation rates as the soot particle grows in size. Using the new chemistry and the soot models we were able to, for the first time, predict the soot in a jet flame formed with m-xylene/n-dodecane blend.

The computed soot distribution is compared with the LII measurements in Figure 8-17(a). For the first time, calculations were able to predict the significant amount of soot leaving the flame zone as observed in the experiments. The predicted soot production region in the flame zone (bottom half) also matched well with the experiment. Computed and measured soot distributions along the centerline are plotted in Figure 8-17(b). As seen in this plot, soot production and growth were predicted well. However, there exist some differences in soot oxidation between the calculations and experiment. It seems the soot in the experiment is getting oxidized at much lower rate.

Soot particles in the model are oxidized in the presence of oxygen through surface reactions. Earlier soot models were oxidizing all the soot particles as the soot particles were not increasing in the size that quickly. In the new soot model, these particles are growing in size rapidly and, thereby, lowered the oxidation rate. However, as seen in Figure 8-17 (b), this oxidation did not match with that noted in the experiment. Calculations for this m-xylene/n-dodecane blend were repeated after increasing the sensitivity of oxidation to the particle surface area. That means, as the soot particle grows the oxidation rate falls more quickly than before. Resulted soot distributions in the mid-section and along the centerline are compared with the measurements in Figs. Figure 8-18 (a) and (b), respectively. Near perfect match between the

computations and measurements may be found in these figures. This suggests that further studies need to be performed for understanding soot oxidation, especially in the flames formed with aromatic fuels.

For understanding how good our new soot model (the one used in Figure 8-17) is in predicting the flames other than the ones established in our laboratories, we have considered several flames that were reported in the literature. Saffaripour et al. at University of Toronto, Canada (Saffaripour et al. 2014) have studied n-decane and Jet-A flames. They have reported their measurements along with their best simulation results. As expected, their calculations resulted good comparisons for the soot in the production and growth regions, but failed significantly in the oxidation regions of the flame. We have simulated these flames using our new soot model and SERDP-2015 gas-phase mechanism and the results are shown in Figure 8-19 and Figure 8-20. Measurements and predictions of University of Toronto and our predictions for the n-decane flame along radial lines at different heights are shown in Fig. 5-69 and those for the Jet-A flame are shown in Figure 8-20. As noted from these figures, for both these flames our new soot model was able to provide significantly improved results.

We have also simulated the jet flames studied at University of San Diego, CA. Detailed soot measurements are not available; however, one could get some qualitative information through the direct photographs of the flames (Figure 8-21). Results obtained for these flames using our new soot model and SERDP-2015 mechanism are compared with the direct photographs of the flames in Figure 8-21 for various fuels. Flame heights and the sooting tendencies were predicted very well. Calculations have captured the leakage of soot from the flame zone noted in the toluene flame. Note that earlier calculations with our old soot model could not predict these flames satisfactorily. This improved soot model was used in the simulations of the jet flames presented in the next section of the report.

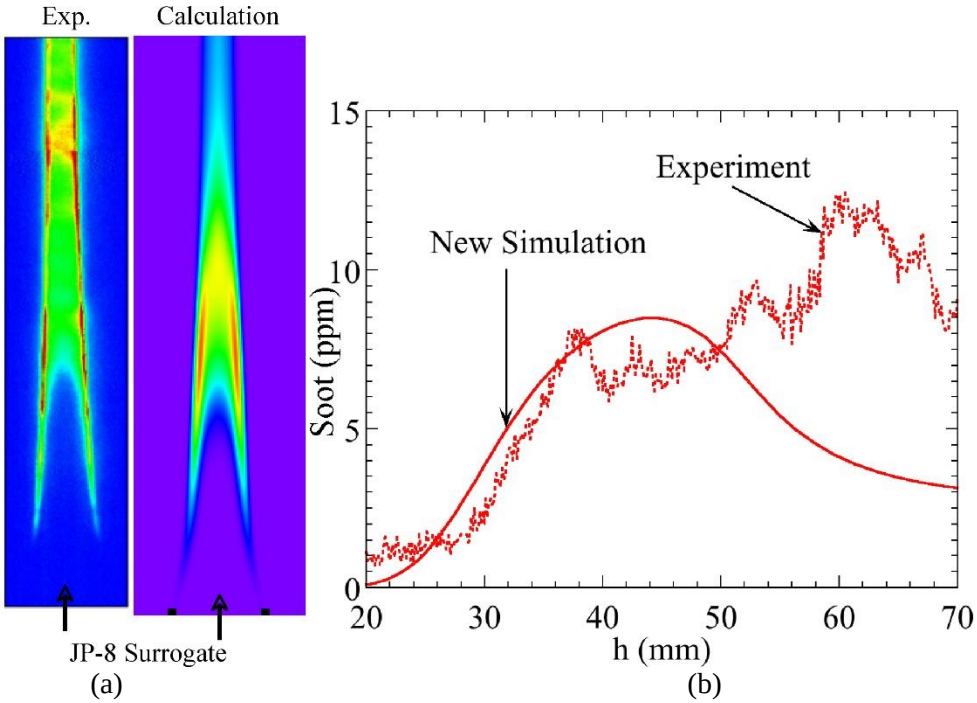

Figure 8-17. M-xylene/n-dodecane flame calculated with new soot model. (a) Comparison of measured (left) and computed (right) distributions of soot. (b) Measured and computed soot distributions along the centerline.

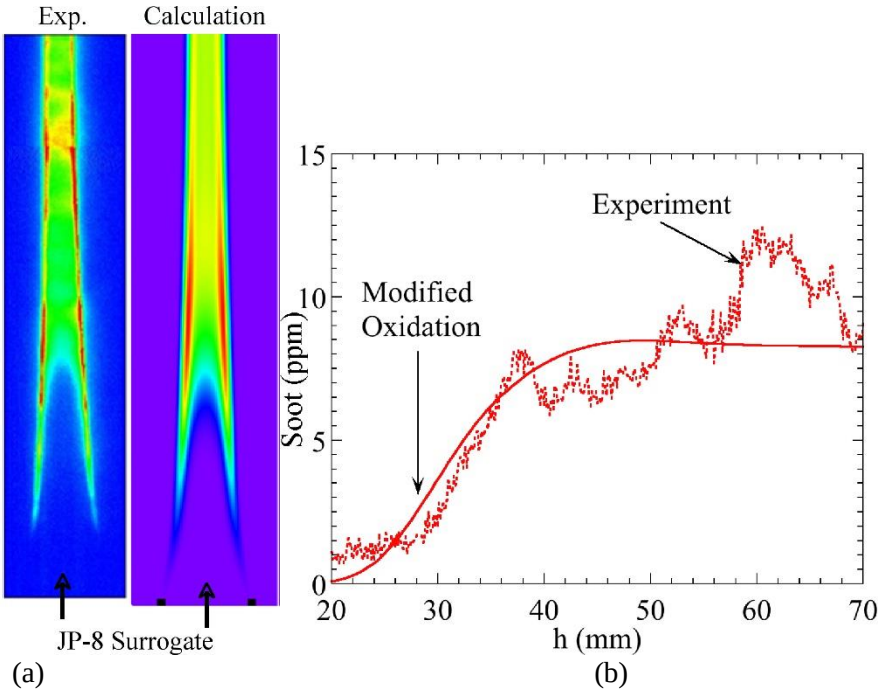

Figure 8-18. M-xylene/n-dodecane flame calculated with new soot model after modifying the soot oxidation rate. (a) Comparison of measured (left) and computed (right) distributions of soot. (b) Measured and computed soot distributions along the centerline.

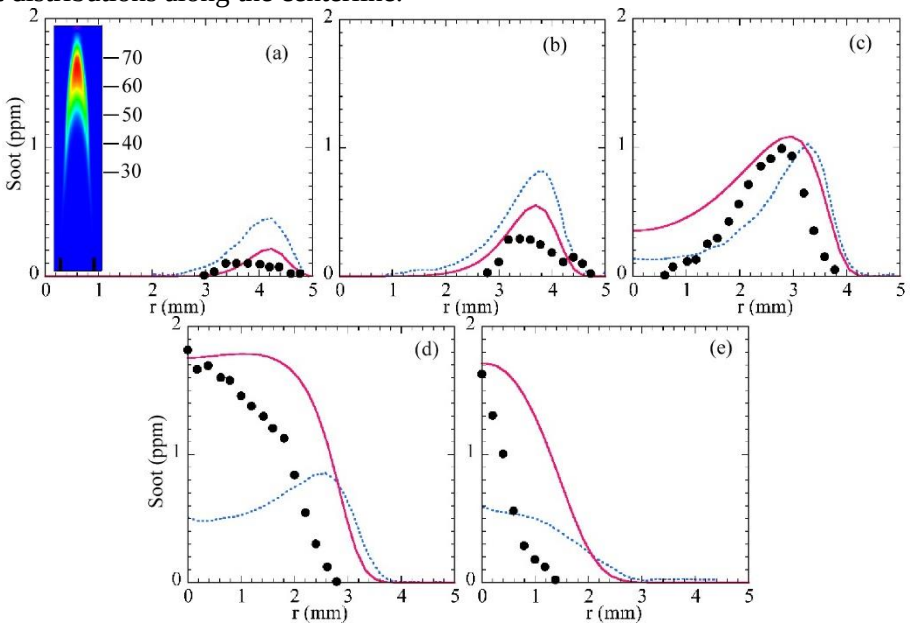

Figure 8-19. Comparison of radial distributions of soot at different heights for n-decane flame of University of Toronto. Symbols, broken lines and solid lines, represent measurements, University of Toronto predictions and our predictions, respectively. (a) h = 30 mm, (b) h = 40 mm, (c) h = 50 mm, (d) h = 60 mm, and (e) h = 70 mm.

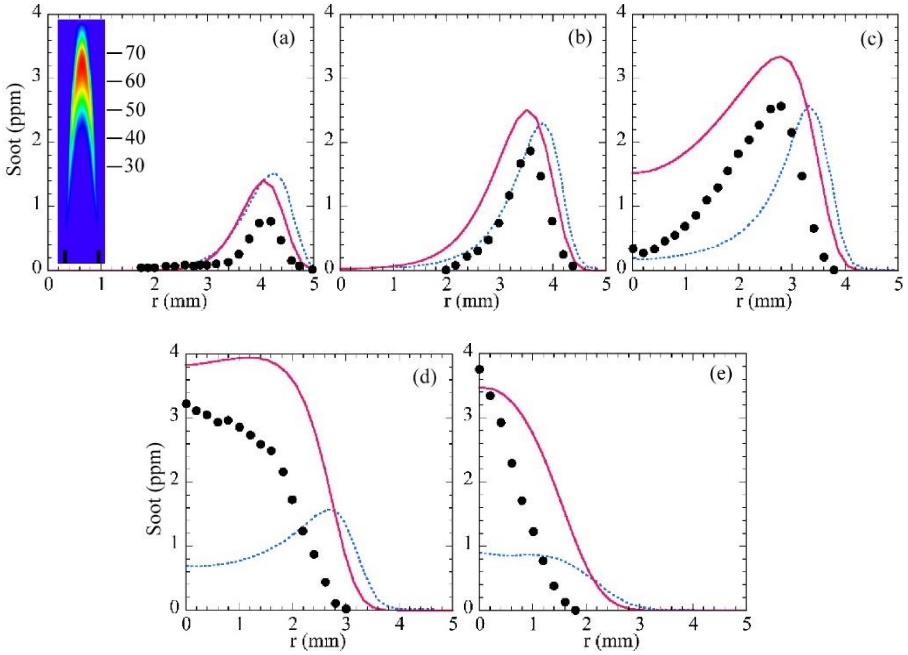

Figure 8-20. Comparison of radial distributions of soot at different heights for Jet-A flame of University of Toronto. Symbols, broken lines and solid lines, represent measurements, University of Toronto predictions and our predictions, respectively. (a) h = 30 mm, (b) h = 40 mm, (c) h = 50 mm, (d) h = 60 mm, and (e) h = 70 mm.

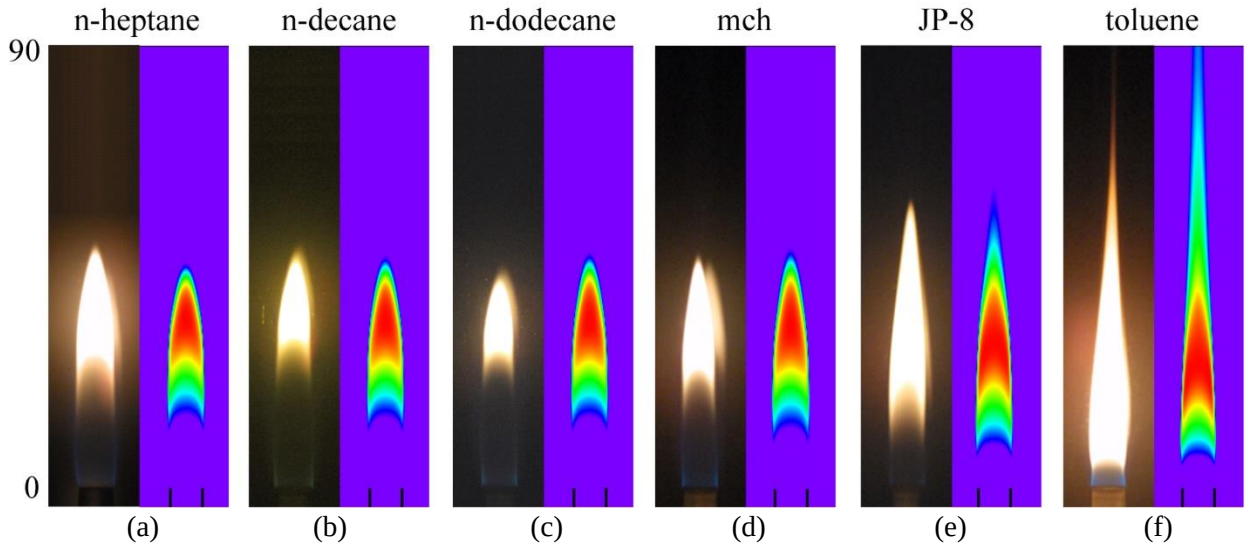

Figure 8-21. Comparison of predicted soot distributions with the direct photographs of flames formed with various fuels. Experiments were performed at University of San Diego.

8.3.3 Simulation of Fuel Effects using the Improved Soot Model in UNICORN

The improved kinetics and soot model led to dramatic improvements in the agreement between the experimental and modeling results for the co-flow flames. Figure 8-22 and Figure 8-23 compare the experimental and modeling distributions of soot for the non-premixed and partially-premixed fuel jets. For both non-premixed and partially-premixed flames, the simulations capture the overall structure of the soot field quite well. The experimental soot field for the m-xylene flame at 0.2 slpm shows the highest levels of soot in an annular region and also that the flame is sooting – that the soot never completely oxidizes. These same characteristics are present in the simulations. *To our knowledge, no other current soot simulations can capture these characteristics for a fuel containing an aromatic species while at the same time capturing the soot fields of the paraffinic fuels.* The simulations also capture the shift in the flame structure of the m-xylene flame when air is added to the fuel jet in the phi=6 flame. The phi=6 m-xylene flame is a non-sooting flame with a closed tip. For both non-premixed and partially-premixed conditions, the flame heights are also captured quite well.

In addition to capturing soot structure well, the simulations capture the centerline volume fraction of soot in the flames very well. Figure 8-24 and Figure 8-25 compare the centerline soot profiles for the experimental and modeling results. (Note that the "spikes" in the soot observed in the data are due to pixel-to-pixel variation in the ICCD camera; they are not real.) For the non-premixed, m-xylene flame, the peak soot volume fraction along the centerline is approximately 8ppm. The simulations predict a peak volume fraction of about 8.5ppm, then the volume fraction decreased to about 3ppm. The decrease is not observed in the experiments. For the non-premixed flames of the paraffinic fuels, the peak soot levels range from 4ppm for the n-heptane fuel to approximately 5 ppm for the iso-octane and methylcyclohexane fuels. The simulations have peak soot volume fractions along the centerline ranging from 4.5ppm for n-heptane to approximately 6ppm for iso-octane. This level of agreement is excellent for soot predictions.

For the partially-premixed flames of m-xylene, the measured peak volume fraction along the centerline is approximately 7ppm and the predicted is 4.5ppm. For the partially-premixed flames of the paraffinic fuels, the measured peak soot volume fractions are between 2 and 3 ppm, and the predicted values are 1.5 to 2ppm. Given the range of fuel chemistries used in these experiments and simulations, the quantitative agreement is excellent.

In order to compare the simulations and experimental data for aromatic species, the mole fractions for aromatic species in the simulation results were converted to concentrations and each concentration was weighted by a cross-section for LIF taken from the literature (see Y. Wang, 2015). The same cross-section was used for all species with the same number of aromatic rings. The result was summed for all one and two ring species to compare to LIF from small aromatic and for species with three or more rings to compare to the LIF from large aromatic species.

Figure 8-26 and Figure 8-27 compare the experimental and modeling results for small aromatic species, which contain 1 or 2-rings, for non-premixed and partially-premixed flames. The spatial distribution of the LIF in the simulations and experiments for the m-xylene flames compares well. The signal at the exit of the fuel tube is from the-xylene and the signal higher in the flame is from small aromatics that form as the fuel reacts under fuel-rich conditions. For the paraffinic fuels, the spatial distribution of the LIF from small aromatics is well captured by the simulations for the partially-premixed flames. The agreement is not as good for the non-premixed flames of the paraffinic fuels. The measurements show the

peak LIF is an annular region whereas the simulations show the peak LIF along the centerline. Still the overall agreement is quite good.

The poorest agreement between the simulations and experiments occurs for the large aromatic species in Figure 8-28 and Figure 8-29. For both non-premixed and partially premixed conditions, the simulations predict that the maximum LIF from species with three or more rings occurs in a conical region along the centerline, corresponding to a triangular region in the 2D images. In the experimental data, the LIF from large aromatic species has maximum signal levels in annular regions, not on the centerline.

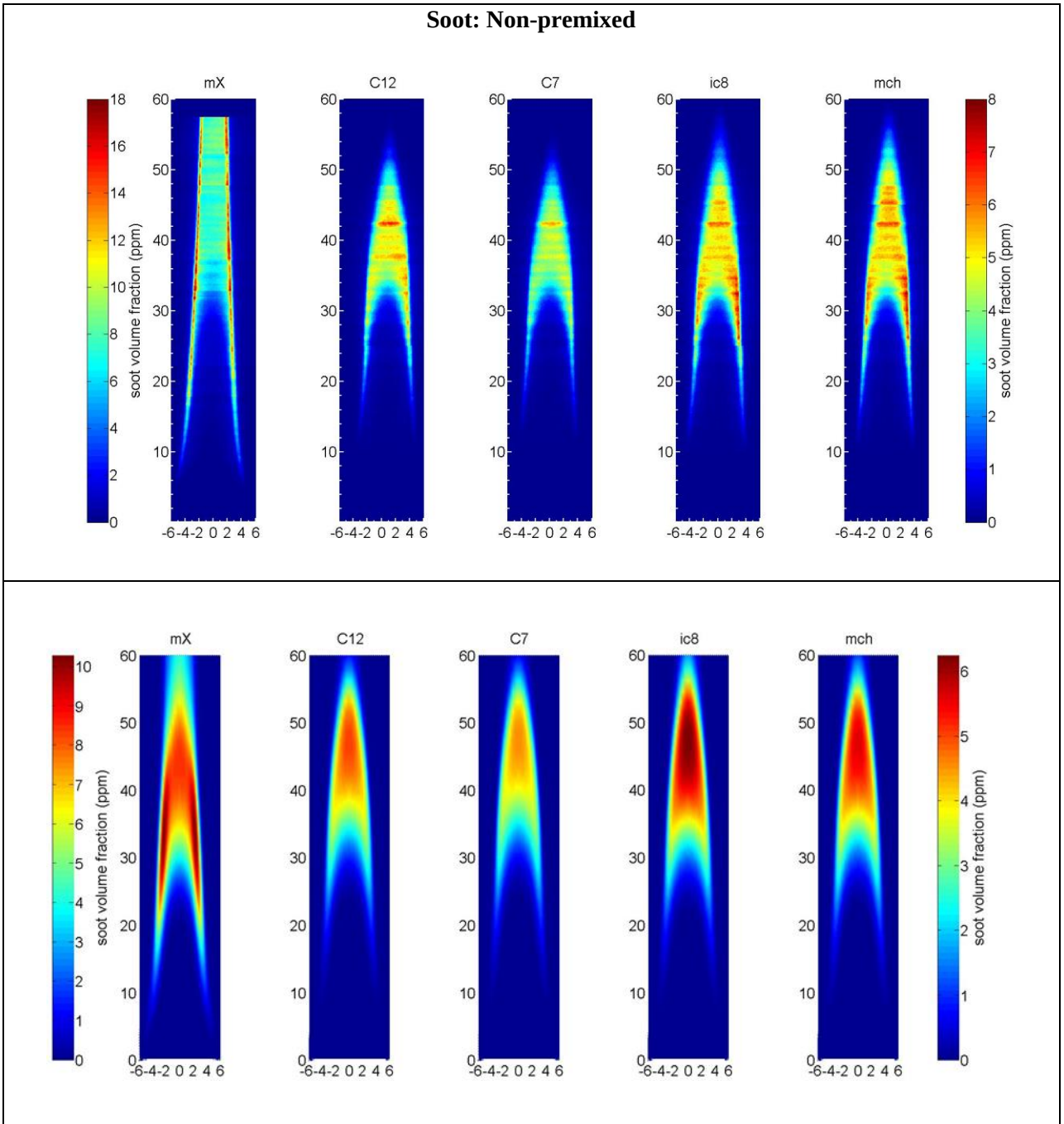

Figure 8-22. Comparison of measured (top) and predicted soot distributions for non-premixed co-flow flames (phi = infinity) with 0.2 slpm nitrogen.

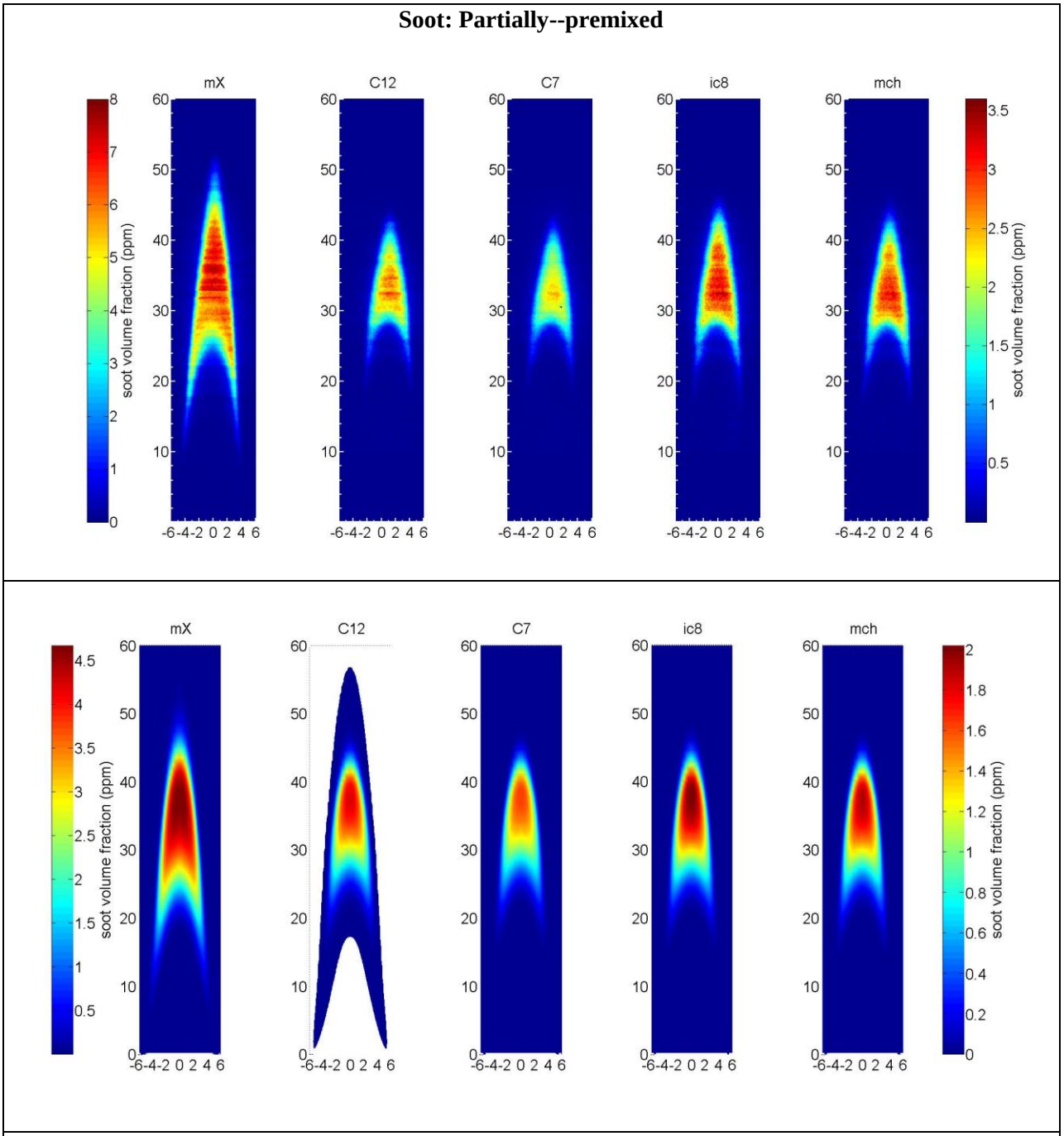

Figure 8-23. Comparison of measured (top) and predicted soot distributions for partially-premixed co-flow flames (phi = 6) with 0.2 slpm nitrogen.

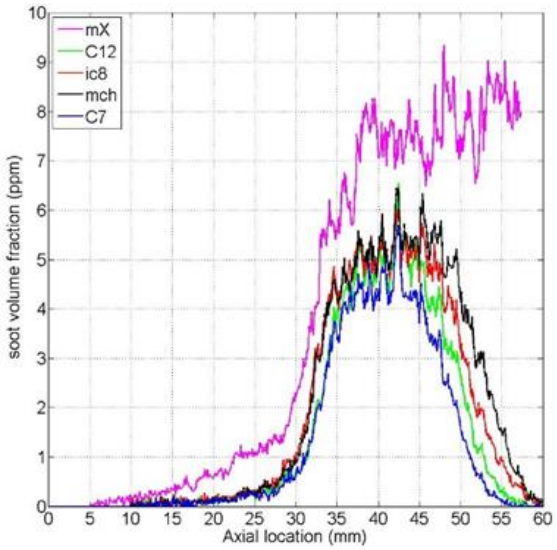

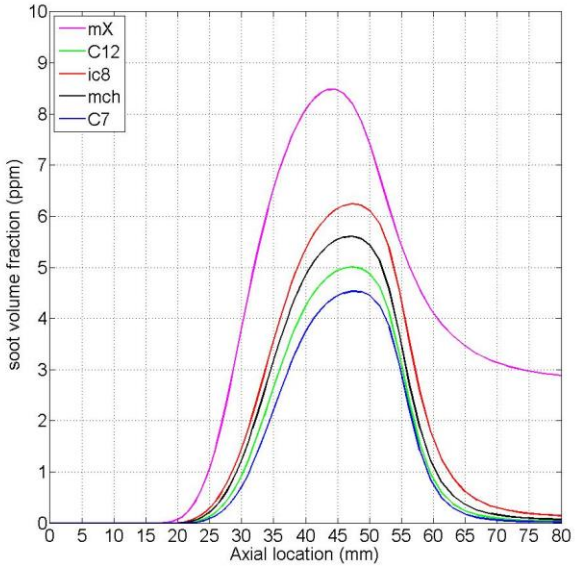

Figure 8-24. Comparison of measured (top) and predicted centerline profiles of soot for non-premixed co-flow flames (phi = infinity) with 0.2 slpm nitrogen.

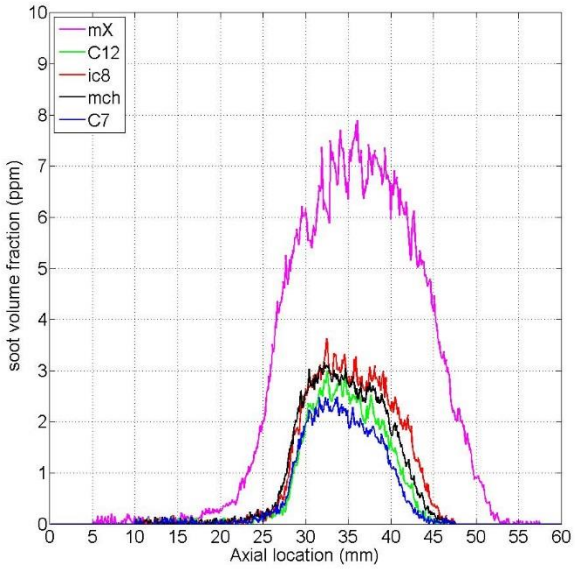

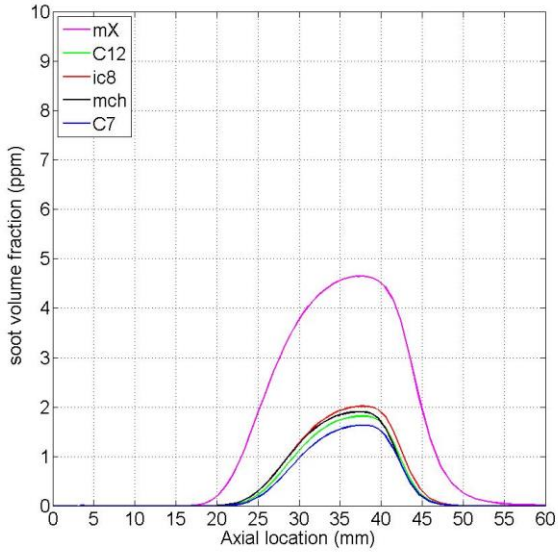

Figure 8-25. Comparison of measured (top) and predicted centerline profiles of soot for partially-premixed co-flow flames (phi = 6) with 0.2 slpm nitrogen.

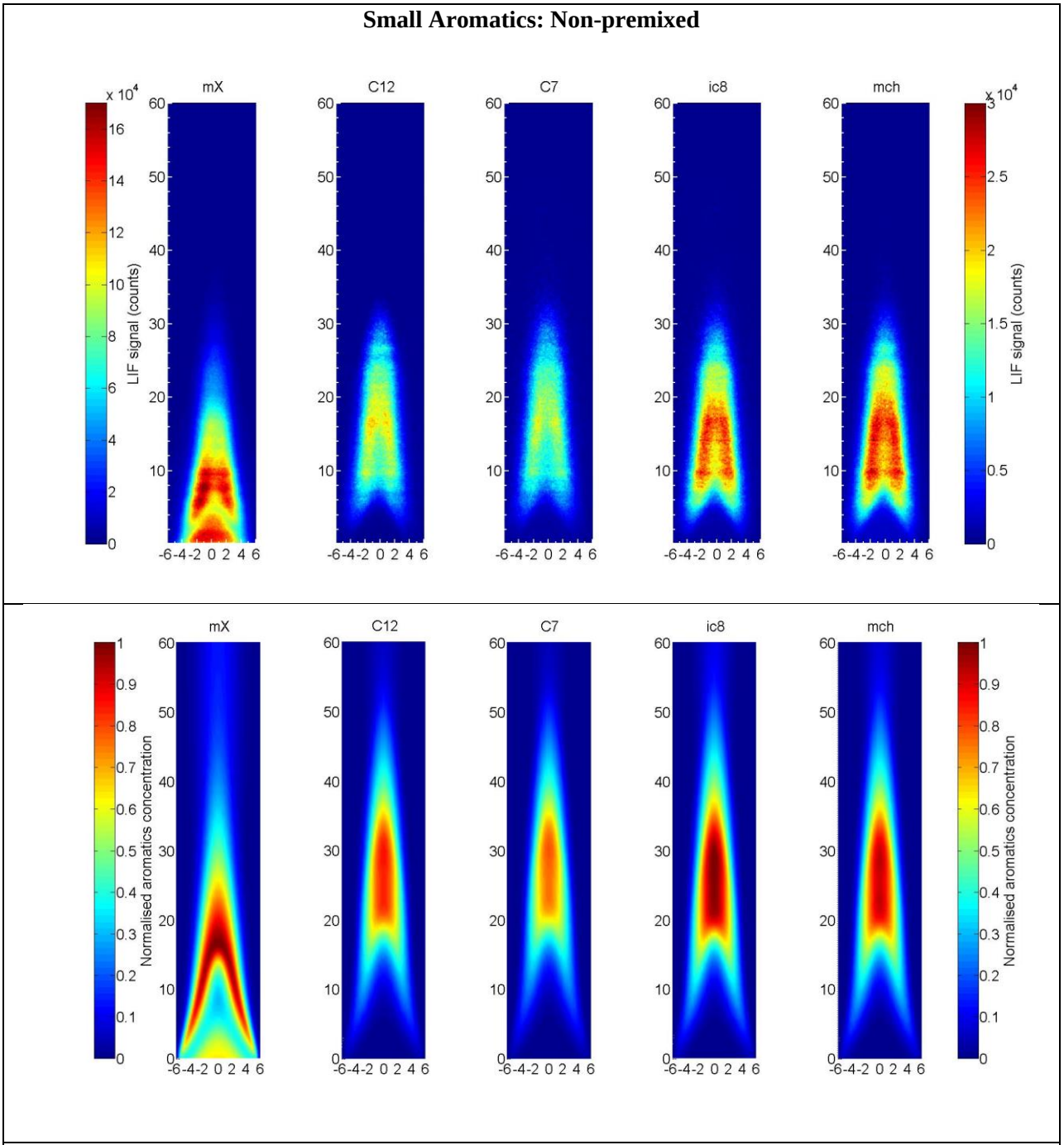

Figure 8-26. Comparison of measured (top) and predicted distributions of small aromatic species for non-premixed co-flow flames (phi = infinity) with 0.2 slpm nitrogen.

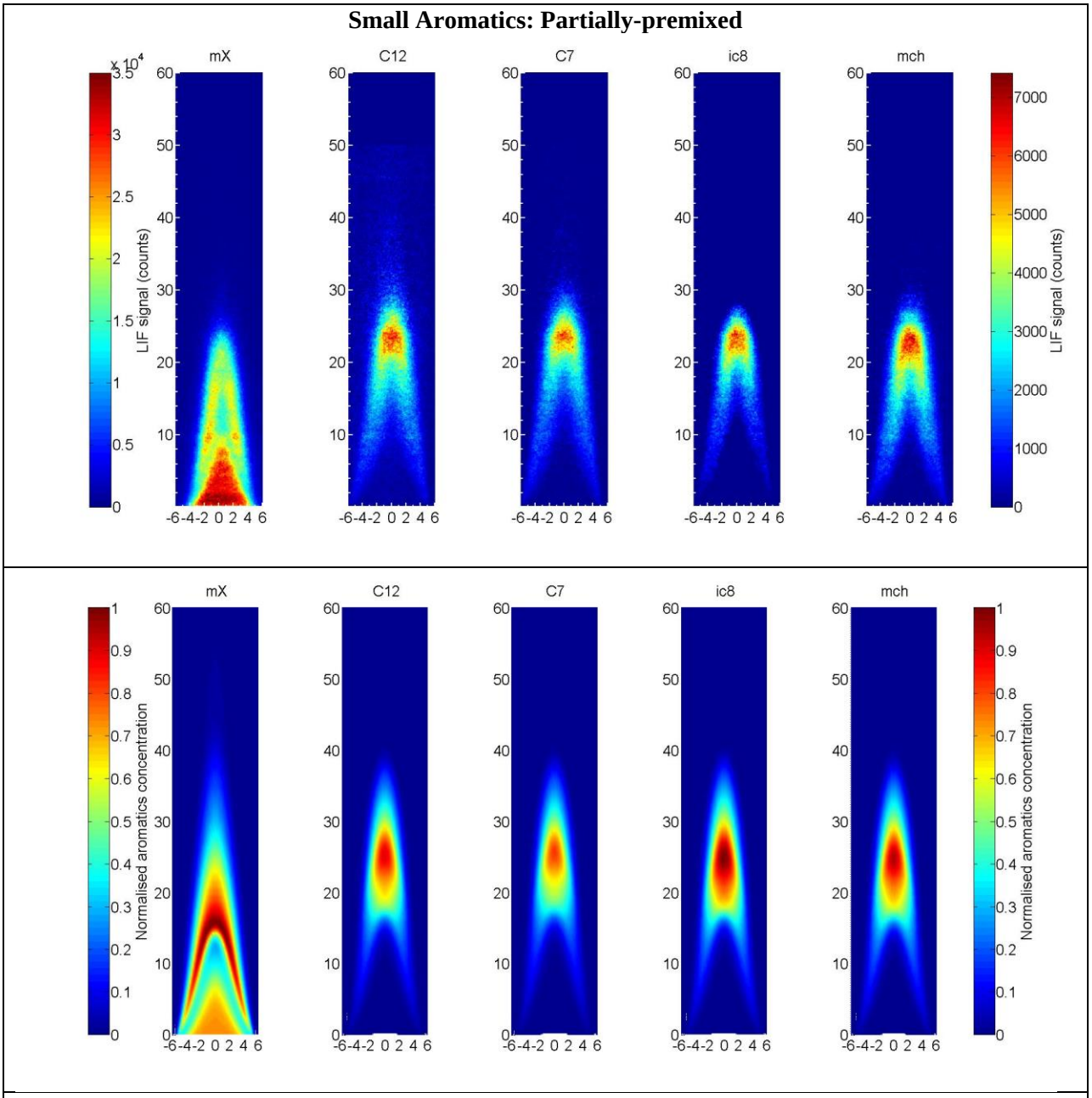

Figure 8-27. Comparison of measured (top) and predicted distributions of small aromatic species for partially-premixed co-flow flames (phi = 6) with 0.2 slpm nitrogen.

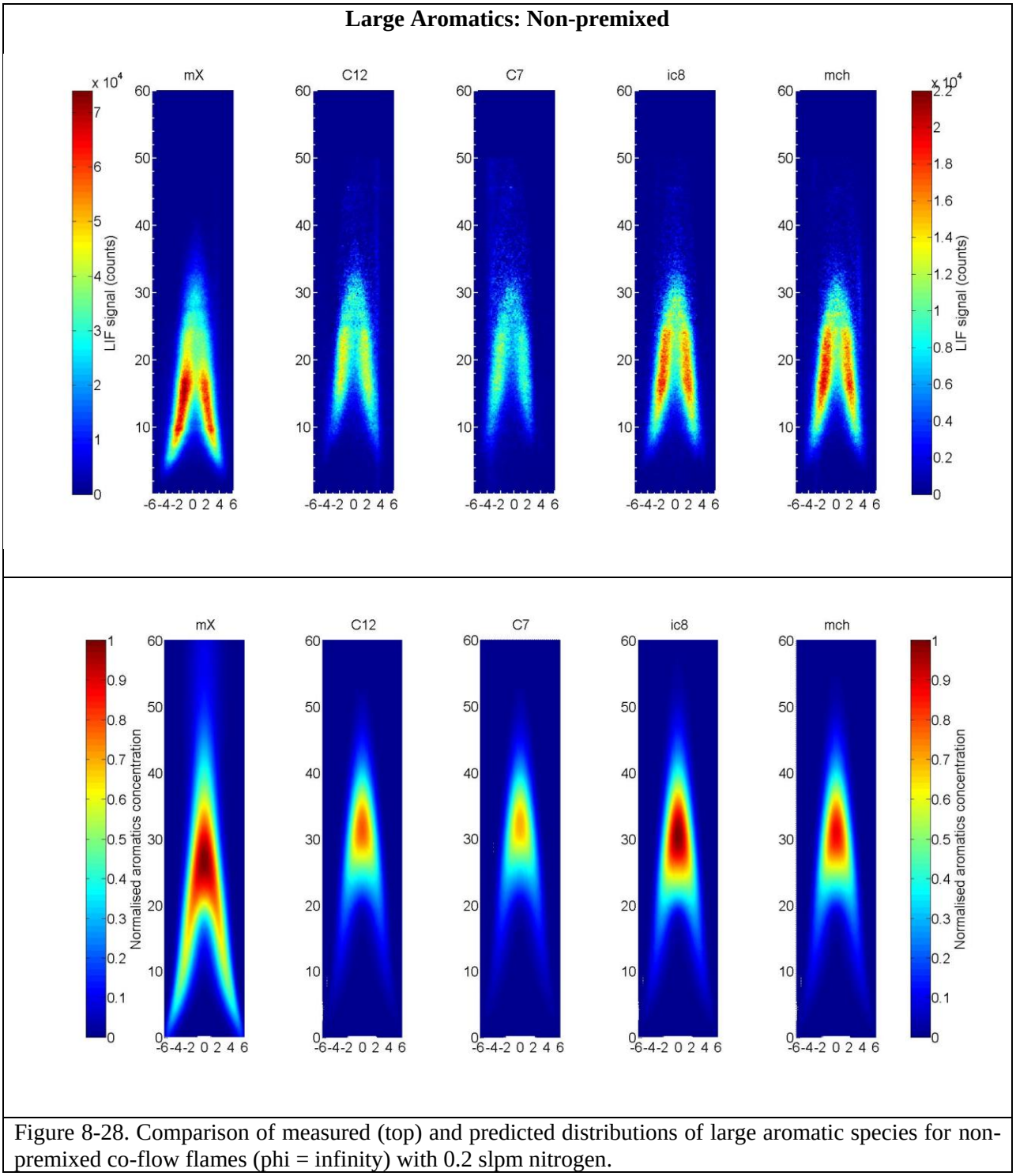

Figure 8-28. Comparison of measured (top) and predicted distributions of large aromatic species for non-premixed co-flow flames (phi = infinity) with 0.2 slpm nitrogen.

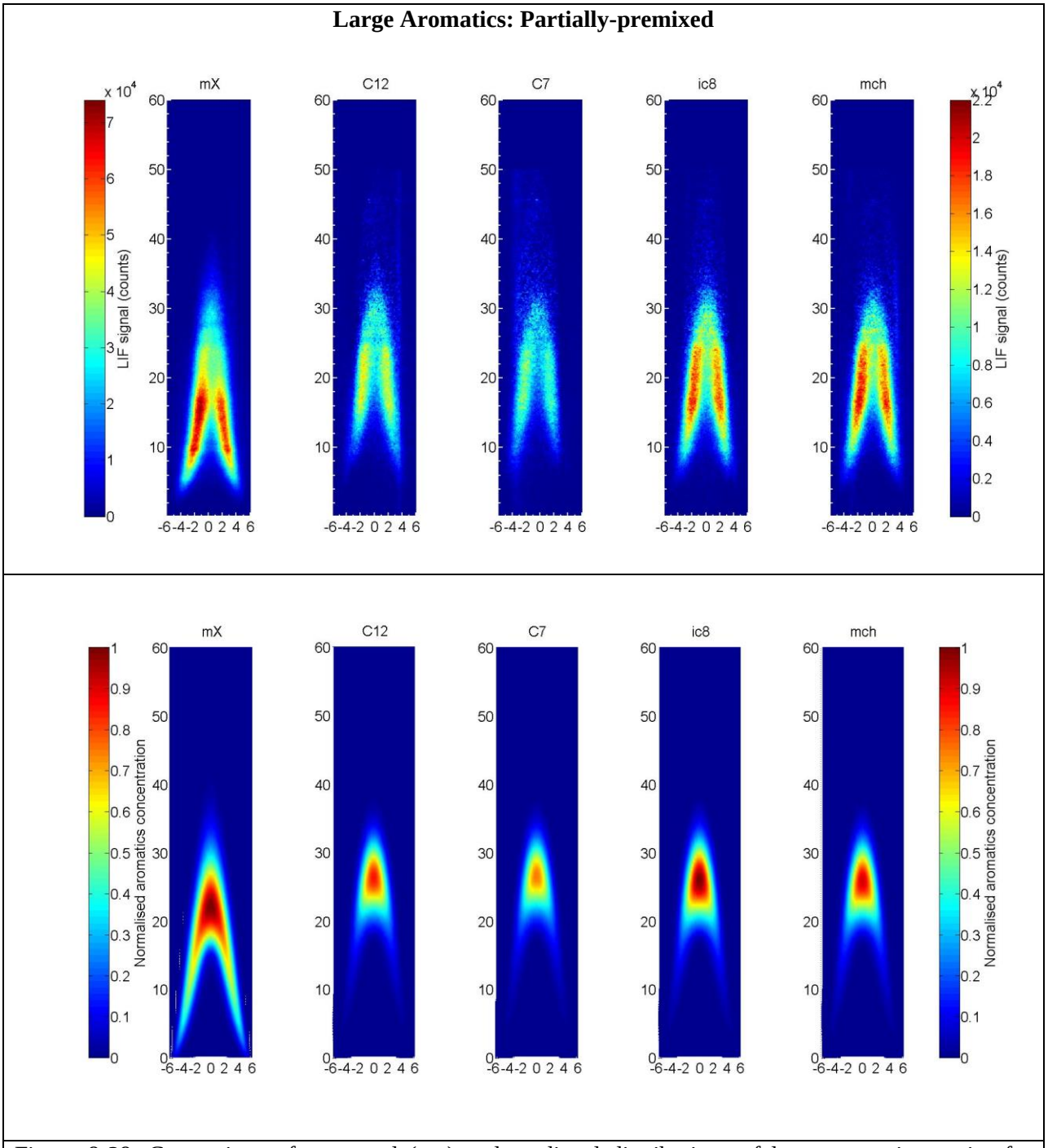

Figure 8-29. Comparison of measured (top) and predicted distributions of large aromatic species for partially-premixed co-flow flames (phi = 6) with 0.2 slpm nitrogen.

8.4 Comparisons of Test Fuels and Actual Fuels

In addition to the four test fuels, two actual fuels were studied in the jet flames: JP-8 and an alternative fuel synthesized with a Fischer-Tropsch process. The fuels are compared in Table 8-4 on a mole fraction basis. The amount of aromatics in the m-xylene/n-dodecane mixture was set at 25% by volume, the maximum amount permitted by the JP-8 specifications for fuels without two-ring aromatics. The 25% volume fraction mole fraction corresponds to 38% mole fraction because of the differences in molecular weight and density between n-dodecane and m-xylene. The FT fuel is nearly all iso-paraffins, whereas the iso-octane/n-dodecane fuel is only 38% iso-paraffins. Thus, the test fuel would be expected to produce lower levels of soot and aromatics based on the relative impact of n-paraffins and iso-paraffins on the formation of soot and aromatic species.

Table 8-4. Comparison of Test Fuels and Actual Fuels.

	JP-8	m-xylene/ n-dodecane	FT Fuel	iso-octane/ n-dodecane
Single-ring aromatics	18.8%	38.2%	~0%	0%
Two-ring aromatics	1.5%		~0%	0%
n-paraffins	16.5%	61.8%	2%	61.8%
iso-paraffins	36.5%	0%	96%	0%
cyclo-paraffins	26.5%	0%	2%	38.2%

Figure 8-30 and Figure 8-31 compare the centerline profiles for aromatic species and soot volume fraction for the JP-8 and m-xylene test fuel for non-premixed and partially premixed conditions. For small aromatic species, the signal levels are higher for the JP-8. This difference is likely due to the presence of the two-ring aromatic species that are present in the JP-8; the two-ring species have larger fluorescence cross-sections than the single ring species. The two-ring aromatic species and the soot volume fraction are much more similar. So even though the JP-8 has lower total concentration of aromatic species, it produces similar amounts of soot and aromatic species to the m-xylene test fuel. The similarity can be attributed to the much greater propensity of the two-ring species to react to form higher molecular weight PAH and eventually incipient soot particles. Thus, the m-xylene test fuel is a reasonable surrogate for JP-8 in producing HAPs that are aromatic and also in the production of soot.

Figure 8-32 and Figure 8-33 compare the centerline profiles for aromatic species and soot volume fraction for the FT fuel and iso-octane test fuel for non-premixed and partially premixed conditions. The soot levels for the FT fuel are approximately 30% higher than for the iso-octane fuel, which is consistent expected trends. However, the laser-induced fluorescence (LIF) levels for the FT fuel are much higher than expected since the fuel does not contain any aromatic species. The probable reason for high LIF signal is believed to be the presence of trace oxygenated species in the FT fuel remaining from the process that created the fuel. Mass spectrometer measurements that will be completed over the next year will verify this hypothesis.

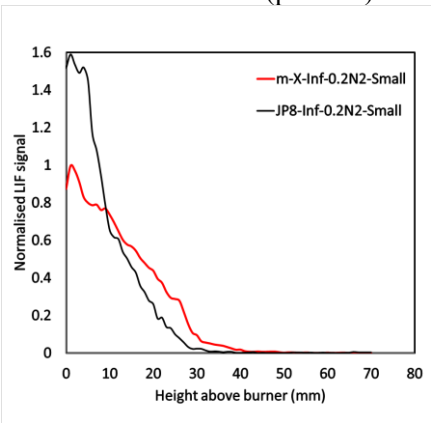

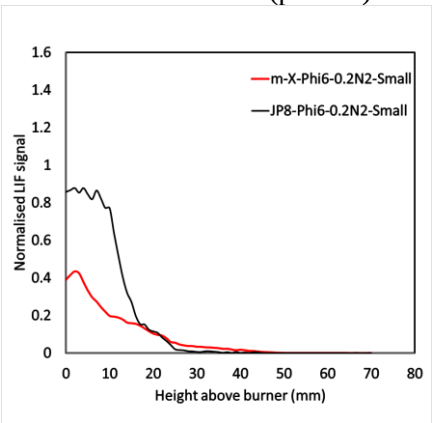

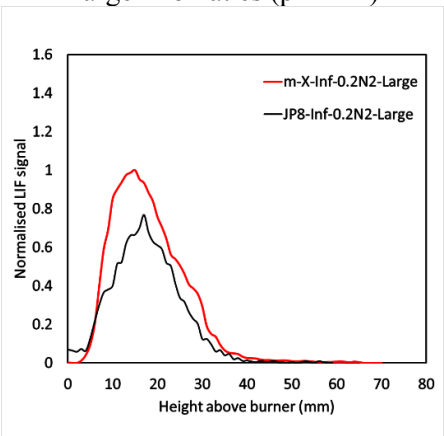

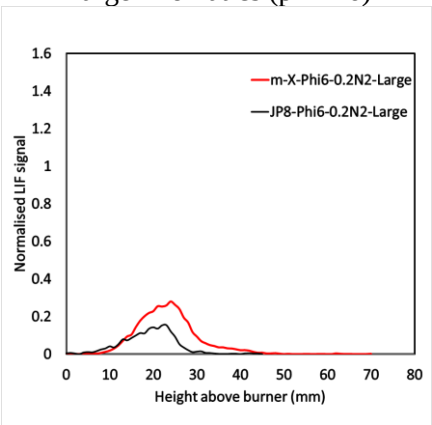

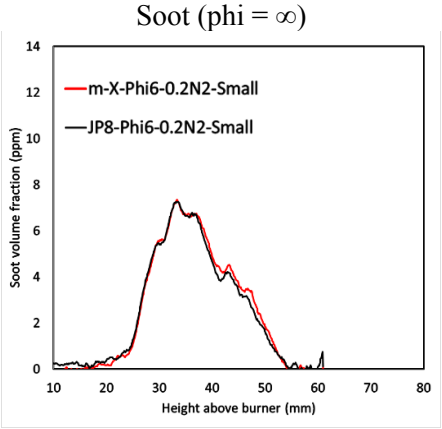

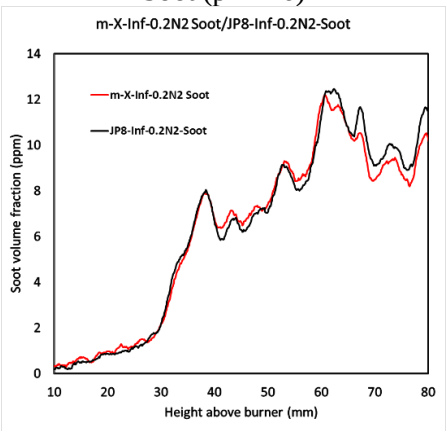

Figure 8-30. m-xylene/n-dodecane vs. JP8 for (phi = ∞): Experimental soot volume fraction and aromatic species for co-flow jet diffusion flame.

Figure 8-31. m-xylene/n-dodecane vs. JP8 for (phi = 6): Experimental soot volume fraction and aromatic species for co-flow jet diffusion flame.

Small Aromatics (phi = ∞)

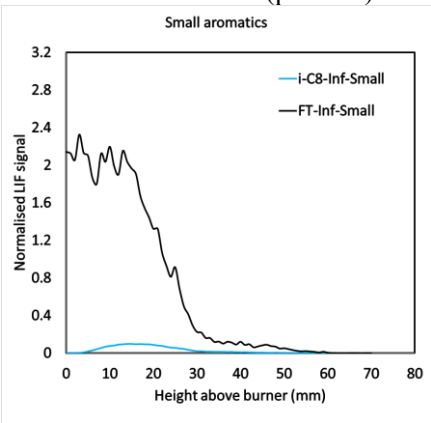

Small Aromatics (phi = 6)

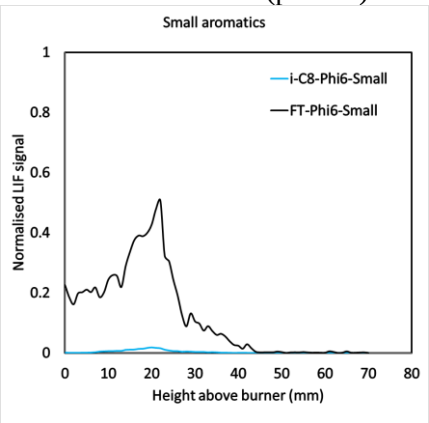

Large Aromatics (phi = ∞)

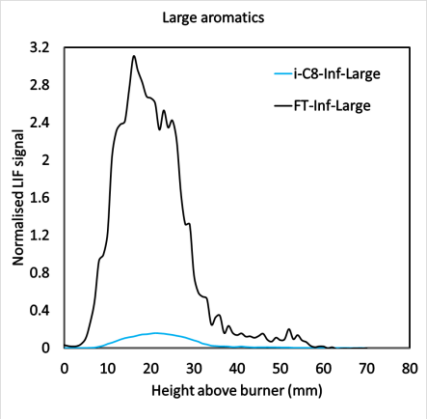

Large Aromatics (phi = 6)

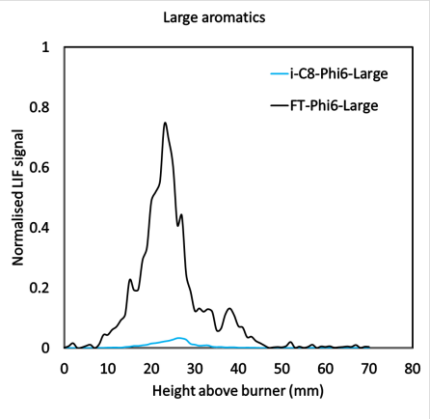

Soot (phi = ∞)

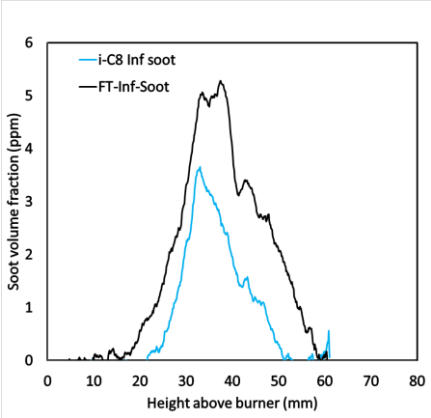

Soot (phi = 6)

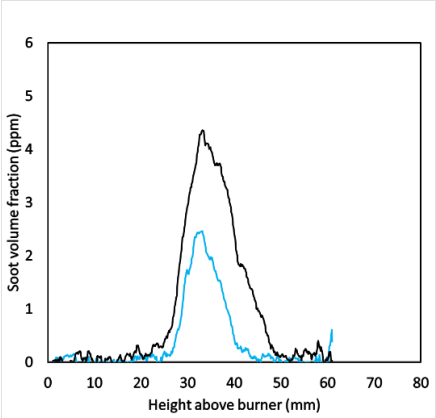

Figure 8-32. Iso-octane/n-dodecane vs. FT for (phi = ∞): Experimental soot volume fraction and aromatic species for co-flow jet diffusion flame.

Figure 8-33. Iso-octane/n-dodecane vs. FT for (phi = 6): Experimental soot volume fraction and aromatic species for co-flow jet diffusion flame.

9 MODEL COMBUSTOR STUDIES

9.1 Experimental Results

Experiments were conducted in the model combustor to determine whether increasing the boiling point of the binary mixture would have an effect on the amount of soot produced in a combustor under fuel-rich conditions. (Experiments in the Referee Combustor, discussed in Section 10, investigated the effect of fuel volatility on UHC and PM under combustion conditions that are overall fuel-lean.) The hypothesis behind these tests is that changes in volatility may affect the vaporization of fuel droplets in a way that would increase emissions. The expected trend is that increasing boiling point of the fuel would lead to increased emissions of UHC, soot and PM. Soot emissions were measured in the model combustor for n-heptane/n-dodecane and n-hexadecane/n-dodecane as well as pure dodecane. The boiling points of the n-heptane, n-dodecane and n-hexadecane are respectively, 98°C, 216°C, and 286°C. In addition, JP-8 was run as a reference fuel to test consistency of operation of the combustor prior to running the relatively more expensive binary fuel blends. The JP-8 was provided by Dr. Tim Edwards of WPAFB and is from the JP-8 supply designated as POSF-5699.

Figure 9-1 shows the data for the two binary mixtures and for JP-8. Two separate experiments were conducted for each fuel. Each experiment consisted of four sweeps in overall equivalence ratio from 1.0 to 1.8 and then 1.8 to 1.0, with increments of 0.1. The figure includes all of the data points along with best fit regression fits to the data. An issue with systematic drift of the reference light intensity was encountered during these experiments. The data were adjusted to account for this drift, but its effect could not be completely compensated. The effect of this drift is most evident at lower equivalence ratios were soot volume fraction is nearly zero.

As expected, both of the binary mixtures, which consisted of normal alkanes, produced substantially less soot than the JP-8. Within experimental uncertainty, the soot volume fraction of the n-heptane/n-dodecane and n-hexdecane/n-dodecane fuels are the same at each equivalence ratio. Therefore, the hypothesis of increasing soot volume fraction with increasing boiling point of the fuel is not confirmed. It is possible that the design injector and bluff-body in the model combustor (Figure 3-17) leads to such rapid levels of droplet vaporization and mixing that the fuel-air mixture is nearly homogeneous prior to the start of combustion. If this is the case, the effects of increasing boiling point would not be evident in the experiment. The scope of the work that could be conducted in the model combustor for the SERDP program did not permit implementing diagnostics to measure the homogeneity of the fuel-air mixture or making modifications to test other designs of the injector and bluff-body that would have lower levels of vaporization and mixing.

If the fuel-air mixture in the dump combustor is homogeneous, chemical effects of increasing the average molecular weight of fuel could still be present. An effect of average molecular weight on soot volume fraction is included in the definition of the Threshold Soot Index, which has been used to correlate the relative propensity to soot among fuels (Calcote and Manos). The average molecular weights of the n-heptane/n-dodecane fuel and n-hexadecane/n-dodecane fuels are 141.3 and 183.6, respectively.

In order to determine whether molecular weight had an effect on soot volume fraction for homogeneous fuel-air mixtures, soot measurements were made for the n-hexadecane/n-dodecane fuel in the jet-flame burner. The results of these experiments are compared to the results for n-heptane/n-dodecane in Figure 9-2 and Figure 9-3. Figure 9-2 compares the 2-D LII distributions from the two fuels under non-

premixed conditions. The 2-D soot field are nearly identical for the two fuels. Figure 9-3 compares the centerline soot profiles for the two fuels, which shows that the n-heptane fuel has slightly lower soot levels. The data suggest that the n-heptane fuel is producing slightly less soot, but the difference in the soot from the two fuels is within experimental uncertainty.

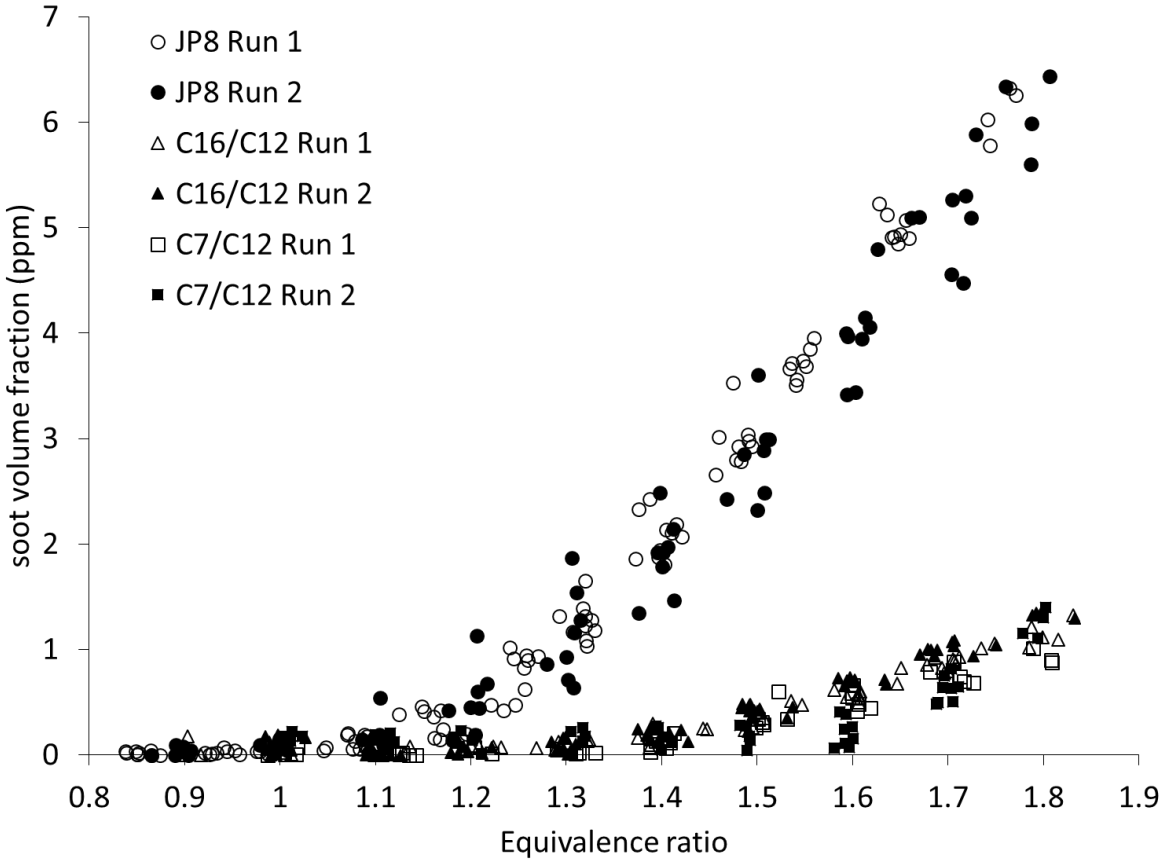

Figure 9-1. Comparison of Soot at Combustor Exit for n-heptane/n-dodecane fuels and JP-8 as a function of equivalence ratio.

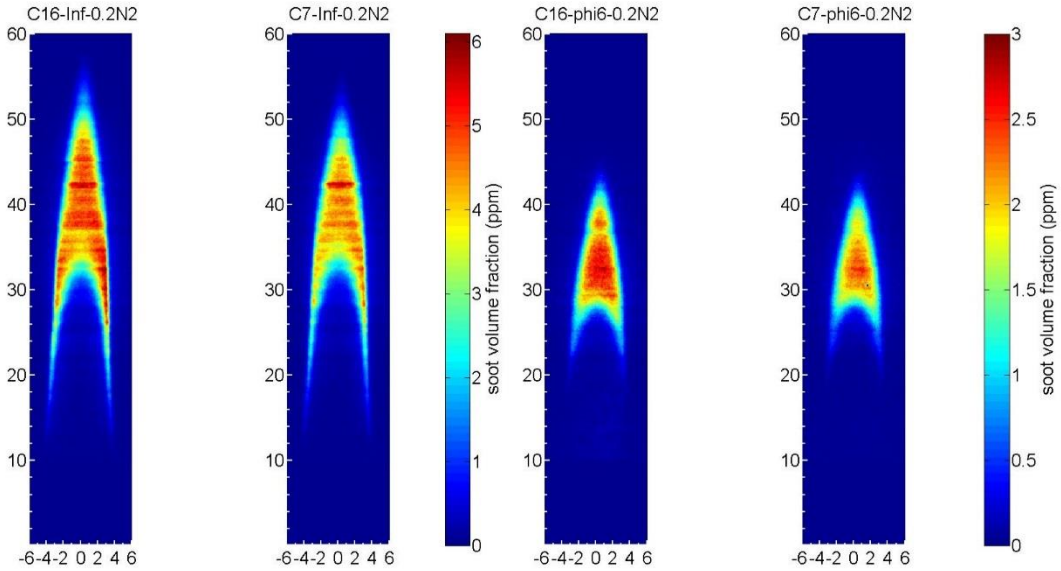

Figure 9-2. Comparison of Soot fields in n-heptane/n-dodecane, pure n-dodecane and n-hexadecane/n-dodecane for non-premixed and partially-premixed (jet phi=6) conditions.

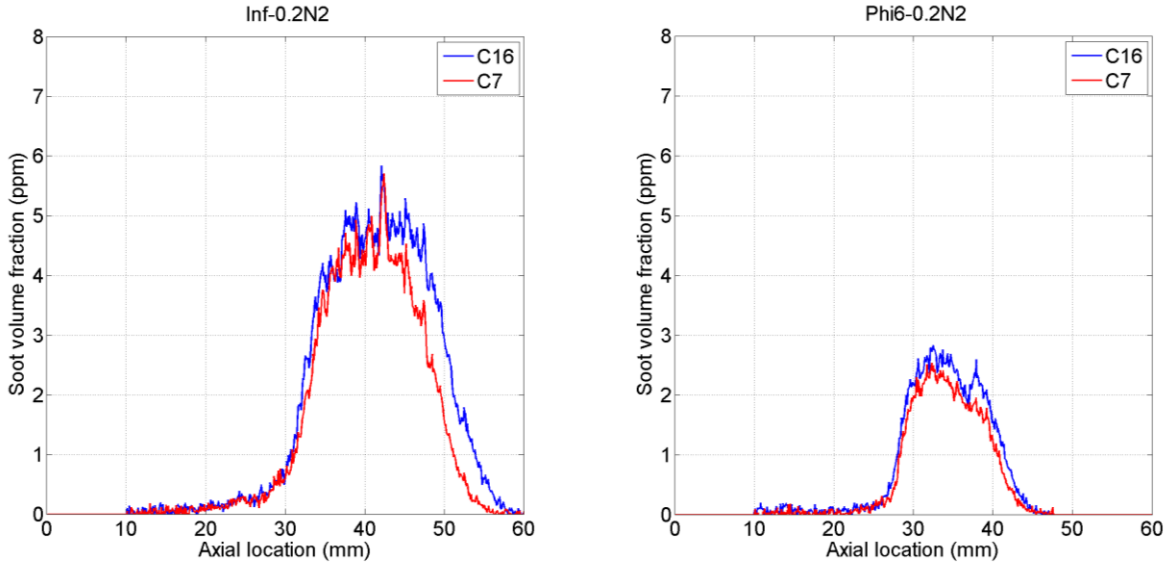

Figure 9-3. Comparison of centerline soot profiles for n-heptane/n-dodecane (C7) and n-hexadecane/n-dodecane (C16) for non-premixed and partially-premixed (jet phi=6) conditions.

9.2 Simulation of Soot in Model Combustor

One approach to developing kinetic model for a surrogate fuels is to formulate detailed chemical kinetic models for each of its components. Typically these components are tested in laboratory experiments like shock tubes and flat-flame burners. Even though the surrogate models can also be validated against the data obtained in the fundamental experiments, such validation is necessary but not sufficient. It is important to realize how well a surrogate fuel and its chemical description mimic the real fuel under environments where those fuels are used. Toward meeting this requirement in the development of surrogate fuels, Penn State University has setup an experimental program using a dump combustor operating at high pressures (Mordaunt, 2005). Even though the design of this combustor became complex for including the key flow features of a gas turbine combustor, yet is simple enough for modeling. Recently, several validation experiments were performed for JP-8 fuel and several of its surrogate mixtures using this dump combustor (Iyer, 2012). It was found that JP-8 produced very low amount of soot when the equivalence ratio was less than 1.2 and then produced soot that increased exponentially with equivalence ratio. JP-8 surrogate mixtures also exhibited similar trends. For understanding the effects of equivalence ratio on soot formation, reacting flows in the dump combustor are simulated using UNICORN code. Calculations are performed for different fuel-rich conditions at 5-atm pressure. Sooting and emission characteristics near the dump section and in the exhaust are analyzed and compared with the experiments. The model combustor is described in Section 3.4.

The axisymmetric feature of the combustor geometry allows the reacting flow in the combustion chamber to be simulated using a simplified model shown in Figure 9-4. The injector bluff body is modeled with a 5.56-mm diameter, 30-mm long tube. The cooling flow is modeled as a shroud flow passing through an annular gap of 3 mm between the combustor wall and the outer boundary. The combustor wall is treated as 1.5-mm-thick solid body with thermal characteristics same as those of stainless steel. The fuel and airflow rates are matched with those used in the experiment. Premixed fuel-air mixture with a specified equivalence ratio is used for the flow entering between the central and outer bluff bodies. An axial velocity of 37.8 m/s (matching with 32 g/s air flow used in the experiment) with 45-degree swirl is prescribed at the chamber entrance. For simplicity, flat velocity profiles are used. The temperature of the fuel-air jet is 500 K. The velocity of the cooling flow (matching with the air flow used in the combustor) is set as 10 m/s. The fuel used is JP-8.

A semi-detailed chemical-kinetics model proposed by H. Wang (2015) for the combustion of JP-8 is used. This mechanism was developed from the lumped reactions for fuel cracking and detailed oxidation reactions for cracked products (JetSurf v.0.2). It has been further modified for the combustion of JP-8 through adjusting the lumped pyrolytic reactions of fuel cracking and reducing it through sensitivity analysis. The final mechanism consisted of 38 species and 436 reactions. Turbulence is modeled using standard k-e approach. While the flow-turbulence interaction is modeled through turbulent viscosity, turbulent thermal conductivity and turbulent diffusivity, the turbulence-chemistry interaction is ignored. Chemical reaction rates are computed using Arrhenius expressions supplied with the chemical-kinetics mechanism.

Soot in the flowfield is simulated assuming it as a gaseous species while solving the flow equations and as mono-sized particles while calculating the formation and growth processes. As a result, two conservation equations--one for the soot volume fraction and the other for the soot number density are added to the Navier-Stokes flow equations. Soot nucleation, agglomeration and oxidation processes are

modeled as described in Mouis et al. (2012). A simple radiation model for gaseous species, based on the optically thin-media assumption, is incorporated into the energy equation. Only radiation from CH_4, CO, CO_2, and H_2O is considered in this study. Radiation from soot is modeled assuming it as blackbody type. Soot nucleation and growth are assumed to be resulting from local acetylene. Soot oxidation is considered primarily due to the presence of O_2, O and OH. Finally, soot agglomeration is treated as a source term in the soot number density equation.

The computational domain is discretized using a non-uniform grid system of 251x126. Grid points are clustered near the dump section where the flame is stabilized for enhancing the accuracy of the simulations. Simulations are performed on a single cpu, intel i7-920 Personal Computer with 16.0 GB of memory. Typical execution time is ~30 s/time-step. Stably oscillating solutions are typically obtained in about 30,000 time steps starting from the solution obtained using a global combustion chemistry model. No ignition source was needed as the high temperatures and CO, CO_2 and H_2O species available from the global initial solution were sufficient for sustaining the flames in the detailed-chemistry simulations.

Experiments using the dump combustor were performed using JP-8 fuel and surrogate mixtures for various equivalence ratios. For evaluating the sooting propensity of different surrogate mixtures with respect to that of real JP-8, soot data in the exit plane were obtained using line-of-sight, laser extinction measurements (Iyer, 2012). It was observed that the soot emission, even though found to be less sensitive to the fuel used (real or surrogates), it increased steeply with the equivalence ratio for all the fuels. The purpose of the current study is to simulate these experiments for understanding the observed effects of equivalence ratio on soot.

Calculations are performed for the axisymmetric model of the dump combustor shown in Figure 9-4 for various equivalence ratios. Velocities of the fuel and cooling flows and their temperatures were not altered while changing the equivalence ratio. All calculations are performed at a pressure of 5 atm. Negligible soot was predicted for equivalence ratios less than 1.2. On the other hand, predicted soot was found to increase exponentially with phi for fuel-rich cases. Results obtained for equivalence ratios between 1.2 and 1.7 are shown in Figure 9-5. For each case, temperature distributions are shown in the left half and the distributions of soot are shown in the right half. The unsteady RANS simulations at elevated pressure of 5 atm predicted dynamic flows for all equivalence ratios. Instantaneous flowfields shown in Fig. 5-56 are obtained at random times. Due to the strong inflow swirl the fuel jet expanded radially outward in a conical shape soon after exiting from the annular passage surrounding the central bluff body. The dynamic fuel jet seems shedding pockets of unburned fuel into products as noted in Figure 9-5 (a) and (d). These fuel pockets got burned quickly and did not show up in downstream direction.

Interestingly, the flow structure changed significantly as the equivalence ratio was increased. Fuel jet became more dynamic at higher equivalence ratios as evidenced from the increased shedding of the fuel pockets. This is due, in part, to the drop in temperature of the combustion products, which decreases molecular viscosity and enhances instabilities. The high burning velocity at phi = 1.2 consumed all the fuel very quickly within a height of 20 mm. A strong vortex shedding along the combustor wall can be noticed in Figure 9-5(a). The conjugate heat transfer from products in the combustion chamber to the cooling air in the shroud region is enhancing the vortex dynamics. The vortex shedding near the wall decreased with equivalence ratio. This may be expected from the reduced temperature (or density) gradients near the combustor wall when fuel got richer.

Very little soot is formed when phi was 1.2. The outer corner near the dump section seems trapping small amount of soot. Relatively cold temperature in this region (due to cooling from walls) and the

entrainment of fuel allow soot to form and stay unburned. Small amount of soot started forming and traveling along the combustor wall at equivalence ratio of 1.4. Note that no soot is formed inside the fuel cone in the cases of phi = 1.2 and 1.4. This scenario has changed at phi = 1.5. Significant amount of soot started forming in the fuel cone region and its concentration increased rapidly with equivalence ratio. This sooting behavior correlates well with the noted decrease in temperature. As the 500-K fuel jet hits the combustor wall and fills the space nearby, the temperature in that region changed dramatically from ~ 2300 K to 500 K, which did not provide appropriate environment for soot growth. On the other hand, combustion products in the region downstream of the fuel cone decreased gradually from ~ 2300 K to ~ 1800 K with equivalence ratio, which allowed soot to form and grow.

The local flow structure near the dump section for equivalence ratios 1.2 and 1.7 are compared in Figure 9-6. Results for the former case are shown in frames (a), (c) and (e), those for the latter case are shown in frames (b), (d) and (f). The color schemes used for these plots are shown at the top. The distributions of temperature and soot radiation are plotted in frames (a) and (b). While the velocity vectors are superimposed on the temperature fields, iso contours of heat release rate (HRR) are superimposed on soot-radiation distributions. Dramatically different flame stabilizations may be noted through comparing the HRR contours for these two cases. When phi was 1.2, flame got anchored along the edges of the fuel jet. However, for high equivalence ratio case (phi = 1.7), flame was initially formed along the inside edge of the fuel jet, but later on (h > 10 mm) it formed closer to the centerline away from the fuel jet. Soot radiation in the high equivalence ratio case is confined to the central core region. Note that even though there is some soot in the regions close to the combustor wall [cf Fig. 5-56(e)] radiation from this soot is negligible due to low local temperatures.

The OH and CO distributions for phi = 1.2 and phi = 1.7 cases are shown in Figure 9-6 (c) and (d). Here, iso contours of O_2 are superimposed on OH distributions. In lower equivalence-ratio case, all the oxygen is consumed along the edges of the fuel jet and the burning intensity (based on OH concentration) increased in some regions. Interestingly, accumulation of CO may be noted in the outermost corner at the dump section. This could be due to the fuel pockets, as seen in Figure 9-6(c), getting separated from the fuel jet and burning slowly in the corner recirculation zone. Flame front in the case of higher equivalence ratio [Figure 9-6(d)] is along a column downstream of the central bluff body. Even though most of CO is confined to this column, some CO got carried away with the motion of the vortices and entrained into the corner recirculation zone.

Distributions of JP-8 and H_2 for phi = 1.2 and phi = 1.7 cases are shown in Figure 9-6 (e) and (f). Contours of the lowest hydrocarbon cracked products (CH_4) are superimposed on JP-8 distributions. The fuel-rich condition of phi = 1.2 should have some fuel left in the combustion products. However, not only JP-8 but also CH_4 got consumed within the region close to the fuel jet [Figure 9-6(e)]. Interestingly, all the hydrogen part of the excess fuel got converted into H_2 and the carbon part of the excess fuel got oxidized to form CO. Absence of cracked fuel components (other than H_2) in the products reiterates the insignificance of the detailed fuel pyrolysis. For phi = 1.7, significant amount of CH_4 is found in the combustor along with JP-8 [Figure 9-6(f)]. In contrast, most of H_2 is found in the cylindrical region downstream of the central bluff body. Overlying the temperature distribution in Figure 9-6(b) on fuel distribution in Figure 9-6(f) suggests that the unburned fuel in the combustor could be divided into two categories. The unburned fuel in the region where temperature is high (> 1200 K) is converted into H_2 and CO and that in the region where temperature is low (< 800 K) is converted into smaller hydrocarbons. Studying these regions would help understanding the emission characteristics of the combustor.

The computed and measured soot at the exit plane for different equivalence ratios are compared in Figure 9-7. These simulations were conducted using the SERDP-2015 chemical kinetic model, developed in the current program. The simulations used the m-xylene fuel mixture as a surrogate for JP-8. Simulations for the other binary mixtures were completed only at a phi=1.6 because of the computational time required for these simulations. The experimental data for JP-8 in the model combustor are from a previous study at Penn State (Iyer et al.) because the data from the current study were not yet available when the simulations were conducted. The simulation results compare well with trends in the new experimental results presented in Figure 9-1. The simulations show the same overall increasing trend of soot volume fraction with increasing equivalence ratio. They also show a substantial decrease in soot for the n-heptane fuel compared to the m-xylene fuel, which served a surrogate for JP-8. Unfortunately, simulations could not be conducted for n-hexadecane because it is not included kinetic mechanism.

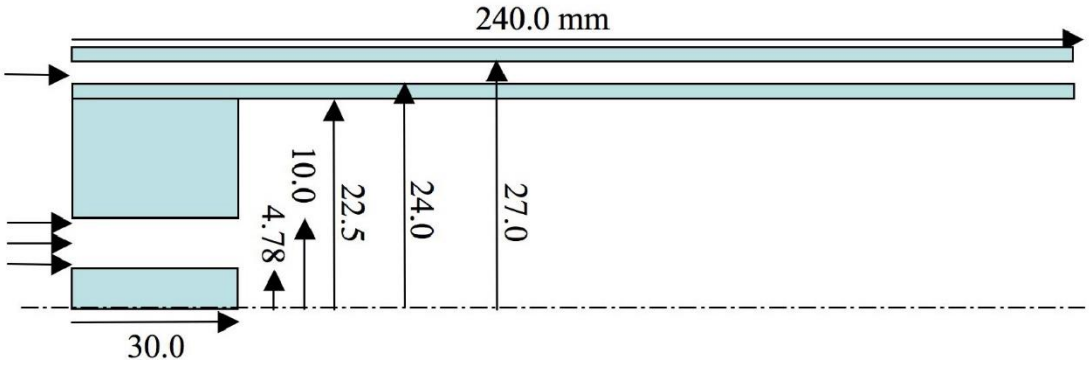

Figure 9-4. Axisymmetric model of the dump combustor used in CFD analysis. Conjugate heat transfer through the combustor outer wall between the burned gases and cooling air is modeled.

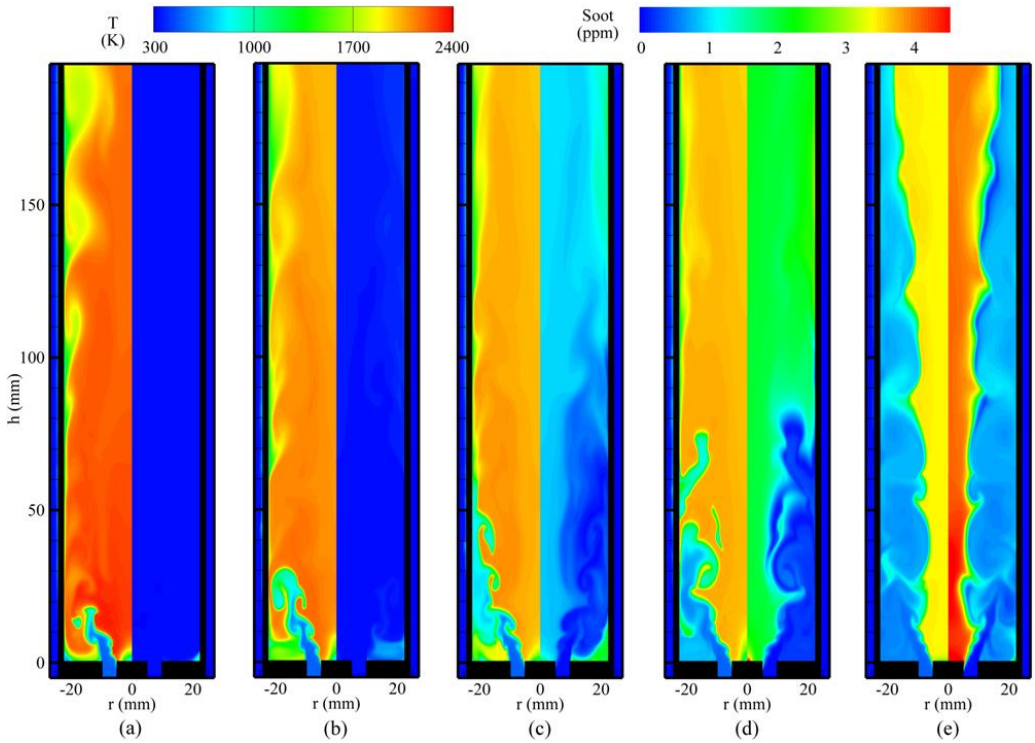

Figure 9-5. Computed temperature fields (left halves) and soot distributions (right halves) in the combustor for different equivalence ratios. Premixed mixtures of JP-8 and air with equivalence ratios of (a) 1.2, (b) 1.4, (c) 1.5, (d) 1.6, and (e) 1.7 are injected into the combustion chamber. Instantaneous flowfields obtained at random times are shown.

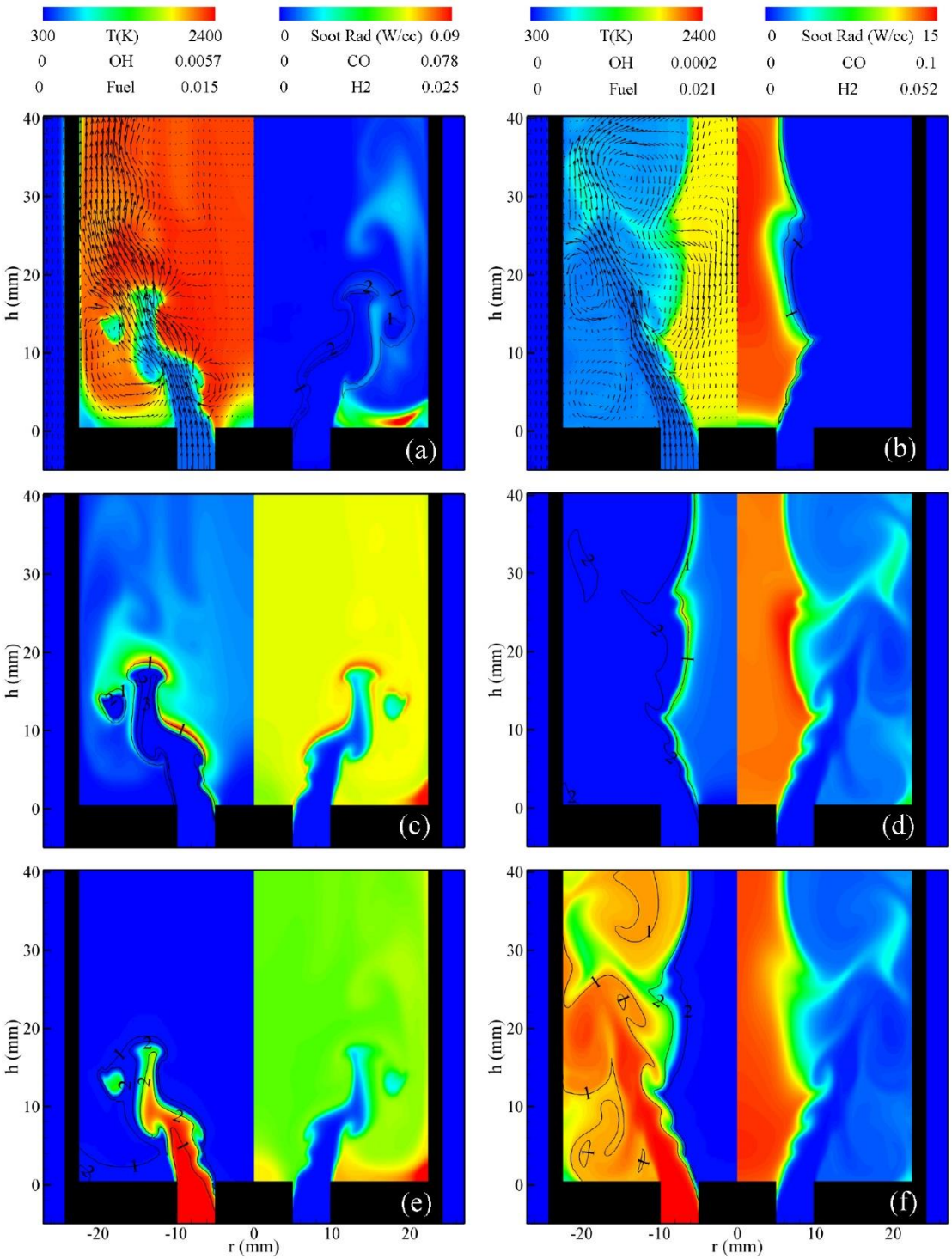

Figure 9-6. Flowfields near the dump section for equivalence ratios 1.2 (a, c, and e) and 1.7 (b, d, and f). Temperature and soot radiation are shown in the left and right halves, respectively in frames (a) and (b). Velocity field (left half) and heat-release-rate contours (right half) are superimposed. OH and CO distributions are shown in frames (c) and (d) in the left and right halves, respectively. O_2 contours are superimposed on the left halves. Fuel and H_2 distributions are shown in frames (e) and (f) in the left and right halves, respectively. CH_4 contours are superimposed on the left halves.

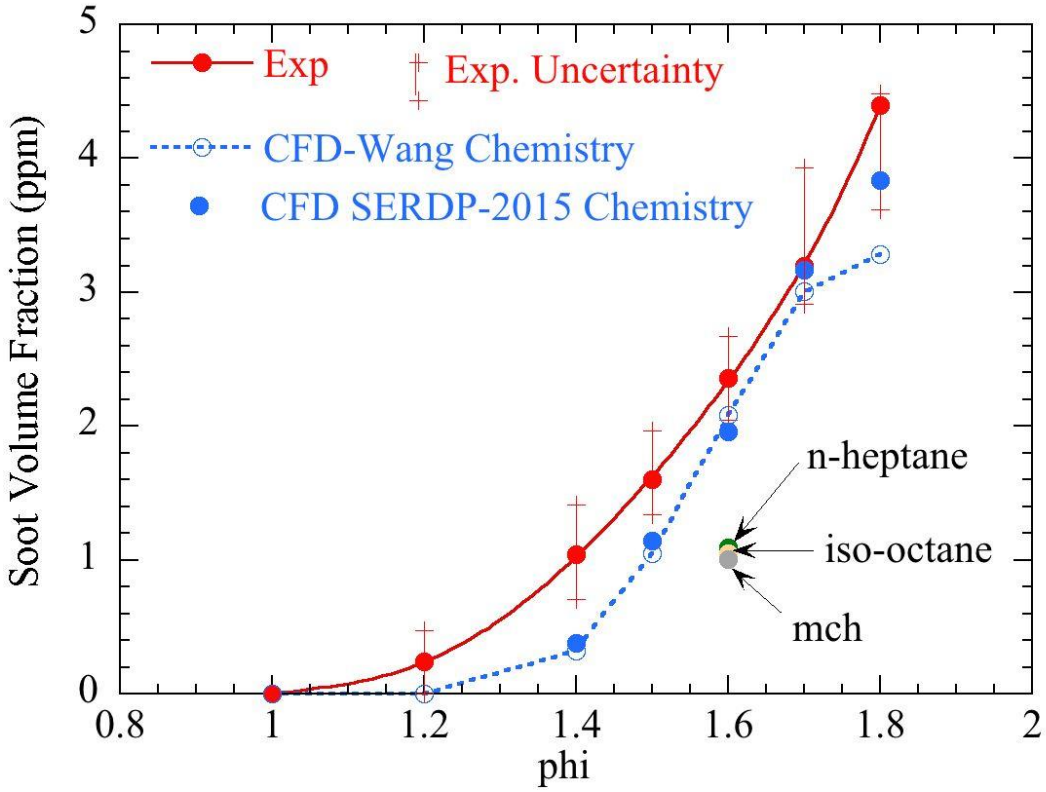

Figure 9-7. Computed (dashed line) and measured (solid line) soot volume fractions at the exit plane of the dump combustor for m-xylene fuel as function of equivalence ratio. Predicted soot volume fraction for paraffinic fuels at phi=1.6 are shown as individual points. The bars between + symbols show the data scatter among experiments performed on different runs and while increasing and decreasing the equivalence ratio.

10 REFEREE COMBUSTOR STUDIES

The combustor performance for the surrogates and a conventional jet fuel was measured for equivalence ratios (phi) near lean blowout (LBO). Figure 10-1 shows the combustor in operation for a typical condition with Jet A fuel. For these conditions, the flame observable by visible radiation is seen to be in the near field region of the fuel injectors. As the reactants flow further downstream they are further diluted by flow through the dilution jets and the effusion cooling passages. Because of structural concerns, the combustor design is heavily effusion cooled, resulting in low overall equivalence ratios. An estimate of the airflow into the primary zone (defined here as the total airflow flow through the swirler plus 25% of the primary dilution jet flow) is 18% of the overall airflow. Using this definition of primary zone air, the ratio of the equivalence ratio in the primary zone to the overall combustor is roughly 5.5.

Emissions measurements were made over a range of conditions from overall phi = 0.11 down to LBO. The high phi end of the measurements was set to avoid high thermo-acoustic instabilities of the combustor, potential "sooting" of windows and subsequent complications on the measurements. The LBO levels are shown in Figure 10-2. It is notable that the highest lean blowout values were observed for the n-C_{12}/i-C_8 surrogate.

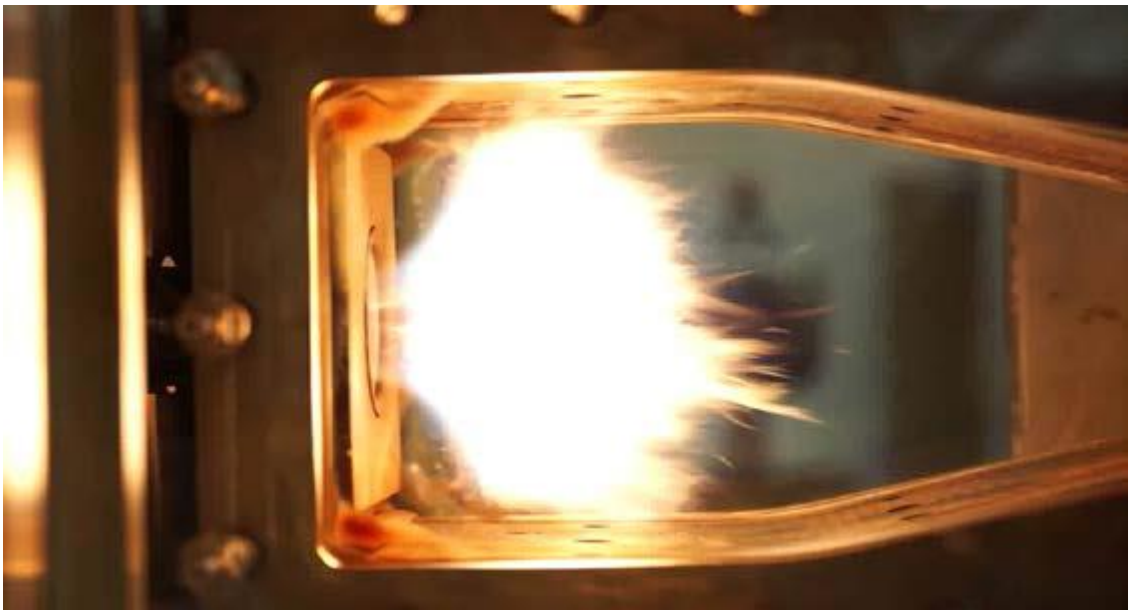

Figure 10-1. Referee combustor operating on Jet A fuel at 207 kPa, T_{air} = 394 K, and phi = 0.1.

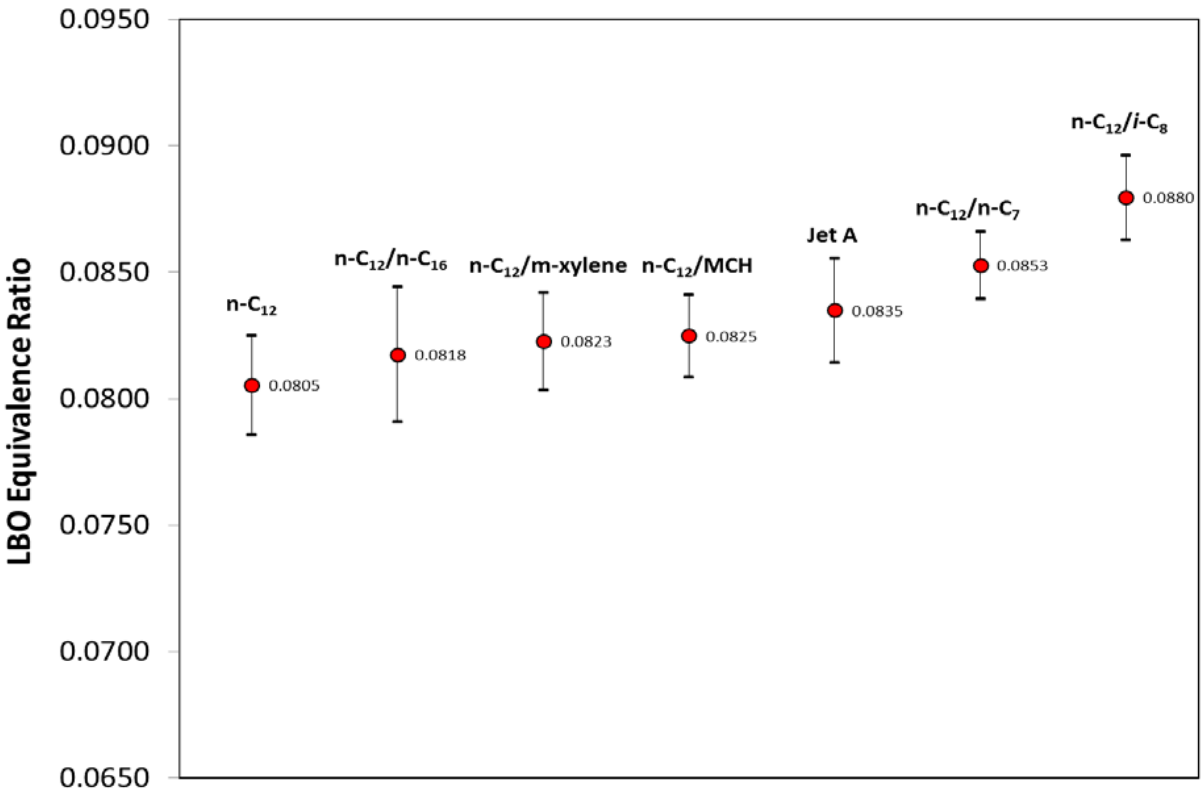

Figure 10-2. LBO Equivalence Ratio for the Test Conditions.

Combustion efficiencies based on gaseous emissions measurements were calculated using guidelines from SAE ARP 1533 (SAE 2013). Figure 10-3 shows the combustion efficiencies as a function of phi for each fuel. Combustion efficiencies ranged from ~78% at near LBO to 88% for the highest phi shown. The efficiency trends as a function of phi were very similar for all fuels, but significant differences between the fuels are observed. As shown, n-C_{12} was consistently the most efficient fuel for this range of phi's, while fuels with aromatics (Jet A and n-C_{12}/m-xylene) and the n-C_{12}/n-C_{16} produced the lowest efficiency. Note that the fuel efficiencies begin to merge as the phi, i.e. combustion temperatures increase.

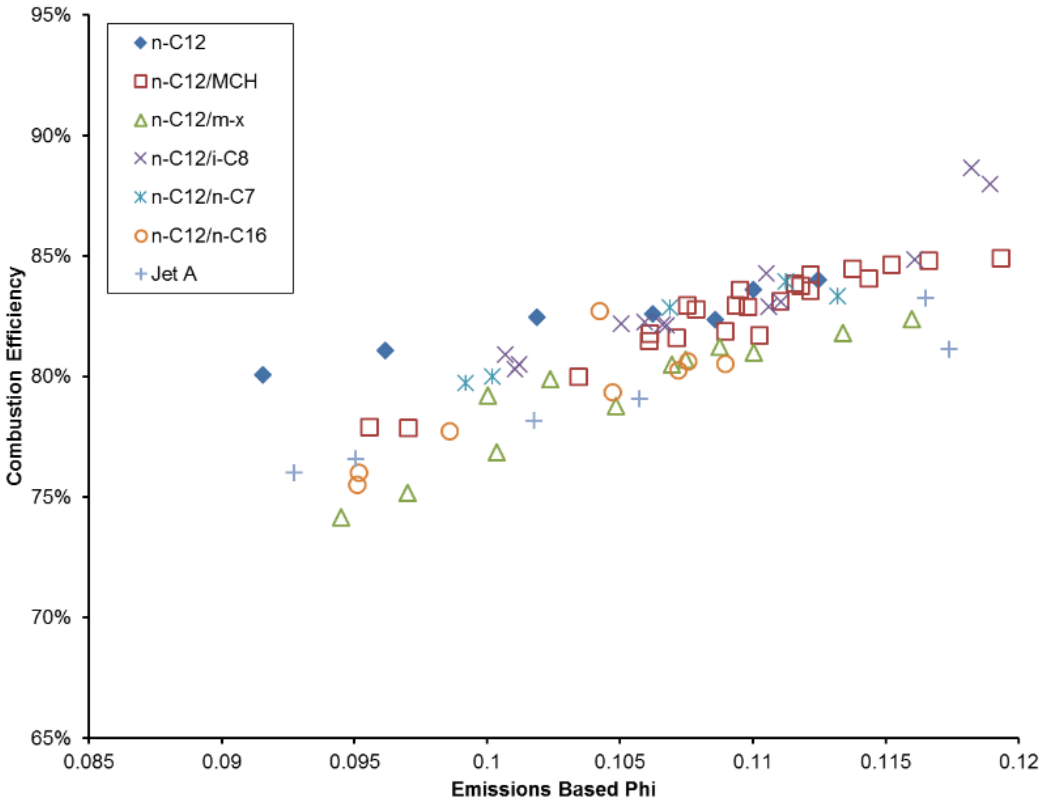

Figure 10-3. Apparent Combustion Efficiency calculated from SAE ARP 1533.

10.1 Gas-phase Emissions

The impact of fuel composition on PM and gaseous emissions were investigated by operating and sampling the combustor at several steady-state conditions for a wide range of phi's. It was noticed that samples collected using the two probes near the walls were ingesting water used to cool the exhaust stream, mostly at higher phi which required higher cooling water flowrates. As such, all emissions data reported herein were collected using only the center probe.

The emissions-based phi were calculated using the guidelines in the SAE ARP 1533 (SAE 2013). The method uses a carbon balance between reactants and products (i.e., mostly CO, CO_2 and unburned hydrocarbons) to determine the fuel-to-air ratio. The phi's were within 5-10% for the lower fuel flows (near LBO), which demonstrates relatively good fuel/air mixing at the point of sampling for those conditions. Repositioning the probes further downstream would likely improve the agreement in phi; however, it would also exacerbate the problem of cooling water entering the probes.

Gas phase and particulate emissions were extracted through the center emissions probe. The CO_2, CO, and UHC emissions are shown in Figure 10-4 to Figure 10-6. The results are expressed in terms of emissions indices. The CO_2 EI increased with an increase in phi, indicating more complete combustion as phi increased. The UHC and CO exhibit the opposite trend, increasing as lean blowout is approached.

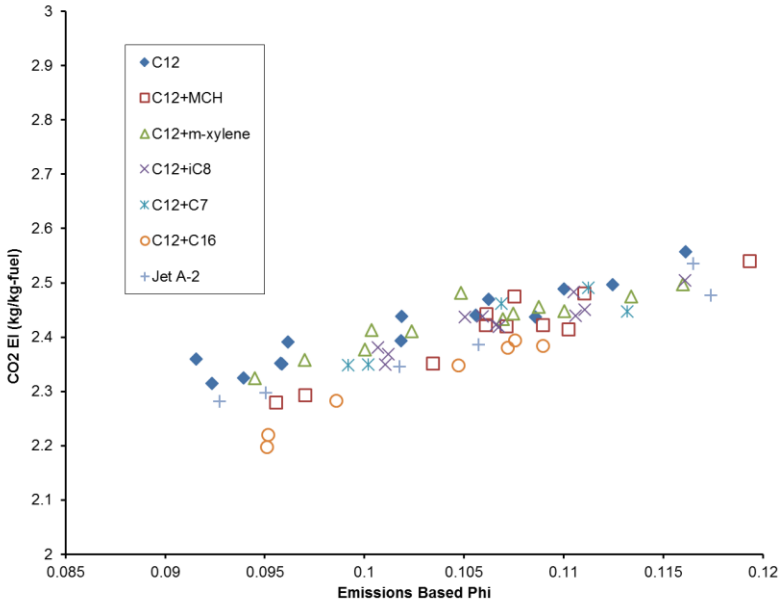

Figure 10-4. CO_2 Emissions at Equivalence Ratios Near LBO.

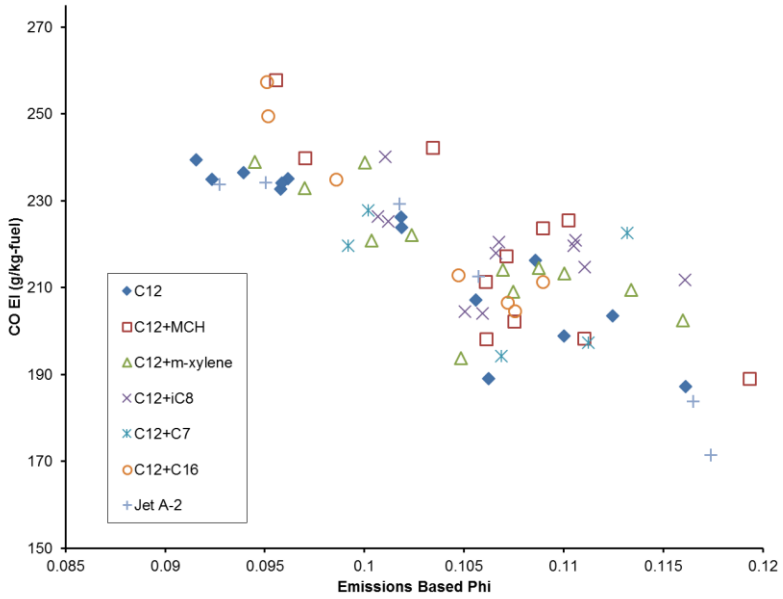

Figure 10-5. CO Emissions at Equivalence Ratios Near LBO.

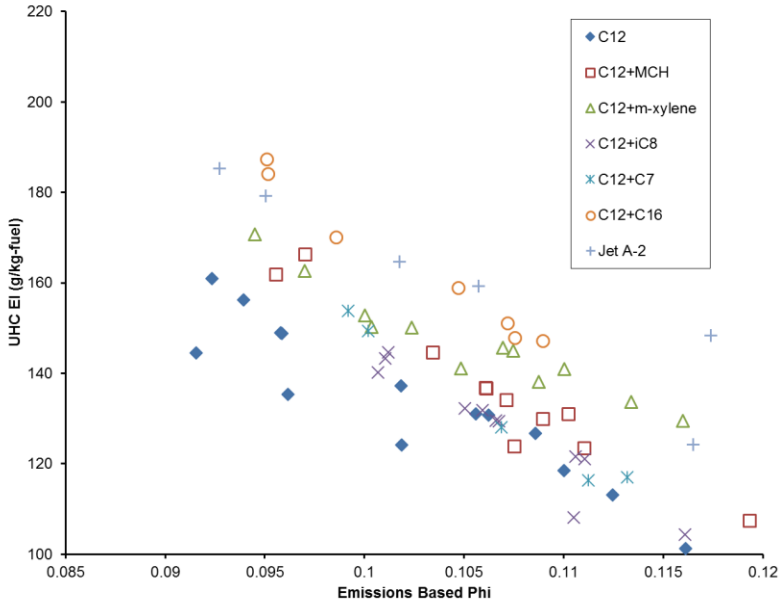

Figure 10-6. UHC Emissions at Equivalence Ratios Near LBO.

Hydrocarbon emissions were monitored using both online (FID and FTIR) and offline analysis (bag sampling and charcoal tube sampling with subsequent analysis) techniques. The combination of techniques allowed both total hydrocarbon and targeted compound identification and quantification. Targeted

compounds include: light hydrocarbon products (e.g., methane, ethane, ethylene, and propane), select hazardous air pollutants (e.g., n-hexane, benzene, toluene, and xylenes), and all surrogate fuel components.

Emissions indices for several of the C_1-C_4 compounds are shown in Figure 10-7 and Figure 10-8. With a few exceptions the levels of each of the emission components were similar across all of the fuels. For all fuels the highest concentration was found for ethylene, followed by either propylene or acetylene, with n-butene at much lower levels. It can also be seen in Figure 10-8 that the n-alkanes in the C_1-C_4 were found in lower concentrations than the alkenes. Methane was seen as the most prominent of the alkanes, decreasing concentrations observed as the number of carbons increased in the n-alkanes. Butane and iso-butene were below detectable limits for all of the fuels. The iso-octane fuel was the only fuel that exhibited significant levels of iso-butylene.

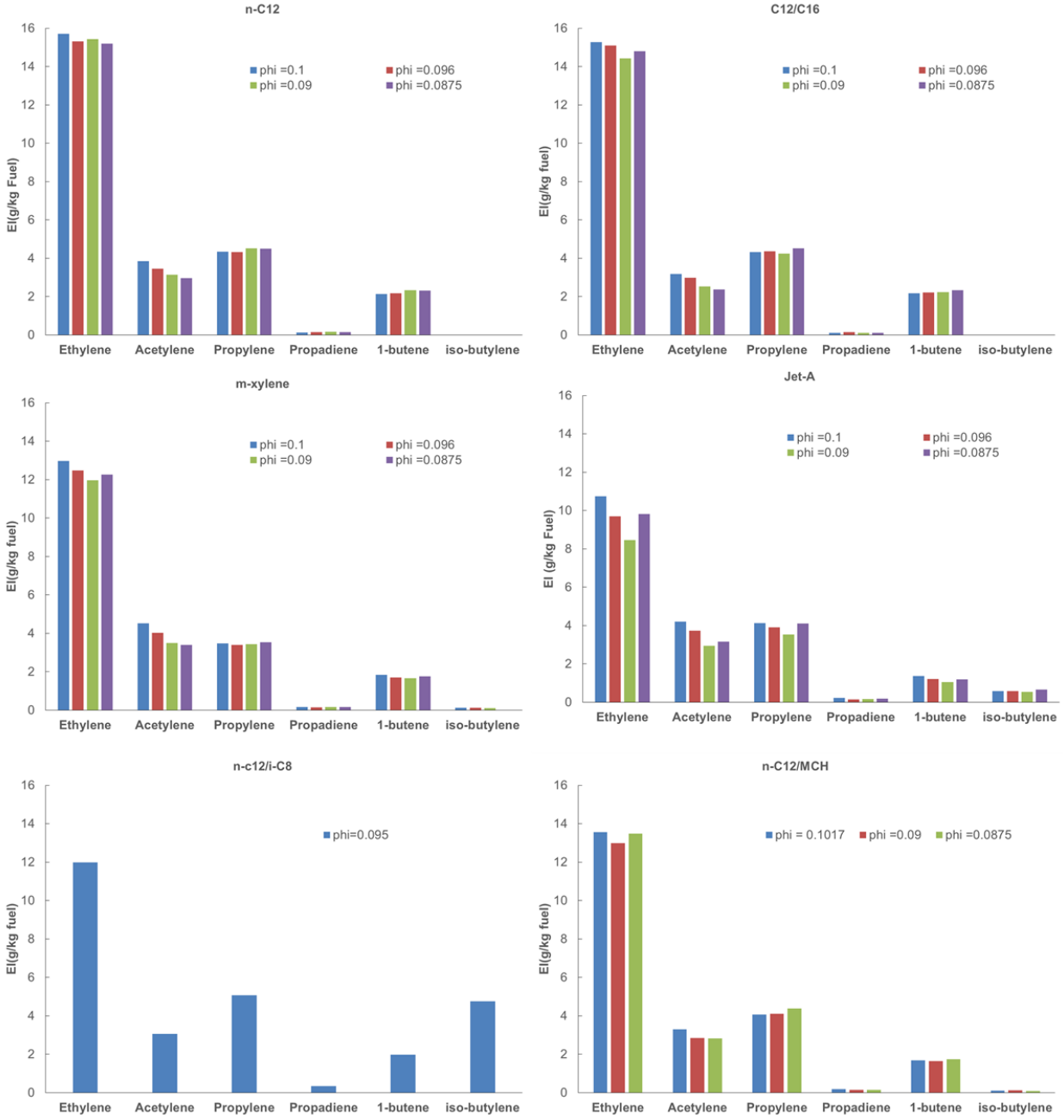

Figure 10-7. C_1-C_4 components in Combustor Exhaust (1-Alkenes and Propadiene).

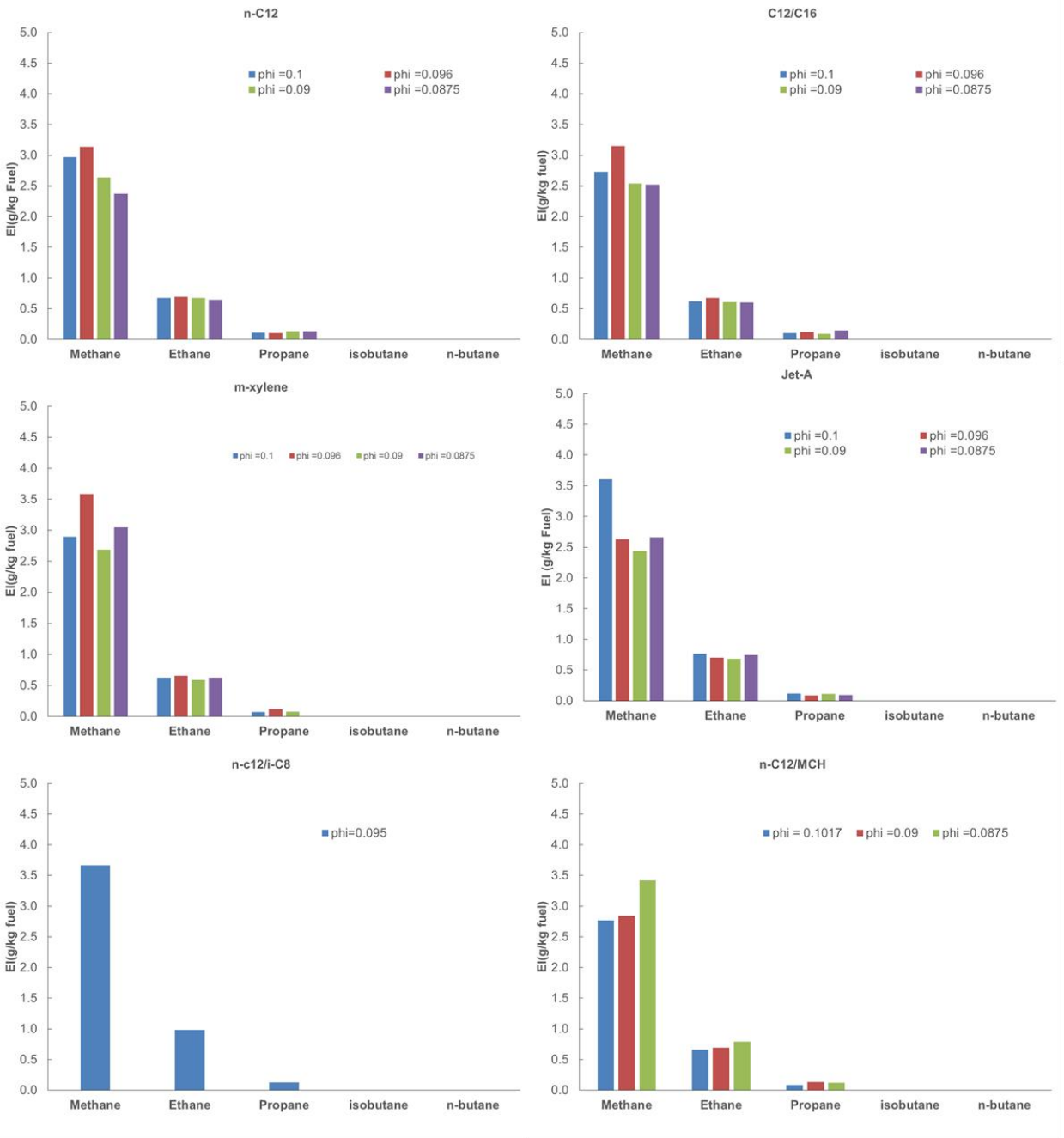

Figure 10-8. C_1-C_4 Components in Combustor Exhaust (Alkanes).

Benzene, and toluene emissions produced by the surrogate fuels are shown in

Figure 10-9 to Figure 10-10. The levels of the two compounds in the exhaust were relatively flat and showed a large variation in levels as a function of the chemical composition of the surrogates. The benzene and toluene were highest for the m-xylene mixture which contains a large aromatic fraction. The MCH fuel mixture was observed to produce similar concentrations of benzene relative to the m-xylene fuel, while all other fuels produced little to undetectable levels of benzene. Figure 10-10 shows that the MCH surrogate produced much lower levels of toluene than the m-xylene, while all of the other surrogates produced little to no toluene. Figure 10-11 shows formaldehyde concentration for the combustion of the surrogates. The formaldehyde concentration varies more with chemical composition than with phi. The highest values for formaldehyde were seen for the iso-octane while the lowest levels were observed for the m-xylene and Jet-A.

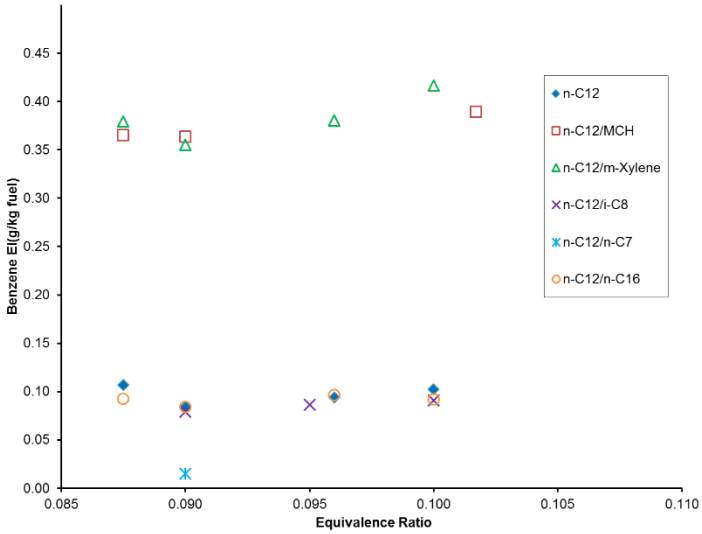

Figure 10-9. Benzene Emissions Index.

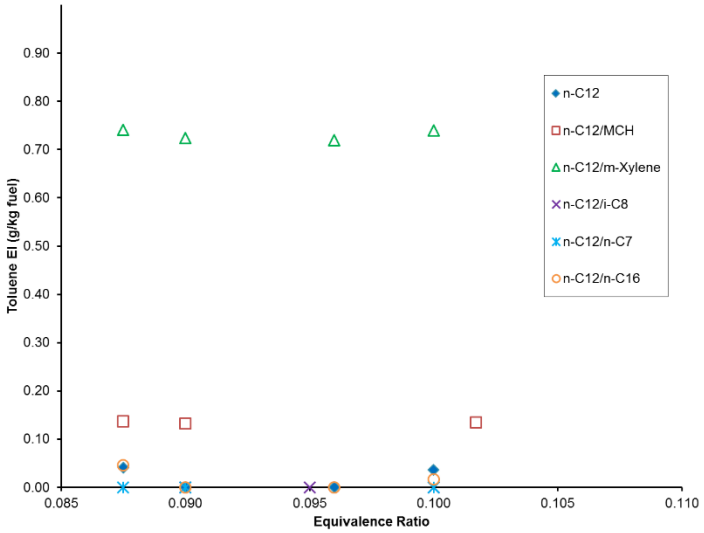

Figure 10-10. Toluene Emissions Index.

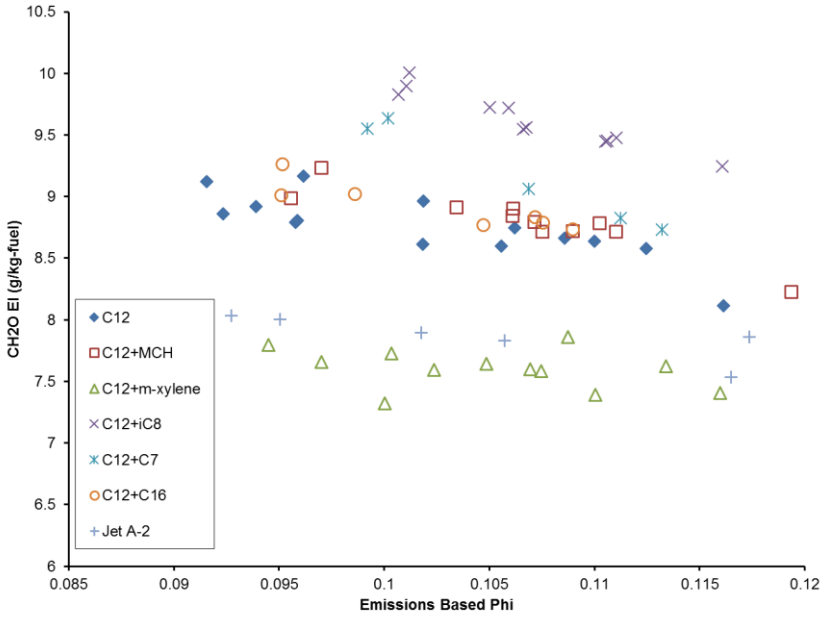

Figure 10-11. Formaldehyde Emissions Index.

The targeted surrogate fuel component analysis allowed the determination of the amount of raw unburnt fuel present in the exhaust. Figure 10-12 shows the percentage of unreacted fuel relative to the unburned hydrocarbons in the exhaust. Note that the results from the n-C16 data are not shown due to difficulties with sample integrity. The results show that the highest fraction of the UHC is reacted fuel, which passed through the combustor without reacting.

The individual component conversions (i.e., mass of component reacted divided by the mass of component fed) for both n-C_{12} and the second blending component. Figure 10-13 shows the relative reactivity, i.e., the ratio of the second component conversion (X_2) to n-C_{12} conversion ($X_{n\text{-}C12}$); a relative reactivity ratio of one indicates both components react similarly upon combustion, whereas an increase or decrease in the ratio would indicate an increase of decrease in the reactivity of component 2 compared to n-C_{12}, respectively. The figure shows that m-xylene has a lower reactivity than the other surrogate compounds, which exhibit similar reactivity to that of n-C_{12}. While the lower conversion ratio of m-xylene could be due to m-xylene production, production of m-xylene for the other surrogates was minimal, which suggests that the lower conversion rate is due to lower reactivity.

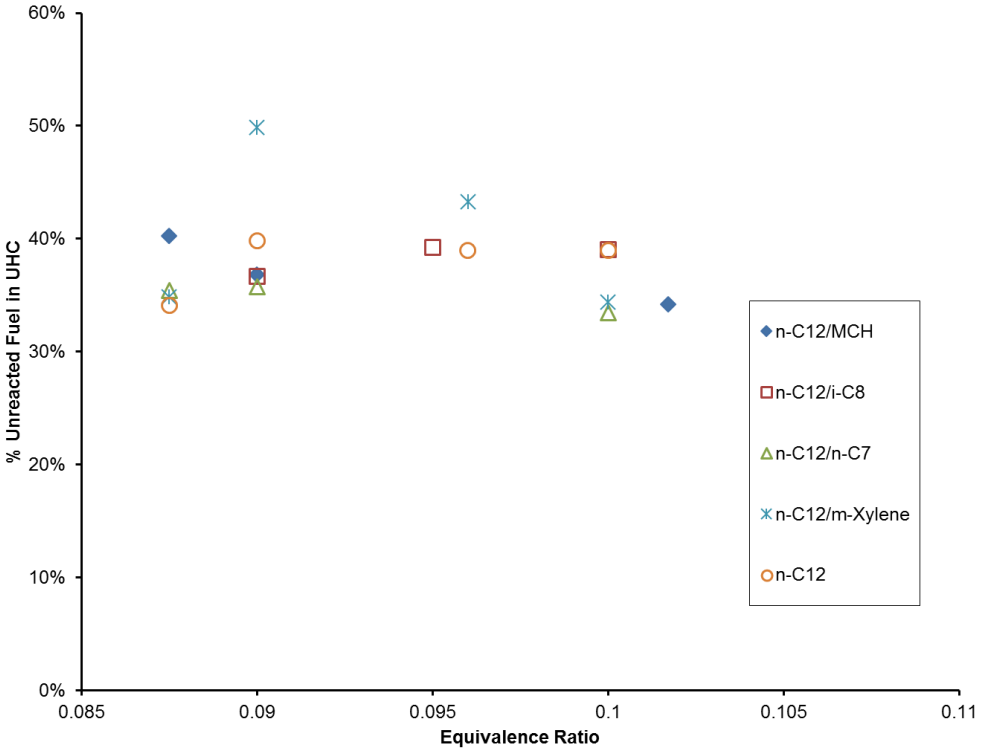

Figure 10-12. Unreacted Fuel Fraction in the UHC.

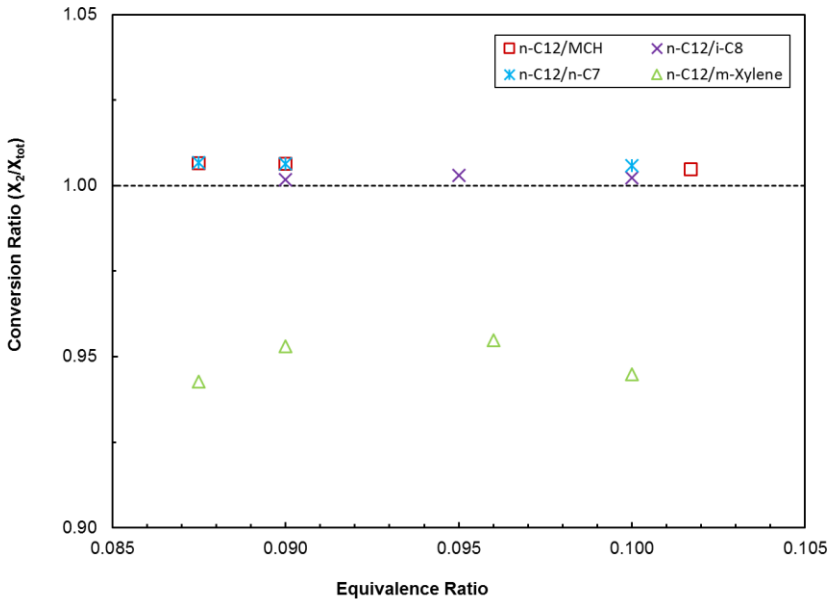

Figure 10-13. Relative Reactivity of Second Surrogate Component Compared to that of n-C_{12}.

10.2 PM Emissions

Particulate measurements were extracted through the center probe. The Particle emission indices are shown in

Figure 10-14. It is noteworthy, that since a volatile particle remover (VPR) was not used, and due to the relatively high concentration of unburned hydrocarbons found at these low phi's, these PM emissions likely contain significant concentrations of volatile PM (e.g., organic aerosols) in addition to the non-volatile (i.e., soot) PM. The particle number emission indices (EIn) increased exponentially as a function of ER. Although the EIn produced by this combustor are significantly lower than for actual turbine engines, the trends as a function of phi (at low phi's) are consistent with those observed previously with these same surrogates on a T63 engine Cain, et al. (2013). The highest particle numbers occurred for the Jet A and the M-xylene/dodecane surrogate, which both contain large fractions of aromatic compounds, while the particle numbers measured for the rest of the compounds were all one to three orders of magnitudes lower. It is notable that at the highest overall equivalence ratio shown, the particle number concentration increases with the boiling point of the second component with the high boiling point n-C12/n-C16 surrogate showing highest particle numbers. It is evident that the organic species may have contributed to the measured particle numbers. The n-C12/n-C16 blend has a relatively high initial boiling and end points, which contributed to its poor combustion characteristics at these conditions. For future studies under very fuel lean conditions, a volatile particle remover (VPR) is recommended to prevent the contribution of volatile PM on the non-volatile particle number measurement

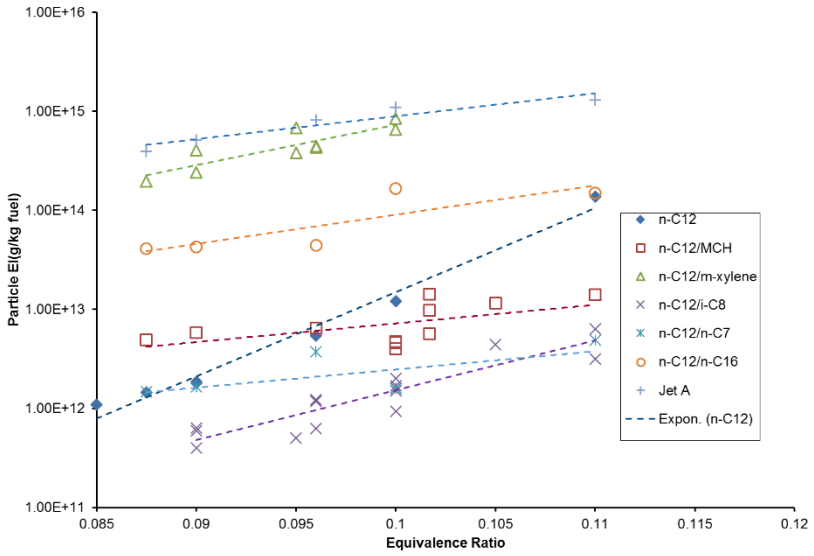

Figure 10-14. Particle number Emission Indices.

The impact of fuel hydrogen-to-carbon ratio (H/C) on PM emissions were explored. Average EI_n for the range of 0.090< ER<0.100 was selected since data were available for all fuels and it avoided the aforementioned instability region. Figure 10-15 shows the PM vs the H/C ratio at phi = 0.10. The curve at phi = 0.09 (not shown) had the same shape. As anticipated, the fuels with aromatic content (lower H/C) produced the highest PM emissions. The total particulate matter for all of the fuels except the C_{12}/C_{16} blend was seen to follow the H/C curve. It is thought that the C_{16} may be higher due to its increased condensation in the exhaust as result of its higher dew point.

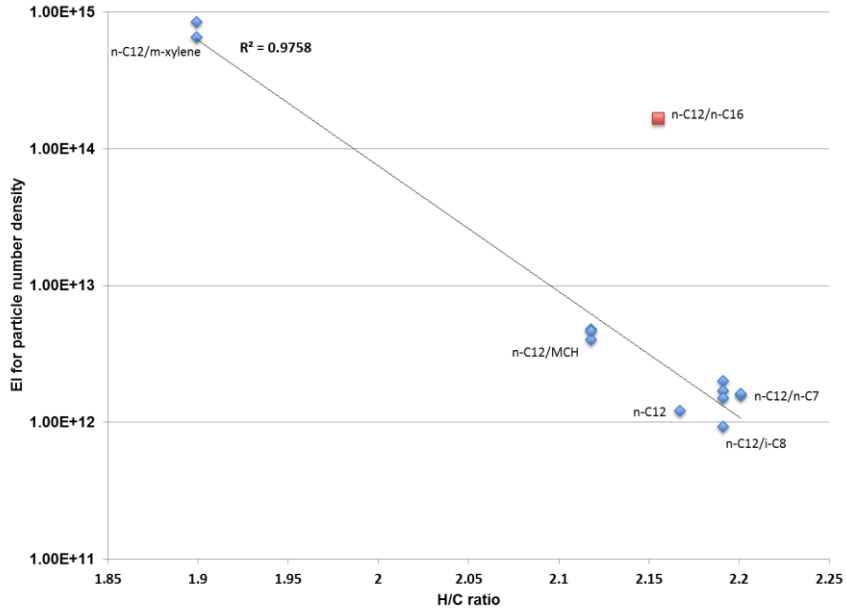

Figure 10-15. Particle Number Density vs HC ratio.

10.3 Summary of findings

The emissions from five surrogates and n-dodecane were studied in a region that produced stable combustion over a range of equivalence ratios roughly 10-30% above the LBO equivalence ratio.

A. The unburned hydrocarbons consisted of high levels (30-50%) of unreacted fuels, which composed the largest fraction of the UHC's.
B. A comparison of the reactivity of second surrogate compound relative to that of n-C_{12} showed that the m-xylene was less chemically reactive than the other compounds.
C. For the C_1-C_4 emissions it was found that the alkene concentrations were highest relative to the alkanes, with ethylene as the species of highest concentration.
D. For C_1-C_4 alkanes methane was present in the highest proportion, and the concentration of the alkanes dropped as the carbon number increased.

11 T63 ENGINE STUDIES

11.1 Effects on Engine Performance

The basic engine performance was similar over the full power range for all fuels evaluated. However, some slight differences were observed, which are most likely related to the varying hydrogen content of the fuels. Figure 11-1 shows a comparison of the overall mass flow as a function of power setting. Figure 11-2 reports the emission index for the total NOx emissions. The required mass flows for a specific power setting were very similar, with minor reduction with increasing hydrogen content (possibly related to higher energy content per mass). The total NOx emissions were comparable, but increased slightly with higher hydrogen content. This may be due to increases in the primary zone temperature during combustion as hydrogen content increases. A specific study or analysis to evaluate the effect of composition on adiabatic flame temperatures would be required to verify this observation.

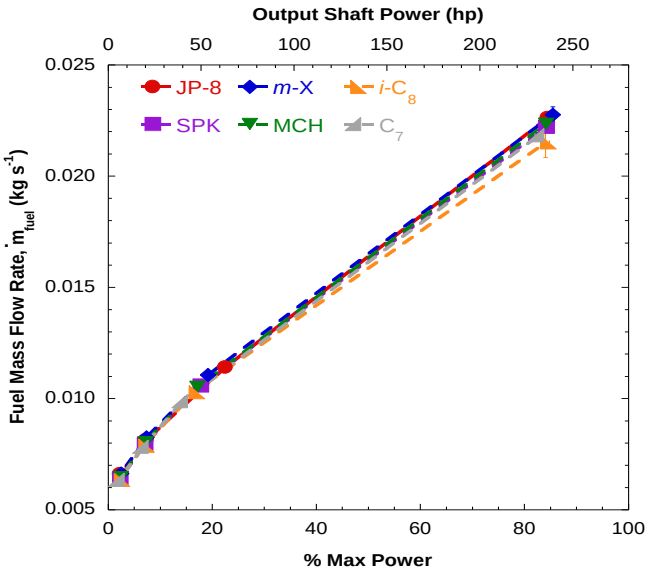

Figure 11-1. Comparison of measured mass fuel flow rate for T-63 engine testing with six fuels.

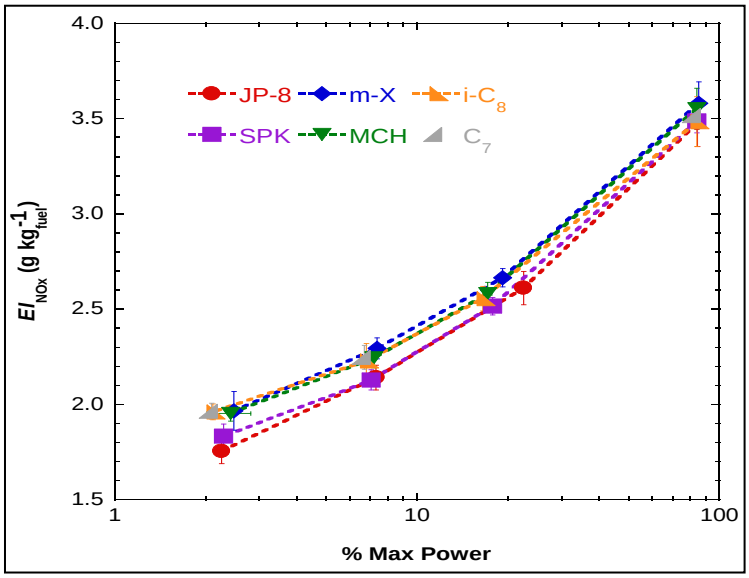

Figure 11-2. Comparison of total NO_x Emission Index for T-63 engine testing with six fuels.

Emissions indices of other major emissions were also consistent with the varying hydrogen content of the fuels; CO_2 and CO both showed corresponding decreases with increasing hydrogen content. CO and total unburned hydrocarbons emission indices were reduced by approximately an order of magnitude as the engine power increased from Idle to the highest power setting. The large decrease in hydrocarbon emissions resulting from an increase in engine power is consistent with previous studies and is attributed to improved combustion efficiency at the higher operating temperature (Spicer, et al., 2009; Anderson et al., 2006).

11.2 Speciation of Minor Combustion Products

The surrogate composition was much more evident on the emissions of speciated minor emissions. In particular, the aromatic emissions were very sensitive to fuel composition, which is important, as this molecular class is known to be a precursor to soot formation. A comparison of the EI for benzene as a function of fuel type and power setting is shown in Figure 11-3. Similar trends were observed for other

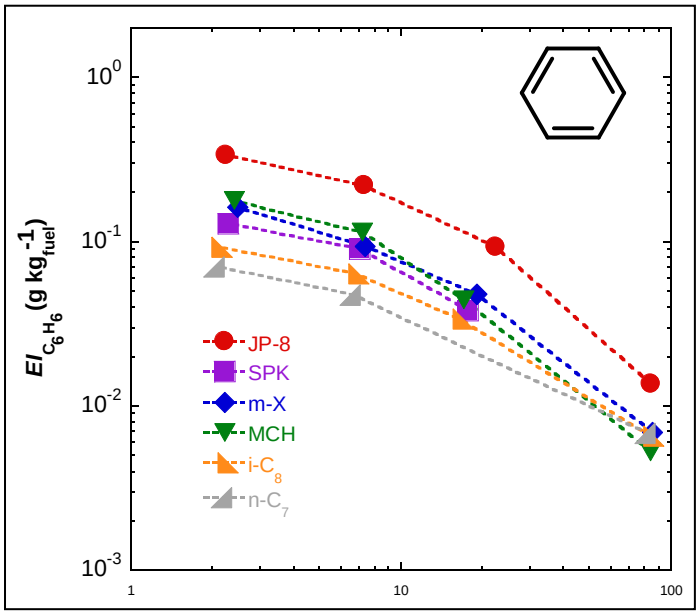

Figure 11-3. Comparison of the emission indices of benzene as a function of power setting and fuel type.

speciated aromatic emissions. The three surrogates without aromatics (*i.e.*, methylcyclohexane, *iso*-octane and *n*-heptane blends) emitted significantly lower aromatic compounds, while the JP-8, F-T and *m*-xylene/*n*-dodecane fuels had substantial aromatic emissions. This trend can be primarily attributed to either direct emission of uncombusted aromatic compounds in the neat fuels or increased rates of production due to precursors in the binary fuel blends. The formation of aromatic compounds during F-T fuel combustion was most likely intensified by the highly-branched nature of the fuel. This can result in formation of combustion intermediates and products more prone to ring formation reactions (*e.g.*, propargyl radicals and propylene). The branching ratio of the fuels did also affect the formation of other species, such as ethylene, which is primarily formed during thermal decomposition via □-scission reactions. Aromatic emissions for testing with *m*-xylene are most likely due to direct decomposition and reaction of this compound during combustion.

Aldehyde emissions were observed as minor products during combustion of the various fuels in this study. In general, a decrease in aldehyde EI values with increasing engine power was observed for all fuels. Linear aldehydes were emitted at the highest yields for all fuel and engine powers, with the exception of the *m*-xylene/*n*-dodecane blend emitting large amounts of *o,m,p*-tolualdehyde due to direct production from *m*-xylene in the fuel. The methylcyclohexane, *iso*-octane and *n*-heptane blends produce similar yields of aldehydes as the F-T fuel, which is reasonable because these fuels are primarily paraffinic in nature. It was observed that JP-8 emitted the least amount of aldehydes at each engine power and fuel combination tested.

Comparison of individual species emissions normalized to other compounds in the exhaust may provide insight into the controlling reaction pathways and emission propensity for different compounds classes and how these affect combustion efficiency. Knighton *et al.* (2007) and Yelvington *et al.* (2007) observed linear relationships between formaldehyde production (or CO_2) and other hydrocarbons in the exhaust of a CFM56-2-C1 turbofan engine. In the Knighton work, three fuels were tested: a baseline (17.5% aromatics), high aromatic (21.8%) and high sulfur content JP-8 (1600 ppm). Correlations between formaldehyde and the hydrocarbons were observed to be independent of the fuel composition. Anderson

et al. (2011) observed a linear relationship between ethylene and other unburned hydrocarbons, but noted different slopes for JP-8 and Fischer-Tropsch fuels. The emission indices of benzene and acetaldehyde in this study normalized to ethylene EI values as a function of fuel type and engine power are shown in Figure 11-4 and Figure 11-5, respectively. These plots show that speciated emissions correlate linearly with ethylene, with high sensitivity of the correlation on the fuel composition. Similar

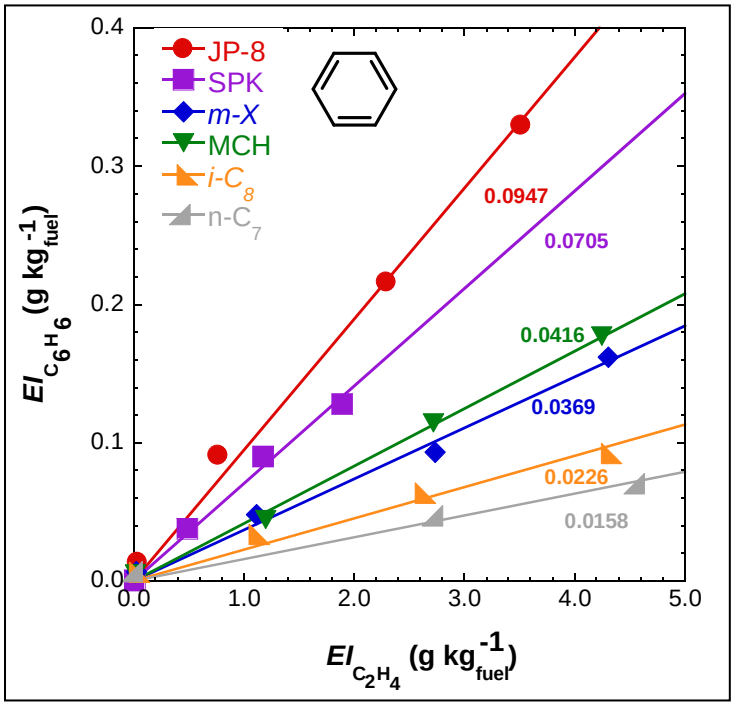

Figure 11-4. Correlation between emission indices for benzene and ethylene. Symbols denote the fuels tested and numbers displayed are the linear slopes.

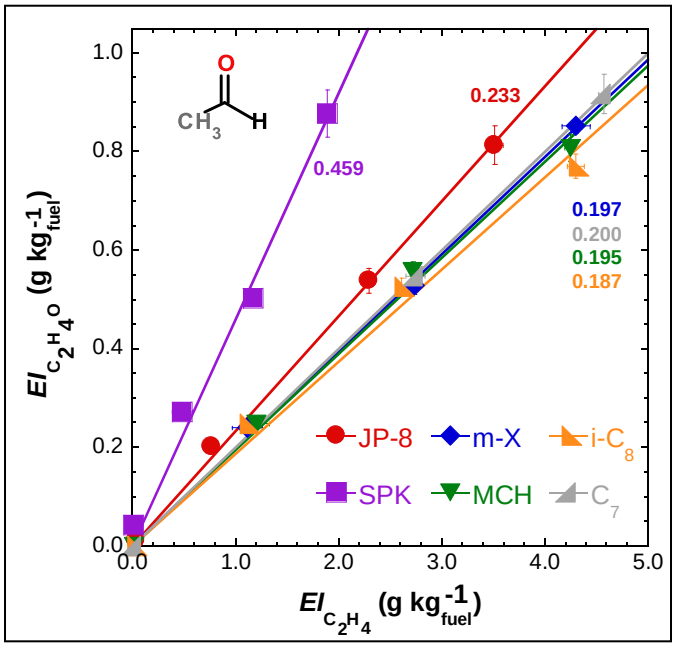

Figure 11-5. Correlation between emission indices for and acetaldehyde to ethylene. Symbols denote the fuels tested and numbers displayed are the linear slopes.

Correlations were observed for other gaseous emissions. These statistical differences in the slopes of the correlations indicate that the fuel chemistry affects the selectivity of species formation during combustion. This interdependency has significant implications in the development of accurate and robust chemical kinetic models for alternative fuels. More specifically, it will assist in identifying and correlating the controlling and pertinent reaction pathways for specific fuel chemistries and can be used as control sets for model and mechanism optimization. Further analysis is being performed to provide additional insight into the differing emissions trends.

11.3 Physical Properties of Soot Emissions

The effect of chemical composition on PM production showed a significantly higher dependence than those observed for the gaseous emissions. The Particle Number Emission Index as a function of fuel type and power setting is shown in Figure 11-6. As expected, the particle emissions increased with higher engine power for all fuels, due to increased rate of soot formation at elevated combustion temperatures and pressures. The paraffinic surrogates have much lower soot propensity than the fully formulated fuels and the *m*-xylene/*n*-dodecane blend, which can be attributed to the role of chemical structure on soot formation rates (Corporan, 2004). The fuels with aromatics, which are direct precursors for soot formation, had much higher PM emissions. With respect to the paraffinic fuels, those with cyclic and high branching had a higher propensity for soot than the linear paraffins. This is due to the increase propensity to form reactive intermediates, which are prone to ring formation, closure and dehydrogenation reactions, resulting in subsequent molecular growth. In general, these observations are consistent with previous alt fuel and chemical class studies, and with simplified soot formation mechanisms, where the rate of formation of soot intermediates affects overall PM emissions. This data can be extremely useful for evaluating the chemical

kinetic models and mechanisms currently under development. Further analysis of PM emissions, including the effect of fuel composition of the particle size distributions and mass emission is being performed and will be subsequently reported.

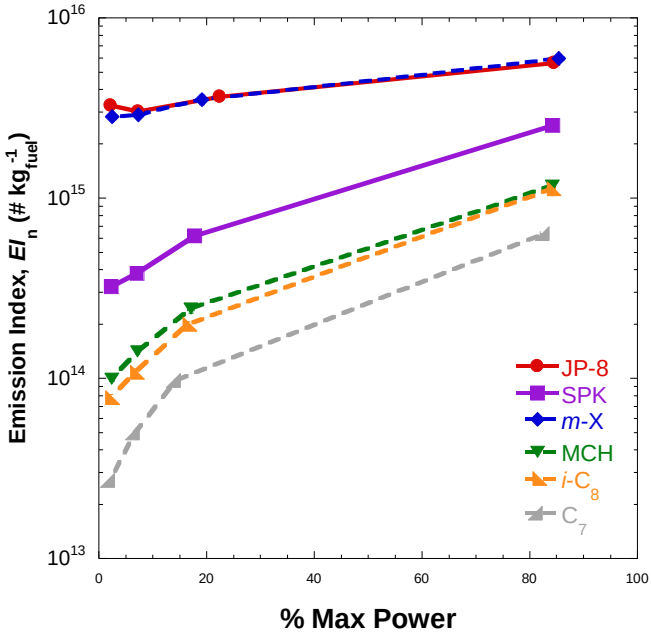

Figure 11-6. Particle Number emission indices as a function of engine power for fuel type.

Estimates of the number and mass of particles that are analyzed by micro-FTIR spectroscopy were calculated. Results show that this method is quite sensitive and probes a wide range of particles: as few as 10^4 particles (~ 5 pg) to as many as 10^9 particles (~ 100 ng). The number of deposited particles peaks around stage 12 for total number and stage 11 for total mass, as shown in Figure 11-7.

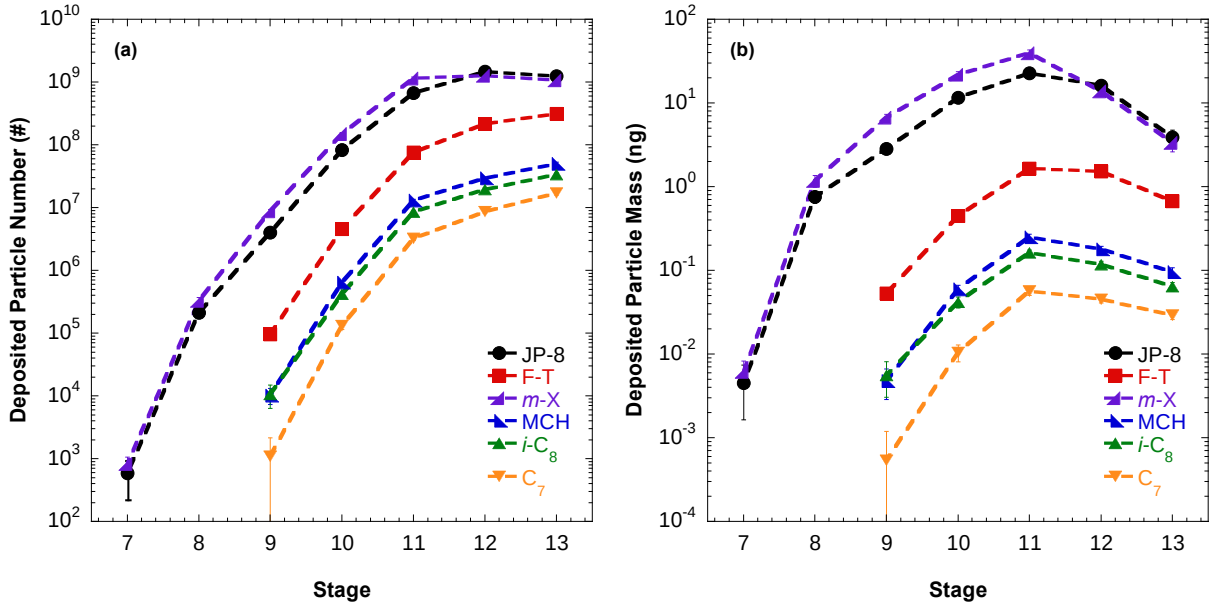

Figure 11-7. Estimated (a) number and (b) mass of particles deposited on stages 7-13 for each fuel (symbols) at low-speed ground idle. Values are representative of one deposition spot (*i.e.*, nozzle) for the sampled PSDs, experiment sampling times and a density of ρ = 1.5 g cm^{-3}.

11.4 Chemical Properties of Soot Emissions

A typical averaged, baseline-corrected and smoothed spectrum for T63 soot particles is shown in Figure 11-8. Various chemical groups are observed in the mid-IR spectra collected: C-H (acetylene, paraffinic and aromatic), C-O (various), C=O, C=C and substituted aromatics. The assignments of vibration modes to all absorption peaks are described elsewhere (Cain *et al.*, 2010). Sulfate can potentially contribute to absorption in the range 1000 – 1200 cm^{-1} (Kirchner *et al.*, 2003). However, contribution of sulfate is likely minor because all fuels tested in this study (excluding JP-8) contain no sulfur. Estimates of the molar ratios between functional groups detected in the samples are made through an analysis of the corresponding IR spectra and IR spectra from a set of standard compounds that contain the same functional groups (Cain *et al.*, 2010).

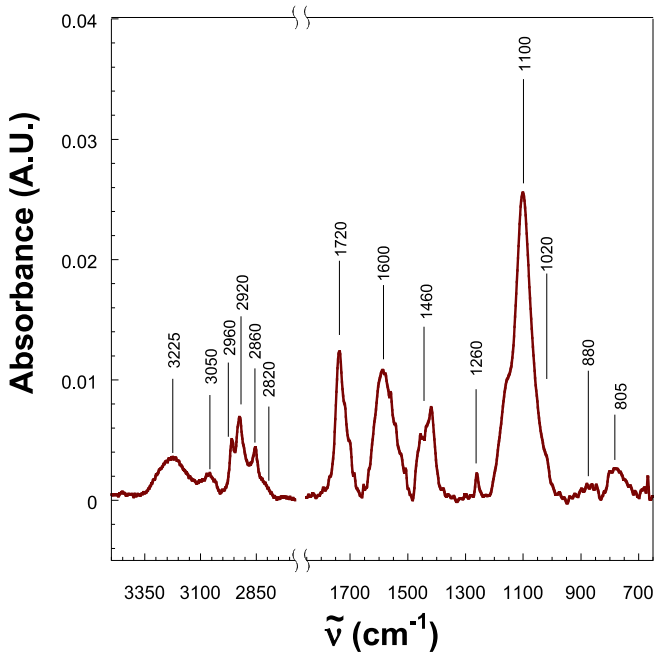

Figure 11-8. A processed (averaged, baseline-corrected and smoothed) micro-FTIR spectrum for T63 aircraft soot that is typical of the six fuels tested. The sample shown is for Fischer-Tropsch, 85% power and stage 9.

11.4.1 Chemical Properties with n-Heptane/n-Dodecane Fuel

Micro-FTIR results are shown in Figure 11-9 for testing with the n-heptane/n-dodecane fuel. Nearly all relative group concentrations are observed to be approximately constant over the sampled size range. The particles contain much more paraffinic C-H and C-O than acetylene C-H and C=O groups.

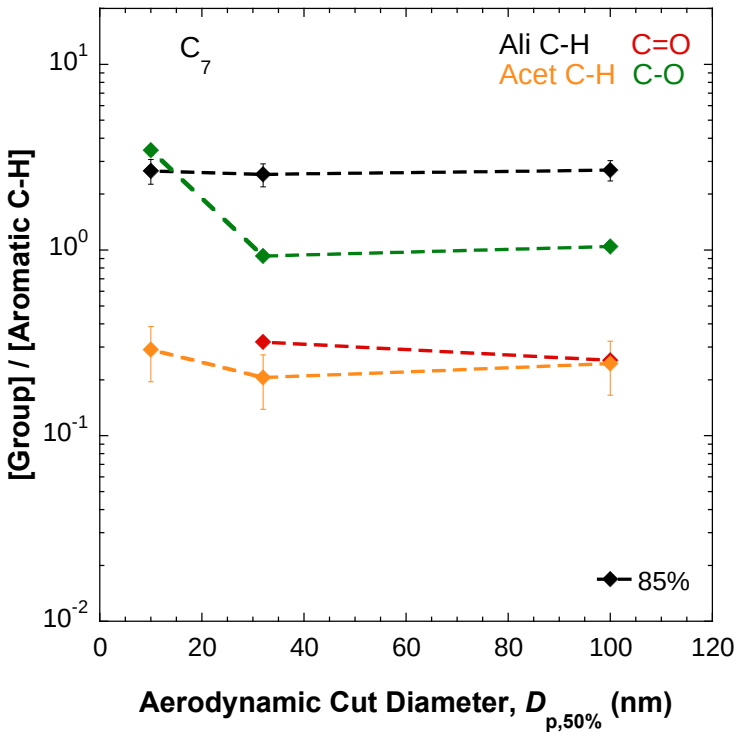

Figure 11-9. Group concentration ratio as a function of particle size for *n*-heptane/*n*-dodecane blend. Colors denote functionality and symbols denote engine power.

11.4.2 Chemical Properties with iso-Octane/n-Dodecane Fuel

Spectroscopy measurements show similar ranking of group concentrations (see Figure 11-10) to the *n*-heptane blend: paraffinic C-H and C-O are higher than C=O and acetylenic C-H. Results for this fuel show that the values increase with engine power, as well as particle size (excluding acetylene C-H at low-speed idle).

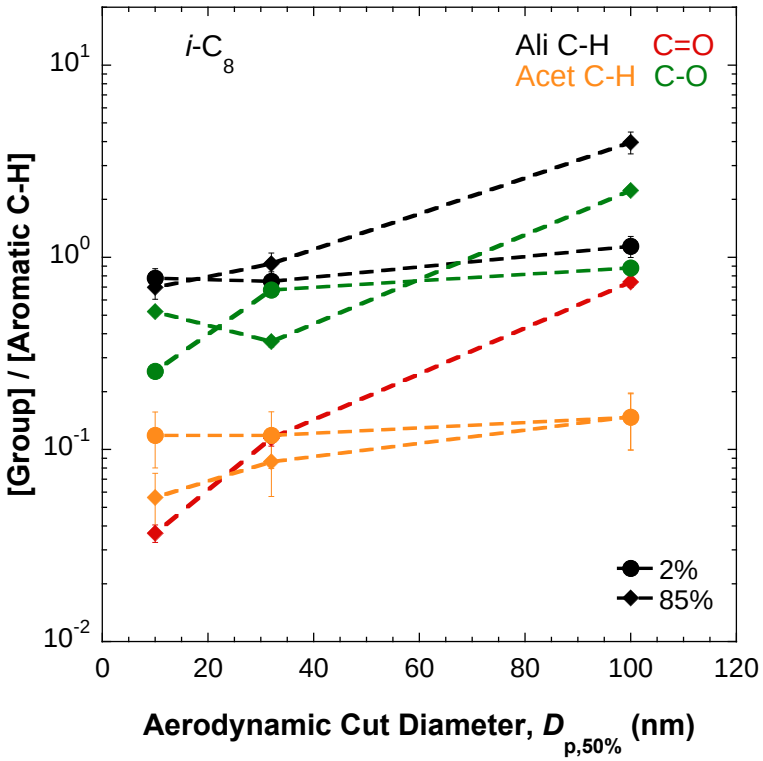

Figure 11-10. Group concentration ratio as a function of particle size for *iso*-octane/*n*-dodecane blend. Colors denote functionality and symbols denote engine power.

11.4.3 Chemical Properties with m-Xylene/n-Dodecane Fuel

Group concentration ordering in Figure 11-11 for the m-xylene/n-dodecane blend is the same for *iso*-octane and *n*-heptane. The trend with particle size, however, is different. Most cases (group at a particular engine power) do not increase (overall) from 10 nm to 100 nm; rather, they exhibit a rise-then-fall behavior with increasing size. Moreover, not all groups consistently observe an increase in value from low-speed idle to cruise.

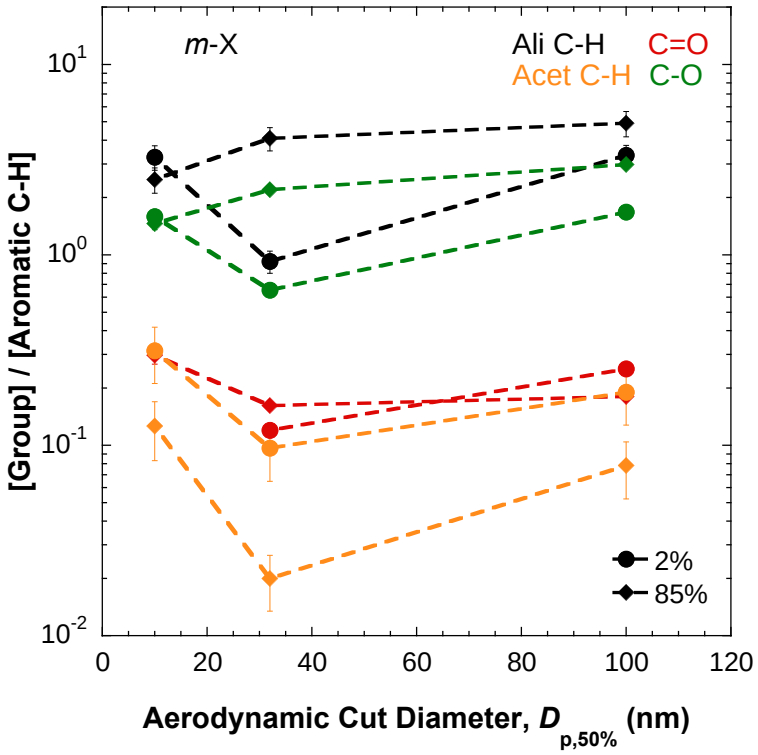

Figure 11-11. Group concentration ratio as a function of particle size for *m*-xylene/*n*-dodecane blend. Colors denote functionality and symbols denote engine power.

11.4.4 Chemical Properties with Methylcyclohexane/n-Dodecane Fuel

Micro-FTIR results for the MCH blend are similar to those for *iso*-octane and *n*-heptane. Specifically, the groups are ordered in similar fashion and their trends with engine power and particle size are nearly the same. One noticeable difference is the continual increase in group concentration above 32 nm; the value is approximately constant at 100 nm for many cases.

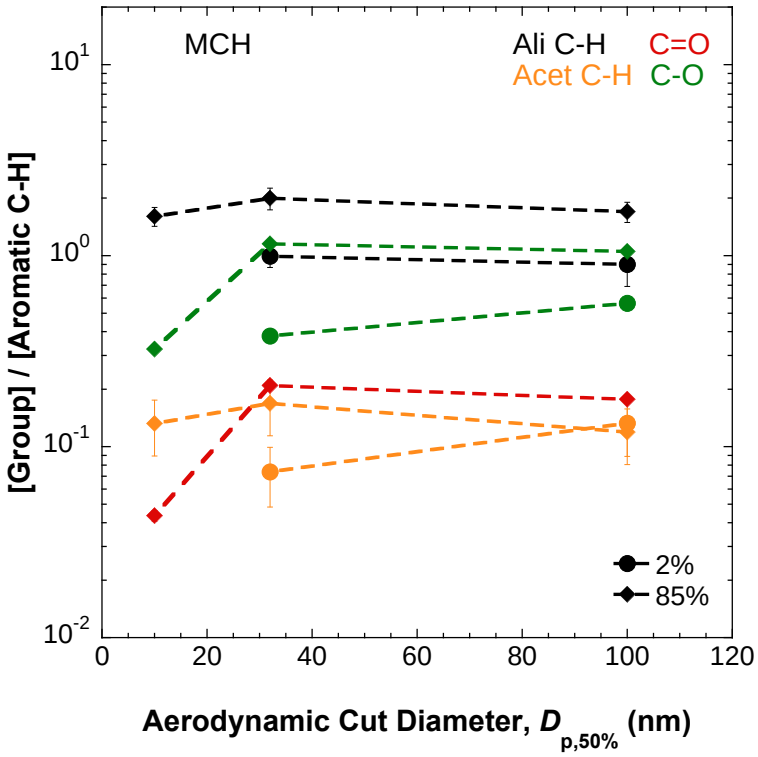

Figure 11-12. Group concentration ratio as a function of particle size for *methylcyclohexane*/*n*-dodecane blend. Colors denote functionality and symbols denote engine power.

11.4.5 Discussion of Chemical Properties of Soot

The concentrations of [paraffinic C-H], [acetylene C-H], [C=O] and [C-O] (relative to [aromatic C-H]) measured by micro-FTIR spectroscopy are displayed in Figure 11-9 through Figure 11-12 for the size-resolved samples collected at the lowest and highest engine power settings. Results show that there are two distinct ordering sets among the fuels tested. For JP-8 and F-T fuels, the following trend is observed: [paraffinic C-H] ≈ [C-O] > [acetylene C-H] > [C=O]. This trend is slightly different for all the alternative fuel surrogates: [paraffinic C-H] > [C-O] > [C=O] > [acetylene C-H]. Among all the particle sizes and fuel/engine power combinations, values of [group]/[aromatic C-H] are in the range of 0.3-7.0 for [paraffinic C-H], 0.01-1.0 for [C=O], 0.2-5.0 for [C-O] and 0.07-0.7 for [acetylene C-H].

Trends with particle size are observed for the data. For the three engine powers tested, all four relative concentrations increase from 10 nm to 100 nm in nearly all cases of JP-8 and Fischer-Tropsch fuels. The response is less clear for the binary fuel blends. The relative concentrations for *m*-xylene and *iso*-octane blends increase in many cases but decrease or are approximately constant in some. Ratios in most power settings are constant for the MCH blend, while the ratio values decrease or remain constant for the *n*-heptane blend. Concentration ratio trends with engine power are a bit different than for particle size. The overall increase from low-speed idle to cruise is largely positive for JP-8 and the *n*-heptane blend, with few decreases in the ratio among all four groups. For F-T, the *m*-xylene and *iso*-octane blends, the response is mixed between increasing, decreasing and remaining constant. An increase is observed for more cases than remaining constant for the MCH blend.

In regards to the ranking of concentration ratio values for the fuels tested, no consistent trend is observed with particle size (Figure S5) or engine power (Figure S6). However, it is observed that values for the Fischer-Tropsch, *m*-xylene and *n*-heptane blends are consistently above those for other fuels, with JP-8 being towards the bottom in many cases. Dividing the concentration ratio for each fuel by the ratio for JP-8 at each point in the test matrix (particle size and engine power) aids this observation. For the paraffinic C-H group, average values (relative to JP-8) are 4.8 (*m*-X), 2.6 (C_7), 1.8 (MCH), 1.6 (F-T) and 1.4 (*i*-C_8). They remain above unity for F-T (2.0), *m*-X (1.4) and C_7 (1.8), but are slightly below unity for the MCH (0.97) and *i*-C_8 (0.91) blends, in the case of acetylene C-H. For the C-O group, all fuels but one (MCH: 0.83) have average concentrations greater than JP-8: C_7 (4.1), *m*-X (3.6), 2.2 (F-T) and *i*-C_8 (1.1). The data for C=O is rather limited for the MCH, *i*-C_8 and C_7 blends due to high signal to noise for many of their samples. However, measurements for *m*-X and F-T fuel gave average values of 5.0 and 2.3, respectively.

One point of interest is the difference in particle chemistry between JP-8 and *m*-xylene fuels. The particle size distributions and total concentrations at each engine power are remarkably similar. However, micro-FTIR spectroscopy measurements show that the particle chemistry for these cases is quite different. Further investigation is needed to understand the importance of the observed chemistry to soot formation and growth.

There are many necessary factors (*e.g.*, combustion performance and sustainability) that govern the selection of future aviation fuels (Edwards *et al.*, 2010). The environmental impact of emissions is an important factor that needs to be assessed when selecting alternative fuels. Particle chemistry is critical to assessing impact of aircraft emissions because particles emitted into the atmosphere can form clouds and react with trace gaseous species. The C=O and paraffinic C-H groups are key to these processes, respectively. Measurements for F-T and *i*-C_8 fuels reveal that the paraffinic C-H group is 1-2 times greater than JP-8 over the deposited size range. Values for other fuels are slightly larger than JP-8: x1-6 for C_7, x0.5-3.5 for MCH and x2-6 for *m*-X. Thus, alternative fuels will have more paraffinic hydrocarbons available for heterogeneous reactions than JP-8. The C=O relative concentrations are mostly larger than JP-8 values at 32 nanometers and near unity at 100 nanometers. It is anticipated that soot from F-T and the surrogates tested would be only marginally more CCN active than JP-8 soot because there are much more particles near 32 nm in the PSD than 100 nm but the 32 nm particles are less CCN active than 100 nm.

The concentration of particulate emissions is critical in estimating its environmental impact. Research on emissions from potential alternative fuels has routinely observed that the soot number density and mass for alternative fuels are less than conventional fuel values (*e.g.*, JP-8) for the same engine. The same is observed for the fuels tested with the T63 turboshaft engine. Figure 11-13 and Figure 11-14 compare the spatial emission rate for tests conducted in this study with some of the available literature values. The spatial emission rate (number or mass-per-kilometer) may be calculated from the emission index (*EI*), fuel mass flow rate and aircraft speed (*V*):

$$Spatial\ Emission\ Rate_{n,m} = ER_{n,m}/V = EI_{n,m} \cdot \dot{m}_{fuel}/V. \qquad (9.1)$$

The figures show that the total number and mass of particles emitted-per-kilometer at cruise engine power may decrease by a factor of 2 and 5, respectively, upon switching to Fischer-Tropsch (Sasol) in the T63 engine. All surrogates but the *m*-xylene blend show larger emissions reductions than F-T: a factor of

4, 4 and 8 lower than JP-8 for MCH, *i*-C_8 and C_7, respectively. Mass emissions reductions are by factors of 15, 15 and 43 for MCH, *i*-C_8 and C_7, respectively.

The chemical characterization results must be combined with the mass and number concentration data to understand total environmental impact of aircraft emissions. It was observed at cruise power that soot from F-T and the binary fuel mixtures have more paraffinic hydrocarbons available for heterogeneous reactions than JP-8 soot, and the CCN activity was estimated to be marginally higher than JP-8 soot. Concentration measurements show that the number of particles produced by those fuels (except *m*-X) is 2-8 times less than JP-8. One conclusion is that the aromatic class has a greater environmental impact than JP-8 since it produces the same amount of particles which will alter the atmosphere's chemistry to a greater extent and be slightly more CCN active. The conclusion of environmental impact relative to JP-8 is less definitive for F-T, MCH, *i*-C_8 and C_7 because it is unclear whether the reduction of their concentration is enough to overcome its observed chemistry-related effects. Clearly further studies are needed.

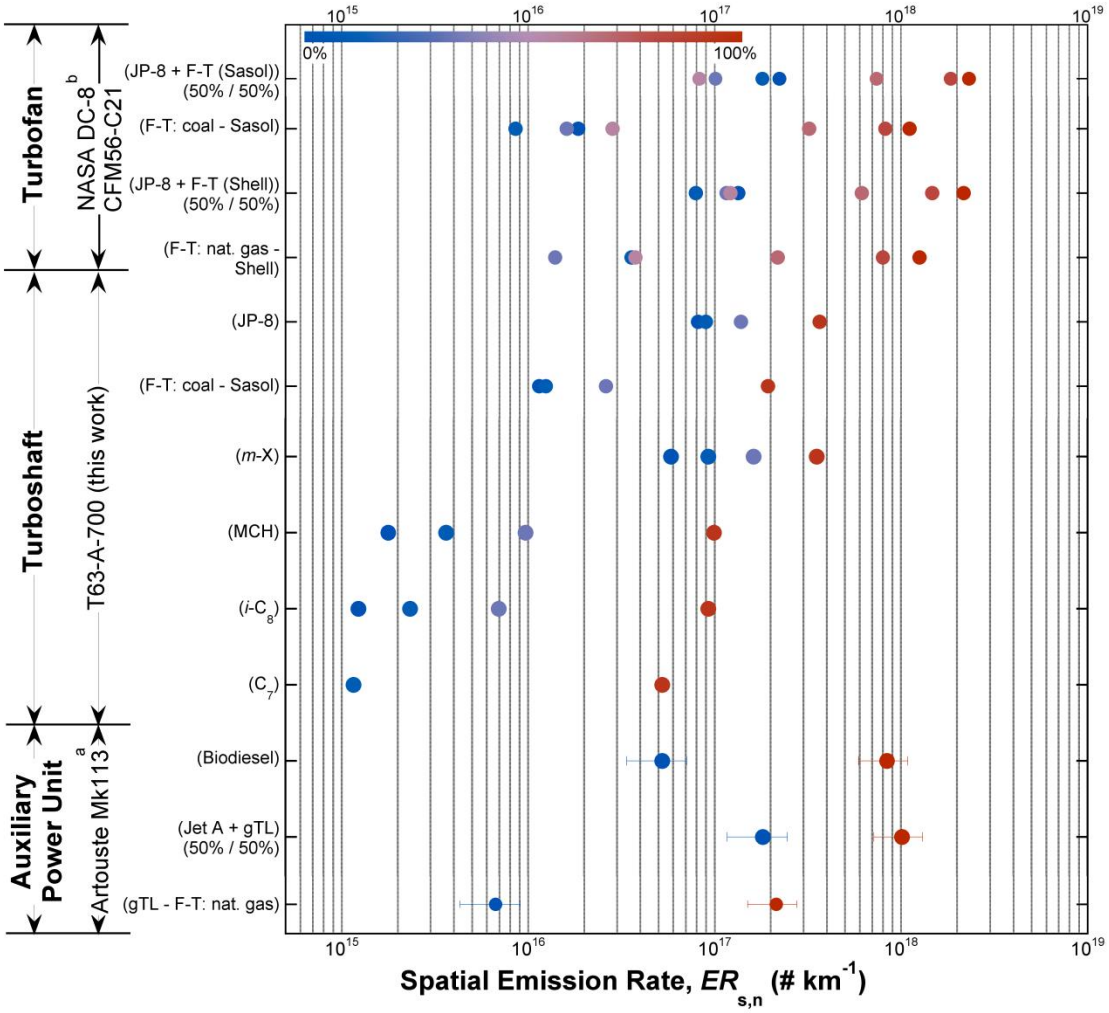

Figure 11-13. Plot showing the number of particles emitted-per-kilometer traveled for various engine technologies. Values assume an aircraft speed of 1 mi hr^{-1}. Symbol colors denote the engine power (% maximum power), as shown in the figure. Data from this work is shown between the data of [a](Lobo *et al.*, 2011) and [b](Bulzan, *et al.*, 2010).

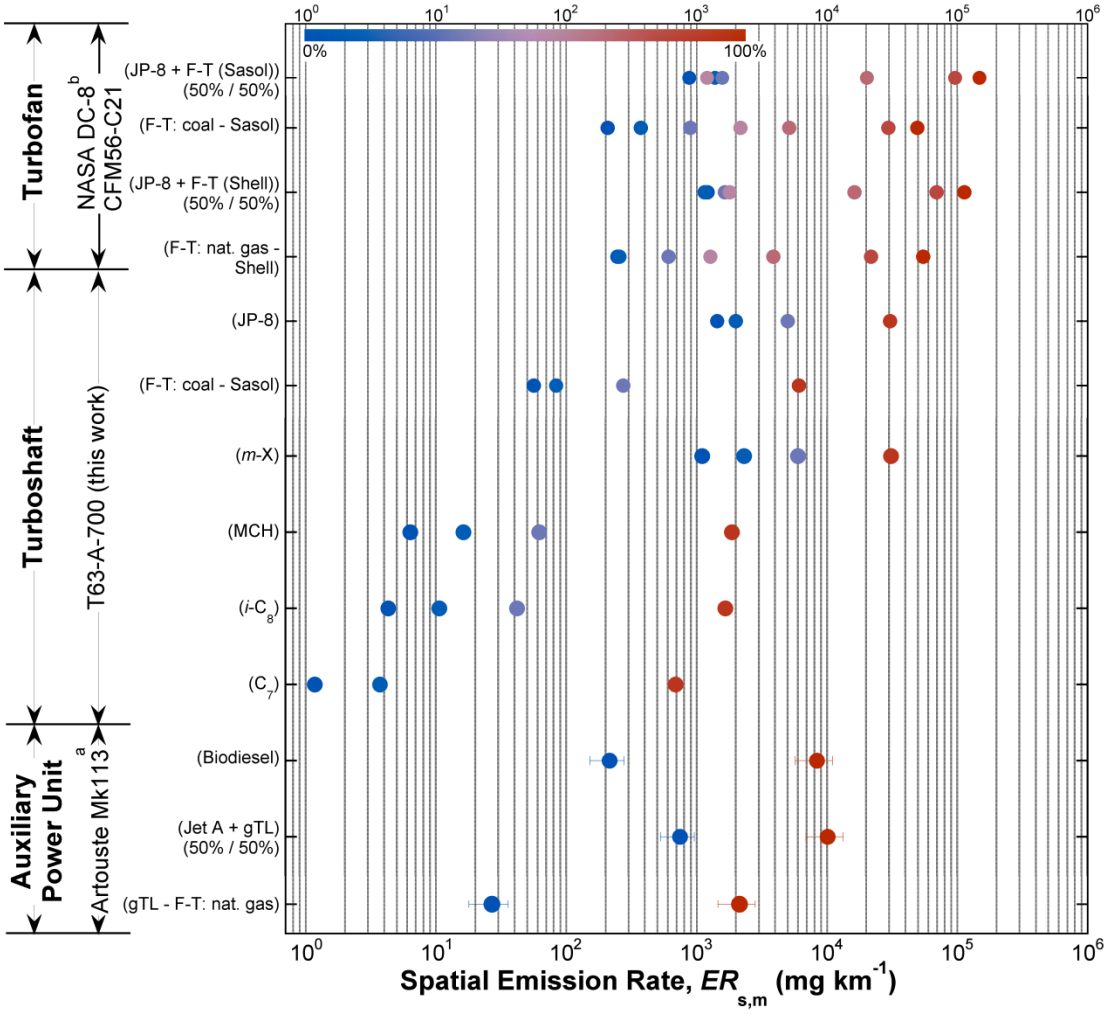

Figure 11-14. Plot showing the mass of particles emitted-per-kilometer traveled for various engine technologies. Values assume an aircraft speed of 1 mi hr^{-1}. Symbol colors denote the engine power (% maximum power), as shown in the figure. Data from this work is shown between the data of [a](Lobo *et al.*, 2011) and [b](Bulzan, *et al.*, 2010).

11.5 Unburned Fuel Emissions

Qualitatively, there is interest in determining whether unburned jet fuel is emitted from the T63 during operation. This can be determined by comparing control samples to those obtained during testing. GC-MS profiles were performed for T-63 engine emissions at idle and compared to a profile of the fuel, spike onto a charcoal tube and then extracted, as shown in Figure 11-15. While the results are not quantitative due to the complexity of the fuel component distribution, it is clear that these two chromatograms represent similar mixtures. The peaks at 25 minutes represent the internal standards spiked into the fuel mixtures. Some of the peaks eluting prior to 5 minutes in the exhaust chromatogram are volatile components produced during combustion which are not present in the neat fuel chromatogram (top), such as butadiene and benzene. The distributions are very similar between 10 and 20 minutes and

represent the hypothesis that a significant portion of the emissions from this engine (operated at idle) are unburned fuel. Further validation that these species are unburned fuel components can be made by more detailed comparison of the GC chromatogram, as shown in Figure 11-16. Based on the relative concentrations of identical/specific compounds in the exhaust sample compared to the neat jet fuel, it is clear that these compounds are completely unreached fuel compounds.

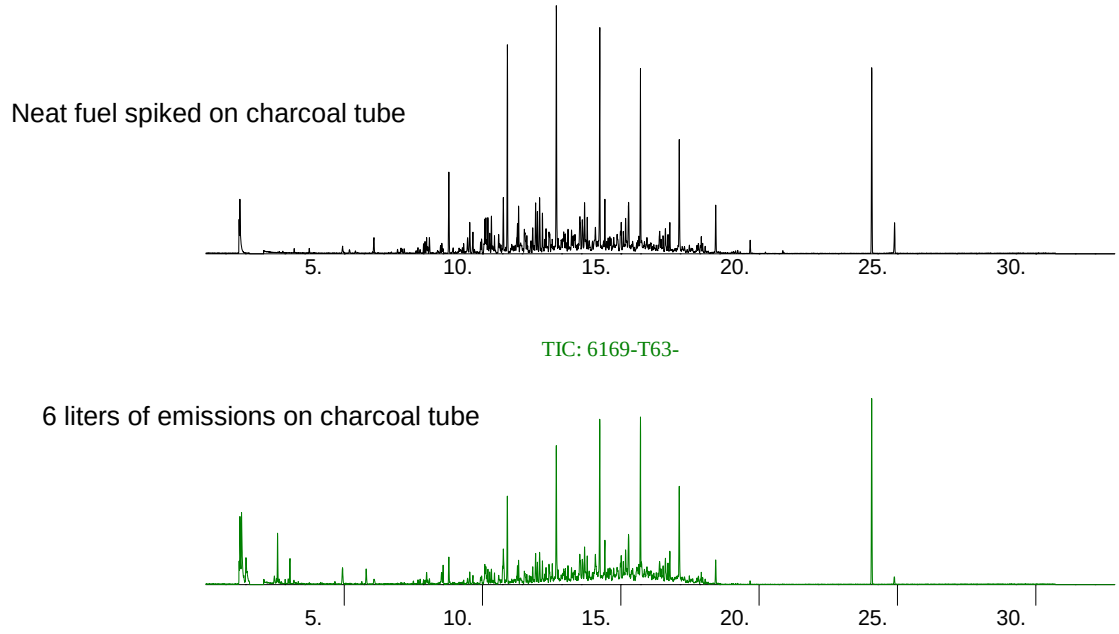

Figure 11-15. Comparison of neat fuel (top) and hydrocarbons captured from T63 idle engine emissions.

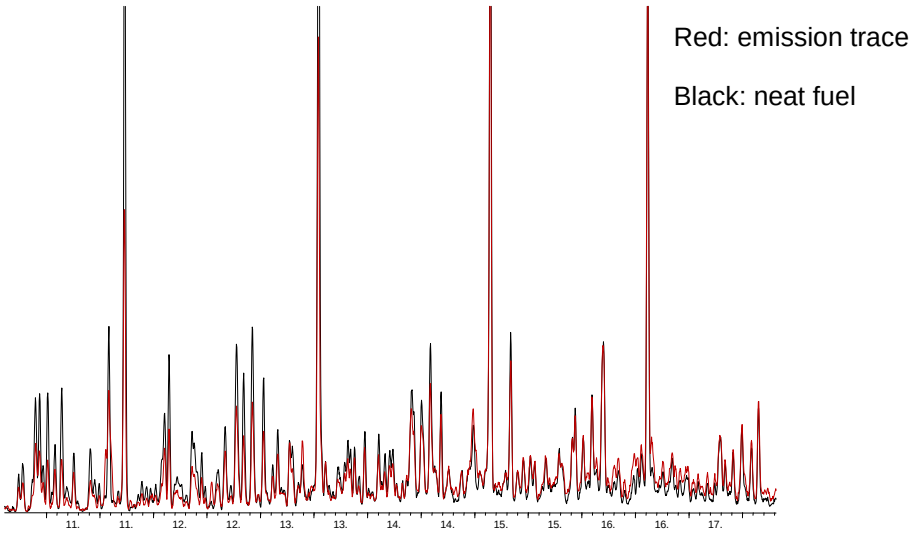

Figure 11-16. Comparison of major components in jet fuel and emissions of T63 (idle condition).

An attempt was made to quantify the percentage of the total unburned hydrocarbon emissions that the unreacted fuel comprises. This was accomplished by using the known internal standard (normal eicosane) concentration and the constant response/mol-carbon atom of the GC-FID. Using this approach, the mass of "fuel" collected on the charcoal tube could be determined, corrected to gas phase ppmV carbon, and compared to the unburned hydrocarbon concentration (UHC) from a continuous monitor used during the test. The continuous monitor is measuring both the reaction products and unburned fuel being emitted from the engine. Results shown in Table 11-1 indicate that the majority of unburned hydrocarbon emissions are from unburned reactant material. While compounds such as alkenes are clearly reaction products (not in the neat fuel) but could not be separated from the fuel response due to complexity, the great majority of compounds are unreacted fuel components.

Table 11-1. Charcoal tube response versus continuous monitor (UHC) response for T63 at idle power conditions.

Engine/Fuel condition	Fuel by charcoal tube (ppmC)	UHC by on-line FID (ppmC)	% of total UHC response
T63/JP-8 (6169) / IDLE	496	672	73%
T63/JP-8 (6169) / IDLE	495	685	72%
T63/JP-8/ 25% aromat. / IDLE	388	642	60%

While unreacted fuel represents the majority of the hydrocarbon emissions under these conditions, a slight shift in the distribution of fuel components as compared to the unreacted fuel was observed. Figure 11-17 compares the weight percent of speciated hydrocarbons as a function of carbon number for the emissions sample and control fuel sample for the major hydrocarbon classes. The data shows that the relative concentration of the more volatile components of the fuel from the exhaust sample are lower than in the parent fuel. This observation may be related to vaporization of the fuel droplet as it is exposed to combustion conditions; the volatile components are preferentially vaporized and combusted, reducing the less volatile components survive the high temperature zone and are emitted. It should be noted that this assertion must be further studied to verify that that this shift is not due to sample transport and collection artifacts.

Other recent studies with model mixtures have also shown the presence of unburned hydrocarbon emissions at idle conditions which exactly match the fuel being combusted. On the contrary, research reactors where the fuel is completely premixed and prevaporized, such as the well-stirred reactor, have not shown this behavior. These observations illustrate the need to account for physical transport effects to be able to accurately predict unburned hydrocarbon emissions during operation.

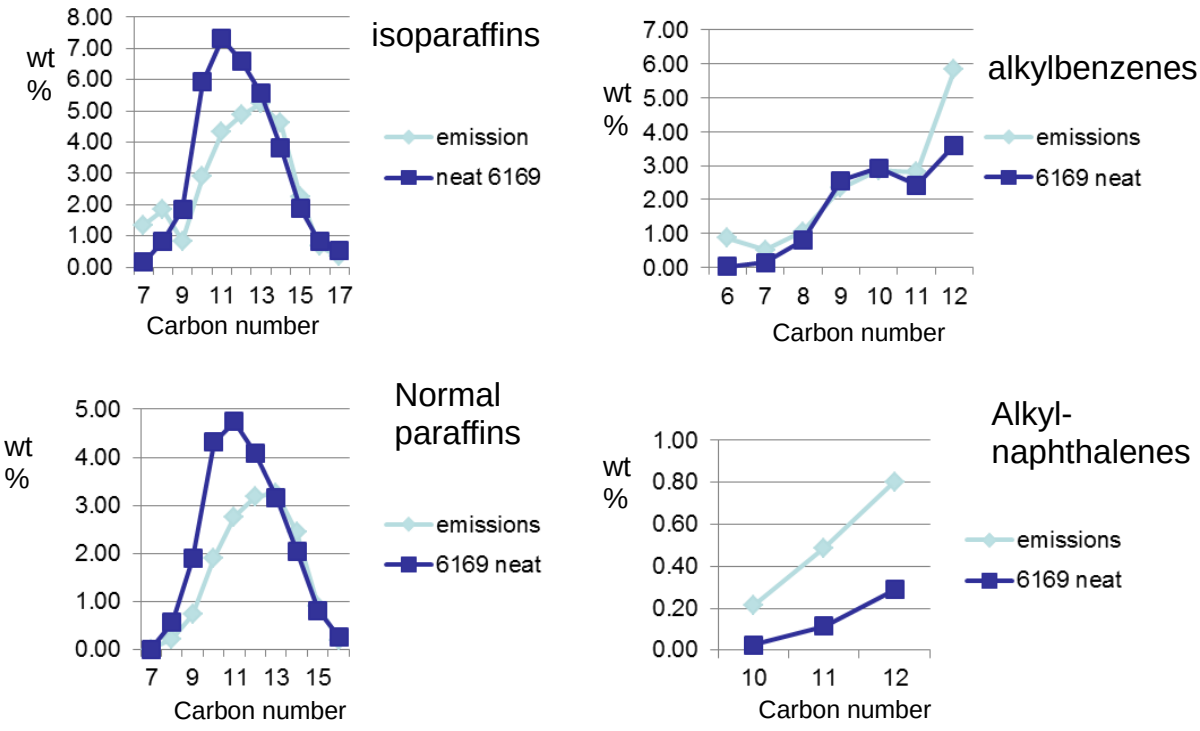

Figure 11-17. Changes observed in distribution of emissions show that less volatile components are more likely to be combusted and that alkyl aromatics are formed during combustion.

12. Conclusions and Recommendations

In conclusion, this program has addressed the near-term objectives identified on page 26 in the Federal Alternative Jet Fuels Research and Development Strategy*. That is: (1) establish a national data base for alternative fuels (Q2NO1) and (2) examine the dependence of variations in jet fuel composition on magnitude and types of combustion emissions (Q2NO3). In addressing these national objectives this program has: (1) established an emissions data base for the combustion of five test fuels in: (i) a well stirred reactor, (ii) shock tube, (iii) laminar premixed and (iv) non-premixed jet flames, (v) a dumb research combustor, (vi) a single swirl cup referee combustor, and (vii) a T-63 gas turbine engine; (2) developed, evaluated and significantly improved the accuracy fuel sensitive emissions models especially for soot; (3) established an improved scientific understanding of how alkanes and aromatic compounds can effect emissions; (4) provided a scientific explanation of the combustion processes responsible for the linear relationship between the concentrations of different hydrocarbon species and gas turbine engine operating conditions; (5) developed improved combustion chemistry models for m-xylene and polycyclic aromatic hydrocarbons which are critical for future soot model development and evaluation; and (6) provided the first ever model predictions and evaluation of hazardous air pollutants. The research fuels consisted of binary mixture of n-dodecane and a second hydrocarbon representative of one of the four main classes of hydrocarbons that are present in alternative fuels. The mixtures were blended to give different chemical and physical properties expected in practical alternative fuels.

Indeed, this program provides an excellent science base for addressing the mid-term and far-term objectives identified on page 26 in the "Federal Alternative Jet Fuels Research and Development Strategy" June 2016. It is recommended that SERDP initiate a follow on program that addresses the mid-term and far-term research and development objectives given in the federal strategy. That is : (1) expand the national data base to include data and analysis new practical alternative fuel candidates (Q3MO2), (2) develop correlations and parametric relationships between practical alternative jet fuels and combustion emissions (Q2MO3), and (3) develop modeling capability to predict jet engine combustion emissions as a function of alternative fuel composition (Q2LO1). It is recommended the following tasks be addressed.

- Demonstrate the capability of formulating chemical kinetic models (detailed/skeletal/reduced) that can be used to make accurate estimates of emissions (soot, hazardous air pollutants, etc.) from combustion devices burning "practical" liquid hydrocarbon fuels with a broad range of physical and chemical properties.
- Quantify the impact of reducing the number of species in chemical kinetic models on the accuracy associated with emissions.
- Identify and quantify the liquid fuel parameters that have the largest impact on emissions and provide insights into how fuels could be optimized to give low emissions in combustion systems.
- Develop and evaluate a tool that offers the potential of being used to optimize combustion system design and fuel characteristics for low emissions.
- Develop models that are applicable to combustor relevant higher pressures and temperature conditions for practical alternative jet fuels similar to those developed on the Navy's Mobility Fuels program or used in the National Jet Fuel Combustion Program (NJFCP).
- Demonstrate models' ability to capture variations in emissions with changes in engine power levels (P3, T3, flow-rates, etc.)
- Develop and demonstrate a new, innovative approach that can be used to estimate soot emissions, with a better than the current-state-of-the-art accuracy, when burning fuels with a broad range of physical and chemical properties in different combustion systems.

*https://www.whitehouse.gov/sites/default/files/federal_alternative_jet_fuels_research_and_development_strategy.pdf.

ACKNOWLEDGEMENTS

The financial support of the Department of Defense Strategic Environmental Research and Development Program (SERDP) for this project is greatly appreciated. We wish to thank Dr. Robin Nissan, SERDP Program Manager, for his support and guidance and Braxton Lewis for his editoral comments and recommendations. All program participants wish to give a special thanks to Ms. Angela Wedding for making all of the arrangements for our numerous internal review meetings at Wright-Patterson AFB and for editing our Interim and Final Reports. Jobs well done.

REFERENCES

Anderson, B. E., Beyersdorf, A. J., Hudgins, C. H., Plant, J. V., Thornhill, K. L., Winstead, E. L., Ziemba, L. D., Howard, R., Corporan, E., Miake-Lye, R. C., Herndon, S. C., Timko, M., Woods, E., Dodds, W., Lee, B., Santoni, G., Whitefield, P., Hagen, D., Lobo, P., Knighton, W. B., Bulzan, D., Tacina, K., Wey, C., VanderWal, R., Bhargava, A., (2011) "Alternative aviation fuel experiment (AAFEX)" NASA/TM-2011-217059; National Aeronautics and Space Administration: Hampton, VA.

Anderson, B. E., Chen, G., Blake, D. R., (2006) "Hydrocarbon emissions from a modern commerical airliner," Atmos. Environ., 40, pp. 3601.

Anderson, B.E., et al., (2011) "Alternative Aviation Fuel Experiment (AAFEX)," NASA/TM–2011-217059, Washington, D.C., February, 2011.

Anneken, D., Striebich, R., DeWitt, M. J., Klingshirn, C., Corporan, E., (2012) "Development of a method to identify and quantify hazardous air pollutants from turbine engine emissions," ACS Preprints-Div. Fuel Chem., 57.

Balagurunathan, J. (2012). Investigation of Ignition Delay Times of Conventional (JP-8) and Synthetic (S-8) Jet Fuels: A Shock Tube Study. Master Thesis, University of Dayton, Dayton, Ohio.

Barlow, R. S., Dunn, M. J., Sweeney, M. S. and Hochgreb, S. (2011) "Unexpected effects of preferential transport in turbulent premixed flames," Paper 2C03, 7th US National Combustion Meeting, Atlanta, GA, March 20-23, 2011.

Bhargava, A., Colket, M., Sowa, W., Casleton, K., and Maloney, D., (2000) "An experimental and modeling study of humid air premixed flames," Journal of Engineering for Gas Turbines and Power - Transactions of the ASME, 122(3), pp. 405–411.

Bittner, J. D., and Howard, J. B. (1981). Composition profiles and reaction mechanisms in a near-sooting premixed benzene/oxygen/argon flame. Symposium (International) on Combustion, 18, 1105.

Blunck, D., Cain, J., Striebich, R.C., Vijlee, S.Z., Stouffer, S.D., Roquemore, W.M., (2012) "Fuel-rich Combustion Products from a Well-Stirred Reactor Operated using Traditional and Alternative Fuels," 2012 Central States Combustion Meeting.

Blunck, D., Zeppieri, S., Gross, J., Stouffer, S., and Colket, M., (2015) "Hydrocarbon Emissions from a WSR Near Lean Blow-Off", submitted to the AIAA Aerospace Sciences Meeting, Jan.

Blust, J., Ballal, D., Sturgess, G., (1997) "Emissions Characteristics of Liquid Hydrocarbons in a Well Stirred Reactor", 33rd AIAA/ASME/SAE/ASEE Jt. Propuls. Conf. Exhib. AIAA.

Blust, J.W., Ballal, D.R., Sturgess, G.J., (1999) "Fuel Effects on Lean Blowout and Emissions from a Well-Stirred Reactor," J. Propuls. Power., 15, pp. 216–223.

Briones, A., Sekar, B., Zelina, J., Pawlik, R., Stouffer, S., (2008) "Numerical modeling of combustion performance for a well-stirred reactor for aviation hydrocarbon fuels," 44th Joint Prop. Conf., AIAA 2008-4565.

Bulzan, D., Anderson, B., Wey, C., Howard, R., Winstead, E., Beyersdorf, A., Corporan, E., DeWitt, M. J., Klingshirn, C., Herndon, S., Miake-Lye, R., Timko, M., Wood, E., Tacina, K. M., Liscinsky, D., Hagen, D., Lobo, P., Whitefield, P., (2010) "Gaseous and particulate emissions results of the NASA Alternative Aviation Fuel Experiment (AAFEX)," In ASME Turbo Expo: Pow. for Land, Sea and Air, Glasgow, pp. GT2010-23524.

Burcat, A., Scheller, K., and Lifshitz, A. (1971). Shock-tube investigation of comparative ignition delay times for C1-C5 alkanes. Combust. Flame, 16, 29.

Burcat, A., and Radhakrishnan, K. (1985). High temperature oxidation of propene. Combust. Flame, 60, 157.

Cain, J. P., (2011) " Development of a novel heterogeneous kinetics reactor and chemical characterization of soot particles," PhD Dissertation, University of Southern California, Los Angeles.

Cain, J., DeWitt, M.J., Blunck, D., Corporan E., Striebich, R., Anneken, D., Klingshirn, C., Roquemore, W.M., Vander Wall, R., (2013) "Characterization of Gaseous and Particulate Emissions from a Turboshaft Engine Burning Conventional, Alternative, and Surrogate Fuels," Energ. Fuel., 27, pp. 2290–2302.

Cain, J. P., Gassman, P. L., Wang, H., Laskin, A., (2010) "Micro-FTIR study of soot chemical composition-evidence of paraffinic hydrocarbons on nascent soot surfaces," Phys. Chem.,., 12, pp. 5206.

Calcote, H. F., and Manos, D. M., "Effect of Molecular Structure on Incipient Soot Formation," *Combustion and Flame*, Vol. 49, No. 1-3, 1983, pp. 289–304.

doi: 10.1016/0010-2180(83)90172-4

Chen, Y.-C., Lee, W.-J., Uang, S.-N., Lee, S.-H., Tsai, P.-J., (2006) "Characteristics of polycyclic aromatic hydrocarbon (PAH) emissions from a UH-1H helicopter engine and its impact on the ambient environment" Atmo. Env., 40, pp. 7589.

Cheng, M.-D., Corporan, E., DeWitt, M. J., Landgraf, B., (2009) "Emissions of volatile particulate components from turboshaft engines operated with JP-8 and Fischer-Tropsch fuels," Aero. and Air Quality Res., 9, (2), pp. 237.

Cheng, M.-D., Corporan, E., DeWitt, M. J., Spicer, C. W., Holdren, M. W., Cowen, K. A., Laskin, A., Harris, D. B., Shores, R. C., Kagann, R., Hashmonay, R., (2008) "Probing emissions of military cargo aircraft: description of a joint field measurement strategic environmental research and development program," J. of the Air & Waste Man. Assoc., 58, (6), pp. 787.

Chowen, C., Wey, ed., (2004) "Aviation Particle Emissions Workshop," NASA/CP-2004-213398.

Colket, M.B. and Seery, D.J., (1993) "Reaction Mechanisms for Toluene Pyrolysis", in Twenty-Fifth Symposium (International) on Combustion, The Combustion Institute, Pittsburgh, pp. 883-891.

Colket, M., Zeppieri, S. Dai, Z., Kim, W., Hollick, H. and Hautman, D., (2013) "Alternative Fuels Modeling for Navy Applications", ONR Contract N00014-12-C-0408. UTRC Report No. R5.100.0123, June.

Corporan, E., DeWitt, M., Wagner, M., (2004) "Evaluation of soot particulate mitigation additives in a T63 engine," Fuel Proc. Tech., 85, pp. 727.

Corporan, E., Edwards, T., Shafer, L., DeWitt, M. J., Klingshirn, C., Zabarnick, S., West, Z., Striebich, R., Graham, J., Klein, J., (2011) "Chemical, thermal stability, seal swell, and emissions studies of alternative jet fuels," Energy & Fuels, 25, pp. 955.

Corporan E., Stouffer, S.D., DeWitt, M.J., Hendershott, T.H., Klingshirn, C.D., (2015) "Evaluation of Fuel Aromatic Impacts on Combustion Characteristics in a Newly Developed Turbine Engine Combustor Research Facility at AFRL," IASH 2015, the 14th International Symposium on Stability, Handling, and use of Liquid Fuels, Charleston, South Carolina USA,4-8 October 2015.

Corporan, E., Monroig, O., Wagner, M., (2004) "Influence of fuel chemical composition on particulate matter emissions of a turbine engine," ASME Turbo Expo: P. for Land, Sea and Air, GT2004-54335.

Corporan, E., Reich, R., Monroig, O., DeWitt, M. J., Larson, V., Aulich, T., Mann, M., Seames, W., (2005) " Impacts of biodiesel on pollutant emissions of a JP-8-fueled turbine engine," J. of the Air & Waste Man. Assoc., 55, pp. 940.

Corporan, E., DeWitt, M. J., Belovich, V., Pawlik, R., Lynch, A. C., Gord, J. R., Meyer, T. R., (2007) "Emissions characteristics of a turbie engine and research combustor burning a Fishcer-Tropsch jet fuel," Energ. Fuel., 21, pp. 2615.

Curran, H. J., Gaffuri, P., Pitz, W. J., and Westbrook, C. K. (1998). A Comprehensive Modeling Study of n-Heptane Oxidation. Combust. Flame, 114, 149.

Dagaut, P., and Cathonnet, M. (2006). The ignition, oxidation, and combustion of kerosene: A review of experimental and kinetic modeling. Prog. Energy Combust. Sci., 32, 48.

Darius, D., Chaumeix, N., and Paillard. (2009). Pyrolysis and oxidation of n-decane, n-propylbenzene and kerosene surrogate behind reflected shcok waves. Combustion generated fine carbonaceous particles: proceedings of an international workshop held in Villa Orlandi, Anacapri, May 13-16, 2007, H. Bockhorn, A. D'Anna, A. F. Sarofim, and H. Wang, eds., KIT Scientific Publishing, Karlsruhe, 720.

Davis, S. G., Wang, H., Brezinsky, K. Law, C. K., (1996) "Laminar burning speeds and oxidation kinetics of benzene/air and toluene/air flames," Proceedings of the Combustion Institute 26, pp. 1025-1033 (1996).

DeWitt, M. J., Corporan, E., Graham, J., Minus, D., (2008) "Effects of aromatic type and concentration in Fischer-Tropsch fuel on emissions production and material compatibility," Energy & Fuels, 22, pp. 2411.

Dooley, S., Won, S. H., Heyne, J., Farouk, T. I., Ju, Y., Dryer, F. L., Kumar, K., Hui, X., Sung, C.-J., Wang, H., Oehlschlaeger, M. A., Iyer, V., Iyer, S., Litzinger, T. A., Santoro, R. J., Malewicki, T., and Brezinsky, K. (2012). The experimental evaluation of a methodology for surrogate fuel formulation to emulate gas phase combustion kinetic phenomena. Combust. Flame, 159, 1444.

Dworkin S. B., Zhang Q., Thomson M. J., Slavinskaya N. A., Riedel U. (2011) "Application of an Enhanced PAH Growth Model to Soot Formation in a Laminar Coflow Ethylene/Air Diffusion Flame", Combustion and Flame, Vol. 158.

Edwards, T., Moses, C., Dryer, F., (2010) "Evaluation of combustion performance of alternative aviation fuels," 46th AIAA/ASME/SAE/ASEE Joint Propulsion Conference & Exhibit, Nashville.

Farouk, T.I., and Dryer, F.L., (2014) "Isolated n-heptane droplet combustion in microgravity: "Cool-Flames" – Two-stage combustion, Combustion and Flame, 161, 565-581.

Flora, G., Nagulappali, A., Saxena, S., Kahandawala, M. S. P., Sidhu, S. S., (2011) "Simulation of Reflected Shock Combustion Experiments Using Multiple Computational Approaches," Proceedings of 7th meeting of the US Sections of the Combustion Institute.

Flora, G., Saxena, S., Kahandawala, M. S. P., and Sidhu, S. S., (2011) "Investigation of Ignition Delay Time for n-Dodecane and n-Dodecane/m-Xylene Mixtures," Proceedings of 7th meeting of the US Sections of the Combustion Institute.

Frenklach, M., and Harris, S. J., (1986) "Aerosol dynamic modeling using the method of moments," Journal of Colloid and Interface Science, Vol. 118, No. 1, pp. 252-261.

Frenklach, M., Clary, D. W., Gardiner, W. C., and Stein, S. E. (1985). Detailed kinetic modeling of soot formation in shock-tube pyrolysis of acetylene. Symposium (International) on Combustion, 20, 887.

Frenklach, M., and Wang, H. (1991). Detailed modeling of soot particle nucleation and growth. Symposium (International) on Combustion, 23, 1559.

Frenklach, M., and Wang. H., (1994) "Detailed mechanism and modeling of soot particle formation," Soot Formation in Combustion, H. Bockhorn (Ed.), pp. 165-192, Springer-Verlag, Berlin.

Gardiner, W. C. (2000). Gas-Phase Combustion Chemistry. Springer New York, New York, NY.

Gerstle, T., Virag, P Wade, M. (1999) "Aircraft Engine and Auxiliary Power Unit Emission Testing: Vol. 1." United States Air Force: IERA RS-BR-TR-1999-0006.

Glarborg, P., Kee, R.J., Grcar, J.F., and Miller, J.A.(1986) "PSR: A FORTRAN Program for Modeling Well Stirred Reactors," Technical Report SAND86-8209, Sandia National Laboratories.

Glassman, Irvin, (1987) Combustion, Second Edition , Academic Press, London.

Gokulakrishnan, P., (2011) personal communication.

Goodwin, D., Malaya, N., Moffat, H., and Speth, R. (n.d.). Cantera: an object-oriented software toolkit for chemical kinetics, thermodynamics, and transport processes. Version 2.1.1. https://code.google.com/p/cantera/.

Gudiyella, S., Malewicki, T., Comandini, A., Brezinsky, K., (2011) "High pressure study of m-xylene oxidation", Combustion and Flame, 158(4), Special Issue on Kinetics, pp687-704.

Gudiyella, Soumya, (2012), "An Experimental and Modeling Study of the Combustion of Aromatic Surrogate Jet Fuel Components," University of Illinois at Chicago.

Hall, J. M., Rickard, M. J. A., and Petersen, E. L. (2005). Comparison of Characteristic Time Diagnostics For Ignition and Oxidation of Fuel/Oxidizer Mixtures Behind Reflected Shock Waves. Combust. Sci. Technol., 177, 455.

Hassanaly, M., Raman, V., and Colket, M., (2015) "Influence of Fuel Stratification on Turbulent Flame Propagation", submitted to the AIAA Aerospace Sciences Meeting, Jan..

Herndon, S. C., Shorter, J. H., Zahniser, M. S., Nelson, D. D., Jayne, J., Brown, R. C., Miake-Lye, R. C., Waitz, I., Silva, P., Lanni, T., Demerjian, K., Kolb, C. E., (2004) "NO and NO_2 emission ratios measured from in-use commercial aircraft during taxi and takeoff," Env. Sci. & Tech., 38 (22), pp. 6078.

Herndon, S. C., Wood, E. C., Northway, M. J., Miake-Lye, R. C., Thornhill, L., Beyerdorf, A., Anderson, B. E., Dowlin, R., Dodds, W., and Knighton, W. B., (2009) "Aircraft Hydrocarbon Emissions and Oakland International Airport", Environmental Science and Technology, 43, pp. 1730-1736.

Iyer, V. R., (2012) "Effect of Aromatic Components in Surrogate Fuels on Soot in Co-Flow Flames and a Model Gas Turbine Combustor," Ph. D. thesis submitted to the Graduate School College of Engineering, The Pennsylvania State University.

Iyer, V.R., Iyer, S.S., Linvesky, M.J., Litzinger, T.A.. Santoro, R.J., Dooley, S., Dryer, F.L. and Mordaunt, C.J. "Simulating the Sooting Propensity of JP-8 with Surrogate Fuels from Hydrocarbon Liquids," Journal of Propulsion and Power, Vol. 30, No. 5 (2014), pp. 1410-1418.

Kahandawala, M. S. P., "Investigation of Fuel Composition Effects on Particle And Polycyclic Aromatic Hydrocarbon Emissions," Ph.D. Dissertation, University of Dayton, Dayton (OH), 2004.

Kang, T. and D. C. Kyritsis, "A combined experimental/computational investigation of stratified combustion in methane-air mixtures," Energy Conversion and management 48 (2007) 2769-2774.

Kang, T. and D. C. Kyritsis, Combustion Science and Technology, 177: 2191-2210, 2005.

Karalus, M., (2013). Master's Thesis, "An Investigation of Lean Blowout of Gaseous Fuel Alternatives to Natural Gas," University of Washington.

Katta, V. R, Newman-Lehman, T., Seshadri K., and Roquemore, W. M., "Lean blowout limits for JP-8 and their parent components," (2011) AIAA-2011-0413, 49th AIAA Aerospace Sciences Meeting, Orlando, FL, January 4-7.

Katta, V.R., Zeppieri, S.P., Colket, M.B., and Roquemore, W.M., (2014) "Computation of Flame Propagation through Stratified Fuel-Air Mixtures", presented at the Central States Section of the Combustion Institute, March 16-18.

Kee, R. J., Miller, J. A., Jefferson, T. H., (1980) "CHEMKIN: A General-Purpose, Problem-Independent, Transportable, Fortran, Chemical Kinetic Code Package," Technical Report SAND80-8003, Sandia National Laboratories.

Kee. R. J., Grcar, J. F. , Smooke, M. D., Miller, J. A.,(1985) "A Fortran Program for Modeling Steady Laminar One-Dimensional Premixed Flames," Technical Report SAND85-8240, Sandia National Laboratories.

Kennedy, I. M., (2007) "The health effects of combustion-generated aerosols," Proc. Combust. Inst., 31, pp. 2757.

Kinsey, John S., (2009) "Characterization of Emissions from Commercial Aircraft Engines during the Aircraft Particle Emissions experiment (APEX) 1 to 3," EPA-600/R-09/130, Washington, D.C., October.

Kirchner, U., Vogt, R., Natzeck, C., Goschnick, J., (2003) "Single particle MS, SNMS, SIMS, XPS, and FTIR spectroscopic analysis of soot particles during the AIDA campaign," J. of Aero. Sci., 34, pp. 1323.

Knighton, W. B., Herndon, S. C. and Miake-Lye, R. C. (2009) "Aircraft engine speciated organic gases: Speciation of unburned organic gases in aircraft exhaust," EPA-420-R-09-902, United States Environmental Protection Agency, May 2009.

Knighton, W. B., Rogers, T. M., Anderson, B. E., Herndon, S. C., Yelvington, P. E., C., M.-L. R., (2007) "Quantification of aircraft engine hydrocarbon emissions using proton transfer reaction mass spectrometry," J. Propul. Power., 23, pp. 949.

Kumar, K. and C-J. Sung, Laminar Flame Speeds and Extinction Limits of Preheated n-Decane/O2/N2 and n-Dodecane/O2/N2 Mixtures Combustion and Flame, Combustion and Flame 2007, 151, 209-224.

Kumar S., and Ramakrishna, D., (1996) "On the solution of population balance equation by discritization-I, A fixed pivot technique," Chemical Engineering Science, Vol. 51, No. 8, pp. 1311-1332.

Lefebvre, A., Ballal, D., (2010) "Gas Turbine Combustion Alternative Fuels and Emission," CRC Press, Boca Raton, FL, pp 145.

Li, H., Owens, Z. C., Davidson, D. F., Hanson, R. K., (2008) "A Simple Reactive Gasdynamic Model for the Computation of Gas Temperature and Species Concentrations behind Reflected Shock Waves. Int.," J. Chem. Kin, 40, pp. 189.

Lindstedt, P. R., (1994) "Simplified soot nucleation and surface growth steps for non-premixed flames," Soot Formation in Combustion, H. Bockhorn (Ed.), pp. 417-439, Springer-Verlag, Berlin.

Lobo, P., Whitefield, P. D., Hagen, D. E., Rye, L. J., Blakey, S., Wilson, C. W., Williams, P. I., Christie, S., Raper, D., Uryga-Bugajska, I., Pourkashanian, M., (2011) "SAE E31 methodology development and associated PM emissions characteristics of aircraft APUs burning conventional and alternative aviation fuels; PARTNER-COE-2011-005; The Partnership for Air Transportation Noise and Emissions Reduction: Cambridge."

Lutz, A. E., R. J. Kee, J. F. Grcar, F. M. Rupley, (1997) "OPPDIF: A Fortran Program for Computing Opposed-Flow Diffusion Flames," Technical Report SAND96-8243, Sandia National Laboratories.

Mansour, A., Benjamin, M., Steinthorsson, E., (2000) "A New Hybrid Air Blast Nozzle for Advanced Gas Turbine Combustors", Proceedings of ASME TurboExpo, 2000-GT-0117.

Manzello, S.L., Lenhert, D.B., Yozgatligil, A., Donovan, M.T., Mulholland, G.W., Zachariah, M.R., Tsang, W., (2007) Soot particle size distributions in a well-stirred reactor/plug flow reactor. Proc. Combust. Inst. 31, 675–683.

Marinov, N. M., Pitz, W. J., Westbrook, C. K., Lutz, A. E., Vincitore, A. M., and Senkan, S. M. (1998). Chemical kinetic modeling of a methane opposed-flow diffusion flame and comparison to experiments. Symposium (International) on Combustion, 27, 605.

Marple, V. A., Olson, B. A. (1999) "A micro-orifice impactor with cut sizes down to 10 nanometers for diesel exhaust sampling," Report PTL Publication No. 113.

Marple, V. A., Rubow, K. L., Behm, S. M. (1991) "A microorifice uniform deposit impactor (MOUDI): description, calibration, and use," Aero. Sci. and Tech., 14, pp. 434.

McAllister, S., Chen, J.-Y., Fernandez-Pello, A.C., (2011) "Fundamentals of Combustion Processes", Springer New York, New York, NY.

Miake-Lye, R.C., (2010) "AAFEX Gaseous Emissions : Criteria, Green House Gases and Hazardous Air Pollutants, Presentation at AAFEX Workshop," AIAA Meeting, Orlando, FL, 22-25, January 2010.

Mordaunt, C. J., (2005) "Dual Fuel Issues Related to Performance, Emissions, and Combustion Instability in Lean Premixed Gas Turbine Systems," Ph.D. Thesis, The Pennsylvania State University.

Mouis, A.G., Menon, A., Katta, V., Litzinger, T.A., Linevsky, M., Santoro, R.J., Zeppieri, S.P., Colket, M.B., and Roquemore, W.M., (2012) "Effects of m-xylene on aromatics and soot in laminar, N2-diluted ethylene co-flow diffusion flames from 1 to 5 atm," Combustion and Flame, 159, 3168-3178.

Mueller, M. and Pitsch, H, (2013) "Large Eddy Simulation of soot evolution in an aircraft combustor", Physics of Fluids 25, 110812.

Nagulapalli, A. (2015). Methylcyclohexane Ignition Delay Times Under a Wide Range of Conditions. Master Thesis, University of Dayton, Dayton, Ohio.

Nenniger, J., Kridiotis, A., Chomiak, J., Longwell, J., Sarofim, A., (1984) "Characterization of a toroidal well stirred reactor," Proc. of the Combust. Instit., 20, pp. 473.

National Institute for Occupational Safety and Health, (1994a) "Hydrocarbons, Aromatic, Method 1501," in NIOSH Manual of Analytical Methods (NMAM), Fourth Edition - Third Supplement., Cincinnati (OH),

National Institute for Occupational Safety and Health (1994b), "Hydrocarbons, BP 36°-216 °C, Method 1500," in NIOSH Manual of Analytical Methods (NMAM), Fourth Edition - Third Supplement., Cincinnati (OH), 1994.

Onasch, T. B., Jayne, J. T., Herndon, S. C., Mortimer, P., Worsnop, D. R. and Miake-Lye, R. C., (2006) "Chemical Properties of Aircraft Engine Exhaust Aerosols Sampled During APEX." NASA/TM-2006-214382 ARL_TR_3903: Appendix J.

Onasch, T. B., Jayne, J. T., Herndon, S., Worsnop, D. R., Miake-Lye, R. C., Mortimer, I. P., Anderson, B. E., (2009) "Chemical properties of aircraft engine particulate exhaust emissions," J. Propul. Power, 25, pp. 1121.

Python Software Foundation. (n.d.). Python 2.7. http://www.python.org.

Pope, C. A., III, Dockery, D. W., Schwartz, J., (1995) "Review of epidemiological evidence of health effects of particulate air pollution," Inhal. Toxicol., 7, pp. 1.

Ranzi, E., M. Dente, A. Goldaniga, G. Bozzano, T. Faravelli, Lumping procedures in detailed kinetic modeling of gasification, pyrolysis, partial oxidation and combustion of hydrocarbon mixtures. Prog.

Energy Combust. Sci., 27 (1), pp. 99-139 (2001). Mechanism retreived from http://creckmodeling.chem.polimi.it/kinetic.html

Reaction Design, (2011) CHEMKIN PRO, http://www.reactiondesign.com.

Ritter, E.R., Bozzelli, J.W., and Dean, A.M. (1990), "Kinetic Study on Thermal Decomposition of Chlorobenzene Diluted in H2," J.Phys.Chem., 94, 2493.

Rolon, J. C., Aguerre, F., and Candel, S., *Combust. Flame* 100:422 (1995)

Rogers, F., Arnott, P., Zielinska, B., Sagebiel, J., Kelly, K. E., Wagner, D., Lighty, J. S., Sarofim, A. F., (2005) "Real-time measurements of jet aircraft engine exhaust," J. of the Air & Waste Man. Assoc., 55, (5), pp. 583.

Roquemore, W. M. Litzinger, T. A., (2011) SERDP Final Report,WP-1577, Combustion Science to Reduce PM Emissions from Military Platforms, www.serdp.org/Program-Areas/Weapons-Systems-and-Platforms/Noise-and-Emissions/Air-Emissions/WP-1577

Saffaripour, M., Veshkini, A., Kholghy, M., and Thomson, M. J., (2014) "Experimental investigation and detailed modeling of soot aggregate formation and size distribution in laminar coflow diffusion flames of Jet A-1, a synthetic kerosene, and n-decane," Combustion and Flame, 161, 848-863.

Santoro, R. J., Semerjian, H. G., Dobbins, R. A. (1983) "Soot Particle Measurements in Diffusion Flames," Combustion and Flame, 51, pp.203-218.

Saylam, A., Ribaucour, M., Pitz, W. J., and Minetti, R. (2007). Reduction of large detailed chemical kinetic mechanisms for autoignition using joint analyses of reaction rates and sensitivities. Int. J. Chem. Kinet., 39, 181.

Saxena, S., Flora, G., Kahandawala, M., Sidhu, S., (2011) "A Shock Tube Experimental Study and Modeling of M-xylene Ignition Delay," 49th AIAA Aerospace Sciences Meeting including the New Horizons Forum and Aerospace Exposition. , Orlando FL.

Sirjean, B., Dames, E., Sheen, D. A.,You, X.-Q., Sung, C., Holley, A. T., Egolfopoulos, F. N., Wang, H., Vasu, S. S.,Davidson, D. F.,Hanson, R. K., Pitsch, H., Bowman, C. T., Kelley, A., Law, C. K., Tsang, W., Cernansky, N. P.,Miller, D. L.,Violi, A., Lindstedt, R. P., (2009) "A high-temperature chemical kinetic model of n-alkane oxidation," JetSurF version 1.0, September 15, 2009 (http://melchior.usc.edu/JetSurF/Version1_0/Index.html).

Smith, G.P., David M. Golden, Michael Frenklach, Nigel W. Moriarty, Boris Eiteneer, Mikhail Goldenberg, C. Thomas Bowman, Ronald K. Hanson, Soonho Song, William C. Gardiner, Jr., Vitali V. Lissianski, and Zhiwei Qin. Retreived from www.me.berkeley.edu/gri_mech/

Society of Automotive Engineers, "Procedure for the Calculation of Gaseous Emissions From Aircraft Turbine Engines," SAE: Warrendale, PA 2013; SAE Aerospace Recommended Practice ARP 1533B.

Spicer, C. W., Holdren, M. W., Riggin, R. M., Lyon T. F., (1994) "Chemical composition and photochemical reactivity of exhaust from aircraft turbine engines," Ann. Geophysicae 12, pp. 944-955.

Spicer, C. W., Holdren, M. W., Cowen, K. A., Joseph, D. W., Satola, J., Goodwin, B., Mayfield, H., Laskin, A., Alexander, M. L., Ortega, J. V., Newburn, M., Kagann, R., Hashmonay, R., (2009) "Rapid measurements of emissions from military aircraft turbine engines by downstream extractive sampling of aircraft on the ground," Results for C-130 and F-15 aircraft, Atmos. Environ., 43, pp. 2612.

Spicer, C. W., Holdren, M. W., Riggin, R. M., and Lyon, T. F., (1994) "Chemical Composition and Photochemical Reactivity of Exhaust from Aircraft Turbine Engines," Ann. Geophysicae, v. 12, pp. 944-955.

Spicer, C. W., Holdren, M. W., Smith, D. L., Hughes, D. P., Smith, M. D., (1992) "Chemical Composition of Exhaust from Aircraft Turbine Engines," Journal of Engineering for Gas Turbines and Power – Transactions of the ASME, v. 114, pp. 111-117.

Stouffer, S.D., Ballal, D.R., Zelina, J., Shouse, D.T., Hancock, R.D., Mongia, H.C., (2005) "Development and Combustion Performance of High Pressure WSR and TAPS Combustor", 43rd AIAA Aerosp. Sci. Meet. Exhib., AIAA-2005-1416.

Stouffer, S.D., Hendershott, T.H., Monfort, J.R. , Corporan, E., (2016) "Combustion Characteristics in a Single Cup Combustor Using Jet A and Research Fuels", Paper for Central States Section of the Combustion Institute, Knoxville, Tennessee, May 15-17, 2016.

Stouffer, S., Pawlik, R., Justinger, G., Heyne, J., Zelina, J., Ballal, D., (2007) "Combustion performance and emissions characteristics for a well-stirred reactor for low volatility hydrocarbon fuels," 43rd Joint Prop. Conf., AIAA-2007-5663.

Stouffer, S., Striebich, R.C., Frayne, C.W., Zelina, J., (2002) "Combustion Particulates Mitigation Investigation Using a Well-Stirred Reactor," 38th AIAA/ASME/SAE/ASEE Jt. Propuls. Conf. Exhib., AIAA 2002-3723.

Timko, M. T., Onasch, T. B., Northway, M. J., Jayne, J. T., Canagaratna, M. R., Herndon, S. C., Wood, E. C., Miake-Lye, R. C., Knighton, W. B., (2010) "Part II: Chemical properties of particulate matter," J. Eng. Gas Turb. Power, 132, pp. 061505-1.

Tokmakov, I.V., and Lin, M.C., (2004), "Combined Quantum Chemical/RRKM-ME Computational Study of the Phenyl + Ethylene, Vinyl + Benzene, and H + Styrene Reactions," J.Phys. Chem. A, 108:9697-9714.

Turns, Stephen R., (1996) "An Introduction to Combustion: Concepts and Applications," McGraw-Hill, New York, NY.

Vijlee, S.Z., (2014) "Effects of Fuel Composition on Combustion Stability and NOX Emissions for Traditional and Alternative Jet Fuels," PhD Dissertation, University of Washington.

Wang, H., "Chemical-kinetics models for JP-8 fuel," private communications with V. Katta, (2015).

Wang, H., Xiaoqing Y., Ameya, V., Scott, J., Davis, G., Laskin, A., Egolfopoulos, F., , Chung, K. L., (2007) "USC Mech Version II. High-Temperature Combustion Reaction Model of H_2/CO/C_1-C_4 Compounds," http://ignis.usc.edu/USC_Mech_II.htm, May 2007.

Wey, C. C. (2004) "Overview of the Aircraft Particle Emissions experiment (APEX) Program," Aircraft Particle Emissions Workshop, Cleveland, OH.

Wey, C. C., Anderson, B. E. (2006). "Aircraft Particle Emissions experiment (APEX)" NASA/TM-2006-214382 ARL-TR-3903.

Won, S.H., Jiang, B., Dievart, P., Sohn, C.H., and Ju, Y., (2015) "Self-sustaining n-heptane cool diffusion flames activated by ozone," Proceedings of the Combustion Institute, 35, 881-888.

Yasunaga, K., and Tranter, R. S. (2013). Speciation in Shock Tubes. Cleaner Combustion, F. Battin-Leclerc, J. M. Simmie, and E. Blurock, eds., Springer London, London, pp. 143–161.

Yelvington, P. E., Herndon, S. C., Wormhoudt, J. C., Jayne, J. T., Miake-Lye, R. C., Knighton, W. B., Wey, C., (2007) "Chemical speciation of hydrocarbon emissions from a commercial aircraft engine," J. Prop. Power, 23, pp. 912.

You, X., Egolfopoulos, F. N., and Wang, H. (2009). Detailed and simplified kinetic models of n-dodecane oxidation: The role of fuel cracking in paraffinic hydrocarbon combustion, Proc. Combust. Instit., 32, 403.

Zelina, J., Striebich, R., Ballal, D., (1994) “Pollutant emissions research using a well stirred reactor,” AIAA-94-3827-CP.

Zeppieri, S. and Colket, M., (2014) “Fingerprint of Hydrocarbon Emissions from Gas Turbine Exhaust at Low Power”, Combustion Science and Technology. (under final review).

Zhu, J., Irrera, A., Choi, M. Y., Mulholland, G. W., Suo-Anttila, J., Gritzo, L. A. (2004) “Measurement of light extinction constant of JP-8 soot in the visible and near-infrared spectrum,” International Journal of Heat and Mass Transfer 47, pp. 3643-3648.

Appendix A: Results from Initial Lean Blowout Experiments

A.1 Experiments with Heptane/Dodecane

Lean blowout experiments were conducted using the Heptane/Dodecane surrogate. Emissions data was obtained using an FTIR for online concentration measurements. The emissions data was acquired at a rate of 1/8 Hz. A typical lean blowout trace of equivalence ratio and temperature is shown in Figure A-1. As the equivalence ratio is gradually reduced, the temperature in the reactor and the reactor wall temperature decrease. The process is carried out at a slow rate because of the coupling between the wall temperature and the heat loss from the reactor. As the temperature in the reactor decreases, the wall temperature, in turn, decreases, which further increases the heat loss from the reactor, lowering the combustion temperature. The lean blowout limit was reached at an equivalence ratio of 0.425, resulting in a temperature of approximately 1360 K.

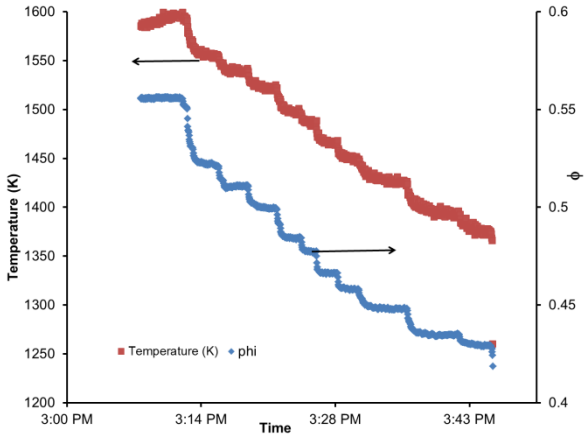

Figure A-1. Temperature and Equivalence ratio of the Reactor Operating on Heptane/Dodecane Surrogate as the Lean Blowout Limit is Approached.

Emissions data from the WSR measured by the FTIR are shown in Figure A-2 plotted against the temperature measured in the WSR. The graph on the left show the major species (CO, CO2, and H2O) and shows the drop in production of H_2O and CO_2 as temperature is decreased (equivalence ratio is decreased) along with the increase in CO as the temperature is decreased. The emissions from four other unburnt hydrocarbons CH_2O, CH_4, C_2H_2, and CH_4 are also shown in Figure A-2. The concentration of these components is seen to increase dramatically as the lean blow out limit is approached. It is planned to explore the possibility of extracting information on other species from the saved spectral content files from the FTIR.

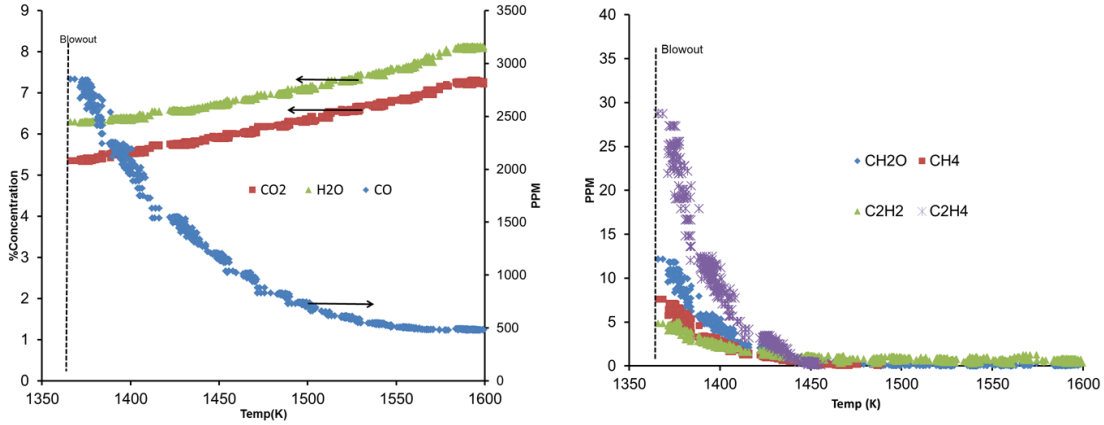

Figure A-2. Emissions from the WSR on the Approach to Lean Blowout for n-Heptane/n-Dodecane Surrogate Fuel.

A.2 Experiments with Methylcyclohexane/n-Dodecane

Lean blowout experiments were conducted for the methylcyclohexane/n-dodecane surrogate fuel. It was found that the lean blowout limit was reached at an average equivalence ratio of 0.428, resulting in a temperature of approximately 1360 K, which were close to the values measured previously for the n-heptane/n-dodecane fuel. The emissions data obtained for a typical blowout with methylcyclohexane/n-dodecane surrogate fuel is shown in Figure A-3. The shapes of the curves are all similar to those shown previously in Figure A-2 for n-heptane/n-dodecane

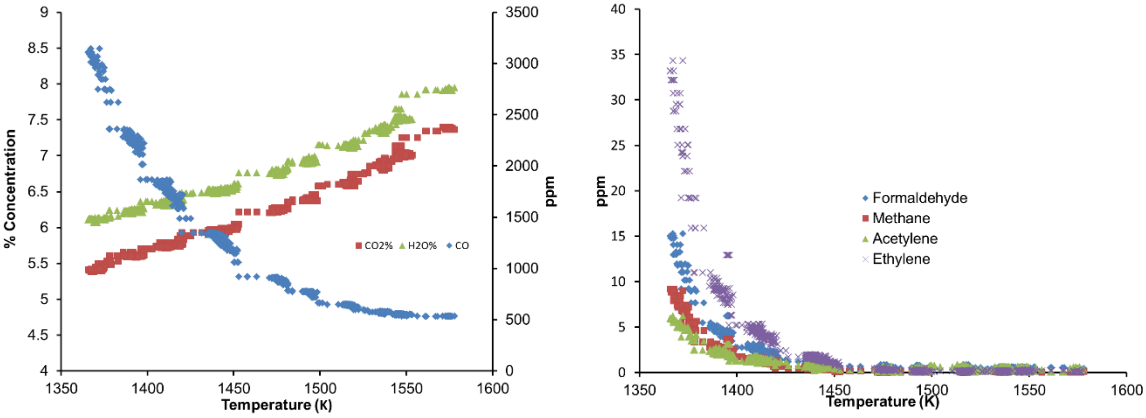

Figure A-3. Emissions from the WSR as Lean Blowout is approached for MCH/Dodecane .

Appendix B Composition of Actual Fuels included in Final Report

T63 Experiments

	Synthetic Paraffinic Kerosene (SPK)	**JP-8**
Aromatics	0.4%	16.7%
n-paraffins	0%	20.1%
iso-paraffins	96.8%	32.8%
cyclo-paraffins	2.8%	27.4%
Naphthalenes	0%	2.2%

Well-stirred Reactor Studies (Fuel-rich experiments)

	Sasol FT Fuel (SPK fuel in T-63 studies)	**JP-8**
Aromatics	0.4%	16.7%
n-paraffins	0%	20.1%
iso-paraffins	96.8%	32.8%
cyclo-paraffins	2.8%	27.4%
Naphthalenes	0%	2.2%

Co-Flow Flame Studies

	Fischer-Tropsch (FT) Fuel	**JP-8**
Aromatics	-	18.8%
n-paraffins	2%	16.5%
iso-paraffins	2%	36.5%
cyclo-paraffins	96%	26.5%
Naphthalenes	-	1.5%

PUBLICATIONS

Archival Publications

Colket, M. "Particulate Emissions," in Gas Turbine Emissions, ed. T. Lieuwen and V. Yang, Cambridge University Press, 2013.

Katta, V.R., and William M. Roquemore, C/H atom ratio in recirculation-zone-supported premixed and nonpremixed flames, Proceedings of the Combustion Institute, Vol. 34 (2013) 1101-1108.

Katta, V. R. and W. M. Roquemore, "Preferential diffusion in bluff-body stabilized turbulent premixed flames," Eleventh International Workshop on measurement and Computation of Turbulent Flames, July-26-28, 2012, Darmstadt, Germany.

Mouis, A.G., Menon, A. Katta, V. Litzinger, T.A., Linevsky, M., Santoro, R.J., Zeppieri, S.P., Colket, M.B., Roquemore, W.M., (2012) "Effects of m-xylene addition on aromatics and soot in laminar, N2-diluted ethylene co-flow diffusion flames from 1 to 5 atm", *Combustion and Flame* 159:10 3168-3178.

Viswanath Katta and William Roquemore, "Formation of a cool diffusion flame and its characteristics," Proceedings of the Combustion Institute, Vol. 36, 2016.

Conference Proceedings

Katta, V. and William Roquemore, "Numerical studies on soot formation in a dump combustor," 2016 Spring Technical Meeting of the Central States Section of the Combustion Institute, May 15-17, 2016, Knoxville, TN.

R. D. Stachler, J. S. Heyne, J. D. Miller, S. D. Stouffer, S.P. Zeppieri, M.B. Colket, and W. M. Roquemore, "Well Stirred Reactor Emission Studies of Fuel Surrogates," 2016 Spring Technical Meeting of the Central States Section of the Combustion Institute, May 15-17, 2016, Knoxville, TN.

Katta, V. and William Roquemore, "Simulation of an opposing-jet cool diffusion flame," 2016 Spring Technical Meeting of the Central States Section of the Combustion Institute, May 15-17, 2016, Knoxville, TN.

Makwana, A., Jain, A., Linevsky, M., Iyer, S., Santoro, R., Litzinger, T., Xuan, Y. & O'Connor, J. (2016). "Effects of fuel structure on soot precursors in a laminar co-flow flame" Meeting of Eastern States Section of the Combustion Institute, Princeton University, Mar. 13-16, 2016.

Katta, V. and William Roquemore, "Fuel effects on the performance of a recirculation-zone supported burner," AIAA-2016-0448, 54th AIAA Aerospace Sciences Meeting and Exposition, San Diego, Jan. 04-08, 2016.

Giacomo Flora, Jeremy P. Cain, Moshan S. P.Kahandawala, Matthew DeWitt, Edwin Corporan, Sukh S. Sidhu, "Time-dependent Speciation of Ethylene Combustion under Fuel-Rich Condition", 9th National Combustion Meeting.

Flora, G., Cain, J. P., Kahandawala, M.S.P., DeWitt, M., Corporan, E., and Sidhu, S.S., Time-dependent Speciation of Ethylene Combustion under Fuel Rich Conditions—a Novel Shock Tube Approach, submitted to the 9th U. S. National Combustion Meeting, May 17-20, 2015

Makwana, Y. Wang, M. Linevsky, S. Iyer, R. Santoro, T. Litzinger, J. O'Connor, Capturing Soot Formation with the Use of Iso-Octane as a Surrogate for Fischer-Tropsch Fuel, 9th U. S. National Combustion Meeting, May 17-20, 2015

Katta, V. R., YeFu Wang, M. Linevsky, S. Iyer, Thomas Litzinger, R. Santoro, and William Roquemore, "Modeling soot in flames with complex fuels," Proceedings of the U. S. National Meeting of the Combustion Institute, May 17-20, 2015, Cincinnati, OH.

Blunck, D., Zeppieri, S., Gross, J., Stouffer, S., and Colket, M., (2015) "Hydrocarbon Emissions from a WSR Near Lean Blow-Off", presented at the 53rd AIAA Aerospace Sciences Meeting, Jan. 5th, 2015.

Hassanaly, M., Koo, H., Raman, V., and Colket, M., (2015) "Influence of Fuel Stratification on Turbulent Flame Propagation", presented at the 53rd AIAA Aerospace Sciences Meeting, Jan. 5th, 2015.

Katta V. R. and W. M. Roquemore, "Modeling of Emissions in a Laboratory Swirl Combustor," Paper No. GT2015-43977, Proceedings of ASME Turbo Expo 2015: Turbine Technical Conference and Exposition, June 15 - 19, 2015, Montreal, Canada.

Katta, V. R., YeFu Wang, M. Linevsky, S. Iyer, Thomas Litzinger, R. Santoro, and William Roquemore, "Evaluation of Soot Models in Computing Jet Flames formed with n-Dodecane and iso-Octane," Paper No. AIAA-2015-1384, AIAA Science and Technology Forum and Exhibit, Jan 5-9, 2015, Orlando, FL

Katta, V. R., Stephen Zeppieri, Meredith Colket, William Roquemore, "Modeling Flame Propagation and Quenching in Stratified Mixtures," Paper No. AIAA-2015-1385, AIAA Science and Technology Forum and Exhibit, Jan 5-9, 2015, Orlando, FL.

Colket, M., "Challenges and Uncertainties in Use of Surrogate Fuels for Emulating Combustor Performance", presented to 52nd AIAA Aerospace Sciences Meeting, National Harbor, MD, January 13, 2014

Viswanath Katta, Stephen Zeppieri, Meredith Colket, William Roquemore, "Computation of Flame Propagation Through Stratified Fuel-Air Mixtures," 2014 Spring Technical Meeting of the Central States Section of the Combustion Institute, March 16-18, 2014, Tulsa, OK.

Viswanath Katta, YeFu Wang, Thomas Litzinger, M. Linevsky, S. Iyer, R. Santoro, and William Roquemore, "Soot in Jet Diffusion Flames Established with various Fuel Blends," 2014 Spring Technical Meeting of the Central States Section of the Combustion Institute, March 16-18, 2014, Tulsa, OK.

Wang, Yefu, Suresh Iyer, Thomas A. Litzinger, Robert Stantoro. Soot and Aromatic Species in Non-premixed and Partially-premixed Laminar Jet Flames, Eastern States Section of the Combustion Institute Fall Technical Meeting, Clemson, SC, Oct. 13-16, 2013.

Colket, M., "Use of Alternate Fuels for Aviation: Concerns of GT Industry", Presented to the 6th Annual Fuel and Combustion Research Meeting Multi-Agency Coordinating Council for Combustion Research, Washington, DC, September 23-26, 2013

Katta, V. and William Roquemore, "Preferential Diffusion in Bluff-Body Stabilized Turbulent Premixed Flames," 14th International Conference on Numerical Combustion, San Antonio, TX, April 8-10, 2013.

Katta, V. R. and Roquemore, W. M. (2012) C/H atom ratio in recirculation-zone-supported premixed and nonpremixed flames, Proceedings of the Combustion Institute, Vol. 34 (2013) 1101-1108

Katta, V. R. and Roquemore, W. M. (2013) "Vortex/Flame Interactions and Transition to Turbulence," AIAA 2013-2876, 43rd Fluid Dynamics Conference, June 24-26, 2013, San Diego, CA.

Blunck, D., Cain, J., Striebich, R., Vijlee, S., Stouffer, S., Roquemore, W., "Fuel-rich Combustion Products from a Well-Stirred Reactor Operated using Traditional and Alternative Fuels," *2012 Central States Combustion Meeting*, Dayton, OH (2012).

Colket, M., Zeppieri, S., Dai, Z., Hautman, D., "Fuel Research at UTRC", presented to the 5th Annual Fuel Research Meeting, Multi-Agency Coordinating Council for Combustion Research, Sandia National Laboratories, Livermore, CA, September 17-20, 2012.

Colket, M., Zeppieri, S., Dai, Z., Kim, W., Hautman, D., "Ignition and LBO Results in Research Combustor using Fuels with Broad Property Range", Presentation at the Fuels Properties ad Kinetics Workshop, JANNAF, Monterey, AC, December 4th, 2012. V. R. Katta, W. M. Roquemore, "Relationships among hydrocarbon species in opposing-jet nonpremixed flames formed with different fuels," Paper No. 12S-122, Spring Technical Meeting of the Central States Section of the Combustion Institute, Dayton, OH, April 22-24, 2012.

Zeppieri, S., and Colket, M., Hydrocarbon fingerprint in gas turbine emissions, Stephen Zeppieri, Meredith B. Colket

Fall Technical Meeting of the Eastern States Section of the Combustion Institute, Storrs, CT Oct 9-12, 2011

Mouis, A.G., Iyer, V.R., Linevsky, M., Litzinger, T.A., Santoro, "Effects of m-xylene, dodecane and JP - 8 addition on soot in laminar, N2-diluted ethylene co-flow diffusion flames from 1 to 5 atm," Fall Technical Meeting of the Eastern States Section of the Combustion Institute, Storrs, CT Oct 9-12, 2011

Cain, J., Blunck, D., Corporan, E., DeWitt, M., Striebich, R., Anneken, D., Klingshirn, C., Roquemore, W., "Characterization of Gaseous and Particulate Emissions from a Turboshaft Engine Burning Conventional, Alternative and Surrogate Fuels," *2012 National Meeting of the American Chemical Society*, Philadelphia, PA, (2012).

Katta, V. R. and Roquemore, W. M. (2012) Relationships among hydrocarbon species in opposing-jet nonpremixed flames formed with different fuels, Proceedings of the Spring Technical Meeting of the Central States Section of the Combustion Institute, Dayton, OH, April 22-24, 2012.

Reports

Roquemore, W. M. and Litzinger, T. A., The science of emissions from alternative Fuels, Interim Report, SERDP WP-2145, October 2012.

Roquemore, W. M. and Litzinger, T. A., The science of emissions from alternative Fuels, Interim Report 2, SERDP WP-2145, June 2014.

Papers in Review and Preparation

R. D. Stachler, J. S. Heyne, S. Zeppieri, J. D. Miller, S. D. Stouffer, M. Colket, and W. M. Roquemore, "Alternative Fuel Studies Using a Well Stirred Reactor," Energy & Fuels, 2016 (in preparation).

Makwana, A., Wang, Y., Linevsky, M., Iyer, S., Santoro, R., Litzinger, T., & O'Connor, J., "Effects of Fuel Composition on Aromatic Species and Soot in Jet Diffusion Flames", in preparation for Combustion and Flame

Wang, Y., Makwana, A., Linevsky, M., Iyer, S., Santoro, R., Litzinger, T., & O'Connor, J., "Effects of Fuel Composition on Aromatic Species and Soot in Partially-premixed Jet Flames", in preparation for Combustion and Flame

Makwana, A., Wang, Y., Linevsky, M., Iyer, S., Santoro, R., Litzinger, T., & O'Connor, J., "Effects of Fuel Volatility on Soot in Model Gas Turbine Combustor", in preparation for Journal of Propulsion and Power

Giacomo Flora, Jeremy P. Cain, Moshan S. P.Kahandawala, Sukh S. Sidhu, “Fuel structure Effects on Surrogate Alternative Jet Fuel Ignition Delay Times”, manuscript currently under internal review

Giacomo Flora, Jeremy P. Cain, Moshan S. P.Kahandawala, Sukh S. Sidhu,“Fuel structure Effects on Surrogate Alternative Jet Fuel Emission”, manuscript currently under internal review.